NASA/TM—2001-209981

Small-Scale Spatial Fluctuations in the Soft X-Ray Background

Kip D. Kuntz
NASA Goddard Space Flight Center, Greenbelt, Maryland

National Aeronautics and
Space Administration

Goddard Space Flight Center
Greenbelt, Maryland 20771

February 2001

Cover Illustration: This design was used in most (though not all) of the editions of the *Histoire de L'Academie Royale de Sciences* printed by the L'Imprimerie Royale (Paris). There exist at least two plates distinguished by the engraver's initials on the protractor (not visible in this copy). This illustration, an example of the "T" plate, is a copy of the engraving found in the 1757 edition, which is not as finely struck as other copies, but was more accessible to a scanner due to a wider than usual binding margin. The edition from which this copy was taken is in the collection of Drs. Principe and Kuntz.

Available from:

NASA Center for AeroSpace Information
7121 Standard Drive
Hanover, MD 21076-1320
Price Code: A17

National Technical Information Service
5285 Port Royal Road
Springfield, VA 22161
Price Code: A10

ABSTRACT

Title of Dissertation: SMALL-SCALE SPATIAL FLUCTUATIONS IN THE SOFT X-RAY BACKGROUND

K. D. Kuntz, Doctor of Philosophy, 2000

Dissertation Directed by: Prof. Stuart N. Vogel,
Department of Astronomy

In order to isolate the diffuse extragalactic component of the soft X-ray background, we have used a combination of *ROSAT* All-Sky Suvey and *IRAS* 100 μm data to separate the soft X-ray background into five components.

We find a *Local Hot Bubble* similar to that described by Snowden et al (1998).

We make a first calculation of the contribution by *unresolved Galactic stars* to the diffuse background.

We constrain the normalization of the *Extragalactic Power Law* (the contribution of the unresolved extragalactic point sources such as AGN, QSO's, and normal galaxies) to 9.5 ± 0.9 keV cm^{-2} s^{-1} sr^{-1} keV^{-1}, assuming a power-law index of 1.46.

We show that the remaining emission, which is some combination of Galactic halo emission and the putative diffuse extragalactic emission, must be composed of at least two components which we have characterized by thermal spectra. *The softer component* has $\log T \sim 6.08$ and a patchy distribution; thus it is most probably part of the Galactic halo. *The harder component* has $\log T \sim 6.46$ and is nearly isotropic; some portion may be due to the Galactic halo and some portion may be due to the diffuse extragalactic emission. The maximum upper limit to the strength of the emission by the diffuse extragalactic component is the total of the hard component, $\sim 7.4 \pm 1.0$ keV cm^{-2} s^{-1} sr^{-1} keV^{-1} in the $\frac{3}{4}$ keV band.

We have made the first direct measure of the fluctuations due to the diffuse extragalactic emission in the $\frac{3}{4}$ keV band. Physical arguments suggest that small angular scale ($\sim 10'$) fluctuations in the Local Hot Bubble or the Galactic halo will have very short dissipation times ($\sim 10^5$ years). Therefore, the fluctuation spectrum of the soft X-ray background should measure the distribution of the diffuse extragalactic emission. Using mosaics of deep, overlapping PSPC pointings, we find an autocorrelation function value of ~ 0.0025 for $10' < \theta < 20'$, and a value consistent with zero on larger scales. Measurement of the fluctuations with a $\delta I/I$ method produces consistent results.

SMALL-SCALE SPATIAL FLUCTUATIONS IN THE SOFT X-RAY BACKGROUND

by

K. D. Kuntz

Dissertation submitted to the Faculty of the Graduate School of the
University of Maryland, College Park in partial fulfillment
of the requirements for the degree of
Doctor of Philosophy
2000

Advisory Committee:

Prof. Stuart Vogel, Chairman
Prof. Daniel I. Fivel
Prof. Richard Mushotzky
Prof. Eve Ostriker
Dr. Steven L. Snowden
Prof. Sylvain Veilleux

PREFACE

Meae culpae

First, I apologize profusely to my readers; my style is prolix and baroque, and the dissertation is long. Second, I apologize for the format. I know that most readers expect to receive the dissertation in the official format. I have turned to the two-column, single-spaced, ten-point journal format, not only because it looks better and is easier to read, but it decimates the fewest forests. Third, I apologize for insufficient gravitas.

I would also like to apologize for a matter of notation, about which I was very careful in the earlier chapters, and quite sloppy in the later chapters. The 0.1-0.284 keV energy band is sometimes referred to as band R1L2, and sometimes as band R82. Both of these bands are the same. Band R12 is slightly different from band R82, but not sufficiently so as to make a difference for most purposes. Sometimes these bands are referred to collectively as the "$\frac{1}{4}$ keV" band, but I have tried to eliminate most of those instances. The 0.44-1.21 keV band is referred to as the R45 band, but occasionally I slip and refer to is as the "$\frac{3}{4}$ keV" band. The 1.21-2.04 keV band is sometimes called the "1.5 keV" band. Other works using the *ROSAT* PSPC usually use these same bands, but often refer to them slightly differently, For example, the 0.44-2.04 keV band often is called the 0.5-2.0 keV band. Then, of course, there are a few individuals who have created non-standard bands; in those cases I have tried to refer to them in a way that will make their relation to the standard bands apparent.

I could also apologize for the diffuse nature of the term "Soft X-ray Background", as that term sometimes means 0.1-0.5 keV, and sometimes $E < 2$ keV. However, that terminology has been mixed for a long time, so I decline to take the blame.

Some Administrative Matters

Chapter 3, together with Appendix D, is contained in Kuntz & Snowden (1998), a manual for use of the mosaicking software. At the beginning of the project it was thought that the existing mosaicking software was sufficient, but repeated tinkering led to its wholesale reconstruction, and thus the need for a new manual.

Chapter 4, on the tracers of absorption, began as an attempt to understand the absorption of X-rays by the ISM. I was led to examine a number of results in the literature, and at times the examination got out of hand; this chapter was the result. There are a number of interesting issues buried in this chapter that I hope to revisit in the future, such as curious results obtained by Arabadjis & Bregman (1999).

Chapter 5 and Chapter 6, on the TAE, are in press (set for the 1 November issue of the Astrophysical Journal) as "The Deconstruction of the Spectrum of the Soft X-ray Background". I *did* need to determine a good spectrum for the SXRB in order to do a good deabsorption (and to pursue some other topics, such as X), but the treatment here is a bit of an indulgence, though a profitable one. Appendix A and Appendix E cover related issues that were raised during seminar presentations about the TAE.

Chapter 7 (with Appendix F), on the X-ray contribution due to stars, was originally projected due to the need for a measure of the variance due to unresolved stellar X-ray sources. The question of how much of the TAE could be due to stars provided a more immediate motive. It was thought that a simple galactic model, together with the Schmitt, Fleming, & Giampapa (1995) and Schmitt (1997) data would be adequate. The Guillout et al. (1996) paper led me to believe that my problem had already been solved. However, the difference in energy bands modeled and the concentration of resolved sources rather than the unresolved sources, did not allow application of the results to my problem. Contacting the author was of little use: his proprietary software was too complex and too directed to other problems to be easily applied to mine, and the author became unavailable due to the XMM launch. So I took a month and built my own. After another round of improvements, this chapter will be submitted to the Astrophysical Journal.

Chapter 8, on deabsorption, is necessary and (almost) completely uninteresting. Clearly, the absorption of X-rays by the ISM is more complex than we would like to admit, and many of the required data do not exist. Those data will be very hard to obtain, but will have major implications for the general study of the ISM.

Chapter 10, on fluctuations, is the ostensible reason for the dissertation, as supported by an ADP grant. A number of difficulties make the results somewhat less useful than one might have hoped (as might be implied by the introductory quote). Nevertheless, the results may be a useful base for future study of a clumpy diffuse IGM. The essential results, together with bits of Chapter 8 and Chapter 2, and together with some projected work described in Chapter 11, are expected to turn into a paper over the next two years, during which I will be funded by an ADP grant to pursue this work.

This dissertation was formatted with LaTeXusing a the aastex style file as modified by M. Pound, M. Regan, and, very likely, others. The style file was further modified to better handle figure and table numbering, reduce the wasted space in references, and to include a number of other tweaks.

REFERENCES

Arabadjis, J. S., & Bregman, J. N. 1999, ApJ, 510, 806, submitted
Guillout, P., Haywood, M., Motch, C., & Robin, A. C. 1996, A&A, 316, 89
Kuntz, K. D., & Snowden, S. L. 1998, Cookbook for analysis procedures for *rosat* xrt observations of extended objects and the diffuse background, part ii: Mosaics, Technical report, NASA/GSFC
Schmitt, J. H. M. M. 1997, A&A, 318, 215
Schmitt, J. H. M. M., Fleming, T. A., & Giampapa, M. S. 1995, ApJ, 450, 392

DEDICATION

To he who made it possible,
Dr. Dr. Prof. L.M.A.F.P.

ACKNOWLEDGEMENTS

As with any work of this length, there are many individuals and institutions who have contributed to its nascence.

My greatest thanks go to *Steve Snowden*, who made the mistake of inviting me to work with him for the summer of 1994, and then was foolish enough to invite me back to work on a thesis. He has shown patience approaching infinite with my (sometimes egregious) mistakes, with my pursuit of the inconsequential, and with the all too frequent absences in which I worked to renovate either the house at 2329 North Calvert Street, or the neighborhood in which it stands.

Richard Mushotzky fronted for this project within the Laboratory for High Energy Astrophysics. I have not been the most flexible graduate student with which he has worked, I've been slow and methodical when what was really wanted was results. And even then I was off by a factor of $4\pi 10^6$.

Stuart Vogel agreed to front for this project within the Department of Astronomy. More importantly, he found a source of funding for the first several months of this project.

John Wang, before his untimely death, had agreed to be a member of my disseration committee. In the early stages he provided acute insights about the thesis process, and I had looked forward to his guidance on the fluctuation analysis. I miss his warm and witty presence even more than I miss his advice.

The remainder of my committee, *Sylvain Veilleux, Eve Ostriker,* and *James J. Kelly* displayed remarkable restraint and patience. Dr. Kelly, in particular, took the responsibility to act as the Dean's Representative at, literally, the last moment.

Keith Jahoda practiced great forebearance in providing guidance in what I suspect he (rightly) thought a fool's errand. Many times he has set aside his own work at length and at short notice to restrain my galloping misconceptions.

Robin Shelton has provided many stimulating conversations in which we attempted to determine the extent of knowledge about the halo and LHB, and how that knowledge had come to be. I am also thankful for the several collaborative projects in which she included me long before I had proved myself capable.

Rick Schafer helped me to understand some of the background for Chapter 10 during the early parts of this project, and provided many interesting discussions about propagating uncertainties through Fourier transforms.

Fran(tic) Verter introduced me to a number of new problems in the ISM, and encouraged me to further study of the X-ray method of determining X.

Eli Dwek, and *Tom Sodroski* helped me understand the ISM as seen by *IRAS*, and provided moral support when I was the organizer of the Building 2-Building 21 ISM bag-lunch series.

Peter Teuben often inquired after my progress and made a number of very useful suggestions for finding a way to analyse the ACFs.

Richard Rand provided a sounding board for some of the discussion about the halo, and its relation to those of other galaxies, in Chapter 6.

At the University of Leicester, *Bob Warwick* provided the thesis topic, who was perplexed by excess variations in his $\frac{1}{4}$ keV data, and who posed the question as to their nature. (I suppose I should also thank *Colin Barber* for *not* pursuing this course of investigation.)

At the Evangelische Studienwerk, Villigst, *Dr. Eberhard Müller* provided great hospitality during my visit to Weil der Stadt. There I spent several pleasant afternoons drafting parts of Chapter 8 while sitting under the gaze of Kepler.

My path through the sometimes labyrinthine University bureaucracy was smoothed by *Thelma Bublitz*, *Maryann Philips*, and *Ms. Zita.* Though it is tradition for graduate students to complain about University administration, the rapaciousness of the bursar's office, etc., I must acknowledge that the University administration has done much to support me, transparently, *without my request*,

such as deferring my student loans.

At Goddard, *Maybelline Burrell* and the *GSRP* office, who handled the funding of the first several months of this project, and have been helpful ever since.

Finally, I must also thank that person who set into motion the whole curious chain of events that led me not only to start a thesis, but to start one dealing with the ISM, a topic that I had learned to loathe under different masters. Without *Laura Danly*, this thesis, 2329 Calvert Street, and L.M.A.F.P. would not have happened, and I surely would not have become the person I am today, let alone be as happy as I am.

Other Acknowledgements

This research was supported in part by the NASA GSRP program through the GSFC/LHEA. This research was also supported in part by the NASA ADP program.

This research has made use of data obtained through the High Energy Astrophysics Science Archive Research Center Online Service (HEASARC), provided by the NASA/Goddard Space Flight Center.

This research has made use of data obtained through NED.

This research has made use of data obtained through SIMBAD.

This research has made use of the Schlegal, Finkbeiner, & Davis maps of the *IRAS* 100 μm emission obtained from Douglas Finkbeiner in advance of publication.

Table of Contents

List of Tables

List of Figures

Chapter 1: Introduction

Parturient montes, nascetur ridiculus mus, attamen labor quam perutilis.

-not Horace, Ars Poetica, line 168

Abstract

This chapter introduces the astrophysical problem that the dissertation was intended to address: to place limits on the existence of the "missing" baryons in the local universe in the form of warm-hot filaments of gas in the intergalactic medium. We argue that the soft X-ray band ($E < 1$ keV) is the most likely energy band in which to detect these filaments, and that the observational difficulties in this band, though grave, are surmountable.

1. Introduction

Observations have shown the baryon density at high redshift to be consistent with that predicted by big-bang nucleosynthesis models (Burles & Tytler 1998), but at low redshifts, the best accounting of stars, stellar remnants, and hot gas ($\log T > 7.0$) reveals an embarrassing deficit of baryons (Fukagita, Hogan, & Peebles 1998). The cosmological models of Cen et al. (1995) suggest that, depending upon the nature of the dark matter and the form of the universe, as much as 30% to 50% of the low-redshift baryonic matter may be in the form of warm-hot gas *filaments* in the intergalactic medium (IGM) with $5.0 < \log T < 7.0$, and should emit strongly in the *ROSAT* bandpass < 2 keV. However, some 70-80% of the X-ray background in the 0.5-2.0 keV band has been resolved into point sources (Hasinger et al. 1998). If the missing baryons are in the form of hot gas, that gas must not emit too strongly above ~ 0.75 keV, and thus must have temperatures $\sim 10^6$ K, and should show strong emission in the 0.1-0.284 keV or $\frac{1}{4}$ keV band.

Extragalactic studies are difficult at 0.1-0.5 keV band due both to the greater absorption by the Galactic ISM than at higher energies and to the addition of a number of Galactic emission components whose emission is minimal at higher energies. Nonetheless, the study of the *spatial fluctuations* in the 0.1-0.284 keV and 0.44-1.21 keV bands, especially when coupled to a similar study at higher energies, can yield valuable constraints on the distribution of the extragalactic gas that may contain the missing baryons, the distribution of the Galactic halo gas, and upon the population of point sources emitting in the 0.1-1.0 keV bands.

We proposed to study these spatial fluctuations using large (~ 10 square degree) mosaics of overlapping *ROSAT* PSPC pointings, which would provide the largest product of collecting area, field of view, and cumulative exposure for any mission of the foreseeable future. The mosaics were to be created in two different energy bands, the 0.1-0.284 keV band (also called the $\frac{1}{4}$ keV, R12, or R82 band), and the 0.44-1.21 keV band (also called the $\frac{3}{4}$ keV, or R45 band). (Due to the carbon edge, the *ROSAT* PSPC has virtually no response in the 0.284-0.44 keV band.) Cen & Ostriker (1999) estimated that some 7 keV cm^{-2} s^{-1} keV^{-1} of the soft X-ray background at 0.7 keV was due to emission from large scale filamentary structure in the intergalactic medium. Initial calculations made the detection of such filaments hopeful. On the scale of the largest point spread function in a *ROSAT* PSPC pointing, $10'$, given a modest exposure, 10 ks, the relative uncertainty in SXRB (just the root of the total number of counts) is $\sim 31(\sim 11)\times10^{-6}$ counts s^{-1} arcmin^{-2}, in the R82(R45) band mosaic which translates into $\sim 3(\sim 1)$ keV cm^{-2} s^{-1} keV^{-1} at 0.7 keV.

Of course, there are difficulties with such a calculation; any single filament will not have so large a flux, (at the time of the proposal, the emission of any single filament had not yet been predicted in print) and there would likely be many of these structures of various brightnesses along the line of sight. Thus, although one might not expect to detect any single such object, one would expect to be able to measure the power spectrum the fluctuations in the background caused by such objects.

Initial calculations showed that the uncertainty in the autocorrelation function, the standard method for measuring the power spectrum of fluctuations, would, once the information for all of the mosaics were combined be about a factor of two lower than the best yet measured in the 0.5-2.0 keV energy band (Chen et al. 1994). Once the conversion is made of their ACF from the broad 0.5-2.0 keV band to the narrower 0.44-1.21 keV band that we use, we expected to do about a factor of eight better; in reality, we have done about a factor of seven better.

Studies on large scales are essential to the detection of fluctuations for more than an increase in the detection sensitivity. If, as suggested by the cosmological models of Bryan & Norman (1998), the large scale structure has a low filling factor, then one needs a very large region of study to ensure a reasonable probability of including at least one such structure. Such a large-scale study has not been previously possible; only by searching the *ROSAT* archive for large numbers of overlapping PSPC exposures, and the application of our unique mosaicking software has this study become possible. At the time the project was begun, the actual filling factor for any of the models was poorly characterized, and remains so.

In the following section we will flesh-out the recent theoretical innovations that motivate the study of fluctuations at $\frac{1}{4}$ keV and $\frac{3}{4}$ keV and describe the difficulties of such study. In Section 3 we will describe the necessary parts of the research program and provide a chapter-by-chapter description of the following dissertation.

2. Motivation

2.1. Missing Baryons - Why To Look at the 0.1-1.2 keV Background

The baryonic density calculated from standard big-bang nucleosynthesis using measurements of the D/H ratio in Lyman limit systems is $\Omega_b h_{70}^2 = 0.0394 \pm 0.00286$ (Burles & Tytler 1998). A number of investigators have matched cosmological models to spectra of the Lyman alpha forest to find similar values of the baryonic density at $z \sim 3$ (Zhang et al. 1997; Hernquist et al. 1996). Despite the large amount of matter shown to exist in the hot ($\log T \sim 7.0$) intergalactic medium of galaxy clusters, a complete census of matter in stars and gas in galaxies, groups, and clusters in the low-redshift universe accounts for only about 1/3 of the baryon density predicted by nucleosynthesis (Fukagita, Hogan, & Peebles 1998; Cen & Ostriker 1999). Where is the remaining 2/3? If it emits, it must emit in some region of the spectrum either hidden from us, such as the extreme UV, where Galactic absorption obscures all but the brightest sources, or in some spectral region that has been poorly explored.

Hydrodynamical simulations of the universe, such as those by Cen et al. (1995), have shown that gravitational accumulations of matter lead not only to the well known and observed hot shocked gas in galaxy clusters ($T = 10^{7.0-7.8}$), but also to substantial sheets and filaments of cooler ($T = 10^{6.0-7.3}$) gas at low redshift. This cooler gas, forming large-scale structures, should dominate X-ray emission at energies below 1 keV. Ostriker & Cen (1996) have shown that a wide range of models (CDM, HDM, and *COBE* normalized models) require between 30% and 50% of the baryons in the current epoch to be in this cooler gas with $10^{5.0} < T < 10^{7.0}$. It should be noted that the *COBE* limits on intergalactic gas (Mather et al. 1994) apply only to gas with $T \sim 10^8$.

If the gas that forms the large-scale structure is hotter than $T \sim 10^{6.5}$ K, then the gas should have been detected in the *ROSAT* $\frac{3}{4}$ keV band. However, it is common knowledge that there is a distinct *lack* of diffuse emission at energies above 0.5 keV; Hasinger et al. (1998) has resolved some 80% of the X-ray background at this energy into point sources (mostly AGN). This understanding requires qualification. Hasinger et al. (1998) has resolved some 80% of the X-ray background in the 0.5-2.0 keV band; the primary uncertainty being the exact level of the SXRB. The lower portion of this band, the 0.5-1.0 keV is known to be contaminated by emission from the Galaxy, but the absolute value of that contamination can not be determined at present. All one can measure is the excess above an extrapolation of the extragalactic background whose spectral shape and emission strength is measured at higher energies ($E > 2$ keV). There may even be some contamination in the 1.0-2.0 keV band (see Chapter 6). Of that contamination, there is no currently available technique for separating the Galactic component from any putative extragalactic component. Thus, it is suggested that although Hasinger et al. (1998) have nearly completely resolved the SXRB into point sources in the 1.0-2.0 keV band, there is still "wiggle room" for a diffuse extragalactic component at $E < 1$ keV.

Measurements of the autocorrelation function in a combined 0.5-2.0 keV band at scales from $2'$ to several degrees are consistent with unresolved point sources just under a point source detection limit of 10^{-14} ergs cm^{-2} s^{-1} (Chen et al. 1994), but, the *measured* ACFs in that band are very strongly limited by noise (compared in particular with the ACF in the 1.0-2.0 band measured by Soltan & Hasinger 1994) and the claims based upon the ACF are derived by fitting a functional form to the measured ACFs.

If, however, instead of being at $T = 10^{6.5}$ K, the gas is as cool as $T = 10^{6.0}$ K, then it will be virtually undetectable in the *ROSAT* 0.44-1.21 keV band, but will dominate the *ROSAT* 0.1-0.284 band. Due to the greater observational difficulties in the 0.1-0.284 keV band than in the 0.44-1.21 band, the 0.1-0.284 band has not recieved the same attention given to higher energies. For example, the X-ray $\log N - \log S$ curve was determined only for energies greater than 0.5 keV, and fluctuation analyses are rarely performed at energies as low as 0.5 keV.

At the time this project was begun it appeared that the cosmo-hydrodynamical models made very different predictions about the distribution of gas in large-scale structures, depending sensitively upon the unknown cosmological parameters. Some models produced sparsely distributed, small, high surface brightness clumps, while others produced very densely distributed, low surface brightness filaments. Although direct comparisons of the clumping due to different models of the universe have not yet been published, one can get a good flavor of their difference by comparing the X-ray simulations in Bryan & Norman (1998) and Cen & Ostriker (1999). The spatial distribution of hot gas, and thus the fluctuations it produces in the soft X-ray background, could depend strongly on cosmological parameters, lending greater impetus to this project. More recent work by Pierre, Bryan, & Gastaud (2000) suggests that the strength of the filaments does depend upon cosmological parameters, though somewhat perhaps more weakly than previously thought, and Davé et al. (2000) states categorically that cosmological parameters have a non-negligible effect on the warm-hot IGM, but that the differences have not yet been fully explored.

In summary, cosmological hydrodynamic models suggest that there may be a large reservoir of baryons in warm-hot gas, in filaments in the IGM, and observations suggests that the gas does not reside in the hotter phases, but, if it exists, should be most apparent in the 0.1-1.0 keV band.

2.2. Observations of 0.1-1.2 keV Fluctuations

Soltan et al. (1996) measured the autocorrelation function (ACF) in the R6 band ($E \sim 0.73$-1.56 keV) as well as in the R5 band ($E \sim 0.56$-1.21 keV). The two were very different (see their Figure 2a), the R6 ACF dropping to indetectability for scales greater than $\sim 6°$, while the R5 ACF has a significant value at 6° and a slow decline to zero only at $\sim 30°$. The difference was attributed to the higher Galactic contamination in the lower energy band, and great consideration was given to using the ACF in the R5 band to remove this contamination from the R6 band. On large scales the R6 ACF appears to match well ACF's measured at higher energies (2 - 10 keV) and provides a good measurement down to $12'$. However, the dismissal of the R5 ACF as being unduly contaminated with Galactic emission may have been a bit hasty, it may, rather, have been of sign of more interesting phenomena at lower energies, such as large scale structures of 10^6 K gas.

The Leicester group, studying the UK Medium Deep Survey has been attempting to model fluctuations from R12 band ($E \sim 0.1$-0.284 keV) *ROSAT* data. Assuming that the emission of the Galactic foreground is unabsorbed, and assuming that extragalactic and Galactic halo emission is absorbed by the total H I column in a given direction, they noticed that after removing the emission due to the Local Hot Bubble (LHB) and deabsorbing the remaining extragalactic flux, that there remained greater than anticipated residuals (Barber, Warwick, & Snowden 1995; Warwick et al. 1997). These fluctuations had sizes 15′ - 30′ and amplitudes of ∼20%. These fluctuations are not related to known clusters and have too large an angular extent for their flux to be due to previously unknown clusters.

Thus, there is some evidence that there may be fluctuations in the soft X-ray background at energies for which the X-ray background has entirely resolved into point sources. However, at these energies, interpretation of X-ray images becomes much more difficult than at higher energies.

2.3. The Observational Difficulties Below 0.284 keV ...

Galactic Absorption: Measurement of fluctuations at $\frac{1}{4}$ keV is complicated by stronger Galactic absorption than at higher energies; a typical Galactic column density toward a high-Galactic-latitude field is 10^{20} cm^{-2}. This column absorbs ∼65% of the Galactic halo/extragalactic flux at $\frac{1}{4}$ keV, but only ∼5% at $\frac{3}{4}$ keV. This absorption not only reduces the signal but, due to the uncertainty in the column density, can produce spurious structure.

The Multiplicity of Emission Components: In the 0.1-0.284 keV band there are many more emission components than there are at higher energies. In the 2-10 keV energy range, the spectrum is dominated by the extragalactic power-law (EPL) which is due to the many types of unresolved extragalactic point sources (AGN, QSOs, etc.). When the extragalactic power-law spectrum, measured at energies > 1.5 keV is extrapolated into the lower energy bands, there is a clear excess that is well modeled by two thermal components with $T = 10^{6.0-6.5}$ (Chen, Fabian, & Gendreau 1997; Miyaji et al. 1998) that are loosely called "Galactic components". These components are the Local Hot Bubble (LHB, a region of $T = 10^{6.0}$ plasma surrounding the sun), and the Galactic halo, which would include any diffuse extragalactic emission. In Chapter 5 we will see that there are problems with previous decompositions of the spectrum of the SXRB. There are, in fact (see Chapter 6), an even larger number of components, but the increased number of components does not add any significant complexity.

From shadowing experiments using the disks of spiral galaxies, the extragalactic flux in this energy band is thought to be ∼30 keV cm^{-2} s^{-1} sr^{-1} keV^{-1} (Barber & Warwick 1994; Snowden & Pietsch 1995; Barber, Roberts, & Warwick 1996; Cui et al. 1996), a value that matches that expected from the extrapolation of the higher energy power law, which is thought to be due to the superposition of extragalactic point sources. However, the value is derived from a few very small areas on the sky, and although all of the determinations agree fairly well, the limited sampling cannot adequately constrain the flux in other directions, where it may be significantly higher. From the modeling of 0.1-0.284 keV *RASS* data (ignoring regions where the model is known to have difficulties) Snowden et al. (1998) found that somewhat more than half of the received 0.1-0.284 keV emission is due to the LHB. Of the remainder, one quarter to perhaps all could be extragalactic. Tighter limits on the diffuse extragalactic emission are placed in Chapter 6 and Chapter 7.

2.4. ...And Why They May Not Be So Horrible

Despite the Galactic signal being comparable to or greater than the extragalactic signal, nature has been forgiving. Fluctuations due to foreground emission (the sum of the LHB and Galactic halo emission) are likely to be small, and the fluctuations due to the Local Hot Bubble in the 0.1-0.284 keV band can be measured in mosaics made in carefully chosen parts of the Galactic plane where Galactic absorption blocks the emission not due to the LHB. Preliminary work has shown these fluctuations to be small. In the 0.44-1.21 keV band, the LHB has a very much smaller emission (Snowden, McCammon, & Verter 1993; Kuntz, Snowden, & Verter 1997), and thus does not produce a substantial 0.44-1.21 keV foreground.

The Galactic halo is also likely to be smooth on the scales of interest. The crossing time of a clump capable of producing the Warwick $\frac{1}{4}$ keV fluctuations, if they are in the Galactic halo, is a mere 10^6 years, suggesting that fluctuations on this scale are unlikely to persist unless replenished by an as yet unknown mechanism. Reasonable heating mechanisms are likely to affect only the large scales. Halo supernovae, which have fluxes comparable to that of the Galactic halo even as old remnants, would affect the 5° - 10° angular scales (Shelton 1998). Nearby galactic fountains have not been conclusively detected with either X-ray or UV absorption line surveys, and therefore should not effect the high latitude sky. Measuring fluctuations at $\frac{1}{4}$ keV may place interesting constraints on the existence of halo supernovae. Thus, although one can argue that the halo can be *expected* to be smooth, any measurement of structure in the 0.1-1.21 keV band will be of interest for understanding the Galactic halo.

3. Outline

To study the spatial fluctuations one must find the appropriate data; regions where there are many overlapping long exposures. The non-cosmic backgrounds must be removed from the individual exposures, and the exposures mosaicked together. The foreground due to the LHB must be removed, and the remaining image corrected for absorption by the Galactic ISM. The fluctuations in the resultant image can then be studied using autocorrelation or other methods.

Chapter 2 describes all of the different types of data used, from the X-ray data themselves to the H I and *IRAS* 100 μm data used in correcting for the absorption by the Galactic ISM. Also included is a discussion of the models which are used to convert count-rates to physical quantities. (This discussion is continued in Appendix A.) The second section of this chapter reviews the data selection criteria and briefly describes the selected data. Tables containing a complete list of the selected X-ray data are given in Appendix B. The third section describes the reduction of the X-ray data; the formation of images, the removal of non-cosmic backgrounds, and the correction for instrument response. Some minor reduction tools are presented in Appendix C

Chapter 3 describes the process by which individual pointings can be mosaicked together to form images covering several square degrees. The most significant problem is correcting for long-term variation in the non-cosmic backgrounds. This chapter describes the algorithm by which the relative offsets between observations can be determined. A step-by-step description of the process and the software by which it is accomplished can be found in Appendix D

Correcting the X-ray images for absorption due to the Galactic ISM, the process of "deabsorption", requires knowledge of the absorbing column and the spectrum of the radiation being absorbed. The spectrum of the absorbed radiation is not known *ab initio*, but must be determined after the absorbing column is found. The process of deabsorption is discussed in Chapter 4 through Chapter 8.

Chapter 4 describes the current state of understanding of the X-ray absorption cross-sections and abundances of the various components of the ISM. The absorption is produced by metals associated with the molecular, neutral, and ionized components of the ISM. Maps of these components do not exist at the resolution of the X-ray data. This chapter explores the extent to which, on multidegree scales, the total absorbing column is traced by *IRAS* 100 μm emission.

Chapter 5 describes the difficulties with previous measures of the spectrum of the SXRB, and the following chapter solves several of those problems. Chapter 6 describes a large-scale separation of the diffuse soft X-ray background into the foreground emission due to the Local Hot Bubble (LHB) and the background emission due to the Galactic halo and the putative diffuse extragalactic emission, a "deabsorption" of the northern Galactic hemisphere. The chapter contains a determination of the spectrum (actually the broad-band Spectral Energy Distribution or SED) of the background emission, and provides a budget for the SXRB. A short consideration of the southern Galactic hemisphere is provided in Appendix E

Chapter 7 is essential to several different chapters. This chapter calculates the contribution of unresolved Galactic stars to the diffuse X-ray background. The model that is described here is used to calculate the fluctuations due to unresolved point sources in Chapter 10. Ancillary calculations used by this chapter are found in Appendix F.

Chapter 8 considers the computational task of correcting mosaics for absorption. This chapter also considers the extent to which the *IRAS* 100 μm emission traces absorbtion on arcminute scales, and the extent to which the as-yet-unmeasured H II component will contribute to the uncertainty. This chapter displays, sometimes in excruciating detail, the mechanics of deabsorption, and the uncertainties involved. The superfluity of detail is meant to convince the reader that we really have done the deabsorption as well as possible, and minimized the spurious fluctuations that can be introduced by this process.

Chapter 9 contains pictures of the deabsorbed data in a number (surfeit?) of different manners. This chapter also includes a small amount of analysis to demonstrate the degree to which the deabsorption was successful.

Chapter 10 contains the fluctuation analysis. We consider two measures of fluctuations, the autocorrelation function and the $\delta I/I$ measure. Because the data to which we are applying these methods are very different from the usual types of data to which they are applied (our data have very strongly varying exposure, noise, and point source detection limits) we devote considerable discussion to data preparation. We also develop a new version of the $\delta I/I$ measure that is more useful than those used in the past. We then compare our ACFs to previous work. Some of the more tedious derivations, as well as a large amount of graphical output are relegated to Appendix G through Appendix I.

We find that although our ACF in the 0.44-1.21 keV band is better than any previously measured in the broader 0.44-2.04 keV band, there appears to be structure in the ACF of somewhat greater amplitude than the uncertainty which may be due to unremoved point sources and the windowing function. The modeling required to remove these features (or at least place limits upon their reality) has not yet been done. We also show that contributions to the 0.1-0.284 keV band ACF by the LHB are very small, and thus that the contributions in the 0.44-1.21 keV band will be even smaller.

Chapter 11 discusses the progress made in this dissertation towards detecting the "missing" baryons. We show that our ACFs could be improved by further modeling, but that it is not yet known what order of magnitude signal is expected from the warm-hot intergalactic medium. We suggest a number of projects that could tie this dissertation to more concrete results.

REFERENCES

Barber, C., Warwick, R. S., & Snowden, S. L. 1995, in Röntgenstrahlung from the Universe, ed. H. Zimmermann, J. Trümper, & H. Yorke, MPE Report 263, 319

Barber, C. R., Roberts, T. P., & Warwick, R. S. 1996, MNRAS, 282, 157

Barber, C. R., & Warwick, R. S. 1994, MNRAS, 267, 270

Bryan, G. L., & Norman, M. L. 1998, ApJ, 495, 80

Burles, S., & Tytler, D. 1998, ApJ, 499, 699

Cen, R., Kang, H., Ostriker, J. P., & Ryu, D. 1995, ApJ, 451, 436

Cen, R., & Ostriker, J. P. 1999, ApJ, 514, 1

Chen, L.-W., Fabian, A. C., & Gendreau, K. C. 1997, MNRAS, 285, 449

Chen, L.-W., Fabian, A. C., Warwick, R. S., Branduardi-Raymont, G., & Barber, C. R. 1994, MNRAS, 266, 846

Cui, W., Sanders, W. T., McCammon, D., Snowden, S. L., & Womble, D. S. 1996, ApJ, 468, 117

Davé, R., et al. 2000, ApJ, submitted

Fukagita, M., Hogan, C. J., & Peebles, P. J. E. 1998, ApJ, 503, 518

Hasinger, G., Burg, R., Giacconi, R., Schmidt, M., Trümper, J., & Zamorani, G. 1998, A&A, 329, 482

Hernquist, L., Katz, N., Weinberg, D. H., & Miralda-Escudé, J. 1996, ApJ, 457, L51

Kuntz, K. D., Snowden, S. L., & Verter, F. 1997, ApJ, 484, 245

Mather, J. C., et al. 1994, ApJ, 420, 439

Miyaji, T., Ishisaki, Y., Ogasaka, Y., Ueda, Y., Freyberg, M. J., Hasinger, G., & Tanaka, Y. 1998, A&A, 334, L13

Ostriker, J. P., & Cen, R. 1996, ApJ, 464, 27

Pierre, M., Bryan, G., & Gastaud, R. 2000, A&A, submitted

Shelton, R. L. 1998, ApJ, 504, 785

Snowden, S. L., Egger, R., Finkbeiner, D., Freyberg, M. J., & Plucinsky, P. P. 1998, ApJ, 493, 715

Snowden, S. L., McCammon, D., & Verter, F. 1993, ApJ, 409, L21

Snowden, S. L., & Pietsch, W. 1995, ApJ, 452, 627

Soltan, A., & Hasinger, G. 1994, A&A, 288, 77

Soltan, A. M., Hasinger, G., Egger, R., Snowden, S., & Trümper, J. 1996, A&A, 305, 17

Warwick, R., Hutchinson, I., Willingale, R., Kuntz, K., & Snowden, S. 1997, in The Local Bubble, ed. D. Breitschwerdt & M. Freyberg, 321

Zhang, Y., Anninos, P., Norman, M. L., & Meiksin, A. 1997, ApJ, 485, 496

Chapter 2: Data, its Selection and Reduction

Abstract

This chapter presents an overview of the many types of data and pseudo-data used in this analysis. The second second section describes the criteria by which PSPC mosaics were chosen for analysis, and the criteria by which pointings within those mosaics were accepted or rejected. The third section describes the reduction of individual PSPC pointings. The mosaicking of PSPC pointings is described in the following chapter.

1. Data

This section provides a description of the principal data set used, the PSPC observations, as well as the subsidiary data sets necessary for the analysis. We also describe the various "pseudo-data" sets, such as the Raymond & Smith plasma models, that are used in the analysis.

1.1. ROSAT Pointed PSPC Observations

The PSPC pointed observations cover regions with a radius of ~ 1°. The angular resolution for a given pointing varies from $\sim 15''$ on the optical axis to $\sim 10'$ at a radius of ~ 1°. At the edge of the pointing where the resolution is degrading rapidly, the field is also strongly vignetted, so each pointing is restricted to the central $53'$ radius. The PSPC response covers the energy range $0.1\ \mathrm{keV} < E < 2.04\ \mathrm{keV}$. The energy resolution is given by

$$\Delta E/E \approx 0.43\sqrt{0.93/E}. \qquad (2.1)$$

Due to the relatively poor energy resolution, the energy range is divided into seven standard broad bands, R1 through R7.

The data were retrieved from the High Energy Astrophysics Archive at the Goddard Space Flight Center. The bulk of the data retrieved used the "Revision 2" reprocessing. On average, 22% of the exposure time for a given pointing was discarded for having either overly large or unquantifiable backgrounds.

The data reduction of PSPC pointed observations is discussed in §3, while the formation of mosaics is discussed in Chapter 3.

1.2. ROSAT All-Sky Survey

The *ROSAT* All-Sky Survey (the *RASS*), was taken with the prime PSPC camera over ~ 200 days (Snowden et al. 1995; Snowden et al. 1997). Although the angular resolution of the survey was $\sim 3'$, the effective exposure for any position, ~ 600 seconds, does not provide a statistically meaningful number of photons on those scales. The latest release of the *RASS* (Snowden et al. 1997) binned the data to $12'$ pixels.

Because some sources of non-cosmic background contamination vary over long periods of time (particularly the so-called Long Term Enhancements or LTEs, see §3.3.3 below) and the *RASS* covers a much longer time-line than any single PSPC pointing, the *RASS* background contamination removal is on average superior to that for any single PSPC pointing.

The point source removal limits for the *RASS* were nearly uniform and set to the level obtainable for 90% of the survey region; 0.025 counts s^{-1} in the combined R12 band, 0.020 counts s^{-1} in the combined R45 band, and 0.020 counts s^{-1} in the combined R67 band.

1.3. ROSAT Bright Source Catalogue

The *ROSAT* Bright Source Catalogue (Voges et al. 1996) is a catalogue of the sources detected in the *RASS*. Selecting objects from the catalogue with count rates greater than the *RASS* point source detection limits will produce a (nearly-correct) list of objects removed from the *RASS*. This is useful for comparing individual PSPC pointings to the *RASS* to remove residual background contamination.

TABLE 2.1
DATA SUMMARY

Data	Resolution ($'$)	FOV ($'^2$)
RASS	12	All-Sky
PSPC	1-5	53$'$ Radius
Dwingeloo H I	30	$\delta > -37°$
Lockman H I	15	$\sim 15° \times 15°$
DIRAS	5	All-Sky

TABLE 2.2
PSPC PSF-FIELD RADIUS RELATION

PSF[a] Diameter (arcmin)	Field Radius R1L2 (arcmin)	R45	R67
2	12.7	15.7	14.7
3	20.7	21.7	20.7
4	26.7	27.2	25.7
5	32.1	31.6	30.6
6	36.6	36.6	35.1
7	41.6	41.1	39.6
8	45.6	45.1	43.6
9	49.6	49.1	47.6
10	53.6	53.1	51.6

[a] This is the diameter encircling 90% of the energy.

1.4. HI

The bulk of the H I 21 cm data used is from the Dwingeloo survey (Hartmann & Burton 1997) which has complete coverage for $\delta > -37$. The velocity sampling was 1.03 km s^{-1}. The beam size was 36′ and the beam spacing was 30′, somewhat less than fully sampled. Although the data were collected on a regular 30′ grid, the data were interpolated to points spaced $(\Delta\ell, \Delta b) = (30', 30')$. To form images in the coordinates of the X-ray mosaics requires a second interpolation, a problem that could have been avoided if the data had been released as a list of spectra on the original pointing centers.

One key advantage of the Dwingeloo survey is the sidelobe decontamination (Hartmann et al. 1996). The sidelobes were removed using a bootstrapped model of the Dwingeloo response and a self-referential algorithm first developed by Kalberla (1978). The uncertainty after the removal of the sidelobe contamination is $T_a \sim 0.084$ or $N_{HI} \sim 1.6 \times 10^{17}$

1.5. DIRBE-IRAS 100 μm Emission

We have used the de-striped *DIRBE*-corrected *IRAS* 100 μm all-sky survey as presented by Schlegel, Finkbeiner, & Davis (1998) as a surrogate tracer of the total absorbing column density. The *IRAS* data have a high resolution, $\sim$ 5′, but a poor absolute calibration, having a variable gain and offset. The *DIRBE* data, conversely, have poor resolution, 0°.7, but a precise absolute calibration. Schlegel, Finkbeiner, & Davis (1998) used Fourier analysis to de-stripe the *IRAS* 100 μm data, and used the *DIRBE* 100 μm data to correct the *IRAS* calibration.

The systematic uncertainty in the resultant data product is a vexed question, depending as it does on the removal of the zodiacal dust emission, etc.. However, the systematic uncertainty will play a very small rôle in our analysis since we will always be scaling the 100 μm emission to H I emission. Where we have needed the pixel-to-pixel uncertainty we have typically taken the variance over a region 15′ × 15′, about 3 × 3 resolution elements.

The main objective of Schlegel, Finkbeiner, & Davis (1998) was to derive a measure of the total dust column from the 100 μm emission. The 100 μm dust emissivity depends upon the dust temperature. They used the *DIRBE* 240 μm/100 μm ratio to derive the dust temperature. From the dust temperature they then calculated a correction factor X, that, when applied to the 100 μm flux, produces the total dust column density. At high Galactic latitudes dust emission is small, so the uncertainties in the derived dust temperature are large, even when the *DIRBE* data are smoothed.

The efficacy of using the 100 μm emission to trace the total absorbing column and the value of the X correction factor for dust temperature are discussed in a general way in Chapter 4, and are discussed for small fields in Chapter 8.

1.6. Abell Cluster Catalogue

The Abell cluster catalogue used in Chapter 9 to remove known clusters from the mosaics was that of Abell, Corwin, & Olowin (1989) (readily available through the HEASARC) with subsequent corrections.

1.7. Pseudo-Data

Pseudo-data are those large collections of model calculations whose results are often so taken-for-granted that one forgets that they are subject to uncertainty. The model calculations used are not unique but are those commonly used by X-ray astronomers, and were readily available for use.

1.7.1. Thermal Models of X-ray Emission

The connection between band ratios and the physical state of the emitting plasma is made through model spectra. Due to their ready availability, we have chosen to use the 1991 release of the Raymond & Smith (1977) equilibrium model spectra. The applicability of equilibrium models to astronomical diffuse X-ray emission is debatable. However, except in Appendix A, where the problem is discussed more fully, the spectrum models provide no more than a low-resolution spectral shape for use in deabsorption. The equilibrium model spectra provide a convenient set of "basis-vectors" for describing the broadband emission.

1.7.2. Absorption Cross-sections

We have used the Bałucinska-Church & McCammon (1992) cross-sections for all elements save He, for which we have used the cross-section from Yan, Sadeghpour, & Dalgarno (1998). The Bałucinska-Church & McCammon (1992) cross-sections are, save for He, the same used in Morrison & McCammon (1983). The Bałucinska-Church & McCammon (1992) He cross-section is very different from other determinations of the He cross-section. Following Arabadjis & Bregman (1999), we have chosen to use a He cross-section that is more similar to others in the literature.

The elemental cross-sections are, of course, not valid for the same elements when in molecular form. For this reason, among others, we avoid regions with molecular gas for the bulk of the analysis. The elemental cross-sections are also not valid for ionized gas. The few cross-sections quoted for ionized gas may be out of date and should be reconsidered before the controversies mentioned in Chapter 4 can be resolved.

2. Data Selection

The data selection criteria set forth here are those that were applied when the project was started. Little change could be applied to the criteria for the high-*b* mosaics. However, the LHB mosaic criteria could be improved, and there are several other potential mosaics that may be analysed in the future.

2.1. High-*b* Mosaic Criteria

Figure 2.1 shows the positions of individual PSPC pointings over high Galactic latitudes. There are a number of regions containing large aggregates of overlapping (or nearly overlapping) pointings which are potential mosaics. For the study of background fluctuations we have chosen those aggregates that meet the following criteria. 1.) The region must contain a large number of deep exposures and cover a significant area, $\gtrsim$ 10 square degrees. 2.) The region must not contain large angular extent clusters of galaxies, (i.e., avoid the Coma and Virgo clusters). 3.) The region must not contain large angular extent X-ray features due to the Galaxy (i.e., Loop I). 4.) The region must not contain strong high or intermediate velocity clouds. Since the surrogate tracer, the *IRAS* 100 μm emission, is known not to trace high and intermediate velocity clouds, we have excluded these regions where we have no adequate tracer of the total absorbing column. 5.) The region must not contain any molecular gas, as the conversion to total absorbing column density is uncertain in such regions. This condition was considered to be met if the H I column was less than 3×10^{20} cm^{-2}, or, equivalently, if the *IRAS* 100 μm emission was generally $\lesssim 2.5$ MJy sr^{-1}. Small areas within a mosaic containing suspected molecular gas could be removed later.

The regions meeting these criteria are marked in Figure 2.1, are shown in Figure 2.2 with respect to the $\frac{1}{4}$ keV background, and are listed in Table 2.3. Figure 2.3 shows the regions with respect to the *IRAS* 100 μm emission, which can be considered equivalent to the amount of X-ray absorption, while Figure 2.5 shows the distribution of the strength of the *IRAS* 100 μm emission. The distribution of the exposure times within each mosaic is also shown in Figure 2.5. Figure 2.4 shows the velocity distribution of the H I within the fields. These figures demonstrate that all of the criteria are reasonably well met for the seven chosen mosaics.

2.1.1. LHB Mosaic Criteria

Mosaics for the study of the variation of the Local Hot Bubble were chosen with the following criteria. 1.) The region must not contain bright extended sources at any X-ray energy. Because the R2 band has a small amount of response at energies greater than the Carbon edge (0.284 keV), hard sources, even if not readily visible to the eye in the R1 and R2 band maps, may cause considerable contamination. 2.) The region must contain a sufficient column density of H I to block most of the $\frac{1}{4}$ keV band emission originating from beyond the Local Hot Bubble.

Figure 2.6 shows the positions of PSPC pointings in the Galactic plane with reference to the Galactic column density as measured by the *IRAS* 100 μm emission. Of course, with this measure of the column density, there is no way of determining whether the absorbing column is immediately outside the LHB, or whether the

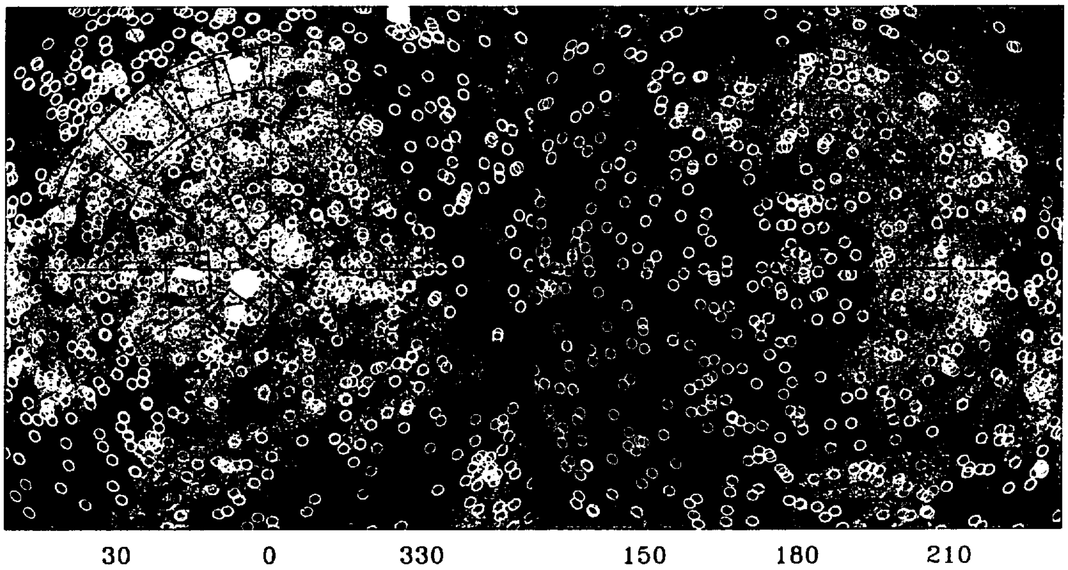

Fig. 2.1.— Maps of the PSPC pointings at high Galactic latitude. The grey-scale is the $\frac{1}{4}$ keV X-ray background. Quadrangles mark the locations of mosaics. Longitudes are marked every 30°, latitudes every 15°. *Left:* The north Galactic pole. *Right:* The south Galactic pole.

TABLE 2.3

FIELDS

Moniker	Field	R.A. deg.	Dec. deg.	ℓ deg.	b deg.	Area[a] sq. deg.	<Exposure> ks
NGPD	035+78	206.3343	26.9168	35.00	78.00	13.8(10.9)	15.5
NGPE	086+74	205.2314	39.3763	86.00	74.00	10.7(8.84)	25.1
LockA	138+52	171.8789	62.5172	138.50	52.00	29.2(25.1)	8.3
LockB	161+51	153.4315	52.5778	161.00	51.25	29.4(23.7)	7.9
NGPF	171+50	149.0283	46.8985	171.00	50.50	21.1(19.5)	7.4
NGPA	220+84	186.0158	26.1826	220.50	84.00	28.8(26.3)	9.2
SGPA	295-89	13.0158	-28.1186	295.00	-89.00	14.3(12.1)	13.7
Hyades	178-22	66.0426	17.2034	178.50	-22.00		
Plane	045+00	288.4274	10.7237	45.00	00.00	22.6(21.4)	3.2

[a] Unmasked area(masked area)

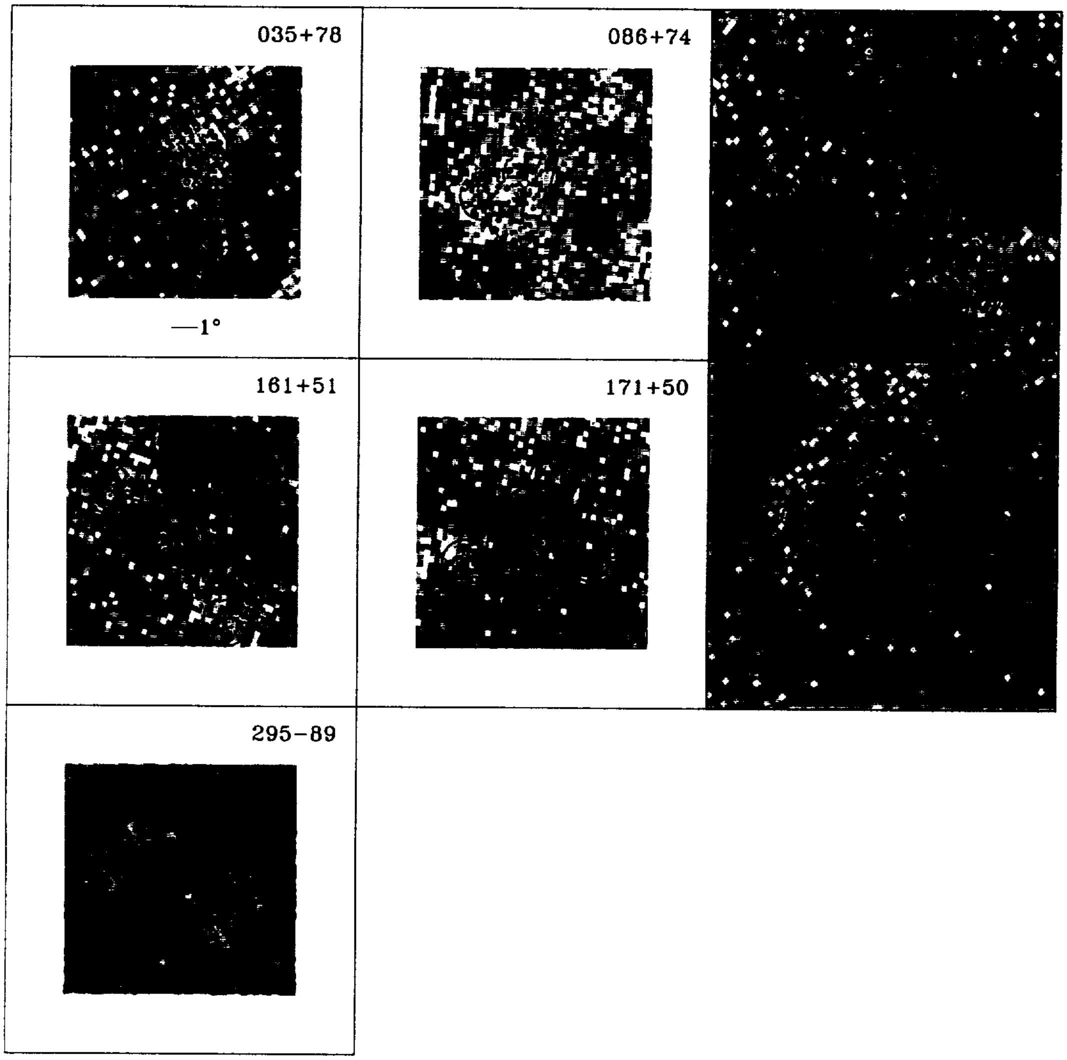

Fig. 2.2.— The $\frac{1}{4}$ keV emission for each mosaic region. The dark lines show the mosaic regions after source exclusion. The scale bar is given at the bottom of the first panel.

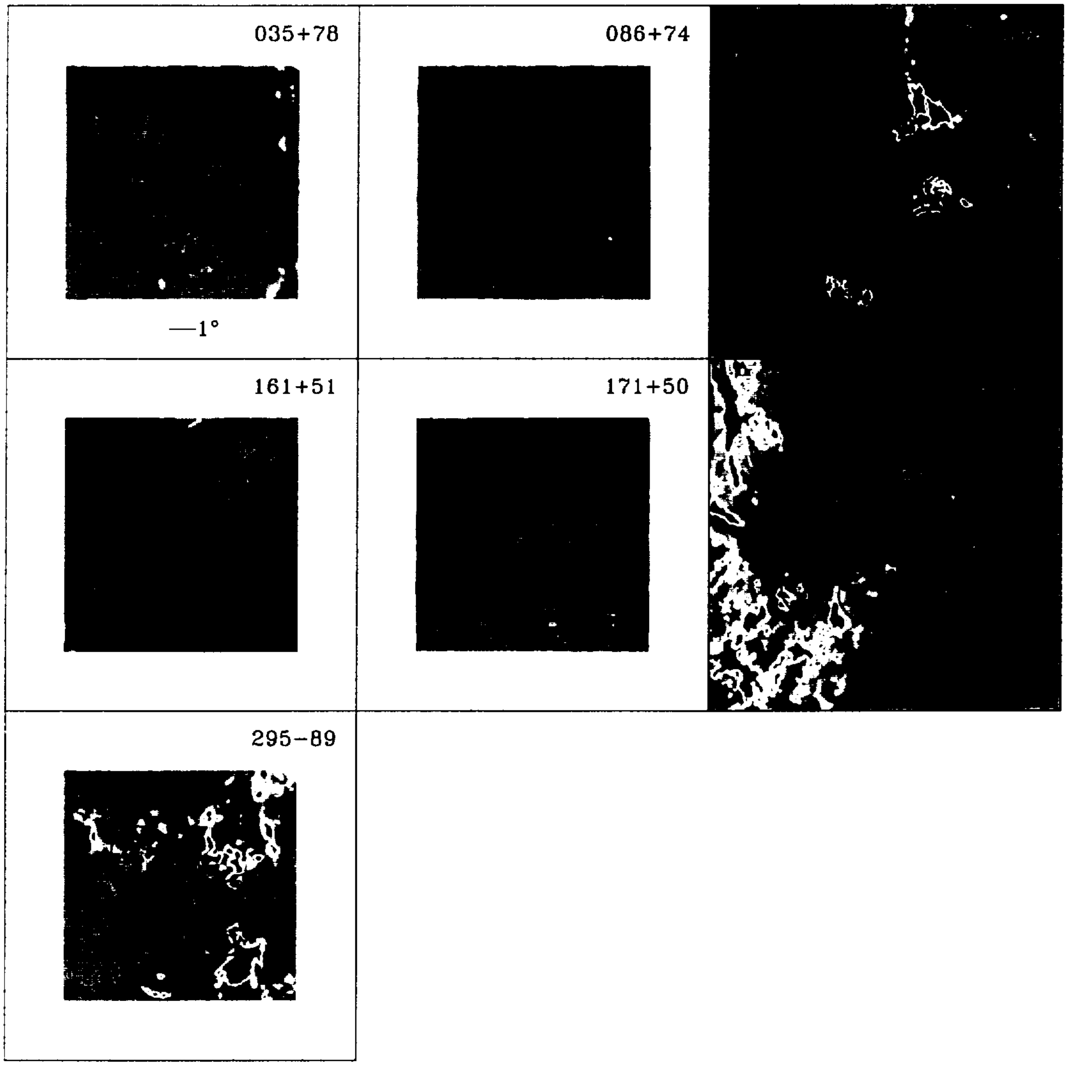

Fig. 2.3.— The *IRAS* 100 μm emission for each mosaic region. The dark lines show the mosaic regions after source exclusion. The scale bar is given at the bottom of the first panel.

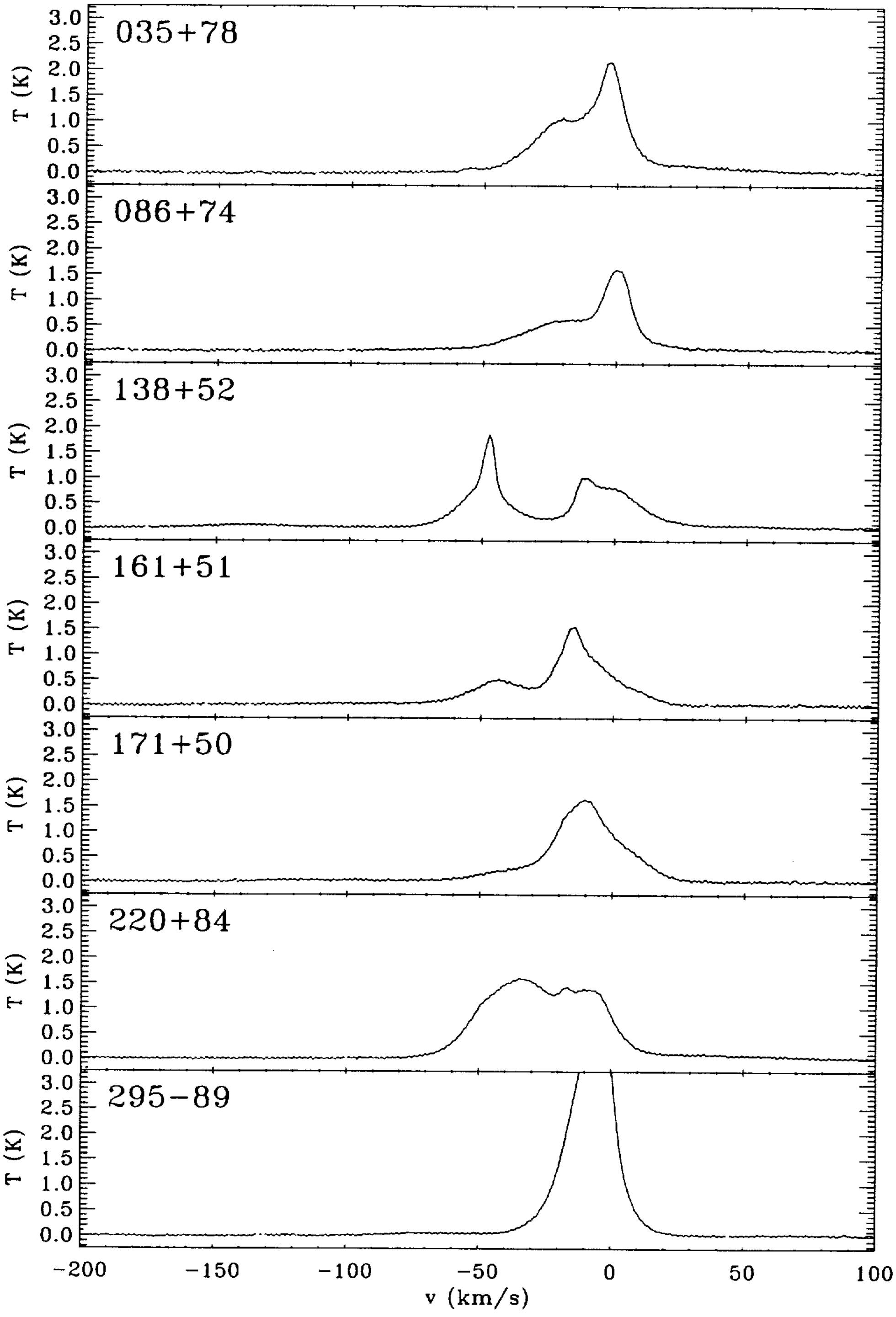

Fig. 2.4.— The H I spectrum in the direction of each mosaic. The light line is the spectrum scaled by a factor of 10.

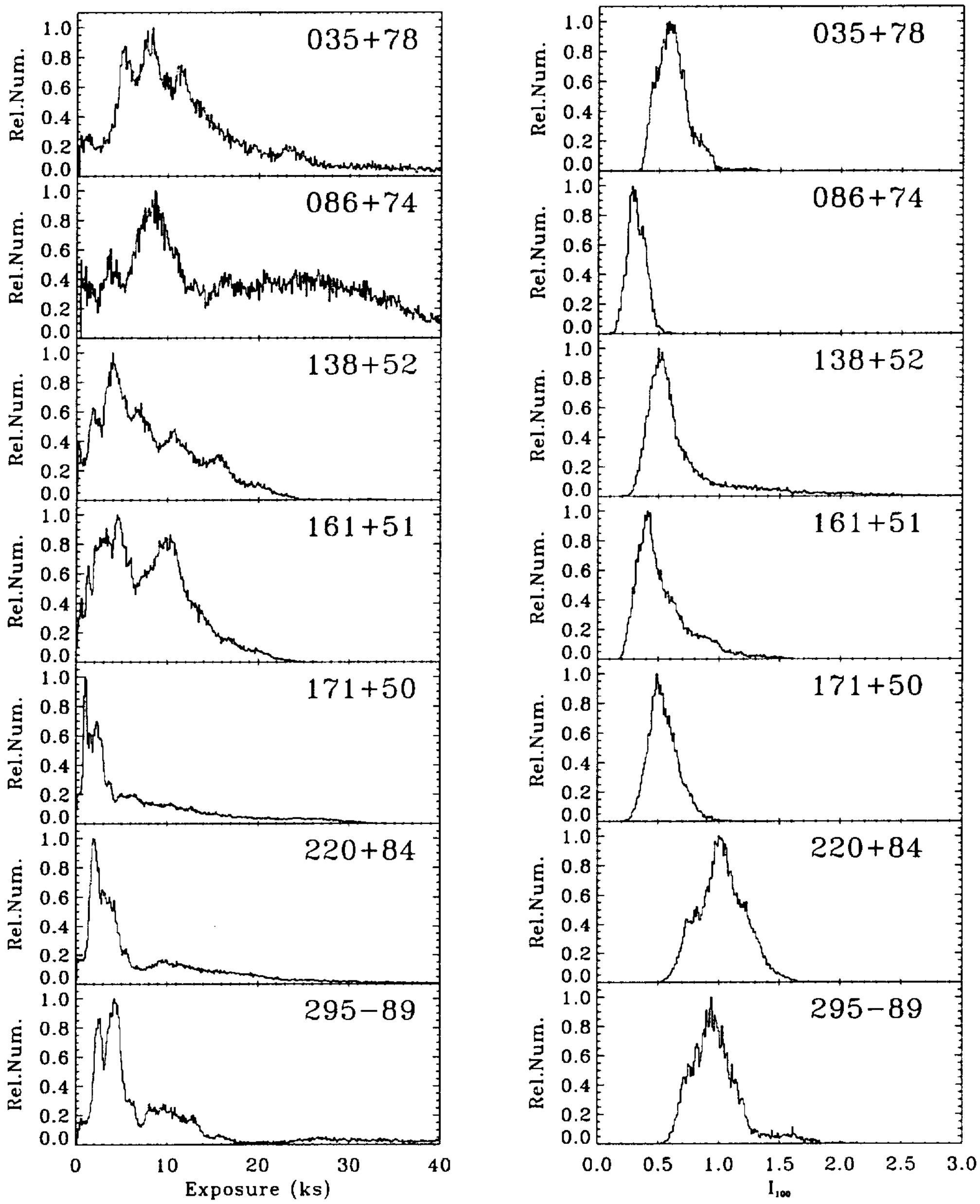

Fig. 2.5.— The distribution of exposure (*left*) and *IRAS* 100 μm emission (*right*) within each mosaic.

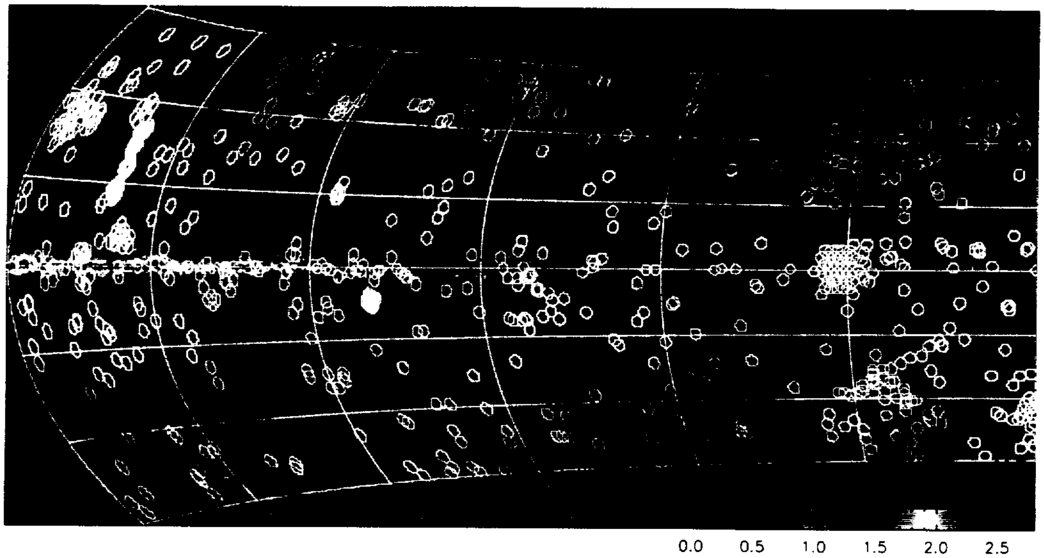

Fig. 2.6.— Map of PSPC pointings in the Galactic disk. The greyscale is the logarithm of the $\frac{1}{4}$ keV optical depth calculated from the *IRAS* 100 μm emission. $\ell = 180°$ is to the right, $\ell = 360°$ is to the left.

column density is distributed along the entire line of sight. However, there are only two large potential mosaics; one in the direction of the Hyades cluster $(\ell, b) = (181°, -22°)$, and one towards a rather anonymous region at $(\ell, b) = (45°, 0°)$. The absorption in the direction of the Hyades is predominately due to the Taurus-Auriga molecular clouds that are just external to the LHB. The absorption in the direction of $\ell = 45°$ is less understood, but the maps of Sfeir et al. (1999) suggest a significant amount of absorption near the LHB boundary.

Although the Hyades mosaic was reduced and analysed (Kuntz, Snowden, & Warwick 1998) it was not included in the dissertation; the large point source population is particularly difficult to model, so fluctuation measurements using this field would be very uncertain.

2.2. Pointing Criteria

Not all pointings overlapping a mosaic of other pointings were used. Typically, pointings with less than 3 ks were removed, as were other pointings for which the background removal was uncertain. Short exposures ($\sim$ 3 ks) were sometimes included if they had significant ($\gtrsim$ 75%) overlap, in which case the region that did not overlap any other pointing was masked out. Regions with less than 0.01 the mean exposure, typically the unoverlapped edges of lower exposures and regions near point sources that had been removed, were masked out. A complete list of the pointings used in each mosaic can be found in Appendix A.

We were able to use a larger number of pointings than originally expected; the original mosaicking software required all of the pointings to have a substantial overlap with at least one other pointing. The version of the mosaicking software developed by Kuntz & Snowden (1998) allowed pointings with little (or no) overlap to be included as well.

3. Data Reduction

This section provides an overview of *ROSAT* PSPC data reduction. The purpose of data reduction is to remove the non-cosmic backgrounds and to correct for the temporal and spatial variation in the detector efficiency. These topics have been discussed elsewhere at length; this chapter provides a summary of previous work keyed to the appropriate sources. Since we are primarily interested in the diffuse background, the detection and removal of point sources are also included under the rubric of data reduction. The first sub-section discusses the instrument, §1.3.2 discusses the "flat-field" correction, §1.3.3 describes the non-cosmic back-

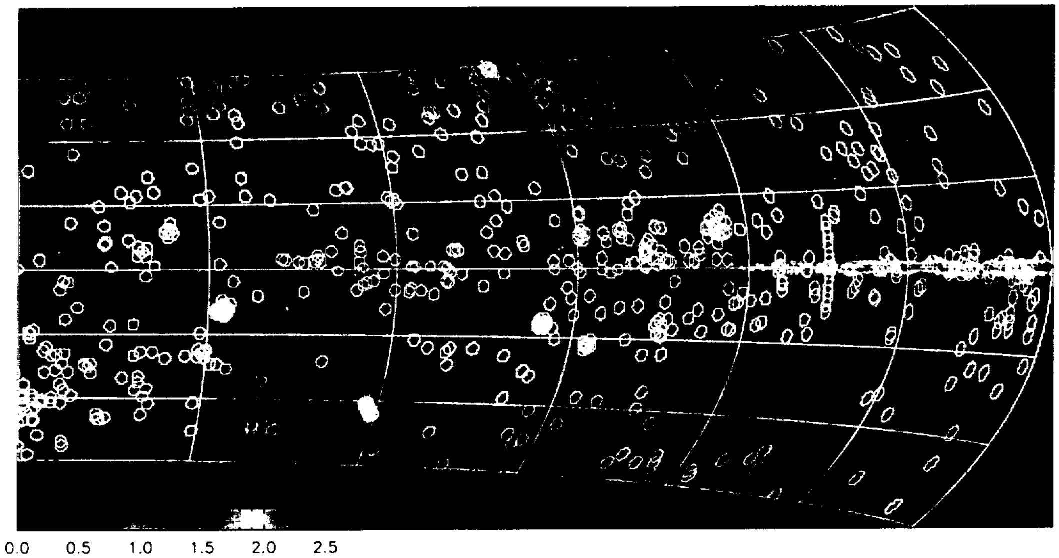

Fig. 2.7.— Map of PSPC pointings in the Galactic disk. The greyscale is the logarithm of the $\frac{1}{4}$ keV optical depth calculated from the *IRAS* 100 μm emission. $\ell = 180°$ is to the left, $\ell = 0°$ is to the right.

grounds and their measurement, §1.3.4 describes the point source removal algorithm, and §1.3.5 describes the output data products.

3.1. The Instrument

The *ROSAT* satellite carried a pair of Position Sensitive Proportional Counters (PSPC). The first, PSPC C, was used for the *ROSAT* All-Sky Survey and a few pointed observations before 25 January 1991, when, due to loss of attitude control, the spacecraft tumbled and scanned the detector over the sun. The second, PSPC B, was nearly identical to the first, and was used from January 1991 to the end of the *ROSAT* mission, when the detector's gas was depleted. All of the PSPC pointed observations used here were taken with PSPC B.

PSPC B was operated in two different gain states. Before 11 October 1991 it was operated at the same gain as PSPC C. After that date the gain was reduced by ~ 30% to eliminate a "warm spot" (low-level leakage events) that appeared as the detector degraded.

For each detected photon, the instrument produced a time, an (x, y) detector position, and an 8-bit pulse height that is photon-energy dependent. The Standard Analysis Software System (SASS) (Gruber 1992; Voges et al. 1992) corrected the pulse height for temporal and spatial variation in the gain to produce a pulse-height invariant (PI) channel that is independent of the gain state of the detector. The SASS also coverts the detector coordinates to sky coordinates.

The full 0.1-2.4 keV energy range of the PSPC is covered by the 256 PI channels. However, the energy resolution is much lower than the PI channel spacing,

$$\frac{\Delta E}{E} \approx 0.43\sqrt{\frac{0.93}{E}}, \qquad (2.2)$$

so that the $\Delta E/E$ at 0.1 keV is ~ 1.3 and the $\Delta E/E$ at 1.0 keV is ~ 0.41. Given the low energy resolution, and that the count rate for the diffuse cosmic background in any given PI channel is small, for studies of the diffuse background the PSPC energy range is broken into six standard bands, R1 through R7, excluding R3[1]. The PI channels and approximate energy range for each band are given in Table 2.4, and the band response functions are shown in Figure 2.8. Although the energy coverage of the bands is often redundant (i.e., the R1 and R2 bands cover much of the same energy range) the

---

[1] The R3 band exists, but it has a small response on either side of the carbon absorption edge. It served primarily as a gap to more distinctly separate the $\frac{1}{4}$ keV and the $\frac{3}{4}$ keV data.

bands have been formed from different PI channel ranges and thus are *statistically independent.* Given the statistical independence and the difference in energy centroids, even the R1 and R2 bands can be used to form a hardness ratio, or an X-ray "color", that is capable of distinguishing, for example, between different thermal models. (For an extensive set of band ratios as a function of emission model temperature and absorbing column density see Snowden et al. (1997).)

In the low gain mode, the R1L band (sometimes also called the R8 band) must be substituted for the R1 band. In the high gain state, channels 7 and below are set to zero by the pulse hight discriminator; in the low gain state, channels 10 and below contain no usable data.

3.2. Detector Efficiency

Map Formation: (See Snowden et al. (1994), §§3.1, 3.2) The X-ray equivalent of the "flat-field" is the detector efficiency map. The detector efficiency maps for PSPC B data were made differently for the R1 and R2 bands than they were for the R4-R7 bands. The R1 and R2 band detector efficiency maps were created from the $\sim$ 11 days of scanning mode data taken with the PSPC B to finish the *ROSAT* All-Sky Survey (RASS). Point sources, bright extended objects, and periods with high non-cosmic background were removed from the data, and all the remaining photon detections were mapped in detector coordinates. From this image was subtracted the modelled particle background and the after-pulse background[2]. The remainder is the detector efficiency map.

Since the cosmic background in the hard bands is approximately a factor of five lower than in the soft bands, the statistics do not allow the employ of the same method for the R4-R7 band maps. Instead, the detector efficiency maps were created from the $\sim$ 180 days of scanning mode data accumulated with the PSPC C. The PSPC C detector efficiency map was then shifted and normalized to the data accumulated with the PSPC B.

Use: (See Snowden et al. (1994), §§3.1, 3.3) Over the course of an exposure, which may be divided into seperate segments spread over days if not weeks, the roll angle of the detector on the sky will change. There is also a 400 second period "wobble" intended to reduce obscuration by the window support structure. To create an effective exposure map in sky coordinates, one divides an exposure into short observation intervals (typically $\sim$ 1 second long) and for each interval shifts, rotates and sums an appropriately scaled copy of the detector efficiency map.

3.3. The Non-Cosmic Backgrounds

There are five different non-cosmic backgrounds that must be removed; the particle background (PB), the after-pulse contamination (AP), short-term enhancements (STE), long-term enhancements (LTE), and scattered solar X-rays (SSX). For each, one must know the spectrum, the spatial distribution, and the strength of the background in order to effect the background subtraction. The particle background and the after-pulse contamination can be separated easily from the other backgrounds and are described individually. The STE, LTE, and SSX backgrounds all enter through the detector window; their detection and measurement is executed simultaneously, and their spatial distributions are all derived from the exposure map, so they will discussed together. The spatial and spectral distribution of the STE cannot be determined *ab initio*, so periods containing STEs are merely removed.

For each of the backgrounds there is a map of the spatial distribution of that background over the detector. The method of generating these maps is described below; except for the SSX background, these maps are temporally invariant and were produced by the *ROSAT* calibration team. Each of the maps is normalized so that the integral over the detector is unity, representing the probability of a single event as a function of location; the map need only be multiplied by the number of events to create (in detector coordinates) a map of the background.

3.3.1. The Particle Background

The particle background is discussed extensively in Snowden et al. (1992) and Plucinsky

---

[2] No other non-cosmic backgrounds need be subtracted as, with the exception of the after-pulse background, all the others will be vignetted in the same manner as the cosmic photons.

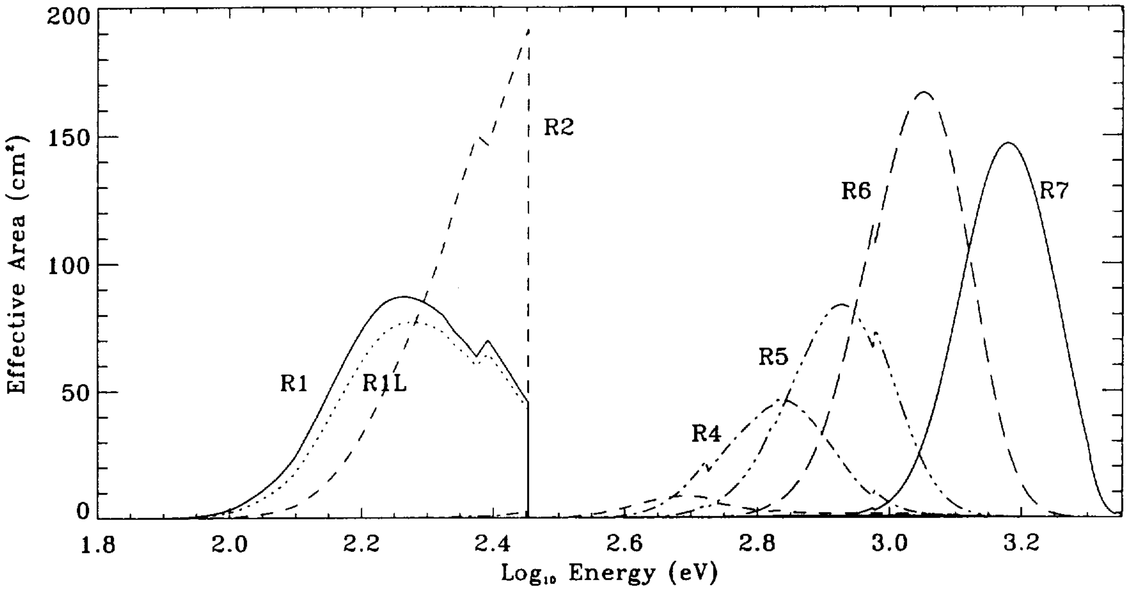

Fig. 2.8.— The broad energy bands.

TABLE 2.4

BROAD BAND DEFINITIONS

Band	PI Channel	Energy[a] (keV)
R1	8-19	0.11-0.284
R1L=R8	11-19	0.11-0.284
R2	20-41	0.14-0.284
R3	42-51	0.20-0.83
R4	52-69	0.44-1.01
R5	70-90	0.56-1.21
R6	91-131	0.73-1.56
R7	132-201	1.05-2.04

[a] 10% of peak response.

et al. (1993) as well as Snowden et al. (1994), §4.1. Some 99.83% of the particle background events are rejected by the five-sided vetoing and logic discrimination of the instrument, and so are not included in the data. Still, given the high incidence rate, the particle background remains significant, especially at higher energies where the X-ray rate decreases as $E^{-\alpha}$, where $1.4 < \alpha < 2.0$. Typically the particle background provides 10% of the counts in the R7 band.

There are two different particle backgrounds that must be measured. The *internal* particle background is observed when the detector is in (or out) of the focal plane and the filter wheel is closed. The internal background is composed primarily of energetic charged particles. The *external* particle background is most clearly observed when either the detector is out of the focal plane and the filter wheel is open or the detector is in the focal plane, the filter wheel is open, and the instrument is pointed at the unilluminated earth. In neither of these cases is the external particle background observed independently from the internal particle background. The external background is composed of particle induced Al Kα X-rays, and a component that is thought to be electrons with energies of a few keV.

The clearest evidence for the external background is obtained when the detector is out of the focal plane but the filter wheel is open. The detector itself is square, but is masked by the window mounting plate to a circular opening. When the filter wheel is closed, the rates in the corners of the detector, under the mask, are similar to the values in the center of the detector. When the filter wheel is opened, the count rate in the corners does not increase, though the rate in the unmasked region of the detector does. The Al Kα component is only detected where the detector is unmasked. Further, the external background bears the faint imprint of the shadow of the window support structure.

There is no concrete way of knowing whether the external background increases or decreases when the detector is moved into the focal plane, but the brief observation of the unilluminated earth (178 s, immediately before the detector was pointed at the sun) suggests that the external background does not increase significantly.

Measurement: The Master Veto Rate (MV) is the rate at which the instrument rejects particle background events using five-sided vetoing and logic selection. The mean MV rate is a function of the geocentric position of the satellite; below a threshold MV rate of about 220 counts s^{-1}, the MV rate as a function of geocentric position is relatively constant. MV rates over this threshold (which occur less than about one percent of the time) are very erratic and typically occur in proximity to the particle belts or the South Atlantic Anomaly.

Both the internal and the external particle backgrounds are well correlated with the MV rate for MV rates below about 220 counts s^{-1}. Thus, the total particle background for any observation can be determined from the MV rate so long as the MV rate is below the threshold.

Spatial distribution: The spatial distribution of the external particle background was measured while the detector was out of the focal plane and the filter wheel was closed. The only spatial variation within the "accepted" detector region[3] is a slight increase with distance from the detector center. The external particle background map used for data reduction is a constant with the slight radial dependence.

The spatial distribution of the internal particle background was measured while the detector was out of the focal plane and the shutter was open. To within the uncertainties, the spatial variation was limited to the shadow of the window support structure. The external particle background map used for data reduction is a de-vignetted detector map, which imitates a constant background shadowed by the window support structure.

Spectrum: The spectrum of the internal particle background is

$$S_P(PI) = a_1(PI + 0.5)^{-a_2} + a_3 \qquad (2.3)$$

where PI is the pulse-height invariant channel. The external particle background has the same form, with the addition of the Al Kα line. There is no detectable MV dependence of a_2, while the MV dependence of a_1 and a_3 depends upon the epoch of the data.

---

[3] The accepted detector region is that area which is not masked and excludes regions near the edge of the physical detector where the vetoing is inefficient due to the variable electric field near the attachment points of the high-voltage anodes.

3.3.2. The After-Pulse Contamination

The after-pulse (AP) contamination is discussed by Plucinsky et al. (1993), §§1, 3.1, 3.3.2, and 3.4. The after-pulse contamination was first observed as an increase in the count rates of the lowest PI channels. The events that produced this increase occurred within 0.35 ms and within a few arcminutes of a previous event. These events are thought to have been due to negative ion formation in the counter gas.

The AP contamination is reduced by accepting only those events which occur more than 0.35 ms after a previous event. Since many of the events that produce the AP counts are particle background events that are rejected by the vetoing (and thus not recorded as events), rejecting all events that occur less than 0.35 ms after a previous event will not remove all of the AP counts. The remaining AP contamination can contribute $\sim$ 15% of R1 band counts, and thus is a significant background. The AP contamination is time-variable and need not be correlated with the MV rate

Spectrum: Although the spectrum of the AP contamination is given by

$$P_{AP}(PI) = e_1 e^{\frac{-e_2[PI+0.5]}{e_3}} \left[\frac{PI+0.5}{e_3}\right] \qquad (2.4)$$

where PI is the pulse-height invariant channel, e_1, e_2, and e_3 can rarely be determined from the data. The AP spectrum is generally modeled in a more empirical manner.

Measurement: The AP contamination is determined in the following manner. A PI channel spectrum is formed from all events occurring greater than 0.35 ms after a previous event. This is taken as a first order approximation of the true spectrum. A PI channel spectrum is formed from all events occurring less than 0.35 ms after a previous event. This "AP" spectrum will contain predominately AP events, but will also contain photon events and particle background events. If CR is the total count rate from our first our "true" spectrum, then the exposure represented by the AP spectrum will be

$$CR * (0.35 - 0.25)/1000s \qquad (2.5)$$

since no events are recorded in the 0.25 ms after a previous event. To first order, one can remove the photon and PB events from the AP spectrum by subtracting from it the "true" spectrum scaled to the exposure time of the AP spectrum.

To determine the number of AP counts, N_{AP}, one fits the "true" spectrum by

$$N_{AP}AP + N_T RS(T) + SSX + PB \qquad (2.6)$$

where AP is the corrected AP spectrum derived above, N_T is the normalization of a Raymond & Smith thermal spectrum, $RS(T)$, folded through the detector response, SSX is the measured scattered solar X-ray background, and PB is the measured particle background. The thermal spectrum models a combination of the cosmic background and the LTE. The temperature of the model is varied to provide the best fit.

Spatial distribution: The spatial distribution of the AP contamination was determined from data taken during the All-Sky Survey completion as well as several long pointed exposures with high AP rates.

3.3.3. The SXX, STE, and LTE Backgrounds

3.3.3.1. Descriptions *SSX:* Solar X-rays are scattered off of the earth's atmosphere along the observation line of sight. The reduction software uses a standard model atmosphere evaluated for the observation time and position and an empirical two-component solar X-ray spectrum to model Thompson scattering and fluorescent scattering by the principal species (Snowden & Freyberg 1993).

STE: A short-term enhancement is a period of increased background with time scales from several minutes to a few hours, though STE's of the longer periods are unusual. The enhancements are typically soft, affecting the $\frac{1}{4}$ keV bands more than the $\frac{3}{4}$ keV bands. There are several suggested origins for the STE's: aurorae, solar flares momentarily increasing the SSX, and enhanced charged-particle precipitation during periods of increased geomagnetic field activity. Given the difficulty of determining the true origin of any single STE, data segments that are contaminated are simply removed; there is no *a priori* means of determining the spatial distribution of the contamination.

LTE: Long-term enhancements (LTEs in the American literature, LXEs in the German literature) are discussed at length in Snowden et al. (1994) §4.5 and Snowden et al. (1995) §3.1.4. Suggestions about their physical origin, which is unknown, are discussed in Freyberg (1998) and Cox (1998). LTEs are periods of increased background with time scales from several hours to several days[4]. The emission is vignetted to the same degree as the diffuse background, indicating that the LTE is due to photons rather than particles (Snowden et al. 1994) The emission is soft, but the hardness generally increases with emission strength.

The absolute strength of the LTE emission is unknown. The RASS I (Snowden et al. 1995) has made the best measure to date ($< 30 \times 10^{-6}$ counts s^{-1} $arcmin^{-2}$ to $> 300 \times 10^{-6}$ counts s^{-1} $arcmin^{-2}$) over baselines of several days. However, such a measure can not produce more than a local minimum; whether the LTE ever goes to zero, or has some finite value cannot be measured in this way.

There is evidence that the minimum LTE measured during the *RASS* is the true minimum LTE as the *RASS* count rates agree well with other all-sky surveys executed over the last twenty years. There is some evidence that suggests that the minimum LTE value is near zero (Snowden et al. 1995); a *ROSAT* observation of the moon (Schmitt et al. 1991) reveals that the X-ray flux from the unilluminated portion of the moon was comparable to the LTE emission rate. (As pointed out by Snowden et al. (1995), if that X-ray emission were produced on the surface of the moon, then the equivalence may be a misleading serendipity.)

The lunar observations suggest that the LTE originates within cis-lunar space, a suggestion that can be better understood in the light of the surprising X-ray emission by comets such as those of Lisse et al. (1996). It has been suggested that the X-ray emission from comets is the result of solar wind colliding with neutral atoms (Cravens 1996), a process that could also work with the geocorona (Cox 1998). This mechanism is supported by the very weak correlation between the LTE rate and various measures of geomagnetic storms and the solar wind[5]. Cox (1998), in a notorious back-of-the-envelope calculation based on "flaming comets" has suggested that the solar wind interaction with the exospheric hydrogen of the geocorona (through the subsequent recombination) might produce the correct emission rates for the LTE, but that the calculations depend critically on the recombination spectrum.

3.3.3.2. Measurement All of the above phenomena are identified by their temporal signatures. In the case of the STE's, observation segments with anomalously high count rates are merely removed. For the SSX and the LTE backgrounds, the light curve is fit to both backgrounds simultaneously to determine the strength of the backgrounds.

SSX: The light curve of the SSX background depends upon the change of the zenith angle, which can be calculated from the spacecraft attitude, and the column density along the line of sight. The scaling of the SSX background is determined from fitting the model to the light curve. (The current reduction software also allows the scaling to have a linear temporal variation. However, except for some of the longest continuous data sets, such variation is generally not needed.)

Time segments with an SSX background rate over all bands exceding 5 counts s^{-1} are discarded; those time periods are very short, so discarding them removes a large amount of noise while removing only a small amount of signal.

The $\frac{1}{4}$ keV SSX background is dominated by Thompson scattering, while the higher energy bands are dominated by the O Kα flourescence line at 0.53 keV. The two sources do tend to change independently. Thus, the contribution to the R4-R7 bands can be determined from the contribution to the R4 band (since all those bands are dominated by the O Kα line), but the contributions to the R2 band (which contains both the Thompson scattering and the O Kα line) and the R1 band (containing only the Thompson scattering) must be determined seperately.

LTE: The LTE light curve is assumed to be reasonably fit by a low order (less than fifth order) polynomial. From any given observation,

---

[4] Freyberg (1998) makes the curious claim that enhancements last "for typically up to eight hours (i.e. a couple of orbits)". However, a cursory glance at Figure 7 of Snowden et al. (1994) shows that enhancements often last up to several days, and there may be variation on the order of several weeks.

[5] For the wide disparity in opinion about the correlation of the LTE rate and either geomagnetic activity or solar activity compare Snowden et al. (1994) §4.5, Snowden et al. (1995) §3.1.4, and Freyberg (1998).

one can only remove the LTE emission greater than the minimum LTE emission during that observation. Removing the LTE to an absolute level requires comparison of the observation to the equivalent *RASS* field (which is assumed to be free of any LTE emission, but note the caveat several paragraphs above). This comparison is discussed in the following chapter.

3.3.3.3. Spatial Distribution *LTE:* The LTE is vignetted in the same manner as the cosmic emission. The spatial distribution of the LTE is just a scaling of the effective exposure map.

SSX: The SSX is vignetted in the same manner as the cosmic emission, but the SSX emission is also a strong function of zenith angle. Over the diameter of the PSPC field ($< 2^\circ$) the change in SSX with zenith angle is approximately linear. The introduction of this gradient need not be done for every observation interval since the sum of a series of images with different count rates and different gradients will be the sum of the gradients weighted by the count rates. Thus, the gradient can be applied to the sum of the SSX backgrounds from each observation interval.

3.4. Point Source Removal

Point source removal was accomplished with an enhanced sliding box method, where the size of a circular box is scaled to the local PSF. The background was determined from the raw counts in an annulus from the 90% encircled energy radius to 2.5 times that radius. If the raw counts within the 90% encircled energy radius form a 4σ or greater deviation from the background, then a point source was deemed to have been detected. Since the size of the PSF increases with radius, the point source detection limit will be spatially variant (see §3.2.5 of the following chapter).

Given the limited count rate in any single band and the overlap of the energy response, point source detection was executed on the combined R12 band and the combined R47 band.

3.5. Output Products

The output products consist of three images for each band, the raw counts, $C(x,y)$, the sum of the modeled non-cosmic backgrounds, $B(x,y)$, and the effective exposure, $E(x,y)$. There is also a mask, $M(x,y)$, which is zero for regions containing point sources, and regions with very low effective exposure (i.e., under the wagon wheel of the window support structure).

3.6. Execution

The data were reduced following the procedure described in the *Cookbook for Analysis Procedures for* ROSAT *XRT Observations of Extended Objects and the Diffuse Background, Part I: Individual Observations* (Snowden & Kuntz 1998) which describes the Extended Source Analysis Software (ESAS). The ESAS implements the calibration and procedures described in a series of papers about the PSPC (Snowden et al. 1992; Snowden & Freyberg 1993; Plucinsky et al. 1993; Snowden et al. 1994).

The ESAS was developed by S.L. Snowden as a suite of about a dozen individual FORTRAN routines, each of which queried the user for data and control parameters. When faced with the task of reducing over 280 observations, it became necessary to reduce the amount of human interaction necessary for the reduction of each observation. K.D. Kuntz modified the FORTRAN routines so parameters could be passed from one routine to another through data files. These modifications have been incorporated into the current ESAS release, which is available to the entire community through the *ROSAT* Guest Observer Facility at NASA/GSFC. A set of UNIX shell scripts that invoke the FORTRAN routines in the correct order are described in Appendix C.

The steps of the reduction may be summarized as follows.

Initial Time Selection: Time periods when the MV rate exceded the threshold are removed. All events occuring less than 0.35 ms after a previous event are removed.

Subsequent Time Selection: The remaining data are used to create a light curve. All times for which the SSX$>$ 5 counts s^{-1} are removed.

On average, time selection removes $\sim$ 20% of the exposure. This loss is unavoidable; the data that are removed either are uncalibratable or have a very low signal-to-noise ratio.

Light Curve Fitting: The strength of the SSX and LTE backgrounds are determined by fitting the models to the light curve. Observation segments that are significanly above the fit are removed under the suspicion that they contain STEs.

Mapping (also called "casting"): The events remaining after time selection (raw counts) are mapped into sky coordinates, as are the effective exposure, the particle backgrounds (as measured from the MV rate), the SSX, and the LTE.

AP Fitting: Once the particle background and SSX count rates have been determined, the AP count rate can be determined. As described above, and the distribution of the AP counts mapped into sky coordinated.

Background Summation: The PB, SSX, LTE, and AP backgrounds are summed to produce a single background image.

Point Source Removal: The point source detection is done using the raw count image and exposure map, and the mask is created.

The final, reduced image is given by

$$\frac{raw\ counts - modeled\ background}{effective\ exposure}. \tag{2.7}$$

The reduced images were created only to check for reduction problems; the mosaicking software to be discussed in the next chapter does not use reduced images, but rather the raw counts image, the background image, the effective exposure image, and the mask.

4. Uncertainties

4.1. Detector Map & Effective Exposure Map

To produce an effective exposure map the observation is split into observation segments that are sufficiently small that the shift or rotation within any single segment is less than a detector pixel, $14''.957 \times 14''.957$. A typical observation contains 200 different shift/rotation combinations. A pixel of the exposure map ($14''.957 \times 14''.957$ in sky coordinates) will be the weighted sum of all of the detector map pixels that overlaid that position in each of the shift/rotation combinations.

The detector map used for this work is the image, in detector coordinates, of all of the photons that were detected in the ~ 11 days that the PSPC B was used to finish the All-Sky Survey. The uncertainty in a given pixel of the detector map will be the uncertainty in the number of photons detected in that pixel, and will be given by Poisson statistics. If we consider a case where all the obervation segments have the same weight, then the uncertainty of a $14''.957 \times 14''.957$ pixel in the exposure map will be the root of the sum of the counts in all of the detector map pixels that overlaid that position. Table 2.5 contains the typical number of counts at both the center and the periphery of the detector map. Assuming 200 observation segments, there are 200 different detector map pixels that overlay a given exposure map pixel; the percentage uncertainty for a pixel of the effective exposure map will range from ~ 11.5% to ~ 6.8%.

For a $1' \times 1'$ pixel (the size typically used in mosaics) the calculation is similar. However, in this case, one no longer has 200 independent samples; although the number of detector map pixels that overlay a given exposure map pixel will increase a small amount, the number of independent samples will decrease[6]. The uncertainty per pixel will decrease only slightly; for $1'$ pixels the uncertainty ranges from 9.5% to 5.6%. In all cases the uncertainty in the exposure map is much less than the uncertainty due to the counting statistics of individual exposures.

4.2. Spatial and Temporal Gain Variation

Snowden, Turner, & Freyberg (1999) have recently completed a study of the spatial and temporal variation of the PSPC. After the temporal gain corrections of Prieto, Hasinger, & Snowden (1996), they found that there were variations of up to ~ 4% in the gain around the nominal PHA to PI conversion. In particular, the gain in the central $15'$ region of the PSPC was reduced by up to ~ 4%, depending upon the epoch.

The implications of the gain variation are not clear for broad band studies. A change in gain

---

[6] An approximate calculation can be made as follows. Assume that the detector map pixels used to calculate a single $14''.957 \times 14''.957$ exposure map pixel form a square with sides of $\sqrt{200}$ pixels. If one is seeking the uncertainty for an exposure map pixel that is $n \times n$ detector pixels in size, the square of detector pixels that will contribute will be $\sqrt{200} + (n-1)$ on a side. However, there will be only $(\sqrt{200} + (n-1))^2$ independent contributions.

TABLE 2.5
DETECTOR MAP COUNTS

Band	Counts[a]		% Uncer.[b]	
	Edge	Center	Edge	Center
R1	0.39	1.09	11.3	6.96
R1L	0.38	1.09	11.5	6.77
R2	0.62	0.99	8.96	7.10
R4	0.49	0.96	10.1	7.22
R5	0.49	0.98	10.1	7.14
R6	0.50	0.94	9.98	7.30
R7	0.38	0.96	11.5	7.22

[a] Average for a single detector pixel measured over a 16 × 16 pixel box. The "edge" region was selected to be [455:470,225:270]; the "center" region was selected to be [235:250,225:240]

[b] The percent uncertainty was calculated for a single detector pixel using the method described in the text.

changes the PI channel into which a given event is binned. For a broad energy band such as those used here, the effect of the gain reduction depends upon the spectral shape; what is the balance between counts shifted out of one end of the band and those shifted in at the other?

To explore this effect we have taken several Raymond & Smith model spectra of different temperatures, determined their expected PI distribution, and reduced the gain by 4.5% (the counts in each channel are reduced by 4.5% and then increased by 4.5% of the next higher channel.) The results are shown in Table 2.6, where it can be seen that, due to the low spectral resolution of the PSPC, a small change in the gain does little to change the total number of counts. Note also that in most cases the wobble smears the effect of the gain variation so modeling a 4.5% gain shift is conservative.

4.3. Particle Background Map

The total number of counts per detector pixel in the particle background maps measured by Plucinsky et al. (1993) are on the order of 1.02 counts arcmin^{-2} for the internal PB, and 0.40 counts arcmin^{-2} for the external PB. (Here I have combined their data sets 2, 3, and 5 for the internal PB and data sets 1 and 4 for the external PB.) Given these low count values, only direct measurement of large scale structure in the PB map is possible. For bands R4-R7, the variance within the measured PB maps was consistent with a Poisson distribution. In band R1L2, there is a strong residual grid pattern with a 5′ scale (Plucinsky et al. 1993).

Although one cannot measure the grid pattern in the particle background, it is unlikely to cause significant spurious structure. First, the "dither" smears the structure. Second, the mean particle background rate for the sum of the internal and external particle background in the data used by Plucinsky et al. (1993) are on the order of 13×10^{-6} counts s^{-1} arcmin^{-2} for all bands combined. From Table 2.7, one can see that the contribution to any single band will be significantly smaller; in band R1L2 the PB rate will be ~ 1% of the detected cosmic rate, while in band R45 the PB rate will be ~ 4% of the detected cosmic rate[7].

REFERENCES

Abell, G. O., Corwin, H. G., & Olowin, R. P. 1989, ApJS, 70, 1

---

[7] I have used the detected cosmic rate here rather loosely. The detected cosmic rate is the total number of non-LHB photons detected. This is the total number of photons that actually enter the detector that cannot be attributed to the LHB.

TABLE 2.6
EFFECT OF GAIN REDUCTION ON BROAD BANDS

$\log T$[a]	Percent Change						
	R1	R1L	R2	R4	R5	R6	R7
5.8	0.04	0.14	0.54	0.84	0.52	0.62	0.64
6.0	-0.12	-0.03	0.42	0.41	0.40	0.46	0.46
6.2	-0.22	-0.15	0.33	0.14	0.30	0.34	0.34
6.4	-0.24	-0.16	0.34	-0.06	0.13	0.28	0.28
6.6	-0.19	-0.12	0.32	-0.22	0.04	0.24	0.25
6.8	-0.01	0.04	0.33	-0.33	-0.02	0.21	0.23

[a] Raymond & Smith model temperature.

TABLE 2.7
PARTICLE BACKGROUND DISTRIBUTION

Band	Internal	External	
		Continuum	Al Kα
R1L	0.185	0.044	0.000
R2	0.148	0.105	0.000
R3	0.049	0.047	0.000
R4	0.081	0.084	0.000
R5	0.090	0.096	0.000
R6	0.168	0.182	0.189
R7	0.270	0.293	0.804
R1L2	0.333	0.149	0.000
R45	0.171	0.180	0.000
R67	0.438	0.475	0.993

The quantities listed are the percentage of each component in each band for the PSPC B in low gain mode.

Arabadjis, J. S., & Bregman, J. N. 1999, ApJ, 510, 806, submitted

Balucinska-Church, M., & McCammon, D. 1992, ApJ, 400, 699

Cox, D. P. 1998, in The Local Bubble, ed. D. Breitschwerdt & M. Freyberg, 121

Cravens, T. E. 1996, Geophysical Research Letters, 24, 105

Freyberg, M. J. 1998, in The Local Bubble, ed. D. Breitschwerdt & M. Freyberg, 113

Gruber, R. 1992, in Data Analysis in Astronomy IV, ed. V. D. Gesù, 153

Hartmann, D., & Burton, W. B. 1997, Atlas of Galactic Neutral Hydrogen (Cambridge University)

Hartmann, D., Kalberla, P. M. W., Burton, W. B., & Mebold, U. 1996, A&A, 119, 115

Kalberla, P. M. W. 1978, Ph.D. thesis, University of Bonn

Kuntz, K. D., & Snowden, S. L. 1998, Cookbook for analysis procedures for *rosat* xrt observations of extended objects and the diffuse background, part ii: Mosaics, Technical report, NASA/GSFC

Kuntz, K. D., Snowden, S. L., & Warwick, R. S. 1998, in The Local Bubble, ed. D. Breitschwerdt & M. Freyberg, 329

Lisse, C. M., et al. 1996, Science, 274, 205

Morrison, R., & McCammon, D. 1983, ApJ, 270, 119

Plucinsky, P. P., Snowden, S. L., Briel, U. G., Hasinger, G., & Pfeffermann, E. 1993, ApJ, 418, 519

Prieto, M. A., Hasinger, G., & Snowden, S. L. 1996, A&A, 120, 187

Raymond, J. C., & Smith, B. W. 1977, ApJS, 35

Schlegel, D. J., Finkbeiner, D. P., & Davis, M. 1998, ApJ, 500, 525

Schmitt, J. H. M. M., Snowden, S. L., Aschenbach, B., Hasinger, G., Pfeffermann, E., Predehl, P., & Trümper, J. 1991, Nature, 349, 583

Sfeir, D., Lallement, R., Crifo, F., & Welsh, B. Y. 1999, A&A, submitted

Snowden, S. L., et al. 1997, ApJ, 485, 125

Snowden, S. L., & Freyberg, M. J. 1993, ApJ, 404, 403

Snowden, S. L., et al. 1995, ApJ, 454, 643

Snowden, S. L., & Kuntz, K. D. 1998, Cookbook for analysis procdures for *rosat* xrt observations of extended objects and the diffuse background, part i: Individual observations, Technical report, NASA/GSFC

Snowden, S. L., McCammon, D., Burrows, D. N., & Mendenhall, J. A. 1994, ApJ, 424, 714

Snowden, S. L., Plucinsky, P. P., Briel, U., Hasinger, G., & Pfeffermann, E. 1992, ApJ, 393, 819

Snowden, S. L., Turner, T. J., & Freyberg, M. J. 1999, A&A

Voges, W., et al. 1992, in Proceedings of Satellite Symposium 3, Space Science with Particular Emphasis on High-Energy Astrophysics, ed. T. D. Guyenne & J. J. Hunt, 223

Voges, W., et al. 1996, http://www.rosat.mpe-garching.mpg.de/survey/rass-bsc/

Yan, M., Sadeghpour, H. R., & Dalgarno, A. 1998, ApJ, 496, 1044

Chapter 3: Mosaicking

Abstract

The following cookbook describes the process of creating a mosaic from a number of overlapping *ROSAT* PSPC or HRI pointings, whose reduction was described in the previous chapter. The mosaicking process described here is a substantial improvement over previous versions; we have implemented a more complex process that, now that the high resolution maps from the *ROSAT* All-Sky Survey have become publically available, will produce a mosaic with better LTE offset removal especially on large scales, and automatic normalization to the All-Sky Survey. Although this chapter is primarily concerned with describing this new method of mosaicking, the method not utilizing the *ROSAT* All-Sky Survey is described as well.

1. Introduction

Mosaicking[1] is a potentially powerful tool for producing large field-of-view images (several degrees by several degrees) that are much more sensitive than the *ROSAT* All-Sky Survey (the *RASS*). As with any mosaicking technique, determining and removing the zero-point offsets between overlapping pointings is of prime concern. Unlike those who mosaic optical images, we have little astrometric concern, the pixels are large (usually several times the 14.957″ pointed image pixels) compared to the pointing accuracy of the instrument (10″).

As in the previous chapter, it is important to distinguish between *cosmic* and *non-cosmic* backgrounds. The cosmic background is the sum of the counts received from diffuse or unresolved distant sources. The non-cosmic background, usually referred to simply as the "background", is the sum of the counts received from local sources, such as scattered solar X-rays and the Long Term Enhancement (LTE), or produced in the instrument, such as the particle background and the "after-pulse" counts. See Snowden et al. (1994) for an extensive discussion of the PSPC background, Snowden (1998) for the HRI particle background. In general, the cosmic background is what we want, and the background is the nuisance we want to eliminate, though its components may, in themselves, be of interest.

2. The LTE Offset Rate

The principal task in forming a mosaic is to remove the *effect* of any residual offsets between fields: to eliminate any variation in the zero level across the fields. The residual offsets are primarily due to the different LTE offset rate of each exposure, but may also include any over or undersubtraction of the other background components. As was described in Part I, for each individual exposure, the light-curve can be described roughly by a low order polynomial. The global minimum of that polynomial is the true cosmic background signal plus any component constant (over the period of the observation) of the LTE, while the flux above that minimum is clearly due to the LTE. Due to the limited time over which an exposure is made, one cannot be sure that a global minimum (LTE = 0) has been reached. Therefore, although one can take the true cosmic background rate to be the minimum rate observed during the exposure, what remains is still the true cosmic background plus some unknown LTE rate, the LTE *offset*.

Clearly, since the LTE is by definition a time variable phenomenon, the residual offset will be different for different exposures. The following sections describe three methods by which one can determine the LTE offsets for all of the pointings within a mosaic. The first two methods, though implemented in the mosaicking software, are primarily for illustration, as both have potentially serious drawbacks. The third

---

[1] A number of commentators have expressed displeasure at this spelling of the gerund form of "mosaic". Though it may look a bit odd, this form is recognized by dictionaries, following the model of picnicking and panicking. A "c" followed by an "i" should be soft, leading to something sounding like "mō - sā - ĭ - sēng", like "icing".

method is a synthesis of the previous two and is the recommended method. The results of the three methods can be seen in Figure 3.1.

2.1. Direct Comparison to the *RASS*

The first method, direct comparison (DC), is rather simple-minded; one can compare the mean count rate in each pointing to the mean count rate from the matching position in the *ROSAT* All-Sky Survey (the *RASS*);

$$LTE = R_{pointed} - R_{RASS}, \qquad (3.1)$$

where LTE is the residual LTE count rate for a given pointed exposure, $R_{pointed}$ is the mean count rate in that exposure, and R_{RASS} is the mean *RASS* count rate for the area of the sky covered by the pointed observation. It is assumed that the LTE has been correctly removed from the *RASS*, an assumption discussed at length in Snowden et al. (1994) and Snowden et al. (1995).

2.1.1. Point Sources

The above equation also assumes that the point sources have been removed to the same level for both the *RASS* and the pointed observation. In general, the point sources can be removed from the pointed observation to much smaller count rates than in the *RASS* due to the limiting source count rate used for the *RASS* (see Table 3.1) and the typically much longer exposure of the pointed observations. As can be seen in Table 3.3, the total contribution from point sources that are detected in individual pointings but which are fainter than the *RASS* exclusion threshold can be comparable to the LTE offset. To make the comparison properly, one should make a point source mask based upon the *ROSAT* Bright Source Catalogue or BSC (Voges et al. 1996), the catalogue used to make the point source masks for the *RASS*, using the count-rate thresholds listed in Table 3.1.

2.1.2. Uncertainties

For a given pointed exposure there are ~ 90 $12' \times 12'$ *RASS* pixels, each of which has an uncertainty of ~ 25 – 75%. The distribution of the uncertainty of the RASS pixels can be judged from Figure 3.2. The uncertainty in the difference between the mean count rate of a pointed observation and the mean count rate for the same region of the *RASS* is $\sim 5 - 7 \times 10^{-6}$ counts s^{-1} arcmin^{-2} for a single band (see Table 3.3). Figure 3.3 shows a typical *RASS* field and the regions corresponding to the individual pointings in a mosaic. Several of the regions appear to contain "hot" pixels, i.e., those which are either statistically high or contain unremoved point sources. This impression is reinforced by Figure 3.4, where the "hot" pixels appear as outliers. As implemented, these outliers, both positive and negative, are removed before the difference between the pointed observation and the *RASS* is calculated.

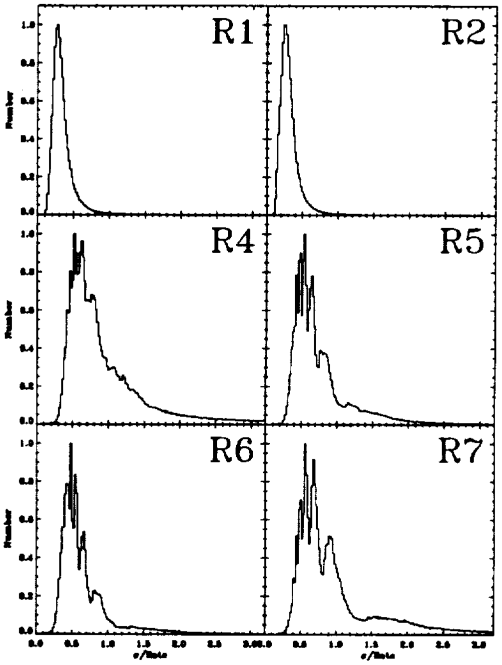

Fig. 3.2.— The distribution of Uncertainty/Rate for a single panel of the *RASS* in the direction of $(\ell, b) = (180, 0)$.

The difficulty with this method is that there is no pointing-to-pointing consistency. Given the uncertainties in the *RASS*, adjacent pointings may be normalized to different values of the diffuse cosmic background; causing obvious "seams" between pointings. The seams can only be seen with difficulty in Figure 3.1 due, in part, to the inherent smoothness of this field.

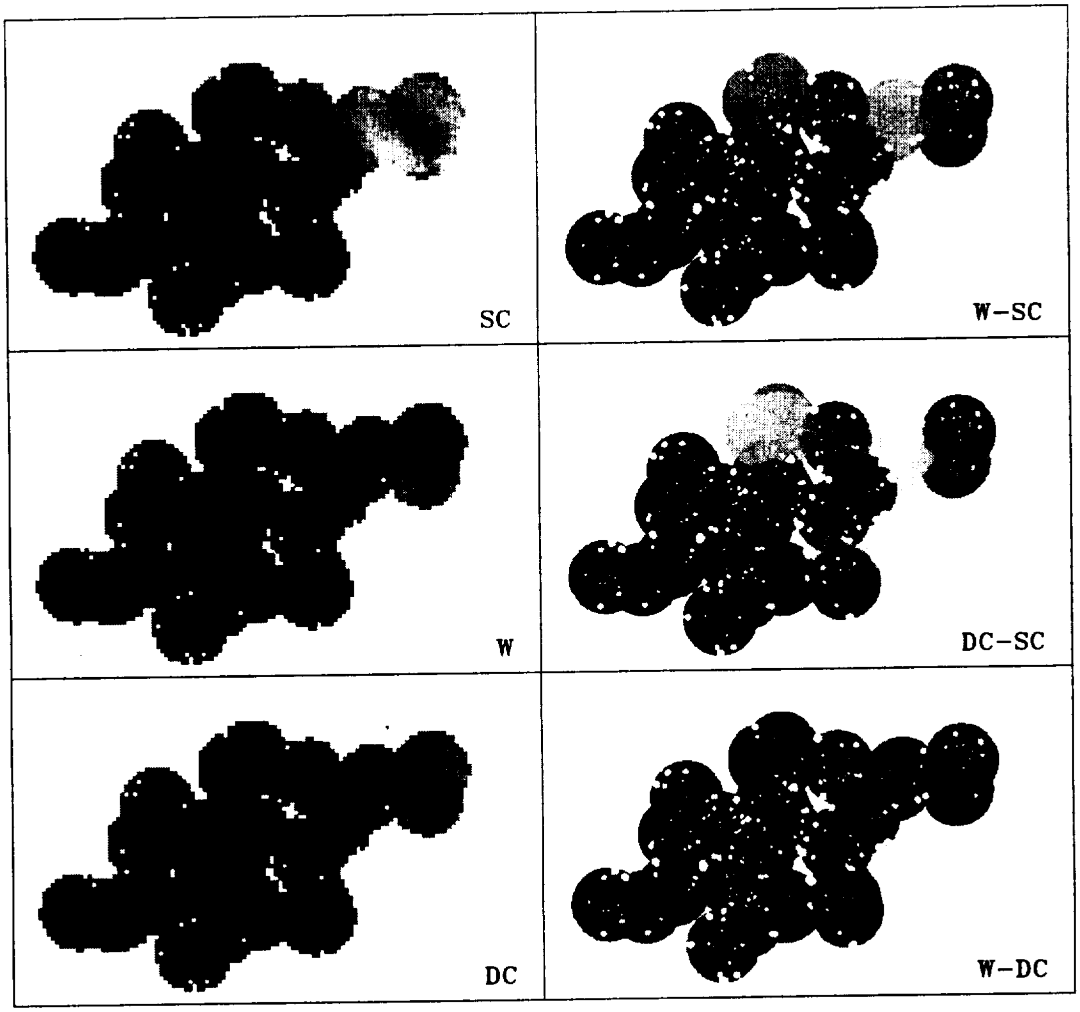

Fig. 3.1.— A mosaic of R2 band pointings where the LTE offset has been determined by three different methods. *Top Left:* Self-consistent solution (SC) adjusted by the difference between the entire mosaic and the *RASS*. *Top Right:* Difference of the equal weighting and self-consistent solutions. *Middle Left:* Equal weighting (W) of self-consistent and direct comparison solutions. *Middle Right:* Difference between the direct comparison and self-consistent solutions. *Bottom Left:* Direct comparison (with the *RASS*) solution (DC). *Bottom Right:* Difference between the equal weighting and the direct-comparison solution. The image mosaics (left-hand column) were binned to $6' \times 6'$ pixels and were further smoothed by a $30'$ radius tophat function. The mean value of the images is $\sim 200 \times 10^{-6}$ counts s^{-1} arcmin^{-2}, with a range from 140 to 230 $\times 10^{-6}$ counts s^{-1} arcmin^{-2}. The difference images (right-hand column) were binned to $1'.5 \times 1'.5$ pixels. The difference have a range from -30 (white) to +30 (black) $\times 10^{-6}$ counts s^{-1} arcmin^{-2}. The {min,max} range for each of the difference images is W-DC: {-7.95,15.68}, DC-SC: {-27.24,21.22}, and W-SC: {-19.07,14.92} in the same units as above. One should not take the uncertainty in the LTE offset to be so large since much of the difference is accounted for by the systematic trend across the image, not pointing-to-pointing variation. *Scale:* Each pointing has a radius of $53'$.

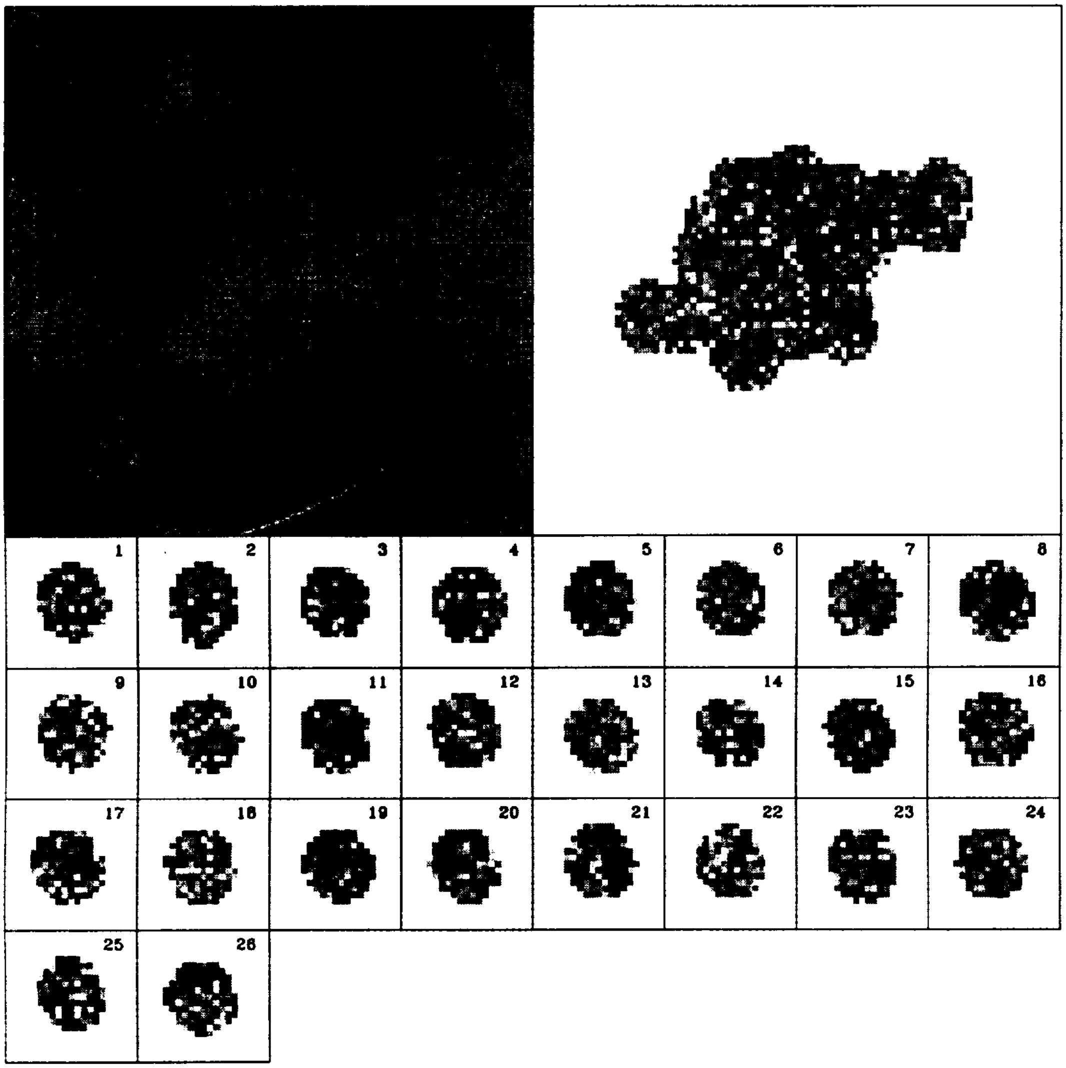

Fig. 3.3.— A demonstration of the hazards of comparing PSPC pointings to the *RASS*. *Top Left:* A typical *RASS* field, in this case centered on $(\ell, b) = (180, 0)$ for band R2. Darker pixels have higher X-ray intensity. Shown is the outline of a mosaic for which the LTE offset is to be found. (The dot in the center is a region missing from the mosaic; not a point source.) *Top Right:* The *RASS* at the location of the mosaic. *Bottom:* The *RASS* at the location of each individual pointing. The size scale is that same as for the panel in the upper right. Note the existence of "hot" pixels in some of these pointings.

Table 3.1
RASS Point Source Exclusion Limits

Band	Limit (counts s^{-1})
R12	0.025
R45	0.02
R67	0.02
R47[a]	0.04

[a] This is an approximation. A point source with a steep spectral index might be detected in R45 but not in R67, meaning that 0.02 counts s^{-1} would be removed from the *RASS*, rather than 0.04 counts s^{-1}.

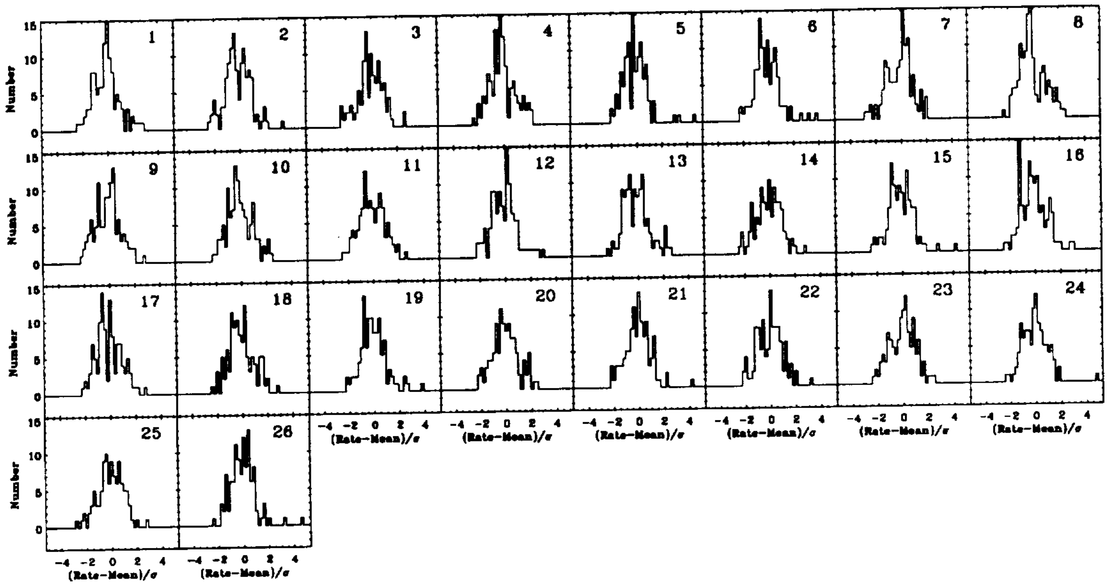

Fig. 3.4.— The distribution of the *RASS* pixel values for each individual pointing (band R12). The horizontal axis is the pixel value minus the mean, divided by the standard deviation of the distribution. Note that the hot pixels in Figure 3.3 are the outliers above 3σ.

2.1.3. Use of the R1 vs. the R1L Band

The *RASS* was executed with the R1 band, while most mosaics will be formed with the R1L band. To convert from one to the other requires some assumptions about the temperature of the emitting gas and the amount of intervening absorption. These assumptions should, of course, be consistent with the R1/R2 band ratio determined from the *RASS*[2].

If the bulk of the $\frac{1}{4}$ keV emission in the field of view is produced by the Local Hot Bubble (LHB), then the appropriate R1L/R1 band ratio can be read from Table 3.2. This table contains the mean R2/R1 band ratio for the LHB, as well as the values at the half-maxima of the distribution (Snowden et al. 1998), the corresponding Raymond & Smith model temperatures, (Raymond & Smith 1977) and the resulting R1L/R1

---

[2] It should also be remembered that the *RASS* was not executed with the same detector used for most of the pointed observations; the cross-calibration of the two detectors is described in Snowden et al. (1994).

band ratios. These values have been calculated assuming both no absorption and an absorption due to the Local Fluff, $\sim 1.5 \times 10^{18}$ cm^{-2}.

If an object other than the LHB fills most of the field of view, one will need to determine the R1L/R1 ratio intrinsic to the object through independent spectral modeling. As a first cut, one could determine the Raymond & Smith model temperature from the R2/R1 band ratio, and use that to determine the R1L/R1 band ratio. The user will have to determine whether such a solution is appropriate.

One other interesting situation is a high-Galactic-latitude pointing containing a contribution from the LHB as well as a contribution from the Galactic halo. From (Snowden et al. 1998), we find that the halo has a lower model temperature ($\log_{10} T = 6.06$) than the LHB ($\log_{10} T = 6.14$). An unabsorbed contribution would increase R1L/R1, since the lower temperature gas would be softer, but the halo emission is absorbed, which hardens the halo contribution to an R1L/R1 ratio closer that of the LHB. When the absorption makes the halo component very hard, it is sufficiently attenuated, that it contributes very little to the total emission. This behavior can be seen in Figure 3.5. As can be seen, for most fields containing the Galactic halo, taking the R1L/R1 ratio of the LHB will be sufficient.

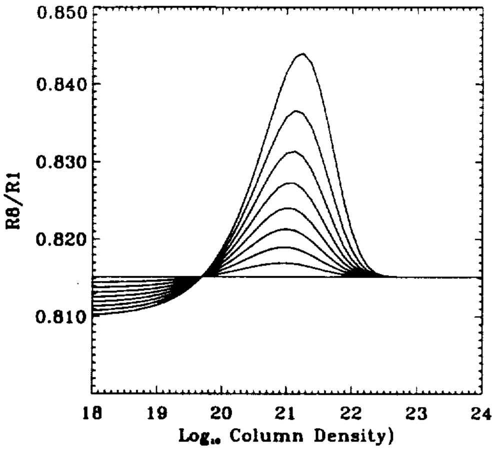

Fig. 3.5.— The behavior of the R1L/R1 ratio as a function of halo emission fraction and absorbing column density. The horizontal line is the value of R1L/R1 for the LHB. Each curve deviating from that line is the value of R1L/R1 as a function of the column density absorbing the halo component. The curves progressively farther from the horizontal show an unabsorbed halo to LHB contribution of 10%, 20%, 30%, to 80%.

2.1.4. Weighting Change

Since the initial release of this software, we have changed the weighting scheme used to compare the *RASS* to the individual pointings. Originally, each pixel in a pointing was weighted by its uncertainty. For low surface brightness objects, where there are only a few counts per pixel, the uncertainty will be correlated with the pixel value, thus significantly biasing the mean. (This will not be a problem with most observations of diffuse but recognizeable objects, only with observations of the diffuse background.)

To correct this problem, we removed the weighting. Without the weighting, pixels at the edge of a pointing where the exposure is low, introduce significant uncertainty into the value of the mean. To reduce this uncertainty we introduced an iterative discard. In each iteration, the mean and variance are calculated. Any pixels that fall outside 3.5σ are removed, and the mean and variance are calculated again. The entire set of pixels, including pixels that have been previously discarded, is then compared to the new standard deviation. The process is repeated until the number of discarded pixels converges, typically three or four iterations.

2.2. Self-Consistent Solution

The self-consistent solution determines the relative LTE offsets between pointings, and then compares the entire mosaic to the *RASS*.

The effect of the different offsets between two overlapping exposures can be removed by comparing the total count rates in the region of overlap. The total count rate is defined as

$$R \equiv \frac{\textit{total counts} - \textit{background counts}}{\textit{exposure time}}, \tag{3.2}$$

where each quantity is summed over the region of overlap. Here, as above, "background" is shorthand for the sum of the particle background, the scattered solar X-rays, the after-

TABLE 3.2

R1L/R1 RATIOS FOR THE LHB

Foreground N_H	R2/R1[a]	log T 0 cm^{-2}[b]	log T 1.5 x 10^{18} cm^{-2}[b]	R1L/R1 0 cm^{-2}[b]	R1L/R1 1.5 x 10^{18} cm^{-2}[b]
-HWHM	1.02	6.093	6.088	0.8088	0.8095
Mean	1.12	6.143	6.138	0.8149	0.8153
+HWHM	1.23	6.214	6.207	0.8234	0.8239

[a] From Snowden et al. 1997.

[b] Column density of absorbtion in front of the LHB emission due to the Local Fluff.

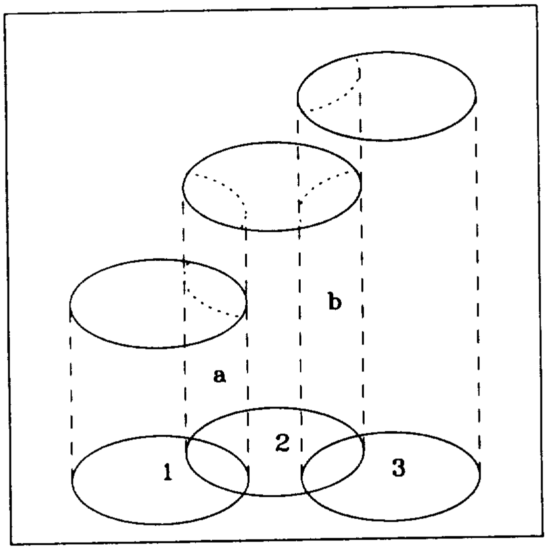

Fig. 3.6.— A graphic portrayal of the determination of the LTE offset. Here there are three exposures (1, 2, and 3) and two regions of overlap (a and b). We thus have the system of equations:

$$R_{1a} - LTE_1 = R_{2a} - LTE_2$$
$$R_{2b} - LTE_2 = R_{3b} - LTE_3$$
$$LTE_1 + LTE_2 + LTE_3 = 0$$

which can be easily solved.

pulse counts, and the portion of the LTE greater than the minimum LTE (during the exposure). Assuming that there is no cosmic source of variation, (e.g., a variable star) the difference in the count rates in the region of overlap is the difference in LTE offset rates between the two exposures. In other words, if S_{12} is the count rate due to cosmic sources in the region of overlap of exposure$_1$ and exposure$_2$, LTE_1 and LTE_2 are the LTE offsets for exposure$_1$ and exposure$_2$, respectively, and R_1 and R_2 are the total count rates in exposure$_1$, and exposure$_2$, respectively, then

$$S_{12} + LTE_1 = R_1, \qquad (3.3)$$

$$S_{12} + LTE_2 = R_2, \qquad (3.4)$$

and thus

$$\Delta LTE \equiv LTE_1 - LTE_2 = R_1 - R_2. \qquad (3.5)$$

At this point, one could subtract the difference in LTE rates (ΔLTE) from the exposure with the larger rate, could add it to the exposure with the smaller rate, or, pardoning the pun, one could split the difference between the two. Although the first option might seem the best, it really does not matter, as the absolute LTE offset is yet to be determined.

The method for multiple exposures is similar. For an example of three exposures,

$$LTE_1 - LTE_2 = R_1 - R_2 \qquad (3.6)$$

$$LTE_2 - LTE_3 = R_2 - R_3 \qquad (3.7)$$

where the R_n – R_m are measured quantities. (See Figure 3.6 for a graphic portrayal.) To these equations can be added the constraint

$$LTE_1 + LTE_2 + LTE_3 = 0, \qquad (3.8)$$

which closes the system and sets the condition that the LTE offset rates are as small as possible. This condition ensures a reasonable solution and essentially "splits the difference".

The advantage of this method is that adjacent pointings are normalized to the same cosmic background rate, and thus visible "seams" can be avoided. However, small errors between pairs of overlapping pointings can accumulate, causing a "drift" in the measured cosmic background level (relative to the true cosmic background level) from one part of the mosaic to another. "Drift" is especially a problem for linear chains of overlapping exposures, but can occur any place the relative LTE offsets are determined by a limited number of pointings, or pointings with low exposure.

2.3. Synthesis

The best method combines the self-consistent method, and its ability to avoid "seams", with the direct comparison to the *RASS*, which avoids the problem of "drift". For a two-pointing mosaic, we wish to combine

$$LTE_1 - LTE_2 = R_1 - R_2 \tag{3.9}$$

from the self-consistent method with

$$LTE_1 = R_1 - RASS_1 \tag{3.10}$$

$$LTE_2 = R_2 - RASS_2 \tag{3.11}$$

where $RASS_1$ and $RASS_2$ are the mean count rates determined from the *RASS* at the positions of the two pointings.

The equations described in the previous section, as implemented, are solved with a singular value decomposition (SVD) algorithm, which is very stable for over-determined sets of equations. The algorithm is sufficiently complicated that most introductory texts merely describe its properties without describing the algorithm itself (e.g., Strang 1976) or provide source code without explanation (Press et al. 1986). Understanding the algorithm itself, however, is not necessary to determine the proper way to combine the above three equations.

Assuming, for the moment, that there are no uncertainties, the above system of equations can be written as

$$\begin{bmatrix} 1 & -1 \\ 1 & 0 \\ 0 & 1 \end{bmatrix} \begin{bmatrix} LTE_1 \\ LTE_2 \end{bmatrix} = \begin{bmatrix} R_1 - R_2 \\ R_1 - RASS_1 \\ R_2 - RASS_2 \end{bmatrix} \tag{3.12}$$

For example, take

$$\begin{aligned} R_1 &= 110 \\ R_2 &= 120 \\ RASS_1 &= 90 \\ RASS_2 &= 110. \end{aligned} \tag{3.13}$$

The self-consistent solution (after comparing the entire mosaic to the *RASS*) would yield

$$LTE_{SC} = \begin{bmatrix} LTE_1 \\ LTE_2 \end{bmatrix} = \begin{bmatrix} 10 \\ 20 \end{bmatrix}. \tag{3.14}$$

while direct comparison with the *RASS* would yield

$$LTE_{DC} = \begin{bmatrix} LTE_1 \\ LTE_2 \end{bmatrix} = \begin{bmatrix} 20 \\ 10 \end{bmatrix} \tag{3.15}$$

The SVD solution of the three equations together yields

$$LTE_{WS} = \begin{bmatrix} LTE_1 \\ LTE_2 \end{bmatrix} = \begin{bmatrix} 13.3333 \\ 16.6666 \end{bmatrix} \tag{3.16}$$

which is $\frac{1}{3}$ the self-consistent solution (LTE_{SC}) (which is represented by 1 equation) plus $\frac{2}{3}$ the direct comparison solution (LTE_{DC}) (which is represented by two equations).

The two solutions should be weighted by their uncertainties, and not by the number of equations representing each. For the simple example above, the weighting can be accomplished by multiplying each direct comparison equation by a factor W,

$$\begin{bmatrix} 1 & -1 \\ W & 0 \\ 0 & W \end{bmatrix} \begin{bmatrix} LTE_1 \\ LTE_2 \end{bmatrix} = \begin{bmatrix} R_1 - R_2 \\ (R_1 - RASS_1)W \\ (R_2 - RASS_2)W \end{bmatrix} \tag{3.17}$$

which yields the solution

$$LTE_{WS} = LTE_{SC} + 2W^2 LTE_{DC} \tag{3.18}$$

or, to weight the solutions equally

$$W = \sqrt{\frac{1}{2}}. \tag{3.19}$$

In this case, each equation should then be further weighted by its uncertainty.

Increasing the number of pointings substantially increases the complexity, and the result is no longer the weighted sum of the two solutions. Figure 3.7 demonstrates this complexity; each curve shows the LTE offset for a given pointing as a function of the weighting applied to the direct comparison equations. The left edge of the plot is the modified[3] self-consistent solution; the right edge is the direct comparison solution; between is the result for various weightings. The

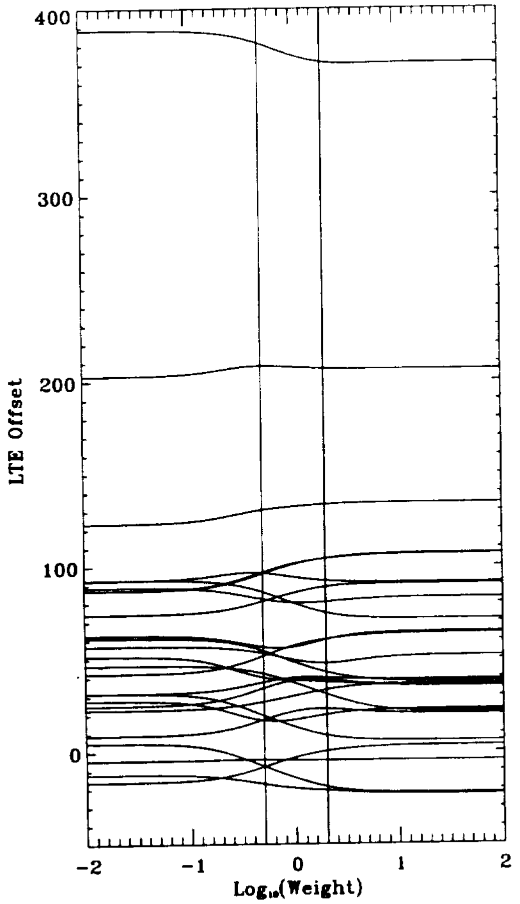

Fig. 3.7.— A demonstration of the change in LTE offset solution as a function of the relative weights of the self-consistent and direct-comparison equations. The left edge is the modified (see text) self-consistent solution for the LTE offsets of the mosaic shown in Figure 3.1. There are twenty-six pointings in this mosaic. The right edge is the direct-comparison solution. Plotted between the vertical bars are the solutions obtained as the relative weight of the direct-comparison equations is increased from 1/100 to 100. Note that not all of the LTE values change monotonically as the weighting is changed.

change from one solution to the other is not monotonic.

It should be noted that the χ^2 will be higher for the weighted solution than for either the self-consistent and direct-comparison solutions, simply because there are more conflicting conditions to be met. However, it should also be remembered that χ^2 loses significance if W is more than one[4].

Once the LTE offset rates are determined for each pointing, the spatial distribution of the LTE offset counts for each pointing is taken to be the distribution of the effective exposure, i.e., that which is put into the mosaic is a scaled exposure map.

2.4. Calculating Offsets in Overlap Regions

Before the total count rate in the overlap region is calculated, the image must be carefully cleaned. First, the heavily vignetted edges must be removed; the low effective exposure, and the resultant low source-detection rates, result in a high uncertainty in the count rates. Excluding regions more than 53″ from the center of the field removes the most heavily vignetted regions.

Second, point sources and bright small-scale extended sources must be removed. As has been noted before, the PSF at the edge of the field is

---

[3] The self-consistent solution was modified by adding a constant. The self-consistent solution produces the relative LTE values; the absolute LTE values had to be obtained by comparing the mosaic to the *RASS*. As soon as one combines the self-consistent and direct comparison equations, no matter how small the weight of the direct comparison equations, they set the absolute LTE value. This LTE value assumes a different cosmic background than does the self-consistent solution. The direct comparison solution assumes a cosmic background that is the mean of the *RASS* values of individual pointings, which is not at all the same as the mean of the *RASS* in the region of the mosaic; even though both cover the same area, they weight it differently.

[4] If n is the number of self-consistent equations, m the number of pointings, W the weighting the direct-comparison equations, LTE_n the fit value of the LTE offset, and using the nomenclature above, then

$$\chi^2 = \frac{\sum_n((R_i - R_j) - (LTE_i - LTE_j))^2}{m + Wn} \qquad (3.20)$$

$$+\frac{\sum_m(W(R_i - RASS_i - LTE_i))^2}{m + Wn} \qquad (3.21)$$

TABLE 3.3
LTE OFFSET (R2)

Pointing	ℓ	b	PSC[a]	SC[b]	WS -0.3[c]	WS 1.0[c]	WS 0.3[c]	DC[d]
rp200020/	180.74	-22.61	21.27	-16.15±5.45	-7.96±5.30	-2.95±3.66	0.35±4.99	3.21±6.98
rp200083/	179.79	-20.73	7.75	-4.47±6.89	-4.15±6.96	-4.46±5.39	-4.62±7.56	-4.73±9.76
rp200441n00/	180.48	-23.54	12.04	9.03±6.51	17.44±6.10	21.86±4.30	23.04±5.81	20.27±8.42
rp200442n00/	178.12	-21.73	12.82	-12.01±6.47	-17.35±6.22	-19.66±4.49	-20.88±6.03	-23.07±8.11
rp200443n00/	179.95	-19.65	10.80	92.74±7.79	86.05±7.13	79.78±4.94	74.63±6.40	71.27±9.02
rp200444n00/	182.33	-21.40	10.35	87.11±7.67	96.76±6.73	101.48±4.78	103.94±6.24	106.42±8.08
rp200776n00/	181.14	-24.13	12.90	42.27±7.66	51.61±7.03	57.19±5.08	60.47±6.61	63.50±8.26
rp200777n00/	180.16	-21.94	6.81	74.05±5.06	81.05±5.16	85.57±3.61	88.70±5.03	90.17±7.30
rp200942/	183.14	-23.12	3.57	202.95±12.51	208.15±8.22	207.42±5.37	206.63±6.71	206.15±8.05
rp200981n00/	177.96	-23.01	3.66	46.70±8.58	42.12±8.00	36.95±5.80	30.97±7.55	21.27±10.26
rp200982n00/	182.40	-22.74	5.32	123.36±10.38	130.48±7.50	132.24±5.17	133.32±6.50	134.02±7.56
rp201504n00/	174.91	-19.69	5.83	27.76±13.37	16.91±8.79	17.32±5.52	19.91±6.42	22.67±7.24
rp700044/	176.42	-20.03	8.40	4.93±9.48	-7.86±7.19	-14.14±4.96	-18.92±6.34	-22.31±7.70
rp900353n00/	179.42	-19.59	13.38	61.28±7.65	54.33±6.99	48.06±4.80	42.75±6.18	37.51±8.83
rp200002sum/	184.12	-23.03	7.26	92.50±13.99	96.35±8.92	93.97±5.55	92.00±6.33	90.93±6.88
rp200912sum/	177.87	-23.33	5.42	56.96±8.69	53.04±8.05	49.31±5.77	47.47±7.30	51.51±9.32
wp200775n00/	179.46	-23.21	6.12	31.66±6.88	37.50±6.75	39.86±5.13	39.75±7.13	38.63±9.14
wp201313/	179.50	-19.38	8.60	388.50±8.36	381.38±7.65	375.23±5.50	371.12±7.40	370.70±10.33
wp201316n00/	175.03	-20.40	3.98	51.60±13.02	39.91±8.73	38.27±5.69	37.52±7.02	36.01±8.40
wp201369n00/	179.54	-21.21	17.32	22.75±5.18	26.96±5.52	30.21±4.05	33.34±5.57	36.31±7.31
wp201747n00/	181.98	-20.52	17.00	24.97±7.72	34.37±6.87	38.41±4.94	38.64±6.55	35.03±8.79
wp200001sum/	181.15	-21.28	13.80	87.04±6.30	95.96±5.89	100.99±4.21	104.09±5.77	106.76±7.90
wp201314sum/	178.06	-19.85	9.93	62.85±8.15	56.36±7.38	56.31±5.35	60.10±6.75	64.26±7.70
wp201315sum/	176.61	-20.28	3.97	31.81±9.08	19.58±7.21	13.37±5.10	8.85±6.66	5.81±8.30
wp201370sum/	177.44	-21.10	6.85	88.81±6.76	82.12±6.21	80.05±4.40	80.50±5.76	82.83±7.45

[a] The point source contamination in the *RASS* for the combined band R1L+R2. The units are 10^{-6} counts s^{-1}.

[b] The self-consistent solution adjusted by the LTE offset determined from the entire mosaic region (67.16×10^{-6} counts s^{-1} arcmin^{-2}). The units are 10^{-6} counts s^{-1} arcmin^{-2}.

[c] The solution of the weighted combination of the self-consistent and direct comparison equations. The number is the $\log_{10}$ of the weight (W) applied to the direct-comparison equations. The units are 10^{-6} counts s^{-1} arcmin^{-2}.

[d] The direct-comparison solution. The units are 10^{-6} counts s^{-1} arcmin^{-2}.

much larger than at the center of the field. Thus, when the edge of one field overlaps the center of another, the same point source, just outside the region of overlap, may enter the region of overlap for one exposure but not for another (See Figure 3.8). Even if the point source lies completely within the overlap region for both exposures, the Poisson variation in point source counts between the two exposures, differential vignetting, as well as possible intrinsic variability of the point source can both cause miscalculation of the background offsets.

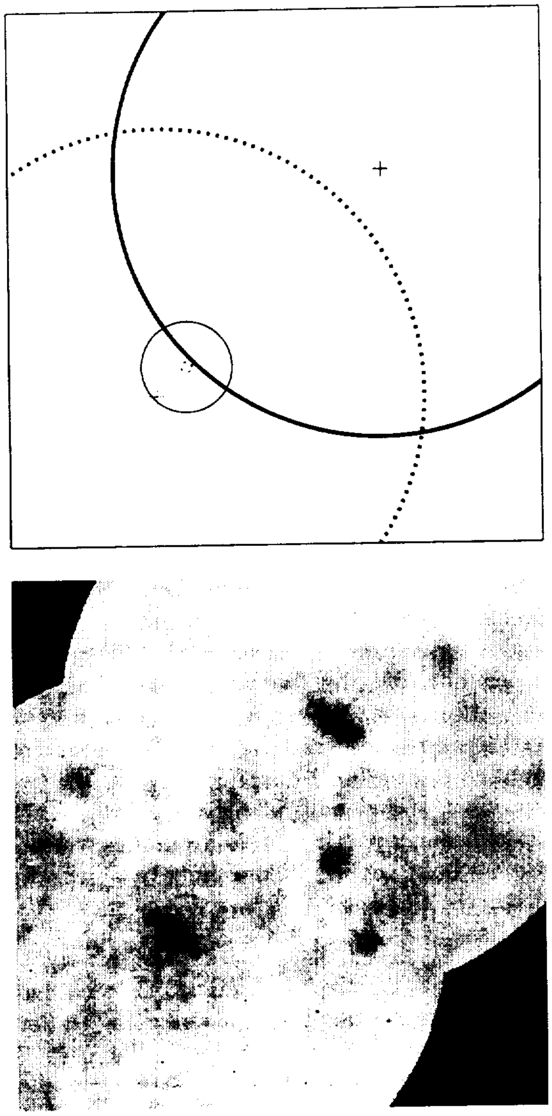

Fig. 3.8.— *Top:* A demonstration of point source problems in the region of overlap. The thick lines represent the edges of two overlapping exposures; the crosses show the exposure centers. The thin lines show the PSF size for a single point source near, but not in, a region of overlap. Although the point source is not in the region of overlap, it contributes counts to the overlap region for one exposure, but not the other. *Bottom:* A mosaic of two observations in the LMC. Both observations have a bright point source near their center which lies just outside of the processed area of the other observation. Note the "fans" produced by not removing the PSF region of a source outside the field of view.

2.4.1. Background Gradients

The above treatment of uncertainty in the count rate in the overlap region assumes that the background is flat. The calculation of the LTE offsets can stumble if there is a strong gradient across the overlap region. Consider the following one-dimensional demonstration, which is shown schematically in Figure 3.9. In the region of overlap, let the cosmic background be represented by a linear function (solid line, top panel). Let the effective exposure be another simple function of position for two overlapping pointings, pointing 1 and pointing 2 (dotted and dashed lines, top panel). The detected counts, as shown as a function of position, are shown for the two exposures in the lower panel.

The overlap routine calculates the count rate in the region of overlap as

$$CR = \frac{\sum \boldsymbol{counts} - \sum \boldsymbol{background}}{\sum \boldsymbol{effective\ exposure}} \qquad (3.22)$$

In this simplified case, $\sum(\boldsymbol{effective\ exposure})$ is the same for both pointings. Assume also, for simplicity, that the background is the same for both pointings. As can be seen in the lower panel, $\sum \boldsymbol{counts}$ will be very different for the two pointings.

Given this extreme example, what is likely in typical fields? Consider a 30$'$ overlap in a region where the cosmic background has a linear gradient, decreasing by n% from one side of the overlap region to the other. One can calculate the count rate in the overlap region that one would determine using both of the exposures. Figure 3.10 plots the difference between the count rates divided by the true count rate as a function of n. Given two pointings, 1 and 2,

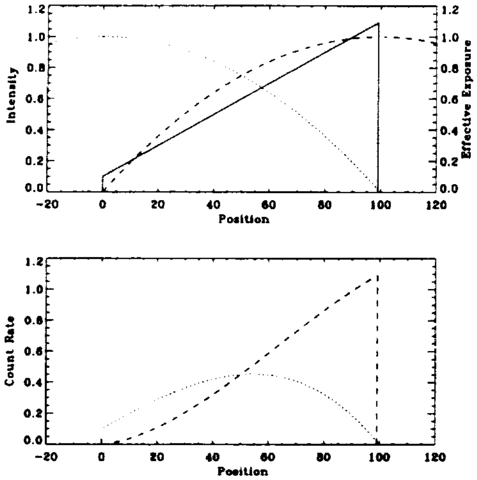

Fig. 3.9.— A demonstration of the effect of a gradient in the cosmic background on the count rates measured in overlap regions. *Top:* The solid line is the cosmic background as a function of position on a one-dimensional sky. The dotted line and the dashed line are the effective exposures as a function of position for two overlapping exposures. *Bottom:* The measured count rates as a function of position for the two exposures, shown only in the region where the two exposures overlap. (No vignetting correction has been applied.) Note that the sum under the curves will not be the same.

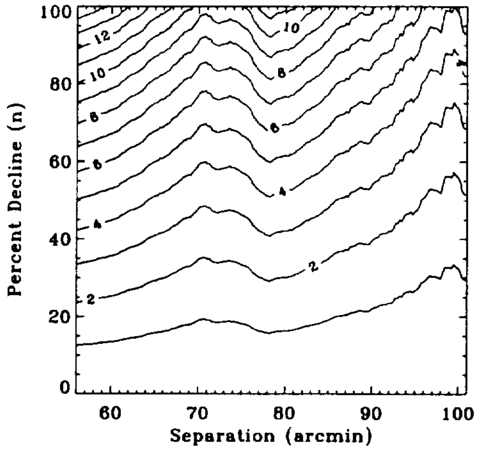

Fig. 3.10.— A measure of the effect of a gradient on the count rates measured in overlap regions. The percentage difference between the count rates determined from two overlapping pointings as a function of the separation of the centers of the pointings and the steepness of the slope of the cosmic background over the region of overlap. The structure in the plot is due to the spoke-and-ring structure of the PSPC window. See text for an complete explanation of the plotted quantities.

and taking all of the following sums to be over the region of overlap, then the percentage difference is

$$\frac{\frac{\sum counts_1}{\sum exposure_1} - \frac{\sum counts_2}{\sum exposure_2}}{\sum true\ count\ rate}. \qquad (3.23)$$

The cosmic background has been taken to be a linear function across the region of overlap. The percent decline is defined as

$$100 \times \frac{Max(background) - Min(background)}{Max(background)}, \qquad (3.24)$$

where the Max(background) is at one edge of the region of overlap and Min(background) at the other.

As can be seen, even for a very steep slope, the difference in counts between the two exposures is only ~10% of the true number of counts. Thus, although gradients can lead to serious problems, for most circumstances the effects will be less than a percent.

2.4.2. The Exclusion Radius

It is tempting to use the exclusion radius to minimize the uncertainty in the count rate in the overlap region. It would appear that increasing the exclusion radius would increase the uncertainty by including an ever larger number of low-signal-to-noise pixels in the more heavily vignetted region. However, for a given separation of two overlapping fields, increasing the exclusion radius includes an ever larger number of high-signal-to-noise pixels near the field center. Thus, it can be seen that the uncertainty in the count rate in the overlap region is *formally* minimized by maximizing the exclusion radius (i.e. excluding as little as possible). The scaled uncertainty per pixel[5] is shown graphically in

---

[5] The scaled uncertainty per pixel is defined as follows: if RT (the rate multiplied by the exposure time) is the

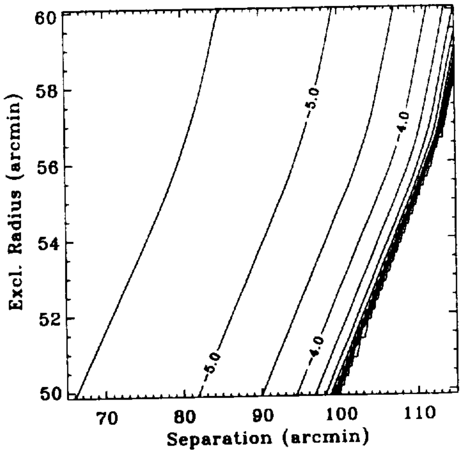

Fig. 3.11.— A graphical representation of the uncertainty in the count rate for the overlap region as a function of field separation (center of field to center of field) and exclusion radius. The plotted quantity is the scaled uncertainty per pixel, the plotted contours are logarithmic from -5.5 to 0 in steps of 0.5. The empty region to the right denotes the combination of exclusion radius and separation for which there is no overlap. The scaling of the uncertainty per pixel is described in the text.

Figure 3.11.

We have not found a criterion which, from first principles, determines the best exclusion radius to use. However, experience has shown that using a 53′ exclusion radius produces reasonable solutions.

2.5. Point Source Detection

Detecting and removing point sources is a multi-step process, given that the same point source may (or may not) be detected several times in overlapping exposures, and false sources may be detected in a short exposure and not seen in longer, overlapping exposures. The problem is further complicated by the fact that not only will the detection limit vary from exposure to exposure, but, due to the variation of the size of the PSF[6], will change drastically from the center to the edge of a single exposure. (See Figure 3.12.)

Once one has detected all of the sources in all of the exposures, the easiest way of sorting through the multiple detections and the possible false detections is to accept only the "best" detections. The "best" detections are those made in the exposure which, at the location of the detection, has the best point source detection limit. That is, for every pixel in the mosaic, one determines which exposure has the best point source detection limit at that point. Then, taking a list of all of the point source detections, and the fields in which each detection was made, one discards all of those detections which were made in the parts of exposures with non-optimal detection limits. The remainder is a "master list" of detections which can then be used to mask out the point sources.

The actual method implemented is slightly more sophisticated. It compares the discarded point source detections with the list of "good" detections to determine which are duplicates, i.e., the same objects as the "good" detections, barely detected in sub-optimal pointings. The rejects that are not duplicates are selected for closer scrutiny; they may be unmasked hot-spots or transient sources, both of which should be excluded. The bottom-left panel of Figure 3.13 shows an example of an unmasked hot-spot detected as a point source, but placed in the reject

---

number of counts in an unvignetted pixel and $V_{i,j}$ is the vignetting function in pixel $\{i,j\}$, the the total number of counts in the overlap region will be

$$\sum_{i,j} RTV_{i,j} \tag{3.25}$$

while the count rate in the overlap region will be

$$\frac{\sum_{i,j} RTV_{i,j}}{\sum_{i,j} TV_{i,j}} \tag{3.26}$$

with the uncertainty

$$\frac{\sqrt{\sum_{i,j} RTV_{i,j}}}{\sum_{i,j} TV_{i,j}} \tag{3.27}$$

The scaled uncertainty per pixel is thus

$$\frac{1}{N}\sqrt{\frac{R}{T}}\frac{1}{\sqrt{\sum_{i,j} V_{i,j}}} \tag{3.28}$$

where N is the number of pixels in the overlap region.

[6] Unless explicitely defined otherwise, the point spread function radius is taken to be the radius at which the point spread function contains ninety percent of the energy for the PSPC, fifty percent for the HRI.

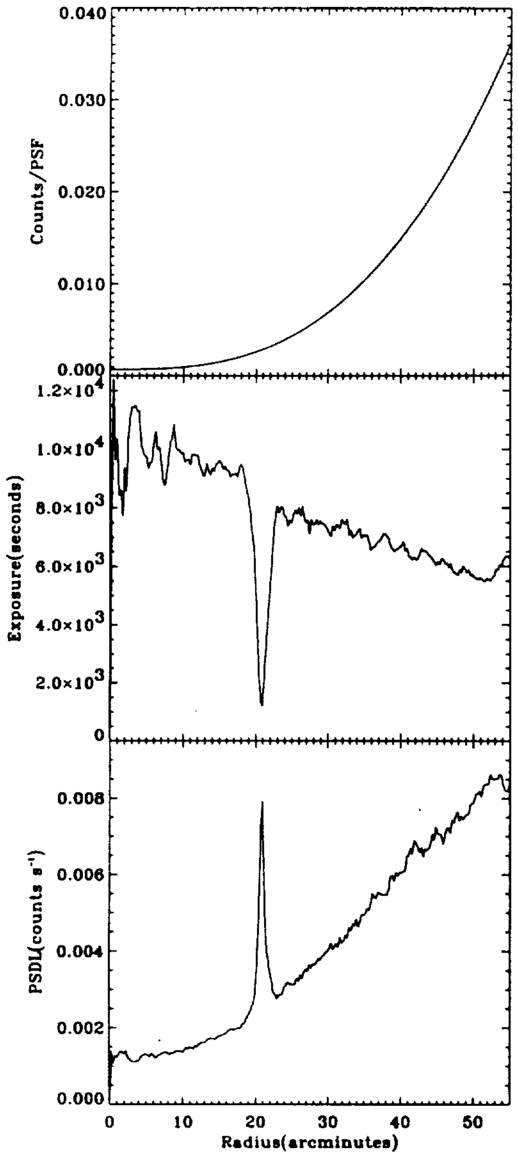

Fig. 3.12.— Point source detection limits. These plots were made from an azimuthally averaged exposure map *det_20_41_b.fits*. *Top:* The point source detection limit for an unvignetted exposure with a uniform background count rate of 450×10^{-6} counts s^{-1} arcmin^{-2} and an exposure of 10 ks. The source of the variation with radius is only the change in the PSF size with radius. *Middle:* The vignetting function. The sharp dip at ~ 21′ is due to the window support structure. *Bottom:* The point source detection limit for a vignetted exposure with a uniform count rate of 450×10^{-6} counts s^{-1} arcmin^{-2}. The variation with radius is due to both the change in the size of the PSF and the decrease in effective exposure.

list. This hot-spot is reproduced in Figure 3.14 at several different contrasts to show its structure. The other rejected detections do not appear to be significant.

Occasionally, when a point source falls right on the boundary between being accepted from one pointing and being accepted from another, there can be problems; each pointing's detection can fall in the other pointing's "accept" region. Such problems are readily found by a brief examination of the "rejected" point sources.

The above method produces a detection limit that varies greatly across the mosaic. Why not, one might ask, use a uniform detection limit that is as bad or worse than the worst detection limit within the mosaic? The difficulty is that the worst detection limit is set by the outer parts of the exposures (typically outside of the inner support ring at ~22′) which provide the bulk of the area of the mosaic. The resulting detection limits are usually worse, sometimes, much worse, than the detection limits of the *RASS*.

2.5.1. Recalcitrant Point Sources

Once the mosaic has been formed, enhancements may exist which appear to be point sources that have not been adequately removed. This may or may not be a real problem. Consider an area where the edge of one field (where the PSF is large) overlaps the center of another field (where the PSF is small). If a point source has been removed, then a larger area of one field will have been removed than has been removed from the other. As a result, there may be a small region with no exposure, there will certainly be a surrounding annulus with low exposure, and a surrounding region with higher exposure. If the "low exposure" is sufficiently small that not all the pixels contain counts *and* the "higher exposure" is significantly greater than the "low exposure", then, in the mosaic, the pixels in the "low exposure" region will be scaled to have the same average count rate as the higher exposure region which means that those *individual* pixels in the "low exposure" region which have counts, will have much higher values than the surrounding area, while those pixels without counts (but which have modeled non-cosmic background counts) will be more negative. Thus, though all of the averages will be

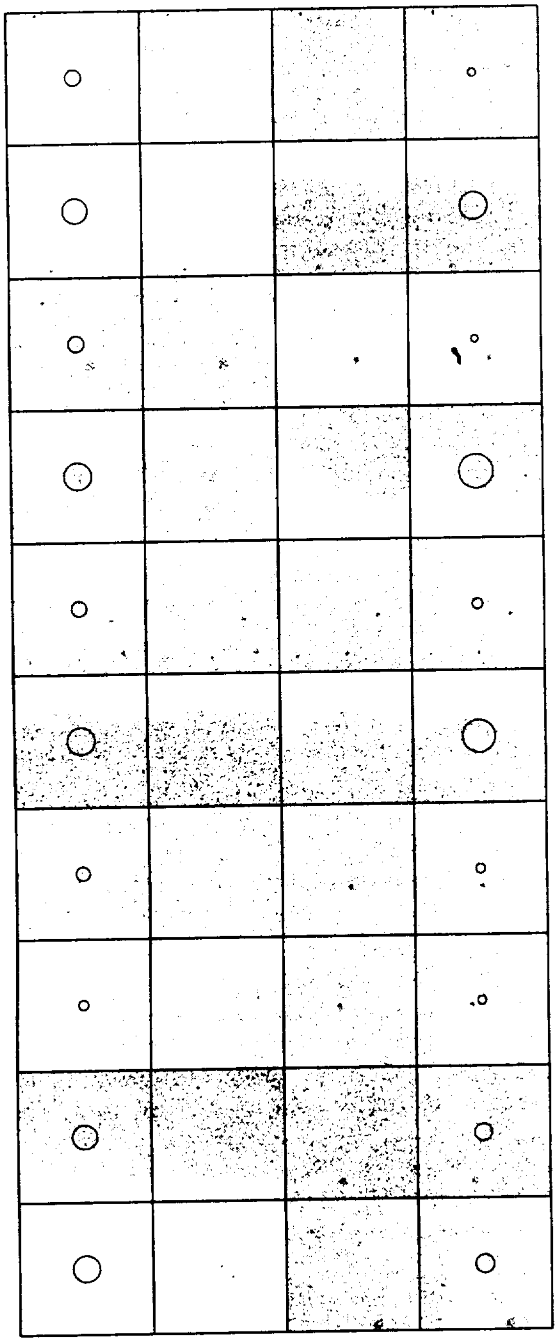

Fig. 3.13.— Comparison of "rejected" sources to better exposures of the same regions. *Left two panels:* ten "rejected detections". The leftmost panel is overplotted with the local PSF. *Right two panels:* the same positions (R.A., dec.) in the pointings with the best point source detection limit at those positions. The right-most panel is overplotted with the local PSF. Each panel has been scaled by the extremes within that panel. Note the strong source in the lowest panel.

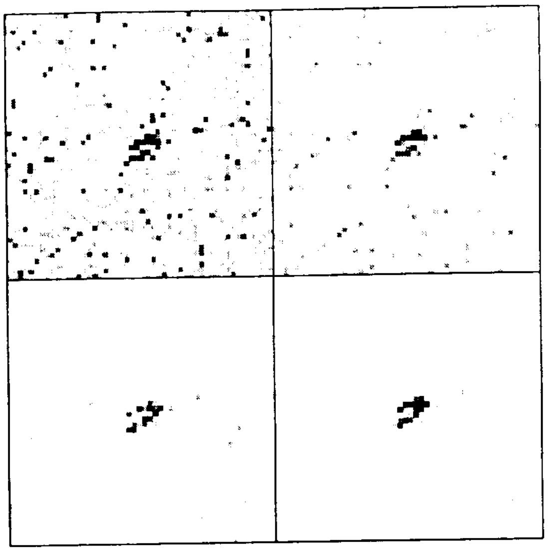

Fig. 3.14.— An unmasked hot-spot. The region is shown at several different contrasts to demonstrate its structure. Note that at low levels it looks vaguely point-like, but that the brightest pixels reveal the spacecraft wobble.

correct, a point source will seem to exist, as the eye more readily perceives positive excursions than the negative excursions. The solutions are to use a larger pixel size, or to mask out the offending region "by hand", or to use an exposure threshold.

Although many residual point sources are of this spurious nature, real residual point sources may occur in mosaics formed from bands R1 or R1L. In this case, the PSF is poorly characterized even at small detector radii, due to the ghost-image problem[7]. The theoretical PSF radii are too small, a problem that is especially notable towards the center of the field. This can be corrected by setting a minimum removal radius of eight 15″ pixels (a 2′ radius).

Residual Point Sources will also appear in

---

[7] When an event occurs in the PSPC it creates a signal in both sets of crossed cathode wires. The x-position of the event is the centroid of the signals produced by the cathode wires running in the y-direction. The y-position of the event is the centroid of the signals produced by the cathode wires running in the x-direction. If the signal from a set of wires is too small to allow centroiding, (i.e., the signal is above the threshold on only one wire) the position of that event is taken to be the iposition of that wire with the greatest signal. This causes faint sources to be spread along the closest set of crossed wires. The faint wings of stronger sources will assume a "screen" pattern.

regions where many short exposures overlap. These point sources were indetectable in any single exposure. At this time, no software has been developed to detect and remove these point sources. If these sources must be removed, one must determine their position manually and proceed as described above for extended sources.

2.5.2. Point Source Detection Limits

If the smallest allowable statistical significance for a detected point source is set to S, then, given Poisson statistics,

$$S = \int_{C=0}^{C_{lim}} P(C, C_{back}) dC, \tag{3.29}$$

$$S = e^{-C_{back}} \sum_{C=0}^{C_{lim}} C_{back}^{C}/C! \tag{3.30}$$

where C_{back} is the number of background counts expected in the area covered by a point source (i.e., one PSF radius) and C_{lim} is the smallest number of counts necessary for the statistical significance of S. At a pixel position [m,n] a radius r from the field center (the optical axis)

$$C_{back}[m,n] = R[m,n] \; \pi \; PSF(r)^2 \; E[m,n] \tag{3.31}$$

where R[m,n] is the background count rate (counts s^{-1} $arcmin^{-2}$) expected in pixel [m,n], E[m,n] is the exposure time (sec), and PSF(r) is the PSF radius (arcmin) at that position. Given a constant exposure and background count rate, the point source detection limit as a function of radius is shown in Figure 3.12a. The slight saw-tooth pattern is due to the Poisson probability being an integral function. Given the exposure map, which shows strong vignetting at the edges of the field (Figure 3.12b) one can derive the a typical point-source detection limit as a function of radius (Figure 3.12c). It should be noted that, due to the shape of this function and the increase of PSF size with radius, the center of a shorter exposure can have a better point source detection limit than the edge of a much longer exposure.

2.6. An HRI Note

The above discussion has been primarily targeted towards the PSPC and is not completely applicable to the HRI. First, although the HRI also is subject to the LTE, the greater part of the offsets between pointings is due to the large uncertainty in the HRI particle background calibration (Snowden 1998). However, the difference in the source of the offset does not change the method of removal. Second, the method of determining offsets is different because there is no *RASS* equivalent for the HRI. The difference in bandpass between the HRI and PSPC is sufficiently large that it sould be unwise to attempt the type of band ratio correction we have employed to scale the *RASS* to the PSPC band R1L. Therefore one can only use the self-consistent method of determining relative offsets.

2.7. "What have I done wrong?"

Once the mosaic has been produced, unless all the exposures were of similar length, or the pixel size was chosen to be quite large, the end result will not look very nice; the boundaries between different exposures will be readily apparent. This type of result can be seen in Figure 3.15. The reason for this ugliness is *not* incorrect background subtraction or a problem with the LTE offset rate, rather, the problem is with the eye.

In the typical *ROSAT* exposure the majority of the pixels do not have detected photons. A longer exposure has more photon-bearing pixels than a shorter exposure. When scaling a shorter exposure to a longer exposure, one increases the values in the few pixels containing detections, rather than increasing the number of pixels with detections. Thus, even when a shorter exposure is scaled to a longer exposure, the two will still look very different. This is graphically demonstrated for a one-dimensional detector in Figure 3.16.

The solution to this problem is to increase the size of the pixels. If, on the basis of aesthetics, one needs to increase the pixel size, then one probably needs to increase the pixel size for scientific reasons, namely, in order to gain enough counts per pixel to have reasonable statistics.

REFERENCES

Press, W. H., Flannery, B. P., Teukolsky, S. A., &

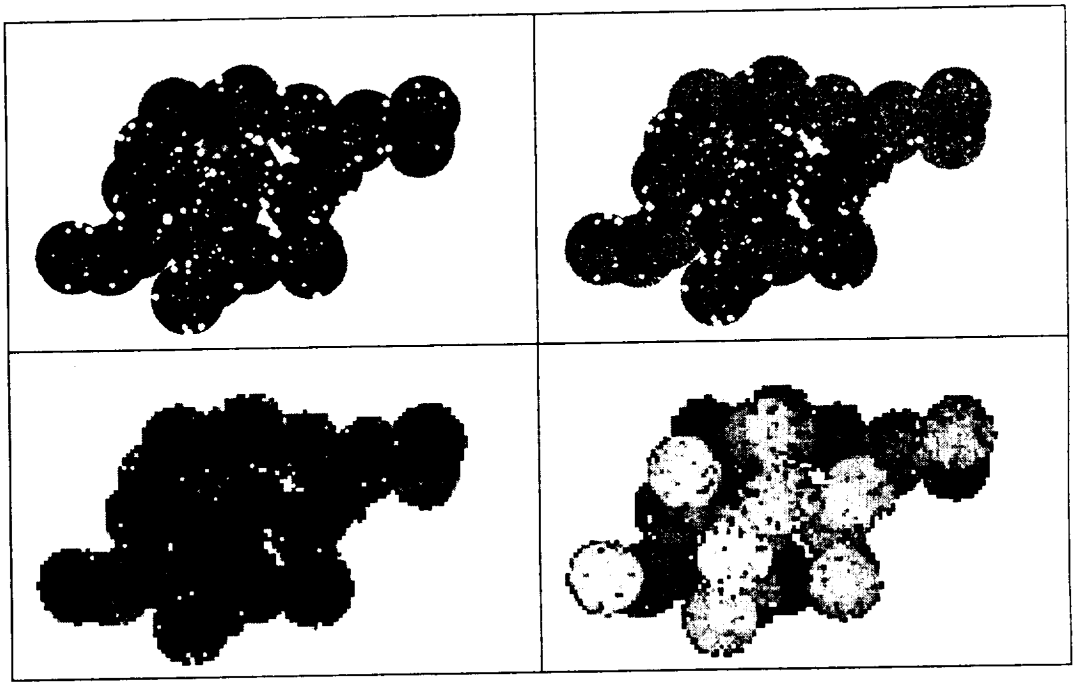

Fig. 3.15.— An example of a "raw" mosaic where the count rates are continuous over exposure boundaries, but scaling of "sparse" images reveals the exposure edges. *Top Left:* A map of the logarithm of the exposure; higher exposure regions are darker. *Top Right:* The "raw" mosaic. Note that the lower exposure regions appear "rougher" than higher exposure regions. *Bottom Left:* The mosaic formed with a sufficiently large pixel size (4 × 4 the size of the "raw" mosaic) that every pixel has nearly the same uncertainty. Note that there *is* structure in this field, but it is not related to exposure boundaries. *Bottom Right:* The uncertainty for the previous mosaic.

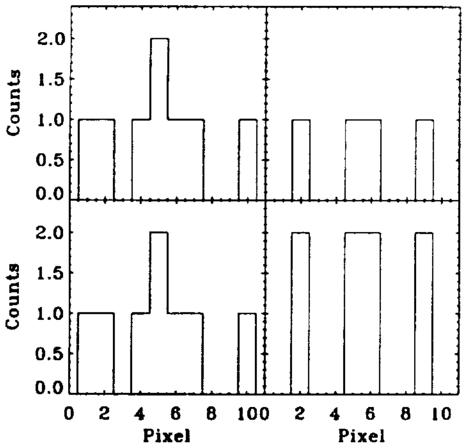

Fig. 3.16.— One dimensional demonstration of the effect of scaling on sparse images. *Top:* Two one-dimensional "images" with the same count rate; the left image has twice the exposure as the right image. *Bottom:* The two images scaled to the same exposure time. Note that the two images will look very different despite the fact they have the same count rates.

Vetterling, W. T. 1986, Numerical Recipes (Cambridge University Press)
Raymond, J. C., & Smith, B. W. 1977, ApJS, 35
Snowden, S. L. 1998, ApJS, 117, 223
Snowden, S. L., Egger, R., Finkbeiner, D., Freyberg, M. J., & Plucinsky, P. P. 1998, ApJ, 493, 715
Snowden, S. L., et al. 1995, ApJ, 454, 643
Snowden, S. L., McCammon, D., Burrows, D. N., & Mendenhall, J. A. 1994, ApJ, 424, 714
Strang, G. 1976, Linear Algebra and its Applications (Academic Press)
Voges, W., et al. 1996, http://www.rosat.mpe-garching.mpg.de/survey/rass-bsc/

Chapter 4: Tracers of Absorption

Abstract

This chapter explores the problem of finding an adequate tracer of the entire X-ray absorbing column. X-ray absorption is produced by H and He (for X-rays with $E < \frac{1}{4}$ keV) and metals (for X-rays with $E > \frac{1}{4}$ keV) distributed through all the phases of the ISM. As dust is likely distributed through all but hottest phases of the ISM, and a high-resolution all-sky survey exists, 100 μm emission by dust has become a commonly used tracer of the X-ray absorbing column. The *IRAS* 100 μm emission has become even more attractive as a tracer since the destriping, recalibration, and dust temperature correction by Schlegel, Finkbeiner, & Davis (1998). However, there are a number of well known (though not always well understood) systematic effects that make 100 μm emission less than an ideal tracer, including unresolved temperature effects in neutral gas, and very uncertain contributions by H II to either 100 μm emission or X-ray absorption. We review the current understanding of the problem and attempt to quantify the uncertainties.

1. Statement of the Problem

When observing X-ray emission from objects beyond the Local Cavity one typically wants to correct for the effects of the absorption. At $\frac{1}{4}$ keV absorption is primarily due to hydrogen and helium, with smaller contributions from oxygen and iron. The relative contributions of the various elements in a completely neutral atomic gas is shown for three *ROSAT* bands in Figure 4.1. The amount of absorption is, of course, quite sensitive to the ionization states, but much less sensitive to chemical state, i.e., C and O *versus* CO. It is generally assumed that the abundance of these absorbers is traced by the abundance of H in its three phases, H II, H I, and H_2. Ideally, then, determining the absorbing column would be accomplished by making a map of H in each phase, and correcting those maps for the change in absorption cross-section due to the mean ionization or chemical state of the absorbing species related to each phase of H. Two problems are immediately apparent; first, metallicity varies (and thus the number of X-ray absorbers per H atom), and second, although H I is well traced by 21 cm emission, no all-sky high-resolution maps (better than 30′) exist of any of the phases of H.

For such reasons, use of the *IRAS* 100 μm emission is particularly appealing. The *IRAS* maps, particularly after the destriping and cross-calibration work of Schlegel, Finkbeiner, & Davis (1998), provide a high resolution (6′) all-sky map of a quantity that might trace all three states of H. Relying on the dubious assumption that the dust to gas ratio is nearly constant , one is left with the complication of finding the dust emis-

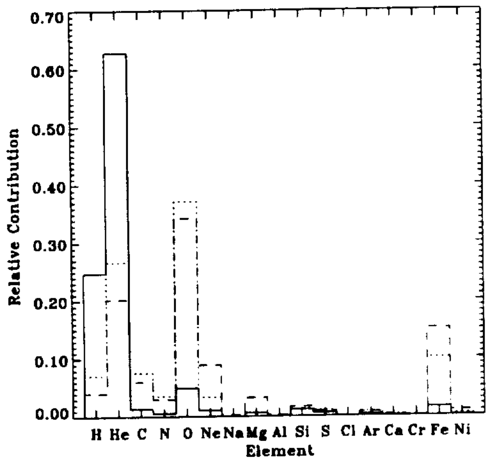

Fig. 4.1.— The relative elemental contributions to the absorption cross-section. *solid:* The relative contributions at $\frac{1}{4}$ keV. *dotted:* The relative contributions at $\frac{3}{4}$ keV. *dashed:* The relative contributions at 1.5 keV. Note that the bands are not dominated by single elements that differ from band to band. Thus, the broad-band *ROSAT* data is not useful for diagnosing elemental abundances.

sivity per H atom for each of the three states, a quantity depending upon a variety dust temperatures along the line of sight. The problem is complicated by the fact that, unlike the H I and H II data, the *IRAS* data is devoid of velocity information, thus complicating the task of identifying the contributions from the different components. Despite the seemingly Sisyphæn nature of this task, the following sections explore the extent to which the *IRAS* 100 μm emission can be used to trace the X-ray absorbing column.

We will first consider the extent to which the *IRAS* 100 μm emission tracks H I in regions that ought to be free of contamination by H_2. As that correlation is quite strong, we then consider the extent to which the H II may or may not be traced. We then consider *IRAS* 100 μm emission in regions with contributions from H_2, and in particular, the extent to which the temperature dust correction of Schlegel, Finkbeiner, & Davis (1998) may be deemed reliable for the purpose of tracing the X-ray absorption column.

2. Dust Emission and ISM

Consider the components to the 100 μm signal, measured over some limited region, as a function of neutral hydrogen column, N_{HI}, as schematically depicted in Figure 4.2. There is a constant component due to the Cosmic Infrared Background (CIB) which will not vary with N_{HI}. To this component can be added the contribution due to H I, which, over most of the high Galactic latitude sky, is the largest contribution. The slope of the relation will be the dust emissivity per H atom, ε_I. This slope will depend upon the dust temperature, but for the moment we will assume that the 100 μm emission has been corrected for dust temperature. Of the H II, some fraction, $f \sim 30\%$, is correlated to the H I (Reynolds et al. 1995), and the remainder is not. If the H II has an emissivity of ε_{II}, then the relation between N_H and I_{100} will have a slope $\varepsilon_I + N_{HI}\frac{N_{HII}}{N_{HI}}f\varepsilon_{II}$, while there will be the added offset, $(1-f)N_{HII}\varepsilon_{II}$, and increased scatter in the I_{100}-N_{HI} relation. Finally, above some threshold, there will be the contribution of H_2, with an emissivity ε_2. The threshold over which H_2 may begin to appear will depend upon the local H I density and the radiation field, and estimates based upon the column density range from 3×10^{20} for high Galactic latitude fields (Reach, Wall, & Odegard 1998) to 5×10^{20} in general (Savage et al. 1977). The amount of H_2 on a given line of sight is, of course, but poorly correlated with H I, so points may fall within a wide region.

This pedantic exercise demonstrates the only tool (currently existing) for diagnosing the *IRAS* 100 μm emission: deviations in the I_{100}-N_{HI} relation. In the following sections we will make use of this schematic to understand limits placed on emissivities, column densities, and temperature deviations.

2.1. Review of SFD

Schlegel, Finkbeiner, & Davis (1998) (henceforth, SFD) created an optical extinction map based upon the *IRAS* and *DIRBE* 100 μm maps. The *DIRBE* map is well calibrated, but has poor resolution ($\sim 0.75°$), while the *IRAS* map has calibration problems, but much higher resolution ($\sim 6'$). Beyond destriping the *IRAS* maps, SFD adjusted the *IRAS* map by both a scale factor and an offset so that the *IRAS* map, when convolved to the *DIRBE* beam, would have the same value as the *DIRBE* 100 μm map. Thus, they obtained a 100 μm map with the *IRAS* resolution, and a calibration nearly as good as the *DIRBE* map.

To determine the relative dust column, they determined the 100μm/240μm band ratio for each pixel in the *DIRBE* map and used a ν^α emission model to determine the dust temperature from that ratio. They then determined a scaling factor X_T between the 100 μm emission at 18.2 K and the 100 μm emission the temperature of the dust. The value $X_T I_{100}$ is the amount of 100 μm emission that would be produced if all the dust were at 18.2 K, i.e., a quantity proportional to the total dust column.

There are two important caveats to be observed. First, SFD did their own Inter-Planetary Dust (IPD) removal from the *DIRBE* data set which is not quite so sophisticated as that produced by Kelsall et al. (1998). The *DIRBE* maps produced by Kelsall et al. (1998) used a sophisticated model of the IPD that relied upon the movement of the spacecraft to produce a time-varying IPD signal. The time-varying portion of the signal in any band could then be re-

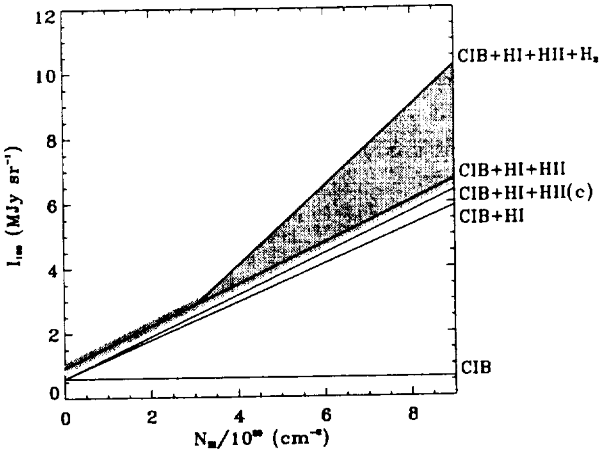

Fig. 4.2.— A schematic depiction of the source of the structure in the I_{100}-N_{HI} relation. We have assumed no temperature variation in the dust associated with H I. The emissivities and relative offsets are reasonably accurate. The shaded region contains the expected distribution of observed points.

moved with minimal effect upon the absolute zero-point. As determining the CIB was the object of this mission, this method was ideal. SFD, conversely, were interested in isolating the contribution due to the Galactic ISM, and their method explicitly removes the CIB. They assume that the spatial distribution of the IPD is well represented by the 25 μm emission, and the spatial distribution of the Galactic emission (in regions without contributions from H_2) is assumed to be well tracked by the H I, as measured by Leiden-Dwingeloo survey (Hartmann & Burton 1997). The magnitude of the IPD emission to be removed from the emission map at a band b is given by that scaling of the 25 μm emission which will minimize the scatter in the relation between band b and the H I emission. As can be seen from SFD Equation 3, a constant offset is also removed in this process[1]. The resulting map will then include *only* that emission which has the same spatial distribution as the Galactic H I.

The offset removed from *DIRBE* 100 μm image, $B_{100} = 0.62 \pm 0.04$ MJy sr^{-1}, compares favourably with the CIB value found by Arendt et al. (1998), 0.66 ± 0.017 MJy sr^{-1}. This offset contains (at least) three components; 1.) the CIB which SFD measure[2] as < 0.5 MJy sr^{-1}, 2.) the constant term of the 25 μm emission map, though this is likely small[3], < 0.12 MJy sr^{-1}, and 3.) the contribution of the uncorrelated H II. This last contribution should be quite small as, overall, the H II should have a $\csc b$ distribution similar to the overall distribution of H I.

The second caveat is that the dust temperature correction is calculated from the ratio of two differently weighted means[4] over a given line of

---

[1] Equation 3 from SFD is

$$\mathbf{D}_b^Q = \mathbf{D}_b - (\mathbf{A}_b + \mathbf{Q}_b\overline{\mathbf{D}}_{25}(\beta))\mathbf{D}_{25} - \mathbf{B}_b \qquad (4.1)$$

where bold face indicates images, and subscripts, bands. The quantity $\overline{\mathbf{D}}_{25}(\beta)$ is the mean 25 μm flux as a function of β, ecliptic latitude. The quantity $\mathbf{D}_b$ is the original *DIRBE* image in band b, and $\mathbf{D}_b^Q$ is the quantity remaining after the IPD removal process.

[2] SFD use a linear regression (as opposed to the quasi-quadratic regression in their Equation 3) to measure the CIB from all data fulfilling the condition that $\beta > 30°$ and $N_H < 200$ K km s^{-1}.

[3] The following quantity is derived by assuming that $\mathbf{D}_{25}$ is formed of two components, the IPD and a constant background. The constant flux is taken to be 192 MJy sr^{-1}, that measured by Hauser et al. (1998) in "High Quality Region B". This quantity was then propagated through SFD Equation 3.

[4] That is, emission in a given band will be

$$\int_0^\infty B_\nu(T(l))dl \qquad (4.2)$$

where B_ν is the Planck function. Thus the emission is a given band will weighted by the emission from re-

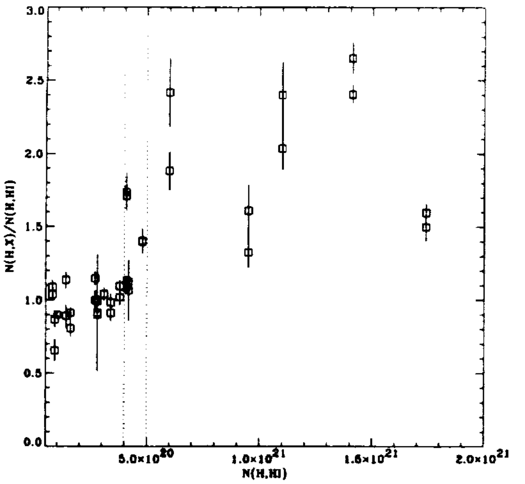

Fig. 4.3.— The ratio of X-ray detected gas to atomic gas plotted as a function of the atomic gas. N(H,X) is the amount of gas setected by X-ray absorption; N(H,HI) is the amount of gas detected by 21 cm radio observations. Note that the data points are "paired" due to there being two X-ray measures per background source. This is a recreation of the Figure 2 in AB97, whose data were kindly provided by the authors.

sight. Any single line of sight will sample several different dust temperature environments. Dust near the disk will sample its local environment, which will change rapidly with position due both to the localized nature of the heating sources and the patchy extinction. Dust at higher z will be subject to a more uniform radiation field, and large-scale variation is expected due to, for example, the Galactic bulge. (See Sodroski et al. (1997) for a detailed three-dimensional model of dust temperature.) It is not clear to what extent sampling different dust environments along the line of sight will effect the dust temperature corrections (a subject far beyond this work) but it should be taken that the dust temperature correction will, by its nature, be no more than an estimate.

2.2. H I

In order to isolate as much as possible the contribution of H I to I_{100}, we restrict ourselves to column densities below the threshold above which H_2 contamination might be expected. The value of that threshold is rather an open question. Savage et al. (1977), using *Copernicus* absorption line spectra of H_2, noted that at columns of 5×10^{20} that the molecular fraction went from negligible to 0.1. Of course, their lines of sight were primarily in the disk, so one might expect a contribution to the H I column density by gas not at all associated with the H_2 clouds, thus raising the threshold. Boulanger et al. (1996), when plotting N_{HI} *versus* I_{100} noted that below $T = 250$ K km s^{-1} ($\sim 4.5 \times 10^{20}$ cm^{-2}), that the relation was fairly tight, but over that value, the dispersion increased, presumably due to contribution from H_2. Arabadjis & Bregman (1999), in a study comparing the X-ray absorbing column, N_X, with N_{HI} in high b lines of sight noted a fairly tight correlation between N_X and N_{HI} below $\sim 5 \times 10^{-20}$ cm^{-2}, but an immediate and substantial increase in the dispersion over that value (see Figure 4.3). Reach, Wall, & Odegard (1998), using the formula in Reach, Koo, & Heiles (1994), suggest that at high b that the threshold is more $\sim 3 \times 10^{20}$ cm^{-2}.

Restricting ourselves for the moment to H I below the most restrictive threshold, we turn to Figure 4.4. Here we have plotted I_{100}/N_{HI} in the top panel for that part of the northern hemisphere with $b > 40°$. The 21 cm data were taken from the Leiden-Dwingeloo survey (Hartmann & Burton 1997) and has a 30′ resolution. The I_{100} data was taken from SFD and was smoothed to approximately the same resolution.

If we disregard those regions with $N_{HI} > 3 \times 10^{20}$ cm^{-2} (the strong white contours) we see that there is still a great deal of variation in the ratio. Reach, Wall, & Odegard (1998), using *DIRBE* data binned to 10° cells, found such variation to be greater than the statistical uncertainty, and, on the basis of 100 μm/240 μm colors, suggest that the scatter in the ratio is due to temperature variation. The strong patterning on many scales supports this conclusion. Comparison of Figure 4.4 with the bottom right panel of Figure 4.5, which incorporates the SFD dust temperature correction, suggests that whereas temperature has some effect, it does not account for the spatial pattern of the variation (unless, of course, there is some serious problem with the SFD dust temperature correction,

---

gions with the temperature at which dust will emit most strongly in that band.

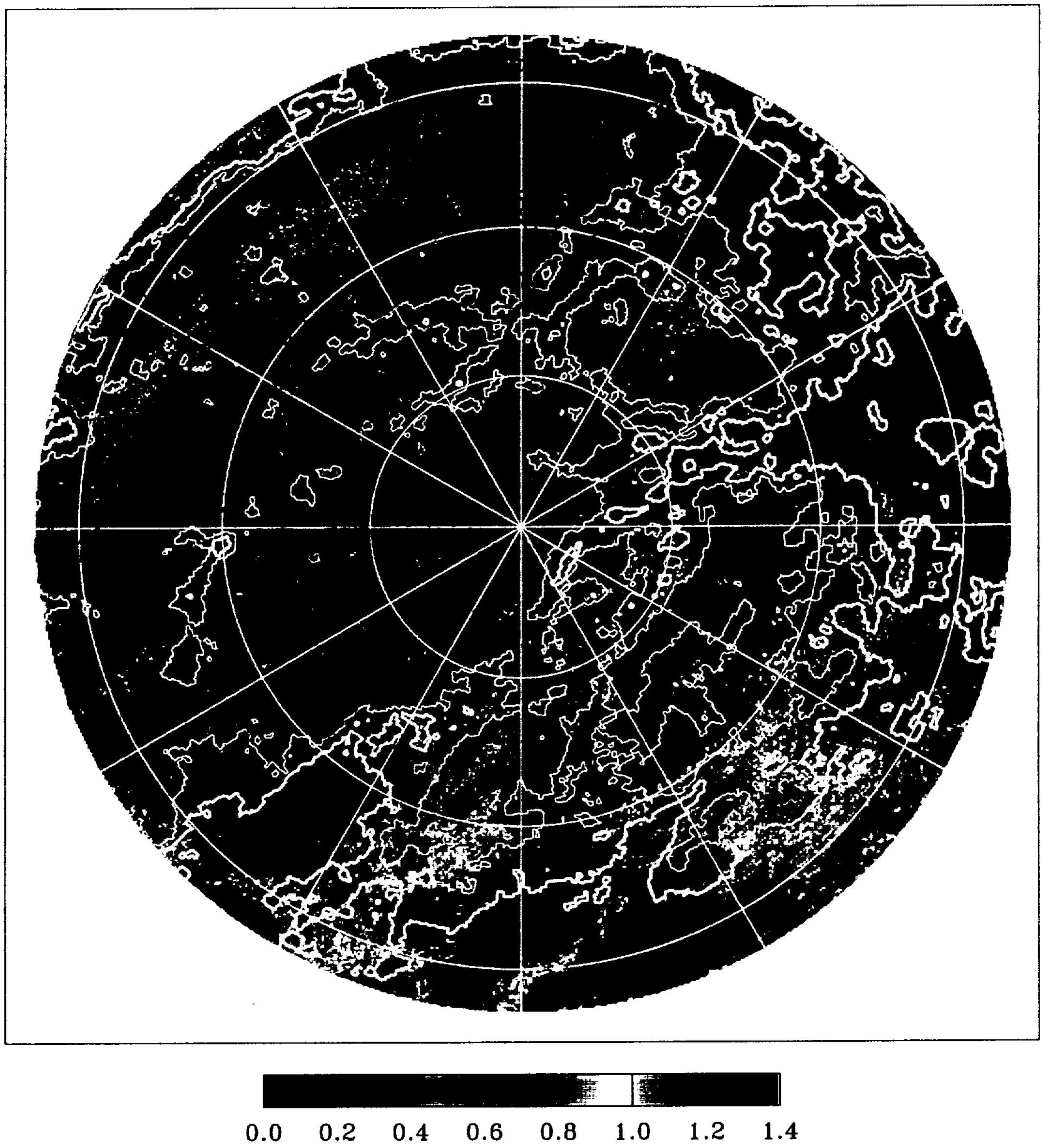

Fig. 4.4.— The angular variation of the I_{100}/N_{HI} ratio for the northern Galactic hemisphere. I_{100}/N_{HI} in Galactic coordinates for the north Galactic pole. 0° is at bottom with ℓ increasing counter-clockwise; $\Delta b = 15°$. The highest gray-scale value is 1.4 MJy sr^{-1}/10^{20} cm^{-2}. The N_{HI} is from the Leiden-Dwingeloo survey, and the column is summed over -100 km s^{-1} $\leq v \leq$ 100 km s^{-1} and represents "disk" gas. The thick white contours mark N_{HI} = 3 × 10^{20} cm^{-2}; the light white contours mark N_{HI} = 2 × 10^{20} cm^{-2}; the black contours mark the Intermediate Velocity Arch (Kuntz & Danly 1996) in -100 km s^{-1} $\leq v \leq$ -70 km s^{-1} at N_H = 10^{19} cm^{-2}. The bright region at (ℓ, b)=(316°, 51°) is the H II region surrounding Spica.

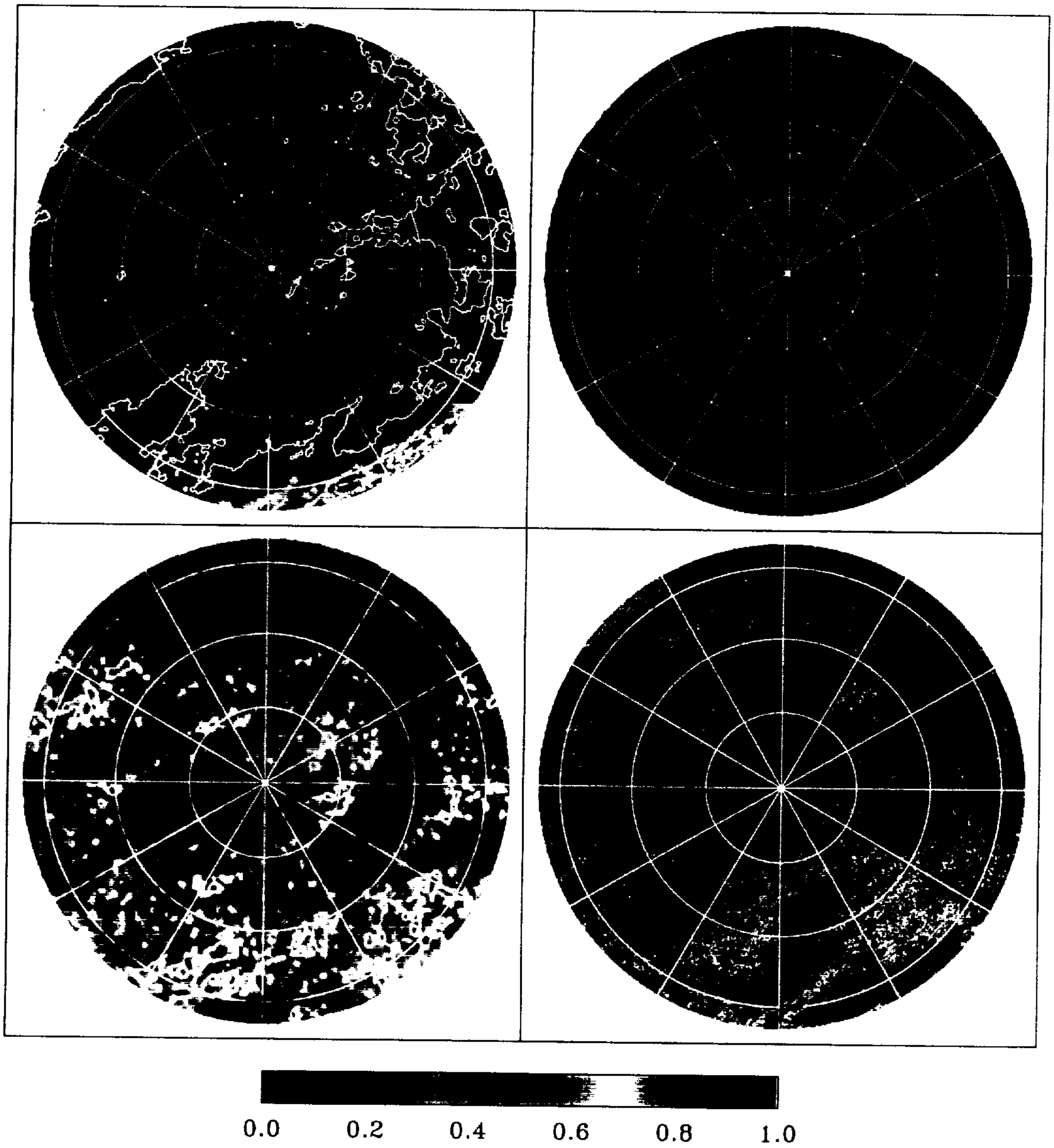

Fig. 4.5.— The angular variation of the I_{100}/N_{HI} ratio for the northern Galactic hemisphere. *Top Left:* The "disk" gas. The highest gray-scale value is 10^{21} cm^{-2}. The contours are as in the previous figure. *Top Right:* The Intermediate Velocity Arch. The highest gray-scale value is 1.5×10^{20} cm^{-2}. The contours are as in the previous figure. *Bottom Left:* The SFD dust temperature correction factor X_T. The highest gray-scale value is 1.4. *Bottom Right:* The $I_{100}/N_{HI(disk)}$ multiplied by the SFD dust temperature correction factor. The gray-scale is the same as for the previous figure.

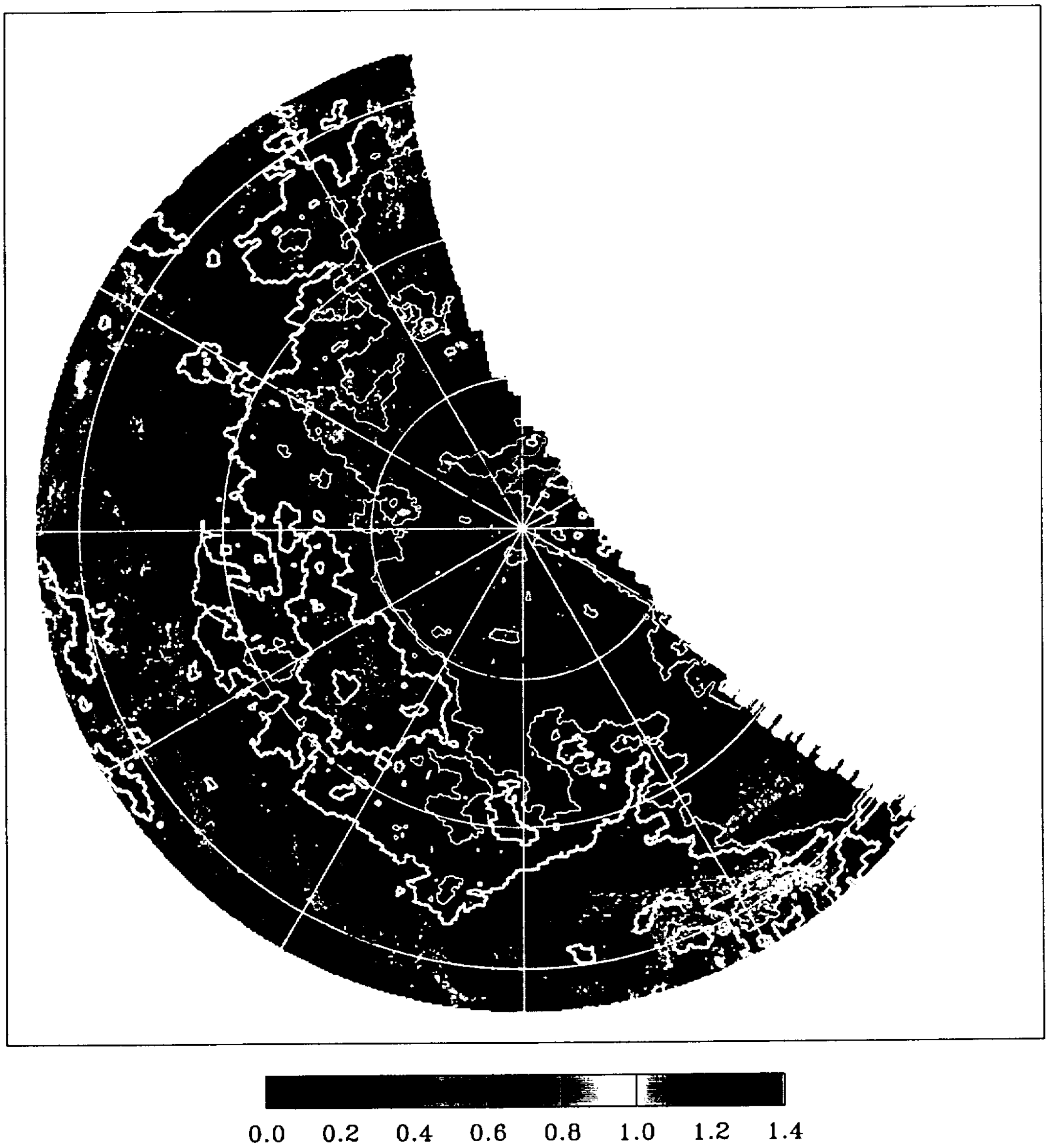

Fig. 4.6.— The angular variation of the I_{100}/N_{HI} ratio for the northern Galactic hemisphere. The panels and scales are as in the previous figures.

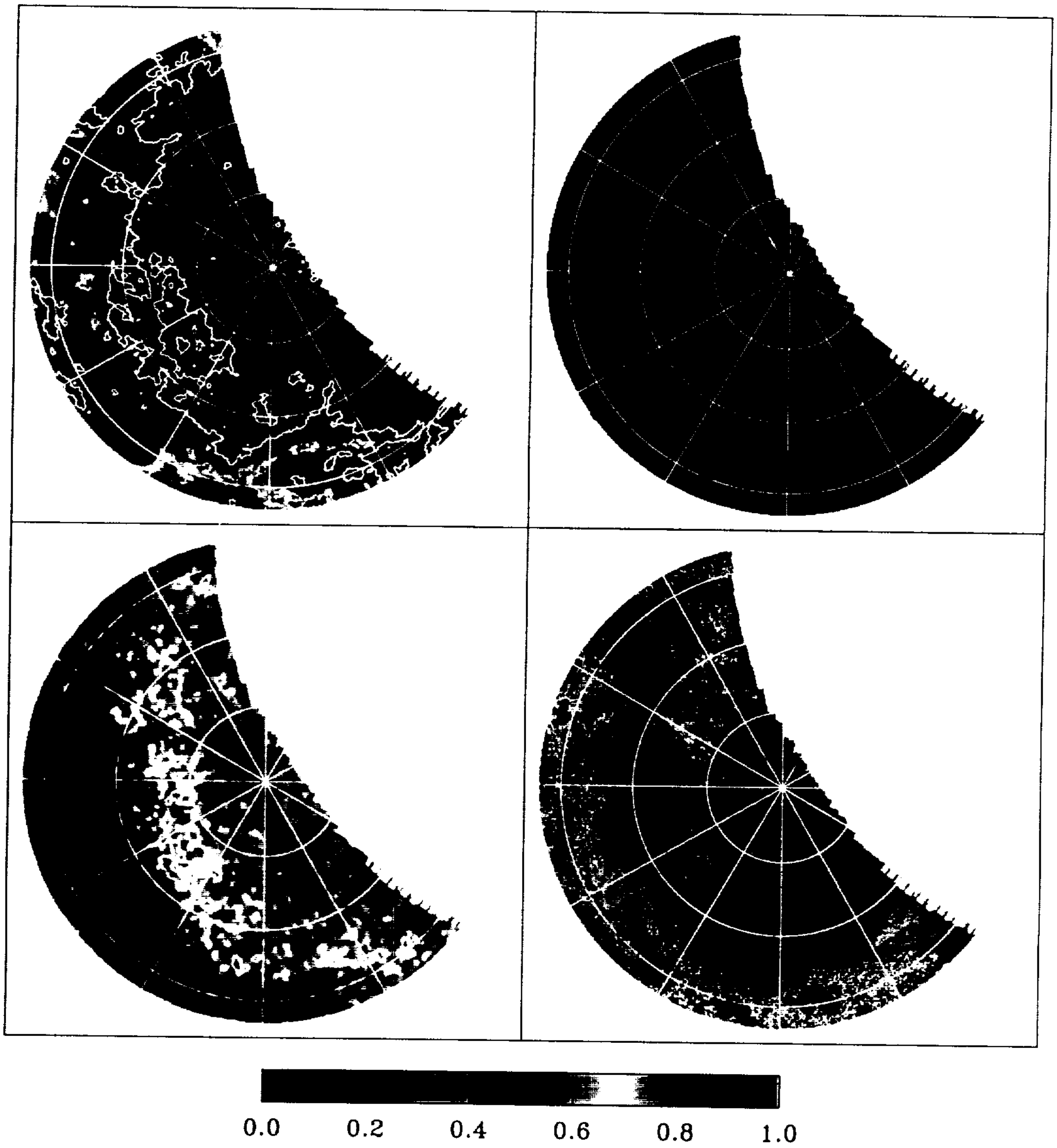

Fig. 4.7.— The angular variation of the I_{100}/N_{HI} ratio for the southern Galactic hemisphere. The panels and scales are as in the previous figure.

which it would be far outside of the scope of this chapter to attempt to diagnose).

From Figure 4.4, one can see that the I_{100}/N_{HI} ratio has some dependence upon N_{HI}, though this is suggested in only some regions and does not explain, for example, the low values in the fourth quadrant, or the low "trough" between 170° and 180°. The low "trough" can, in fact be explained by the presence of intermediate velocity gas[5] between -100 km $s^{-1} \leq v \leq$ -70 km s^{-1}. Removing this intermediate velocity gas from the N_{HI} column improves the I_{100}-N_{HI} relation in those very limited regions with intermediate velocity gas (see the lower right panel of Figure 4.5), but does not account for much of the variation.

2.3. H II

In the canonical model of the H II distribution (Reynolds 1991), the scale-height (910 pc) and planar density (0.025 cm^{-3}) of the H II has been determined from pulsar dispersion measures, which give a direct measure of n_e along the line of sight. These measures imply that $N_{HII}/N_{HI} \sim 0.33$. In the canonical model, $N_{HeII}/N_{He} \sim 0.5$ (Domgörgen & Mathis 1994), thus reducing the absorption cross-section (with respect to that of neutral gas) to 0.62. Thus, H II accounts for about 20% of the X-ray absorbing column. Using the canonical model, Arabadjis & Bregman (1999) calculate $C \equiv N_X/N_{HI} \sim 1.23$.

There have been two recent claims that the H II columns are much smaller. Both Laor et al. (1997) and Arabadjis & Bregman (1999) claim that the H I accounts for all of the absorption seen in the spectra of extragalactic objects. Arabadjis & Bregman (1999) in particular, measure the ratio N_X/N_{HI} (see Figure 4.3) for thirteen lines of sight with $N_{HI} < 5 \times 10^{20}$ cm^{-2} and find the mean $N_X/N_{HI} = 0.972 \pm 0.022$; their 99% confidence interval upper limit to C is 1.023. There are two reasons for suspecting this result. First, if there were no H II the physical lower limit of N_X/N_{HI}, C, must be unity. In order for the uncertainties in N_X/N_{HI} to be consistent with this physical limit, they must be increased by a factor or 2.7. Increasing the uncertainty by this factor expands the upper limit of C to 1.11, allowing for $N_{HII}/N_{HI} \sim .18$, which is still low, but not so shockingly so. The published results of Laor et al. (1997) do not allow a similar re-analysis.

Both Laor et al. (1997) and Arabadjis & Bregman (1999) determined the X-ray absorbing column through spectral fits; Laor et al. (1997) using quasar spectra and Arabadjis & Bregman (1999) using galaxy cluster spectra. Given that these fits were made on objects with different spectral types it is difficult to ascribe the results to systematic problems with the fitting. Both groups propose that their results suggest that the He associated with the H II must appear mostly in the form of He III in order to avoid significant X-ray absorption. It is also suggested that the H II observed by the Reynolds group is not the same H II that produces the pulsar dispersion measures.

A full discussion of this possibility is beyond the scope of this work, but a few obvious considerations can be made. Reynolds (1985) measured a temperature of ~ 8000 K for local ($r < 1$ kpc, $b < 30°$) H II using the forbidden line ratio [S II]/Hα. For one not-so-local field ($r < 3.8$ kpc, $b \sim 20°$) (Reynolds et al. 1995) a similar temperature was determined from Hα line widths. This field would suggest that the spectroscopically observed H II is the same as that seen in the pulsar dispersion measures, but no significant conclusion can be drawn. Conversely, if the H II observed by pulsar dispersion measures has He III/He ~ 0.5, it must have $\log T > 4.8$ (collisional ionization equilibrium) or $\log T > 4.1$ (isochorically cooling gas) according to the calculations of Schmutzler & Tscharnuter (1993). The latter temperature is suggestive given that the cooling curve for an isochoric gas has a minimum at $\log T = 4.0$. In either case, the gas is entering the regime where it may

---

[5] This particular part of the IV gas defines the backbone of the Intermediate Velocity Arch (Kuntz & Danly 1996), and is morphologically related to both lower and high velocity gas. The HVC gas has not been detected at 100 μm despite careful searches (Wakker & Boulanger 1986). Thus, it is not surprising that the intermediate velocity gas might be deficient as well. It is far from clear whether the high velocity clouds are deficient in dust due to grain destruction or whether the temperature of the dust is such that the emission at 100 μm is too small to be teased out of the much larger signal due to the disk gas. The deficiency is not a deficiency in the materials from which to make dust; in detecting high velocity complex M in absorption with *IUE*, Danly, Albert, & Kuntz (1993) showed that at least some of the high velocity clouds are not metal deficient.

be *producing* X-rays that would "fill in" the expected absorption.

For a worst-case scenario, we will continue to assume that the H II is described by the canonical model. For the canonical model some fraction of the H II, as measured by Hα, is correlated with the H I. Thus, the amount of spatial variation in the component of the ISM that is traced only by H II will contain only $\sim$ 12% of the X-ray absorbing column. Of than portion, some portion may be spatially variant, the remainder lost in the uncertainty of the offset.

How well is this component traced by I_{100}? Boulanger et al. (1996), after removing the contribution to I_{100} by H I, searched for any $\csc b$ dependence in the residuals (such as one might expect from the uniform plane-parallel distribution of H II) and found none. Fixsen et al. (1998) attempted to correlate the I_{100} with both H I 21 cm and [C II] 158 μm (as a tracer of H II), and found little emission correlated with [C II] (Arendt et al. 1998). The *COBE* team concentrating on the Galactic emission attempted to determine the emissivity of the H II related gas by fitting

$$I_{100} = \varepsilon_I N_{HI} + \varepsilon_{II} N_{HII} + CIB \qquad (4.3)$$

where N_{HII} was determined from some combination of Hα and dispersion measures for a slected number of lines of sight. Their 3σ upper limit to $\varepsilon_{II}/\varepsilon_I = 0.75$. This value suggests that the total contribution by H II to I_{100} is $\leq 20\%$, and the component that is uncorrelated with H I will contribute $\leq 13\%$.

Thus, the upper limit to the contribution by H II to X-ray absorption is of the same order as the upper limit to its contribution to I_{100}, due to the fact that, by chance, $\varepsilon_{II}/\varepsilon_I \sim \sigma_{II}/\sigma I$, where σ_a is the absorption cross-section of component a. However, since these are upper limits, I_{100} may trace H II much more poorly than does its X-ray absorption, or *vice versa*.

2.4. H$_2$

Given all of the difficulties encountered below the molecular threshold, it might seem foolish to even attempt deabsorption for regions over the threshold. However, X-ray absorption by molecular clouds holds great promise for determining total molecular content (Snowden, McCammon, & Verter 1993; Herbstmeier, Heithausen, & Mebold 1993; Mortiz et al. 1998; Kuntz, Snowden, & Verter 1997), and such studies often use 100 μm emission as a tracer of the total gas content. Thus, there are some valid reasons for pushing into the realm of the absurdly uncertain.

The molecular gas can be detected at some threshold in plots of I_{100} *versus* N_{HI} as a spray of points above the linear I_{100}-N_{HI} relation established at even lower column densities (see Figure 4.2). This effect can be seen in the plot of N_X/N_{HI} *versus* N_{HI} from Arabadjis & Bregman (1999) (Figure 4.3 and Figure 4.8), where the molecular column is seen as an excess of N_X for $N_H \sim 4 \times 10^{20}$ cm^{-2}. Using N_X as a measure of the total column density, we plot N_X *versus* I_{100} in Figure 4.8. The dotted line represents the best fit to the I_{100}-N_X relation for data points without molecular contamination; the points with substantial molecular components fall far above the line and have a substantial scatter around a fit to all of the data (dotted line). It is well known that this is due to 1.) a substantially different dust temperature between neutral and molecular regions and 2.) a substantial spread in temperatures between different molecular regions. SFD attempted to correct the I_{100} for dust temperature; just how well did they do?

Our reanalysis uses the N_X data published in Arabadjis & Bregman (1999). To make a consistent comparison between I_{100} and XI_{100}, we re-extracted the values of I_{100} from the SFD maps and extracted the values of X_T from the same regions. A comparison of our value of I_{100} and that used by Arabadjis & Bregman (1999) (and kindly provided by Dr. Arabadjis) shows only some minor differences, presumably due to different extraction/averaging procedures. The uncertainties used are those published for the N_X and, for the I_{100}, the RMS of the pixels within the extraction region.

The fits to the N_X-I_{100} and N_X-$X_T I_{100}$ relations were made using the BCES($N_X|(X_T)I_{100}$) estimator of Akritas & Bershady (1996), and the uncertainties were estimated using the bootstrap method[6]. The results are shown in Figure 4.9. When fitting to $X_T I_{100}$, we do not use the val-

---

[6] The BCES($X|Y$) estimator finds the best fit to Y given X under the assumption that both variables have uncertaintes and that both variables have intrinsic scatter.

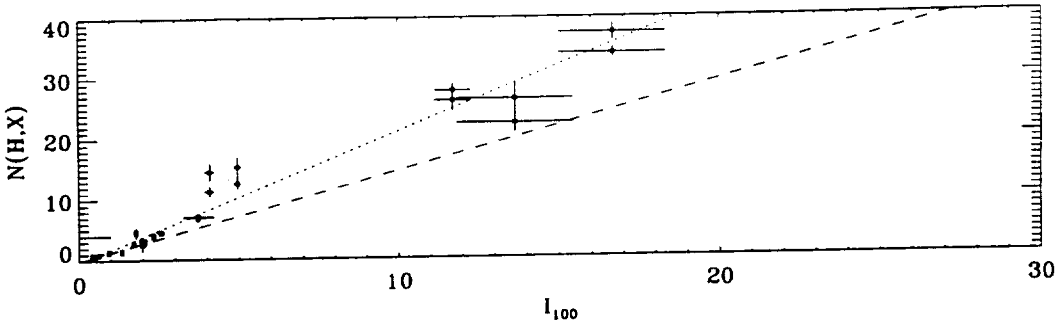

Fig. 4.8.— The amount of gas detected by X-ray absorption *versus* the SFD I_{100} measure of the dust column. The *dashed* line is the fit to points with N(H,X) < 4×10^{20}, the *dotted* line is the fit to all points. We have plotted boxes around the points to aid the eye in distinguishing those with the smallest uncertainties.

ues directly extracted from the SFD data sets. SFD warn that at high Galactic latitudes, where the I_{100} emission is low (and by extension, the I_{140} and I_{240} emission is small) the dust temperature correction factor, X_T will be poorly determined. This is not disastrous, as these regions, having low dust columns, are unlikely to have a substantial molecular component, and so the correction is likely close to unity. Therefore, for the purposes of fitting, we have taken the mean of the X_T values for all points where $X_T < 1.3$ and divided all the X_T values by this mean. For $X_T < 1.3$ we have set $X_T = 1.0$. This removes the large uncertainties for the X_T values near unity in a consistent manner. Since our mean X_T for $X_T < 1.3$ was slightly greater than unity, we will be slightly underestimating the X_T at higher values.

When fitting $X_T I_{100}$ (in opposition to fitting just I_{100}), the difference in emissivity per H atom between the fits using all of the data and fits using data from below the N_H threshold becomes less, and the 1 σ uncertainty regions for the slopes come closer to overlapping. Clearly, the X_T correction is an improvement, and one can see that the dispersion of the data over the molecular threshold has decreased. However, the X_T correction, despite the fact that we have decreased its magnitude slightly to improve the signal-to-noise, is a bit too large. Clearly, increasing the data set will be necessary before determining the correctness of X_T.

The results of the fits are given in Table 4.1 to demonstrate the above trend in a more quantitative manner. The parameters for fitting $N_X = A + BI_{100}$ using only data with $N_X < 4 \times 10^{20}$ cm^{-2} are particularly useful and will be used in the summary to calculate the uncertainties in equivalent X-ray absorbing columns from 100 μm emission.

3. Implications

A summary of the uncertainties in tracing the X-ray absorbing column is given in Table 4.2.

1.) The 100 μm emission traces the H I very well over many degree scales. However, dust temperature effects limit its usefulness over areas less than a few degrees, as there is clear structure on scales down to the resolution limit in maps of I_{100}/N_{HI} in regions with no molecular component. This structure may also be due to H II.

2.) In regions with high or intermediate velocity gas, the I_{100} measure will underestimate the total column due to the well known dust emission deficiency of high velocity gas. This deficiency seems to exist for the higher velocity parts of the Intermediate Velocity Arch, and further work will be necessary to see if it is true for the ~ -60 km s^{-1} gas as well.

3.) H II is poorly traced by I_{100} as the emis-

The bootstrap method of determining the uncertainty in the fit parameters takes an arbitrarily large number of subsamples of the data, fits each sub-sample, and determines the statistical properties of the resulting fit parameters.

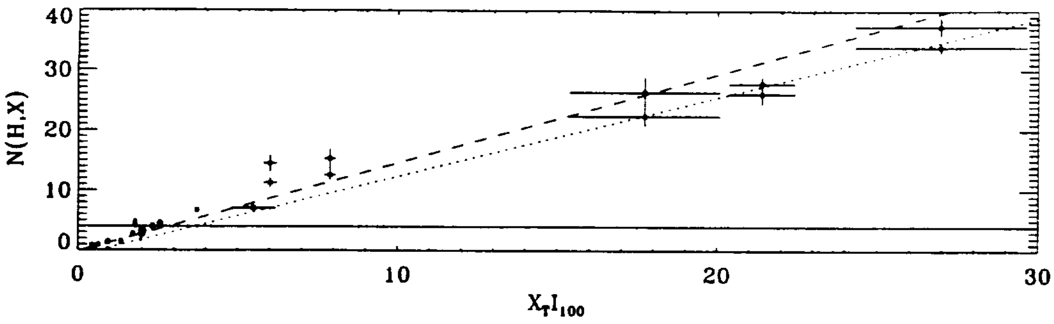

Fig. 4.9.— The amount of gas detected by X-ray absorption *versus* the SFD $X_T I_{100}$ measure of the dust column. The *dashed* line is the fit to points with N(H,X) < 4 × 10^{20}, the *dotted* line is the fit to all points.

sivity per H atom appears to be much smaller in H II than in H I. The impact of this difficulty may be ameliorated by substantial decrease in the absorption cross-section of gas related to H II.

4.) The SFD dust temperature correction offers a substantial improvement in obtaining rough absorption measures for regions with molecular components. The SFD dust temperature correction does not adequately correct I_{100} from diffuse neutral gas, perhaps due to the low emission values of such gas.

5.) Given that there is no all-sky H I survey with resolution smaller than 30′, the best projected survey of H II has a 1° resolution, and surveys of H_2 (through its CO surrogate) have a 1° sampling, the *IRAS* 100 μm survey remains the only tracer on scales between 5′ and 30′.

We will explore the efficacy of using the *IRAS* 100 μm survey on sub-degree scales in the following chapter.

REFERENCES

Akritas, M. G., & Bershady, M. A. 1996, ApJ, 470, 706

Arabadjis, J. S., & Bregman, J. N. 1999, ApJ, 510, 806, submitted

Arendt, R. G., et al. 1998, ApJ, 508, 74

Boulanger, F., Abergel, A., Bernard, J.-P., Burton, W. B., Désert, F.-X., Hartmann, D., Lagache, G., & Puget, J.-L. 1996, A&A, 312, 256

Danly, L., Albert, C. E., & Kuntz, K. D. 1993, ApJ, 416, L29

Domgörgen, H., & Mathis, J. S. 1994, ApJ, 428, 647

Fixsen, D. J., Dwek, E., Mather, J. C., Bennett, C. L., & Shafer, R. A. 1998, ApJ, 508, 123

Hartmann, D., & Burton, W. B. 1997, Atlas of Galactic Neutral Hydrogen (Cambridge University)

Hauser, M. G., et al. 1998, ApJ, 508, 25

Herbstmeier, U., Heithausen, A., & Mebold, U. 1993, A&A, 272, 514

Kelsall, T., et al. 1998, ApJ, 508, 44

Kuntz, K. D., & Danly, L. 1996, ApJ, 457, 703

Kuntz, K. D., Snowden, S. L., & Verter, F. 1997, ApJ, 484, 245

Laor, A., Fiore, F., Elvis, M., Wilkes, B. J., & McDowell, J. C. 1997, ApJ, 477, 93

Mortiz, P., Wennmacher, A., Herbstmeier, U., Mebold, U., Egger, R., & Snowden, S. 1998, A&A, 336, 682

Reach, W. T., Koo, B.-C., & Heiles, C. 1994, ApJ, 429, 672

Reach, W. T., Wall, W. F., & Odegard, N. 1998, ApJ, 507, 507

Reynolds, R. J. 1985, ApJ, 333, 341

Reynolds, R. J. 1991, in The Interstellar Disk-Halo Connection in Galaxies, ed. H. Bloemen, 67

Reynolds, R. J., Tufte, S. L., Kung, D. T., McCullough, P. R., & Heiles, C. 1995, ApJ, 448, 715

Savage, B. D., Bohlin, R. C., Drake, J. F., & Budich, W. 1977, ApJ, 216, 291

Schlegel, D. J., Finkbeiner, D. P., & Davis, M. 1998, ApJ, 500, 525

Schmutzler, T., & Tscharnuter, W. M. 1993, A&A, 273, 318

Snowden, S. L., McCammon, D., & Verter, F. 1993, ApJ, 409, L21

Sodroski, T. J., Odegard, N., Arendt, R. G., Dwek, E., Weiland, J. L., Hauser, M. G., & Kelsall, T. 1997, ApJ, 480, 173

Wakker, B. P., & Boulanger, F. 1986, A&A, 170, 84

TABLE 4.1
FITS TO $N_X = A + B(X)I_{100}$

Fit[a]	A[b] Fit (Bootstrap)[e]	B[c] Fit (Bootstrap)	CIB[d]
		I_{100}	
$N_H < 4e20$	-0.019 ± 0.098 (0.016 ± 0.128)	1.477 ± 0.079 (1.490 ± 0.096)	-0.003 ± 0.139 (0.022 ± 0.149)
$N_H < 5e20$	-0.192 ± 0.119 (0.072 ± 0.259)	1.755 ± 0.086 (1.769 ± 0.100)	0.312 ± 0.121 (0.111 ± 0.316)
All	-0.473 ± 0.299 (0.355 ± 0.481)	2.161 ± 0.094 (2.164 ± 0.105)	0.298 ± 0.096 (0.102 ± 0.304)
		XI_{100}	
$N_H < 4e20$	-0.019 ± 0.098 (0.012 ± 0.109)	1.477 ± 0.079 (1.493 ± 0.077)	-0.003 ± 0.139 (0.034 ± 0.181)
$N_H < 5e20$	-0.192 ± 0.119 (0.049 ± 0.216)	1.755 ± 0.086 (1.758 ± 0.093)	0.312 ± 0.121 (0.117 ± 0.323)
All	0.825 ± 0.242 (0.708 ± 0.457)	1.318 ± 0.039 (1.329 ± 0.054)	-0.773 ± 0.174 (0.583 ± 0.496)

[a] This column lists which portion of the data was used for the fit.

[b] 10^{20} cm^{-2}

[c] 10^{20} cm^{-2} (MJy sr^{-1})$^{-1}$

[d] *Residual* CIB in the SFD 100 μm data set. MJy sr^{-1}

[e] Result of the bootstrap analysis.

TABLE 4.2
UNCERTAINTIES IN EQUIVALENT ABSORBING COLUMNS

Source	Full Field[a] cm^{-2} (original units)	Variation within Field[b] cm^{-2} (original units)
I_{100} Offset	±6.35 × 10^{18} (±0.43 MJy sr^{-1})[c]	None
Columns not traced by I_{100}		
H II[d]	$(1 - f)N_{HII}\sigma_{HII}/\sigma_{HI}$ $= 0.30 \times 10^{20} \csc b$	$(1 - f)N_{HII}\sigma_{HII}/\sigma_{HI}$ $= 0.30 \times 10^{20} \csc b$
H II[e]	$0.16 \times 10^{20} \csc b$	$0.16 \times 10^{20} \csc b$
IV gas	Position Dependent	Calculable from N_{HI}
ϵ_I Variation	None as a local ϵ_I can be determined from the data	TBD
H_2	None for $I_{100} < 2$ MJy sr^{-1}	Suspect areas can be removed

[a] On the order of 10° × 10°.

[b] Scales 2° to 4°.

[c] Calculated from the SFD uncertainty in the offset using the N_X/I_{100} ratio 1.49 determined by the fit to the Arabadjis & Bregman (1999) data listed in Table 4.1.

[d] Assuming the canonical model of the H II layer.

[e] Assuming the low H II absorption suggested by Arabadjis and Bregman (1999).

Chapter 5: The Spectrum of the SXRB

Abstract

The soft X-ray background in the 0.1-1.0 keV band is known to be produced by at least three sources; the Local Hot Bubble (LHB), the extragalactic power law (EPL), and a seemingly Galactic component that lies outside the bulk of the absorption that is due to the ISM of the Galactic disk. This last component, which we call the Trans-Absorption Emission (TAE), has been modeled by a number of groups who have derived disparate measures of its temperature. The differences have arisen from differing assumptions about the structure of the emitting gas and unrecognized methodological difficulties.

We find that spectral fitting methods do not uniquely separate the TAE from the foreground emission that is due the LHB, but the angular variation of the absorption can be used to break this degeneracy. However, large-scale deabsorption studies that have used this variation to determine the strength of the TAE have all had serious flaws, most notably, the lack of sufficient energy coverage.

1. Introduction

The canonical model of the soft X-ray background (0.1-1.0 keV) posits a Local Cavity (in the H I of the Galactic disk) that is filled, at least in part, by hot gas emitting mostly in the $\frac{1}{4}$ keV band. This region of X-ray emitting gas is known as the Local Hot Bubble (LHB). The LHB emission is absorbed by the nearby very tenuous Local Interstellar Cloud (LIC), otherwise known as the Local Fluff. Beyond the Local Cavity there are thicker layers of absorbing gas which partially absorb emission from an isotropic extragalactic component and emission from at least one other component. This latter component we will call the "trans-absorption emission" (TAE) or the "distant component". The local component and the distant component are usually modeled as thermal plasmas. The isotropic extragalactic component, which is most clearly seen at E > 1 keV, and is presumably due to the accumulation of unresolved point sources, is modeled as a power-law, and will be referred to as the Extragalactic Power Law (EPL). The distant component is required to contribute to the observed excess over the extrapolation of the EPL in both the $\frac{1}{4}$ keV and $\frac{3}{4}$ keV bands.

Table 5.1 contains a compendium of measures of the temperature of the thermal components using various techniques. The *ROSAT* measures alone show a wide dispersion. In particular, PSPC spectral fitting produces lower LHB temperatures and higher halo temperatures than do early broad-band measures and PSPC broad-band deabsorption measures. In order to understand the source of this difference, the next section assumes the canonical model and explores the limitations of the methods used for determining the parameters of that model.

We find that although a portion of the difference is due to inadequacies in the spectral fitting method, the bulk of the difference is due to assumptions about the nature of the distant component. Most investigators have assumed that the TAE is due to a single-temperature Galactic halo. We find that none of the existing single-component models satisfies all of the constraints placed upon the data by the angular variation of the absorption of the TAE.

2. Analysis of Previous Results

Using the canonical model described above, several efforts have been made to determine the spectrum of the soft X-ray background. We divide these methods into two groups; spectral fitting of individual PSPC pointings, and all-sky deabsorption of broad-band images. In both of these cases, the data were fit to the function

$$I_O = I_L e^{-(N_f)\sigma(\nu,N_f,S)}$$

TABLE 5.1
COMPENDIUM

Source	T_L		T_{D1}		T_{D2}		Method[a]
	keV	$\log T$	keV	$\log T$	keV	$\log T$	
			Pre-ROSAT Results				
Bloch et al. (1986)	0.077-0.097	5.95-6.05	...	...	...	...	BB
Juda et al.(1991)	0.054-0.136	5.8-6.2	...	...	...	...	BB
Snowden et al. (1990)	0.086	6.0	...	...	...	...	BB
			ROSAT Era Results				
Chen, Fabian & Gendreau (1997)	0.05	5.76	0.12	6.14	...	...	SF
Kerp(1994)	$0.061^{+0.016}_{-0.015}$	5.85 ± 0.1	$0.172^{+0.045}_{-0.035}$	6.3 ± 0.1	...	...	DA
Miyaji et al.(1998)	.057-.09	5.82-6.02	0.142-0.148	6.217-6.233	...	...	SF
Peitz et al.(1998)[b]	...	...	0.135	6.195 ± 0.05[b]	...	...	SF/DA
Sidher(1996)[c]	...	...	0.137(0.216)	6.2 (6.4)[c]	...	...	SF/DA
Snowden et al.(1998)[d]	$0.119^{+0.034}_{-0.012}$	$6.14^{+0.11efg}_{-0.05}$	$0.106^{+0.022}_{-0.018}$	$6.09^{+0.08e}_{-0.08}$	...	...	DA/BB
Snowden et al.(2000)[h]	$0.119^{+0.034}_{-0.024}$	$6.14^{+0.11efg}_{-0.10}$	$0.100^{+0.033}_{-0.030}$	$6.07^{+0.12e}_{-0.16}$	...	...	DA/BB
			ROSAT Results - This Work				
Hyades	$0.103^{+0.002}_{-0.002}$	$6.08^{+0.01i}_{-0.01}$	...	...	...	...	BB
Galactic Plane	$0.108^{+0.005}_{-0.007}$	$6.11^{+0.02ei}_{-0.03}$	...	...	...	...	BB
Chap. 6 §6.1	$0.118^{+0.038}_{-0.023}$	$6.11^{+0.18ef}_{-0.07}$	$0.098^{+0.058}_{-0.037}$	$6.06^{+0.19e}_{-0.20}$	$0.250^{+0.079}_{-0.045}$	$6.46^{+0.12e}_{-0.08}$	DA/BB
Chap. 6 §6.1.4	0.108 ± 0.04	6.10 ± 0.02	0.087 ± 0.003	6.00 ± 0.02	0.180 ± 0.008	6.32 ± 0.02	SF
Chap. 6. §6.1.4	0.127 ± 0.010	6.17 ± 0.03	0.313 ± 0.055	6.56 ± 0.07	...	...	SF
			Post-ROSAT Results				
Parmar et al.(1999)[k]	$0.137^{+0.011}_{-0.022}$	$6.2^{+0.03}_{-0.07}$	$0.7^{+0.4}_{-0.3}$	$6.91^{+0.20k}_{-0.24}$	...	...	SF

[a] BB - Broad-Band Ratios, SF - Spectral Fitting, DA - De-Absorption

[b] Temperature derived from the Mewe-Kaastra (Mewe, Gronenschild, & van den Oord 1985) code. A fit of a Raymond & Smith (1977) spectra to the Mewe-Kaastra spectrum absorbed by 1.5×10^{20} cm^{-2} and folded through the *ROSAT* PSPC response yielded a Raymond & Smith plasma temperature of $\log T = 6.18$. If a Mewe-Kaastra-Leidahl spectrum were used rather than a Mewe-Kaastra spectrum, the Raymond & Smith plasma temperature would be $\log T = 6.17$.

[c] Temperatures derived from the Landini & Monsignori-Fossi (Landini & Monsignori-Fossi 1990) code. Sidher et al. note that Raymond & Smith code would produce a $\log T_D = 6.4$.

[d] A second, hotter component is implied, but not explicitly characterized in this paper. The values given here are not quite the values given in the original paper. Those values had been calculated from band ratios using an older detector response matrix; we have used the current detector response matrix.

[e] Cited range is the FWHM of the distribution. These distributions are dominated by fit and/or data uncertainties; the distribution of temperatures is very narrow. See text §4 for a fuller explanation.

[f] The upper limit is not given by the upper FWHM of the distribution but by the highest R2/R1 ratio permitted by an unabsorbed Raymond & Smith spectra.

[g] These LHB temperatures have not taken into account absorption within the LHB. Assuming an absorbing column $\sim 4 \times 10^{18}$ cm^{-2}, the temperatures drop by $\Delta \log T \sim 0.01$.

[h] This paper assumed a second, hotter component with $\log T_{D2} \sim 6.4$.

[i] This temperature was derived in the anti-center. Snowden, Schmitt, & Edwards (1990) showed that the temperature of the LHB depends upon Galactic longitude, with Galactic center directions having slightly higher temperatures than the Galactic anti-center.

[k] Result obtained with the BeppoSAX LECS. The temperatures were derived using the Mewe-Kaastra-Liehdal code. These results should not be compared to the current work because the Parmar et al. (1999) data selection does not well sample the Galactic halo and the fit methodology does not consider some known physical constraints. The fitted spectrum was the sum of spectra from many locations on the sky. All of the spectra were from relatively low Galactic latitude, most have absorbing columns $> 3 \times 10^{20}$, making the detection of the soft TAE component difficult. When the spectra were fitted individually, the TAE component was fixed to $\log T = 6.9$, rather than being fitted in a simultaneous fit. The foreground absorption used for the LHB component, 7×10^{19} cm^{-2}, is unreasonably high.

$$
\begin{aligned}
&+I_D e^{-(N_b)\sigma(\nu,N_b,S)} \qquad (5.1)\\
&+I_E e^{-(N_b)\sigma(\nu,N_b,S)}
\end{aligned}
$$

where I_O is the observed X-ray flux, I_L is the local (LHB) X-ray emission which may be absorbed by an intervening layer of column N_f, I_D is the distant emission (TAE) and I_E is the contribution due to the EPL. Both the distant and extragalactic components are absorbed by a column N_b. The quantity σ is the absorption cross-section. In the case of spectral fitting, σ is dependent only upon energy (ν), but for broad-band deabsorption we use the *effective* cross-section for a given band which is dependent both upon the magnitude of the absorbing column (N), and upon the spectral shape of the background emission (S).

2.1. Spectral Fitting

Several groups (e.g., Chen, Fabian, & Gendreau 1997 and Miyaji et al. 1998) have attempted to fit the spectrum of the X-ray background as observed in individual PSPC pointings. Attention has focused upon determining the index of the EPL; determination of the temperatures and normalizations of the two thermal components has been incidental. Due to this focus, the *ROSAT* PSPC data have usually been supplemented with *ASCA* observations of the same field in order to gain a greater lever arm for fitting the EPL. Fitting the thermal components is more problematic.

The thermal components occupy only a very limited spectral region in the *ROSAT* range; the emission lies mostly within 0.1-0.4 keV, which is completely outside of the *ASCA* range. At these energies, absorption, and the uncertainty due to its correction, is much greater. Also greater are the non-cosmic contaminants; the Long Term Enhancement (LTE) and the Scattered Solar X-rays (SSX). The LTE is a particular problem for PSPC pointed observations as adequate removal requires a light curve extending over (at minimum) several weeks to months (Snowden et al. 1995; Snowden et al. 1994). Much of the disagreement between different spectral fits has been attributed to inadequate non-cosmic background removal (Miyaji et al. 1998).

Inadequate spectral resolution is also a problem. There are only about five independent spectral resolution elements in the *ROSAT* PSPC energy band, and only three spanning the energies emitted by the thermal components. Thus, even given some *a priori* model of the EPL, the four fit parameters necessary to describe two thermal components are under-determined. In practice, the situation is even worse. Figure 5.1 shows the Raymond & Smith (1977) spectra for three representative thermal components, and a maximal set of independent resolution elements. (As with all future references to the Raymond & Smith spectra in this paper, except in the context of XSPEC, we are using the 1991 release with cosmic abundances.) The bulk of the emission is contained in ~ 2 resolution elements.

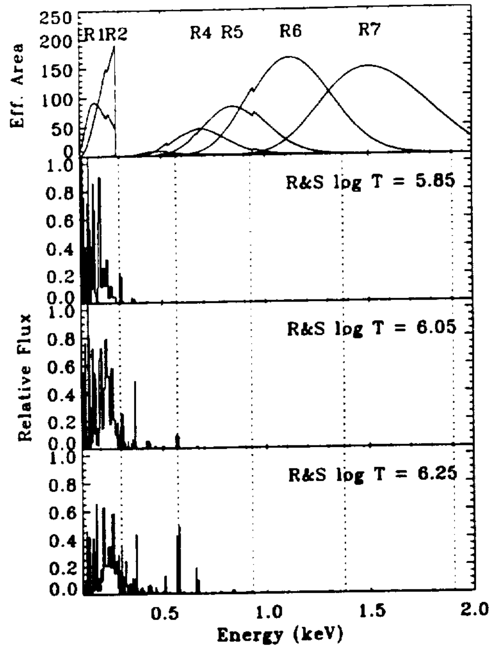

Fig. 5.1.— A comparison of the spectra of thermal components with the available independent spectral elements for the *ROSAT* PSPC. *Top:* the *ROSAT* PSPC band response functions. *Below:* Three thermal spectra spanning the range of temperatures found in the literature. The vertical lines show the divisions between independent spectral resolution elements, i.e., elements with non-overlapping FWHM. The bulk of the emission from Galactic thermal components falls almost entirely within two independent spectral resolution elements.

At the risk of appearing to labour the point, consider the following. The six standard *ROSAT*

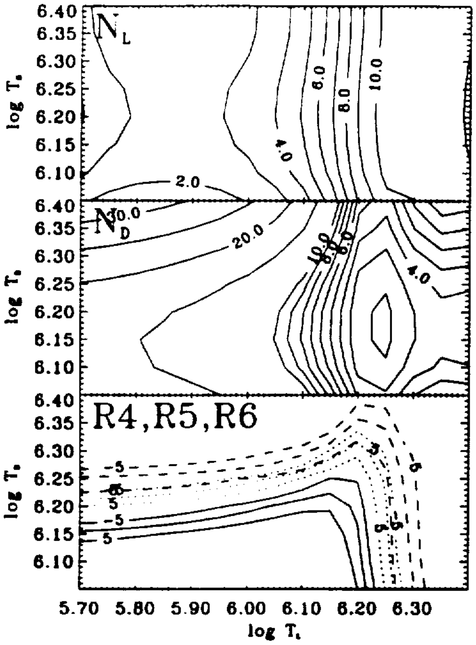

Fig. 5.2.— The degeneracy in the thermal component fit parameters. We have used a "mean" high Galactic latitude background spectrum with a mean absorbing column (N_b) of 1.21×10^{20} cm^{-2} (and $N_f = 0$), have assumed a Chen, Fabian & Gendreau (1997) EPL (their Model A), and have assumed a single-temperature distant component. *Top:* The range of normalizations required for the local emission component, in units of 1000 $n_e n_p L$ (n_e and n_h in cm^{-3} and L in pc), as a function of the local and distant component temperatures. *Middle:* The same as above for the distant component. *Bottom:* The region of parameter space allowed by the R4, R5, and R6 band fluxes, allowing a $\pm 5 \times 10^{-6}$ counts s^{-1} arcmin^{-2} uncertainty in the fluxes. *Solid:* R4, *Dotted:* R5, and *Dashed:* R6. Results are similar for other EPL models, though no EPL model can force the three regions to have significant overlap.

PSPC bands R1-R7 (the R1 and R2 bands forming the $\frac{1}{4}$ keV band, the R4 and R5 bands forming the $\frac{3}{4}$ keV band, and excluding R3 as usual, Snowden et al. 1995) contain all of the information in the PSPC spectrum. The bulk of the information about the thermal components is contained in the R1 and R2 bands. Using only the R1 and R2 bands, given the absorbing column and the EPL, one can choose (within reason) any pair of local and distant temperatures, T_L and T_D, and find some pair of normalizations N_L and N_D that provide the observed R1 and R2 band values. Figure 5.2 shows the ranges of normalizations required over a reasonable range of T_L and T_D[1].

Also shown in Figure 5.2 is the region allowed by the R4, R5, and R6 band values. The horizontal branch of the allowed parameter space represents a "minimal LHB" model, where the $\frac{1}{4}$ keV flux is dominated by the distant emission; the LHB component is then poorly constrained and can assume a broad range of values. The vertical branch of the allowed parameter space represents a "maximal LHB" model, where the $\frac{1}{4}$ keV flux is dominated by the LHB; the distant emission is then poorly constrained and can assume a broad range of values. It should also be noted that the vertical branch falls at the T_L at which the R2/R1 ratio for the local component is a maximum (see Figure 5.3.)

Most of the published parameters of the local and distant thermal components fall in the region allowed by the R4 flux.

The "degeneracy" in the fit parameters can be broken with the addition of *angular* information; if N_b varies over scales smaller than the angular scales of the variation in the emission, then the local and distant normalizations can be determined, and from them, the temperatures. It is not our desire to single out any particular practitioner of spectral fitting for criticism, especially since the thermal parameters were not their prime objective. However, one can easily show that the thermal components fit, *for example*, by Chen, Fabian, & Gendreau (1997) are incorrect. Taking a small strip of the *RASS* in the southern Galactic hemisphere that is free of strong $\frac{1}{4}$ keV structures ($\ell = 165°, -55° > b > -75°$), and assuming that the temperatures of the local and distant emission do not vary with position, one can solve for the normalizations as a function of position. A plot of the normalization as a function of absorbing column density, Figure 5.4, shows a strong correlation between the absorbing column density and the normalization of the distant component. One should

---

[1] The data used in the construction of Figure 5.2 were regions with $b > 45°$, $45° < \ell < 270°$, and $1.1 \times 10^{20} < N_H < 1.3 \times 10^{20}$ cm^{-2}.

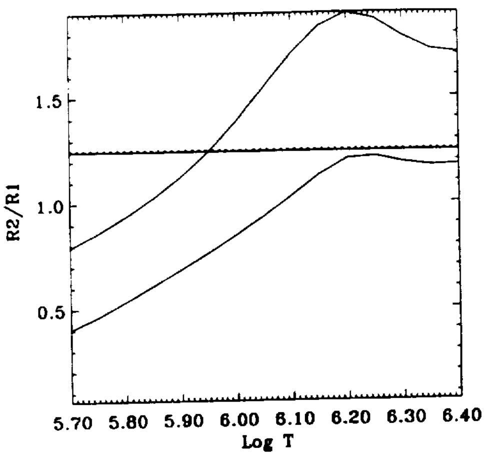

Fig. 5.3.— The R2/R1 ratio as a function of temperature. The top curve is the R2/R1 ratio for the distant component after absorption by a "mean" high Galactic latitude column of 1.21×10^{20} cm^{-2}; the bottom curve is the ratio for the local component. The horizontal line is the ratio for the "mean" high Galactic latitude background. Note that since the local component has an R2/R1 ratio less than the observed R2/R1 ratio in all cases, the distant component must have a temperature greater than $\log T \sim 5.95$.

not expect the emission from beyond the absorbing layer to be correlated with the intervening column density of H I. Therefore, the normalization must be wrong.

Indeed, repeating the exercise using the parameters determined by Snowden et al. (1998), shows no correlation between the absorbing column density and the normalization for the distant component. The uncertainties for the Snowden et al. (1998) parameters are larger than for the Chen, Fabian, & Gendreau (1997) parameters because a softer distant component, absorbed by the intervening column, will require a greater change in N_D before effecting the observed flux.

Consider a spatially invariant background absorbed by a spatially varying column of H I, to which is added a spatially invariant foreground. If one assumes that the background component has a higher temperature than the true background, then the assumed effective absorption cross-sections will be lower than the true effective absorption cross-sections. Thus the expected variation due to absorption (in the value of the transmitted flux) will be smaller than the true variation, and that part of the true variation that is not accounted for by the assumed

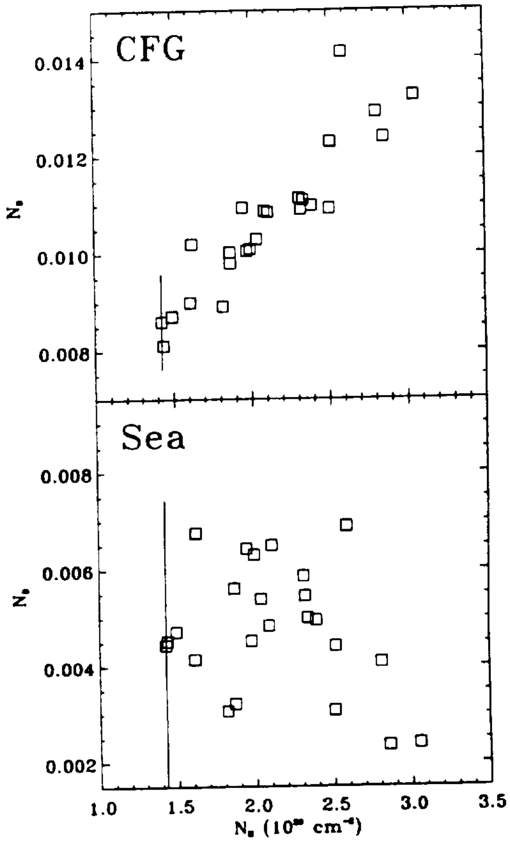

Fig. 5.4.— Checking spectral fit parameters using absorption. *Top:* We have used the temperatures of Chen, Fabian & Gendreau (1997) ($\log T_L = 5.76$ and $\log T_D = 6.14$) to demonstrate how the angular variation of the absorption can be used to check the temperature and normalizations derived from spectral fitting. Since one does not expect the true magnitude of the TAE to be correlated with the absorbing column, the fact that the derived TAE normalization is correlated with N_H indicates that the assumed component temperatures are incorrect. *Bottom:* We have used the temperatures of Snowden et al. (1998) ($\log T_L = 6.12$ and $\log T_D = 6.09$). There is no visible correlation between the TAE normalization and the absorbing column.

variation will be attributed (by whatever fitting mechanism one is using) to a variation in the strength of the background component. Thus, if the assumed temperature of the distant component is wrong, or if the magnitude of the distant component is wrong for any reason, the fitted normalization will be correlated with the absorbing column.

2.2. All-Sky Deabsorption

The second approach to determining the X-ray background spectrum utilizes the Galactic absorption as a tool to separate the local emission from the distant emission. One assumes that at some angular scale the foreground and background emissions are constant at some $\overline{I_L}$ and $\overline{I_D}$, and that the variation in observed X-ray flux is due to absorption by the intervening column. Given a tracer of the absorbing column (e.g., either an H I map or an *IRAS* 100 μm map) one fits the relation in Equation 5.1 to find $\overline{I_L}$ and $\overline{I_D}$.

Since we have very little knowledge of the distribution of N_f, the absorption due to clouds within the LHB, one fits $\overline{I'_L}$ and $\overline{I_D}$ in

$$I_O - I_E e^{-(N_b)\sigma(\nu,N_b,S)} = I'_L + I_D e^{-(N_b)\sigma(\nu,N_b,S)} \tag{5.2}$$

where

$$I'_L = I_L e^{-(N_f)\sigma(\nu,N_f,S)}. \tag{5.3}$$

When using the I'_L determined from several bands to solve for the temperature and emission measure of the local component, a uniform N_f is generally assumed (see § 6.2). N_f is small so, at worst, it can contribute only a few percent error.

2.2.1. $\frac{1}{4}$ keV (The R12 Band)

Snowden et al. (1998) used the single band *RASS* maps of Snowden et al. (1997) to separate the $\frac{1}{4}$ keV (R12 band) emission into foreground and background components over the entire sky. Although these maps have a mean exposure much lower than pointed observations, they have the advantage of having the best possible LTE and SSX removal (Snowden et al. 1995), far better than can be accomplished for any single typical PSPC pointing.

Snowden et al. (1998) assumed that both the local emission and the distant emission were flat on $\sim 4^\circ\!.8$ scales, and they fit Equation 5.1 assuming $N_f = 0$. The fit for each $4^\circ\!.8 \times 4^\circ\!.8$ region was then applied to the center ninth of that region. They used the *IRAS* 100 μm map of Schlegel, Finkbeiner, & Davis (1998) as a tracer of the absorbing column. This map was scaled by the mean value of H I$/I_{100}$ where the 21 cm data (-74 km s^{-1} $< V <$ 24 km s^{-1}) was taken from the Dwingeloo survey of Hartmann & Burton (1997). The EPL was assumed to have a Γ of 1.96 (as per Hasinger et al. 1993) but was normalized to be consistent with the observed upper limit to the extragalactic background in the R12 band (Barber & Warwick 1994; Snowden & Pietsch 1995; Barber, Roberts, & Warwick 1996; Cui et al. 1996); although an inconsistent procedure, the inconsistency is inconsequential, as shown by Snowden et al. (2000). The decomposition of the emission into foreground and background components was done separately for the R1 and R2 bands, and the R2/R1 band ratio was then used to determine the temperatures of the local and distant components.

This method works well if the emission and absorption is well described by the canonical model. If, however, the emission and the absorption are interleaved, then significant overestimates of the distant component will occur. Conversely, if the absorption tracer underestimates the total absorbing column, then the distant emission will be underestimated. Both problems pertain to regions with high and intermediate velocity complexes. (See Herbstmeier et al. 1995 and Kerp et al. 1999 for preliminary studies of this problem.)

As can be seen in Snowden et al. (1998), Figure 8, (and again in our Figure 6.4) the distant emission appears to be strongly mottled, even away from the problematic high velocity clouds, and there is evidence of temperature variation. Surprisingly, none of the structure observed in the $\frac{1}{4}$ keV TAE is seen in the $\frac{3}{4}$ keV band, which is smooth (see Figure 4 in Snowden et al. (1997) or our Figure 6.4). This difference led Snowden et al. (1998) to conclude that the component responsible for the structure in the $\frac{1}{4}$ keV band must not have significant emission in the $\frac{3}{4}$ keV band, and must be different from the component producing the very smooth $\frac{3}{4}$ keV emission. Accordingly, they felt justified in measuring the temperature of the component producing the $\frac{1}{4}$ keV structure from the R2/R1 band ratio alone, leaving the measure of the hotter component to groups concentrating on the $\frac{3}{4}$ keV band.

Note that almost all other measures of the temperature of the TAE assumed a single-temperature component, and therefore measure a significantly higher temperature than Snowden et al. (1998). In this case, visible structure in the $\frac{1}{4}$ keV (R12) band but relative smoothness in the $\frac{3}{4}$ keV (R45) band is understandable; for $\log T = 6.14$, R45/R12 ~ 0.026, so much of the structure visible in the $\frac{1}{4}$ keV band will be reduced to the level of the noise in the $\frac{3}{4}$ keV band.

Since the effective cross-section for a given energy band depends upon both the column density of the absorbing gas and the spectral shape of the background emission, one must assume a spectral shape (or temperature) for the distant emission before separating the observed emission into local and distant components. After the local/distant separation one can take the band ratios of the distant component to determine a new spectral shape for the distant emission, and repeat the process.

Did the assumption of the initial temperature of the distant emission bias the subsequent measure of the temperature of the distant emission? For a range of local and distant temperatures, we assumed a fixed single-temperature distant component, and determined the normalizations required to produce the total observed R1 and R2 band emission. Using those temperatures and normalizations we then created vectors of flux *vs.* absorbing column for both bands. Using a method similar to that used in Snowden et al. (1998), those vectors were then fit to derive the local and distant emission values, assuming the cross-sections appropriate for a distant component with $\log T_D = 6.09$. We used the R2/R1 band ratio from the resulting components to compute a "derived" temperature. Figure 5.5 shows the "derived" temperature for a range of true (or input) local and distant temperatures. One can see that for many temperatures, the Snowden et al. (1998) method (without iteration) could produce a biased measure of the temperatures. However, for temperatures near the assumed temperature, the bias is small and does not preclude finding the true temperature through iteration. For all reasonable cases, the biases are $\Delta \log T_L < 0.02$ and $\Delta \log T_D < 0.04$, and so are on the order of the systematics of the analysis (e.g., choice of plasma emission model).

2.2.2. $\frac{3}{4}$ keV

A large-scale deabsorption technique was used in Snowden et al. (1997) to demonstrate the existence of the X-ray emitting bulge with a temperature of $\log T = 6.6$ which dominates the Galactic center and the Loop I region, but does not affect most of the high Galactic latitude sky.

Pietz et al. (1998) took an interesting, though Procrustean, approach to determining the TAE in the $\frac{3}{4}$ keV band. They applied simultaneous spectral fits to three deep PSPC images from the same region of the sky, each with a different absorbing column, to determine the temperature of the local and distant components. This method minimizes the problems with inadequate non-cosmic background subtraction and avoids the degeneracy described in §2.1.

They then used the fitted temperature for the TAE to fit a single-temperature hydrostatic equilibrium model of the Galactic halo to the observed $\frac{3}{4}$ keV distribution. Given 1) that the high Galactic latitude $\frac{3}{4}$ keV emission is smooth, 2) that one does not expect the canonical model to work well near the plane, where the classical "infill" problem[2] remains unsolved, 3) that the flattened halo model produces very little variation at high Galactic latitude, and 4) that the flattened halo model has its greatest variation in the direction of Galactic center where the multiple emission components are very confused, it is not surprising that the Pietz et al. (1998) model is a "good fit" at $\frac{3}{4}$ keV. Their fitting has found the high Galactic latitude normalization, but is not good at constraining the variation with latitude, since the region with the greatest lever arm is also the region that must be excluded due to Galactic absorption and confusion with Loop I.

Pietz et al. (1998) used a very limited number

---

[2] The "infill" problem is as follows: at $\frac{3}{4}$ keV and 1.5 keV the average emission level in the Galactic plane is roughly the same as the average emission at high Galactic latitude, despite the fact that one would expect Galactic disk to "shadow" the extragalactic flux. See, for example, Sanders et al. (1983). Thus, there must be an additional Galactic source of diffuse $\frac{3}{4}$ keV and 1.5 keV emission that almost exactly compensates for the emission that is absorbed by the Galactic disk. However, that source of emission remains unkown.

of PSPC pointings towards a fairly atypical region (Draco) to make a local/distant separation at $\frac{1}{4}$ keV. They then claim that the distant component of the $\frac{1}{4}$ keV flux (excluding regions with High Velocity Clouds or known structures such as Loop I) is produced solely by the extrapolation to $\frac{1}{4}$ keV of the $\frac{3}{4}$ keV emission produced by their Galactic halo model. Their evaluation of the degree to which this extrapolation accounts for the angular structure of the $\frac{1}{4}$ keV emission is overly optimistic; as they have no LHB model, they can always attribute poorly fitting regions to the effects of the LHB.

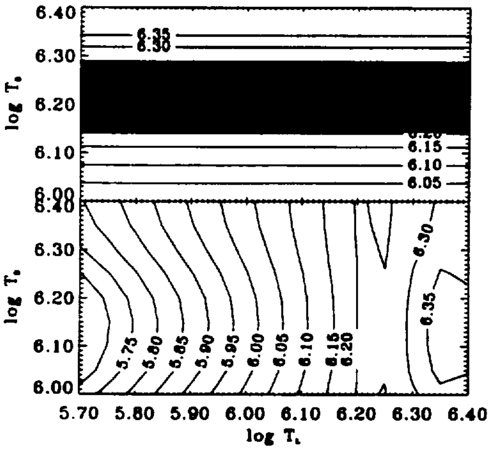

Fig. 5.5.— A demonstration of the bias due to the method of Snowden et al. (1998). Input temperatures for both local and distant components were used to calculate a model of the observed flux as a function of absorbing column density. Those model data were then analyzed using the method of Snowden et al. (1998) to find "derived" temperatures for the local and distant components. The difference between the input and "derived" temperatures measures the bias in the Snowden et al. (1998) analysis. The axes are the input temperatures, the contours are the "derived" temperature. *Top:* The "derived" temperature of the distant component as a function of the true local and distant temperatures. The shaded region produces measured R2/R1 ratios that do not correspond to any temperature. *Bottom:* The "derived" temperature of the local component as a function of the true local and distant temperatures. Making a bad initial assumption will produce an incorrect (biased) measure of the distant temperature, but iteration will produce the correct distant temeperature.

2.2.3. Synthesis

In Snowden et al. (2000), a large (but by no means comprehensive) catalogue of 378 *ROSAT* $\frac{1}{4}$ keV band shadows[3] was used to determine the values of the foreground and background emission in the R1 and R2 bands for many very localized regions at high Galactic latitude for both the northern and southern Galactic hemispheres. The $\frac{3}{4}$ keV band emission was determined for the same regions by subtracting the absorbed EPL from the observed emission and deabsorbing the remainder. It was found that although both the distant $\frac{1}{4}$ keV and $\frac{3}{4}$ keV band emission varied by a factor of five, there was no clear correlation between the distant $\frac{1}{4}$ keV emission and the distant $\frac{3}{4}$ keV emission (see the Figure 15 from Snowden et al. 2000). The lack of correlation was used to support the argument made in Snowden et al. (1998) that the distant component producing the bulk of the $\frac{1}{4}$ keV emission is not the same thermal component producing the $\frac{3}{4}$ keV emission.

2.3. Summary

Spectral fitting methods are incapable of determining the parameters of the thermal components due to absorption uncertainty, poor noncosmic background subtraction, and inadequate spectral resolution. The two large-scale deab-

---

[3] An X-ray shadow is traditionally defined as a region that has a deficit of X-rays and the region of the deficit is spatially matched to an H I 21 cm or 100 μm emission feature. Snowden et al. (2000) expand that definition to regions with an excess of X-rays, where the excess is matched to the decrease in some measure of the absorbing column.

sorption studies, executed in different bands, are each blind to the analysis in the other. Snowden et al. (1998) posited two components to the TAE, but for historical reasons deferred the necessary analysis in the $\frac{3}{4}$ keV band to expand the proof of their case. Pietz et al. (1998) attempted to extrapolate their $\frac{3}{4}$ keV results into the $\frac{1}{4}$ keV band, but without taking into account the structure of the LHB, or the possibility of additional halo components.

The Snowden et al. (1998) self-consistent solution for the temperature of the distant component derives a low temperature distant component ($\log T \sim 6.07$)[4] that produces little $\frac{3}{4}$ keV emission. Assuming that both the $\frac{1}{4}$ keV and the $\frac{3}{4}$ keV distant emission are produced by the same thermal component requires a higher temperature ($\log T > 6.14$) but, as shown in Figure 5.4 and § 2.1, the higher temperature is inconsistent with the observed angular variation of the emission with absorbing column. Further, the extensive shadowing study by Snowden et al. (2000) shows that the distant $\frac{3}{4}$ keV emission is not correlated with the distant $\frac{1}{4}$ keV emission.

Therefore, the distant emission, the TAE, must have more than a single thermal component and, in fact, may have multiple thermal components. The temperature of those components may be spatially variable. The intensity is undoubtedly variable. Due to the limitations of the data, no more than an incremental improvement can be made by extending the Snowden et al. (1998) analysis to the R4-R7 bands. In the following chapter, we will assume the TAE to be composed of two thermal components, a soft thermal component with temperature T_S dominating the $\frac{1}{4}$ keV band, and a hard thermal component with temperature T_H dominating the $\frac{3}{4}$ keV band. We will derive model temperatures for those components, and will evaluate the extent to which further thermal components may exist.

REFERENCES

Barber, C. R., Roberts, T. P., & Warwick, R. S. 1996, MNRAS, 282, 157

Barber, C. R., & Warwick, R. S. 1994, MNRAS, 267, 270

Bloch, J. J., Jahoda, K., Juda, M., McCammon, D., Sanders, W. T., & Snowden, S. L. 1986, ApJ, 308, L59

Chen, L.-W., Fabian, A. C., & Gendreau, K. C. 1997, MNRAS, 285, 449

Cui, W., Sanders, W. T., McCammon, D., Snowden, S. L., & Womble, D. S. 1996, ApJ, 468, 117

Hartmann, D., & Burton, W. B. 1997, Atlas of Galactic Neutral Hydrogen (Cambridge University)

Hasinger, G., Burg, R., Giacconi, R., Hartner, G., Schmidt, M., Trümper, J., & Zamorani, G. 1993, A&A, 275, 1

Herbstmeier, U., Mebold, U., Snowden, S. L., Hartmann, D., Burton, W. B., Moritz, P., Kalberla, P. M. W., & Egger, R. 1995, A&A, 298, 606

Juda, M., Bloch, J. J., Edwards, B. C., McCammon, D., Sanders, W. T., Snowden, S. L., & Zhang, J. 1991, ApJ, 367, 182

Kerp, J. 1994, A&A, 289, 597

Kerp, J., Burton, W. B., Egger, R., Freyberg, M. J., Hartmann, D., Kalberla, P. M. W., Mebold, U., & Pietz, J. 1999, A&A, 342, 213

Landini, M., & Monsignori-Fossi, B. C. 1990, A&AS, 82, 229

Mewe, R., Gronenschild, E., & van den Oord, G. H. J. 1985, A&AS, 62, 197

Miyaji, T., Ishisaki, Y., Ogasaka, Y., Ueda, Y., Freyberg, M. J., Hasinger, G., & Tanaka, Y. 1998, A&A, 334, L13

Parmar, A. N., Guainazzi, M., Oosterbroek, T., Orr, A., Favata, F., Lumb, D., & Malizia, A. 1999, A&A, submitted

Pietz, J., Kerp, J., Kalberla, P., Burton, W. B., Hartmann, D., & Mebold, U. 1998, A&A, 332, 55

Raymond, J. C., & Smith, B. W. 1977, ApJS, 35

Sanders, W. T., Burrows, D. N., McCammon, D., & Kraushaar, W. L. 1983, in Supernova Remnants and their X-ray Emission, ed. J. Danziger & P. Gorenstien, 361

Schlegel, D. J., Finkbeiner, D. P., & Davis, M. 1998, ApJ, 500, 525

Sidher, S. D., Summer, T. J., Quenby, J. J., & Gambhir, M. 1996, A&A, 305, 308

Snowden, S. L., Cox, D. P., McCammon, D., & Sanders, W. T. 1990, ApJ, 354, 211

Snowden, S. L., Egger, R., Finkbeiner, D., Freyberg, M. J., & Plucinsky, P. P. 1998, ApJ, 493, 715

Snowden, S. L., et al. 1997, ApJ, 485, 125

Snowden, S. L., Freyberg, M. J., Kuntz, K. D., & Sanders, W. T. 2000, ApJS, in press

Snowden, S. L., et al. 1995, ApJ, 454, 643

---

[4] The temperatures quoted here from Snowden et al. (1998) and Snowden et al. (2000) are not quite the temperatures found in those papers. The values here have been recalculated from the R2/R1 band ratios using an updated detector response matrix, while the Snowden et al. papers used earlier versions to remain consistent with previous papers.

Snowden, S. L., McCammon, D., Burrows, D. N., & Mendenhall, J. A. 1994, ApJ, 424, 714
Snowden, S. L., & Pietsch, W. 1995, ApJ, 452, 627
Snowden, S. L., Schmitt, J. H. M. M., & Edwards, B. C. 1990, ApJ, 364, 118

Chapter 6: The Spectrum of the TAE

Abstract

We show that the TAE cannot be characterized by a single thermal component; no single-component model can be consistent with both the spectral energy distribution of the TAE emission *and* the angular variation due to absorption by the Galactic disk. Under the assumption that the LHB does not vary on scales smaller than $\sim 5^\circ$, we use the angular anticorrelation of the *ROSAT* All-Sky Survey with the Galactic absorption to separate local from distant emission components, and to fit the spectral energy distribution of the resulting distant emission.

We find that the emission is best described by a two-thermal-component model with $\log T_S = 6.06^{+0.19}_{-0.20}$ and $\log T_H = 6.46^{+0.12}_{-0.08}$. The soft component has a patchy distribution, while the hard component appears nearly constant over the high Galactic latitude sky. This two-thermal-component TAE fits the *ROSAT* spectral energy distribution significantly better than single-component models, and is consistent with *both* angular variation and spectral constraints. This two-thermal-component model is similar to the halo emission seen in external spiral galaxies.

1. Introduction

We attempt to determine the thermal structure of the TAE by combining the all-sky deabsorption method of Snowden et al. (1998) with six-band Spectral Energy Distribution (SED) fitting. Ideally, to determine the thermal and spatial structure of the TAE, one would use the angular structure of the absorbing column to separate the emission in each band into local and distant components, and then one would determine what combination of thermal components would produce the spectrum (or SED) of the distant emission. Unfortunately, the separation of the emission of any band into local and distant components requires knowledge of the spectrum of the distant component in order to calculate the appropriate effective cross-sections. Thus, any determination of the nature of the distant emission requires iterative solution of both the separation into local and distant components and the modeling of the thermal component structure. The extent to which such a process can be successful is strongly limited by the interplay of the response of the instrument, the spectrum of the emission, the energy dependence of the absorption cross-sections, and the available range of absorption column density.

In the following sections, we will briefly describe the available X-ray data and some considerations concerning the measurement of the absorbing column. Section 3 describes the limitations to the separation of the X-ray data into local and distant components that were alluded to above. Section 4 describes the external constraints that can be used to set the non-TAE parameters in Equation 5.2. Finally, we detail the iterative method used to separate the local and distant components and to determine the thermal structure of the distant emission.

2. Data

2.1. The RASS

The X-ray data are the single-band *RASS* maps of Snowden et al. (1997), which have $12' \times 12'$ pixels. Of these band maps, the combined R1 and R2 bands (the R12 band) map forms a "$\frac{1}{4}$ keV" map, the combined R4 and R5 bands (the R45 band) map forms a "$\frac{3}{4}$ keV" map, and the combined R6 and R7 bands (the R67 band) map forms a "1.5 keV" map. Histograms of the statistical significance of the pixels in each band are given in Figure 6.1. Given the long temporal baseline possible with the *RASS*, the LTE and SSX removal were far better than is possible with any single pointed PSPC

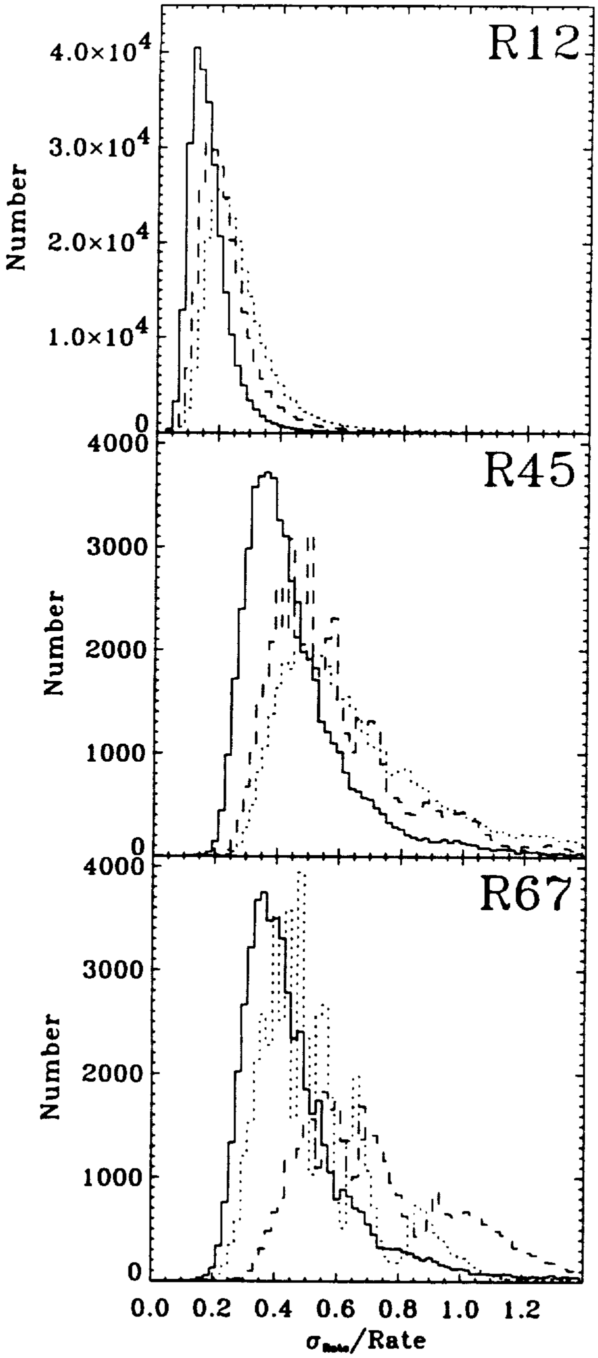

Fig. 6.1.— Histograms of the statistical significance of individual 12′ × 12′ pixels in individual and combined bands of the *RASS*. For bands R4-R7, only pixels in the north polar cap ($b > 55°$, $45° < \ell < 270°$) were used. In each panel, the solid line is the combined band, the dotted line is the lower energy band, and the dashed line is the higher energy band.

observation[1]. Some systematics remain. Even in seemingly uniform regions, a high contrast stretch of the raw *RASS* images will reveal the scan pattern, more strongly at $\frac{3}{4}$ keV than at $\frac{1}{4}$ keV .

The R1 and R2 band maps have had point sources removed to a level of (R1+R2)=0.025 counts s^{-1} while the R4-R7 band maps have had point sources removed to a level of (R4+R5)=0.2 counts s^{-1} and (R6+R7)=0.02 counts s^{-1}. Correction of the *RASS* bands for the band-variable point source removal is discussed in §4.1.

For reasons that will become apparent shortly, the analysis was restricted to $b > 55°$, $45° < \ell < 270°$; the selection in Galactic longitude was set to exclude the Galactic center/Loop I emission. Within this region we also removed pixels contaminated by extended sources, Coma, Virgo, and A1367.

2.2. The Absorbing Column

We have taken as a tracer of the absorbing column the *IRAS* 100 μm maps of Schlegel, Finkbeiner, & Davis (1998), as no other tracer of the absorbing column has either all-sky coverage, or angular resolution comparable to that of the *RASS*. As has been discussed in Arendt et al. (1998) 100 μm emission traces, to varying degrees, the molecular, neutral atomic, and ionized atomic components of the ISM. (For a review see Chapters 3 & 5 of Kuntz 2000.)

Low velocity disk H I appears to be well traced by the 100 μm emission, but the 100 μm emissivity of the H I does appear to vary (Reach, Wall, & Odegard 1998). The high and intermediate velocity H I appears to have very low 100 μm emissivity, and is essentially invisible at 100 μm, meaning that the *IRAS* 100 μm maps in regions with intermediate ($-100 < v < -75$ km s^{-1}) or high ($v < -100$ km s^{-1}) velocity clouds will underestimate the absorbing column (Wakker & Boulanger 1986).

Only upper limits to the 100 μm emissivity of the H II have been determined, so the 100 μm emission should be considered a poor tracer of

---

[1] Removal of residual background contamination for individual PSPC pointings after reduction with the ESAS software (Snowden & Kuntz 1998) can only be done by reference to the *RASS*. The method is described by Kuntz & Snowden (1998).

the ionized gas (Arendt et al. 1998).

The emissivity of the molecular gas is a very strong function of the cloud temperature. The work of Schlegel, Finkbeiner, & Davis (1998) attempted to correct for the cloud temperature in order to produce maps of the true dust column density, but the accuracy of this correction, denoted by X, is not well understood. Therefore the absorbing column of molecular gas (even if one assumes a constant dust-to-hydrogen-nucleon ratio) may be poorly determined by the *IRAS* 100 μm emission. However, molecular gas covers only a small portion of the high Galactic latitude sky, appearing only where the H I column is greater than 3×10^{20} cm^{-2} (Reach, Wall, & Odegard 1998), and the H I 21 cm/*IRAS* 100 μm ratio is quite sensitive to the presence of molecular material.

The dominant tracer of absorption is H I. (At $\frac{1}{4}$ keV He provides roughly half of the physical absorption, while at energies > 0.5 keV metals provide nearly all of the absorption.) The amount of absorption due to H II is a matter of debate (Arabadjis & Bregman 1999; Laor et al. 1997); the cumulative absorbing column due to H II appears to be less than 0.2 that of the absorbing column due to H I at $\frac{1}{4}$ keV and may be significantly smaller.

Since the 100 μm emission is very good at tracing the H I, and the H I 21 cm/100 μm ratio is very sensitive to the presence of H_2, the 100 μm emission is the single best tracer of the total absorbing column. That the 100 μm emission is not sensitive to H II is offset by the X-ray absorption being less sensitive to H II. To convert from the native units of dust emission (MJy sr^{-1}) to absorbing column, we use the ratio of $N(\mathrm{H\ I})/XI_{100} \sim 1.475$ determined from the northern Galactic hemisphere ($b > 45°$) where $N(\mathrm{H\ I}) < 3 \times 10^{20}$ cm^{-2}, a value which varies by $\sim 5\%$, depending upon the latitude and column density limits used.

We have removed the regions where N_H with $v < -75$ km s^{-1} has column densities above 1×10^{19} cm^{-2}. This selection removes the strongest intermediate and high velocity clouds, which are known to be deficient in *IRAS* 100 μm emission.

3. Limits

Optical Depths: In order to separate the distant emission from the local emission, one must have absorption over a wide range of optical depths within a limited angular region. (The region must be small in order for the assumption of a spatially invariant local and distant X-ray emission made by Equation 5.1 to be valid.) In practice, the smallest τ must be $\lesssim 1$, in order to produce a good measure of I_D, the distant emission, and the largest τ must be $\gtrsim 2$ in order to produce a good measure of I_L, the local emission. Either of these limits can be relaxed if the other end of the optical depth range extends well beyond its limit. If the first condition is not met, but the latter is, I_D may be estimated from $I_D = (I_O - I_L)e^{\tau}$, where I_O is the observed flux.

Since the absoption cross section, $\sigma \propto E^{-8/3}$, regions fulfilling the τ requirements at $\frac{1}{4}$ keV generally do not fulfill the τ requirements at $\frac{3}{4}$ keV or 1.5 keV (see Figure 6.2). Separation at $\frac{1}{4}$ keV is usually possible if $\overline{N_H} < 4 \times 10^{20}$ cm^{-2}, whereas separation at $\frac{3}{4}$ keV is generally only possible if $\overline{N_H} \gg 4 \times 10^{20}$ cm^{-2}. Thus, while $\frac{1}{4}$ keV separation into I_D and I_L is usually possible at high Galactic latitude, $\frac{3}{4}$ keV separation is generally only possible at low latitude.

Count Rates: The difficulty in separating I_D from I_L at $\frac{3}{4}$ keV is exacerbated by the $\frac{3}{4}$ keV count rates, which are typically one-tenth of the count rates at $\frac{1}{4}$ keV (note the lower statistical significance of higher energy band pixels in Figure 6.1). Thus, separation of the *RASS* is generally possible for the R1 and R2 bands, individually, but at higher energy, it is only possible in the combined R45 and R67 bands.

Regions with sufficiently high column densities to show good $\frac{3}{4}$ keV shadows are typically near the Galactic plane, where there are likely to be many emission components (and absorbing screens) along a given line of sight. Thus, although there are regions for which the local/distant separation is mathematically possible, those regions are unlikely to produce a meaningful measure of either the local or the distant emission.

4. External Constraints

4.1. Properties of the EPL

The EPL is the aggregate of unresolved sources. It must be the result of a complex convolution of source populations with different spectra, the

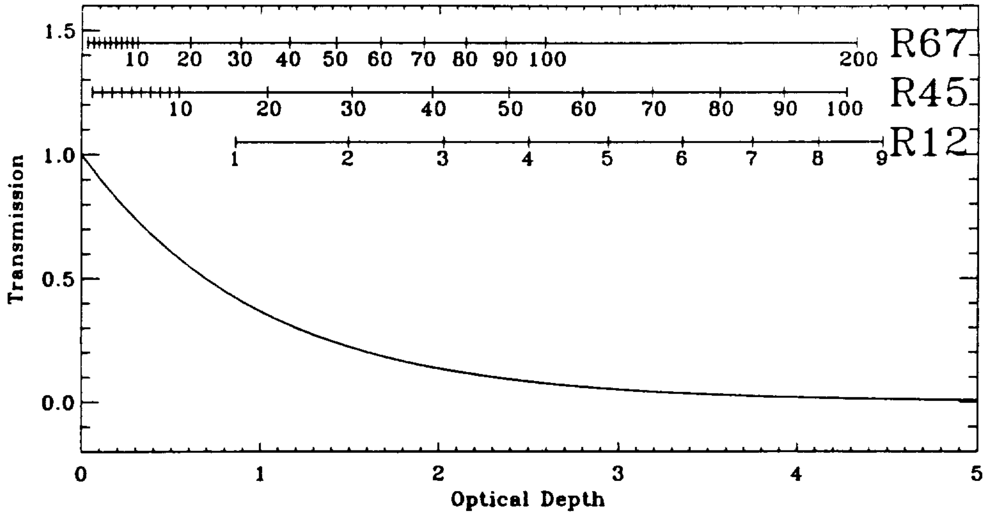

Fig. 6.2.— The column densities at various energies necessary to produce a given optical depth. The column density marked on each bar is in units of 10^{20} cm^{-2}. We have assumed a $\log T = 6.05$ thermal background in band R12, and a $\log T = 6.35$ thermal background for both R45 and R67.

distribution of redshifts, and the distribution of intrinsic absorption. None of the existing populations of point sources thought to compose the EPL has spectra as hard as that of the EPL. Given the cosmological significance of the EPL, a number of groups have attempted to measure the photon index (Γ) and normalization (N_Γ) of the EPL (i.e., the spectrum of the aggregate of unresolved sources). Indices measured from *ROSAT* data alone have been higher than those measured from *ASCA*, which provides a significantly longer, absorption free, lever arm (e.g. Chen, Fabian, & Gendreau 1997). It has been suggested by a number of authors that this discrepancy is due to calibration uncertainties in the *ROSAT* PSPC. Fits using both *ROSAT* and *ASCA* data tend to indices more similar to the *ASCA* values. We have chosen the values of Chen, Fabian, & Gendreau (1997), $\Gamma = 1.46$, $N_\Gamma = 10.5$ keV cm^{-2} s^{-1} sr^{-1} keV^{-1}, as being representative of a number of recent measures of the EPL from joint *ROSAT/ASCA* fits.

The Chen, Fabian, & Gendreau (1997) point source removal limit for the region from which the $\Gamma = 1.46$, $N_\Gamma = 10.5$ EPL was derived was ~ 0.00524 counts s^{-1} for the R47 band. To correct to the point source detection limit of the *RASS* , nearly an order of magnitude larger, we used the $\log N - \log S$ relation of Hasinger et al. (1998) and have assumed a photon index for the point sources between the point source removal limits of Chen, Fabian, & Gendreau (1997) and the *RASS* . We have assumed that those point sources can be characterized by the point sources detected by Chen, Fabian, & Gendreau (1997) at somewhat lower fluxes ($\lesssim 0.00524$ counts s^{-1} but $\gtrsim 0.0003$ counts s^{-1}). A $\Gamma = 2.54$ index was derived by Chen, Fabian, & Gendreau (1997) for a sample of confirmed QSO's detected in this flux interval. However, the confirmed QSO sample is softer than the complete sample of objects in this flux interval, so a harder index may be more apropriate. We have performed the analysis using both $\Gamma = 2.00$ (the value used by Hasinger et al. (1998) in their construction of a log N-log S relation) and $\Gamma = 2.54$ for the point source correction.

Caveat: Although much effort has been expended to determine the spectra of individual sources, the spectrum of the unresolved extragalactic background, the EPL, is unknown in the $\frac{1}{4}$ keV band. We have assumed that the power law that describes the extragalactic background for $E > 1.0$ keV extends into the $\frac{1}{4}$ keV band.

It has been suggested that the spectrum of the extragalactic background turns up below 1 keV. However, that turn-up can not be too great; Snowden et al. (2000) show that the isotropic extragalactic background at $\frac{1}{4}$ keV cannot be more than $\sim 325 \times 10^{-6}$ counts s^{-1} $arcmin^{-2}$. If the spectrum breaks at 1 keV, then $\Gamma < 1.64$; if it breaks at 0.75 keV, then $\Gamma < 1.67$. Thus, even if there is a turn-up in the extragalactic spectrum, the effect is small.

4.2. $\frac{3}{4}$ keV Emission from the LHB

Given all of the caveats placed on $\frac{3}{4}$ keV local/distant separation in §3, any external constraint on the magnitude of the local $\frac{3}{4}$ keV emission is useful. Lines of sight useful for measuring the local component of the $\frac{3}{4}$ keV emission must be chosen carefully. The highest signal-to-noise measure of the local $\frac{3}{4}$ keV emission remains that of Snowden, McCammon, & Verter (1993) towards MBM 12, (a molecular cloud situated just inside the LHB) which yields 2σ upper limits of 23×10^{-6} counts s^{-1} $arcmin^{-2}$ ($\frac{3}{4}$ keV) and 39×10^{-6} counts s^{-1} $arcmin^{-2}$ (1.5 keV). In this direction, the $\frac{1}{4}$ keV flux is 385×10^{-6} counts s^{-1} $arcmin^{-2}$.

If the temperature of the LHB is $\sim \log T_L = 6.10$, then the R45/R12 ratio is 0.017, and the $\frac{3}{4}$ keV count rate due to the LHB in the direction of MBM 12 is 7.1×10^{-6} counts s^{-1} $arcmin^{-2}$, well below the upper limit and similar to the measured value of $\sim 5 \times 10^{-6}$ counts s^{-1} $arcmin^{-2}$. At high Galactic latitudes, where the LHB flux is on the order of $400 - 600 \times 10^{-6}$ counts s^{-1} $arcmin^{-2}$, the $\frac{3}{4}$ keV counts due to the LHB will be $8.75 - 13.25 \times 10^{-6}$ counts s^{-1} $arcmin^{-2}$, which is a substantial fraction of the high Galactic latitude $\frac{3}{4}$ keV flux, typically $\sim 35 \times 10^{-6}$ counts s^{-1} $arcmin^{-2}$. Thus, ignoring the LHB contribution at $\frac{3}{4}$ keV in the manner of Pietz et al. (1998) is unwise.

5. The Iterative Algorithm

We use a bicyclic iterative scheme to solve for the distant component in each band and, simultaneously, fit two thermal components to the resulting SED. The process is described graphically in Figure 6.3. Given the difficulty of performing a local/distant separation in the R4-R7 bands, we have treated those bands somewhat differently than the R1 and R2 bands; the R1 and R2 bands are separated into local and distant components with a method similar to that used by Snowden et al. (1998), while the R4-R7 bands are corrected only for Galactic absorption after the contribution of the LHB has been removed. The lack of correlation between the $\frac{1}{4}$ keV and $\frac{3}{4}$ keV bands, as well as the low model temperature found for the $\frac{1}{4}$ keV emission by Snowden et al. (1998) suggested that there is little contribution from the $\frac{1}{4}$ keV TAE emission to the $\frac{3}{4}$ keV TAE emission (when compared to the much greater flux at $\frac{1}{4}$ keV) and *vice versa*. The fitting algorithm begins with the assumption, but the assumption is not reified by the fitting algorithm.

The first cycle (the left side of Figure 6.3) iteratively determines the temperature of the softer component from the bands R1 and R2, after separating the local from the distant emission. The second cycle (the right side of Figure 6.3) iteratively determines the temperature of the harder component from the bands R4 through R7. Each cycle passes to the other the extrapolation into the complementary band range of the component it has fit. The first cycle finds the single best thermal component fit to the R1 and R2 bands, and extrapolates that component into the R4-R7 bands. That extrapolation is then subtracted from the R4-R7 data, and a single thermal component is fit to the remainder. That thermal component is then extrapolated to the R1-R2 band range, where it is subtracted from the R1-R2 data. The process is then repeated.

5.1. Details of Local/Distant Separation

The process by which the distant emission is separated from the local emission in bands R1 and R2 is similar to that used by Snowden et al. (1998). Both the local and distant emissions are assumed to be spatially invariant over $4^\circ.8 \times 4^\circ.8$ regions. The *bulk* of the distant emission in the R12 band is assumed to come from a single thermal component. From both *RASS* single band images (R1 and R2) is subtracted the contribution of the EPL, after absorption by the Galactic ISM, and the contribution to that band from the hard thermal component, also after absorption by the Galactic ISM. The X-ray data from each $4^\circ.8 \times 4^\circ.8$ region are then binned by the absorbing column density into 1×10^{19} cm^{-2} wide bins. The binned data are then fit by Equation 5.2, assuming some $\log T$ for the distant emission. The Lampton, Margon, & Bowyer (1976) criteria are

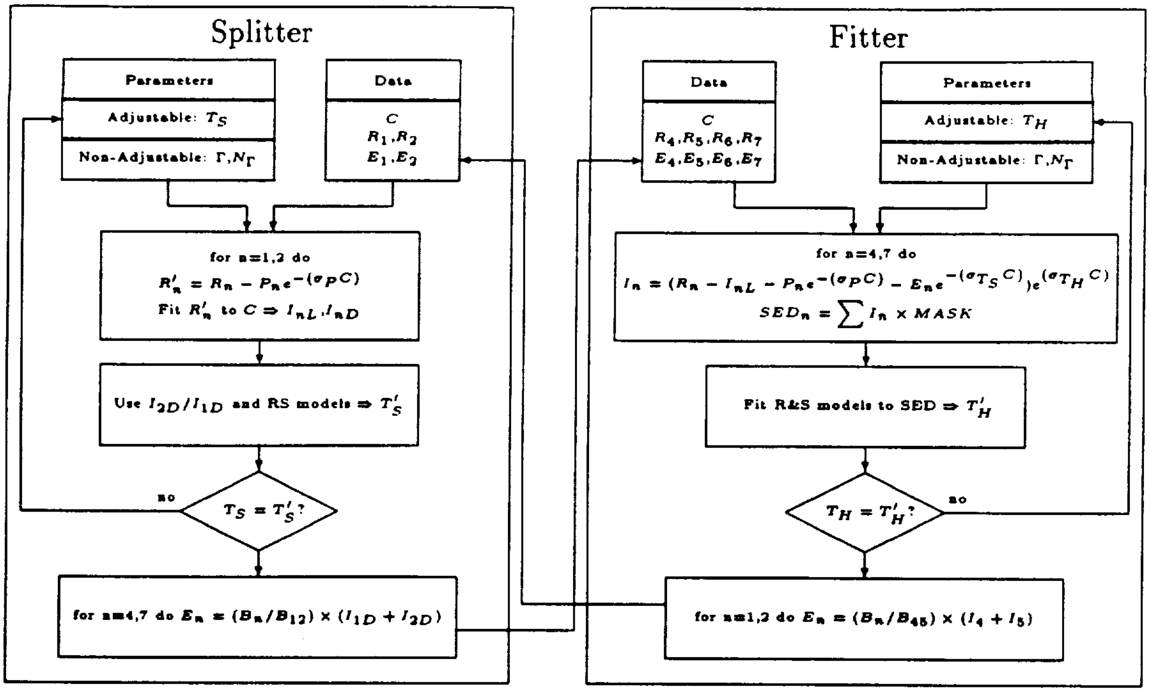

Fig. 6.3.— Flowchart for the bicyclic iterative fitting of two thermal components to the SED of the TAE. T_S is the model temperature of the softer component (which is fit in the left iterative cycle) and T_H is the model temperature of the harder component (which is fit in the right iterative cycle). R_n is an image of the observed emission in band n, E_n is an image of the emission extrapolated from other energies into band n, I_n is an image of the TAE emission in band n, corrected for absorption, P_n is the value of the extragalactic power law in band n, and C is the absorbing column. The subscripts L and D denote the *local* and *distant* components. B_n is the band value derived from a Raymond & Smith spectrum. The "$T = T'$?" is a consistency check for the temperature of the component.

used to determine the uncertainties in the fit parameters. The fitting is done for each 4°.8 × 4°.8 region for which the $\overline{N_H} < 4 \times 10^{20}$ cm^{-2}. The 4°.8 × 4°.8 regions overlap by 1°.6, so the solutions are applied only to the center ninth of the region (1°.6^2).

In their work, Snowden et al. (1998) found that the uncertainty in the distant component could be substantially reduced by taking the quantity

$$I'_D = (I_O - \overline{I}_L)e^{\tau} \qquad (6.1)$$

rather than the value produced by the fit. We have followed this procedure, although, owing to slight differences in the fitting procedure, we find that the improvement is less significant.

Once the separation is accomplished for both the R1 and the R2 band images, the hardness ratio is determined for the distant component. This leads to a new estimation of the $\log T_S$ for the distant emission, and the process is repeated until the assumed temperature and the temperature recovered from the hardness ratio agree to $\Delta \log T_S < 0.005$. Convergence typically occurs in three iterations.

5.2. Details of the R4-R7 SED Fitting

From each *RASS* single band image is subtracted the contribution from the EPL, absorbed by the Galactic ISM, the contribution from the soft thermal component that dominates the R1 and R2 bands, absorbed by the Galactic ISM, and the contribution by the LHB, without absorption. The image of the remainder in each band is spatially smoothed by a three pixel boxcar and is then deabsorbed (i.e., multiplied by e^{τ} where τ is the effective cross-section multiplied by the column density) assuming some $\log T_H$

for the distant emission.

After all four bands have been deabsorbed in this manner, the mean deabsorbed SED for a region with $b > 55°$ and $45° < \ell < 270°$ is calculated. A thermal model is fitted to this SED to determine the new $\log T_H$, and the process is repeated until $\Delta \log T_H < 0.005$. Convergence typically occurs in three iterations. Convergence between the two halves of the iteration usually occurs in three or four iterations.

6. Analysis of Current Results

The results of the local/distant separation and the SED fitting are shown in Figure 6.4. The top images show the soft and hard components in the bands in which they dominate, and below that are their uncertainties (3σ for the soft, 1σ for the hard). The third row contains the spatial distribution of the temperature of the two components. For the soft band the temperature is in the form of the R2/R1 band ratio, while for the hard component the temperature is the fitted Raymond & Smith (1977) equilibrium temperature. The fourth row contains the absorbing column, and the raw R47 band image.

6.1. The TAE

6.1.1. The Soft Component

The temperature of the soft component was derived from the R2/R1 ratio over the north polar cap region ($b > 45°$, $45° < \ell < 270°$, excluding regions with strong X-ray clusters of galaxies or strong ($N_H > 10^{19}$ cm^{-2}) high and intermediate velocity clouds). The histogram of the R2/R1 band ratio over the north polar cap region is shown in Figure 6.5, along with the conversion to Raymond & Smith model temperatures (assuming cosmic abundances). The FWHM of the R2/R1 ratio is 0.610-1.290, and the distribution is asymmetric, with a strong high R2/R1 tail. The values in the high tail do not correspond to a Raymond & Smith model temperature, and thus indicate that the bulk of the dispersion is due not to an intrinsic spread of temperatures, but to the uncertainty of the local/distant split. The mean uncertainty in R2/R1, obtained by propagating the uncertainties in the distant components of R2 and R1 is sufficient to produce the entire observed FWHM. Unlike Snowden et al. (1998), we have not smoothed the distant emission images before calculating the R2/R1 ratios, so our uncertainties are somewhat higher.

In order to minimize the effects of the tail we have chosen to characterize the R2/R1 ratio by the mode. The mode is 0.950; the corresponding model temperature is $\log T_S = 6.056$. Snowden et al. (1998) found $\log T = 6.09$ (FWHM = 6.01 - 6.17) for the soft distant component,

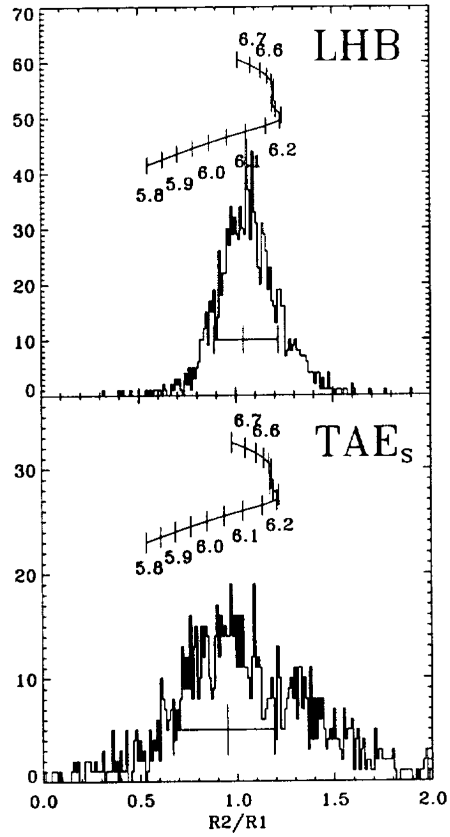

Fig. 6.5.— The distribution of the R2/R1 band ratios for the LHB and TAE. The squiggle above the histogram shows the conversion to Raymond & Smith model temperature. For the TAE, both the R2/R1 ratio and Raymond & Smith conversion are after deabsorption. For the LHB the histogram is of the R2/R1 ratio derived from I'_L values; the temperature conversion assumes a 4×10^{18} cm^{-2} absorption. Note that only the lower branch of the temperature conversion is of interest as the upper branch would over-predict the R47 flux.

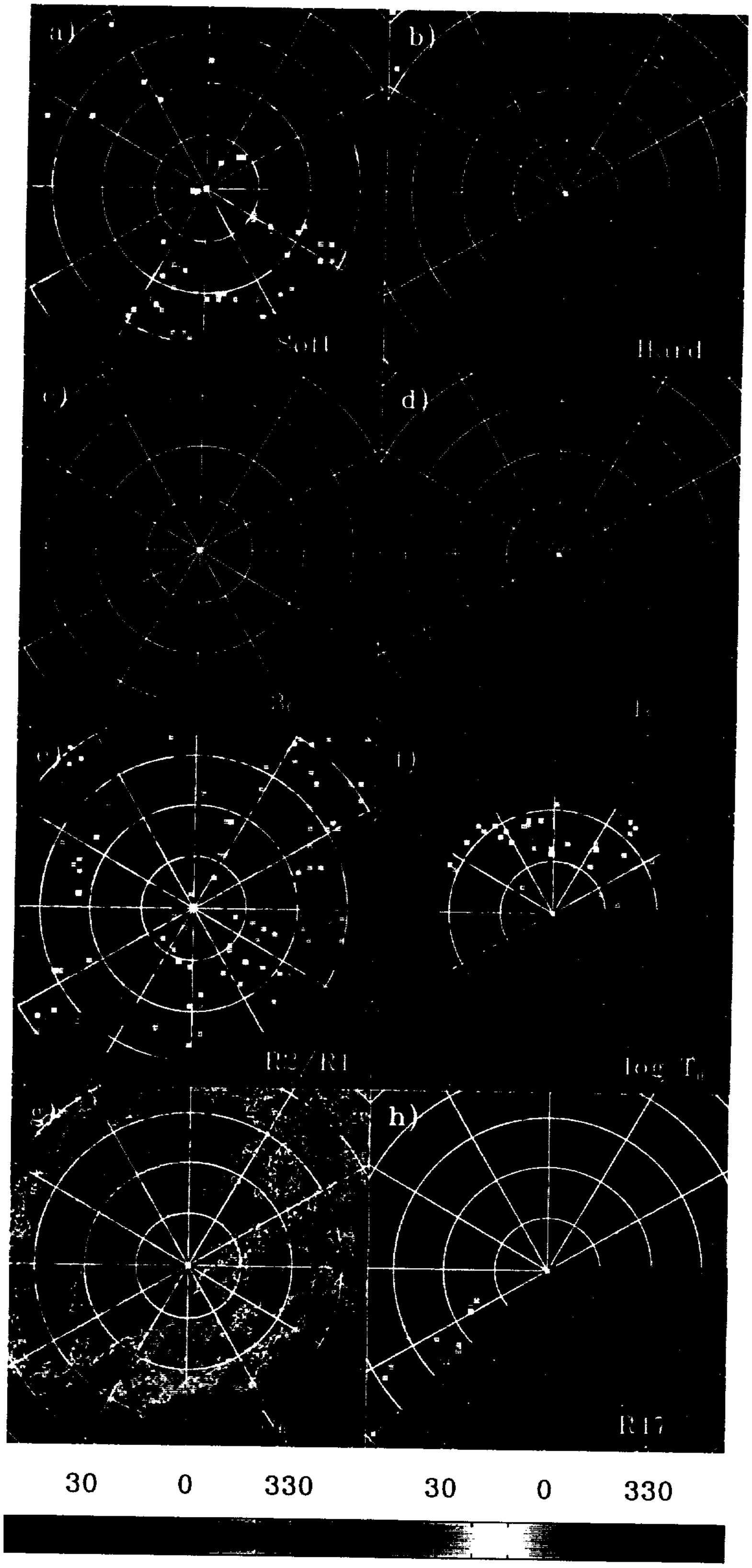
a)
Soft
b)
Hard
c)
d)
e)
R2/R1
f)
log T
g)
h)
R17
30
0
330
30
0
330

Fig. 6.4.— *Previous page:* The spatial distribution of measured quantities. All images are of the northern Galactic hemisphere. Galactic longitude 0° is down, 90° is on the left. The longitude spacing is 30°, the latitude spacing is 15°. Note that the pixelization is 1°.6. *a:* The soft TAE component as seen in the R12 band. Greyscale: minimum 0, maximum 5×10^{-3} counts s^{-1} arcmin^{-2}. *b:* The hard TAE component as seen in the R47 band. Greyscale: minimum 0, maximum 5×10^{-4} counts s^{-1} arcmin^{-2}. *c:* The 3σ uncertainty of the soft TAE component. Greyscale as in *a*. *d:* The 1σ uncertainty of the hard TAE component. Greyscale as in *b*. *e:* The R2/R1 band ratio for the soft component. Greyscale: minimum 0, maximum 3. *f:* The log of the fitted temperature of the hard TAE component. Greyscale: minimum 6.0, maximum 7.0. *g:* The absorbing column density. Greyscale: minimum 0, maximum 4×10^{20} cm^{-2}. *h:* The observed R47 band flux. Greyscale as in *b*. Note that the bulk of the observed structure is due to the scan paths.

without an extrapolation of a hard thermal component. If we follow Snowden et al. (1998), and ignore the extrapolation of the hard component, we find an R2/R1 ratio of 0.92, with a corresponding model temperature of $\log T = 6.040$. Since we used a much more restricted portion of the sky, and a different fitting algorithm, the difference between the value from Snowden et al. (1998) and our value (without the extrapolation of the hard component) is a good measure of the systematic uncertainties.

Systematics: Most of the systematics in the local/distant separation have been discussed in Snowden et al. (1998). The magnitude of the distant component is not correlated with the absorbing column, though the uncertainty will be. The value of the R2/R1 ratio for the distant component is not correlated with the value of R2, R1, or the magnitude of the absorbing column. Snowden et al. (2000) discuss the variation of the R2/R1 ratio of the distant component with Galactic latitude and longitude and they find none. We are not so sensitive to the variation of R2/R1 with position as were Snowden et al. (2000) because, although this study has a greater number of pixels, the Snowden et al. (2000) study carefully chose regions to have a large dynamic range in absorption.

Although the R2/R1 ratio of the distant component is not correlated with N_H, the derived temperature of the distant component may still be systematically affected by the absorbing column. If the absorbing column is systematically underestimated, one might overestimate the model temperature, and that overestimate may depend upon the absorbing column. As can be seen in Figure 6.6, for the approximate background temperature and range of columns used ($N_H < 4.0 \times 10^{20}$ cm^{-2}), the overestimate has little dependence on absorbing column. If $N_{HII}/N_{HI} \sim 0.33$ (Reynolds 1991) and $\sigma_{HII}/\sigma_{HI} \sim 0.62$ (assuming that $N_{HeII}/N_{He} \sim 0.5$ as per Domgörgen & Mathis 1994) then the absorbing column due to H II will be ~ 0.2 times that due to H I. Assuming a distant component temperature of $\log T = 6.15$, if one does not account for the 20% extra absorption due to the H II, one would overestimate the distant component temperature by $\Delta \log T \sim 0.05$.

One might also expect to find that the lack of a sufficient dynamic range in the absorption

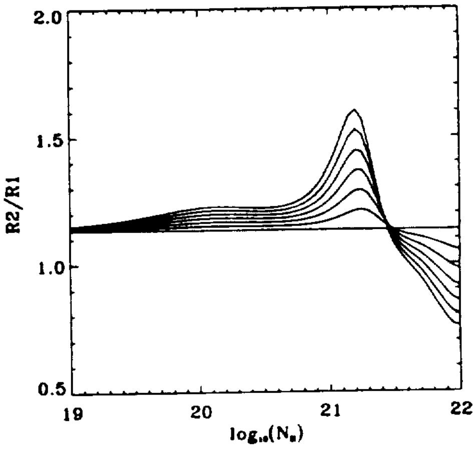

Fig. 6.6.— The derived R2/R1 ratio as a function of N_H if N_H were underestimated. We assumed the distant emission to have $\log T = 6.15$ and measured the R2/R1 ratio of the deabsorbed emission when the absorbing column had been underestimated by (from bottom to top) 0% to 30% in steps of 5%.

might produce a systematically high (or low) estimate of the distant component. We recalculated the R2/R1 ratio using only those $1^{\circ}.6^2$ pixels with "good" fits, defining "good" fits to be those for which the 1σ lower limit was greater than zero. The difference between this value of R2/R1 and that calculated from all of the pixels was insignificant.

6.1.2. The Hard Component

The temperature of the hard component was derived from fitting the R4-R7 SED. The uncertainty of the value was determined from the dispersion of the temperatures found from fitting the SED of each $1^{\circ}.6^2$ region. The histogram of the distribution of temperatures is shown in Figure 6.7. The mode of the temperature distribution was $\log T_H = 6.46$ and the FWHM of the distribution was 6.38-6.55.

To within the uncertainties, the spatial distribution of the temperature of the hard component is uniform. The gradient from bottom to top in Figure 6.4 matches the scan pattern seen in the *RASS* images; the pattern has an amplitude of $\Delta \log T \sim 0.1$.

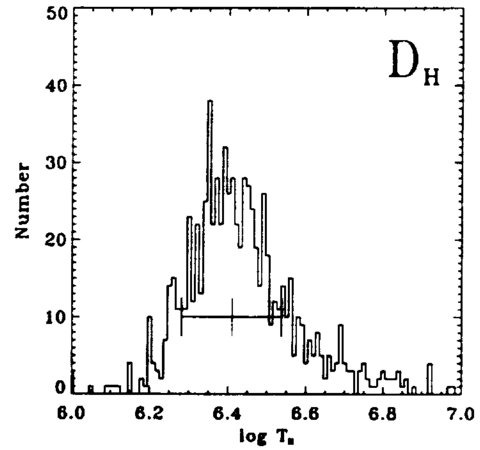

Fig. 6.7.— The distribution of the temperatures produced by fitting Raymond & Smith models to the R4-R7 SED after the emission due to the LHB and the soft component of the TAE have been removed.

6.1.3. Comparisons

Comparison of the components: If the TAE were produced by a single component, then one would expect the R12 and R45 bands for the TAE to be correlated. The lack of correlation is shown in Figure 6.8.

Comparison of one- and two-component models: Given the R1 and R2 measures of the TAE (from the local/distant separation), and the R4-R7 measures of the TAE (from direct *RASS* observation), we can construct the SED for each $1^{\circ}.6^2$ region on the sky. We can then measure the relative goodness of fit for both the one- and two-component models.

To minimize the introduction of a bias through deabsorption, we created an absorbed SED from that part of the sky with $0.95 < N_H/10^{20} < 1.15$ cm^{-2}. For all bands we have taken the SED elements to be $I_O - (I_L + I_E)$ where I_E is the contribution due to the absorbed EPL. We have then fit the two component model to each $1^{\circ}.6^2$ pixel using the previously derived temperatures, and determined the mean χ^2 per fit, $\overline{\chi^2_\nu} = 3.43$

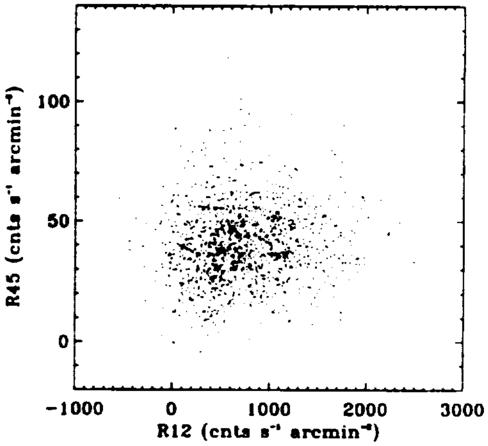

Fig. 6.8.— Correlation of the $\frac{1}{4}$ keV (R12) band emission of the TAE and the $\frac{3}{4}$ keV (R45) band emission of the TAE. The points are shown without error bars for clarity.

($\nu = 4$).

The temperature of the single-component model was determined iteratively in a manner similar to that used for the two-component model. We fit a single-component model to the SED used for the two component fit. That temperature was then used to do the R1 and R2 band local/distant separation, and to redetermine the SED. The single-component model was refit to the R1-R7 SED, and the procedure was repeated until sucessive fits produced the same value. We then found the temperature for which a single-component model had the best mean χ^2 per fit, $\overline{\chi^2_\nu} = 6.79$ ($\nu = 5$) at $\log T = 6.22$. If the single-component model were correct, one would expect that the temperature produced by fitting the SED should be consistent with that found from the R2/R1 ratio. Using $\log T = 6.22$ as the TAE temperature in the local/distant separation, we find the unabsorbed R2/R1 band ratio to be 1.00, equivalent to a Raymond & Smith model temperature of $\log T = 6.08$. Therefore, although our procedure attempts to make the temperatures found by SED fitting and by local/distant separation consistent, no single-component model can be made consistent.

Comparison of the χ^2 show that the two-component TAE model is clearly a significantly better fit. Results for a "mean" SED derived from a limited range of absorbing column density ($0.95 < N_H/10^{20} < 1.15$) can be seen for both models in Figure 6.9. The single-component temperature derived here is consistent with other single-component analyses. The relatively poor fit of the single-component model is due to forcing the SED fit to be consistent with the local/distant separation.

More Components?: The data are clearly insufficient to determine the existence of further components; any combination of thermal components that mimic the two derived here will work as well. The spatial distribution of the temperature of the hard component (Figure 6.4) suggests that that temperature may vary with position. Whether there is a single component with a spatially variable temperature, or several components with different temperatures must, at this point, remain a semantic distinction.

Conversely, one can ask if the hard thermal component is actually due to some component of the extragalactic background. If it is due to the unresolved extragalactic point sources, then the

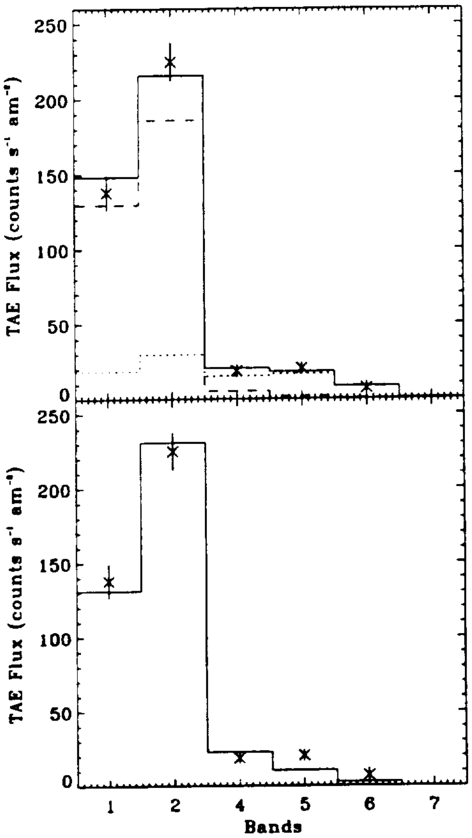

Fig. 6.9.— Fitting one- and two-component TAE models to the R1-R7 band SED. Both panels use a "mean" SED calculated from all regions where $0.95 < N_H/10^{20} < 1.15$ and ($45° < \ell < 270°, b > 55°$). The uncertainties are representative of those of the individual $1.^\circ 6^2$ pixels for which the fits were made. *Top:* The data are the ×, the solid line is the best fit two-component TAE model, the dotted line is the hard component, the dashed line is the soft component. *Bottom:* The data are the ×, the solid line is the best fit one-component TAE model. Note that the SED used for the one-component model is slightly different from that used for the two-component model. See text for explanation. Note that the relative χ^2 values given in the text were derived from all of the pixels within ($45° < \ell < 270°, b > 55°$) while the fits shown are to the mean of a subsample of the pixels used.

spectrum of the background must turn up at ~ 1 keV, but turn back down before the $\frac{1}{4}$ keV band; possible, but contrived. If it is due to a diffuse extragalactic background, then that background resembles a thermal plasma.

It is likely that some portion of the hard thermal component is due to unresolved Galactic stars. Stellar X-ray emission is usually modeled by thermal plasmas with $\log T \sim 6.3$–6.5. A calculation of the X-ray flux due to stars, similar to that made by Guillout et al. (1996), shows that no more than $\sim 17\%$ of the hard component flux can be due to unresolved stellar point sources. At high Galactic latitudes, in directions of nominal diffuse background levels, only $\sim 14\%$ of the $\frac{3}{4}$ keV and 1.5 keV band flux which is not due to the LHB or the EPL can be due to unresolved stars.

Comparison of point source spectrum models: As noted in §4.1, one must correct the *RASS* for point sources below the *RASS* removal limit but brighter than those discarded by Chen, Fabian, & Gendreau (1997) when measuring the spectrum of the EPL. The spectrum of those sources is poorly understood in the $\frac{1}{4}$ keV and $\frac{3}{4}$ keV bands. The results presented above use $\Gamma = 2.00$ for the point source correction. If a $\Gamma = 2.54$ spectrum were used instead, the changes to the derived temperatures is minimal; $\Delta \log T < 0.001$ for all of the components.

Comparison of plasma models: From Table 5.1 it will be remembered that the model temperature derived depended, to some degree, upon the plasma model used. To some extent, this disagreement is immaterial; no plasma model has been able to reproduce the line spectrum of the diffuse X-ray background (Sanders et al. 1998; Vallerga & Slavin 1998; Deiker et al. 1997). Therefore, the model temperatures derived here may be nothing more than convenient markers on an artificial but universally accessible scale. However, these markers certainly allow comparison of some measure of the relative temperatures of the gas.

Using XSPEC (Arnaud 1996) to fit Mewe-Kaastra-Leidahl models to unabsorbed Raymond & Smith models convolved with the *ROSAT* response, both models using cosmic abundances, we find that

$$\log T_{MKL} \sim 0.92 + 0.83 \log T_{RS}. \tag{6.2}$$

Thus, the equivalent MKL temperatures will be systematically lower than the Raymond & Smith values quoted here.

6.1.4. The Diffuse Background Budget

Table 6.1 presents the budget for the diffuse soft X-ray background toward the north Galactic pole ($b > 85°$, $45° < \ell < 270°$, with the region around the Coma Cluster excluded). The line marked "Remainder" is the total observed flux from which has been subtracted the contributions from the LHB, the EPL, and the point source correction necessary for point sources not excluded from the *RASS*, but too bright to have been included in the Chen, Fabian, & Gendreau (1997) formulation of the EPL. Hard and soft thermal components with $\log T_H = 6.46$ and $\log T_S = 6.06$ were fit to the remainder to determine their normalizations. The final line shows what portion of the remainder is due to unresolved stellar X-ray sources. It should also be noted from the work of Snowden et al. (2000) that of the remainder no more than 80×10^{-6} counts s^{-1} arcmin^{-2} in the $\frac{1}{4}$ keV band can be truly extragalactic. (That is, after the removal of the EPL, the minimum flux observed originating from beyond the Galactic H I layer is 80×10^{-6} counts s^{-1} arcmin^{-2}.)

6.1.5. Spectral Fitting Redux

Using the knowledge gained above, one can return to the spectral fitting method. We have used three deep pointed PSPC exposures to test the consistency of our broad-band RASS results with more detailed spectral fitting. Whereas Pietz et al. (1998) selected pointings that were close together but had different absorbing columns, we used maps of the distant $\frac{1}{4}$ keV emission to choose directions with different TAE intensities. We then searched the *ROSAT* archive at the HEASARC for pointed observations longer than 10 ks in those directions, and which did not include clusters of galaxies or particularly bright point sources. Table 6.2 details these observations. The three observations, one exposure of the Lockman Hole deep survey, one of an AGN, and one of a star, were then prepared for spectral fitting. We first examined the light curves of the observations and eliminated times of bright scattered solar X-ray contamination,

TABLE 6.1
DIFFUSE BACKGROUND BUDGET

Component	Observed Fluxes[a]			Fluxes Before Absorption[b]		
	10^{-6} counts s^{-1} $arcmin^{-2}$			10^{-6} counts s^{-1} $arcmin^{-2}$		
	R12	R45	R67	R12	R45	R67
Total Observed[a]	1036.6	122.3	122.6			
LHB	622.0	12.2	0.6			
EPL	83.6	57.1	105.4	245.6	60.5	107.4
PSC	19.5	8.9	11.4			
Remainder	311.5	44.1	4.7			
Best Fit Soft[d]	251.5	5.8	0.2	649.3	6.7	0.2
Best Fit Hard[e]	43.8	39.5	12.6	97.0	41.8	13.0
Stars[f]	8.7	5.5	1.7			

[a] *RASS* data taken from $b > 85°$, $45° < \ell < 270°$

[b] Mean absorbing column was 1.32×10^{20} cm^{-2}

[c] The best fit emission measure was 4.7×10^{-3} cm^{-6} pc.

[d] The best fit emission measure was 2.1×10^{-3} cm^{-6} pc.

[e] Unresolved stellar X-ray sources which contribute to the hard thermal component.

TABLE 6.2
POINTED OBSERVATIONS USED

Observation	N_H	ℓ	b	Exposure(ks)	
				Total	Useful
rp900029a04	0.56×10^{20}	149.51	53.16	46.7	46.7
rp700996n00	2.16×10^{20}	217.00	55.45	19.6	14.4
rp200721n00	1.88×10^{20}	86.55	40.91	46.9	28.0

TABLE 6.3
SPECTRAL FITS

Model	$\log T_L$	N_L[a]	$\log T_{D1}$	N_{D1}[a]	$\log T_{D2}$	N_{D2}[a]	χ^2_ν	ν
2 Comp	6.10 ± 0.02	1.28 ± 0.53	6.00 ± 0.02	< 0.77	6.32 ± 0.02	0.64 ± 0.24	1.22	450
		0.73 ± 0.14		1.72 ± 0.60				
		2.61 ± 0.04		4.14 ± 0.89				
1 Comp[b]	6.17 ± 0.03	1.76 ± 0.04	6.56 ± 0.07	< 0.05			1.39	452
		1.28 ± 0.04		0.20 ± 0.09				
		2.61 ± 0.04		< 0.05				
1 Comp[c]	6.10 ± 0.02	1.28 ± 0.24	6.31 ± 0.23	0.64 ± 0.35			1.26	450
		0.09 ± 0.14	6.24 ± 0.02	1.25 ± 0.42				
		1.58 ± 0.26	6.13 ± 0.01	3.01 ± 0.71				

[a] Units are 10^{-3} photons cm^{-2} s^{-1} keV^{-1} in a solid angle of 8.54×10^{-5} sr

[b] The temperature of the absorbed thermal component was constrained to be the same for all data sets. The normalization of the extragalactic power law was fixed at the fitted value from the two-component model.

[c] The temperature of the absorbed thermal component was fitted independently for all the data sets.

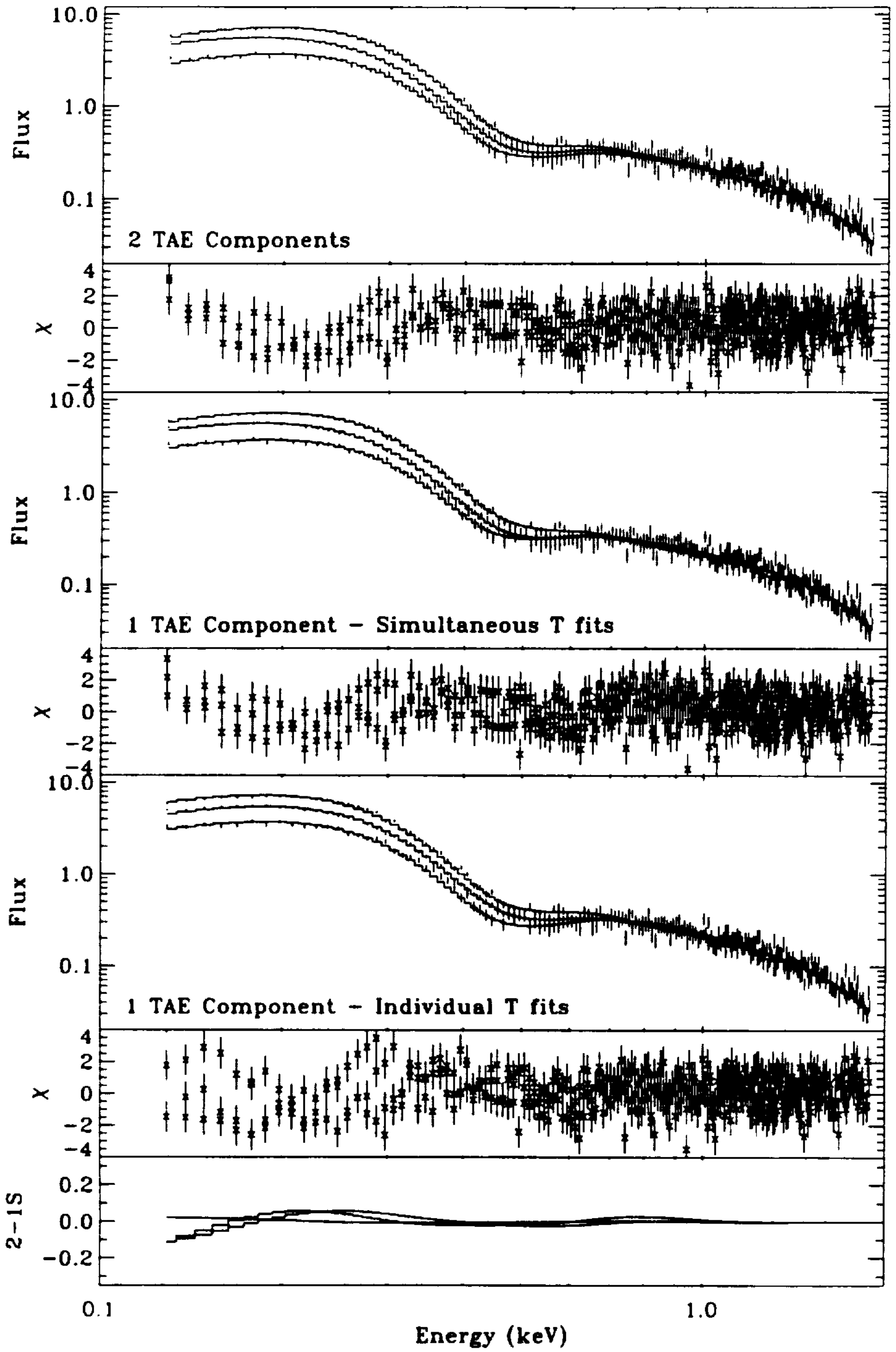

Fig. 6.10.— Simultaneous fits of three PSPC spectra from deep pointings. *Top:* Fit by a model containing the EPL, LHB and a two-component TAE. *2nd Panel:* The residuals to the two-component fit. *3rd Panel:* Fit by a model containing the EPL, LHB, and a one-component TAE; all the spectra are fitted with the same temperature TAE. *4th Panel:* The residuals to the one component fit. *5th Panel:* Fit by a model containing the EPL, LHB, and a one-component TAE; each spectrum is fitted with its own TAE temperature. *6th Panel:* The residuals to the one-component fit. *Bottom:* The best fit two-component models minus the best fit one-component models, where the one-component models were required to have the same TAE temperature, i.e. the models in the third panel.

short-term enhancements (most likely a background due to auroral X-rays), and long-term enhancements (the observations were relatively unaffected by the last). We examined images of the data and created an extraction region which included most of the area inside of the ring of the window-support structure but excluded the targets of the AGN and stellar observations. The same extraction region was used on all observation data sets. We binned the data into pulse-height channels with a minimum of 25 counts and created ancillary region files (ARFs).

XSPEC V.10 was used to fit the three observations simultaneously with several different models. We first fit the data with the two-component TAE model: an unabsorbed thermal spectrum for the LHB, two absorbed thermal spectra for the TAE, and the absorbed EPL. For the fit we fixed the power-law slope to the Chen, Fabian, & Gendreau (1997) value of 1.46 but allowed the normalization to vary. (The fitted normalization was 12.1 keV cm^{-2} s^{-1} sr^{-1} keV^{-1}.) The temperatures of the three thermal components were allowed to vary but they were constrained to be the same for all three data sets. The normalizations of the local component and the soft absorbed component were fit independently for the three data sets but the normalizations of the hard thermal component and power law were constrained to be the same. The data were fit in the 0.12-1.90 keV band. Table 6.3 lists the results, which show a reasonable goodness of fit ($\chi^2_\nu = 1.22$ with $\nu = 450$). The fitted values of the temperatures are consistent with our broad-band analysis.

We also fit the data with the one-component TAE model: an unabsorbed thermal spectrum for the LHB, one absorbed thermal component for the TAE, and the absorbed EPL. The temperatures of the thermal components and the normalization of the power law were constrained to be the same for all data sets but the normalizations for the thermal components were fit individually. With two fewer fitted parameters the reduced χ^2 value increased from 1.22 to 1.38. This rather significant reduction in the quality of the fit relative to the two-component model supports our claim that the one-component model cannot, in general, be fit simultaneously to multiple directions on the sky. Examination of the fitted parameters (Table 6.3) reveals a much higher temperature for the absorbed thermal component ($\log T \sim 6.56$), and lower values for the normalizations. The fitting algorithm forced the local emission to accept a portion of the distant emission.

To examine the situation further, we allowed the temperature of the absorbed thermal component in the one-component model to be fit individually to each data set. This produced a considerable improvement in the χ^2 value, to 1.26, now with the same number of fitted parameters as the two-component model. However, the fitted values for the temperatures (Table 6.3) were completely inconsistent with a constant value (as expected with the large change in the quality of the fit). The brighter the $\frac{1}{4}$ keV TAE the cooler the fitted temperature. This is exactly the expected result if the $\frac{1}{4}$ keV intensity arises from a different emission component than the $\frac{3}{4}$ keV intensity. Thus the two-component model is completely consistent with the detailed spectral fits of the three observations while the one-component model is not.

The results listed in Table 6.3 also demonstrate the ease with which the fitting algorithm can shift intensities and spectral parameters between one component and another. The choice of details used for the spectral model strongly affects the results which are obtained. The two separate fits to the one-component model provide an excellent example. In the first case, when the temperature of the TAE is constrained to be the same for all three data sets, the fitted temperature is very high and the fitted intensities are very low; such low intensities are inconsistent with the variation of the halo emission which has been determined by shadowing experiments. This is clearly the case with the observation in the high-intensity direction (towards the Draco enhancement) where the fit provides a low value for the upper limit; flux from the TAE has been shunted to the LHB.

The difference between the temperature derived for the hot component by spectral fitting and that derived by SED fitting should not be considered too seriously; the two methods have very different systematics. Whereas, in the bicyclic iteration, the normalization and temperature of the LHB was very strongly constrained by the anticorrelation with the absorbing column, in the spectral fitting, the properties of the LHB are less strongly constrained, and so the fitting routine can distribute flux among the various components more freely, producing the best fit for those three particular spectra.

6.2. The LHB

Overview: The local/distant split that produces the R1 and R2 measures of the TAE also provides a measure of the emission due to the LHB. We find an LHB temperature of $\log T_L = 6.11$ (FWHM = 6.04-6.26) from the R2/R1 band ratio 1.06 (FWHM = 0.920-1.220). Although Snowden et al. (1998) and Snowden et al. (2000) contain detailed discussions of a similar analysis, as applied to the LHB, several points are worth noting. First, the temperature of the LHB, as derived by this analysis or by spectral fitting, depends sensitively upon the temperature found for the TAE. The total R1 and R2 band emission must be conserved, and the imposition of a given TAE temperature will determine the temperature to be found for the LHB. However, there are some checks upon the temperature of the LHB. Since, in the Galactic plane, the column density in many directions is sufficient to block background $\frac{1}{4}$ keV emission, one can determine the R2/R1 ratio for the LHB without TAE contamination. After marshaling some essential data about the LHB, we will compare our measure of the LHB temperature to those in the literature.

Shape and Size: The shape of the LHB was determined by Snowden et al. (1998) from the all-sky deabsorption, but the size can not be set without knowing the emission measure within the LHB. The standard scaling of the LHB is given by the observation of the molecular cloud MBM 12, which produces a barely significant $\frac{1}{4}$ keV shadow, implying that it is just barely within the LHB emission. The distance to MBM 12 has recently be redetermined to be $\sim$ 90 pc by Sfeir et al. (1999). Thus, the high scaling of Snowden et al. (1998), 0.23 pc $(10^{-6}$ counts s^{-1} arcmin$^{-2})^{-1}$, should be used.

Internal Absorption: Sfeir et al. (1999) has compiled a homogeneous data set of 456 lines of sight with Na I D absorption spectra with which they have mapped the Local Cavity. Their comparison of the Snowden et al. (1998) LHB contours to the Local Cavity shows that the bulk of the LHB fits inside the distance at which the cumulative column density is significantly less than 2×10^{19} cm^{-2} (in the Na I D line, $W_\lambda = 10$mÅ); only some of the more peripheral regions of the LHB overlap directions/distances with such high column densities.

Absorption of the LHB emission is produced by the Local Interstellar Cloud (LIC) and several similar clouds within $\sim$ 5 pc. A mean absorbing column due to these features can be derived from Hutchinson, Warwick, & Willingale (1998) who showed that the mean absorbing column within $\sim$ 50 pc was about 4×10^{18} cm^{-2}, about a factor of two greater than the highest LIC column densities (Lallement et al. 1995). We will use this value for the mean absorption of the LHB. It corresponds to approximately 3.6% absorption of the $\frac{1}{4}$ keV emission. Other investigators have used greater columns; Sidher et al. (1996) used 6.6×10^{18} cm^{-2} ($\sim$ 5.9% absorption), Kerp (1994) and Pietz et al. (1998) used 1×10^{19} cm^{-2} ($\sim$8.7% absorption), and Parmar et al. (1999) used 7×10^{19} cm^{-2} ($\sim$ 43% absorption). The last of these values is completely incompatible with optical absorption line studies.

Temperature: The model temperature of the LHB can be determined from the R2/R1 (or R2/R1L) ratio in a direction in which absorption by the Galactic ISM blocks $\frac{1}{4}$ keV emission from more distant sources. Figure 6.11 demonstrates the difficulty of this problem. Numerous strong features visible in the $\frac{3}{4}$ keV band, mostly supernovae and super-bubbles, penetrate the Galactic absorption to contaminate the local emission, and increase the R2/R1 ratio. One can calculate the hardness ratio in a large window towards the anticenter in between known sources of contamination, and one finds that the temperature is $\sim \log T = 6.10$ (R2/R1 = 1.057). The temperature of the LHB towards the Galactic center does seem to be higher (Snowden, Schmitt, & Edwards 1990; Snowden et al. 2000), but the contamination by the Galactic bulge "leaking" through the absorption does not allow a determination with this data set.

One might think to avoid most sources of contamination by sampling just off of the Galactic plane. The only region that is near the Galactic plane and has a substantial absorbing column ($10^{21} < N_H < 2.0 \times 10^{21}$ cm^{-2}) is the region of the Taurus-Auriga molecular clouds. Absorption line data place these clouds at $\sim$ 120 pc, so there is little room for extra emission

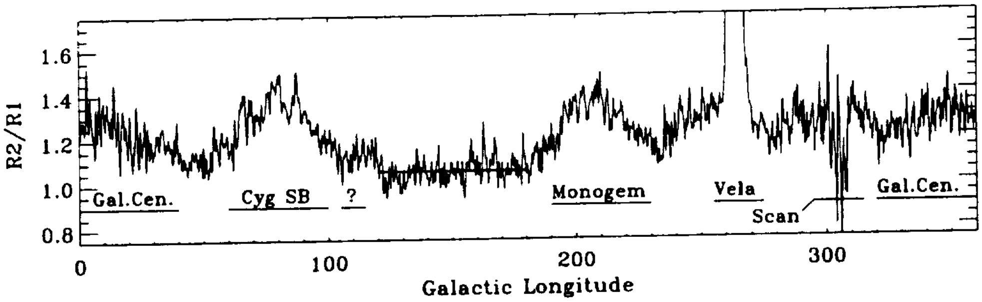

Fig. 6.11.— The $\frac{1}{4}$ keV hardness ratio as a function of Galactic longitude for the region within 5° of the Galactic plane. Brighter, hotter, absorbed features that "leak" into the R12 band are labeled. "Scan" refers to region with poor exposure due to a missing scan. The horizontal bar overlaying the data shows the mean hardness ratio over the given ranges of Galactic longitude.

components between the LHB (radius ~ 100 pc in this direction) and the absorbing clouds. A sample of the *RASS* of ~ 360 square degrees yields a R2/R1 = 1.02 ± 0.01, or an equivalent Raymond & Smith model temperature of $\log T = 6.09 \pm 0.01$

Thus, the current analysis produces an LHB temperature through broad-band ratios that is consistent with independent measures also made with broad-band ratios. The significantly lower temperatures found by the spectral fitting of past analyses are due to the need for a much higher temperature TAE, when one assumes that the TAE is due to a single thermal component.

7. Discussion

Historical Background: The discovery of the soft X-ray emission that we have come to associate with the LHB occurred as the result of attempts to measure the soft extrapolation of the extragalactic power law (Bowyer, Field, & Mack 1968; Bunner et al. 1969; Davidsen et al. 1972). The ubiquity of the $\frac{1}{4}$ keV emission was a mystery that was not to be solved by the discovery of instrumental effects or incorrect modeling of the particle background, though these problems remain. (See, for example, the discussion of the Long Term Enhancements and the earth as a "flaming comet" in Cox 1998.) The $\frac{1}{4}$ keV emission anti-correlation with the total neutral hydrogen column led to two main schools of thought. The first, the absorption model (Bowyer, Field, & Mack 1968; Bunner et al. 1969; Davidsen et al. 1972), was that the ubiquitous emission was extragalactic and absorbed, though it was found that the absorption cross-sections could not produce the observed dynamic ranges (McCammon et al. 1976; Long, Agrawal, & Garmire 1976; Burrows et al. 1984) or band ratios (Bloch et al. 1986; Burrows 1989; Juda et al. 1991). The second, the displacement model (Sanders et al. 1977; Cox & Snowden 1986; Cox & Reynolds 1987; Snowden et al. 1990), was that the emission was proportional to the unabsorbed path length, which was roughly anti-correlated to the total column. There was a third model, the embedded cloud model, Jakobsen & Kahn (1986), based somewhat on the McKee & Ostricker (1977) model of the ISM, that suffered from many of the same problems as did the absorption model (Burrows 1989). The advent of X-ray shadows (Snowden et al. 1991; Burrows & Mendenhall 1991), observed early in the *ROSAT* era, showed that both models were, to some extent, correct.

It was clear that the soft X-ray background was composed of at least three components, the LHB, the EPL, and some component beyond the Galactic absorption, which we have called the TAE. Although the Draco shadows ($\ell = 89° - 91°, b = 38° - 40°$) were the first glimpse of a hot Galactic halo, it was not the long-theorized Galactic corona (Spitzer 1956); the $\frac{1}{4}$ keV TAE was too patchy (Burrows & Mendenhall 1991; Snowden et al. 1991; Snowden et al. 1994). It was suggested that the $\frac{1}{4}$ keV and $\frac{3}{4}$ keV TAE were due to different components (Burrows & Mendenhall 1991) as the $\frac{3}{4}$ keV emission was much smoother than the $\frac{1}{4}$ keV emission. Like the infamous Leiden-Groningen H I 21 cm data split that produced the artificial separation between high and intermediate velocity clouds, the *RASS* was split between the $\frac{1}{4}$ keV and $\frac{3}{4}$ keV bands and analysed by different groups.

Summary of the Argument: The current work attempts to effect the obvious synthesis of the two bands. Our results have shown that the TAE is composed of at least two thermal components, perhaps more. The result is based on five arguments: 1) That the TAE of the R12 and R45 bands are not correlated, 2) That no single component can produce both the observed anti-correlation of emission and absorbing column and a consistent SED, 3) That the two-component models fit the SED better than any single-component model, 4) That single component models are not acceptable because they do not allow the LHB to have a temperature that is consistent with that measured by the R2/R1 ratio in the Galactic plane where there is no "leaking" background emission, and 5) That the two component model is more consistent with detailed spectral fitting than are the single component models. The argument that the $\frac{3}{4}$ keV emission is much smoother than the $\frac{1}{4}$ keV emission is no more than suggestive. With the exception of such strong features as the Draco enhancement, a single-temperature model, in order to get the proper R45/R12, will necessarily scale down the structures seen in the R12 band. Since much of the emission in the R45 band is due to the EPL, the small variations due to the TAE would become difficult to detect in the R45 band.

Although we posit two (or more) components to the TAE, the components are not neatly segregated into the $\frac{1}{4}$ keV and $\frac{3}{4}$ keV bands; ~15% of the $\frac{3}{4}$ keV band flux (before absorption) is produced by the soft component, while ~10% of the $\frac{1}{4}$ keV band flux (also before absorption) is produced by the hard component. Because the soft component does not have a significant trend with Galactic longitude, global analyses that utilize only the R4-R7 bands, such as Wang (1997), will not be significantly affected by our analysis.

Global Properties of the TAE: The mean surface brightness of the soft TAE component is ~ 642 counts s^{-1} $arcmin^{-2}$ or $\sim 2.6 \times 10^{-8}$ ergs cm^{-2} s^{-1} sr^{-1} over the 0.1-2.0 keV range; for the hard component, ~ 110 counts s^{-1} $arcmin^{-2}$ or $\sim 8.5 \times 10^{-9}$ ergs cm^{-2} s^{-1} sr^{-1} over the 0.1-2.0 keV range. Even away from Loop I ($\ell = 330° \pm 60°$) and the Draco enhancement ($\ell \sim 90°$), the soft component is quite mottled, though the azimuthally averaged distribution is quite constant. The hard component, away from Loop I, is smooth (see Figure 6.4).

These characteristics suggest that the hard component might be identified with the Galactic corona or a Galactic halo in hydrostatic equilibrium (Wang 1997; Pietz et al. 1998), though that identification is by no means certain. If the hard component is the corona, with what is the soft component to be identified?

The missing piece in halo studies is often the distance to the emission, and this study is no exception. Several studies have set the $\frac{1}{4}$ keV *terminus a quo*. The $\frac{1}{4}$ keV shadowing clouds in Draco have distances $z > 180$ pc (Lilienthal et al. 1991). Benjamin et al. (1996) found distances of $z \sim 285 \pm 75$ pc to an infrared cirrus cloud in the Lockman hole that shadows the distant X-ray emission. The determination of the *terminus ad quem* is more difficult. The attempts to use high and intermediate velocity clouds are difficult as the disk absorption is much stronger, and there have been suggestions that the high velocity clouds may have X-ray emitting bow-shocks. A search for $\frac{1}{4}$ keV shadows due to high velocity complex M ($1.5 < z < 4.4$ kpc) was equivocal (Herbstmeier et al. 1995). A trivial upper limit is set by the shadowing of the extragalactic background by several galaxies (Barber & Warwick 1994; Snowden & Pietsch 1995; Barber, Roberts, & Warwick 1996; Cui et al. 1996). Distance determinations for the $\frac{3}{4}$ keV emission by shadowing are even more difficult as high and intermediate velocity clouds do not have sufficient column density to produce a measurable shadow.

External Galaxies: Observations of external galaxies provide further clews to the distribution of the TAE. The $\frac{1}{4}$ keV flux due to the TAE (both components) is ~ 706 counts s^{-1} $arcmin^{-2}$, while the $\frac{3}{4}$ keV flux is ~ 47 counts s^{-1} $arcmin^{-2}$. Thus, despite the absorption by our own galaxy, the closer external galaxies should have detectable halos.

The X-ray halos of face-on galaxies are contaminated by the point sources in the disk, but this contamination has diminished as resolution has improved. The best study to date is that of the closest face-on Milky Way analogue, M101, which was observed by the *ROSAT* PSPC (Snowden & Pietsch 1995). If we use the relative D_{25} values for the two galaxies to scale to the equivalent of the galactocentric radius of the sun, a radius of $\sim 8'.5$, and if we assume that the entire M101 flux, after point source removal, is due to the halo, we find 1570 counts s^{-1} $arcmin^{-2}$ at $\frac{1}{4}$ keV, while the flux at $\frac{3}{4}$ keV at that radius is indistinguishable from the background. Significant $\frac{1}{4}$ keV flux ($\sim$ 350 counts s^{-1} $arcmin^{-2}$) extends to $\sim 20'$. (The scale length of the $\frac{1}{4}$ keV emission is $\sim 0.4D_{25}/2$, and the scale length of the $\frac{3}{4}$ keV emission would appear to be similar.) Thus, both the strength and extent of the soft component of the TAE is consistent with that observed in M101. The temperature determined from the R2/R1 ratio for the M101 halo is, however, cooler, $\log T = 5.86$.

Edge-on spiral galaxies for which extra-planar X-ray emission has been detected are often strong star-burst galaxies. Three non-starburst edge-on spiral galaxies have *ROSAT*-detected X-ray halos: NGC 891, NGC 4631, and NGC 4565. Of these, NGC 4565 has the lowest stellar formation rate (SFR, as measured by L_{FIR}/D_{25}^2) and has no detected extended diffuse ionized gas (DIG). Vogler, Pietsch, & Kahabka (1996) detected some extraplanar diffuse X-ray emission, but were unable to determine a scale-height, and could only say that the temperature was consistent with a few times 10^6 K gas. NGC 4631, which has a higher SFR, is a disturbed galaxy that may be interacting (Weliachew, Sancisi, & Guélin 1978; Rand, Kulkarni, & Hester 1992; Rand & Stone 1996; Donahue, Aldering, & Stocke 1995). It has a strong nuclear star formation, and nuclear Hα filaments, which may be related to a $\frac{1}{4}$ keV emission region. The $\frac{3}{4}$ keV emission has a HWHM z-extent of almost 3 kpc, a radial extent of about 3 kpc (0.25 $D_{25}/2$), and a temperature $\log T_{RS} = 6.48$ (Wang et al. 1995) or $\log T_{MKL} = 6.31$ (Dahlem, Weaver, & Heckman 1998). NGC 891, which has an even higher SFR, has a more uniformly extended X-ray halo; the $\frac{3}{4}$ keV emission has a HWHM z-extent of 2.1 kpc, a radial scale length of 4.1 kpc (0.3 $D_{25}/2$), and a temperature of $\log T = 6.54$ (Bregman & Houk 1997).

The only extragalactic detection (in an edge-on spiral) of a component that might be similar to the soft component of the TAE is that by Wang et al. (1995) in NGC 4631, where they detect a component with $\log T < 5.78$. Dahlem, Weaver, & Heckman (1998) also detect a component with $\log T = 5.76$, but Read, Ponman, & Strickland (1997) do not. Such a soft component could not be detected in NGC 891 due to the higher Galactic absorption. Lack of detection of the soft TAE component in external galaxies is not surprising; it is subject to strong absorption by both the Milky Way and the host galaxy. If the soft component has a lower scale-height than the hard component, then not only will the absorption by the host galaxy be important, but the *ROSAT* resolution would not allow separation of the soft TAE from disk emission.

Pure Speculation: Both NGC 4631 and NGC 891 have SFRs, based upon L_{FIR}/D_{25}^2, that are similar to that of the Milky Way (Rand 1998). Both NGC 4631 and NGC 891 have halo temperatures that are consistent with the $\log T = 6.46$ that we have found for the hot component of the TAE. Given the similarities of halo temperature, and that the extent of the extra-planar diffuse ionized gas is roughly dependent upon the SFR, it seems likely that the smooth hard component of the TAE has z-scale heights $\sim$ 2 kpc, somewhat smaller than the 4 kpc exponential scale height fitted by Pietz et al. (1998). Both M101 and NGC 891 imply that the hard component should have a radial scale length $\sim 0.35D_{25}/2$. or $\sim$ 4 kpc, which is much smaller than the 15 kpc scale length fitted by Pietz et al. (1998), but implies a much more disk-like distribution than the model of Wang (1997).

The $\frac{3}{4}$ keV emission in the Milky Way is quite symmetric, the mean flux in the south being very similar to that of the north, the emission is quite symmetric in NGC 891, and the asymmetry of NGC 4631 is thought to be an inclination effect (Wang et al. 1995). With a disk-like distribution, this symmetry would argue that the hard component is hot gas in hydrostatic equilibrium, where the symmetry across the disk is enforced by the gravitational potential.

The soft component, however, is very different. The soft component is patchy, and there is a distinct north-south asymmetry in the $\frac{1}{4}$ keV TAE; the northern hemisphere is about 1.9 times stronger than the southern hemisphere (Snowden et al. 1998), and the temperature of the soft component in the southern hemisphere may be lower than that of the north (Snowden et al. 1998) as is implied by Figure 11 of Snowden et al. (2000). These properties suggest that the soft component is the result of local phenomena. Perhaps the soft component is composed of the plumes of hot gas ejected from Galactic chimneys. Snowden et al. (1998) suggested that the Draco enhancement was the extraplanar breakout of the Cygnus superbubble, though the intervening mid-latitude absorption makes testing this model difficult. (It is interesting to note that such a model suggests that the Draco emission occurs to $z \sim 2$ kpc.) However, as the $\frac{1}{4}$ keV TAE is not restricted to lower latitudes any local phenomenon must be fairly uniformly distributed or must send gas to fairly high z. Shelton (1998) has suggested that supernovae remnants in the halo might dominate the soft X-ray emission and produce the patchy structure.

As has been pointed out by Gehrels & Williams (1993) in the context of stellar coronae, the cooling curve for a hot thin plasma has two local minima at temperatures that would emit in the soft X-ray range. Of course, the exact temperatures of those minima ($\log T = 5.9$ and 6.6) do not agree particularly well with the observed temperatures ($\log T = 6.06$ and 6.46). Reference to Schmutzler & Tscharnuter (1993) shows that the location of the minima of the cooling curve are sensitive to the metallicity and previous ionization history of the gas. It is only *suggestive* that the minima of the cooling curve may correspond to the temperatures of the dominant components. In this case, the ubiquity of the soft component suggests that the soft component may represent some part of the hard component at a more advanced age.

Future Work: Determining the true thermal structure of the Galactic halo will be difficult. Next generation X-ray instruments will have lower background contamination, but typically will have small fields-of-view, so using angular variations caused by absorption to separate local and distant components will be more difficult. Although spectral resolution will be good at $\frac{3}{4}$ keV, the spectral resolution below the carbon edge, where the LHB and the soft component of the TAE has most of their emission, remains poor. Experience with the DXS has shown that given high spectral resolution, understanding the spectrum of the LHB is still difficult, and the parameter space allowed by non-equilibrium plasma codes is large.

Attention will also need to be given to incorporating the X-ray TAE into our understanding of the halo optical/UV emission/absorption line ratios. Many line ratios are adequately explained by photoionization due to massive disk stars, whose ionizing radiation is absorbed and hardened by passage through the gaseous disk (see, for example, the review by Rand 1998). However, there are still outstanding difficulties, such as the run of line ratios with z-height, in which the X-ray halo may play a part.

REFERENCES

Arabadjis, J. S., & Bregman, J. N. 1999, ApJ, 510, 806, submitted

Arendt, R. G., et al. 1998, ApJ, 508, 74

Arnaud, K. A. 1996, in Astronomical Data Analysis Software and Systems V, ed. G. Jacoby & J. Barnes, 17

Barber, C. R., Roberts, T. P., & Warwick, R. S. 1996, MNRAS, 282, 157

Barber, C. R., & Warwick, R. S. 1994, MNRAS, 267, 270

Benjamin, R. A., Venn, K. A., Hiltgen, D. D., & Sneden, C. 1996, ApJ, 464, 836

Bloch, J. J., Jahoda, K., Juda, M., McCammon, D., Sanders, W. T., & Snowden, S. L. 1986, ApJ, 308, L59

Bowyer, C. S., Field, G. B., & Mack, J. E. 1968, Nature, 217, 32

Bregman, J. N., & Houk, J. C. 1997, ApJ, 485, 159

Bunner, A. N., Coleman, P. L., Kraushaar, W. L., McCammon, D., Palmieri, T. M., Shilepsky, A., & Ulmer, M. 1969, Nature, 233, 1222

Burrows, D. N. 1989, ApJ, 340, 775

Burrows, D. N., McCammon, D., Sanders, W. T., & Kraushaar, W. L. 1984, ApJ, 287, 208

Burrows, D. N., & Mendenhall, J. A. 1991, Nature, 351, 629

Chen, L.-W., Fabian, A. C., & Gendreau, K. C. 1997, MNRAS, 285, 449

Cox, D. P. 1998, in The Local Bubble, ed. D. Breitschwerdt & M. Freyberg, 121

Cox, D. P., & Reynolds, R. J. 1987, ARA&A, 25, 303

Cox, D. P., & Snowden, S. L. 1986, Advances in Space Research, 6(2), 97

Cui, W., Sanders, W. T., McCammon, D., Snowden, S. L., & Womble, D. S. 1996, ApJ, 468, 117

Dahlem, M., Weaver, K. A., & Heckman, T. M. 1998, ApJS, 118, 401

Davidsen, A., Shulman, S., Fritz, G., Meekins, J. F., Henry, R. C., & Friedman, H. 1972, ApJ, 177, 629

Deiker, S., Kelley, R. L., Lesser, A., McCammon, D., Porter, F. S., Stahle, W. T. S. C. K., & Szymkowiak, A. E. 1997, in Proceedings of the Seventh International Workshop on Low Temperature Detectors, 113

Domgörgen, H., & Mathis, J. S. 1994, ApJ, 428, 647

Donahue, M., Aldering, G., & Stocke, J. T. 1995, ApJ, 450, L45

Gehrels, N., & Williams, E. D. 1993, ApJ, 418, L25

Guillout, P., Haywood, M., Motch, C., & Robin, A. C. 1996, A&A, 316, 89

Hasinger, G., Burg, R., Giacconi, R., Schmidt, M., Trümper, J., & Zamorani, G. 1998, A&A, 329, 482

Herbstmeier, U., Mebold, U., Snowden, S. L., Hartmann, D., Burton, W. B., Moritz, P., Kalberla, P. M. W., & Egger, R. 1995, A&A, 298, 606

Hutchinson, I. B., Warwick, R. S., & Willingale, R. 1998, in The Local Bubble, ed. D. Breitschwerdt & M. Freyberg, 283

Jakobsen, P., & Kahn, S. M. 1986, ApJ, 309, 682

Juda, M., Bloch, J. J., Edwards, B. C., McCammon, D., Sanders, W. T., Snowden, S. L., & Zhang, J. 1991, ApJ, 367, 182

Kerp, J. 1994, A&A, 289, 597

Kuntz, K. D. 2000, Ph.D. thesis, University of Maryland

Kuntz, K. D., & Snowden, S. L. 1998, Cookbook for analysis procedures for *rosat* xrt observations of extended objects and the diffuse background, part ii: Mosaics, Technical report, NASA/GSFC

Lallement, R., Ferlet, R., Lagrange, A. M., Lemoine, M., & Vidal-Madjar, A. 1995, A&A, 304, 461

Lampton, M., Margon, B., & Bowyer, S. 1976, ApJ, 208, 177

Laor, A., Fiore, F., Elvis, M., Wilkes, B. J., & McDowell, J. C. 1997, ApJ, 477, 93

Lilienthal, D., Wennmacher, A., Herbstmeier, U., & Mebold, U. 1991, A&A, 250, 150

Long, K. S., Agrawal, P. C., & Garmire, G. P. 1976, ApJ, 206, 411

McCammon, D., Meyer, S. S., Sanders, W. T., & Williamson, F. O. 1976, ApJ, 209, 46

McKee, C. F., & Ostricker, J. P. 1977, ApJ, 218, 148

Parmar, A. N., Guainazzi, M., Oosterbroek, T., Orr, A., Favata, F., Lumb, D., & Malizia, A. 1999, A&A, submitted

Pietz, J., Kerp, J., Kalberla, P., Burton, W. B., Hartmann, D., & Mebold, U. 1998, A&A, 332, 55

Rand, R. J. 1998, Proc. Astron. Soc. Aust., 15, 106

Rand, R. J., Kulkarni, S. R., & Hester, J. J. 1992, ApJ, 396, 97

Rand, R. J., & Stone, J. M. 1996, AJ, 111, 190

Raymond, J. C., & Smith, B. W. 1977, ApJS, 35

Reach, W. T., Wall, W. F., & Odegard, N. 1998, ApJ, 507, 507

Read, A. M., Ponman, T. J., & Strickland, D. K. 1997, MNRAS, 286, 626,668

Reynolds, R. J. 1991, in The Interstellar Disk-Halo Connection in Galaxies, ed. H. Bloemen, 67

Sanders, W. T., Edgar, R. J., Liedahl, D. A., & Morgenthaler, J. P. 1998, in The Local Bubble, ed. D. Breitschwerdt & M. Freyberg, 83

Sanders, W. T., Kraushaar, W. L., Nousek, J. A., & Fried, P. M. 1977, ApJ, 217, L87

Schlegel, D. J., Finkbeiner, D. P., & Davis, M. 1998, ApJ, 500, 525

Schmutzler, T., & Tscharnuter, W. M. 1993, A&A, 273, 318

Sfeir, D., Lallement, R., Crifo, F., & Welsh, B. Y. 1999, A&A, submitted

Shelton, R. L. 1998, ApJ, 504, 785

Sidher, S. D., Summer, T. J., Quenby, J. J., & Gambhir, M. 1996, A&A, 305, 308

Snowden, S. L., Cox, D. P., McCammon, D., & Sanders, W. T. 1990, ApJ, 354, 211

Snowden, S. L., Egger, R., Finkbeiner, D., Freyberg, M. J., & Plucinsky, P. P. 1998, ApJ, 493, 715

Snowden, S. L., et al. 1997, ApJ, 485, 125

Snowden, S. L., Freyberg, M. J., Kuntz, K. D., & Sanders, W. T. 2000, ApJS, in press

Snowden, S. L., Hasinger, G., Jahoda, K., Lockman, F. J., McCammon, D., & Sanders, W. T. 1994, ApJ, 430, 601

Snowden, S. L., & Kuntz, K. D. 1998, Cookbook for analysis procdures for *rosat* xrt observations of extended objects and the diffuse background, part i: Individual observations, Technical report, NASA/GSFC

Snowden, S. L., McCammon, D., & Verter, F. 1993, ApJ, 409, L21

Snowden, S. L., Mebold, U., Hirth, W., Herbstmeier, U., & Schmitt, J. H. M. M. 1991, Science, 252, 1529

Snowden, S. L., & Pietsch, W. 1995, ApJ, 452, 627

Snowden, S. L., Schmitt, J. H. M. M., & Edwards, B. C. 1990, ApJ, 364, 118

Spitzer, L. 1956, ApJ, 124, 20

Vallerga, J., & Slavin, J. 1998, in The Local Bubble, ed. D. Breitschwerdt & M. Freyberg, 79

Vogler, A., Pietsch, W., & Kahabka, P. 1996, A&A, 305, 74

Wakker, B. P., & Boulanger, F. 1986, A&A, 170, 84

Wang, Q. D. 1997, in The Local Bubble, ed. D. Breitschwerdt & M. Freyberg, 503

Wang, Q. D., Walterbos, R. A. M., Steakley, M. F., Norman, C. A., & Braun, R. 1995, ApJ, 439, 176

Weliachew, L., Sancisi, R., & Guélin, M. 1978, A&A, 65, 37

Chapter 7: The Stellar Contribution to the SXRB

Abstract

Using stellar luminosity functions derived from *ROSAT* data, the contributions of Galactic stars to the diffuse X-ray background are calculated for *ROSAT* PSPC passbands. The model follows that of Guillout et al. (1996), but uses *ROSAT* rather than *Einstein* data to determine the intrinsic luminosity distributions. The model provides nearly the correct number of stellar sources in deep *ROSAT* surveys, though it may underestimate the number of stars at low fluxes.

The contribution of unresolved stellar sources to the *ROSAT* All-Sky Survey at the Galactic poles is 8.28, 5.46, and 1.66 × 10^{-6} counts s^{-1} $arcmin^{-2}$ in bands R12 ($\frac{1}{4}$ keV), R45($\frac{3}{4}$ keV) and R67(1.5 keV), respectively, which is equivalent to 1.8, 1.2 and 0.35 $\times 10^{-13}$ ergs cm^{-2} s^{-1} deg^{-2}. These values correspond to 2%, 19%, and 37% of the TAE emission. The uncertainty in the normalization could increase this quantity by a factor of ~ 1.6.

1. Introduction

1.1. Motivation

Recent advances in the study of the diffuse soft X-ray background have attempted to place limits on the amount of emission from a diffuse extragalactic background. Cen & Ostriker (1999) suggested that such a background might exist in the $\frac{1}{4}$ keV and $\frac{3}{4}$ keV range as a result of gas accretion on sub-cluster size objects forming filamentary structures on cosmological scales, the exact form of these structures being very sensitive to the cosmological model. At higher energies (above 1 keV) truly diffuse X-ray extragalactic emission is ruled out as such gas would produce unacceptably large perturbations in the microwave background. Such considerations do not hold at $\frac{1}{4}$ keV, but the multiplicity of backgrounds (at least two diffuse Galactic components, as well as unresolved Galactic point sources, and unresolved extragalactic sources) make the detection of a diffuse extragalactic background difficult. *ROSAT* observations have been used to attack the problem on several different fronts.

The extragalactic background due to unresolved point sources can be characterized as a power-law at E>1 keV, and a variety of results, including recent Chandra observations The work of (Mushotzky et al. 2000) suggests that this power-law extends, without a break, to lower energies. Snowden et al. (2000) and Kuntz & Snowden (2000), following the work of Snowden et al. (1998), have studied the emission that is not due to unresolved extragalactic sources. Snowden et al. (1998) separated the $\frac{1}{4}$ keV emission originating from beyond the Galactic absorption from that due to the Local Hot Bubble and this work was extended by Kuntz & Snowden (2000) to the remainder of the *ROSAT* band. Snowden et al. (2000) placed an upper limit to the diffuse extragalactic emission at $\frac{1}{4}$ keV. Although Kuntz & Snowden (2000) characterized the emission originating beyond the Galactic absorption in the $\frac{3}{4}$ keV band, they were not able to effect a separation of the emission from beyond the Galactic absorption into its various components, the Galactic halo, the diffuse extragalactic emission, and unresolved Galactic point sources. Thus, although there is almost no doubt that there is a Galactic halo, the upper limit to the diffuse extragalactic emission in the $\frac{3}{4}$ keV band remains the total emission originating beyond the Galactic absorption. Included in the measure of the emission originating beyond the Galactic absorption was the contribution due to unresolved Galactic point sources. It is thus necessary to calculate that contribution to further tighten the limits on the diffuse extragalactic background.

From the model of Cen & Ostriker (1999), the diffuse extragalactic background will not be smooth, and the clumpiness is a function of the cosmological model. This dissertation seeks to place limits on the spatial fluctuations that might be due to the diffuse extragalactic background, thus it is necessary to know the degree of fluctuation due to unresolved Galactic point sources.

It is thus particularly interesting for the study of the diffuse extragalactic background to study the luminosity function of Galactic point sources, that is to say, stars.

1.2. Previous Work

A stellar log N-log S relation in the form of a cumulative luminosity function (CLF, the number of sources, N, with fluxes greater than S) has been calculated by Guillout et al. (1996) from a mixture of *Einstein* IPC and *ROSAT* PSPC data, using the Bienaymé, Robin, & Crézé (1987) model of the spatial distribution of stars. The Guillout et al. (1996) study concentrated on comparing the model distribution of stellar sources with observed count rates as a function of position, the complement of the information required for studies of the diffuse X-ray background.

There are a number of difficulties in applying the published Guillout et al. (1996) CLF to the problem of unresolved stellar sources. First, the Guillout et al. (1996) study published the CLF for the entire *ROSAT* PSPC band-pass. Studies of the diffuse X-ray background are generally interested in only some portion of that band-pass. Given the strong differences in the absorption by the ISM from one end of the band-pass to the other, no simple scaling can be applied to the published relations to obtain, for example, the relation for the $\frac{1}{4}$ keV band. Second, as can be seen in Guillout et al. (1996), and again in our Figure 7.1, although older stars have lower X-ray luminosities, their population is considerably larger and they dominate the luminosity function, especially at lower flux levels. However, this is the population that is the least well characterized in the Guillout et al. (1996) study; they were forced to take data from *Einstein* IPC studies of field stars. Far superior *ROSAT* studies have since become available (Schmitt, Fleming, & Giampapa 1995; Schmitt 1997) Third, because the source population has a finite distance limit, the CLF will increase to lower flux levels, but will turn over and become constant below some limiting flux. The published relations do not reach the "turn-over" point, so it is difficult to know how far to extrapolate in order to determine the total point source contribution.

The following model calculation uses the best current data to derive the luminosity function at high Galactic latitude, which will be of greatest interest to those studying the diffuse extragalactic background. Rather than the CLF, we calculate the more useful form,

$$N(S)d\log S, \tag{7.1}$$

which allows the calculation of

$$\int_0^{S_l} SN(S)d\log S, \tag{7.2}$$

the flux in unresolved sources. The model is, in principle, capable of calculating the stellar contribution at low Galactic latitudes, but some poorly determined input parameters greatly increase the uncertainties near the Galactic plane.

2. Data

In order to calculate the contribution of stellar sources, the stellar populations were binned by spectral type $\mathcal{S_T}$ and age $\mathcal{A}$. We used the spectral-type divisions of Schmitt, Fleming, & Giampapa (1995) and Schmitt (1997) and the age divisions of Guillout et al. (1996), all of which are listed in Table 7.1.

The division by age follows Guillout et al. (1996): the 0-0.15 Gyr class is represented by the Pleiades (171 *ROSAT* detected members, ~ 0.1 Gyr, 115 pc), the 0.15-1.0 Gyr class is represented by the Hyades (191 detected members, ~ 0.6 Gyr, 45 pc), and the 1.0-10.0 Gyr class is represented by the field population.

The data are insufficient to determine the X-ray luminosity functions for subsamples of the 1-10 Gyr field population, which, especially for the later type stars, will be nearly uniformly distributed through the age range. However, stars in the 1-2 Gyr age range will have a very different z-height distribution than stars in the 5-10 Gyr age range. Thus, for calculation, the stars in the 1-10 Gyr age class are subdivided into the age ranges used by Bienaymé, Robin, & Crézé (1987) (see Table 7.2) although the same X-ray

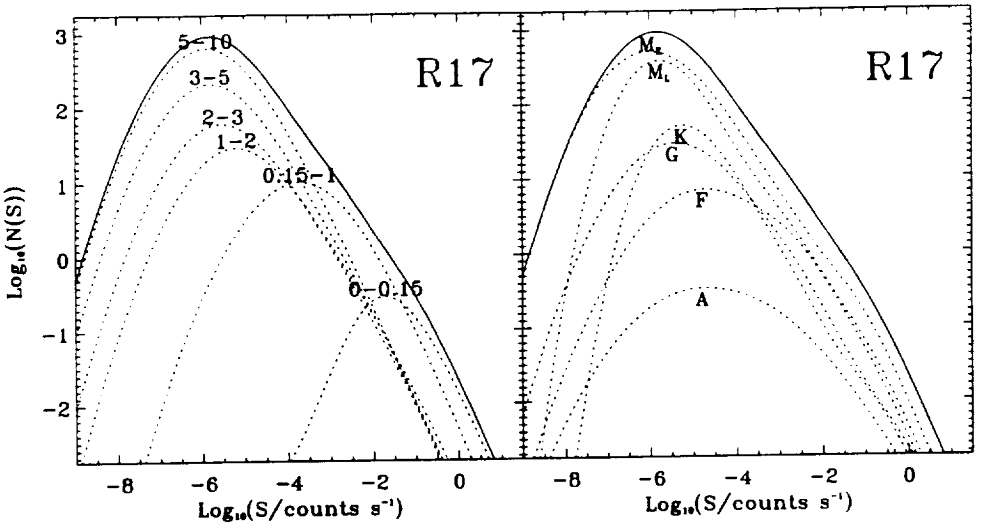

Fig. 7.1.— The luminosity function, $N(S)d\log S$, for band R17 shown with the fractional contributions of the different age classes (*left*) and spectral types (*right*).

luminosity function for all the age sub-divisions in the 1-10 Gyr age class.

A number of other well-studied clusters could be included with the Hyades for a sample of stars in the 0.15-1.0 Gyr group; Coma Berenices (42 detected members, ~ 0.5 Gyr, 80 pc) and Praesepe (56 detected members, ~ 0.6 Gyr, 160 pc). X-ray emission from Coma Berenices members is similar to that from Hyades members (Randich, Schmitt, & Prosser 1996), while that from Praesepe members is lower than that from (coeval) Hyades members (Randich & Schmitt 1995). Given that the Hyades would seem to be representative of its age class, and that there is a relatively larger sample available from the Hyades cluster than from other clusters, the other clusters have not been included in this age class. However, it should be borne in mind that the Hyades luminosities may need to be adjusted downwards to truly represent its age class.

Although X-ray emission has been detected from nearly every spectral type, the dominant contribution by stellar sources is from low-mass main sequence dwarfs, due both to intrinsic luminosity and the number of sources.

Stars of spectral type A have been excluded from the model. The intrinsic X-ray luminosity probability distribution is poorly determined for the younger age classes, and is currently undetermined for the 1-10 Gyr age class, which would dominate the emission from the A spectral type[1]. The intrinsic X-ray luminosities, where measurable, are about an order of magnitude below those of F stars, and the mid-plane number density is lower than F stars, by a factor of 0.005 for the 1-10 Gyr age class. Since the younger age classes will have low z-heights, the error introduced will be minimal for high Galactic latitudes. Guillout et al. (1996) estimate the maximum contribution from A stars to be ~ 2%.

White dwarfs have also been excluded from the calculation as their contribution is typically two orders of magnitude below that of main-sequence stars in band R12, and significantly lower in band R47.

RS CVn systems have been excluded from the calculation. Although they have high luminosities, the median intrinsic luminosity, $\mu \sim 30.3$ (Dempsey et al. 1993), their number density is quite low, probably less than 1×10^{-4} pc^{-3} (Ottmann & Schmitt 1992) as is their scale height (~ 325 pc).

Giants and super giants have been excluded from the calculation as their proper calculation would require extensive analysis beyond the

---

[1] To determine the intrinsic luminosity function for the old disk A stars, one would need access to the *ROSAT* All-Sky Survey data from which the Bright Source Catalogue (Voges et al. 1999) was formed in order to determine the upper limits for undetected stars.

scope of this paper. Nearly all giants are X-ray sources with $\log L_X \sim 27.3$, similar to solar type stars (Schröder, Hünsch, & Schmitt 1998; Hünsch et al. 1998) but the source population is much smaller, and more closely restricted to the plane.

We have also excluded Population II stars from the calculation. If a comparison between disk RS CVn systems and Population II binaries is any indication of the relative emission from single Population I and Population II stars, then the Population II stars should have emission that is more than an order of magnitude below that of Population I stars (Ottmann, Fleming, & Pasquini 1997).

2.1. Model Inputs

For each spectral-type/age-class bin, the contribution to the luminosity function is determined by four parameters: μ and σ, the mean and dispersion of the intrinsic luminosity probability function, c, which describes the z distribution of the stars, and n_0, the mid-plane ($z = 0$) density of stars.

Following Schmitt, Fleming, & Giampapa (1995) and Schmitt (1997), we have assumed that the intrinsic luminosity function for a particular spectral-type/age-class bin is given by the log-normal distribution,

$$P(\log L_x) = \frac{1}{\sigma\sqrt{2\pi}} \exp -\frac{1}{2}\left[\frac{\log L_x - \mu}{\sigma}\right]^2. \tag{7.3}$$

The parameters $\mu(S_T, \mathcal{A})$ and $\sigma(S_T, \mathcal{A})$ were derived from the *ROSAT* data sets listed in Table 7.1.

Since these data sets contain points with upper limits, the parameters were determined by fitting the Kaplan-Meier estimator (Schmitt 1985) of the cumulative distribution function, where the uncertainty in the Kaplan-Meier estimator was taken from Fiegelson & Nelson (1985). The uncertainties were derived using a bootstrap method (Babu & Feigelson 1996). We corrected for binaries in the same manner as Schmitt, Fleming, & Giampapa (1995); we have divided the flux equally between members of binary systems. Guillout et al. (1996) showed that correction for binaries made little difference to the luminosity function.

Since there were no data available for late M stars of the 0-0.15 Gyr and 0.15-1.0 Gyr age classes, the μ for the 1-10 Gyr age class was extrapolated to the younger age classes using the general trend observed in the other spectral classes; a $\Delta \log L_X = 0.92$ decrease between the 0-0.15 Gyr and 0.15-1.0 Gyr classes, and a $\Delta \log L_X = 0.98$ decrease between the 0.15-1.0 Gyr and 1.0-10.0 Gyr classes. For the late M stars the same value of σ was used for each age class, that of the oldest age class; this tends to increase the number of sources with high fluxes.

To convert from X-ray luminosity to count-rates, we used the inverse of the conversion used by the original authors. Schmitt, Fleming, & Giampapa (1995) used the conversion factor[2] $(5.30HR + 8.31) \times 10^{-12}$ ergs cm^{-2} counts^{-1}, where HR, the hardness ratio, is defined by (R47-R82)/(R47+R82) and Rxx is the count rate in band xx. For each spectral type, HR is a linear function of the log of the luminosity. (See Appendix F.) Typically, that linear relation was determined for a span of $\log L_X$ smaller than used in the model calculation and unreasonable values of HR could be obtained; HR was limited to the range -1 to 0. Stern, Schmitt, & Kahabka (1995) used the conversion 6.0×10^{-12} ergs cm^{-2} counts^{-1}, which is somewhat softer than that used by Schmitt, Fleming, & Giampapa (1995). Stauffer et al. (1994) used a conversion of $\sim 8.4 \times 10^{-12}$ ergs cm^{-2} counts^{-1} (for $N_H = 0$), characteristic of $\log T = 7.06$. Due to the shape of the conversion curve, this is also the conversion factor for $\log T = 6.88$.

The spatial distribution for each age-class was assumed to be given by equations A1 and A2 of Bienaymé, Robin, & Crézé (1987), where $c(\mathcal{A})$, the axial ratio for ellipsoids describing the disk populations, were taken from the "best fit" column of their Table 1 and are listed in our Table 7.2.

To maintain some consistency between the initial mass function (IMF), the stellar formation rate (SFR), and the σ_z-Age relation, the mid-plane density of each spectral-type/age-class bin, $n_0(S_T, \mathcal{A})$, was derived in a manner similar to that used by Guillout et al. (1996). The disk was assumed to have an age of 10 Gyr, a constant SFR, and an invariant IMF. The IMF was

---

[2] This relation was derived for a Raymond & Smith model two component corona fitted to a small number of high S/N spectra. See Fleming et al. (1995) for a complete description.

TABLE 7.1

STELLAR DATA

Type	B-V	M_V	0-0.15 Gyr			0.15-1 Gyr			1-10 Gyr		
			No.[a]	μ $\log L_X$	σ $\log L_X$	No.[a]	μ $\log L_X$	σ $\log L_X$	No.[a]	μ^b $\log L_X$	σ^b $\log L_X$
A[e]	-0.01-0.29	...	16/39	28.51±0.26	0.99±0.16	10/35	27.84±0.39	0.93±0.29	16/62[d]	...	...
F	0.3-0.6	...	30/33	29.39±0.07	0.32±0.06	57/60	28.93±0.05	0.28±0.03	28/29	28.00±0.14	0.96±0.14
G	0.61-0.8	...	19/26	29.39±0.20	0.67±0.18	27/33	28.64±0.12	0.39±0.05	29/38	27.36±0.17	0.82±0.13
K	> 0.8	< 8	40/44	29.46±0.07	0.42±0.04	51/86	28.29±0.06	0.45±0.08	17/17	27.62±0.17	0.48±0.12
M(early)	> 0.8	8-15	44/55	29.19±0.05	0.32±0.04	56/174	27.89±0.14	0.72±0.12	66/78	26.86±0.10	0.77±0.10
M(late)	> 0.8	> 15	0	29.12[g]	0.49[g]	0	28.20[g]	0.49[g]	16/19	27.22±0.22	0.49±0.24
Spatial Distribution			Bienaymé et al. Eq. A1			Bienaymé et al. Eq. A2			Bienaymé et al. Eq. A2		
Stellar Sample			Pleiades			Hyades			Field Stars d<13 pc for F & G stars d<7 pc for K & M stars		
Data[f]			Stauffer et al. (1994), PSPC			Stern et al. (1995), RASS Pye et al. (1994), PSPC			Schmitt et al. (1995), PSPC Schmitt (1997), PSPC		

[a] The number of detected stars in the sample divided by the total number of stars in the sample.

[b] Since Schmitt (1997) and Schmitt et al. (1995) convert from PSPC counts to luminosity using $(5.30\mathrm{HR} + 8.31)\times10^{-12}$ erg cm^{-2} s^{-1} [count s^{-1}]$^{-1}$ where HR is a hardness ratio, and since HR is luminosity dependent, the σ derived from Schmitt (1997) and Schmitt et al. (1995) data are likely to be systematically larger than those derived from other data sets where the PSPC count to luminosity conversion was made with a standard 6×10^{-12} erg cm^{-2} s^{-1} [count s^{-1}]$^{-1}$. This difference in conversion may also introduce a very small offset between these luminosities and those of the other age classes.

[c] The uncertainties were determined as described in the text. Our fit values were similar to those of Schmitt, Fleming, & Giampapa (1995) and Schmitt (1997), and we have retained their values.

[d] Number in the *RASS* Point Source Catalogue (Hünsch et al. 1999). In the $r < 13$ pc sample of Schmitt (1997) there are four A stars, none of which were detected.

[e] Spectral-type A is not used in the model calculations. Note the large uncertainties in the parameters of the intrinsic luminosity distribution. The parameters could not be calculated for the field sample as the detected fraction for a sample of main-sequence A stars within 30 pc is ~ 1/3, and upper limits for the non-detections have not been published.

[f] "PSPC" refers to data obtained from pointed PSPC observations, "RASS" refers to data extracted from the *ROSAT* All-Sky Survey.

[g] Extrapolated from the 1.0-10.0 Gyr class due to lack of data. See text.

TABLE 7.2

MID-PLANE STELLAR DENSITIES

Type	Age Group (Gyr)					
	0-0.15	0.15-1	1-2	2-3	3-5	5-10
A	2.16×10^{-4}	3.93×10^{-4}	1.01×10^{-4}	2.55×10^{-7}	0	0
F	2.93×10^{-4}	6.14×10^{-4}	4.40×10^{-4}	2.59×10^{-4}	2.29×10^{-4}	6.99×10^{-5}
G	2.78×10^{-4}	5.82×10^{-4}	4.17×10^{-4}	2.88×10^{-4}	4.39×10^{-4}	9.15×10^{-4}
K	3.31×10^{-4}	6.93×10^{-4}	4.96×10^{-4}	3.42×10^{-4}	5.22×10^{-4}	1.18×10^{-3}
M(early)	4.28×10^{-3}	8.96×10^{-3}	6.42×10^{-3}	4.43×10^{-3}	6.75×10^{-3}	1.53×10^{-2}
M(late)	2.45×10^{-3}	5.12×10^{-3}	3.67×10^{-3}	2.53×10^{-3}	3.86×10^{-3}	8.73×10^{-3}
c[a]	0.0140	0.0279	0.0457	0.0662	0.0867	0.0958

[a] Parameter describing the ellipticity of the stellar distribution. See equations A1 and A2 of Bienaymé, Robin, & Crézé (1987).

taken from Haywood, Robin, & Crézé (1997):

$$dN = m^{-(1+x)} dm \tag{7.4}$$

where

$$\begin{aligned} x &= 0.7 \text{ for } & m &< 1 m_\odot \\ x &= 1.5 \text{ for } & 1 m_\odot \leq m &< 3 m_\odot \\ x &= 2.0 \text{ for } & m &\geq 3 m_\odot . \end{aligned} \tag{7.5}$$

The total number of stars was normalized by comparing the number produced by the above formula with $r < 7$ pc in the $8 < M_V < 15$ range (i.e., the K and early M stars) with the number actually observed (79). The fraction of the number of stars in each age-class was calculated using the main-sequence lifetimes listed in Scalo (1986) and the mass-absolute magnitude-spectral type relations of Kroupa, Tout, & Gilmore (1993).

2.2. Method

For each spectral-type/age-class bin, the intrinisic luminosity distribution was evaluated for $\Delta \log L_X = 0.1$ intervals. For each distance interval, $\Delta r =$ 1pc, from 0 to 3000 pc, the value of $\log L_X$ was adjusted for r^{-2} diminution and absorption by the ISM. The vertical distribution of the ISM was taken from Lockman (1984), and was assumed to be plane-parallel. The absorption cross-sections were taken from Morrison & McCammon (1983). The absorption was calculated assuming that the stellar emission is well described by an equilibrium plasma model with $\log T = 6.4$. Although the bulk of the stars lie beyond the bulk of the absorption (see Figure 7.2), only the R12 band reaches column densities for which $\tau = 1$. (The next most sensitive band is R17, for which $\tau \sim 1$ at $\sim 5.5 \times 10^{20}$ cm^{-2}.) Thus, the luminosity function is not too sensitive to absorption by the ISM.

The intrinsic luminosity function was then interpolated to a standard $\Delta \log (S/\text{counts s}^{-1}) = 0.1$ spacing, and scaled by the size of the volume element and the relative stellar density for that z-height. The luminosity function for each spectral-type/age-class was summed over z-height, and scaled by the total number of stars in that spectral-type/age-class.

The aggregate luminosity function for band R17 is shown in Figure 7.1 for the north Galactic pole. As might be expected, the luminosity function is dominated by the older age classes because, although their intrinsic luminosities may be an order of magnitude smaller than the younger age classes, they account for the bulk of the number of sources. For similar reasons, the luminosity function is dominated by the longer-lived spectral classes. The high-count-rate end of the luminosity function is strongly influenced by the younger age-classes as they have larger intrinsic luminosities and smaller scale-heights.

The lower half of Figure 7.3 shows the effect of the changes of parameters on the cumulative luminosity function of a single spectral-type/age-class. The increments for each of the parameters are their typical uncertainties. As can be seen, except for the uncertainty in n_0, which would

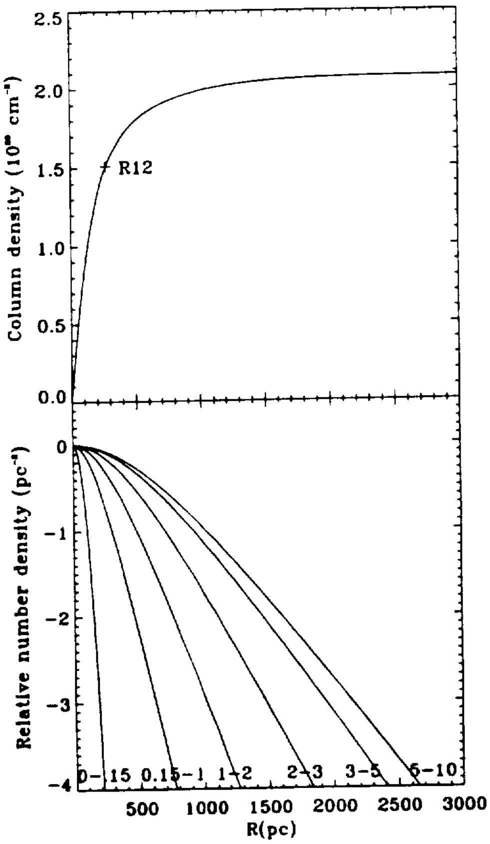

Fig. 7.2.— The relative surface number densities for each age group as a function of z-height, compared to the absorbing column through which they are observed. *Top:* The total absorbing column through which and object of z-height R is observed. The $\tau = 1$ point for band R12 is marked; to achieve the same τ for band R47 requires a much greater column density. *Bottom:* The relative surface densities for stars of a given age group at a z-height R. Each curve has a mid-plane number density of unity.

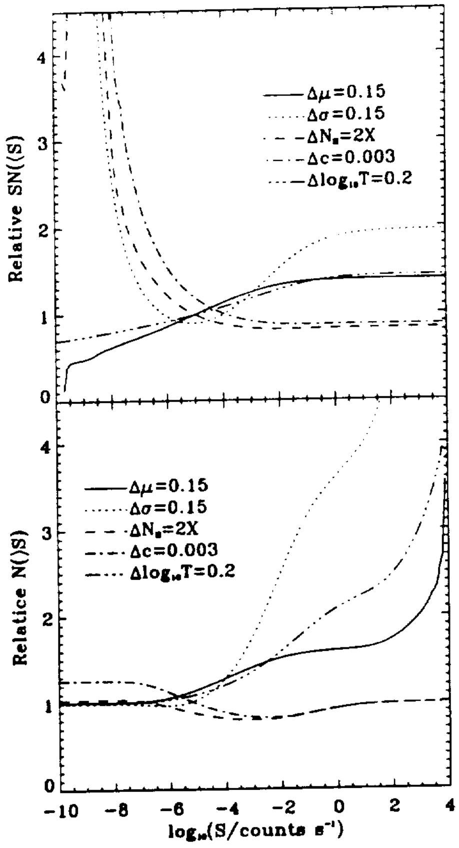

Fig. 7.3.— The effect of uncertainties of the input parameters on the unresolved flux (*top*) and the cumulative luminosity function (*bottom*) shown as the ratio between the luminosity functions. For the M(early), 1-2 Gyr age class we show the luminosity function calculated with a single parameter increased by Δ, where the Δ is the typical uncertainty divided by the fiducial luminosity function.

cause increases at all count rates. uncertainties in σ, T_{eff}, and μ only cause significant changes for count-rates above 10^{-2} counts s^{-1}. Uncertainties in c and N_H cause very little change at any count rate.

3. Comparisons

3.1. The Guillout et al. Model

It is difficult to check our model against that of Guillout et al. (1996) because, although their c values can be reconstructed from their Figure 3, their μ values recovered from their references, and their n_0 values approximated from their description of the IMF and SFR, the σ values are provided in neither the references nor the paper proper. Figure 7.4 shows the results of our model broken into the same age/spectral classes as Guillout et al. (1996) and can be compared directly to their Figure 8.

The two models agree fairly well except for the "late M" class. For this class we find a factor of ~ 10 more sources than Guillout et al.

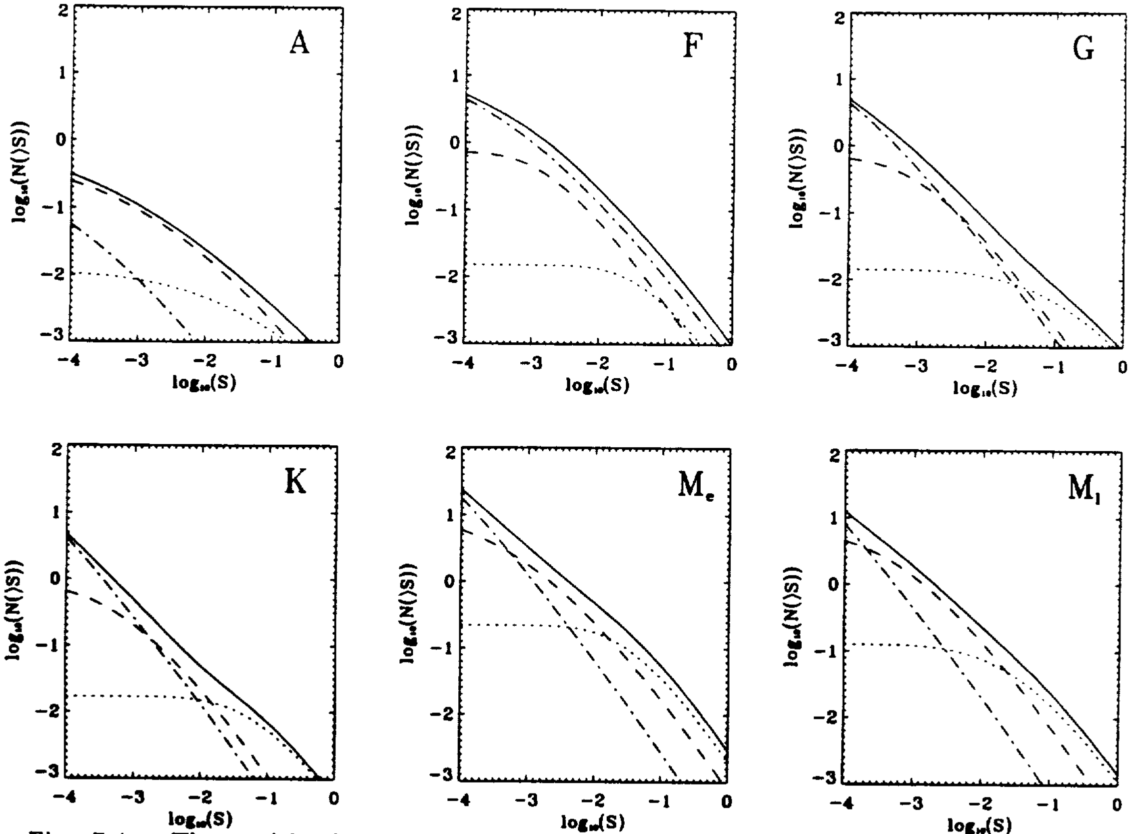

Fig. 7.4.— The model calculations for the north Galactic pole subdivided by age and spectral class. *Solid:* the total luminosity function for the spectral class, *Dotted:* the contribution from the 0-0.15 Gyr age class, *Dashed:* the contribution from the 0.15-1 Gyr age class, and *Dot-Dashed:* the contribution from the 1-10 Gyr age clasess. M_e and M_l indicate for the early and late M stars respectively.

(1996); it is not clear whether this due to a different IMF, a different low-mass cut-off (0.08 $M_\odot$ was used here), or merely a different mass-to-spectral-type conversion.

The current model uses the same c values as Guillout et al. (1996). The values of n_0 can be checked for those spectral-type/age class bins for which Guillout et al. (1996) provide plots of the cumulative luminosity function that extend below the "turn-over". The n_0 agree fairly well (to within a factor of ~ 2).

Since the values of μ used by Guillout et al. (1996) are known, one could, in principle, reconstruct the values of σ used from their Figure 8. However, the computational effort outweighs the usefulness of this test. The values of σ used for the current model are clearly superior given the greater completeness of the data from which they are drawn. Overall, the values of σ used here appear to be somewhat larger than those used by Guillout et al. (1996), causing a horizontal shift of the cumulative luminosity function to higher count-rates. The current cumulative luminosity function matches the Guillout et al. (1996) values between $\log S = -4.2$ and $\log S = -2.7$. At higher luminosities, our band R17 cumulative luminosity function grows to 1.6 that of Guillout et al. (1996) at $\log S = -0.6$, while at lower luminosities, our cumulative luminosity function grows to 1.3 that of Guillout et al. (1996) at $\log S = -4.8$. The overall comparison of the two models can be seen in Figure 7.5.

3.2. Point Source Counts

We have checked our model against the number of stellar point sources found in surveys and against the stellar log N-log S relation of Kraut-

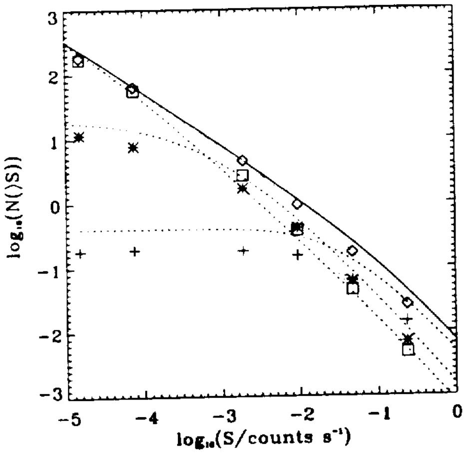

Fig. 7.5.— Comparison between the current model and that of Guillout et al. (1996). *Solid:* the total CLF for the current model, *Dotted:* the current model CLF for various age groups, ◇: the total Guillout CLF, □: the Guillout CLF for 1-10 Gyr, ✱: for 0.15-1 Gyr, +: for 0-0.15 Gyr.

ter et al. (1999). The comparison is listed in Table 7.3 and shown for the R47 band in Figure 7.6.

As can be seen, the model somewhat underestimates the number of stellar sources for deep *ROSAT* surveys in band R47, but the predictions are within Poisson uncertainties, with the exception of the survey of Carballo et al. (1995), which has a low identification fraction, and the survey of Boyle, Wilkes, & Elvis (1997). The unpredicted number listed in the Table is the number of sources with flux above the survey limit at the (l, b) position of the survey, in $\deg^{-2}$, multiplied by the survey area and the fraction of sources for which identifications have been made (the "ID completeness").

The bright end of the model can be compared to the Krautter et al. (1999) log N-log S relation for band R17 (shown for three values of S) and matches reasonably well for $\log S < 0$. The difficulty with this comparison is that Krautter et al (1999) do not note whether this relation is for $b = 90°$ or for some lower Galactic latitude. Predictions for both $b = 90°$ and $b = 30°$ are given in the table. Transforming the Krautter et al. (1999) log N-log S function to the R47 band using their mean stellar hardness ratio, $HR = 0.11 - 0.12$, we find that our model slightly underestimates the observed function.

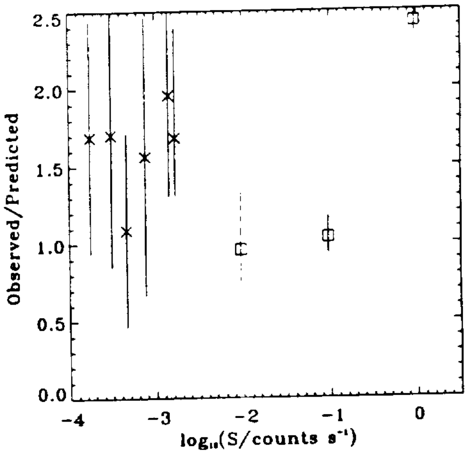

Fig. 7.6.— The band R47 predicted cumulative luminosity function with measured values. ◇: deep surveys listed in Table 7.3, □: values from the Krautter et al (1999) log N-log S relation.

There are two potential methods for correcting the model. The first is to adjust the normalization, that is, scaling the whole model. This will increase the number counts at all count-rates by a factor of ~ 1.6. This would increase the number of K and early M stars in the solar neighborhood to 118, which is well outside the Poisson uncertainty. Such an increase might be accomodated if the IMF/SFR were changed[3]. The second method would be to change the shape of the cumulative luminosity function; increasing μ or σ for any of the young populations would preferentially increase number counts at higher count-rates without increasing the number counts at lower count-rates.

---

[3] However, it should be noted that the most likely change necessary for the IMF/SFR, on the grounds of stellar observations, is to decrease the low-mass end of the IMF at early epochs to account for the seeming defficiency of old late M stars (Bessell & Stringfellow 1993). The normalization used only K and early M stars, and it is not clear whether the observational evidence can tolerate any similar reduction in the number of early M stars. If so, the relative contribution of young stars would be increased, thus increasing the cumulative luminosity function at higher count-rate.

4. Model Description

It is instructive to see how the luminosity function changes with detection band, Galactic latitude, and Galactic longitude.

Figure 7.7 shows the stellar luminosity function at the north Galactic pole for several *ROSAT* bands. The R12 band is substantially different from the R45 band due both to the different instrumental response (which produces a horizontal shift in the curves) and the differing effects of absorption (which increases the number counts below the peak and decreases them above the peak, though not at the highest fluxes).

Figure 7.8 shows the ratio of the stellar luminosity function at $b = 30°$ to that at the Galactic pole for the R12 and R47 bands. We have assumed a plane-parallel absorption model. For typical deep *ROSAT* surveys, there is a factor of ~ 2.5 greater number of sources at $b = 30°$ than at $b = 90°$ in band R47. The increase in number counts for band R12 is less severe due to absorption. As can be seen from the Figure, at $b = 30°$ the effect of the Galactic radial density gradient is negligible.

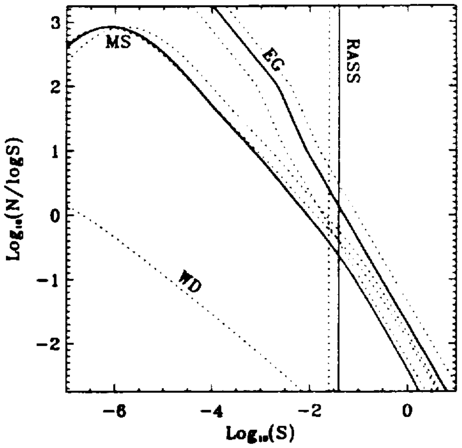

Fig. 7.9.— The luminosity function for main-sequence stars, white dwarfs, and extragalactic objects, for band R12 (*dotted*) and band R47 (*solid*). The relations are shown for a total $N_H = 5 \times 10^{19}$ cm^{-2} (further to the right) and for $N_H = 2.1 \times 10^{20}$ (further to the left). For band R47, the relations for the different values of N_H are indistinguishable. The band R47 relation for white dwarfs is not shown, but would be significantly below the R12 relation. The point source detection limit for the *ROSAT* All-Sky Survey is also shown.

5. Results

Figure 7.9 shows the luminosity functions in PSPC bands R12 (dotted) and R47 (solid) for main-sequence stars, white dwarfs, and the extragalactic luminosity function derived by Hasinger et al. (1998)[4]. For band R47, above the RASS detection limits, stellar sources account for one third to one half of point sources, in agreement with a number of studies, while for band R12, the fraction depends upon the total absorbing column.

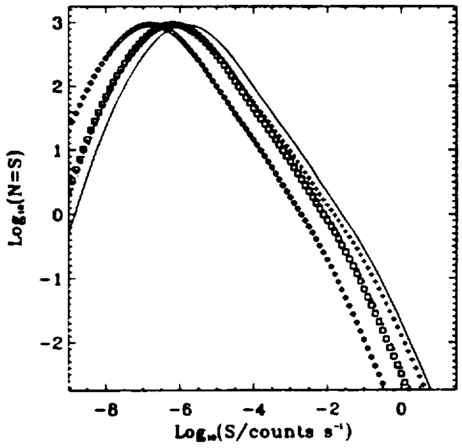

Fig. 7.7.— The luminosity function for different bands in the direction of the north Galactic pole. *Solid line:* band R17 +: band R12, ☐: band R45, ◇: band R67, *Dotted line:* band R47 (almost indistinguishable from band R45).

Figure 7.10 shows the contribution to the *RASS* of unresolved stellar sources as a function of Galactic latitude. The model predicts the unresolved stellar contribution to the diffuse X-ray background measured by the *ROSAT* All-Sky Survey to be

$$8.28 \times 10^{-6} \text{ counts s}^{-1} \text{ arcmin}^{-2} \text{ (band R12)},$$

---

[4] The white dwarf luminosity function is shown to demonstrate its inconsequentiality. It was calculated using the data of Fleming et al. (1996) with the assumption that intrinsic X-ray luminosity of white dwarfs extends down to at least $\log L_X = 27.5$

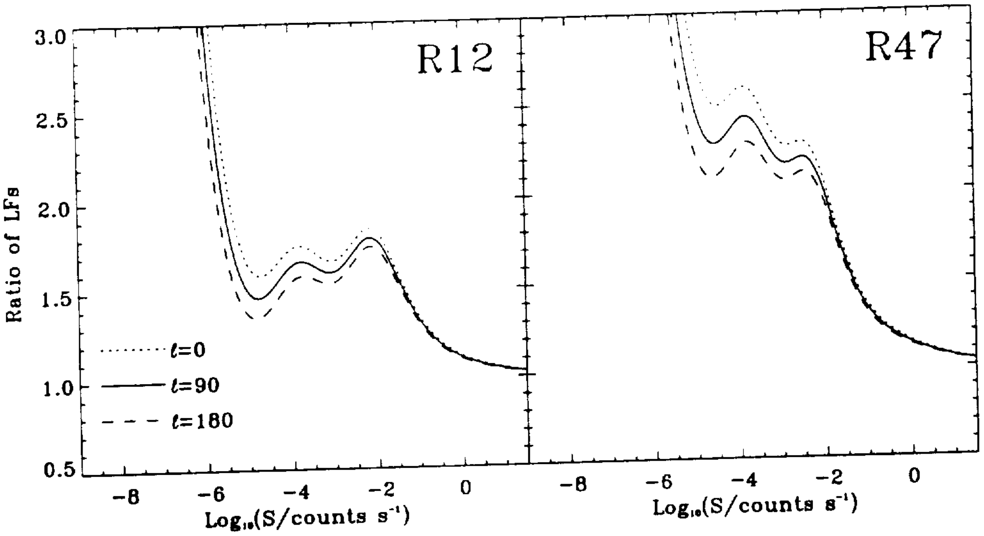

Fig. 7.8.— The ratio of the luminosity function at $b = 30°$ to the luminosity function at $b = 90°$. *Solid:* The ratio for $\ell = 90°$, *Dotted:* the ratio for $\ell = 0°$, *Dashed:* the ratio for $\ell = 180°$.

5.46×10^{-6} counts s^{-1} $arcmin^{-2}$ (band R45), and

1.66×10^{-6} counts s^{-1} $arcmin^{-2}$ (band R67)

for the north Galactic pole. Using the standard stellar conversion factor of 6×10^{-12} erg cm^{-2} $count^{-1}$, the unresolved stellar contribution is

1.80×10^{-13} ergs cm^{-2} s^{-1} deg^{-2} (band R12),

1.18×10^{-13} ergs cm^{-2} s^{-1} deg^{-2} (band R45), and

3.58×10^{-14} ergs cm^{-2} s^{-1} deg^{-2} (band R67).

It should be noted that the Fleming et al. (1995) conversion ranges from 3 to 8.3×10^{-12} erg cm^{-2} $count^{-1}$ for hardness ratios in the range -1 to 0.

In bands R12, R45, and R67, the unresolved stellar sources can account for, at most, 2%, 19% and 37% of the flux that is thought not to be due to the Local Hot Bubble or the unresolved extragalactic point sources (essentially the component that Kuntz & Snowden (2000) attribute to the Galactic halo) The variation of the contribution from unresolved stellar sources with Galactic latitude would be unnoticeable in the *RASS* given the uncertainty in the *RASS* and, more importantly, the variable effects of Galactic absorption.

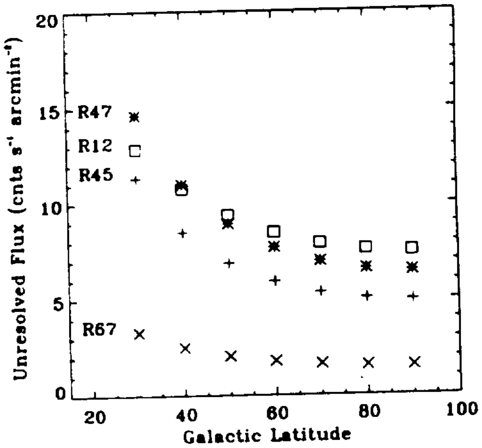

Fig. 7.10.— The contribution of unresolved stellar sources to the *RASS* as a function of Galactic latitude. It is assumed that the point source removal limits were 0.025 counts s^{-1} in band R12 and 0.02 counts s^{-1} in band R45 and band R67.

If the normalization suggested by the deep surveys discussed in §3.2 is correct, then these values would increase by a factor of ~ 1.6.

TABLE 7.3

PREDICTIONS

Survey	(ℓ, b) 2000	Band	Area deg^2	ID Comp.	Source Limit 10^{-3} c/s	Pred.	Obs.
Bower et al. (1996)	(96.4, 29.8)	47	0.21	0.90	.763	1.9	3
Schmidt et al. (1998)	(149.5, 53.5)	47	0.28	1.00	.459	2.8	3
Zamorani et al. (1999)	(270.2,-51.8)	47	0.20	0.84	.309	2.4	4
McHardy et al. (1998)	(85.0, 75.9)	47	0.17	1.00	.175	3.0	5
Carballo et al. (1995)	(162.6, 51.1)	47	2.20	0.57	1.42	4.6	9
Boyle, Wilkes, & Elvis (1997)	various	47	3.92	0.89	1.7	11.9	20
Comparison to measured log N-log S function							
Krautter et al. (1999)	various	47			9.52	0.40-0.72	0.6
		47			95.2	0.030-0.038	0.04
		47			952	0.0014-0.0016	0.004
Krautter et al. (1999)	various	17			17	0.6-1.01	0.6
		17			170	0.058-0.073	0.04
		17			1700	0.0032-0.0036	0.004

6. Future Improvements

In the future, this model will be applied to the problem of the X-ray "infill" of the Galactic plane. A number of improvements will be made.

1.) The M_V-mass relation has been improved by (Henry & McCarthy 1993), and there is likely to be a better low-mass IMF available. (Bessell & Stringfellow (1993), for example, suggest that there is a deficit of old late M stars.) Since the M stars dominate the main-sequence luminosity function, changes in the number of M stars could cause significant changes in the luminosity function.

2.) Schmitt, Fleming, & Giampapa (1995) and Schmitt (1997) have shown that the hardness ratio of a star depends upon its luminosity; fainter stars are softer/cooler. This change can amount to a change of a factor of two in the flux-to-counts conversion factor from one end of the probability distribution to the other. Since the intrinsically more luminous stars have less negative hardness ratios the conversion factor is higher for higher luminosity stars; the high luminosity tail is attenuated and the low luminosity tail is augmented. Although the hardness ratio dependent conversion was used for the 1-10 Gyr population, the luminosity-hardness-ratio relation has not yet been determined for the younger populations.

3.) The field A star luminosity distribution should be determined. This will be important for working close to the plane.

4.) Similarly, the RS CVn luminosity function should be included for work near the Galactic plane.

5.) The Hyades luminosity function could be improved by the point source data from pointed PSPC observations. These data are in-hand, but have not been examined.

6.) The contribution from OB stars and giants of all spectral classes needs to be reassessed.

REFERENCES

Babu, G. J., & Feigelson, E. D. 1996, Astrostatistics (Chapman & Hall)

Bessell, M. S., & Stringfellow, G. S. 1993, ARA&A, 31, 433

Bienaymé, O., Robin, A. C., & Crézé, M. 1987, A&A, 180, 94

Bower, R. G., et al. 1996, MNRAS, 281, 59

Boyle, B. J., Wilkes, B. J., & Elvis, M. 1997, MNRAS, 285, 511

Carballo, R., Warwick, R. S., Barcons, X., Gonzalez-Serrano, J. I., Barber, C. R., Martinez-Gonzalez, E., Peres-Fournon, I., & Burgos, J. 1995, MNRAS, 277, 1312

Cen, R., & Ostriker, J. P. 1999, ApJ, 514, 1

Dempsey, R. C., Linsky, J. L., Fleming, T. A., & Schmitt, J. H. M. M. 1993, ApJS, 86, 599

Fiegelson, E. D., & Nelson, P. I. 1985, ApJ, 293, 192

Fleming, T. A., Molendi, S., Maccacaro, T., & Wolter, A. 1995, ApJS, 99, 701
Fleming, T. A., Snowden, S. L., Pfeffermann, E., Briel, U., & Greiner, J. 1996, A&A, 316, 147
Guillout, P., Haywood, M., Motch, C., & Robin, A. C. 1996, A&A, 316, 89
Hasinger, G., Burg, R., Giacconi, R., Schmidt, M., Trümper, J., & Zamorani, G. 1998, A&A, 329, 482
Haywood, M., Robin, A. C., & Crézé, M. 1997, A&A, 320, 428
Henry, T. J., & McCarthy, D. W. 1993, AJ, 106, 773
Hünsch, M., Schmitt, J. H. M. M., Schröder, K.-P., & Zickgraf, F.-J. 1998, A&A, 330, 225
Hünsch, M., Schmitt, J. H. M. M., Sterzik, M. F., & Voges, W. 1999, A&AS, 135, 319
Krautter, J., et al. 1999, A&A, 350, 743
Kroupa, P., Tout, C. A., & Gilmore, G. 1993, MNRAS, 262, 545
Kuntz, K. D., & Snowden, S. L. 2000, ApJ
Lockman, F. J. 1984, ApJ, 283, 90
McHardy, I. M., et al. 1998, MNRAS, 295, 641
Morrison, R., & McCammon, D. 1983, ApJ, 270, 119
Mushotzky, R. F., Cowie, L. L., Barger, A. J., & Arnaud, K. A. 2000, Nature, in press
Ottmann, R., Fleming, T. A., & Pasquini, L. 1997, A&A, 322, 785
Ottmann, R., & Schmitt, J. H. M. M. 1992, A&A, 256, 421
Randich, S., & Schmitt, J. H. M. M. 1995, A&A, 298, 115
Randich, S., Schmitt, J. H. M. M., & Prosser, C. 1996, A&A, 313, 815
Scalo, J. M. 1986, Fundamentals of Cosmic Physics, 11, 1
Schmidt, M., et al. 1998, A&A, 329, 495
Schmitt, J. H. M. M. 1985, ApJ, 293, 178
Schmitt, J. H. M. M. 1997, A&A, 318, 215
Schmitt, J. H. M. M., Fleming, T. A., & Giampapa, M. S. 1995, ApJ, 450, 392
Schröder, K.-P., Hünsch, M., & Schmitt, J. H. M. M. 1998, A&A, 335, 591
Snowden, S. L., Egger, R., Finkbeiner, D., Freyberg, M. J., & Plucinsky, P. P. 1998, ApJ, 493, 715
Snowden, S. L., Freyberg, M. J., Kuntz, K. D., & Sanders, W. T. 2000, ApJS, in press
Stauffer, J. R., Caillault, J.-P., Gagné, M., Prosser, C. F., & Hartman, L. W. 1994, ApJS, 91, 625
Stern, R. A., Schmitt, J. H. M. M., & Kahabka, P. T. 1995, ApJ, 448, 683
Voges, W., et al. 1999, A&A, 349, 389
Zamorani, G., et al. 1999, A&A, 346, 731

Chapter 8: Deabsorption

Abstract

This chapter discusses the optimal manner by which to correct X-ray images for absorption due to the Galactic ISM in the absence of high-resolution (~ 1′) surveys of tracers of the total absorbing column. This chapter treats three issues. First, although the *IRAS* 100 μm survey is adopted as the best currently available high-resolution (~ 5′) "surrogate" tracer of the absorbing column, it is necessary to scale the "surrogate" tracer to approximate most closely the true absorbing column, without having a measure of that absorbing column other than the absorbed X-ray images. Second is the purely technical issue of the optimal algorithm for calculating the emission from beyond the absorbing column using the observed absorbed emission and the map of the surrogate tracer. Third is the uncertainty in the deabsorbed emission, particularly the uncertainties that produce spurious spatial variation in the measured deabsorbed emission.

We remove regions with significant molecular contribution by removing regions with H I column densities greater than 3×10^{20} cm^{-2}. We find that the *IRAS* 100 μm emission is a better tracer of the total X-ray absorbing column than the H I 21 cm emission. The 100 μm emission may be a better tracer of the absorbing column because 1.) it traces dust (i.e., absorbers) rather than the gas containing the absorbers or 2.) it traces all phases of H (H_2, H I, and H II), rather than just the neutral component. The best agreement between X-ray absorbing column and 100 μm emission occurs when the 100 μm emission is scaled to the column density of H I in the velocity range ±75 km s^{-1}. Although we have little knowledge of the distribution of H II, and H II is poorly traced by 100 μm emission, we show that the error produced by absorption by H II is $< 3\%$ in band R12 and $< 1\%$ in band R45.

1. Introduction

Deabsorption is the process by which one uses a map of the absorbing column density to determine the amount of emission before and behind the screen of absorption. The goal of the operation is either to calculate the mean emission from beyond the absorbing screen, as in Chapter 5, or to determine the structure of the emission from beyond the absorbing screen, as in the following chapter.

1.1. Method

In order to correct for the effects of Galactic absorption, we have assumed the "standard" model for the distribution of the X-ray emission and absorption; the solar system is surrounded by a Local Hot Bubble (LHB) beyond which the bulk of the absorption is due to diffusely distributed material in the Galactic disk. Exterior to the disk is X-ray emission due to the Galactic halo as well as the X-ray emission due to the extragalactic background. The observed X-ray flux, I_O, is given by

$$I_O = I_L + I_D e^{-(N_H)\sigma(\nu, N_H, \mathcal{S}_D)} + I_E e^{-(N_H)\sigma(\nu, N_H, \mathcal{S}_E)} \qquad (8.1)$$

where I_L is the local (LHB) X-ray emission, I_E is the contribution due to the extragalactic background by unresolved point sources, and I_D is the distant component of the X-ray emission including the Galactic halo and the putative emission from a diffuse extragalactic background. Note that we are assuming that the local emission is "flat" on the scale of region being deabsorbed. The $\sigma(\nu, N_H, \mathcal{S})$ is the effective cross-section, which is a function of the energy band, ν, the total absorbing column, N_H, and the shape of the background spectrum, $\mathcal{S}$. Throughout the following chapter, N_H is the total absorbing column density, expressed in terms of the total column density of hydrogen nucleons. In order to simplify the deabsorption process, we produce

$$I'_O = I_O - I_E e^{-(N_b)\sigma(\nu,N_H,\mathcal{S})_E} \qquad (8.2)$$

so that we fit

$$I'_O = I_L + I_D e^{-(N_b)\sigma(\nu,N_H,\mathcal{S}_D)}. \qquad (8.3)$$

In order to accomplish the deabsorption, we must first produce an I_O image by removing the flux due to the unresolved extragalactic point sources, for which we have assumed the functional form given by Chen, Fabian, & Gendreau (1997). One must also correct the X-ray mosaics for the effects of spatially varying point source removal (§2.1). In order to find I_L and I_D we must bin the I'_O image by the absorbing column density, N_H (§2.2), to produce an $I' - N_H$ relation that can be fitted by Equation 8.3.

Before fitting, we must determine $\mathcal{S}_D$, the shape of the spectrum of the X-ray background. This background will include emission by the Galactic halo and the putative extragalactic background, as well as other, as yet unidentified components. The shape of the background spectrum is discussed in §3.

Before creating the $I' - N_H$ relation one must also construct a map of the total absorbing column. No single tracer will follow all of the possible states of the absorbing gas. The bulk of the absorption will be due to gas associated with the neutral hydrogen, but the spatial resolution of existing neutral hydrogen surveys is insufficient ($\sim 30'$) to resolve the fine-scale structure of the H I. The *IRAS* 100 μm survey is the best surrogate tracer, as it has much higher angular resolution ($\sim 5'$), but it may not track the entire H I column, and it traces other components as well (i.e., H_2 and, perhaps, H II). The manner in which we can use the primary tracer (H I 21 cm emission) and the surrogate tracer (the 100 μm emission, I_{100}) to form the best currently-possible tracer of the total absorbing column is discussed in §4.

Once the $I' - N_H$ relation has been fit, and the quantities I_L and I_D have been determined, two different methods can be used to calculate the image of the distant emission. These methods are compared in §5.

1.2. Errors

In each section we will estimate the magnitude of the errors introduced by the deabsorption process. There are three different types of errors to be considered. The first type of error is in the fit coefficients. While the error in the fit parameters is the prime concern if one is attempting to determine the magnitude of the distant emission, when one is interested primarily in the structure of the distant emission, the uncertainty in the fit parameters enters only when one determines the relative size of the fluctuations compared to the background. We will see that the uncertainty in the fit parameters is reduced in band R47 as the foreground emission is negligible and is treated as a fixed parameter.

The second type of error is the deviation of the fit from the mean measured $I'_O - N_H$ relation. The uncertainty in this function contributes to the uncertainty in the residual to the fit. The uncertainty in the value of the fit at a given value of N_H is typically small as the function must fit the observed points. Changing the scaling of the absorbing column, for example, may change the fit parameters, but will do little to change the fitted relation itself. Errors of this type will be dependent on N_H, and should be visible as a correlation of emission with N_H within the image of the distant emission.

The third type of error is in the absorbing column. This is the most serious type of uncertainty for studies of the structure of the distant emission as systematic errors in the absorbing column could cause spurious deviations from the mean $I'_O - N_H$ relation. This type of uncertainty is also the most difficult to determine as the variation in the column density of H II is virtually unknown at small angular scales.

The relative impacts of various types of errors is summarized at the end of §4.

2. I_O

2.1. Point Source Correction

The X-ray mosaic must be corrected for the position-dependent point source detection limit (PSDL) and point source removal. When creating the mosaics, the point sources were removed to the local PSDL. This means that, on average, pixels in regions with lower PSDLs (i.e., better PSDLs) will have more flux removed due to point source removal than will pixels with higher PSDLs. To correct for the spatially variable flux removal, we set a global PSDL which is higher than the PSDL over the bulk of the mosaic. Regions with higher PSDL are removed. To each mosaic pixel is then added the average flux that would be contributed by point sources whose brightnesses fall between the local PSDL and the global PSDL.

There are two classes of point sources for which we must correct. For extragalactic objects, we have used the Hasinger et al. (1998) log N - log S relation[1].

One must also correct for unresolved Galactic stars. The model for creating the luminosity function as seen from earth, including the effects of absorption, is described in Chapter 7[2]. We calculated that model for the Galactic longitude and latitude for each field, for total absorbing columns of 0.5, 1.5, 2.5, and 3.5 × 10^{20} cm^{-2}. For each image pixel, the correction was obtained by interpolating to the correct column density.

The magnitude of the corrections, and the relative amounts due to Galactic and extragalactic point sources can be seen in Figure 8.1 for the field 138+52. As expected, because of the relatively low column densities of our selected fields. the correction is nearly independent of column density in band R47. Note that the correction due to Galactic stars is only about 10% of the correction due to extragalactic point sources where the corrections are the greatest, though a significantly higher fraction where the correction is smaller. Because the total flux of unresolved Galactic stars is small for all point source detection limits, the uncertainty in the observed luminosity function for Galactic stars will have minimal impact upon the point source correction.

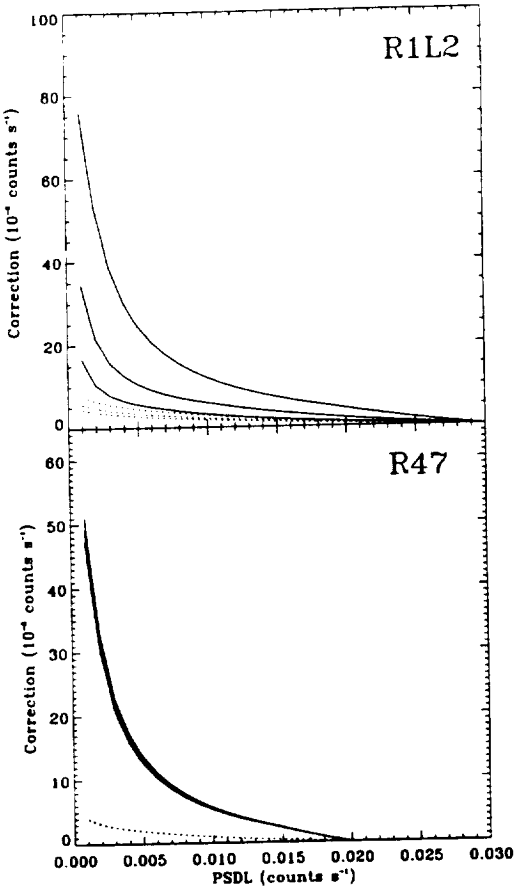

Fig. 8.1.— Typical correction for variable point source detection limits. For both bands R12 and R47 the correction has been made to 0.02 counts s^{-1}. *Solid:* correction due to extragalactic objects, *Dotted:* correction due to Galactic stars. The corrections are shown for three column densities: 10^{20} cm^{-2} (the greatest correction), 2×10^{20} cm^{-2}, and 3×10^{20} cm^{-2}. Typical PSDL are 0.001-0.03 counts s^{-1} in band R1L2 and are 0.0005-0.02 in band R45.

---

[1] Computationally, this process is not a trivial one. The PSDL is in counts s^{-1} after absorption by the local N_H, in a given band. The log N - log S relation is in ergs cm^{-2} s^{-1} after absorption by $N_H = 5 \times 10^{19}$ cm^{-2}, in the R47 band. One must convert both the local and global PSDLs from the count-rate after absorption by N_H to the count-rate after absorption by 5 × 10^{19} cm^{-2} by multiplying by

$$e^{-N_H \sigma(N_H,S)} e^{5\times10^{19}\sigma(5\times10^{19},S)} \neq e^{(5\times10^{19}-N_H)\sigma(5\times10^{19}-N_H,S)},$$

where the spectral shape S is taken to be a power law of photon index 2.0 for consistency with Hasinger et al. (1998). The count-rates are then converted to energies using the conversions of Hasinger et al. (1998) and their log N-log S relation used to determine the average flux per pixel produced by point sources with brightness between the local and global limits. The flux is then converted back to a count-rate in the proper band after absorption by N_H by the reverse of the above process. Note that the correction is dependent upon N_H.

[2] Since the model already includes the effects of absorption, and changing the absorption by factors of two causes little change in the observed luminosity functions. one need not execute the same computational mess required for the extragalactic luminosity function.

2.2. N_H Binning

In order to determine the mean $I'_O - N_H$ relation, once the X-ray mosaic has been corrected for the variable PSDL, the data must be binned by the absorbing column. There are two ways of executing this binning. The crude method is to use the rate images, and to sum the uncertainties in quadrature[3]. A more refined method is to return to the raw count, background count, and effective exposure images, bin each quantity separately, and then determine the X-ray rate for each N_H bin[4]. The crude method weights all pixels evenly and can produce unreasonably large uncertainties in cases where the effective exposure varies greatly (e.g. edge pixels where the effective exposure can be near zero). The more refined method provides more accurate count rates and uncertainties and effectively weights more heavily the higher exposure regions.

It should be noted that in both cases, the uncertainty for the X-ray flux in any N_H bin will be the uncertainty in the mean of that bin. Alternately, one could calculate as the uncertainty the dispersion of the X-ray values in a given bin. However, this latter method produces very large values of the uncertainty per pixel and very poor fits. Since the fits are attempting to determine the mean I_L and the mean I_D, use of the uncertainty of the mean X-ray emission in a given bin is justified.

With the exception of Figure 8.4 and Table 8.2, the refined binning method has been used throughout this paper.

3. σ_{eff}

As can be seen in Equation 8.3, the effective cross-sections are a function of the shape of the background X-ray spectrum, $\mathcal{S}$. We have taken as the background spectrum that found by Kuntz & Snowden (2000). This spectrum is composed of two components, each of which is modeled by thermal equilibrium spectra, with $\log T_S = 6.056$ and $\log T_H = 6.462$. The relative strengths of the two components, $\mathcal{N}_S$ and $\mathcal{N}_H$, varies by a factor of ~ 4, and is dominated by the variation in $\mathcal{N}_S$. We have calculated effective cross-sections for the mean high-Galactic $\mathcal{N}_H/\mathcal{N}_S$, as well as a factor of two higher and lower. Figure 8.2 compares these effective cross-sections with those derived from single-component thermal equilibrium models.

As might be expected, the R1L2 band effective cross-sections are dominated by the soft thermal component, while the R67 band effective cross-sections are dominated by the hard thermal component. The R45 band effective cross-sections, however, are not well represented by either single component within the column density range encountered in the deabsorptions presented here (5×10^{19} cm^{-2} to 3×10^{20} cm^{-2}, see the following section.).

In order to determine the correct $\mathcal{N}_H/\mathcal{N}_S$ for a given field, we first fit Equation 8.3 using the *RASS* data for the field. We then select those parts of the field within a narrow range of column densities for which there are a large number of image pixels, usually $0.9 \times 10^{20} \leq N_H \leq 1.0 \times 10^{20}$ cm^{-2}, and determine the mean absorbing column for that region. Using the I_D determined for bands R1 and R2, reabsorbed by the mean column, as well as the data from bands R4-R7, in the selected parts of the field,

---

[3] If i is the index of the n pixels having $h < N_H < h + \Delta h$, then the X-ray rate, R, its uncertainty, σ, and the absorbing column, N_H for a given bin will be

$$R = \sum_i R_i/n,$$

$$\sigma = \sqrt{\sum_i \sigma_i^2}/n, \text{ and}$$

$$N_H = \sum_i N_{H i}/n$$

respectively, where the subscribed quantities are the pixel values.

[4] If i is the index of the n pixels having $h < N_H < h + \Delta h$, then the X-ray rate, R, its uncertainty, σ, and the absorbing column, N_H for a given bin will be

$$R = \frac{\sum_i C_i - \sum_i B_i}{\sum_i E_i},$$

$$\sigma = \frac{\sqrt{\sum_i C_i}}{\sum_i E_i}, \text{ and}$$

$$N_H = \frac{\sum_i N_{H i} E_i}{\sum_i E_i}$$

respectively, where C_i, B_i, and E_i are the raw counts, background, and effective exposure in pixel i. The uncertainty in the background, B_i, is assumed to be much smaller than the Poissonian uncertainty in C_i.

we form a spectral energy distribution. We determine the values of $\mathcal{N}_H$ and $\mathcal{N}_S$ by fitting the two-component spectrum to the spectral energy distribution in a manner similar to that used in Kuntz & Snowden (2000). Using the values of $\mathcal{N}_H$ and $\mathcal{N}_S$ we can then create a two-component Raymond & Smith model spectrum from which to calculate the σ_{eff}.

3.1. The Uncertainty due to σ_{eff}

One can calculate the effect of using a σ_{eff} derived from a one-component model spectrum when the "true" background is produced by the two-component spectrum described above. For column densities from 5×10^{19} cm^{-2} to 3×10^{20} cm^{-2} we have calculated

$$I_O = 1 + e^{-N_H \sigma(N_H, S)} \qquad (8.4)$$

at 5×10^{18} cm^{-2} intervals where the background spectrum was the two component model. We fit the I_O-N_H relation where σ_{eff} was calculated using a single thermal component model of the background spectrum. We then calculated the fractional difference in the I_L and I_D fit parameters and determined the maximum fractional deviation between the true and fitted relations. The results are given in Table 8.1. The greatest effect is upon the fit parameters, I_L and I_D, with fractional differences up to 10%. However, the fractional difference between the true I_O-N_H relation and the fit to that relation are very small, $< 0.9\%$. This source of uncertainty will not directly contribute to the production of spurious fluctuations.

Errors due to an uncertainty in $\mathcal{N}_H/\mathcal{N}_S$ will be substantially smaller than those listed in Table 8.1.

4. N_H

4.1. Some Considerations

Deabsorption requires a tracer of the total absorbing column, N_H. The material responsible for the absorption exists in at least three phases of the ISM, the H I, the H II, and H_2. High resolution maps of these three phases do not exist. However, the dominant phase is H I, which is traced by the *IRAS* 100 μm emission, I_{100}, for which there is a high resolution (5′) all-sky

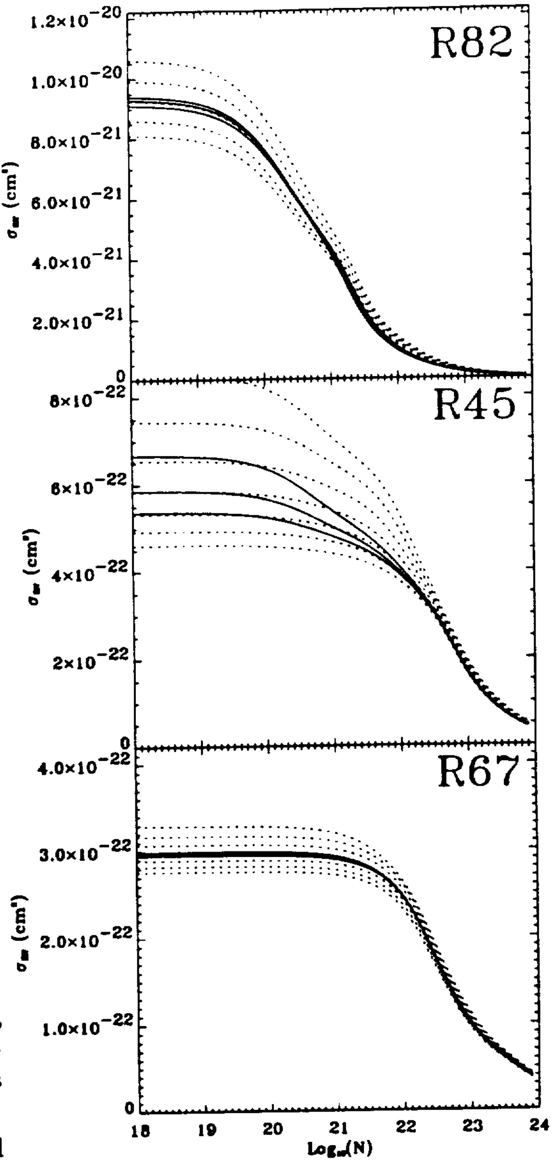

Fig. 8.2.— Comparison of effective cross-sections. In each panel the three solid lines represent two-thermal component emission models for the Galactic halo taken from Kuntz & Snowden (2000). The $\mathcal{N}_H/\mathcal{N}_S$ for the three lines are from top to bottom, 1.13, 0.56, and 0.28. The dotted lines represent single-component thermal equilibrium models: *Top:* $\log T$ = 6.0 to 6.2, $\Delta \log T = 0.05$, *Middle Row:* $\log T$ = 6.2 to 6.5, $\Delta \log T = 0.05$, *Bottom Row:* $\log T$ = 6.3 to 6.6, $\Delta \log T = 0.05$. Lower temperature models have higher effective cross-sections. Band R82 is the same as band R1L2.

TABLE 8.1
EFFECT OF SPECTRAL SHAPE

Band	$\mathcal{N}_H/\mathcal{N}_S$	I_L	I_D	Residual[b]	
				min.	max.
		$\times 10^{-2}$	$\times 10^{-2}$	$\times 10^{-4}$	$\times 10^{-4}$
R1L2	1.14	-2.72	1.00	-3.33	2.67
R1L2	0.56	-5.90	5.44	-4.45	5.79
R1L2	0.28	-7.90	2.53	-6.29	9.23
R45	1.14	9.32	-9.35	-1.94	4.73
R45	0.56	4.29	-4.45	-1.34	2.89
R45	0.28	-3.92	3.55	-3.26	6.86
R67	0.56	4.16	-4.16	-.003	.006

All quantities are fractional differences. The calculations were made by calculating $I_O = 1 + e^{-N_H\sigma_2}$ for the σ_2 calculated from the Kuntz & Snowden (2000) model, and then fit the relation $I_O = I_L + I_D e^{-N_H\sigma_1}$, where the σ_1 were calculated from a one-component thermal equilibrium model.

[a] The R1L2 band comparison was a Raymond & Smith model with $\log T = 6.1$, for R45, $\log T = 6.35$, for R67, $\log T = 6.45$.

[b] The residual is measured over $5 \times 10^{19} < N_H < 3 \times 10^{20}$.

survey. Thus, we attempt to produce a map of the total absorbing column, N_H, by scaling I_{100} to the column density of the H I, that is, *we assume that the magnitude of the total absorbing column density is well approximated by the H I 21 cm column density, but that the structure is better approximated by the higher resolution maps of the dust emission.* However, I_{100} traces the other phases as well, so the problem is not just forming a tracer of N_H, but determining the extent to which the I_{100} traces the dominant phase, and determining whether the deviation of the I_{100} from the H I is due to other absorbing components. We begin by considering the relation between H I and I_{100}, followed by the relation of a bootstrapped N_H to the observed X-ray flux, I_O.

The relation between I_{100} and H I is an interesting topic of its own (Arendt et al. 1998; Reach, Koo, & Heiles 1994; Reach, Wall, & Odegard 1998). Regions with H I columns $> 3\times10^{20}$ usually contain H_2, which is well traced by I_{100} (Reach, Wall, & Odegard 1998). However, in molecular regions, I_{100} will depend sensitively on the dust temperature which is determined at resolutions no better than $\sim 1°$. Given that there are no high resolution maps of H_2 (or its surrogate, CO) for most regions, and the conversion between I_{100} and N_H will be made uncertain due to the dust temperature, regions possibly containing H_2 are best avoided.

In regions not including molecular gas, the H I/I_{100} ratio will depend upon the metallicity, dust to gas ratio, and dust temperature, as well as the column densities of H II. The H I/I_{100} ratio varies on all scales of interest (see Chapter 4), but the dominant source of the variation is unknown. It is understood that I_{100} predominately traces the "warm disk gas"; H I in high or intermediate velocity clouds (HVCs or IVCs) is not well traced by I_{100} either due to decreased metallicity or decreased dust temperatures (Wakker & Boulanger 1986). However, even excluding regions with HVCs and IVCs, the dust temperature correction proposed by Schlegel, Finkbeiner, & Davis (1998) does not remove the H I/I_{100} variation.

The variation of the H I/I_{100} ratio might be due to the column density of H II, which is not yet known for more than small parts of the sky. However, emissivity of dust associated with H II is thought to be much smaller than that associated with H I (Hauser et al. 1998). Thus, it should be kept in mind that since I_{100} *may* trace the H II as well as the H I, it *may* be a better tracer of N_H than H I alone.

It should be noted that even if a perfect correlation could be found between the H I and I_{100}, it would still not be clear which component of the H I contribute to the absorption of

X-rays. The average H I spectrum is characterized by a broad feature centered on ~ 0 km s^{-1} with a turbulent velocity width of ~ 20 km s^{-1} and a scale height of ~ 120 pc (Lockman & Gehman 1991). There are broader components, with velocity widths of 40 km s^{-1} and 80 km s^{-1} and scale heights of ~ 280 pc and ~ 715 pc (Lockman & Gehman 1991). There may be an even broader component with an even greater scale height (Kalberla et al. 1997). There are also components centered at intermediate ($50 \leq v \leq 100$ km s^{-1}) and high ($v \geq 100$ km s^{-1}) velocities whose z-heights tend to increase with their velocity.

The extragalactic background will clearly be absorbed by all of these components. However, the Galactic halo emission may or may not be absorbed by high-z components; as the z-height of the Galactic halo emission is unknown and the z-heights of the absorbers are only poorly known. The problem is compounded as preliminary investigations have suggested that some high velocity clouds may produce X-ray emission (Kerp et al. 1999). Thus, it is not clear whether including H I with velocities $\gtrsim 75$ km s^{-1} will improve the fits to Equation 8.3.

4.2. Overview of Method

The tracer of N_H must meet two requirements. The tracer must have the correct spatial distribution of absorbers, that is, the correct "structure", and the tracer must have the correct column density of absorbers, that is, the correct "scaling". Since we are interested only in small fields, on the order of 15° × 15°, the problem is somewhat simplified.

The method used to create a map of N_H from I_{100} is to first remove regions affected by molecular gas, that is, regions with H I $> 3 \times 10^{20}$ cm^{-2}. We then find the velocity range of H I that most closely matches the structure seen in the I_{100} map. We then remove all regions with significant H I emission outside of this velocity range. The I_{100} image is then scaled by the best linear relation between I_{100} and H I.

In general, the I_{100} is best matched by H I in the ± 75 km s^{-1} range, as determined by minimizing the scatter in a linear H I to I_{100} relation. Removing the regions with significant column densities of high velocity gas (HVG, i.e., H I with $|v| > 75$ km s^{-1}) does improve the fits to Equation 8.3, and removal of the HVG to column densities of 1.5×10^{19} cm^{-2} is sufficient.

4.3. Details

This section discusses the experiments that were performed to reach the method and parameters described above. The experiments were performed to answer a series of questions: What velocity range of H I best mimics the I_{100} structure? Should the strong high velocity gas structures be removed, and if so, to what column density must they be removed? Are there significant absorption components besides the H I, or is the I_{100} tracing some other component as well? This last question can be reformulated as an inquiry whether the H I/I_{100} variation traces a variation in the column density of absorbers or merely variation in dust emissivity within the H I.

To explore these questions we used a single X-ray mosaic, 138+52, as it covers a large area, has a large range of absorbing columns, and for which, in addition to the Dwingeloo data, we have a higher resolution H I data set provided by J. Lockman. This mosaic is located in the direction of the Lockman Hole, which has been discussed by Snowden et al. (1994). Images of the X-ray and tracer data for this region are shown in Figure 8.3.

No part of the area shown in Figure 8.3 has column densities, as measured by H I 21 cm, great enough to contain molecular gas. Almost a quarter of the mosaic is covered by H I with $|v| > 75$ km s^{-1}, but very little is covered by significant column densities of high velocity gas. The H I/I_{100} ratio has a $\sim 30\%$ variation. Although a portion of that variation does seem to have the same structure as the H I, both low and high column density regions can be found having the same H I/I_{100} ratio.

Both the *RASS* image and the mosaic show structure due to absorption. The I'_O-N_H relations are shown in Figure 8.4 for both the *RASS* and the mosaic for different measures of N_H.

The *structure* of the N_H is set by our choice of I_{100} as a tracer. It can be modified, presumably to make the tracer more closely conform to the true N_H, by masking out regions where the smoothed I_{100} structure does not match that of

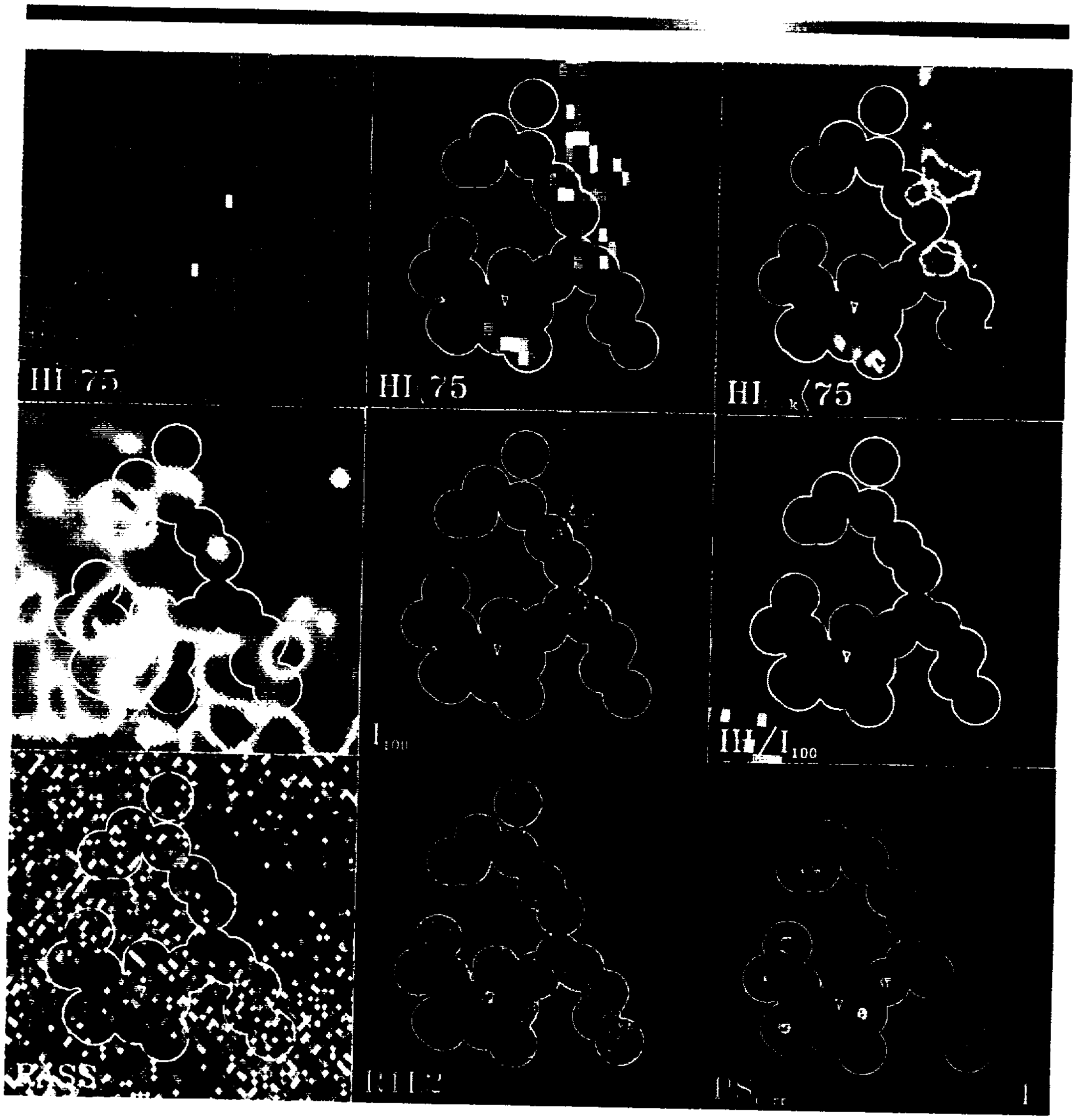

Fig. 8.3.— Images of the 138+52 soft X-ray mosaic and tracers of the absorbing column. Each image is 12°8 on a side, the individual PSPC pointings have 53′ radii. *Top Row:* from left, the Dwingeloo H I data for the high velocity gas ($|v| > 75$ km s^{-1}) greyscale from 0 to 2.5×10^{20} cm^{-2}, white contour at 1.5×10^{19} cm^{-2}; the Dwingeloo H I data for the "disk" gas ($|v| < 75$ km s^{-1}), greyscale from 3×10^{19} cm^{-2} to 2.8×10^{20} cm^{-2}; the Lockman H I data for the "disk" gas ($|v| < 75$ km s^{-1}), greyscale from 0 to 3.0×10^{20} cm^{-2}. *Middle Row:* from left, the Schlegel, Finkbeiner & Davis (1998) temperature correction factor, X, greyscale from 0.8 to 1.3; the Schlegel, Finkbeiner & Davis (1998) destriped *IRAS* 100 μm data, greyscale from 0.1 MJy sr^{-1} to 4.3 MJy sr^{-1}; the H I/I_{100} ratio, greyscale from 0.5 to 3.5. *Bottom Row:* from left, the *RASS*, greyscale from 4 to 14 $\times 10^{-4}$ counts s^{-1} arcmin^{-2}; the R1L2 X-ray mosaic, greyscale from 4 to 10 $\times 10^{-4}$ counts s^{-1} arcmin^{-2}; point source correction, greyscale from 0 to 1×10^{-4} counts s^{-1}. The scale bar is shown in the lower right-hand corner.

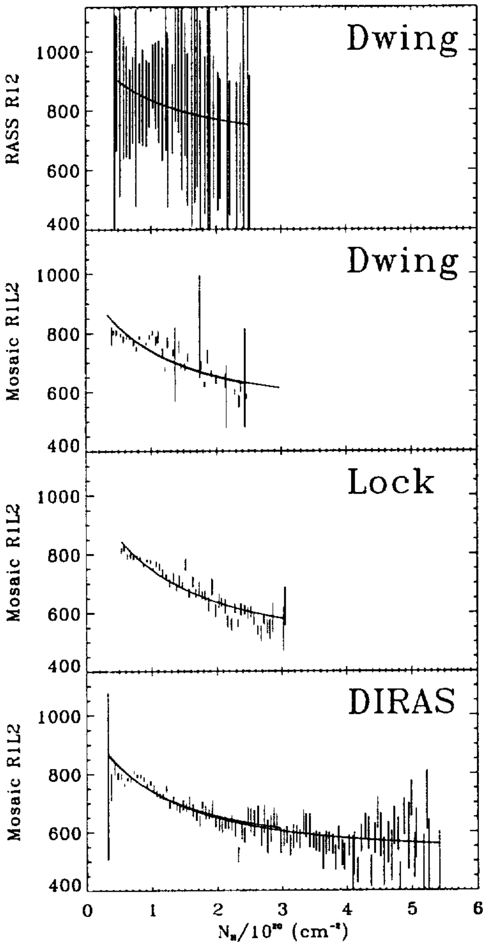

Fig. 8.4.— Comparison of the I'_O-N_H relations for mosaic region 138+52. *Top:* the *RASS* data *vs.* the Dwingeloo 21 cm data, *Upper Middle:* the band R1L2 mosaic *vs.* the Dwingeloo data, *Lower Middle:* the band R1L2 mosaic *vs.* the Lockman 21 cm data, and *Bottom:* the band R1L2 mosaic *vs.* the *IRAS* 100 μm data scaled to the Dwingeloo 21 cm column density.

the much more coarsely sampled N_H. Changing the structure of the N_H tracer has the effect, after the data have been binned by N_H, of moving individual image pixels from one N_H bin to another; the mismatch between the tracer and the true N_H increases the scatter in the I'_O-N_H relation. The *scaling* of the N_H is set by the H I velocity range to which we fit the I_{100}-H I relation, and by the "H I scaling" process. Changing the scaling of the N_H stretches the N_H axis, changing the curvature in the I'_O-N_H relation, but does not change the scatter in that relation. Finally, one could attempt to use the variation in the H I/I_{100} ratio to employ a position dependent scaling.

How can one test the general prescription given in the previous section? One might try to find the method of scaling the I_{100} to the H I that minimizes the χ^2 when fitting Equation 8.3 to the I'_O-N_H relation. As noted above, changing the structure will change the scatter in the I'_O-N_H relation, so finding the method that gives the best approximation of the *structure* of the N_H (as measured by the I'_O-N_H relation) is easy.

Conversely, determining the method that gives the best *scaling* is difficult. If one fits

$$I'_O = I_L + I_D e^{-(\mathcal{K}N_H)\sigma(\nu,\mathcal{K}N_H,\mathcal{S})} \qquad (8.5)$$

where $\mathcal{K}$ is the scaling of the N_H, then if one increases $\mathcal{K}$, I_D will decrease and I_L will increase to compensate, producing a nearly identical fit [5]. The χ^2 surface is very poorly structured, having many local minima. Thus, although I_L and I_D, the parameters in which one is really interested, are very sensitive to $\mathcal{K}$, there is no way of testing $\mathcal{K}$.

4.3.1. Scaling

An example of the difficulty of testing $\mathcal{K}$ is given by an attempt to determine whether H II might trace significant absorption. Some $\sim$ 33% of the H II is thought to be correlated with H I (Reynolds 1991). Thus, if one attempted to fit Equation 8.5 using the H I as a measure of N_H, one ought to find $\mathcal{K} > 1$. (The best estimate is $\mathcal{K}$ should be 1.2[6].) However, besides any con-

---

[5] Fitting Equation 8.5 is non-trivial. There are two possibilities, and choosing the algorithmically simpler leads to disaster. Equation 8.5 was fit using a non-linear routine, the down-hill simplex or amoeba method. The simplest way of fitting the equation is to bin the X-ray data by N_H only once, then for each evaluation, scaling the N_H by $\mathcal{K}$, determining the new σ_{eff}, and calculating the model I_O. The better way of fitting the equation is to bin the X-ray data by $\mathcal{K}N_H$ for each evaluation. The simpler method, for some reason that is not clear, tends to run away, producing very small $\mathcal{K}$. It appears that it may be producing the largest $\mathcal{K}$ consistent with $I_L = 0$. The better method produces a very poorly behaved χ^2 surface because slight changes in $\mathcal{K}$ will change the bin into which a given pixel is placed. If there are two pixels with similar N_H both of which have anomalously high X-ray fluxes, the goodness of fit can be strongly influenced by whether those two pixels end up in the same N_H bin or not.

[6] We have assumed that

sideration of the χ^2 surface, there is another problem. Since the emission by the N_H tracer is linear with column but absorption is exponential with column, and the emission data is much lower resolution than the absorption data, any clumping in the absorbing column should lower $\mathcal{K}$ below unity. To explore this problem we fit Equation 8.5 using the X-ray mosaic for band R1L2, the Dwingeloo data ($\sim 30'$ resolution) and the Lockman data ($\sim 9 - 15'$ resolution). The results are shown in Table 8.2. Although $\Delta\mathcal{K} \sim 0.004$ was sufficient to produce a 1σ change in χ^2, (using the Lampton, Margon, & Bowyer (1976) criteria) yet we find other local minima with nearly the same χ^2 but a $\Delta\mathcal{K}$ of up to 0.2, as can be seen in the two results given for the Dwingeloo data in Table 8.2.

Given the quality of the data, that the fitted value of $\mathcal{K} \sim 1$, and that we have little knowledge of the distribution of H II, we have set $\mathcal{K}$ to unity. At worst, this assumption will introduce a small error in I_D and I_L; it will not effect the scatter of the data around the mean $I'_O - N_H$ relation.

4.3.2. The I_{100}-N_H Relation

We have assumed that the magnitude of the absorbing column density is best approximated by the H I 21 cm column density, while the structure is best approximated by the *IRAS* 100 μm dust emission. We must now determine the optimal way to scale the I_{100} image to the H I 21 cm image.

We know that the 100 μm emission data predominately trace that which is known as "disk" gas. If the H I velocity limits are too broad, one will include structures not traced by I_{100}. Conversely, restricting the H I velocity limits too much will exclude structures that are traced by the I_{100}. To compare the column of H I to I_{100} we binned the *IRAS* data to the same pixel areas contained by the Dwingeloo data set. We then fit the linear relation[7]

$$I_{100} = a + b\frac{HI}{10^{20}}. \tag{8.6}$$

An example fit is shown in Figure 8.5.

As can be seen in Figure 8.5, it is not entirely clear that a simple linear fit reflects reality. If, for example, above a threshold of $\sim 1.5 \times 10^{20}$ cm^{-2} there is some additional component of I_{100} that does not contribute to the H I, one would be inclined to make a fit with a much shallower slope, as shown in the right panel of Figure 8.5. This is similar to the behavior produced by molecular gas, which on average increases the I_{100} emission at column densities greater than 3×10^{20} cm^{-2}. Given the low apparent threshold of the effect, $\sim 1.5 \times 10^{20}$ cm^{-2}, molecular gas should not be causing this effect. H II should not depend upon column density in this manner.

If we look at I_{100} *vs.* H I using the higher resolution Lockman data (Figure 8.6), we see that most of the low column density structure seen in the Dwingeloo H I to I_{100} relation is removed by higher resolution. The high I_{100} values at high H I values are due to dense cloud cores that are not sufficiently resolved by the Dwingeloo data. A simple linear fit is consistent with the Lockman data, and the best fit to the Lockman data is consistent with the best fit to the Dwingeloo data. Thus, the simple linear fit is sufficient in both cases.

The spray of points to higher I_{100} in the right-hand panel of Figure 8.6 raises another question. If small high-column-density regions are not detected by H I due to the low resolution

---

$$\mathcal{K}N_{HI}\sigma_{HI} = N_{HI}\sigma_{HI} + N_{HII}\sigma_{HII}$$

which is equivalent to

$$N_{HI}\sigma_{HI} + N_{HI}\frac{N_{HII}}{N_{HI}}\sigma_{HI}\frac{\sigma_{HII}}{\sigma_{HI}}$$

$$= N_{HI}\sigma_{HI}(1 + \frac{N_{HII}\sigma_{HII}}{N_{HI}\sigma_{HI}}).$$

Using the values given in Chapter 4 we find that $\mathcal{K} \sim 1.2$.

[7] It is well known that since least-squares fitting generally minimizes in only one direction, there is a difference when fitting between "what is H I given I_{100}". (H I$|I_{100}$) and "what is I_{100} given H I?", ($I_{100}|$H I). Since we will be taking I_{100} images and converting them to images that are the equivalent of H I, our formulation would appear to be backwards. We justify our backwardness in the following manner.
We expect H I to be close to the total absorbing column. We know that at a given value of H I, I_{100} will have a range of values due to the IR emission of other components, such as molecular gas. Fitting using equation 8.6 will minimize this scatter. Pixels with additional molecular gas will bias the fit to somewhat larger value of b. Fitting the relation

$$HI = a' + b'I_{100}$$

will minimize in the direction perpendicular to the known scatter. Points with additional molecular gas will produce an even stronger bias in b.

TABLE 8.2
FITTING WITH SCALED N_H

N_H	I_L	I_D	$\mathcal{K}$[a]	χ^2_ν	ν
Dwingeloo	538.4	393.4	1.037	12.46	35
Dwingeloo	493.8	403.0	0.820	12.47	35
Lockman[b]	510.3	492.9	1.027	4.188	35
Lockman[c]	492.2	460.7	1.039	4.904	35

Regions including 1.5×10^{19} cm^{-2} in $|v| > 75$ km s^{-1} were excluded from the fit. The uncertainties are discussed in the text. However, it should be noted that with $\mathcal{K}$ fixed, the uncertainties in I_L and I_D are ~ 8.1 and ~ 14.5 respectively. With $\mathcal{K}$ free to vary, the uncertainties are somewhat larger; ~ 8.5 and ~ 18.1 respectively.

[a] Formally uncertainties are ~ ±0.004. Varying the region used in the fit can change $\mathcal{K}$ by up to ~ 0.2, as can be seen by comparing the two Dwingeloo data fits.

[b] Binned to the Dwingeloo pixel areas.

[c] Original ~ 9 – 15′ resolution.

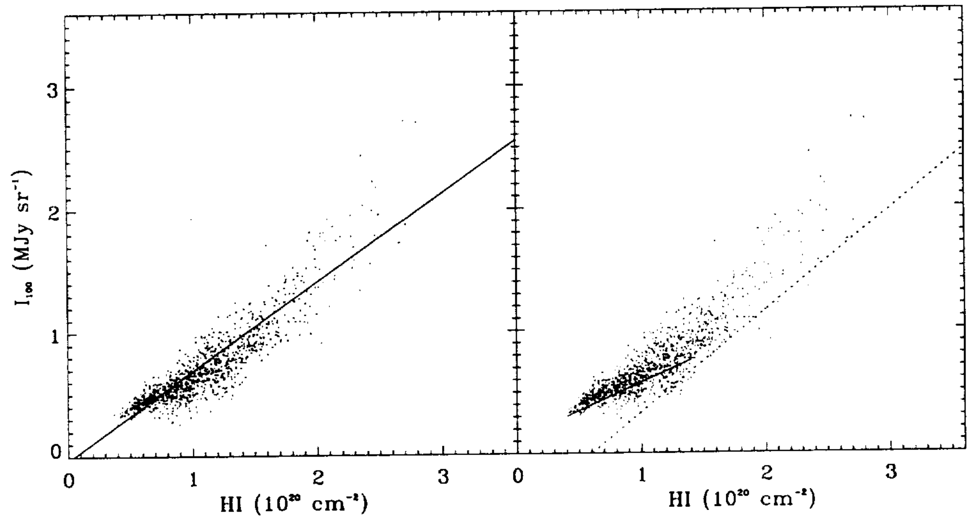

Fig. 8.5.— Example *IRAS* 100 μm emission to Dwingeloo H I 21 cm emission scaling. *Left:* Best linear fit. *Right:* An alternative, the solid line is a "by-eye" fit to the lower bound of the H I to I_{100} relation, the dotted line shows a possible region of avoidence due to a component that contributes to the I_{100} but not the H I. See text for discussion.

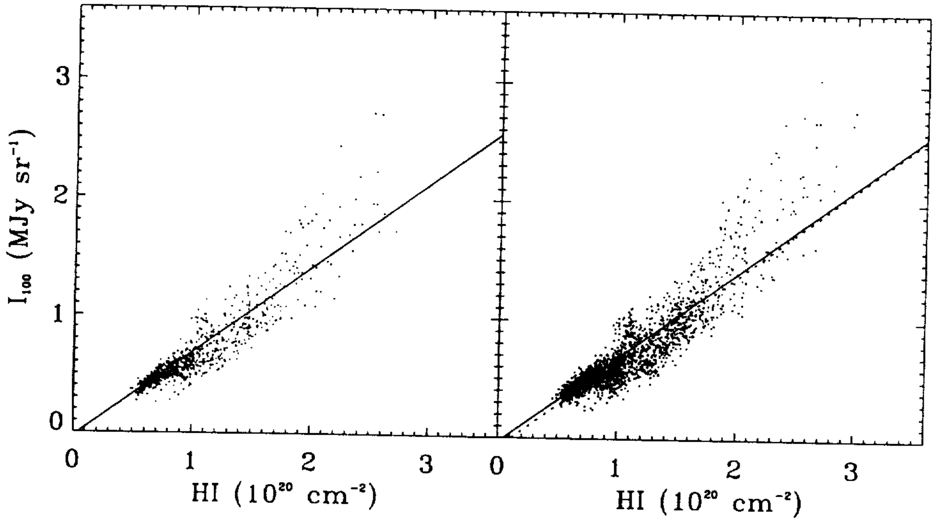

Fig. 8.6.— Example *IRAS* 100 μm emission to Lockman H I 21 cm emission scaling. *Left:* Both the Lockman data and the I_{100} data were rebinned to the Dwingeloo pixel areas. The line is the fit to the Dwingeloo data shown in the previous figure. *Right:* The same data set. The I_{100} data has been smoothed to the Lockman resolution ($\sim 9 - 15'$) and both data sets have been binned to $15'$. The solid line is the same fit as in the previous figure. The dotted line is the best fit to the I_{100} - Lockman H I relation.

of the Dwingeloo survey, how can we be sure that regions containing molecular gas have been removed? We find that although at no place in the field is the H I column density greater than 3×10^{20}, there are regions where the scaled I_{100} does reach those column densities (see Figure 8.4). Those regions are noted by contours on the I_{100} panel of Figure 8.3. Comparison of these regions with the study of Reach, Koo, & Heiles (1994) shows that all *IRAS* clouds with detected CO emission fall within the $N_H > 3 \times 10^{20}$ cm^{-2} contours, where the N_H is derived from I_{100}. Thus, excluding points with $N_H > 3 \times 10^{20}$ cm^{-2}, where the N_H is derived from I_{100}, will be reasonably efficient at removing regions with molecular gas.

Since, as seen in Chapter 4, and again in Figure 8.3, the H I/I_{100} ratio is spatially variable, the mean H I/I_{100} will vary with fit region. We were interested in knowing how the fit values changed with fit region.

Table 8.3 contains the fit results. Although the velocity resolution of the data was much finer, the velocity regions tested were limited to ± 50 km s^{-1}, ± 75 km s^{-1}, ± 100 km s^{-1}, and the entire Dwingeloo velocity range ($-450 < v < 400$ km s^{-1})[8]. Fits were made for a square region surrounding the X-ray mosaic, for the same region but with the I_{100} poor high velocity gas (HVG) removed to various column density limits, and for the region covered by the mosaic. (In the last case, the HVG was removed to the 1.5×10^{19} cm^{-2} level.) It has been assumed that the random uncertainties in the *IRAS* data are all the same, and they have been set to unity

---

[8] Given the broad velocity distribution of the H I, one can assume that the structure seen within the chosen velocity range will extend to more extreme velocities. To compensate for having removed the high velocity wings one can scale the H I column within the chosen velocity range using the factor

$$f = \frac{\langle \mathrm{HI}(-450 \text{ km s}^{-1} < v < 400 \text{ km s}^{-1}) \rangle}{\langle \mathrm{HI}(\text{chosen range}) \rangle},$$

where the means are taken over regions not excluded due to structure at more extreme velocities (i.e., regions without HVCs). This scaling factor is typically on the order of 1.05 to 1.20 when comparing the ± 100 km s^{-1} and ± 50 km s^{-1} velocity ranges to the entire velocity range.
However, since this factor only scales the H I image, it can not effect the structure, and thus it can not change the goodness of fit for either the $I_{100} - N_H$ relation or the $I'_O - N_H$ relation. It will only change the final fit parameters, I_L and I_D.

TABLE 8.3

I_{100} TO H I SCALING

Mask[a]	H I Δv	I_{100} a	I_{100} b	I_{100} χ^{2b}	XI_{100} a	XI_{100} b	XI_{100} χ^{2b}
All	All	0.0452±0.0204	0.5187±0.0189	0.0359	0.1074±0.0217	0.5181±0.0202	0.0402
	±100	-0.0657±0.0176	0.6926±0.0175	0.0190	-0.0157±0.0186	0.7028±0.0186	0.0207
	±75	-0.0480±0.0168	0.7053±0.0174	0.0186	0.0006±0.0178	0.7173±0.0186	0.0200
	±50	0.0608±0.0177	0.7690±0.0226	0.0318	0.0870±0.0178	0.8109±0.0228	0.0280
HVG $> 3.5 \times 10^{19}$	All	-0.0665±0.0219	0.6440±0.0215	0.0259	-0.0328±0.0224	0.6732±0.0219	0.0281
	±100	-0.0593±0.0194	0.6905±0.0205	0.0196	-0.0227±0.0198	0.7195±0.0210	0.0218
	±75	-0.0464±0.0185	0.7018±0.0203	0.0187	-0.0095±0.0190	0.7314±0.0209	0.0208
	±50	0.0383±0.0186	0.7755±0.0247	0.0269	0.0676±0.0185	0.8218±0.0247	0.0268
HVG $> 1.5 \times 10^{19}$	All	-0.0717±0.0212	0.6957±0.0230	0.0168	-0.0314±0.0214	0.7174±0.0231	0.0184
	±100	-0.0378±0.0195	0.6983±0.0224	0.0154	0.0036±0.0197	0.7201±0.0226	0.0169
	±75	-0.0274±0.0189	0.7047±0.0223	0.0148	0.0146±0.0191	0.7263±0.0224	0.0164
	±50	0.0040±0.0180	0.8391±0.0260	0.0165	0.0450±0.0181	0.8676±0.0262	0.0175
Mosaic	All	-0.0779±0.0294	0.7117±0.0316	0.0528	-0.0355±0.0311	0.7391±0.0335	0.0586
	±100	-0.0474±0.0269	0.7194±0.0310	0.0484	-0.0042±0.0284	0.7475±0.0327	0.0539
	±75	-0.0321±0.0259	0.7196±0.0306	0.0465	0.0124±0.0276	0.7468±0.0325	0.0521
	±50	-0.0154±0.0238	0.8451±0.0331	0.0515	0.0284±0.0258	0.8787±0.0358	0.0547

[a] The high velocity gas, "HVG", is defined as HI outside ±75 km s^{-1}. These regions are excluded from the fit. The mosaic mask excluded the HVG at the 1.5 x 1019 cm^{-2} level.

[b] The uncertainty used in the calculation of χ^2 was assumed to be the same for all pixels. The uncertainty was taken to be unity, so this quantity is not a "real" χ^2 but is the second moment with respect to the fit.

for the calculation of a modified χ^2. The best agreement between H I and I_{100}, as determined by the modified χ^2, occurs for the ±75 km s^{-1} velocity interval. Removing HVG (here defined as emission in velocities outside ±75 km s^{-1}) to a level of 1.5×10^{19} cm^{-2} produced the best fits in terms of χ^2. Removing the HVG to the level of 1.5×10^{19} cm^{-2} also brings the fitted scale factor b for all the velocity ranges (save for ±50 km s^{-1}) more closely into agreement.

Although there are 30% spatial variations in the H I/I_{100} ratio, restricting the region of the fit to just that of the mosaic, still excluding HVG to the level of 1.5×10^{19} cm^{-2}, did not make a significant change.

The same fits were made using XI_{100}, the temperature corrected *IRAS* 100 μm data, in place of I_{100}. The XI_{100} fits were always slightly worse than the I_{100} fits. Thus, by our criteria, the temperature correction proposed by Schlegel, Finkbeiner, & Davis (1998) does not help in regions where H I $< 3 \times 10^{20}$ cm^{-2}. This is not surprising as the resolution of the temperature correction is low (~ 0.7°) and the correction is derived from the ratio of the 100 μm and 240 μm emission, both of which will have small values and large uncertainties in regions of such low column density.

4.3.3. The I'_O-N_H Relation

For each of the H I($|v| < 75$ km s^{-1}) to $(X)I_{100}$ fits in Table 8.3, the total absorbing column, N_H was taken to be

$$N_H = \frac{[(X)I_{100} - a] \times 10^{20}}{b} \qquad (8.7)$$

and the N_H was fit to the X-ray emission using Equation 8.3. The results are shown in Table 8.4. Removing the HVG to the level of 1.5×10^{19} cm^{-2} does improve the fits to the I'_O-N_H relation. Using XI_{100} did not produce as good a fit as I_{100}. Figure 8.7 shows the fit and an image of the residual to the fit.

4.3.4. Another Structure/Scaling Method

The H I/I_{100} ratio is spatially variable. It is not known whether this variation is due to a

TABLE 8.4

I_{100} FITTING TO THE X-RAY MOSAIC

Mask[a]	Range	I_{100}			XI_{100}		
		I_L[b]	I_D[b]	χ^2	I_L[b]	I_D[b]	χ^2
All	±75	533.580	417.391	3.807	552.208	389.364	3.447
HVG> 3.5×10^{19}	±75	535.791	406.744	2.937	545.375	392.695	3.160
HVG> 1.5×10^{19}	±75	525.447	405.643	2.318	535.095	391.735	2.144
Mosaic	±75	521.861	407.830	2.191	529.036	394.793	2.526

[a] The high velocity gas, "HVG", is defined as HI outside ±75 km s^{-1}. These regions are excluded from the fit. The mosaic mask excluded the HVG at the 1.5×10^{19} cm^{-2} level.

[b] Typical uncertainties are $I_L = \pm 8.10$ and $I_D = \pm 14.5$.

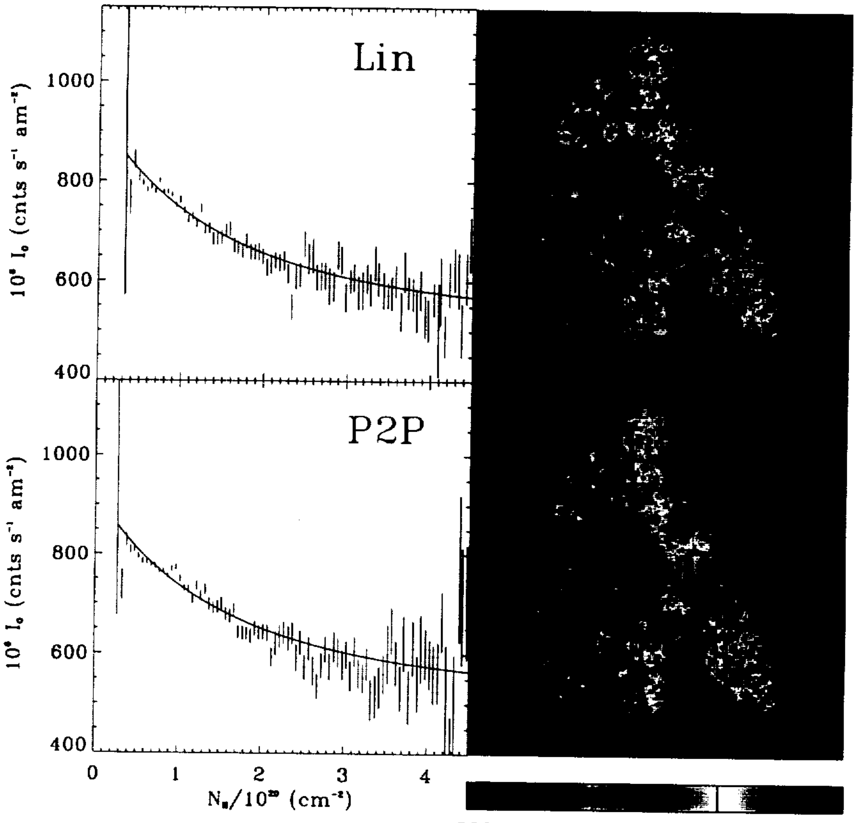

Fig. 8.7.— Example fits of I_{100} to the X-ray absorption, and the residuals to the fits. In all cases regions with HVG> 1.5×10^{19} have been removed for the I_{100} to H I scaling, the ±75 km s^{-1} velocity interval of the H I has been used, and the H I column density in that velocity interval has been scaled to the total H I column density. *Left:* The I'_O-N_H relation. *Right:* The residual to the fits. The grey-scale is the I_O - fit. *Top:* Fit used a linear relation between I_{100} and H I. *Bottom:* Fit used the point-by-point scaling.

TABLE 8.5

POINT-BY-POINT SCALING/FITTING

Mask	Range	I_{100}			XI_{100}		
		I_L^{a}	I_D^{a}	χ^2	I_L^{a}	I_D^{a}	χ^2
All	±75	529.469	411.191	4.613	530.490	408.720	4.619
HVG$> 3.5 \times 10^{19}$	±75	522.592	413.826	3.456	523.229	412.006	3.375
HVG$> 1.5 \times 10^{19}$	±75	521.943	403.406	2.583	521.677	403.275	2.260
Mosaic	±75	519.316	408.243	2.648	519.053	408.150	2.588

[a] Typical uncertainties are $I_L = \pm 8.10$ and $I_D = \pm 14.5$.

change in dust temperature, a change in dust to gas ratio, or, perhaps, the addition of ionized hydrogen containing dust. If the variation is due to the presence of an absorber not correlated with the H I, then I_{100} is a better tracer of the total absorbing column, and the variation should be preserved, as in the fits above. If, however, the variation in the H I/I_{100} ratio is due to a variation in the dust temperature, that variation ought to be minimized.

One can retain the high resolution structure of the I_{100} image while removing the large scale H I/I_{100} variation by smoothing the H I/I_{100} image by a large amount (say 30′ since that is the H I resolution) and setting the absorbing column to be the I_{100} image multiplied by the smoothed ratio image. This is essentially a high-pass filter.

The results can be seen in Table 8.5. For the cases tested, the fits using this "point-by-point" scaling are significantly worse than the linear scaling used in the previous fits, suggesting that the H I/I_{100} variation is not due merely to variation of the dust emissivity within the H I or a variation in the dust-to-gas ratio, but rather to emission from dust that traces some other gas component. From Figure 8.7 (*bottom*) one can see that the residuals to the fit are not considerably different in structure than those found with the linear scaling.

4.4. Uncertainties in N_H

There are two forms of errors in the N_H, scaling errors which, as we have seen above, effect I_L and I_D, but do very little to the value of the fitted value of I'_O, and structure errors, which produce spurious variations in the output I_D image.

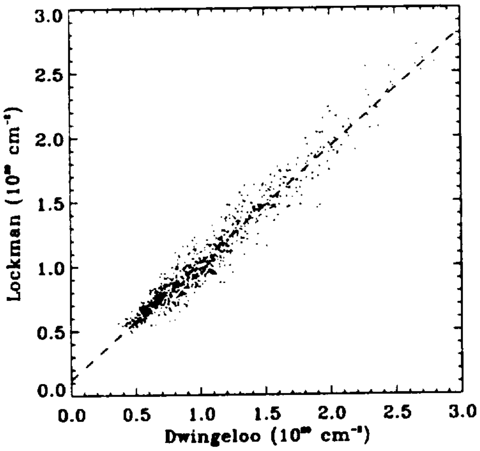

Fig. 8.8.— Comparison of the Dwingeloo and Lockman data sets.

4.4.1. N_H Scaling Errors

There are two forms of scaling errors. The first is a simple offset in the value of the column density. In this case, the error will be the same at all column densities. (As a result, the effect of the error will be smaller at higher column densities.) The second is an error in the scaling between some observed quantity and the value of the column density. In this case, the error will become large as the column density increases.

4.4.1.1. N_H Baseline – An Offset Error Although we use the Dwingeloo data set as the primary tracer of the total absorbing column towards the X-ray mosaics, in the direction of the mosaic 038+52, we have a higher resolution data set ($\sim 9-15'$) provided by J. Lockman. (The same data set was used in Snowden et al. 1994). The two data sets are compared in Figure 8.8, where the Lockman data were binned to the same pixel areas as the Dwingeloo data. The line is the best fit linear relation between the two:

$$\begin{aligned} Lockman &= (0.1208 \pm 0.0084) \\ &+ (0.9036 \pm 0.0086) * Dwingeloo. \end{aligned} \tag{8.8}$$

The Dwingeloo data appear to be systematically lower than the Lockman data at lower column densities.

The Dwingeloo data were cleaned of sidelobe contamination by a sophisticated self-referential algorithm. The Lockman data were cleaned of sidelobe contamination by reference to the Bell Laboratories Survey (Stark et al. 1992), whose sidelobe contamination has been extensively studied and shown to be small (Lockman, Jahoda, & McCammon 1986; Kuntz & Danly 1992). Kalberla et al. (1997) suggested that the baselines of the Bell Laboratories Survey were over-subtracted, meaning that the Lockman data should be lower than the Dwingeloo data. Where the problems lie is not clear. The systematic difference is less than $\sim 7 \times 10^{18}$ within the $0.5-2.0 \times 10^{20}$ cm^{-2} range. The systematic uncertainty quoted by Snowden et al. (1994), 5×10^{18} cm^{-2}, is in reasonable agreement.

The impact of a systematic uncertainty in the H I column density can be calculated. For column densities from 5×10^{19} cm^{-2} to 3×10^{20} cm^{-2} we have calculated

$$I_O = 1 + e^{-N_H \sigma(N_H, S)} \tag{8.9}$$

at 5×10^{18} cm^{-2} intervals. We then fit I_O-N_H relation with an N_H vector that was either increased or decreased from the true amount by 5×10^{18} cm^{-2}. We then calculated the fractional difference in the I_L and I_D fit parameters and determined the maximum fractional deviation between the true and fitted relations. The results are given in Table 8.6. The effect on either the fit parameters I_L and I_D or on the value of the value of the I_O - N_H relation are negligeable.

We have calculated the same quantity for a $\Delta N_H = 5 \times 10^{19}$, the equivalent H I column density of H II, given the canonical distribution of H II, $7 \times 10^{19} \csc b$, and the canonical H II absorption cross-section, 0.62 that of H I. Significant errors occur for the fit parameters, but the difference between the fitted and measured $I'_O - N_H$ relations are still insignificant. This calculation, of course, has assumed that the H II is smoothly distributed. A patchy distribution is discussed below.

4.4.1.2. Error in the $I_{100} - N_H$ Relation - A Scaling Error

As can be seen from Table 8.3, the spread in the values of b in

$$I_{100} = a + b\frac{HI}{10^{20}} \tag{8.10}$$

is ~ 0.09. The change in b causes a change in N_H that is dependent on the derived N_H. We have calculated the effect of $\Delta b = 0.09$ in a manner similar to that used in the previous section. As we have assumed the same value of a in both cases, the calculated change is an upper limit. Note that the change in I_L and I_D is larger at higher energies; due to the lack of curvature in the $I'_O - N_H$ relation, the fit can shift flux from the foreground to the background more easily than at lower energies. However, it should be noted that since, in practice, the foreground in band R47 is fixed, the uncertainty in the R47 background flux will be minimized. The uncertainties in the residual to the fit are again negligeable.

4.4.2. N_H Structure Errors

Of the sources of uncertainty considered, this is the only one that contributes to the production of spurious fluctuations. N_H structure errors are errors in counting the number of hydrogen nucleons along the line of sight. These errors arise because I_{100} is a measure of the dust emissivity, which may not be proportional to the number of hydrogen nucleons. We consider two cases. In the first, we assume that the H I traces the bulk of the absorption and the variations in the H I/I_{100} are due to dust emissivity effects. In the second, we assume that the I_{100} traces both the H I and H II, and then, assuming that the variation in H I/I_{100} are due to variation in the column density of H II, caculate the effect of the H II.

TABLE 8.6
EFFECT OF ΔN_H

Band	I_L	I_D	Residual^a	
			min.	max.
		$\Delta N_H = 5 \times 10^{18}$		
R1L2	-3.51×10^{-3}	4.13×10^{-2}	-4.59×10^{-4}	8.04×10^{-4}
R45	-1.81×10^{-3}	-4.66×10^{-3}	-8.29×10^{-6}	1.11×10^{-5}
R67	-1.95×10^{-4}	1.68×10^{-3}	-3.17×10^{-7}	3.95×10^{-7}
		$\Delta N_H = 5 \times 10^{19}$		
R1L2	-3.24×10^{-2}	4.59×10^{-1}	-3.62×10^{-3}	7.38×10^{-3}
R45	-1.68×10^{-2}	4.58×10^{-2}	-5.44×10^{-5}	1.10×10^{-4}
R67	-1.96×10^{-3}	1.69×10^{-2}	-7.91×10^{-7}	1.27×10^{-6}
		$\Delta N_H = 5 \times 10^{19}$, I_L fixed		
R45		2.68×10^{-2}	-5.03×10^{-5}	6.76×10^{-5}
R67		1.48×10^{-2}	-3.77×10^{-5}	3.72×10^{-5}

All quantities are fractional differences.

^{a}The residual is measured over $5 \times 10^{19} < N_H < 3 \times 10^{20}$.

TABLE 8.7
EFFECT OF $\Delta b = 0.09$

Band	I_L	I_D	Residual^a	
			min.	max.
R1L2	2.70×10^{-2}	1.62×10^{-2}	-4.30×10^{-3}	2.67×10^{-4}
R45	9.72×10^{-2}	-9.65×10^{-2}	-1.15×10^{-4}	6.09×10^{-5}
R67	1.07×10^{-2}	-1.07×10^{-2}	-3.23×10^{-5}	1.69×10^{-5}
		I_L Fixed		
R45		1.15×10^{-2}	-3.85×10^{-3}	3.75×10^{-3}
R67		-6.50×10^{-3}	-2.27×10^{-3}	2.29×10^{-3}

All quantities are fractional differences

^{a}The residual is measured over $5 \times 10^{19} < N_H < 3 \times 10^{20}$.

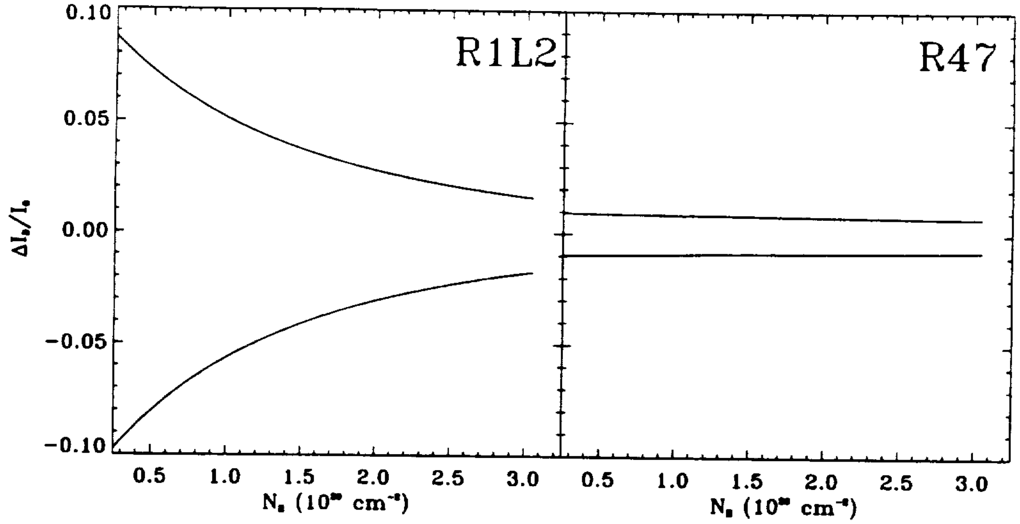

Fig. 8.9.— The fractional amplitude of spurious fluctuations in band R1L2 produced by uncertainties in the absorbing column. An uncertainty of 1.5×10^{19} cm^{-2} was assumed. The plotted value is the change due to this uncertainty in the predicted observed flux, divided by the true distant flux. See text for discussion.

4.4.2.1. Systematic Variations in H I/I_{100}

As can be seen in Figure 8.3, the H I/I_{100} ratio varies on 30′ scales, and higher resolution data show variation on smaller scales. In the 138+52 field, on 30′ scales, for a given value of I_{100}, the r.m.s. variation in H I is $\sim 1.6 \times 10^{19}$ cm^{-2}. If we assume that this dispersion is a measure of the error in the absorbing column, we can calculate the error in the transmitted X-ray flux (i.e., the residual to the fit to the $I'_O - N_H$ relation). This residual to the fit, ΔI_O, as a fraction of the true distant flux, I_D, is shown in Figure 8.9.

If we assume that the variation in H I/I_{100} ratio does not reflect variations in the absorbing column, then the variation in I_{100} can produce $\sim$ 10%($\sim$ 1%) uncertainties in the measured fluctuations in band R1L2(R47). The spurious fluctuations suggested by Figure 8.9 are likely to be a gross exaggeration; §4.3.4 suggests that, at least on the 30′ scales, the variation in the H I/I_{100} ratio *is* more likely to be due to the I_{100} tracing additional components of the total absorbing column than changes in IR emissivity.

4.4.2.2. H II As has been repeatedly mentioned, the spatial distribution of H II is unknown and its mean column density as a function of Galactic latitude is poorly known. The Wisconsin Hα Mapper (WHAM) survey (Reynolds et al. 1998) is currently mapping Hα emission at an angular resolution of 1° over that part of the sky visible from Wisconsin. Although maps have not yet been produced, the variation of Hα emission on scales of a few degrees is 30%, or an equivalent column density of $\sim 3 \times 10^{19}$ cm^{-2} (Reynolds 1999), assuming that Hα is a direct measure of the column density of H II.

If the variation in the H I/I_{100} ratio were due to emission from dust related to H II, and the variation in H II were comparable to that observed by Reynolds, then the emissivity of dust related to H II, ϵ_{II}, would be 0.88 times the emissivity of dust related to H I[9], ϵ_I. This is

---

[9] The measured emissivity, that is, the value of b in Equation 8.6 $\equiv \epsilon_M$, is given by Equation 8.13. The r.m.s of I_{100} at a given value of H I is assumed to be the scatter introduced by the emission of dust related to the H II. If, for a given value of H I, we assume that -1σ value of I_{100} represents I_{100} emission exclusively from H I (see Figure 1 of Chapter 4), then the r.m.s value, ΔI_{100}, represents the variation in the contribution to I_{100} due to dust related to H II. Assuming that the 3×10^{19} cm^{-2} found by Reynolds is twice the characteristic r.m.s. of the H II column density for 1° pixels (i.e. that 3×10^{19} cm^{-2} represents the peak-to-peak value), then then $\epsilon_{II} \sim 0.50$ and $\epsilon_I \sim 0.57$. The measured r.m.s. of I_{100} for values of H I in the 1.0-2.0$\times 10^{20}$ cm^{-2} range is 0.15, when calculated from ΔH I bins that are 5×10^{18} cm^{-2} wide. We

not too unreasonable given that the best 3σ upper limit to $\varepsilon_{II}/\varepsilon_I \sim 0.75$ (Arendt et al. 1998). Thus attributing the variation in the H I/I_{100} ratio to emission by dust related to the variable column of H II is not unreasonable.

The potential problem is that while both the I_{100} emission and the X-ray absorption are due to the weighted sum of the contributions from each H component (H I, H II, and H_2), the weights for absorption and emission are different. We can calculate the effect of the differing weights in the 138+52 field. The true absorbing column is

$$N_H(\text{true}) = \text{H I} + 0.62\text{H II}. \tag{8.11}$$

The measured absorbing column is

$$N_H(\text{measured}) = \frac{\varepsilon_I \text{H I} + \varepsilon_{II}\text{H II}}{\varepsilon_M}, \tag{8.12}$$

where

$$\varepsilon_M = \varepsilon_I + \frac{\text{H II}}{\text{H I}}\varepsilon_{II}. \tag{8.13}$$

One can calculate the I'_O using the true N_H and fit using the measured N_H. The results are shown in the fit column of Table 8.8 for an assumed uniform H II column density of 2.2×10^{19}, the value used by Snowden et al. (1994) for this field. One can also calculate the effect of a variation of the H II column density on the measured deabsorbed flux. For a $\pm 1.5 \times 10^{19}$ cm^{-2} column density of H II, we find an error of $\pm 1.5\%$($\pm 0.2\%$) in the deabsorbed flux in band R1L2(R45) given $\varepsilon_{II} = 0.5$ (see the "Deabs." column of Table 8.8). However, one should note the uncertainty of the many values that entered this calculation.

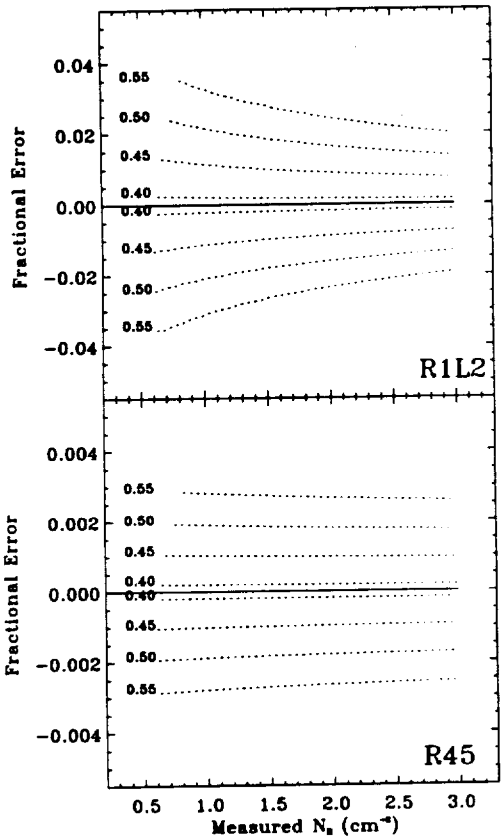

Fig. 8.10.— The fractional amplitude of spurious fluctuations produced by fluctuations in the column density of H II. It was assumed that the mean H II column density was 2.2×10^{19} cm^{-2} and that the fluctuations have an amplitude of 1.5×10^{19} cm^{-2}.

4.4.3. N_H Errors

Table 8.9 summarizes the uncertainties due to errors discussed in this section. As the deviation of fits from the mean $I'_O - N_H$ relation are universally small, they have not been tabulated. The tabulated value for the amplitude of the angular variation in I_D due to variation in the error in N_H, ΔI_D, was calculated on 30′ scales. The error attributed to variations in H I/I_{100} is an extreme upper limit, while that error attributed to H II is likely to be a more accurate representation of the true error.

5. Deabsorption

Once an adequate map of the absorbing column has been obtained, and the mean I_L and I_D have been determined, there are two methods by which to create a map of the distant emission. Both, of course, assume that the local emission is flat.

The obvious method is multiplicative; the map of the distant emission is given by

$$I_D(x,y) = (I'_O(x,y) - \langle I_L \rangle)e^{\tau}, \tag{8.14}$$

---

have assumed that the H II column density in this region is about a quarter of the mean relation (7×10^{19} csc b) as per Snowden et al. (1994).

TABLE 8.8
EFFECT OF H II

ϵ_{II}	ϵ_{II}/ϵ_I	R1L2			R45	
		Fit[a]		Deabs.[b]	Fit[a]	Deabs.[b]
		I_L	I_D	I_D	I_D	I_D
0.40	0.67	-1.10×10^{-2}	-7.04×10^{-2}	2.45×10^{-3}	-3.33×10^{-2}	1.99×10^{-4}
0.45	0.77	-1.48×10^{-2}	-3.33×10^{-2}	1.30×10^{-2}	-3.39×10^{-2}	1.04×10^{-3}
0.50	0.88	-1.79×10^{-2}	4.45×10^{-2}	2.40×10^{-2}	-3.47×10^{-2}	1.93×10^{-3}
0.55	0.99	-2.10×10^{-2}	4.31×10^{-2}	3.53×10^{-2}	-3.54×10^{-2}	2.85×10^{-3}

[a] This is the fractional error in the fit parameters caused by the addition of a uniform H II column density of 2.2×10^{19} cm^{-2}.

[b] This is the fractional error in the deabsorbed flux due to an additional $\pm 1.5 \times 10^{19}$ cm^{-2} of H II assuming the fit including the uniform H II column density of 2.2×10^{19} cm^{-2}.

TABLE 8.9
ERROR SUMMARY

Source	Scale	I_D		ΔI_D	
		R1L2	R45	R1L2	R45
σ_{eff}	...	<< 1%	<< 1%	...	...
N_H Scaling (offset)	...	< .3%	< .1%	...	...
N_H Scaling (scaled)	...	< 2%	< 1%	...	...
Δ(H I/I_{100})	30′	...	...	< 8%	< 1%
H II	30′	< 7%	< 3%	< 3%	< .3%

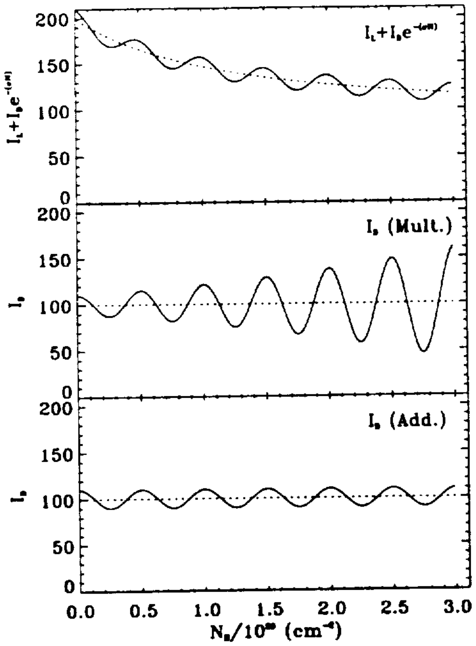

Fig. 8.11.— Demonstration of the effects of the multiplicative and additive methods of deabsorption. *Top:* The observed $I'_O - N_H$ relation, the dotted line being the mean fitted relation, *Middle:* I_D as derived by the multiplicative method, *Bottom:* I_D as derived by the additive method.

where $\tau = N_H(x,y)\sigma(N_H(x,y),\mathcal{S})$. This method assumes that all of the deviation from the mean I'_O-N_H relation is real, and it amplifies all of the uncertainties. A fluctuation analysis performed on a field deabsorbed in this manner will produce an extreme upper limit on the size of fluctuations. Ignoring the systematic uncertainties (i.e., the uncertainies introduced by the deabsorption process), and considering only the statistical uncertainty (i.e., the propagated measurement uncertainty), we find that

$$\sigma_{I_D(x,y)} = \sigma_{I'_O} e^{\tau}. \tag{8.15}$$

The systematic uncertainty will be spatially variant;

$$\sigma_{I_D(x,y)} = e^{2\tau}\sqrt{\sigma^2_{I_L} + \sigma^2_{tau}(I'_O - I_L)^2}. \tag{8.16}$$

However, this may be more conveniently recast as:

$$\sqrt{\sigma^2_{I_L} e^{2\tau} + \sigma^2_{\tau}\langle I_D\rangle^2}. \tag{8.17}$$

A more subtle method used by Barber, Warwick, & Snowden (1995) is additive; the map of the distant emission is given by:

$$I_D(x,y) = I'_O(x,y) - \langle I_L\rangle + \langle I_D\rangle(1 - e^{-\tau}). \tag{8.18}$$

This equation is essentially the residual to the fit to which is added the mean distant emission, that is, if I_F is the fitted value of I'_O, then

$$I_D(x,y) = I'_O(x,y) - I_F + \langle I_D\rangle. \tag{8.19}$$

This method assumes that the distant emission is smooth (equivalent to assuming that any variation is due to the foreground), and minimizes the effect of the uncertainties. If the uncertainties in I_O and N_H were small, a fluctuation analysis performed on a field deabsorbed in this manner would produce a lower limit on the size of fluctuations. However, in the presence of noise this method produces neither limit to the size of fluctuations.

Again considering only the statistical uncertainty, we find that

$$\sigma_{I_D(x,y)} = \sigma_{I'_O}. \tag{8.20}$$

The systematic uncertainty will be

$$\sigma_{I_D(x,y)} = \sqrt{\sigma^2_F + \sigma^2_D}, \tag{8.21}$$

Figure 8.11 demonstrates the different effects of these two methods. Neither method is ideal, though the multiplicative method can be improved by deabsorbing, not to zero column density, but to a small column density, such as 5×10^{19} cm^{-2}.

5.1. Uncertainties

Given the understanding (or lack thereof) of the uncertainties, one may reevaluate the systematic uncertainties of the two methods of deabsorption. The systematic uncertainty for the multiplicative method is given by Equation 8.17; the $e^{\tau}\sigma_{I_L}$ term dominates by an order of magnitude. The systematic uncertainty for the additive method is given by Equation 8.21, but it should be noted that the uncertainty of the fit value, σ_F is usually two orders of magnitude smaller than the uncertainty in the fitted I_D. Therefore, the systematic uncertainty for

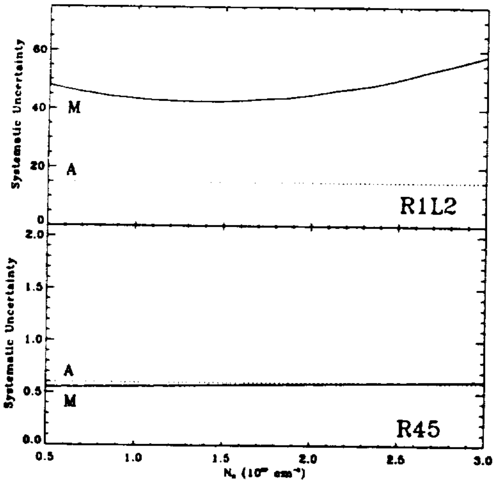

Fig. 8.12.— Comparison of the systematic uncertainties for the multiplicative and additive methods of deabsorption. The systematic uncertainty for the multiplicative method is shown by solid lines; for the additive method, by dotted lines. The uncertainties were calculated for field 138+52 and are in units of 10^{-6} counts s^{-1} arcmin^{-2}.

the additive method is approximately σ_{I_D}. Figure 8.12 shows the systematic errors as a function of N_H for both methods applied to the 138+52 field. The two methods yield similar systematic uncertainties in band R45, but the additive method yields systematic uncertainties that are three times smaller that those of the multiplicative method in band R1L2.

Despite the seeming advantage of the additive method, we use the multiplicative method because our interest is the ***structure*** of the distant component, not its absolute value. The difference in systematic uncertainty is of little consequence as, despite some dependence on N_H, it is primarily a measure of the uncertainty in the mean value of I_D. More important is the pixel-to-pixel uncertainty, which will be smaller by e^τ for the additive method, but this advantage is outweighed by the necessity to assume that there are no fluctuations in I_D.

6. Summary

The greatest difficulty in deabsorbing an X-ray image is finding a tracer of the absorbing column that has a spatial resolution comparable to that of the X-ray image. The *IRAS* 100 μm All-Sky Survey provides a tracer with a resolution of $\sim 5'$, but it is not clear to what extent the 100 μm emission traces the absorbing column related to H II, nor is it clear to what extent the 100 μm emission is influenced by factors other than the total column of hydrogen nucleons (i.e., dust to gas ratio, dust temperature, etc.). However, the analysis shows that 100 μm emission is a better tracer of the total absorbing column than the 21 cm emission of H I; the 100 μm emission does seem to trace variations in the total absorbing column that are not traced by H I.

6.1. Prescription

Using the above information, we can produce a prescription for deabsorbing X-ray mosaics.

First, calculate the correction to the X-ray mosaic for the point source detection limit variation. One should not correct images to a large-point source detection limit: correcting the band R1L2(R47) band image to 0.04(0.02) counts s^{-1} rather than 0.02(0.01) counts s^{-1}, for example, will introduce a 2% variation in the deabsorbed image, as the point source correction is N_H dependent. Although this quantity is much smaller than the uncertainty in any single mosaic pixel, it is comparable to the uncertainty over larger regions.

Second, remove regions with an

$$\mathrm{H\ I}_{(|v|<75\ \mathrm{km\ s^{-1}})} > 3 \times 10^{20}\ \mathrm{cm}^{-2},$$

thus removing regions possibly contaminated with molecular gas. Remove also regions for which the column density for

$$\mathrm{H\ I}_{(|v|>75\ \mathrm{km\ s^{-1}})} > 1.5 \times 10^{19}\ \mathrm{cm}^{-2},$$

thus removing I_{100} deficient high and intermediate velocity gas.

Third, determine the parameters for the linear I_{100}-H I relation,

$$I_{100} = a + b\frac{HI}{10^{20}}, \qquad (8.22)$$

using the region of the mosaic that satisfy the above conditions. Use the $\mathrm{H\ I}_{(|v|<75\mathrm{km\ s^{-1}})}$ for deriving a and b. For some of the mosaics, the dynamic range in the mosaic region will be insufficient to produce good fits; for these mosaics use a larger region to derive a and b. The difference between fit parameters derived for the larger region and those derived from the mosaic region will be small when both are derived over a reasonable dynamic range. From the linear I_{100}-H I relation calculate the total absorbing column as

$$N_H = \frac{[I_{100} - a] \times 10^{20}}{b} \qquad (8.23)$$

Fourth, determine the (rough) shape of the background spectrum. Using the *RASS* for a larger region including the mosaic, determine the I_L and I_D for bands R1 and R2. Given the low exposure of the *RASS* one may need to select a limited range of N_H to execute the I'_O-N_H fitting. Using all of the pixels from the region that fall within some narrow range of absorbing column ($\Delta N_H \sim 1 \times 10^{19}$) determine the mean absorbed SED after the extragalactic power law has been removed. From that SED determine the normalizations of the soft ($\log T = 6.056$) and hard ($\log T = 6.462$) halo components. Using these normalizations, construct the halo spectrum and calculate the effective cross-sections.

Fifth, apply the more refined binning method to the mosaic data to create the mean $I'_O - N_H$ relation, and determine the mean I_L and I_D by fitting Equation 8.3. In principle, one could then check to see if the background spectrum determined from the *RASS* data is appropriate. If not, one could construct a new background spectrum and repeat the process. However, determining the background spectrum from mosaic data is far more difficult than determining the spectrum from the *RASS*; one must correct the mosaic data for the variable point source detection limits, and the band-to-band correction which will depend upon the assumed source spectrum. Using the *RASS* which has a nearly uniform point source removal is much easier.

Sixth, derive the map of the I_D component. Although the additive method may produce a lower systematic uncertainty, the multiplicative method is to be preferred as it yields an identifiable upper limit to the strength of the variation in I_D.

For band R45, one cannot determine I_L by fitting the $I'_O - N_H$ relation because τ changes little for $N_H < 3.0 \times 10^{20}$ cm^{-2}. Therefore, one must use the I_L determined for the R1L2 band, and scale that value to the R45 band using the apropriate emission model. We use a Raymond & Smith thermal model with $\log T = 6.11$, leading to R45/R1L2=0.0185. Given this small scaling factor, the uncertainty in the R45 I_L will be quite small, as will be the uncertainty in I_D.

6.2. Uncertainties

Of the many uncertainties in the deabsorption process, most uncertainties effect the fitted values of I_L and I_D. This uncertainty is important in so far as one is interested in the relative amplitude of fluctuations, $\Delta I_D/I_D$. More troubling uncertainty is the angular variation of the error in N_H. Such variation can produce spurious fluctuations. We have placed an upper limit on the spurious fluctuation by comparing I_{100} with H I, which is known not to trace all the components of N_H. In the R47 band these spurious fluctuations are $\lesssim$ 1%, while at R1L2 they are $\lesssim$ 8%, and could be substantially less. Very rough calculations equating the variation in H I/I_{100} with the variation in the column density of H II suggest spurious fluctuations $\lesssim$ 3% at R1L2 and $\lesssim$ 0.3% at R45.

REFERENCES

Arendt, R. G., et al. 1998, ApJ, 508, 74

Barber, C., Warwick, R. S., & Snowden, S. L. 1995, in Röntgenstrahlung from the Universe, ed. H. Zimmermann, J. Trümper, & H. Yorke, MPE Report 263, 319

Chen, L.-W., Fabian, A. C., & Gendreau, K. C. 1997, MNRAS, 285, 449

Hasinger, G., Burg, R., Giacconi, R., Schmidt, M., Trümper, J., & Zamorani, G. 1998, A&A, 329, 482

Hauser, M. G., et al. 1998, ApJ, 508, 25

Kalberla, P. M. W., Westphalen, G., Mebold, U., Hartmann, D., & Burton, W. B. 1997, in The Local Bubble, ed. D. Breitschwerdt & M. Freyberg, 479

Kerp, J., Burton, W. B., Egger, R., Freyberg, M. J., Hartmann, D., Kalberla, P. M. W., Mebold, U., & Pietz, J. 1999, A&A, 342, 213

Kuntz, K. D., & Danly, L. 1992, PASP, 104, 1256

Kuntz, K. D., & Snowden, S. L. 2000, ApJ

Lampton, M., Margon, B., & Bowyer, S. 1976, ApJ, 208, 177

Lockman, F. J., & Gehman, C. S. 1991, ApJ, 382, 182

Lockman, F. J., Jahoda, K., & McCammon, D. 1986, ApJ, 302, 432

Reach, W. T., Koo, B.-C., & Heiles, C. 1994, ApJ, 429, 672

Reach, W. T., Wall, W. F., & Odegard, N. 1998, ApJ, 507, 507

Reynolds, R. J. 1991, in The Interstellar Disk-Halo Connection in Galaxies, ed. H. Bloemen, 67

Reynolds, R. J. 1999, private communication

Reynolds, R. J., Tufte, S. L., Haffner, L. M., Jaenig, K., & Percival, J. W. 1998, Proc. Astron. Soc. Aust., 15, 14

Schlegel, D. J., Finkbeiner, D. P., & Davis, M. 1998, ApJ, 500, 525

Snowden, S. L., Hasinger, G., Jahoda, K., Lockman, F. J., McCammon, D., & Sanders, W. T. 1994, ApJ, 430, 601

Stark, A. A., Gammie, C. F., Wilson, R. W., Bally, J., Linke, R. A., Heiles, C., & Hurwitz, M. 1992, ApJS, 79, 77

Wakker, B. P., & Boulanger, F. 1986, A&A, 170, 84

Chapter 9: I_D Revealed

Abstract

This chapter describes the details of the application of the deabsorption method to the seven high Galactic latitude mosaics. The cross-correlation of the images of the deabsorbed distant emission and the absorbing column suggests that the deabsorption process produces errors in the image of the distant emission that are small compared to the amplitude of the intrinsic angular variation of the emission.

1. Boring Stuff

The parameters used in and produced by the deabsorption process are listed in Tables 9.2 and 9.3. Much of the information in the tables is depicted in graphic form in the following figures.

The $I_{100} - N_H$ relations are shown in Figure 9.1 both for the region of the mosaic and for a more extended $512' \times 512'$ region. (In the case of mosaics with $1\overset{'}{.}5 \times 1\overset{'}{.}5$ pixels a $768' \times 768'$ region was used.) In only two cases (086+74 and 295-89) do the two measures of the $I_{100} - N_H$ relations diverge; in these cases (indicated by an "E" in the sixth column of Table 9.2), the relation from the more extended region was used.

The distribution of point source detection limits (PSDL) for each mosaic is shown in Figure 9.2. Also shown is the global PSDL to which each mosaic has been corrected (see section 2.1 in the previous chapter). The global PSDL to which a given mosaic was corrected was chosen to require a minimum of correction yet allow $\geq$ 97% of the mosaic to be corrected (regions with PSDLs greater than the global value were discarded).

The shape of the background spectrum was determined from the *RASS* using the "extended regions". The local-distant separation was done in bands R1 and R2, the local component extrapolated to bands R4-R7 assuming a Raymond & Smith model with $\log T = 6.12$. The SED of the distant component was constructed from all six bands, and the normalizations for the soft ($\log T = 6.056$) and hard ($\log T = 6.42$) components were calculated[1] We used the resultant I_L values to calculate the six-band SED of the distant component. We then recalculated $\mathcal{N}_H/\mathcal{N}_S$ and repeated the process until the values of $\mathcal{N}_H/\mathcal{N}_S$ converged. The resulting ratio of the normalizations, hard-to-soft, $\mathcal{N}_H/\mathcal{N}_S$ is given in Table 9.2.

The $I'_O - N_H$ relations are shown in Figure 9.3, where the dotted brackets indicate the range of N_H used for fitting the relations. The results of the fits are given in Table 9.3.

Most mosaics show some divergence from the fitted $I'_O - N_H$ relation at the lowest column densities due to the small number of pixels with such low column densities. The absorbing column density rises above the 3×10^{20} cm^{-2} threshold in three fields, though those regions were removed from the fits. Above this threshold one might not expect the $I'_O - N_H$ relation to follow the extrapolation of the fit due to the presence of molecular gas, as well as the temperature and emissivity variations likely in molecular gas. However, as one can see from mosaics 138+52 and 295-989, at these column densities, the change in I'_O due to a change in N_H is very small. Thus, errors in the I_{100} to N_H conversion will propagate into very small errors in I'_O. One should also note (from Figures 9.4 and 9.5) that the regions with $N_H > 3 \times 10^{20}$ cm^{-2} are quite small, so the measurement error is large. Thus, the goodness of the fit over the column density threshold should not be unexpected.

Images of the distant emission, absorbed by a uniform 5×10^{19} cm^{-2} are shown in Figures 9.4 and 9.5. Also shown are the regions removed from the fit due to $N_H > 3.0 \times 10^{20}$ cm^{-2} (solid

---

[1] This method could not be employed with the 295-89 mosaic. The $I_O - N_H$ relation determined from the *RASS* image showed no anticorrelation. We therefore *assumed* the $\mathcal{N}_H/\mathcal{N}_S$ from the 220+84 field to calculate the σ_{eff}. We then made a local-distant separation using the $I'_O - N_H$ relation from the mosaic (where there is a strong anti-correlation).

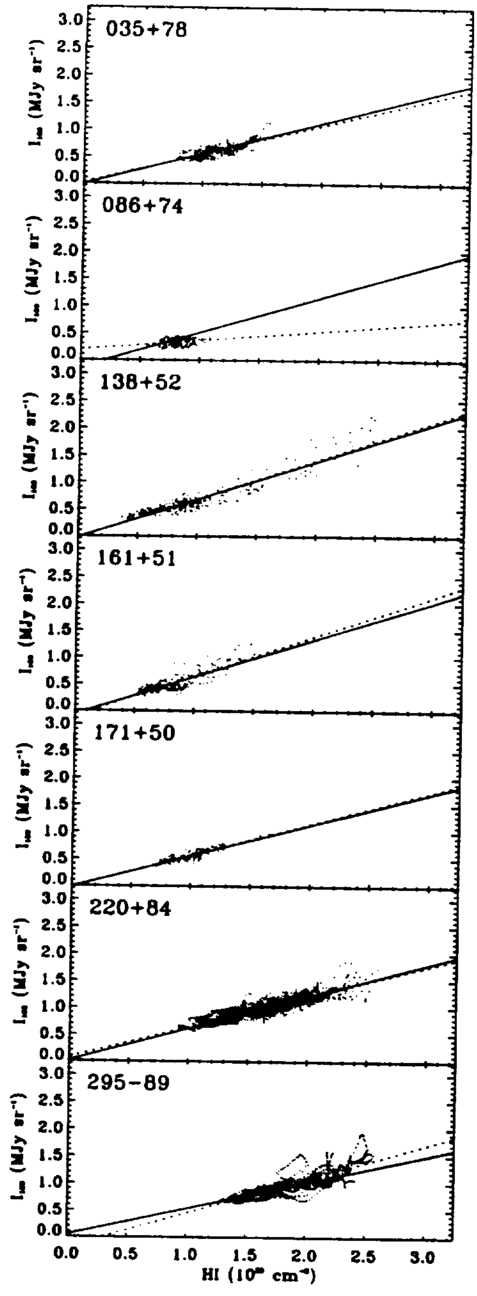

Fig. 9.1.— I_{100}-H I relations for the mosaics. Points are from the region of the mosaic only. The dotted line is the linear relation determined from the mosaic region; the solid line is determined from the extended field. The excursions in the 295-89 field are due to the pixelization of the Dwingeloo data being much smaller than the resolution of the Dwingeloo data.

contours) or $N_{H(|v|>75\mathrm{km\,s^{-1}})} > 1.5 \times 10^{19}$ $\mathrm{cm^{-2}}$ (dashed contours). In order to make these images most useful for understanding the variation of the emission, the plotted quantity is

$$\frac{I_D - \langle I_D \rangle}{\sigma_{I_D}} \tag{9.1}$$

where σ_{I_D} is calculated from a Gaussian fit to the core of the distribution of pixel values. The values of $\langle I_D \rangle$ and σ_{I_D} are given in Table 9.1.

Both the R45 and R1L2 images show variation on many angular scales, from the size of the PSF to the size of the mosaic (i.e., a gradient). Figures 9.6 and 9.7 show the mosaics smoothed by a 121′ sliding box; Figures 9.8 and 9.9 are the high-pass filtered images: the mosaics after the smoothed mosaics has been subtracted.

The mosaics smoothed by 121′ show a variety of structure. Some is clearly due to problems in the mosaicking process; the left-hand "ear" of the R1L2 mosaic of 171+50, the upper "ear" of the R45 mosaic of the same region, and the end-to-end gradients of 035+78 and 086+74. Even if the mosaicking algorithm were perfect, many of these structures would still exist due to large scale variation in background removal in the *RASS*. High-contrast stretches of the *RASS*, particularly in bands R4 through R7, show features along the scan direction. These features will be replicated in the mosaics. Some structure, such as the central enhancement in the R1L2 band mosaic of 220+84, appears to due to structure in the soft X-ray background.

2. Not-So-Boring Stuff

2.1. Quality of the Deabsorption

It is not trivial to determine the amount of distortion in the images of the distant emission due to improper deabsorption. The distortion can not be too gross, else it would be apparent in the images or in the $I_0' - N_H$ relations, but distortions on a given angular scale, whose amplitude is on the order of the uncertainty in the mean flux on that scale, would be difficult to detect.

To gain some insight on the amplitude of such distortions (but, alas, not providing insight on the angular scale of such distortions) we calcu-

TABLE 9.1
IMAGE DISPLAY PARAMETERS

Field	R1L2			R45		
	$\langle I_D \rangle$	$\langle (I_D - \langle I_D \rangle)^2 \rangle$	σ_{I_D}[a]	$\langle I_D \rangle$	$\langle (I_D - \langle I_D \rangle)^2 \rangle$	σ_{I_D}[a]
	10^{-6} Counts s^{-1} arcmin^{-2}			10^{-6} Counts s^{-1} arcmin^{-2}		
035+78	445.0	620.1	477.9	59.9	159.8	138.9
086+74	338.0	528.4	364.0	63.8	161.8	123.2
138+52	315.0	605.5	486.7	24.2	159.4	116.7
161+51	405.3	680.3	579.8	22.4	189.0	170.4
171+50	414.4	934.0	770.9	20.6	282.7	197.4
220+84	559.4	1065.	733.1	51.9	203.1	181.2
295−89	290.8	982.6	722.3	60.7	218.2	146.8

[a] This value determined by fitting a single Gaussian to the distribution of pixels with values greater than zero. Since not all pixels in the mosaics actually contain recorded X-ray photons, the distribution of pixels with values less than zero will be non-statistical; the values will be negative of the modeled background. Thus, they were excluded from the fits. *It can not be emphasized too greatly that because the pixel size is so small, many pixels do not contain counts, and the σ are dominated by counting statistics. These values were only used to clean the images of "hot" pixels.*

TABLE 9.2
DEABSORPTION PARAMETERS I

Field	PS_{lim}		a	b	Reg[a]	$\mathcal{N}_H/\mathcal{N}_S$
	R1L2	R47				
	(counts s^{-1})		(MJy sr^{-1})	(MJy sr^{-1} cm^2)		
035+78	0.020	0.010	+0.0196±0.0319	0.5147±0.0283	M	1.17
086+74	0.030	0.013	-0.1273±0.0200	0.6127±0.0200	E	0.48
138+52	0.030	0.018	-0.0480±0.0232	0.6936±0.0256	M	0.25
161+51	0.030	0.014	-0.1028±0.0248	0.7047±0.0305	M	0.16
171+50	0.040	0.021	-0.0324±0.0215	0.5726±0.0209	M	0.08
220+84	0.040	0.021	+0.0774±0.0103	0.5486±0.0066	M	0.74
295-89[b]	0.025	0.014	+0.0981±0.0106	0.4381±0.0063	E	1.00

[a] "M" means that the HI-to-I_{100} relation was derived only from the mosaic region. "E" means that the relation was derived from a larger area due to the lack of dynamic range within the mosaic region.

[b] See text for the explanation of the method used to determine $\mathcal{N}_H/\mathcal{N}_S$ for this field.

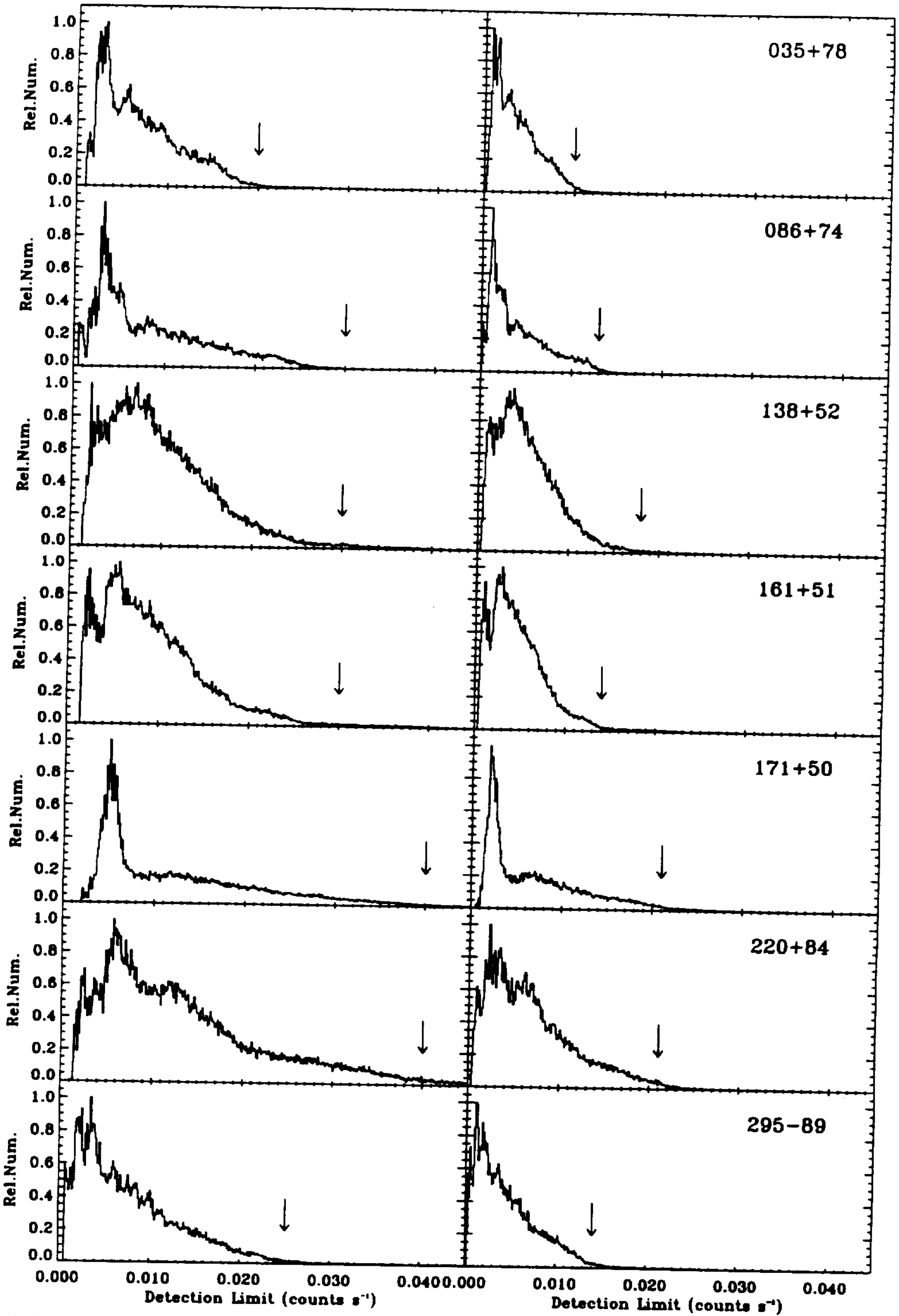

Fig. 9.2.— Distribution of point source detection limits, the relative number of pixels with each detection limit. The arrows indicate the point source detection limits to which each field was corrected in each band. *Left:* Band R1L2, *Right:* Band R45.

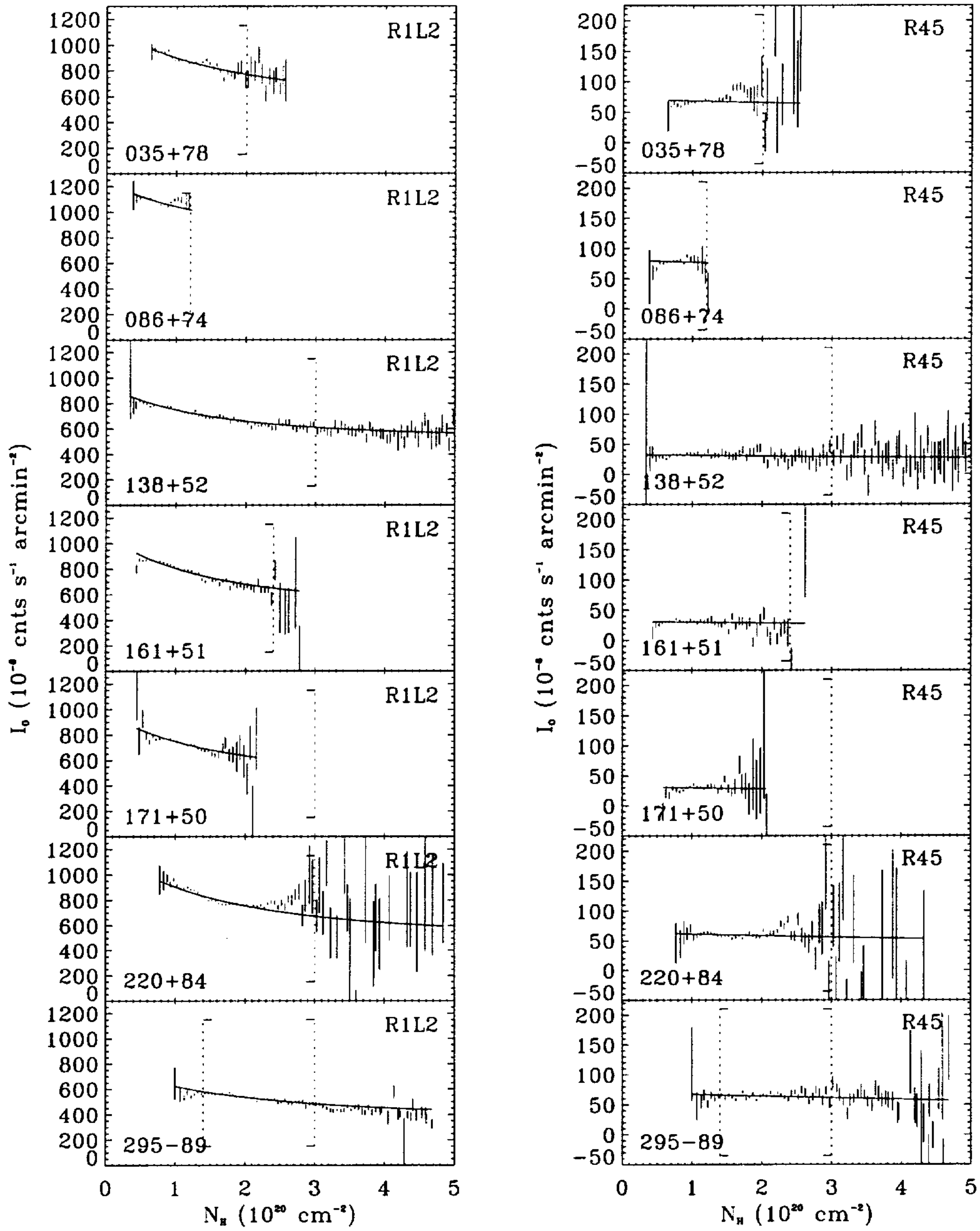

Fig. 9.3.— $I'_O - N_H$ relations for the mosaics. The dashed brackets indicate the range of N_H over which the fit was made.

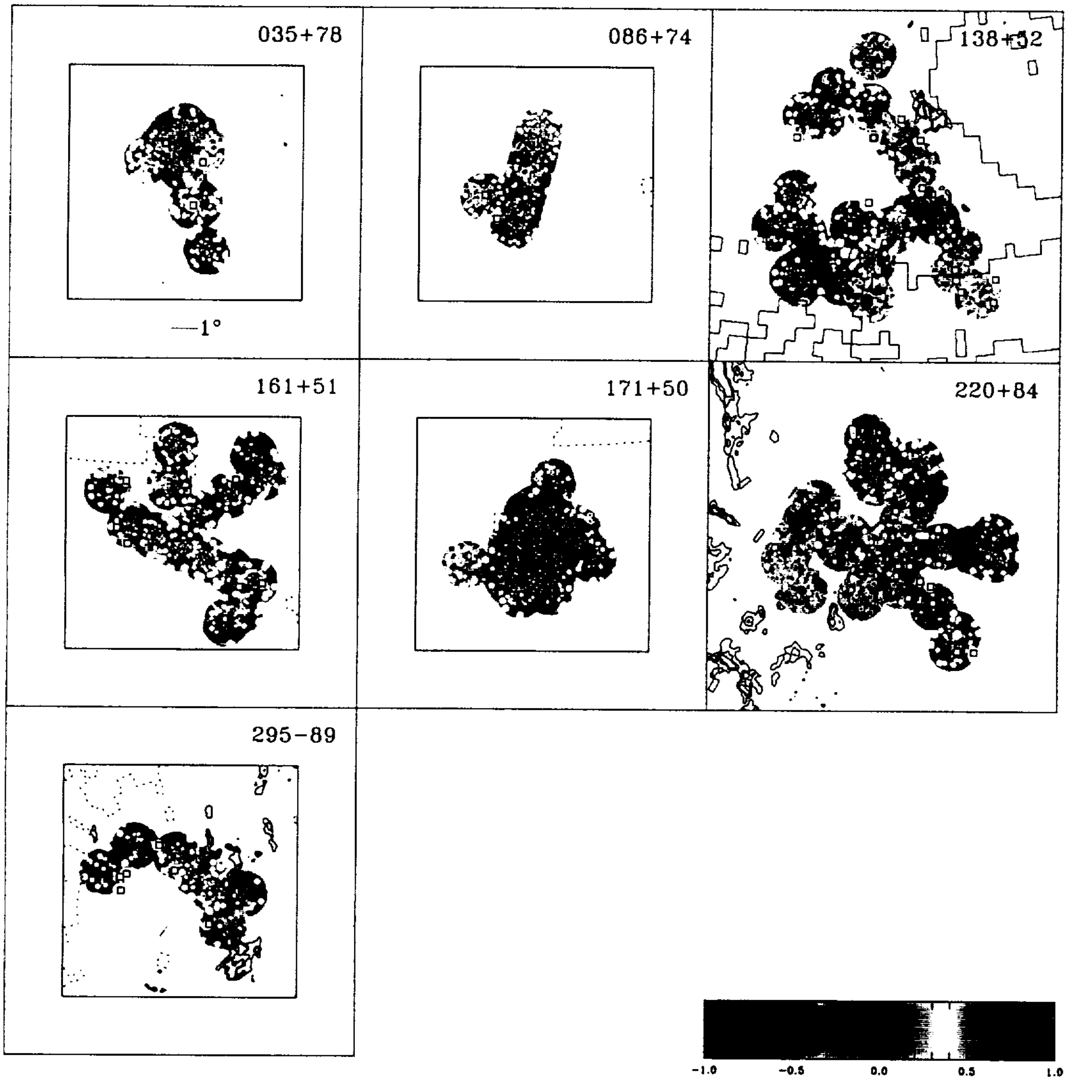

Fig. 9.4.— The R1L2 band images after deabsorption, smoothed by a 10′ boxcar function. Contours denote regions with $N_H > 3 \times 10^{20}$ cm^{-2}. The dashed contours denote regions with IV and HV gas with column density greater than 1.5×10^{15} cm^{-2}. The boxes are locations of Abell clusters. The grey scale is from -1σ to $+1\sigma$, where the σ was measured for the Gaussian core of the distribution of pixel values. The values of σ are given in Table 9.1. The scale is shown in the lower part of the upper left-hand panel.

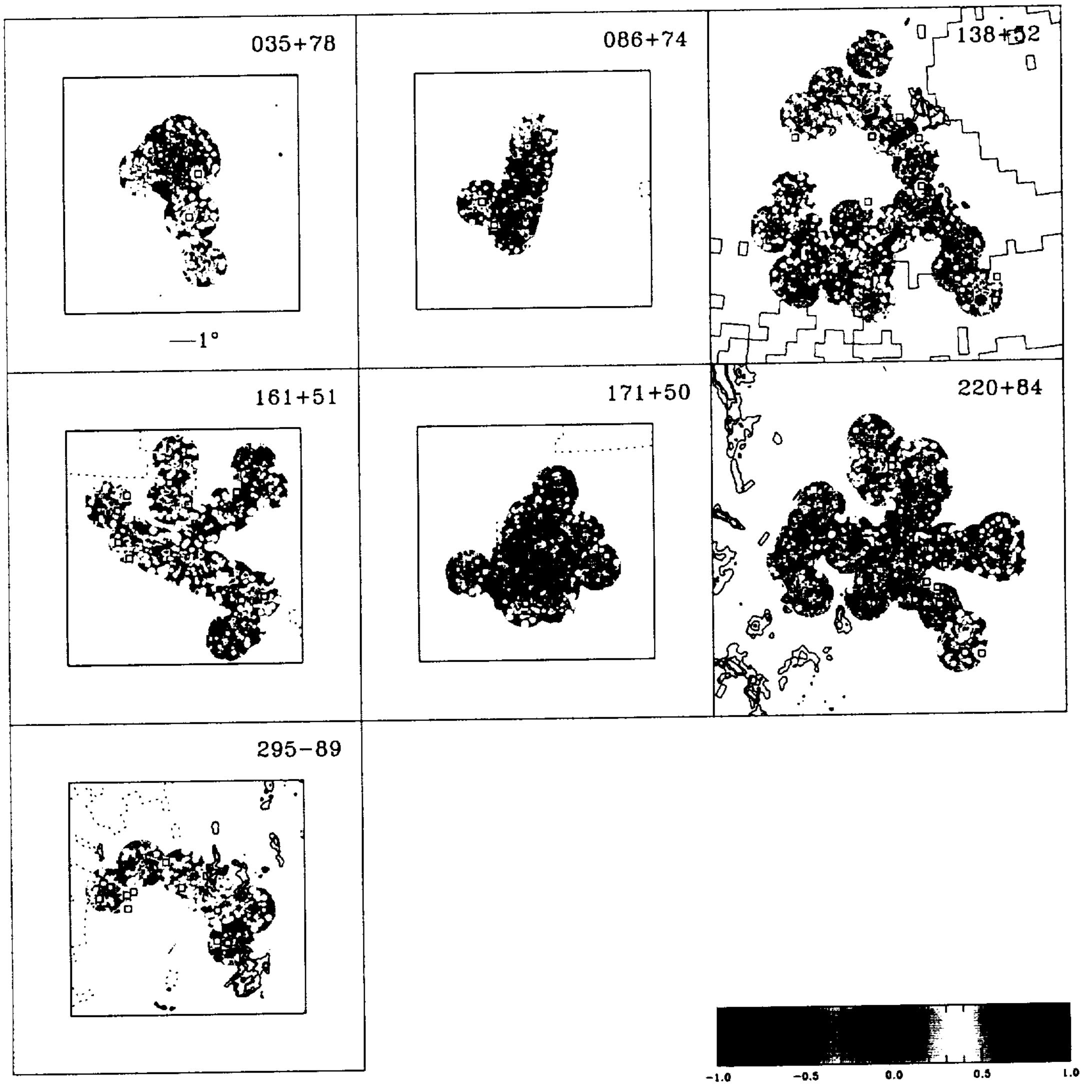

Fig. 9.5.— The R45 band images after deabsorption, smoothed by a 10′ boxcar function. Contours denote regions with $N_H > 3 \times 10^{20}$ cm^{-2}. The dashed contours denote regions with IV and HV gas with column density greater than 1.5×10^{15} cm^{-2}. The boxes are locations of Abell clusters. The grey scale is from -1σ to $+1\sigma$, where the σ was measured for the Gaussian core of the distribution of pixel values. The values of σ are given in Table 9.1. The scale is shown in the lower part of the upper left-hand panel.

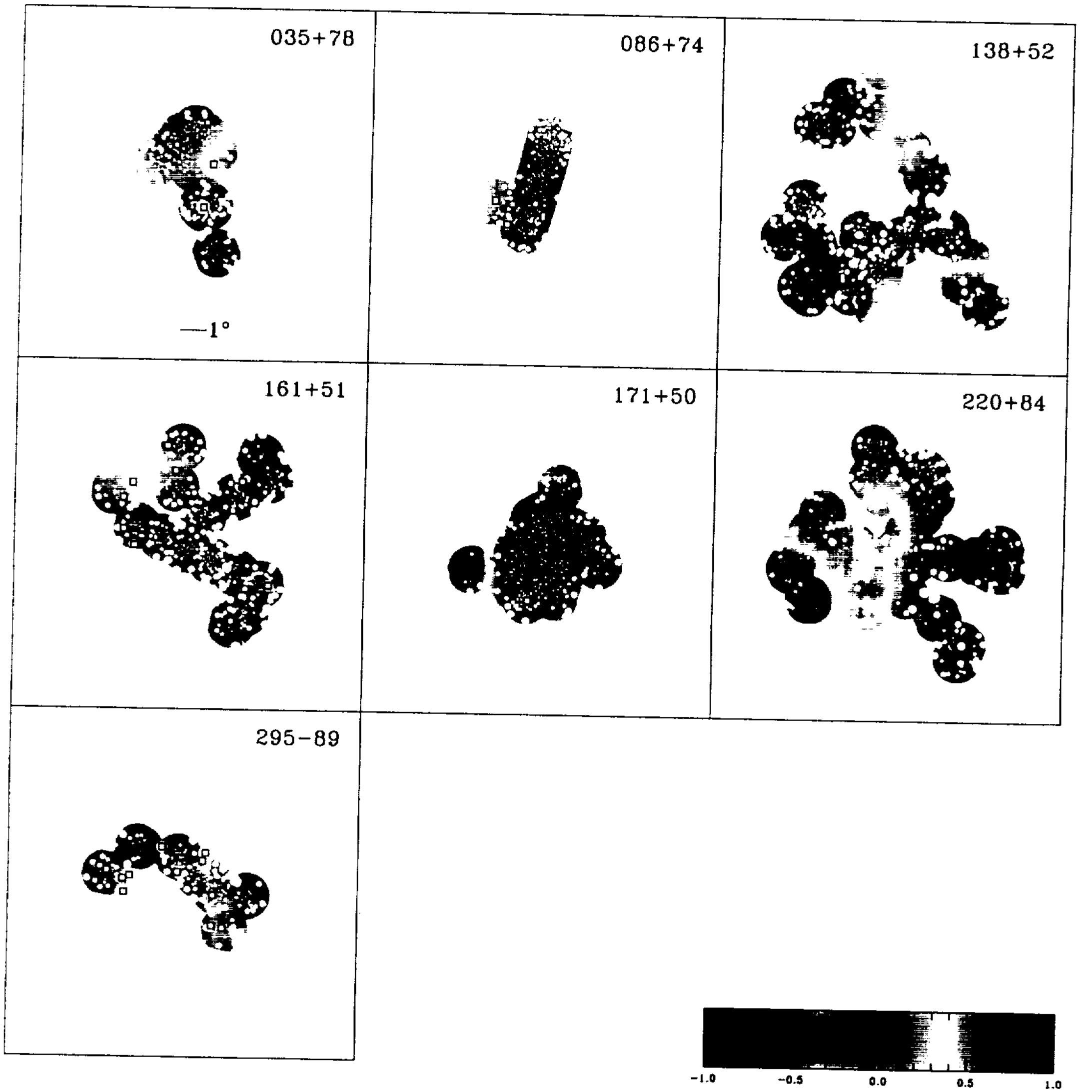

Fig. 9.6.— The R1L2 band images after deabsorption smoothed by a 121′ boxcar. The greyscale is the mean ±200 × 10^{-6} counts s^{-1} $arcmin^{-2}$. Some variation is clearly due to problems with the mosaicking, as the left-hand "ear" on 171+50, but other variation, such as the central portion of 220+84, appear to be due to true variation in the background. The scale is shown in the lower part of the upper left-hand panel.

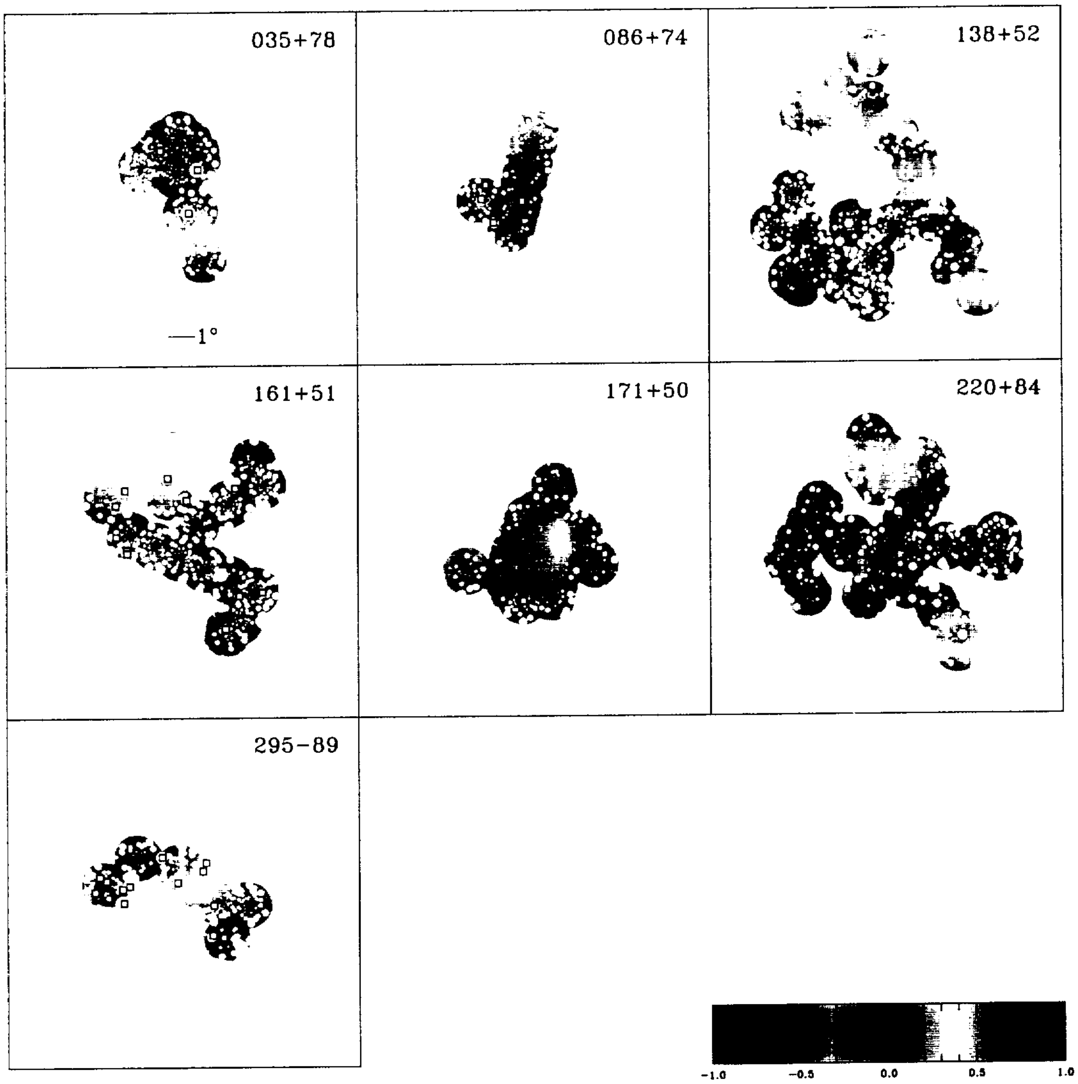

Fig. 9.7.— The R45 band images after deabsorption smoothed by a 121′ boxcar. The greyscale is the mean ±50 × 10^{-6} counts s^{-1} arcmin^{-2}. The variation in the upper "ear" pf 171+50, and the end-to-end variation of 035+78 and 086+74 are likely due to mosaicking problems. The scale is shown in the lower part of the upper left-hand panel.

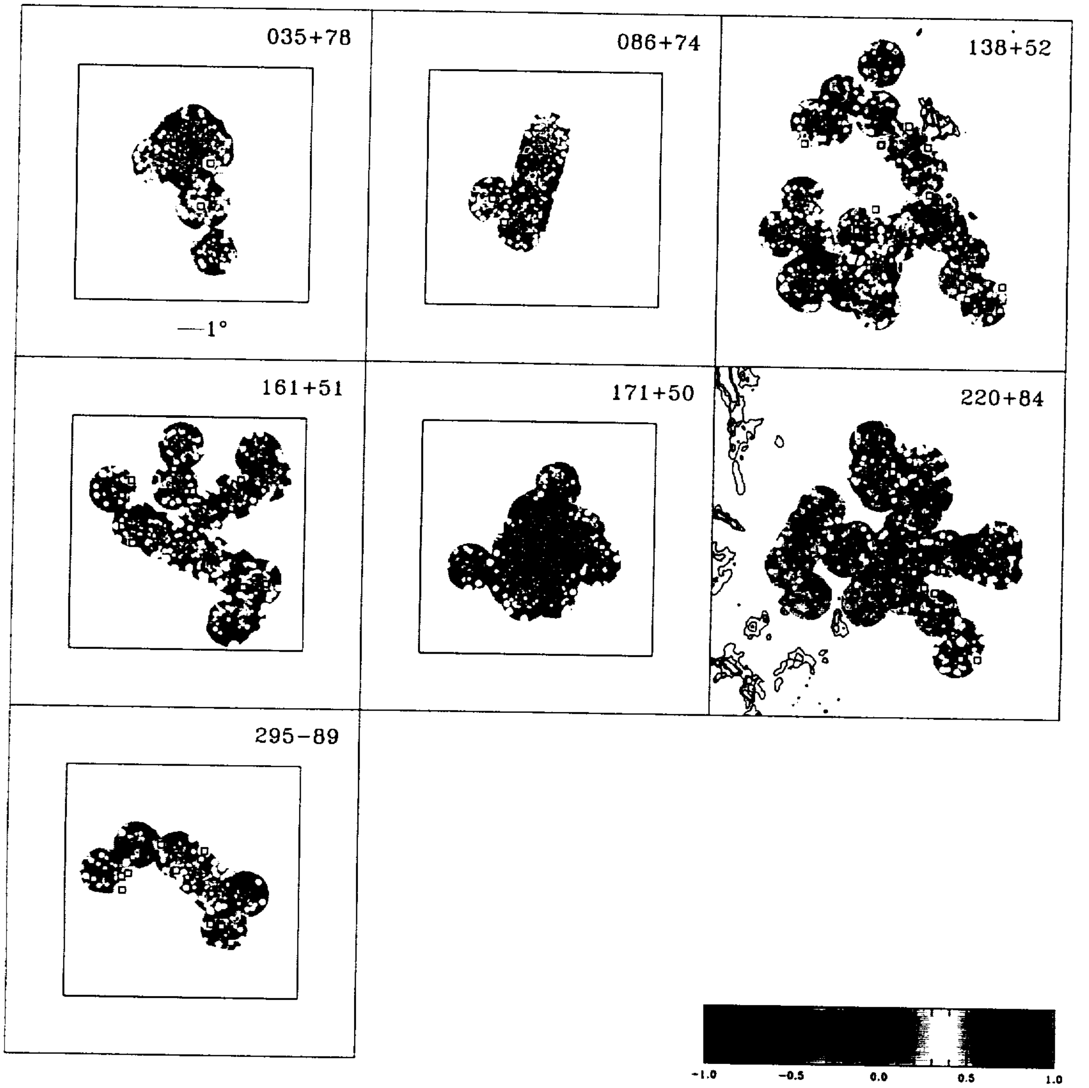

Fig. 9.8.— The R1L2 band images after deabsorption, high-pass filtered with a 121′ threshold, and smoothed with a 10′ boxcar function. The greyscale is as in Figure 9.4. The scale is shown in the lower part of the upper left-hand panel.

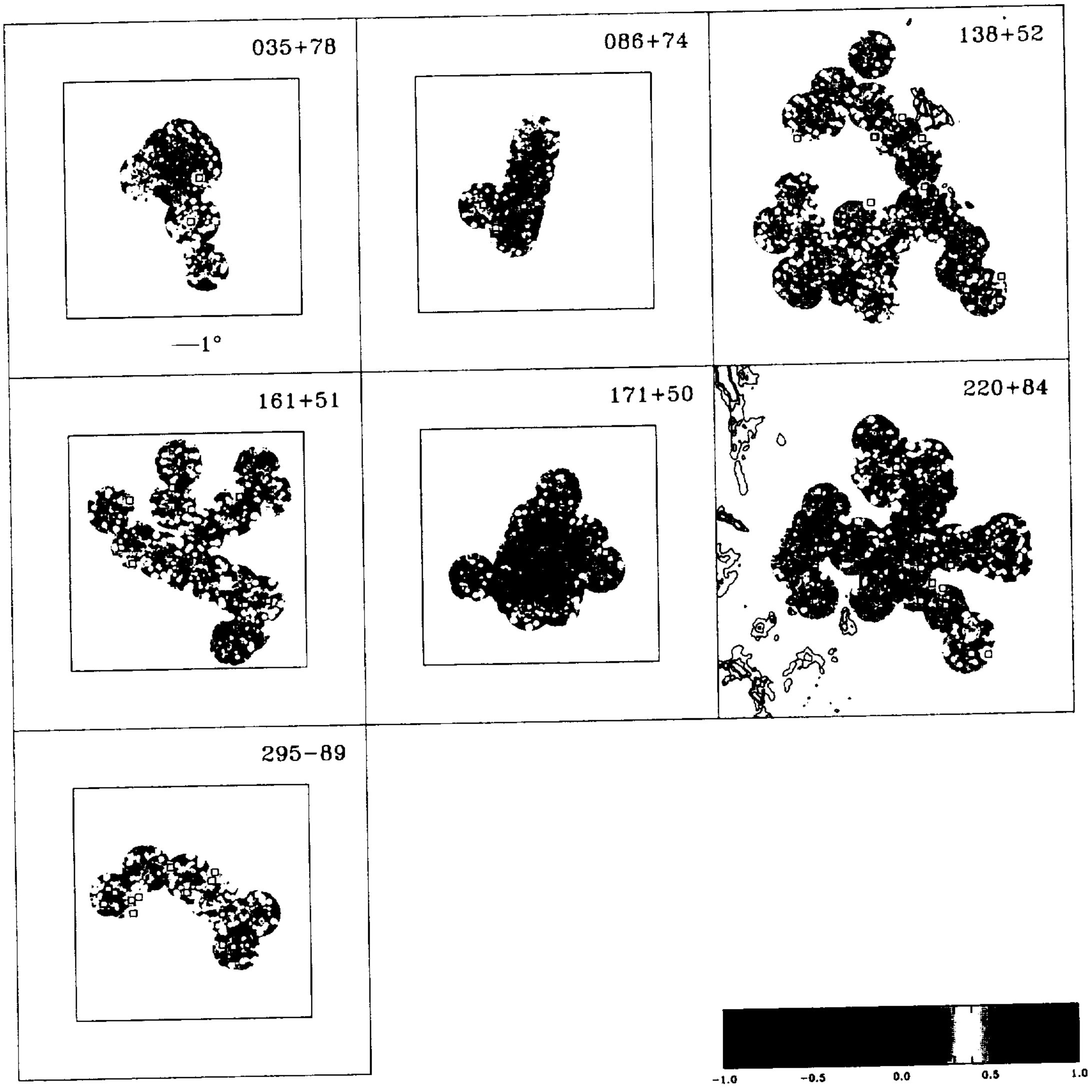

Fig. 9.9.— The R45 band images after deabsorption, high-pass filtered with a 121′ threshold, and smoothed by a 10′ boxcar function. The greyscale is as in Figure 9.5. The scale is shown in the lower part of the upper left-hand panel.

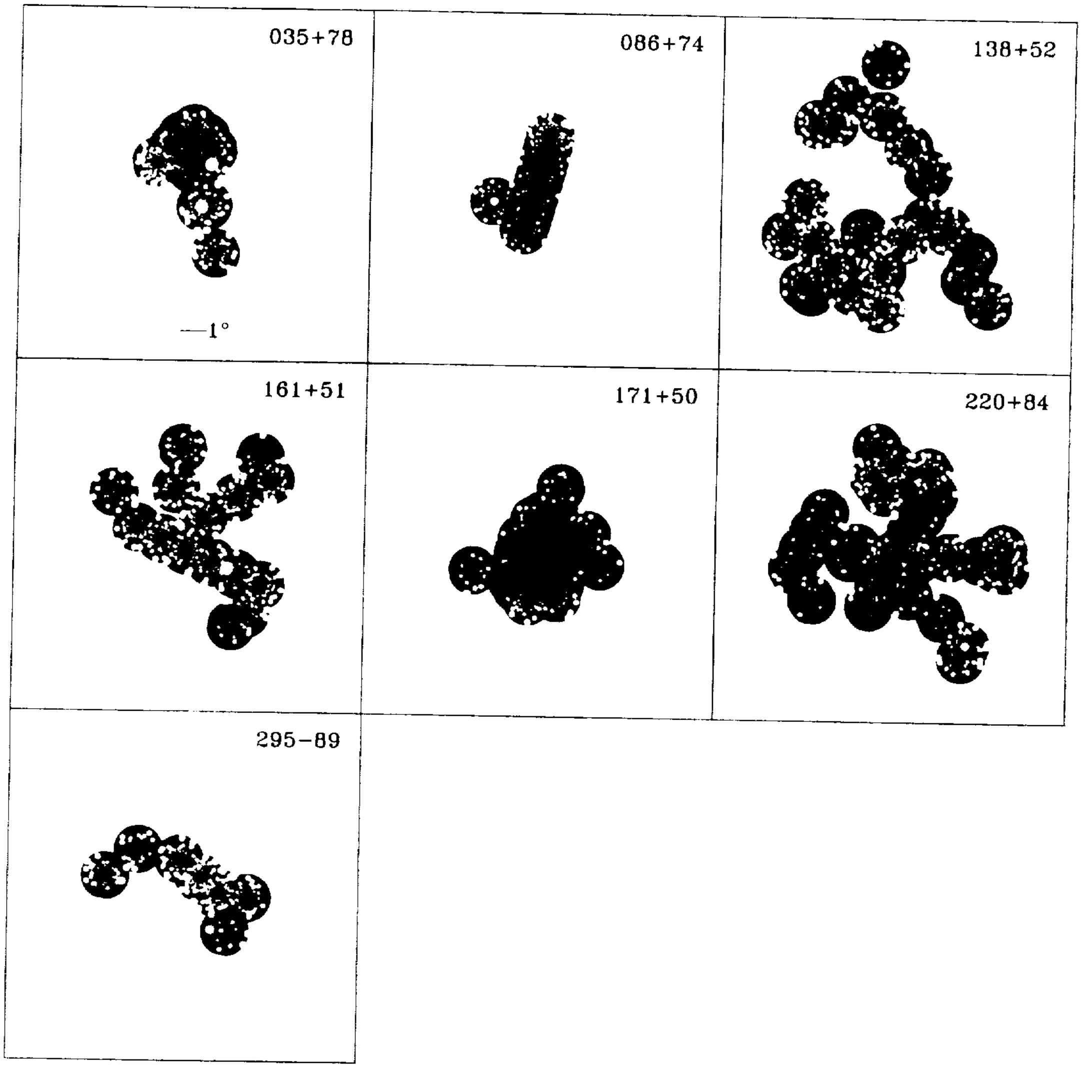

Fig. 9.10.— The relative areas of mosaics with maximum PSF sizes of 10′ (the largest), 5′, and 2′ (the smallest).

TABLE 9.3
DEABSORPTION PARAMETERS II

Field	I_L[a]	I_D[a]	χ^2_ν	ν	N_H[b]	Area
	(10^{-6} counts s^{-1} arcmin^{-2})				(10^{20} cm^{-2})	(degree^2)
			R1L2			
035+78	568.6±20.4	584.1±37.5	5.564	28	0.50-2.0	10.8
086+74	806.9±31.8	432.8±49.5	5.582	17	0.35-1.2	8.68
138+52	530.3±8.1	410.1±14.5	2.713	54	0.00-3.0	28.4
161+51	508.1±11.4	564.1±19.7	4.488	40	0.00-2.4	21.4
171+50	472.7±21.9	511.4±41.0	2.335	36	0.00-3.0	17.0
220+84	523.5±10.5	659.7±26.0	7.881	45	0.70-3.0	17.3
295-89	388.6±10.5	399.4±34.5	1.924	32	1.40-3.0	10.1
			R45			
035+78	10.5	61.2±0.6	4.109	28	0.50-2.0	10.8
086+74	14.9	66.0±0.5	3.317	17	0.35-1.2	8.68
138+52	9.7	23.3±0.5	1.288	54	0.00-3.0	28.4
161+51	9.4	25.7±0.6	1.850	40	0.00-3.0	21.4
171+50	8.7	22.8±0.7	2.141	31	0.60-3.0	17.0
220+84	9.7	54.8±0.5	2.504	45	0.70-3.0	17.3
295-89	7.2	63.2±0.6	2.020	32	1.40-3.0	10.1

[a] These 1σ uncertainties were derived using the LMB criteria.

[b] The range in N_H over which the fit was made.

TABLE 9.4
PEARSON r_s VALUES

Field	R1L2-N_H		R45-N_H		R1L2-R45	
	ii[a]	(ij)[b]	ii[a]	(ij)[b]	UF[c]	HPF[c]
035+78	0.0453071	0.00679737	-0.00070099	0.0105800	0.0404990	0.0512406
086+74	0.0302972	0.00011539	0.00350230	-0.0087495	0.1424650	0.1500020
138+52	0.0046646	-0.00902083	-0.00212031	-0.0148158	0.0787122	0.0709099
161+51	-0.0074366	-0.00649844	-0.00438955	-0.0088455	0.0557257	0.0536091
171+50	0.0164653	0.00156977	-0.00376389	0.0150840	0.0622010	0.0670470
220+84	0.0156349	-0.00390056	0.00578401	-0.0450213	0.0640094	0.0685017
295-89	0.0162464	0.00036065	0.00827481	0.0034546	0.0538589	0.0530195

[a] The Pearson r value for the X-ray image correlated with the N_H image for the same field.

[b] The mean Pearson r value for the X-ray image correlated with the N_H images for the other fields.

[c] The Pearson r value for the R1L2 X-ray image correlated with the R45 X-ray image. *HPF:* the images were high-pass filtered with a cutoff of 120′, *UF:* the images were not filtered.

late the Pearson r value[2], r_s, for the image of the distant emission and the image of the absorbing column:

$$\frac{\sum(I_D - \overline{I_D})(N_H - \overline{N_H})}{\sqrt{\sum(I_D - \overline{I_D})^2}\sqrt{\sum(N_H - \overline{N_H})^2}}. \tag{9.2}$$

If N_H and I_D were completely correlated (or anti-correlated) then the value of r_s would be 1 (or -1); values of r_S near zero would indicate lack of correlation.

Since neither I_D nor N_H are distributed in a statistical sense, we can not use the value of r_s to derive a probability of correlation. However, we can use this value to provide some sense of how small the correlation may be. In Figure 9.11 and Table 9.4 we show the values of r_s for each field (the *ii* column of the table and the boxes in the figure). We then calculate the value of r_s for mismatched pairs, an I_D image paired with the N_H image from another mosaic. (the *ij* column of the table, in which case the measure is the mean of all the mismatched pairs using a given I_D image, and the "×" in the figure).

For both the R45 and R1L2 bands, the value of r_s for an I_D image paired with its N_H image tends to be greater than (i.e., more correlated than) the value of r_s for mismatched pairs, though there are usually mismatched pairs with stronger correlations. The R45 band images appear to be less correlated with N_H than the R1L2 band images. This result suggests that the deabsorption process has over-corrected for the absorption by N_H (under-correction should produce an anti-correlation) and this effect is stronger in band R1L2 than in band R45 (as one might expect any effect to be). However, given that the values of r_s for matched pairs usually lies within the distribution of the values of r_s for mismatched pairs, and in no case does the value of r_s fall very far from the distribution of r_s for mismatched pairs, *the amount of correlation between I_D and N_H must be small, at least compared to the dynamic range of the image.*

2.2. Band-Band Cross-Correlations

We have also considered the cross-correlation of the R1L2 and R45 band images. We have calculated the value of r_s unfiltered and high-pass-filtered images. In both cases, the value of r_s is low, $\lesssim 0.15$, suggesting that there is little correlation between the two bands. Given the results of Chapter 6, such a result might have been expected at least on multi-degree scales.

There is very little difference between the r_s calculated from high-pass-filtered images and that calculated from the filtered images (see Table 9.4 and Figure 9.12), suggesting that the bulk of the correlation between the R45 and R1L2 band images is due to small-angular-scale sources.

---

[2] This value is the equivalent to the zero-offset cross-correlation.

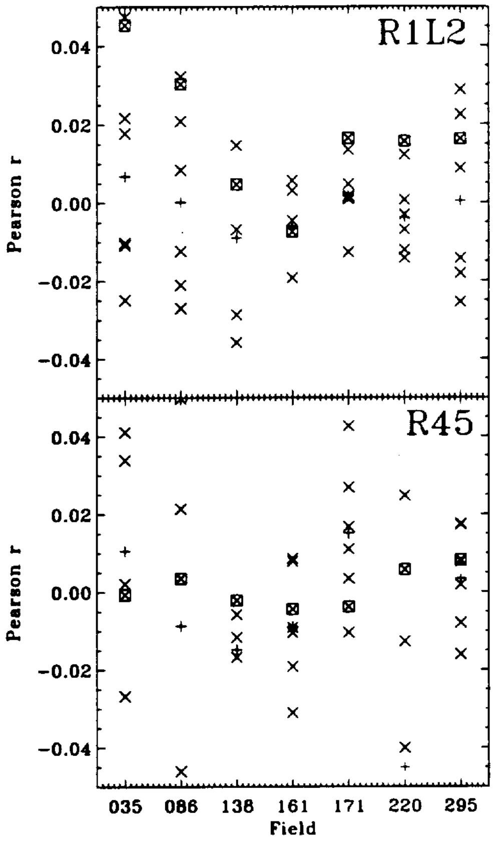

Fig. 9.11.— Pearson r_s values for the cross-correlation of the deabsorbed images with the maps of the absorbing column. *Symbols:* □: r_s for a deabsorbed image and the map of the absorbing column, ×: r_s for a deabsorbed image and maps of the absorbing column for other mosaics, +: the mean of the r_s for a deabsorbed image and the maps of the absorbing column for other mosaics.

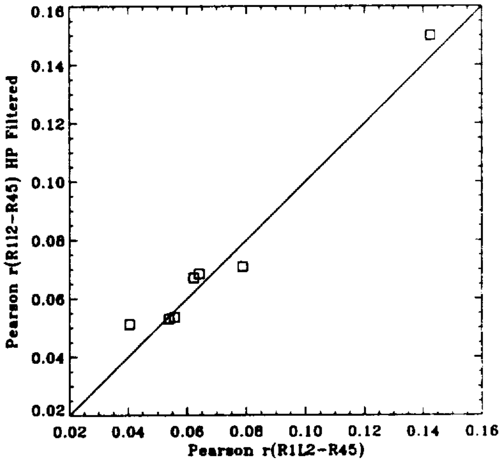

Fig. 9.12.— Pearson r_s values for the cross-correlation of the R1L2 deabsorbed images with the R45 deabsorbed images; *abscissa:* r_s for unfiltered images, *ordinate:* r_s for filtered images.

Chapter 10: Fluctuation Analysis

Abstract

This chapter presents two common measures of the angular correlation function, the autocorrelation function (ACF) and the $\delta I/I$ measure. We discuss here the means by which these measures are applied to the seven mosaicked fields, analyze the extent to which these measures may be affected by systematics, and compare these results to earlier results to determine to what extent these data are useful.

We assume that the observed fluctuations are not due to either the Local Hot Bubble or the Galactic halo, as flucutations on scales smaller than 30′ would be very short lived in either environment. Indeed, an ACF of emission due only to the LHB showed no appreciable signal at scales greater than 3′, the lower limit to which it could be measured. Large scale fluctuations due to calibration difficulties in the *RASS* or emission variation due to the LHB and the Galactic halo are removed by high-pass filtering.

The ACF results remain contaminated by residual point sources, and there may be other systematic effects not yet removed. After removing our estimate for the maximum contribution due to residual point sources we find the ACF; $W(5' < \theta < 35') \sim 0.01$ in the R1L2 band and $W(10' < \theta < 25') \sim 0.0025$ in the R45 band, with no significant signal at larger scales. Our measurement in the R45 band is consistent with the upper limit measured by Chen et al. (1994) in the R47 band.

We have developed a new form of the $\delta I/I$ measure of fluctuations. The results are consistent with the ACF, showing no significant fluctuations at scales greater than 35′ and 25′ in the $\frac{1}{4}$ keV and $\frac{3}{4}$ keV bands respectively.

We find a large variation in the fluctuation spectra determined from different mosaics.

1. Introduction

A cursory examination of the images in the previous chapter shows that there are variations on many scales, from the size of the PSF to the size of the mosaic. The images clearly show the effect of unremoved point sources, point sources that were below the detection threshold of the individual pointings. There may be sources with greater angular extent, similar to the Abell clusters that have been removed, but the summation of many different PSFs at any given location make analysis difficult. The smoothed images show structure on degree scales, and the eye leads one to believe (from the high-pass filtered images) that there may be structure on intermediate scales. How much of that structure is due to overlapping 10′ PSFs remains to be seen.

Structure on large scales is not surprising; the images of the distant component of the diffuse emission in Chapter 6 (Figure 6.4) show structure on degree scales. Most of that structure is in the soft halo component ($\log T = 6.056$) while the harder halo component ($\log T = 6.426$) appears to be much smoother. Of the images studied in this chapter, those in the R1L2 band will be dominated by the soft component. The two components contribute comparable amounts to the R45 band images. Structures on small scales has not been studied but is not expected to be strong; small scale structures tend to dissipate on short time scales in hot plasmas.

In stellar astronomy, a prime difficulty is connecting a theoretically determined HR diagram in (T_{eff}, M_{bol}) with the measured HR diagram in $(B - V, V)$. In this work, the difficulty is connecting some measure of fluctuations in two-dimensional images to the three-dimensional structure of the universe. The first link in this connection is the two-point angular correlation function, $w(\theta)$, which is described in §1.1. The following subsection, §1.2, explores problems introduced by the data that are common to all the methods of measuring fluctuations.

We then consider two methods for measuring fluctuations, the autocorrelation function (ACF) and the $\delta I/I$ measure. The ACF is the most direct measure of $w(\theta)$, but is sensitive to the effects of the PSF, and the uncertainty is inversely proportional to the square of the number of pixels. The $\delta I/I$ measure is a direct calculation of the pixel-to-pixel variance at a given scale. It is somewhat easier to apply, but does not provide a useful measure of $w(\theta)$. The $\delta I/I$ is limited to scales somewhat smaller than the size of the mosaic, but the uncertainty is proportional only to the the inverse of the number of pixels. The ACF is discussed in §2, the $\delta I/I$ measure in §3. Comparison of our results to previous results, (and with our picture of the universe) is discussed in §4. Making the final link to the structure of the universe will, of course, be model dependent. Although the models discussed in Chapter 1 have recently become available, determining whether the range of fluctuations (or lack thereof) seen here is consistent with the model (or *vice versa*) is beyond the scope of this dissertation.

1.1. The Angular Correlation Function

Of the ways to characterize the amount of structure as a function of scale, many are related to the two-point angular correlation function, $w(\theta)$. Following Peebles (1993) one can define $w(\theta)$ in the following manner in terms of point sources. If there is a point source at a given point, then the probability that there is a point source in a solid angle $d\Omega$ at angular distance θ is

$$dP(\theta) = \mathcal{N}[1 + w(\theta)]d\Omega \qquad (10.1)$$

where $\mathcal{N}$ is the angular density of point sources. The probability that two sources exist separated by θ is thus

$$dP(\theta) = \mathcal{N}^2[1 + w(\theta)]d\Omega d\Omega \qquad (10.2)$$

Although this measure can be applied to catalogues of discrete objects, we are more interested in fluxes due to collections of objects. Peebles (1993, §7, Equations 7.62-7.67) develops the formalism for this transformation from counting objects to measuring flux. Consider two differential units of solid angle, $\delta\Omega_i$ and $\delta\Omega_j$ separated by θ_{ij}, each differential unit so small that it can contain at most one source. If the expectation value of the number of sources in the differential $\delta\Omega_i$ is $\langle n_i \rangle = \mathcal{N}\delta\Omega$, then we find that

$$\langle n_i n_j \rangle = \mathcal{N}^2 \delta\Omega_i \delta\Omega_j [1 + w(\theta_{ij})] \qquad (10.3)$$

This formalism can be expanded to the expectation values for the number of objects in extended fields. The extension to fluxes is artificial; one can consider the flux in a pixel to be the number of objects in the pixel, each object having a flux δf. The relation between $w(\theta)$ and the ACF or $\delta I/I$ will derived in the sections below.

One can define a similar two point correlation function such that, given a source at a given point, the probability that there is a point source in a volume dV at a distance r is

$$dP(r) = n[1 + \xi(r)]dV \qquad (10.4)$$

where n is the source density. The relationship between $\xi(r)$ and a measured $w(\theta)$ is complex, relying on the spatial density and luminosity distribution as a function of redshift. If the $w(\theta)$ is measured the flux of an aggregate of sources, then relation is even more complex, as it must include the distributions of all of the different types of objects contributing to the flux.

The general relation between a measured $w(\theta)$ and the distribution and size of diffuse emission is likewise complex and, although it will be discussed in the following chapter, is beyond the scope of this dissertation.

1.2. A Problem

There are a number of ways of characterizing fluctuations, each fraught with its own particular dangers. Each of these methods has a common difficulty; the change in PSF radius with distance from the optical axis. This change is demonstrated in Figure 10.1 and tabulated in Table 10.1. To analyse fluctuations on a given scale, one must include in the mosaic only the central parts of the individual pointings, where the PSF diameter is comparable or smaller than the scale of interest. Otherwise, one would need

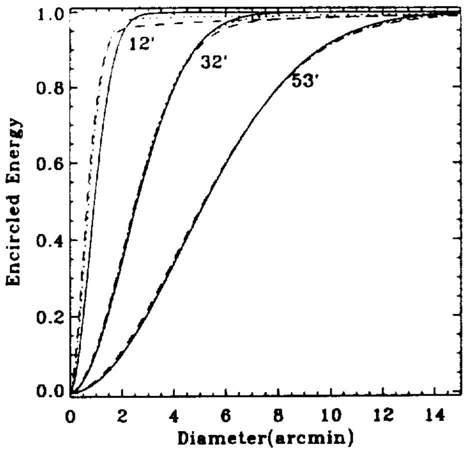

Fig. 10.1.— Comparison of PSF profiles for different bands at different distances from the optical axis. The labels indicate the distance from the optical axis. *Solid:* band R1L2, *Dotted:* band R45, *Dashed:* band R67.

to model the *shape* of the PSF as a function of position within the mosaic; a difficult task since at any given pixel there may be contributions from several different pointings, each with a different PSF size at that pixel. Reducing each pointing to only the central region significantly reduces the area available for analysis.

In order to maximize the available region for analysis, yet still avoid the PSF, ("threading our way twixt one and the other") we have created three mosaics for each field, each mosaic having a different exclusion radius. The three mosaics have an exclusion radii of 12′, 32′, and 53′, allowing a maximum PSFs of ~ 2′, ~ 5′, and ~ 10′ respectively The largest exclusion radius is set by the vignetting function.

2. The Autocorrelation Function - $W(\theta)$

2.1. Equivalent Formulations

The autocorrelation function (ACF) is generally defined as

$$W(\theta) = \frac{\sum_{i,j}(I_i - \langle I \rangle)(I_j - \langle I \rangle)}{\langle I \rangle^2} \tag{10.5}$$

where the sum is over all pairs of pixels i and j that are θ apart. Using the formalism developed by Peebles (1993), one can show that $W(\theta)$ is directly equivalent to $w(\theta)$, the two-point angular correlation function.

The ACF has an advantage over the $\delta I/I$ measure; if $f(u)$ is the image, then the ACF is equivalent to

$$\int_{-\infty}^{\infty} f^*(u) f(u+x)\,du = \int_{-\infty}^{\infty} |F(s)|^2 e^{2i\pi x s}\,ds, \tag{10.6}$$

where $F(s)$ is the power spectrum of the fluctuations.

2.2. Algorithm

There are several different formulations of the autocorrelation function in common use, the most general form of which is

$$W(\theta) = \frac{\sum_{i,i'}(R - \langle R \rangle)(R' - \langle R' \rangle)\sqrt{ww'}}{X^2 \sum_{i,i'} \sqrt{ww'}}. \tag{10.7}$$

where the sum is over all pairs of pixels seperated by θ, R is the count rate in those pixels, and w is the statistical weight given to those pixels. Depending upon the formulation

$$X = \begin{cases} 1 \\ \bar{R} \\ (\sum_i R + \sum_{i'} R')/2 \end{cases} \tag{10.8}$$

We have calculated the ACF using this last form of X to remain consistent with other calculations of the ACF (Soltan & Hasinger 1994; Chen et al. 1994).

For the weights, w, w', one could take the uncertainties calculated in the previous chapter. However, there are difficulties using these uncertainties. As many pixels in the image have only a small number of counts, assuming Poisson statistics, the calculated uncertainties will be strongly correlated with the value of the pixel; in a region of uniform exposure (and thus, uniform true uncertainty) the variation in the number of counts per pixel will cause one incorrectly to weight more strongly the pixels with larger number of counts.

Rather than using the measured uncertainty, we have followed the method of Chen et al. (1994) with modifications. The number of counts

TABLE 10.1

PSPC PSF-FIELD RADIUS RELATION

PSF[a] Diameter	Field Radius R1L2	R45	R67
2	12.7	15.7	14.7
3	20.7	21.7	20.7
4	26.7	27.2	25.7
5	32.1	31.6	30.6
6	36.6	36.6	35.1
7	41.6	41.1	39.6
8	45.6	45.1	43.6
9	49.6	49.1	47.6
10	53.6	53.1	51.6

[a] This is the diameter encircling 90% of the energy.

in pixel (i,j) is given by

$$C_{(i,j)} = EV_{(i,j)}\mathcal{R}_{(i,j)} \tag{10.9}$$

where E is the length of the exposure, $V_{(i,j)}$ is the vignetting function, and $\mathcal{R}_{(i,j)}$ is the cosmic flux. Therefore, assuming Poisson statistics, and assuming that the true variation in the cosmic flux is small, the true uncertainty of pixel (i,j) is

$$\sigma^2_{(i,j)} \propto EV_{(i,j)} \tag{10.10}$$

where, for the purposes of Equation 10.7, the proportionality constant is immaterial and the instrumental background is assumed to be much smaller than the cosmic background. This is the weighting scheme used by Chen et al. (1994). We have modified the weights to account for the relative uncertainties due to deabsorption:

$$w_{(i,j)} = EV_{(i,j)}e^{-\tau_{(i,j)}} \tag{10.11}$$

where $e^{\tau_{(i,j)}}$ is the factor by which pixel (i,j) is deabsorbed.

2.3. Uncertainty

The variance in the ACF is given by

$$\sigma^2_{W(\theta)} = \frac{\sum_{\theta_x,\theta_y|\theta_x^2+\theta_y^2=\theta_0^2} (W(\theta_x,\theta_y) - \overline{W(\theta_0)})^2}{n} \tag{10.12}$$

where n is the number of different measures of $W(\theta = \theta_0)$. The uncertainty in the mean ACF will thus be given by

$$\sigma^2_{\overline{W(\theta)}} = \frac{\sigma^2_{W(\theta)}}{n}. \tag{10.13}$$

This measure of the uncertainty will be unreliable at small θ as there will only be $\pi\theta d\theta/2$ different measures of the ACF. The commonly used "shuffle" method for determining the uncertainty in the ACF, which operates by calculating the ACF of the image after all its pixels have been randomly rearranged, is not applicable to these fields due to the presence of structures with amplitudes greater than that of the noise (See Appendix G).

2.4. Data Preparation

The images used for calculating the ACF are the deabsorbed mosaics that have been further masked to reduce spurious fluctuations. Point sources were detected in the individual images and removed before the mosaicking. Regions with $N_H > 3 \times 10^{20}$ cm^{-2} or IVC/HVC column densities greater than 1.5×10^{19} cm^{-2} have been removed. Regions with a 8′ radius have been removed around every known Abell cluster; larger radii were removed if visual inspection suggested that the cluster emission had a greater extent. A few regions that had X-ray emission similar to that of clusters (but for which there was no identified cluster) were removed, as were a few point sources that had not been detected in individual pointings. A few regions where the deabsorption did not appear to be too sucessful have also been removed.

The images were also cleaned of individual "spurious" pixels; isolated pixels that have count rates greater than $4\sigma_{faux}$ above the mean[1]. These pixels are presumably due to single (or double) photon events in regions with very small effective exposure, and are often on the edge of a masked region. Removing these "spurious pixels" reduces the amplitude of the peak of the ACF at $\theta = 0$, and reduces very slightly the variance of the ACF at all other values of θ.

The deabsorbed images used for calculations include only the flux that could not be attributed to the Local Hot Bubble (LHB) or to the Extragalactic Power Law (EPL, the contribution to cosmic background by unresolved point sources), that is, the images only included the "Galactic halo" and the putative diffuse extragalactic emission. (Those two components together we have called the TAE (Chapter 6), the Trans-Absorptive Emission.) In order to be consistent with previous measures, the display ACFs were corrected to include the EPL component as well;

$$W_{EPL+TAE} = W_{TAE}\left(\frac{R_{TAE}}{R_{TAE}+R_{EPL}}\right)^2 . \tag{10.14}$$

All further ACF values quoted before §4 are for the combined TAE-EPL ACF. The ACF for the R1L2 band is calculated in the same manner as the ACF for the R45 band.

2.5. Application

We have measured the ACFs of each mosaic in each band. The results for a typical mosaic are shown in Figure 10.2. The effect of unremoved point sources can be seen at $\theta \lesssim 10'$, and the effects of large-scale structure can be seen at $\theta \lesssim 100'$. However, it should be noticed that the large-scale structure will have a significant effect on the measurement of the ACF due to small-scale structure.

Consider, for a moment, a not unreasonable model of the sky: assume that there are uncorrelated point sources and assume that the Galactic halo has variations on the scale of a degree. The contribution of the large-scale structure to the ACF will have its greatest amplitude at $\theta = 0$, and will decline as θ increases. Without knowledge of the large-scale structure, one could interpret the same ACF as due to a collection of much smaller scale variations. Thus, if one were attempting to place an upper limit on the contribution of small-scale fluctuations the unrecognized existence of large-scale structure would cause the measured upper limit to be significantly too large.

To achieve the tightest possible constraints on the ACF at $\theta < 1^\circ$ one must remove the influence of the large-scale structure of the halo as much as possible. We have chosen to minimize the impact of the halo by high-pass filtering the mosaics with a low frequency cut-off of 121′, slightly larger than the size of an individual pointing. The high-pass filtering will also ameliorate (but not entirely remove) the effects of offset errors in the mosaicking process. Since we expect the halo emission to have structure on degree scales, high-pass filtering with a cut-off of 121′ will, at worst, remove non-halo structures which, were they detected, would not be separable from halo phenomena.

ACFs are shown both for the mosaic and for the mosaic after high-pass filtering. Similar plots for the other mosaics are given in Appendix H. The ACFs from the high-pass-filtered band R45 mosaics are fairly consistent. Most the ACFs from the high-pass-filtered band R1L2 mosaics are consistent, with the exception of the 086+74 mosaic. Although this mosaic is arguably the best of the seven, as the individual pointings having very high exposure, the bulk of the pointings having substantial overlap, and the entire field having very smooth absorption, the ACF is very different from the others in band R1L2. The image appears to have structure on the $\sim 25'$ scale. Visual inspection of the high-pass-filtered mosaic reveals no peculiarity with respect to the other mosaics[2]. We have removed

---

[1] Calculating the variance of the pixel values is trivial, but calculating a meaningful variance for this purpose is a bit more difficult. A histogram of the pixel values reveals a "well behaved" Gaussian core, and extensive wings. The distribution is better fit with two overlapping Gaussians, the one with lower amplitude having a larger variance. The σ_{faux} used for calculating the cleaning limit was the variance of this broader component.

[2] There are a few point-source like objects remaining in this mosaic, as there are in all of the other mosaics. There

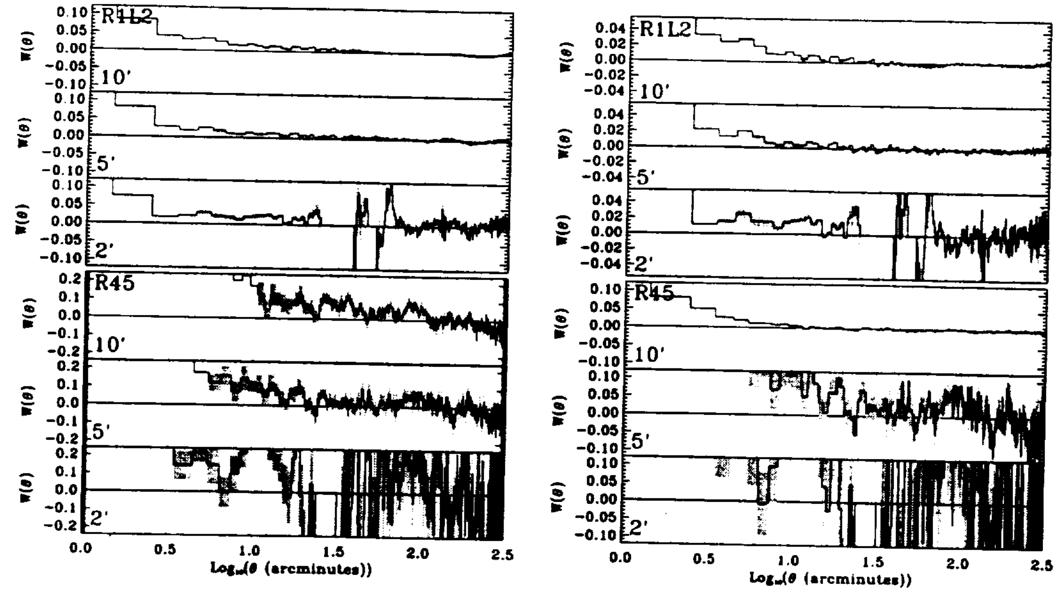

Fig. 10.2.— The ACF of a typical mosaic (161+51). The solid line is the ACF, the shaded region is the uncertainty. The ACF is shown for mosaics where the maximum radius for each pointing has been chosen to produce maximal PSFs of 10′, 5′, and 2′. *Left:* ACFs of the images. *Right:* ACFs of the high-pass filtered images. Note the changes of scales.

this mosaic from further consideration in band R1L2, but its presence should continue to pose a caveat on our conclusions.

2.5.1. Averaging the ACFs

We have found the mean ACF for the seven mosaics by summing the ACF for each mosaic, weighted by the average exposure for the mosaic and by the uncertainty. The effective mean flux ($\overline{R}$) for the coadded ACFs is 527.8(110.2) $\times 10^{-6}$ counts s^{-1} arcmin^{-2} for band R1L2(R45).

In order to reduce the uncertainty at large θ, we arbitrarily clipped individual ACF at the θ at which sequential values of the ACF began to diverge. The exposure weights and the θ_{max} for each ACF is given in Table 10.3. A number of different weighting schemes were tried, but they produced little difference. Restricting the sum to the four best mosaics also changed the mean ACF very little.

The uncertainties for ACFs measured from mosaics with smaller maximum PSFs are significantly worse; the number available pixels is sharply reduced by the demand for a better PSF (see Table 10.2). One would expect $W(5' < \theta < 10')$ to be much lower for the ACF measured from a mosaic with a maximum PSF diameter of 5′ than from a mosaic with a maximum PSF diameter of 10′. However, as can be seen from Figure 10.3, the significantly higher noise in the ACF measured from mosaics with 5′ PSFs completely masks this effect. Therefore, we must not expect to improve upon the ACFs measured from mosaics with 10′ PSFs; any information in the ACF for $\theta < 10'$ will be accessible only by modeling the ACF due to the PSF[3].

2.5.2. The PSF

How much do unremoved point sources contribute to the ACF for θ near the size of the maximum PSF diameter? Figure 10.3 shows the summed ACFs compared to the ACF of the maximum PSF. The ACF of the maximum PSF has been scaled to match the measured ACF

---

are also a few abnormally low patches, as there are in several other mosaics. Masking out these regions in the next iteration may lead to improvement, but such is not likely.

[3] It is for this reason that we have not been more careful in the summation of the 5′ ACFs

TABLE 10.2

MAXIMUM NUMBER OF PIXEL PAIRS

mosaic	R1L2			R45		
	10′	5′	2′	10′	5′	2′
	number of pixel pairs/10^6					
035+78	16.23	4.56	0.31	12.81	4.00	0.34
086+74	19.02	7.86	0.51	19.23	8.36	0.64
138+52	26.34	7.78	0.17	23.18	7.01	0.17
161+51	47.23	14.16	0.25	44.18	13.21	0.31
171+50	49.22	25.98	8.63	33.30	22.14	8.10
220+84	42.08	14.22	0.38	37.64	13.40	0.53
295-89	15.37	4.23	0.05	11.81	3.33	0.06

at the PSF diameter, thus demonstrating the *maximum* contribution that the PSF could have. The extent of the bulk of the ACF is similar to the 90% encircled energy diameter, but it is clear that the ACF of the PSF constains non-negligible signal to much larger scales.

In band R1L2, there is clearly signal above that expected from the PSF on scales $10' < \theta < 25'$, and the ACF made from the 5′ image suggests that the excess may extend to $\theta = 5'$. The situation in band R45 is more equivocal; the 10′ PSF image suggests an excess for $10' < \theta < 25'$, which is supported to nearly the same certainty by the 5′ PSF image. However, the excess signal in band R45 is quite small, comparable to the size of the uncertainty.

Comparison of the measured ACF with the ACF of the PSF is valid to the following extent: the brightest remaining point sources will be in the portion of the mosaic with the worst point source detection limit, which is the region with the largest PSF. Thus, one expects the portion of the ACF due to unremoved point sources to be dominated by objects whose profiles are well described by the maximum PSF. This simple description is somewhat modified by the fact that the number of sources drops sharply as the flux is increased, so the flux (and PSF size) of the sources that dominate the ACF will be the result of a competition between the reduction of the PSF size (and the subsequent reduction of both the point source detection limit and the area over which the point sources could be detected), and the increase in the number of sources per unit solid angle at the point source detection limit. The result of this competition is shown roughly in Figure 10.4, where one can see that the flux contributed by the unremoved point sources is nearly constant with PSF size. Thus, the wings will be due to the largest PSF, but the remainder to the PSF ACF will be much more sharply peaked. Our scaling of the maximum PSF is thus likely to overestimate the contribution from the PSF ACF.

The strongest point sources could be correlated to some extent, as they will be confined to the regions of the image with the worst PSF, and not scattered randomly across the mosaic. For typical point source detection limits, 0.01-0.03 counts s^{-1}, the point source population is dominated by the extragalactic point sources. If we take the "worst PSF" region to be a 10′ wide annulus, then we expect ~ 0.5-5 point sources per pointing[4]. However, since pointings overlap, some fraction of that annulus will have a

---

[4] We have calculated the number of sources as the number of unremoved sources in the 43′-53′ annulus that would have been removed given the PSDL at 43′. This is a crude measure of the "bright" sources in the annulus. We find the following numbers for a single pointing of a given exposure:

Exposure	R1L2		R45	
(s)	PSDL (cts/s)	Number	PSDL (cts/s)	Number
1000	0.017	0.573	0.044	0.964
2000	0.007	1.57	0.017	2.94
10000	0.005	2.59	0.013	8.90

These results suggest that many mosaics will not have correlated sources due to this effect because the mosaic coverage is dominated by low exposure pointings. Most of the mosaics that have a large number of deep (10ks) exposures also have a large amount of overlap (035+78,086+75,161+51), which will reduce the correlation. A possible exception is 295-89.

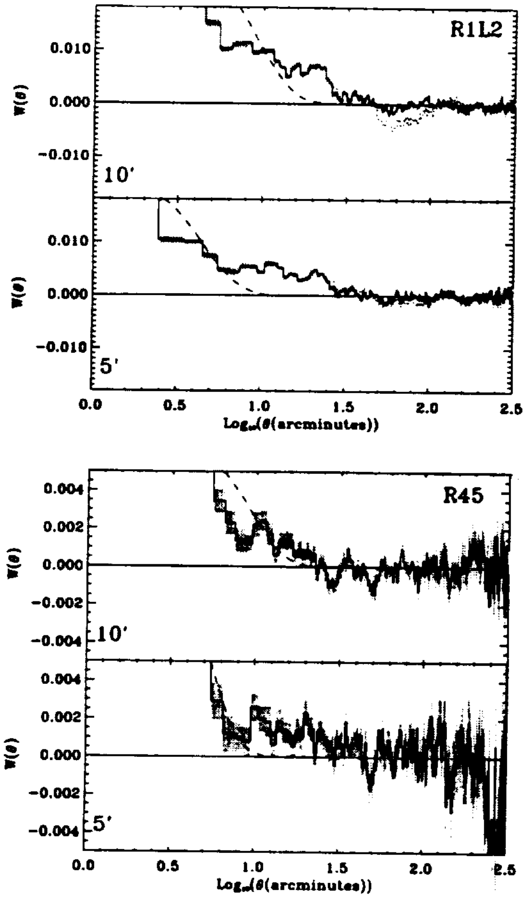

Fig. 10.3.— Mean ACF for high-pass-filtered mosaics. The solid line is the ACF. The shaded region is the uncertainty. The ACF of the maximal PSF is shown as a dashed line. For band R1L2, the addition of the 086+74 mosaic is shown by a dotted line. Note that the high-pass filtering should remove fluctuations above $\log\theta = 2.08$.

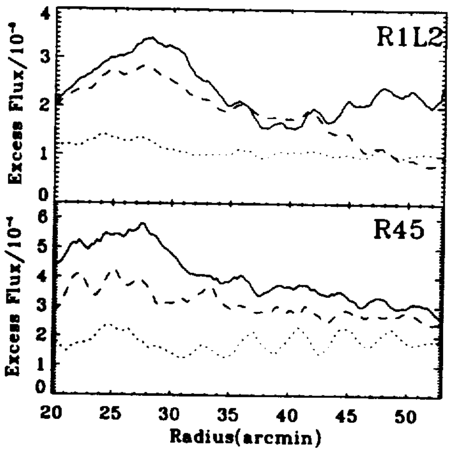

Fig. 10.4.— The unremoved point sources that dominate the ACF: the plotted quantity is the flux of the point sources just below the detection limit; the number of excess sources in an annulus of width 1′ multiplied by the point source detection limit at the radius of that annulus. The number of excess sources is the number of unremoved "bright" sources in an annulus; the number of unremoved sources that would have been removed had the PSDL been that of an annulus whose radius is smaller by 10′. *Solid:* 10 ks exposure, *Dashed:* 5 ks exposure, *Dotted:* 1 ks exposure.

substantially better point source detection limit; the number of unremoved point sources in the region of the worst PSF will be correspondingly decreased to less than ~ 1 per pointing. Therefore, one should not expect correlation from the brightest point sources, but from the fainter point sources with the better PSFs.

The contribution of unremoved point sources to the ACF can be calculated more carefully, but only at great expense. The ACF of unremoved, individual point sources would be the ACF of a complexely weighted sum of all the PSFs in a given mosaic[5]. To address the issue of correlation produced by the variable point source detection limit, one should measure the ACF from simulated mosaics rather than an equivalent model PSF.

It should be further noted that for point sources on a constant background, $W(\theta) < 0$ for large θ. The negative excursions in the measured ACFs may be somewhat removed by more proper modeling of the PSF, increasing the amplitude measured fluctuations in the $10' < \theta < 30'$ range.

3. $\delta I/I$ - A Statistical Method

This method begins with the seemingly simple question; "Could the observed fluctuations be caused by the variation due merely to counting statistics and the unremoved point sources?" For pixels of a given size, one compares their distribution about the mean with that expected from a "flat" background; excess variation may imply fluctuation by the background on the scale of the pixel size. A small note on language: by fluctuation at scale ϕ we mean that the background has intrinsic fluctuations on scale ϕ. Conversely, "lack of fluctuation" on scale ϕ does not mean that the excess variance in $\phi \times \phi$ sized pixels is zero, but that the variance is produced by fluctuations whose intrinsic scale is not ϕ.

The $\delta I/I$ measure is defined as

$$\left(\frac{\delta I}{I}\right)^2 = \frac{\langle (I - \langle I \rangle)^2 \rangle}{\langle I \rangle^2}. \tag{10.15}$$

This quantity is calculated over a range of pixel sizes, $\phi \times \phi$, from the smallest possible to the largest for which reasonable statistics are possible. The smallest pixel size computationally possible for our mosaics we will call the "native" pixel size, and is either $1'$ or $1\overset{'}{.}5$.

3.1. Relation to $w(\theta)$

Using the formalism of Peebles (1993), one can show that this quantity is equivalent to

$$\frac{1}{\langle I \rangle} + \frac{1}{\Omega^2}\left[\int d\Omega_i d\Omega_{i'} w(\phi_{ii'})\right] \tag{10.16}$$

where the integral is over scales smaller than the sizes of the pixels whose variance is being calculated. This is not a particularly interesting formulation but is included here for completeness.

3.2. Algorithm

There are complications in the application of this calculation to mosaicked data; the expected variance in the value of a pixel is spatially variable.

3.2.1. Counting Statistics

The vignetting due to the telescope optics reduces the number of counts with distance from the optical axis, (as well as severely reducing the counts over a limited area due to the window support structure). Thus, the amount of variation due to counting statistics will change from the center of the pointing to the edge. We have used as the variance due to counting statistics the number of counts in a mosaic pixel, and have applied standard propagation of errors through

---

[5] If i is a given pixel, and j is the index of the different pointings (observations) that contribute to the mosaic image at pixel i, then the image whose ACF we seek is

$$\sum_i \sum_j PSF_{i,j} \int_{?}^{PSDL_i} sN(s)ds$$

where PSF is the image of the PSF at that sky location for each pointing, and $PSDL_i$ is the point source detection limit at that pixel (the best of the $PSDL_{i,j}$.), and $N(s)$ is the number of point sources of flux s expected per pixel. The lower limit of the integration is a vexed issue. One certainly would not want to extend the integral to 0, as the very faint sources will be so numerous as to provide a uniform background when measured over individual pixels. Setting the limit to $PSDL_I$ will miss the contribution by sources slightly fainter than $PSDL_i$, that are also slightly more numerous. Perhaps one should set this limit to the source flux for which there is one source per pixel.

TABLE 10.3
SUMMARY

mosaic	θ_{max}[a]		Weight		ϕ_{max}[b]	
	R1L2	R45	R1L2	R45	R1L2	R45
	arcmin				arcmin	
035+78	160	160	25.27	22.07	64	60
086+74	250	250	40.35	39.01	61	53
138+52	355	320	9.09	8.03	109	106
161+51	250	160	13.09	11.92	85	85
171+50	200	100	12.20	10.54	68	68
220+84	320	250	9.82	8.43	126	117
295−89	100	100	22.42	18.81	61	59

[a] The largest scale probed by the ACF.

[b] The largest scale probed by the $\delta I/I$ measure.

the deabsorption process. As, in most mosaics, there are a large number of $1'^2$ pixels that do not contain counts, thus the value of the variance must be used carefully[6]. Binning by a few (where "a few" < 10 for images with 10′ PSFs) removes this problem. As we will shortly see, this binning is not wholly responsible for losing information on scales smaller than the PSF size.

Note that the variance due to counting statistics does not include the uncertainties due to the background subtraction. These will be addressed later.

3.2.2. Point Source Contributions

Due to the change of the size of the PSF with distance from the optical axis, the point source detection limit changes with distance from the optical axis, and thus the contribution of unresolved point sources will also change. One generally assumes the point sources to be uncorrelated, (though it is well known that extragalactic X-ray sources will be correlated) and so the number of sources of a given flux in a given pixel is given by counting statistics; the variance in the number of point sources is the mean number of point sources. If the number of sources in a unit area in the flux interval $S, S+\Delta S$, is given by $n(S)$, and if the minimum detectable point source flux is S_d, then the contribution to the flux in a given pixel is

$$c_{PS} = \Omega \int_{S_m}^{S_d} S n(S) dS \qquad (10.17)$$

and the variance in that flux is

$$\sigma^2_{PS} = \Omega \int_{S_m}^{S_d} S^2 n(S) dS \qquad (10.18)$$

where Ω is the area of the pixel. The value S_m is either the flux of the faintest source, or flux of sources that are so numerous as not to contribute significantly to the variance.

The point sources that contribute to fluctuations of the soft X-ray background are either Galactic (mostly young main sequence stars), or cosmic, typically AGN. The form of the $n(S)$ relations to be used for Galactic point sources is discussed in Chapter 7. For the $n(S)$ relation of the extragalactic sources we use that of Hasinger et al. (1998),

$$\begin{aligned} n(S) &= n_0 s^{-\beta_0} \quad \text{for} \quad s > 18 \\ n(S) &= n_1 s^{-\beta_1} \quad \text{for} \quad 18 > s > 2.66 \\ n(S) &= n_2 s^{-\beta_2} \quad \text{for} \quad 2.66 > s \qquad (10.19) \end{aligned}$$

---

[6] One might think to alleviate this problem in the following manner. The expected variance for a pixel due to counting statistics is the expected number of counts in that pixel, which is given by Equation 10.9, where $\mathcal{R}_{(i,j)}$ is given by

$$\overline{\mathcal{R}}_{LHB} + \overline{\mathcal{R}}_{TAE} e^{-\tau_{TAE}} + \overline{\mathcal{R}}_{EPL} e^{-\tau_{EPL}}.$$

One could then propagate this expression through the deabsorption process to determine the uncertainty of every pixel. However, as this expression ignores the structure in the field, so the measure of the variance will be systematically wrong.

where s is in units of 10^{-14} erg cm^{-2} s^{-1} in the 0.5-2.0 keV band[7], and

$$\begin{aligned} n_0 &= 111.0 & \beta_0 &= 1.94 \\ n_1 &= 238.1 & \beta_1 &= 2.72 \\ n_2 &= 91.0 & \beta_2 &= 2.3 \end{aligned} \tag{10.20}$$

where n_n is in units of degree^{-2}. These values are quite similar to that determined by Mushotzky et al. (2000) for the 0.5-2.0 keV band.

Note that these calculations do not include the effect of the PSF. If the pixel size is smaller than the PSF, then the PSF spreads the flux due to unresolved point sources over several of the surrounding pixels, and effectively decreases the variance due to point sources. Therefore, one should not attempt to apply the $\delta I/I$ measure to scales smaller than the PSF.

3.2.3. The relative contribution

The contribution to the variance by both the counting statistics and the unremoved point sources are exposure dependent. The contribution by unremoved point sources is typically comparable to, to ~ 3 times smaller than, that of counting statistics. Of the contribution by unremoved point sources, less than about a third is due to Galactic sources.

3.2.4. The distribution of values within a single pixel

If σ_B^2 is the variance of the distribution of "true" background sky values, σ_{CS}^2 is the variance due to the counting statistics, and σ_{PS}^2 is the variance due to unremoved point sources, then, since the three quantities are independent, the variance of the measured value in a given pixel will be the sum of the variances. Therefore, the distribution from which the measured value is drawn has a variance

$$\sigma_M^2 = \sigma_{CS}^2 + \sigma_{PS}^2 + \sigma_B^2. \tag{10.21}$$

The σ_M is measured from the mosaics, the σ_{CS} can also be estimated from the mosaics, and the σ_{PS} can be calculated from the point source models. The desired quantity is the σ_B, which is sometimes referred to as the *excess* variance as it is in excess of that expected from counting statistics and the point source models.

For convenience (computational and otherwise) we will take σ_B^2 to be the variance in counts s^{-1} within a pixel of size $\phi \times \phi$. The δI used in Equation 10.15 will thus be σ_B/ϕ^2.

3.2.5. The variance of a collection of pixels

Although every pixel is drawn from a different distribution one must combine them in some way to calculate the background fluctuations. The procedure for combining the pixels is simple; calculate the χ^2 statistic for pixels that have been binned $\phi \times \phi$,

$$\chi^2(\phi) = \frac{1}{\nu} \sum_{(i,j)} \frac{(C - \langle C \rangle)^2}{\sigma_{CS}^2 + \sigma_{PS}^2 + n\sigma_b^2} \tag{10.22}$$

where ν is the number of ϕ^2 sized pixels in the sum and C is the count rate within the pixel (in units of counts s^{-1}). If n is the number of native pixels in a $\phi \times \phi$ sized region, $n\sigma_b^2 = \sigma_B^2$. If the expected variances of the individual pixels was under(over)estimated, then χ^2 statistic for the ensemble of all the pixels will be greater(less) than one. This same operation can be thought of as normalizing all of the distributions from which individual pixels are drawn to have a variance of one). One may thus determine the excess variance (σ_B) by iteration.

We have departed from standard practice in calculating the quantity σ_b rather than σ_B, though it is easy enough to determine one from the other. If n is the number of pixels in a given ϕ^2 sized pixel that are non-zero, then we can include binned pixels that are not "completely filled" into the calculation, with an apropriate weighting. This practice improves one's statistics at all ϕ. As we will see, the quantity σ_b can be more useful than σ_B.

3.3. Uncertainty

The value of χ^2 will, naturally enough, have the properties of the "χ^2 distribution", which is

---

[7] These are the values presented by Hasinger et al. (1998). If one has reason to apply these equations (or is obsessive about checking them) one will notice that given the normalizations in the following lines, the equations produce a discontinuity in $n(s)$ at $s = 18$. The value for the split between β_0 and β_1 should probably be 9.87, not 18.

a well-behaved, though asymmetric, probability distribution. We have defined the uncertainty interval in χ^2 so that

$$\int_{-\sigma}^{\mu} P(\chi^2)d\chi^2 = \int_{\mu}^{+\sigma} P(\chi^2)d\chi^2 = .3415 \quad (10.23)$$

that is, the interval contains the same integrated probability as the standard 1σ interval and is centered on the mean. For $\nu < 20$ this interval is asymmetric due to a large difference between the mean and the mode. The uncertainty in σ_b is just the range of values of σ_b that fulfills this condition.

3.4. Data Preparation

The same data preparation used for the ACFs were used for this calculation.

3.5. Application

Figure 10.5 shows $(\sigma_B(\phi)/I)^2$ for a typical mosaic. This plot is not too satisfactory. If the excess fluctuations were due *only* to uncorrelated fluctuations at or smaller than the native pixel scale, then $\sigma_B(\phi) \propto \phi^{-2}$; very nearly the observed behavior. One is really interested in the deviations from the $1/\phi^2$ behavior. For this reason we find it more useful to consider $\sigma_b(\phi)/I$. The quantity σ_b^2 is the excess variance at the native pixel scale required to produce the observed excess variance at the scale of ϕ . This quantity has the useful property that if there were no fluctuations on scales greater than that of the native pixel, σ_b would be constant. If, on the other hand, the dominate fluctuation scale were Φ, then, roughly, $\sigma_b(\phi) \propto (\phi/\Phi)^2$ for $\phi < \Phi$. Figure 10.5 also shows $(\sigma_b(\phi)/I)^2$ for the same mosaic; the effect of the large-scale fluctuations become immediately apparent. For this mosaic there appear to be fluctuations with $\phi \sim 30'$ as σ_b is constant (to within the uncertainties) for greater ϕ.

Note that we display the quantity $(\sigma_b(\phi)/I)^2$ rather than $\sigma_b(\phi)/I$. If one overestimates the contribution to the variance due to counting statistics or unremoved point sources, then the quantity $(\sigma_b(\phi)/I)^2$ will be less than zero. In order to handle this possibility in the most graceful manner, we do not take the root.

Figure 10.6 shows $(\sigma(\phi)/I)^2$ for a typical mosaic (161+51). Here, as with all the plots of $(\sigma_b(\phi)/I)^2$ given in Appendix H, the value of σ_b has been normalized to a native pixel size of $1' \times 1'$. The quantity I is the mean flux in counts s^{-1} arcmin^{-2}. The upper limit on ϕ is set by the imposed requirement that the number of $\phi \times \phi$ pixels be greater than ten.

The generally good agreement between $\sigma_b(\phi)$ for images where the maximum PSF size was 10′ and for images where the maximum PSF size was 5′ suggests that the characterization of the change in the variance as a function of exposure must be reasonably correct, as the 10′ PSF images (exclusion radius, 53′) sample regions with much larger variance than the 5′ PSF images (exclusion radius, 32′). There are, of course exceptions. For mosaic 171+50 in band R1L2, the reason would appear to be that the 5′ PSF image excludes some regions with poor deabsorption. The discrepancy for mosaic 138+52 in band R45 is nearly within the uncertainties, but its source is unknown.

3.5.1. The Effect of Offsets

In the mosaicking process, each individual pointing is corrected for the non-cosmic background to the flux level of the *RASS* by a uniform offset, $\mathcal{O}_i$. We have not included this uncertainty in the formulation of $\delta I/I$ because the bulk of the uncertainty in the background does not enter as a pixel-to-pixel variation, but rather as an offset[8]. Of course, using a mosaic of pointings means that the offsets will be different for different regions of the mosaic.

We could derive formal uncertainties for the offsets of each of the pointings from the RASS, and thus derive a formal uncertainty for the rel-

---

[8] The lack of pixel-to-pixel variation may not be clear given the treatment in Chapter 2, where we stated that the uncertainty in the exposure mask (from which the non-cosmic background is modeled) is on the order of 10%. Due to the "dither", each 14.″957 x 14.″957 pixel in a single PSPC pointing samples ~ 200 adjacent pixels in the exposure mask. Thus, the difference between to adjacent pixels in a single PSPC pointing will be small because they will have sampled nearly the same set of pixels in the exposure mask. Thus the relative uncertainty for adjacent 14.″957 x 14.″957 pixels will be less than 1.5% Since these pixels are then summed into 1′ or 1.′5 pixels, which are then summed with pixels from other pointings, the relative uncertainty is very small compared to the other variations.

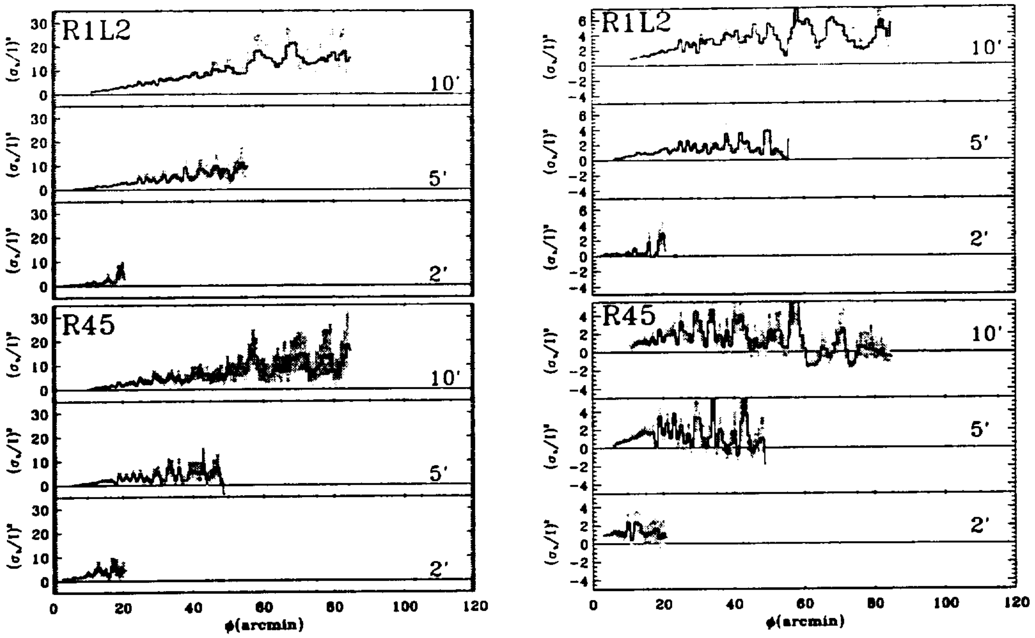

Fig. 10.6.— The $\delta I/I$ measure of a typical mosaic (161+51). The solid line is $\sigma_b(\phi)/I$, the shaded region is the uncertainty. The value of $\sigma_b(\phi)/I$ is shown for mosaics where the maximum radius for each pointing has been chosen to produce maximal PSFs of 10′, 5′, and 2′. *Left:* $\sigma_b(\phi)/I$ for the images. *Right:* $\sigma_b(\phi)/I$ for the high-pass filtered images. Note the changes of scales.

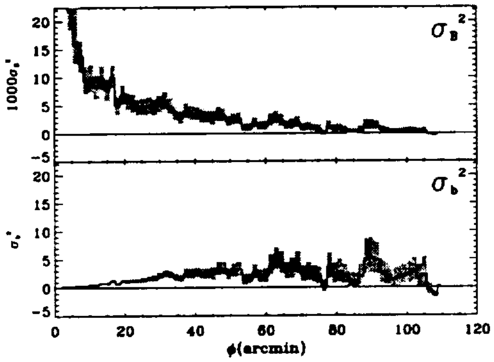

Fig. 10.5.— Comparison of the σ_B and σ_b measures. *Top:* σ_B. *Bottom:* σ_b.

ative offsets of any pair of pointings. Since a large fraction of the uncertainty in the offset of a given pointing is due to the uncertainty in the *RASS* flux, such an error will be a gross overestimate of the true uncertainty of the relative offsets.

We can not determine the $\sigma_b(\phi)$ contributed by the errors in the offsets, but we can determine the behavior σ_b would have as a function of ϕ if the error in the offsets were the sole source of excess fluctuations.

If each pointing in a mosaic has an offset $\mathcal{O}_i$ and an offset uncertainty ς_i, we can create simulations of offset errors. For each pointing we draw a normally distributed random number with a mean of zero and a variance of unity, and multiply that random number by ς_i to get the error in the offset, $\Delta\mathcal{O}_i$. We create an mosaic of the offset errors; the distribution of counts in the mosaic due to the erroneous offsets are modeled in the same way as the original offsets. The value of $\sigma_b(\phi)$ can then be calculated for each simulated mosaic.

Figure 10.7 shows the results for a few trials for a typical mosaic. The quantity $\sigma_B(\phi)$ is

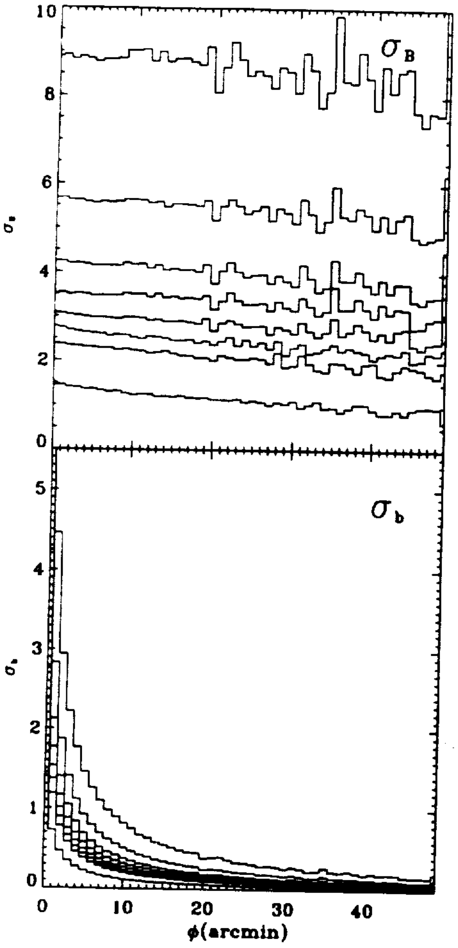

Fig. 10.7.— The effect of offset errors on *top:* $\sigma_B(\phi)$ and *bottom:* $\sigma_b(\phi)$. Plotted are the values of $\sigma_B(\phi)$ and $\sigma_b(\phi)$ for a few simulations of the offset errors in a typical mosaic (086+74).

nearly linear, and the slope is proportional to the overall amplitude of the excess fluctuations. Thus, $\sigma_b(\phi)$ is nearly proportional to $1/\phi$. This is not the behavior of the excess fluctuations in the real mosaics, so the contribution of the offset errors to the excess fluctuations must be small.

3.5.2. Interpretive Difficulties

As with the ACF, there is a difficulty due to "scale-mixing". As was noted in the discussion of $\sigma_B vs. \sigma_b$, the measure of $\sigma_b^2(\Phi)$ is not so much a measure of the excess fluctuations at Φ, but is a measure of excess fluctuations at $\phi \leq \Phi$ (for which $\sigma_b(\Phi) \sim sigma_b(\phi)$) and $\phi \geq \Phi$i (for which $\sigma_b(\Phi) \propto (\Phi/\phi)\sigma_b(\phi)$); it is the shape of the function that tells one at which scales fluctuations exist. As with the ACF, one might expect to understand better the excess fluctuations at $\phi << \Phi$ by high-pass filtering the images with a threshold at Φ. Figure 10.6 contains results for a typical mosaic.

High-pass filtering an image removes all fluctuations at scales greater than the threshold, and decreases the amplitude of the fluctuations at all smaller scales. The variance measured at some scale ϕ is the linear sum of the intrinsic variances at all scales. The variance at some scale of a high-pass-filtered image is the linear sum of the intrinsic variances, each multiplied by a "suppression factor", $[1-(\phi_F/\phi_S)^2]$ (see Appendix I), where ϕ_F is the scale of the fluctuation (not the scale upon which one is measuring) and ϕ_S is the smoothing scale. Since the smoothing scale is 121′, the change in σ_B^2 (and thus σ_b^2) from the image to the high-pass-filtered image (as expressed as a multiplier) should be 0.99993 for fluctuations on the scale of 1′ (i.e., not much), and 0.75 for fluctuations on the scale of 60′. When calculating the excess fluctuation at scale ϕ, one must reduce the variance expected from counting statistics and unremoved point sources, but in this case the scale of the fluctuations is the pixel scale. *We have also multiplied the calculated $\sigma_b^2(\phi)$ by the inverse of the suppression factor before plotting.*

The fact that the $\sigma_b^2(\phi)$ relation in the high-pass-filtered images seems to level off (where it did not in the unfiltered images) would suggest we have isolated the scales of fluctuation. A brief perusal of the figures in Appendix H shows a variety of behaviors for the mosaics in a given band; some level off before reaching the largest measured scale, and some continue to rise.

3.5.3. Averaging

Due to the variety of behaviors, it is difficult to coadd the $(\sigma_b(\phi)/I)^2$ relations in a reasonable manner. We have averaged the relations over those scales which are covered by all mosaics (1′-60′). For band R1L2, the largest-scale fluctuations appear to have $\phi \sim$ 35′-45′, while for band R45, the largest-scale fluctuations appear to have $\phi \sim$ 25′-35′, though there is a great deal of variation from mosaic to mosaic.

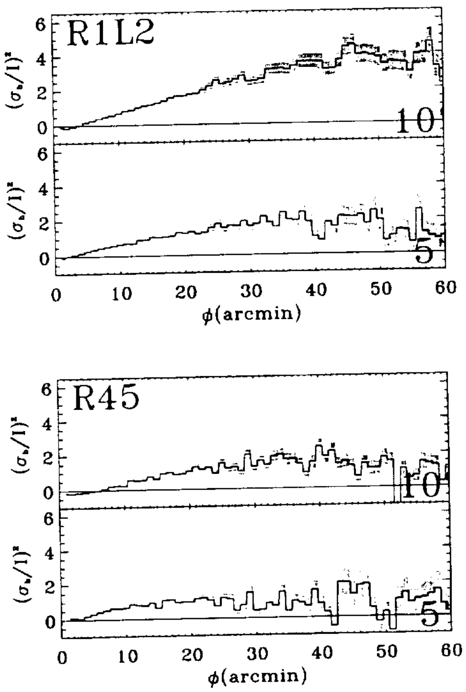

Fig. 10.8.— Mean $(\sigma_b(\phi)/I)^2$ for high-pass-filtered mosaics. The shaded region is the uncertainty.

3.5.4. $\delta I/I$ Summary

The $\sigma_b^2(\phi)$ relations in band R1L2 (for unfiltered images) shows that most mosaics have fluctuations on scales up to the size of the mosaics. Although the same is true for some mosaics in band R45, several mosaics (086+74, 220+84, and 295-89) appear to show minimal fluctuations on scales greater than $\sim 30'$. The large differences in behavior between mosaics for this measure of fluctuations suggests that the similarity seen in the ACFs may be misleading.

4. Results

4.1. Some Considerations

4.1.1. The LHB

It is important to know which component of the SXRB is producing the fluctuations, whether it be the LHB, the Galactic halo, or some extragalactic component. In principle, one can measure the fluctuations due to the LHB; observe a region with a substantial path-length through the LHB (almost any direction) for which there is a sufficient column density of material just outside the LHB to remove the contribution due to other components (not so many directions). This is technically possible in the R1L2 band as $e^{-\tau} = 0.1$ at 3.4×10^{20} cm^{-2}, but is difficult (impossible?) in the R45 band where $e^{-\tau} = 0.1$ at 5.0×10^{21} cm^{-2}.

We have performed an ACF on the R1L2 band image of a mosaic at $(\ell, b) = (45°, 0°)$ with $(\delta\ell, \delta b) = (106', 960')$. In this direction the LHB wall is $\sim$ 107 pc away (assuming that all of the R1L2 flux in the Galactic plane is due to the LHB, and assuming $n_e = 0.005$ cm^{-3}). From the absorption line study of Sfeir et al. (1999), the Na I equivalent width ($W_\lambda(D2)$) due to absorption by the ISM is very small for stars with distances less than 115 pc. At greater distances the equivalent width rises to 80 mÅ; an equivalent width of 50 mÅ corresponds to $N_H = 10^{20}$, or $e^{-\tau} \sim .3$. Thus, at distances slightly greater than that expected for the LHB wall, the ISM becomes optically thick to band R1L2 photons.

The ACF and the high-pass-filtered band R1L2 image is shown in Figure 10.9. There is very little structure on scales larger than 10′. There is also very little structure for $3' < \theta < 10'$ as there will not be many point sources within the LHB. (This will not be true in all directions, consider, for example, the direction of the Hyades.) Thus, the LHB is unlikely to contribute to fluctuations on scales $10' < \theta < 120'$.

4.1.2. The Halo

The contributions due to the halo can only be surmised from what little we know about the Galactic halo. It is still not known whether the X-ray emission in the Galactic halo is due to gas in equilibrium (i.e., virialized in the Galactic potential) or whether it is some non-equilibrium quasi-steady state, such as a cooling flow. Chapter 6 suggests that both may be true, as there is more than one component to the hot Galactic halo. A number of mechanisms have been suggested for heating halo gas, either *in situ* through supernovae or magnetic reconnection, or heating the gas in the disk and ejecting it into the halo through galactic chimneys.

Simulations of supernovae in the Galactic halo by Shelton (1999) show that a SNR at

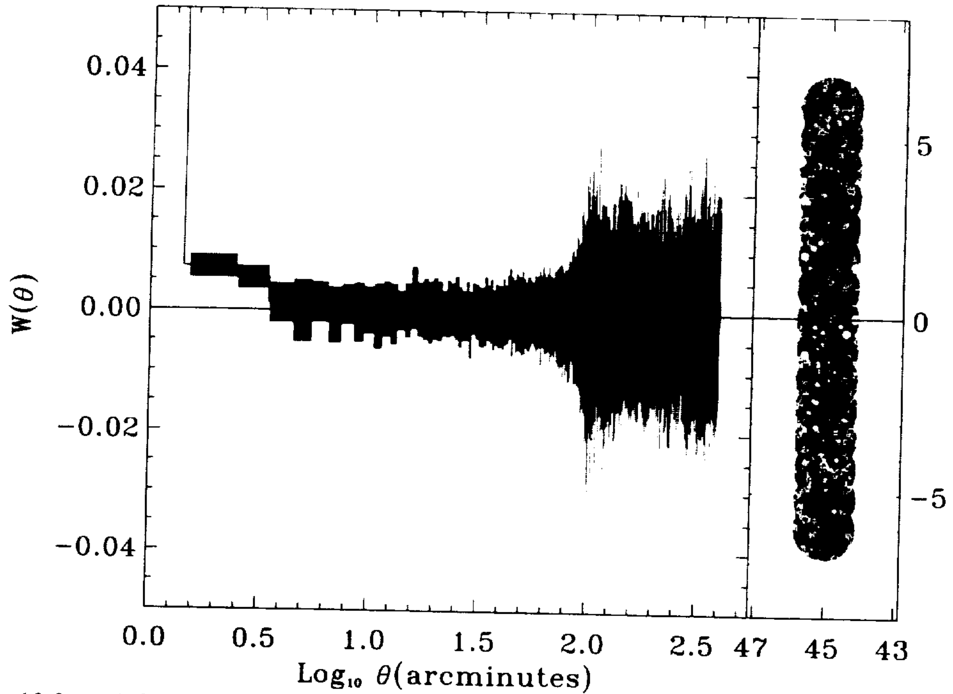

Fig. 10.9.— A band R1L2 ACF for the LHB. *Left:* The ACF for a band R1L2 image towards $(\ell, b) = (45°, 0°)$. The shaded region is the uncertainty. *Right:* The high-pass filtered image of the mosaic.

z = 1 kpc grows to diameter of ∼ 6°. A SNR at z = 0.3 kpc, while not expanding to the same physical dimension due to the higher ambient density, will have a diameter of ∼ 10°. A substantial portion (∼ 400 × 10^{-6} counts s^{-1} arcmin^{-2}) of the R12 band flux from the Galactic halo could be accounted for by overlapping halo SNR, but the flux in band R45 is expected to be almost two orders of magnitude smaller.

Heating by magnetic reconnection, the microflare model of Raymond (1992) for example, is perennially mentioned in this context, likely exists but little work has been done to extend these models to the point where appropriate scales can be determined, perhaps because the physical conditions of the halo are so poorly known.

It has been suggested on the basis of observational evidence that the effluvia from Galactic chimneys is patchy on the scale of several degrees, but at smaller scales, one must resort to physical reasoning. A 10′ radius fluctuation at z = 2 kpc in the halo has a radius of ∼ 6 pc. Consider first an isothermal fluctuation. Assuming a gas temperature of 10^6K, the sound crossing time will be ∼ 3.5 × 10^4 years, implying that fluctuations in the emission due to fluctuations in the density of the emitting plasma, will be short lived.

Consider also an isobaric fluctuation. The emissivity per volume, $\Lambda \propto T^{\alpha}\rho^{2}$, under the condition of pressure equilibrium, will be proportional to $T^{\alpha-2}$. For the Gehrels & Williams (1993) cooling curve, $\alpha \sim 0.2$ for $5.89 < \log T < 6.14$ and $\alpha \sim 0.3$ for $6.65 < \log T < 6.88$; between those regions $\alpha < 0$. Thus, for the range of X-ray emitting plasma temperatures observed ($6.06 < \log T < 6.46$), one must depress the temperature to increase the emissivity (so bright spots will be cooler than the surrounding medium). Such fluctuations, however, are removed by the high conductivity of the surrounding plasma (Field 1965).

Thus, while the contribution of the halo to fluctuations smaller than a few degrees is not known *per se*, and could profit from further work, it seems likely that the halo is not contributing fluctuations on the < 30′ scale. *Thus, once the contamination due to residual point sources is removed, the remaining fluctuations should be due solely to the diffuse extragalactic emission.*

4.2. Comparison with Previous Results

Compared to the extensive literature on ACFs at $E > 2$ keV, the literature below 2 keV is quite restrained. The difficulties due to Galactic absorption have been well appreciated and that, together with a host of other issues (the smaller number of counts due to the extragalactic background, the increasing contribution by the Galactic halo and the LHB, lack of information about the point source spectra below 0.5 keV, ghost images in band R1L2), have impeded efforts. Studies have typically concentrated either on small scales, where the ACF can be derived from a large number of individual deep exposures, or on very large scales, where the *RASS* can be used at energies not effected by Galactic absorption or contamination ($E > 1$ keV). A summary of pertinent ACFs is given in Table 10.4. The remainder of this section will be concerned with the band R45 ACF as there is no comparison to be made for the band R1L2 ACF.

Soltan et al. (1996) calculated the ACF for $\theta < 40°$ from the R5 and R6 band *RASS*. They showed that although the band R6 ACF decreased rapidly from $\theta = 0°$ to $\theta = 5°$and was constant and smaller than the uncertainty at larger scales, the band R5 ACF declined more slowly, to 0.002 at 10°, and was well described by the linear function $W(\theta) = 0.003 - 0.00014\theta$ at larger scales. The band R5 ACF was clearly contaminated by Galactic emission at many scales.

At much smaller scales Soltan & Hasinger (1994), concentrating on the bands least affected by Galactic contamination, measured the ACF in band R67 from 46 deep (> 8 ks) PSPC pointings. They detected a signal at $\theta < 3'$, but at larger θ the signal was much smaller than their small uncertainty. The detected signal was attributed to clusters of galaxies (further discussed in Soltan et al. 1996), and the lack of signal at $\theta > 3'$ was used to place strong constraints on the degree to which X-ray sources could be clustered in the manner of QSOs.

Chen et al. (1994) measured the ACF in the R47 band using a single deep (~ 70 ks) PSPC pointing and a mosaic of six not-so-deep (13~20 ks) pointings. Their ACF is noise limited on all scales (2'-300'), and their tightest constraints were reached by fitting $\alpha(\theta/\theta_0)^{-\gamma}$ to the 2σ upper limits of the data. They again found a very small value of $W(\theta)$ with which to constrain clustering.

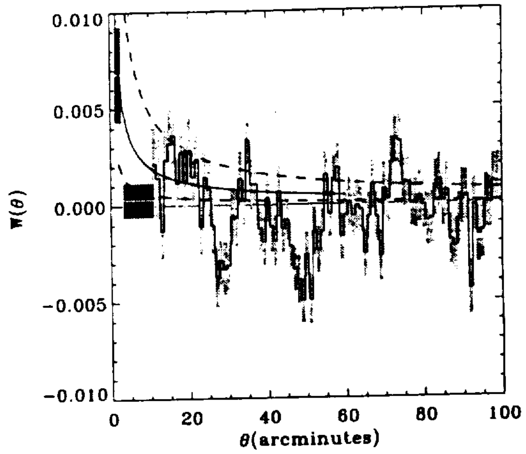

Fig. 10.10.— Comparison of ACFs. The histogrammed data with lightly shaded error bars is the ACF for band R45 after the removal of the maximum contribution from the PSF, scaled as if the fluctuations were due solely to the extragalactic component of the SXRB. (The PSF makes no visible contribution for $\theta > 20'$.) The dark boxes are the ACF calculated by Soltan & Hasinger (1994) for band R67. The lower dashed line is the fitted ACF in band R47 from Chen et al. (1994). The upper dashed line is the same ACF for band R45 *if* all of the fluctuations in band R47 were due to fluctuations in band R45. The thin solid line is the ACF in band R45 using the model of Vikhlinin & Forman (1995).

Direct comparison of our data with these previous measures (Figure 10.10) is initially disheartening. However, it should be realized, first, that the Chen et al. (1994) and Soltan & Hasinger (1994) ACFs have been very carefully cleaned of spurious signals by extensive PSF modeling. Second, by restricting ourselves to the R45 band, we have about half the counts available in the R47 band. For this we have compensated by increasing the area over which the ACF is measured. Third, by measuring the ACF in band R47, Chen et al. (1994) diluted the effects of Galactic contamination that we must possess in full measure.

In Figure 10.10 we show our band R45 ACF after the removal of the maximal PSF contribution under the assumptions that the fluctuations arise solely in the extragalactic background i (i.e., the Galactic halo is assumed to be smooth over the scales of interest). The upper dashed line is the ACF that would be expected if all of the fluctuations measured by (Chen et al. 1994) in the band R47 were due to fluctuations in the band R45; given the very small measure of the fluctuations in band R67 measured by Soltan & Hasinger (1994) (shown as the dark squares), such an assumption seems reasonable. If our removal of the maximal PSF is correct, then our measured ACF is consistent with the fitted value of the Chen et al. (1994) ACF, but it should be noted that the Chen et al. (1994) fitted ACF is a factor of ~ 7 smaller than the actual 2σ upper limits on the data (see their Figure 5b).

The thin solid line is an extrapolation of the the results of Vikhlinin & Forman (1995) to the band R45 ACF. Vikhlinin & Forman (1995) measured the ACF for point sources brighter than some limit. Since both their PSDL and ours was spatially variable, the comparison is difficult; we have taken our PSDL to be the mean PSDL for our mosaics, weighted by average exposure, and have taken for theirs the PSDL for which they have "significant coverage". We then assumed that their ACF characterized all the point sources that they measured but which were not removed in our mosaics, and that there was no other source of fluctuations.

5. Summary

We have measured fluctuations for seven mosaics in bands R1L2 and R45 by two methods; the ACF and the $\delta I/I$ measure. Due to the PSF, the ACF analysis mostly is limited to $\theta > 10'$, and $10' < \theta < 25'$ may still be contaminated by the PSF. Direct measurements of fluctuations arising in the LHB, and physical state of the Galactic halo argue strongly that the observed fluctuations are extragalactic.

For the mean ACF, there are clearly fluctuations in band R1L2 for $5' < \theta < 30'$, where $W(\theta) \sim 0.1$, while the signal is consistent with zero for $\theta > 30'$. In band R45 there may be fluctuations with scales $10' < \theta < 25'$, where $W(\theta) \sim 0.0025$, and those fluctuations are consistent with previous upper limits determined in the R47 band. The $\delta I/I$ measure of fluctuations is consistent with that produced by the ACF.

The $\delta I/I$ measure, which is in some ways a more direct measure of fluctuation, suggests that the mosaics have very different scales and amplitudes of fluctuations (even after fluctuations with scales $> 121'$ are removed), leading one to question the validity of studying the *mean* ACF.

We have shown that the band R1L2 fluctuations due to the LHB are small, and thus the fluctuations contributed by the LHB to the R45 band must be ever smaller. However, it should be noted that due to our choice of energy bands, our data are unabashedly sensitive to fluctuations in the Galactic halo. We do not understand what sources for those fluctuations would be, and physical considerations suggest that small-scale halo fluctuations will be quickly dissipated. Thus, with suitable improvements (such as modeling the ACF produced by unremoved point sources), and a more careful calculation of the halo fluctuations, we will be able to place more stringent limits on the *extragalactic* fluctuations.

REFERENCES

Chen, L.-W., Fabian, A. C., Warwick, R. S., Branduardi-Raymont, G., & Barber, C. R. 1994, MNRAS, 266, 846

Field, G. B. 1965, ApJ, 142, 531

Gehrels, N., & Williams, E. D. 1993, ApJ, 418, L25

Hasinger, G., Burg, R., Giacconi, R., Schmidt, M., Trümper, J., & Zamorani, G. 1998, A&A, 329, 482

Mushotzky, R. F., Cowie, L. L., Barger, A. J., & Arnaud, K. A. 2000, Nature, in press

Peebles, P. J. E. 1993, Principles of Physical Cosmology (Princeton University Press)

Raymond, J. C. 1992, ApJ, 384, 502

Sfeir, D., Lallement, R., Crifo, F., & Welsh, B. Y. 1999, A&A, submitted

Shelton, R. L. 1999, ApJ, 521, 217

Soltan, A., & Hasinger, G. 1994, A&A, 288, 77

Soltan, A. M., Hasinger, G., Egger, R., Snowden, S., & Trümper, J. 1996, A&A, 305, 17

Vikhlinin, A., & Forman, W. 1995, ApJ, 455, L109

TABLE 10.4
COMPARISON OF ACFS

Source[a]	Energy keV	PSDL[b]	N[c]	Γ	θ	$W(\theta)$
Cea94	0.4-2.4(R47)	0.5×10^{-14}	10.9	1.626	$2'$-$30'$	$3.1 \times 10^{-3}(\theta/1')^{-0.8}$[d]
	0.4-2.4(R47)	1.0×10^{-14}	11.9	1.626	$2'$-$300'$	$3.8 \times 10^{-3}(\theta/1')^{-0.8}$[d]
SH94	0.9-2.4(R67)	1.04×10^{-14}[e]	13.4	1.12	$1'$-$3'$	$(6.8 \pm 2.5) \times 10^{-3}$
					$3'$-$11'$	$(0.3 \pm 0.9) \times 10^{-3}$
VF95	0.6-2.0	4×10^{-15}[f]			$0'.5$-$10'$	$0.257(\theta/10')^{-0.8}$[g]
Sea96	0.56-1.21(R5)				2°-3°	3.8×10^{-3}
					10°-14°	1.6×10^{-3}
	0.73-1.56(R6)				2°-3°	1.4×10^{-3}
					10°-14°	5×10^{-5}
K2K	0.4-0.9(R45)	5.80×10^{-14}[h]	10.5	1.42	$10'$-$15'$	0.0031 ± 0.0008[i]
					$15'$-$20'$	0.0028 ± 0.0007
					$20'$-$25'$	0.0015 ± 0.0007
					$25'$-$100'$	-0.0006 ± 0.00014

[a] **Cea94:** Chen et al. (1994), **SH94:** Soltan & Hasinger (1994), **VF95:** Vikhlinin & Forman (1995), **Sea96:** Soltan et al. (1996), **K2K:** this work.

[b] The units are ergs $\mathrm{cm}^{-2}\ \mathrm{s}^{-1}$ in the 0.5-2.0 keV band.

[c] The units are keV $\mathrm{cm}^{-2}\ \mathrm{s}^{-1}\ \mathrm{sr}^{-1}\ \mathrm{keV}^{-1}$. Care must be taken as the different models of the EPL take into account varying contributions from resolved point sources.

[d] These relations are not those given by Chen et al. (1994). Their text states that $W(\theta) = \alpha\theta_{1'}^{-0.8}$ (where we presume the $\theta_{1'}$ implies $\theta/1'$) and that for the $2'$-$30'$ region $\alpha = (-4.86 \pm 3.98) \times 10^{-3}$, and that for the $2'$-$300'$ region $\alpha = (+0.50 \pm 1.68) \times 10^{-3}$. The values given here were derived from their Figure 5b. These are the 95% upper limits of the fits of the functional form shown to the data. The data themselves have 2σ upper limits that are a factor of ~ 7 higher than the 95% upper limits of the fits.

[e] As with the current study, the point source limit is variable. The quoted value is the mean PSDL at $5'$ off-axis; the study limited itself to the central $15'$ of each pointing.

[f] The value quoted is for the PSDL "for a significant region". The maximum PSDL in the best and worst pointings are 5×10^{-14} and 1.2×10^{-15} counts s^{-1}.

[g] The scaling factor was measured from their Figure 2 for the ACF corrected for amplification bias.

[h] The PSDL is variable, the value quoted is the mean over the mosaics, weighted by the mean exposure of the mosaics.

[i] The values are the mean for the given intervals; the quoted uncertainties are the uncertainty of the mean. The r.m.s. of the $25'$-$100'$ interval is 0.002.

Chapter 11: Promiscuous Observations

And a mouse is miracle enough to stagger sextillions of infidels.

-Walt Whitman, Leaves of Grass

Abstract

This chapter summarizes the results of the previous chapters in terms of an interest in the "missing baryons", and the warm-hot IGM (WHIM) that has been predicted to contain them. We review the current knowledge about the WHIM. The fluctuation analyses of Chapter 10 will be applicable after a theoretical prediction of the amplitude and scales of the ACF is made.

The spectral energy distribution analysis of Chapter 6 and Chapter 7 place constraints on the total contribution of the WHIM to the soft X-ray background. We determine the upper limit of the diffuse extragalactic emission to be $< 7.4 \pm 1.0$ keV cm^{-2} s^{-1} sr^{-1} keV^{-1} at energies less than ~ 0.6 keV, and some portion of this value is due to the Galactic halo. We also show that the normalization of the extragalactic power law ($\Gamma = 1.46$) is 9.5 ± 0.9 keV cm^{-2} s^{-1} sr^{-1} keV^{-1}.

1. Cosmological Considerations

1.1. The Status of the Problem

When Chapter 1 was written, a number of different groups had just finished their hydrocosmological simulations, and several of those simulations were available only as pictures on the web. It was clear that all of the simulations put the missing baryons into what has since come to be called the WHIM, the warm-hot intergalactic medium, and it was clear that those baryons were not related to large structures, but the dependencies upon the modelling codes and cosmologies were not clear. There was a clear need for the various groups to compare results to elucidate these dependencies. This synthesis has recently appeared (Davé et al. 2000), and the results, which are nearly independent of the modelling code, can be summarized as follows.

The missing baryons are to be found in the WHIM, at temperatures from 10^5 to 10^7 K. The WHIM is predominately in filamentary structures, though a small percentage is to be found in the coronae of galaxies and virialized structures. The WHIM is found in regions with low over-densities, $(\rho - \overline{\rho})/\overline{\rho}$, peaking at 10 to 30. (The over-density of the local group is $\gtrsim 1500$). The WHIM is not virialized. The heating is due to shocks as gas accretes onto larger structures, and the gas does not cool due to the low density. Heating by supernovae appears to be of only minor importance for the bulk of the WHIM. From an observational perspective, it is interesting to note that the temperature distribution of the WHIM is broadly peaked and strongly evolving, around $\log T \sim 6.45$ for $z = 0$, and $\log T \sim 6.15$ for $z = 1$. The WHIM with the highest densities is also the gas with the highest temperatures, and represents only a tiny fraction of the whole.

Davé et al. (2000) suggest two possible "reality checks". The first is the total amount of flux provided by the WHIM. Davé et al. (2000) attempt to compare a suite of models to the limits at $\frac{1}{4}$ keV (Warwick & Roberts 1998) and $\frac{3}{4}$ keV (Wu, Fabian, & Nulsen 1999), and find them roughly consistent, but more careful calculation of the flux from the simulations should be done. The second reality check is the fluctuations due to the WHIM. These calculations have not yet been done; Davé et al. (2000) do produce a $\xi(r)$, a two-point correlation function, for the simulation, but it is difficult to transform that quantity into $w(\theta)$, an autocorrelation function.

1.2. WHIMsical Detections

1.2.1. Current Claims

Leaving aside detections of extended X-ray emitting gas between close, rich clusters (e.g. Kull & Böhringer 1999) there are two published studies that approach the question of X-ray emission from the low-density WHIM filaments. (Briel & Henry 1995) attempted to detect filaments between pairs of clusters. They found a 2σ upper limit of 3.9×10^{-16} erg s^{-1} cm^{-2} $arcmin^{-2}$ in band R6 (given the assumptions $z = 0.14$, $\log T = 7.06$ and metallicity 0.3 solar) and a 2σ upper limit of 3.1×10^{-16} erg s^{-1} cm^{-2} $arcmin^{-2}$ in band similar to R45 (given the assumptions $z = 0.14$, $\log T = 6.76$ and metallicity 0.3 solar). This is clearly an ideal way to look for filaments, so long as the clusters are sufficiently separated that one is not seeing overlapping cluster halos where one might expect gas with a similar temperature, though of different origin.

Scharf et al. (2000) make a clear detection of a "filamentary" object in band R47, at a flux level of 1.6×10^{-16} ergs s^{-1} cm^{-2} $arcmin^{-2}$, but it is not clear whether the object is a filament of the type discussed by Davé et al. (2000). This X-ray filament is aligned with a filamentary region of enhanced galactic density, and there are three candidate clusters along the filament. This is the best candidate to date, but it would be interesting to compare the mass overdensity within this filament to those proposed by Davé et al. (2000) to see what fraction of the WHIM is contained in structures such as these; is this a typical filament, or is this a higher density object? A note in passing: if the Scharf et al. (2000) detection is a real filament, the fact one filament was found in 22 $30' \times 30'$ fields suggests, with the usual caveat about small-number statistics, that such filaments should be commonly detectable.

1.2.2. Future Claims

Three types of proposals have been put forth for the direct detection of these filaments. M. Pierre and collaborators have proposed (Pierre, Bryan, & Gastaud 2000) direct imaging with XMM-Newton. In opposition to the work of Davé et al. (2000), they make much of the importance of the correct modeling of supernovae. Careful perusal of their proposal shows that one can detect only the $\lesssim 10\%$ of the WHIM that is peripheral to virialized clumps (and has very different properties than the rest of the WHIM) by direct imaging in the X-ray, not the 90% that actually resides in filaments. Detecting the WHIM by this method is like detecting a dog on the basis of a few cat hairs.

The second and third types of proposal are spectroscopic. The *Constellation-X* proposal suggests that the bulk of the WHIM will be detectable with that instrument after only 200 ks given a sufficiently bright background QSO. Alternatively, a similarly long "blank-sky" spectroscopic observation will detect the WHIM in emission to at least $z = 0.04$. Both spectroscopic observations rely on the strength of the O VII ($E = 0.654$ keV) line for gas in the WHIM range. Given that the new generation of detectors have resolution on the order of a few eV at 1 keV, the IGM lines will be easily distinguishable from those of the Galactic halo for $z > 0.01$.

2. The Current Work

There are three predictions about the WHIM that hydrodynamical simulations of the universe ought to make in order to allow a comparison to the universe itself; the total flux, the spectrum, and the angular distribution. The predictions have not yet been published for most hydrodynamical simulation. To what extent does this work place limits on these values?

2.1. Total Flux

The upper limit on the WHIM emission is the total trans-absorptive emission (TAE), that emission that is from beyond the Galactic absorption, but not part of the extragalactic power law (EPL). What is the magnitude of the TAE? To answer this question we must revisit the analysis of the *RASS* data in Chapter 5 and Chapter 6. The primary reason for embarking on a study of the TAE was the need to characterize the spectral shape of the TAE for deabsorption calculations. The primary scientific focus of those chapters was the thermal structure of the Galactic halo. Given this focus, it was most reasonable to characterize the uncertainties in the temperatures as the dispersion of the val-

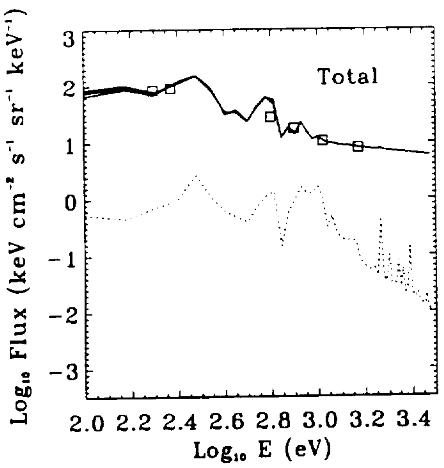

Fig. 11.1.— Graphical decomposition of the soft X-ray background. The *RASS* broad-band measurements *(boxes)* and the model of the total SXRB spectrum at 50 eV resolution *(solid)*. *Dashed:* the contribution of unresolved Galactic stars. See text for further description. Note that the spectral resolution of the model is 50 eV, much smaller than the *ROSAT* resolution.

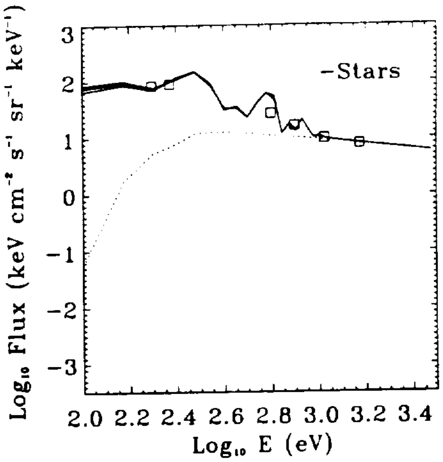

Fig. 11.2.— Graphical decomposition of the soft X-ray background. The *RASS* broad-band measurements *(boxes)* and the model spectrum at 50 eV resolution *(solid)* after the removal of the unresolved Galactic stars. *Dashed:* the contribution of unresolved extragalactic sources after absorption by the Galactic disk. See text for further description.

ues of the temperatures measured in individual 1°.3 × 1°.3 image pixels, and to pay little heed to the absolute magnitude of the emission. In any case, the strength of the soft component varies greatly with position, though the strength of the hard component is reasonably constant. If, however, one is interested in the strength of the TAE in order to place an upper limit on the strength of the emission due to diffuse extragalactic emission, then a somewhat different analysis is needed.

For simplicity, we have chosen to analyse the region used for the "budget" calculations in Table 6.1 ($45° < \ell < 270°, b > 85°$). The steps to deconstruct the total soft X-ray background into its components are depicted graphically in four figures beginning with Figure 11.1. The first panel shows the SED of the total diffuse background (squares) after correction for band-to-band difference in point source detection limits. The small vertical lines within the symbols are the propagated uncertainties. The solid line is our model of the total diffuse background at a resolution of 50 eV, far smaller than the PSPC resolution. The dotted line is the spectrum due to the unresolved Galactic stars, as calculated by an improved version of the model in Chapter 7. As the stars are distributed throughout the absorbing medium, the displayed spectrum is the stellar spectrum appropriately convolved with the absorption.

The second panel (Figure 11.2) shows the SED after the contribution of the unresolved Galactic stars has been removed. The dashed line is the absorbed spectrum of the extragalactic power law (EPL) due to unresolved individual extragalactic point sources. Here we have used the formulation of (Chen, Fabian, & Gendreau 1997) ($\Gamma = 1.46, N_\Gamma = 10.5$ keV cm^{-2} s^{-1} sr^{-1} keV^{-1}), however, unlike our previous treatment, we have renormalized the EPL so that the sum of all of the known components produce observed band R7 flux[1] Without this renormalization, the EPL produces too much flux in band R7.

---

[1] Since the bulk of the emission in the R7 band is due to the EPL, this method essentially sets the band R7 flux of the EPL to the observed flux ($\sim 40 \times 10^{-6}$ counts s^{-1} arcmin^{-2}) minus 0.9×10^{-6} counts s^{-1} arcmin^{-2} (for the unresolved Galactic stars) and 0.6×10^{-6} counts s^{-1} arcmin^{-2} for the TAE. This process is clearly iterative. However, the subtraction of the TAE contribution has little effect on the normalization of the EPL.

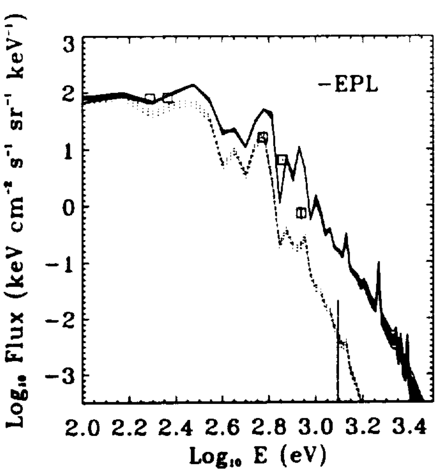

Fig. 11.3.— Graphical decomposition of the soft X-ray background. The *RASS* broad-band measurements *(boxes)* and the model spectrum at 50 eV resolution *(solid)* after the removal of the unresolved extragalactic sources. *Dashed:* the contribution of the Local Hot Bubble. See text for further description.

The third panel (Figure 11.3) shows the background after the subtraction of the EPL. The dotted lines are the contribution due to the Local Hot Bubble (LHB); the middle line is the best fit and the other two are the plus and minus one sigma. The uncertainty in the LHB value has be added to the measurement uncertainties in quadrature. The model of the background was calculated for each of these values of the LHB, each of which is plotted.

The fourth figure (Figure 11.4) is the background after subtraction of the LHB and after correction for Galactic absorption. Following the analysis of Chapter 6, we assumed a two component TAE; for each value of the LHB we have calculated $\pm 1\sigma$ extremes. We have plotted the extremes for the total TAE (solid), the soft component (dotted), and the hard component (dashed). Both the temperatures and normalizations of the components were fit. The temperatures are very similar to those found for the entire North Galactic hemisphere in Chapter 6; $\log T_S = 6.08 \pm 0.03$ and $\log T_H = 6.43 \pm 0.01$.

So how much of this need be included in the upper limit to the diffuse extragalactic emission? First, note that the band R12 emission is patchy, and thus likely to be related to the Galactic halo.

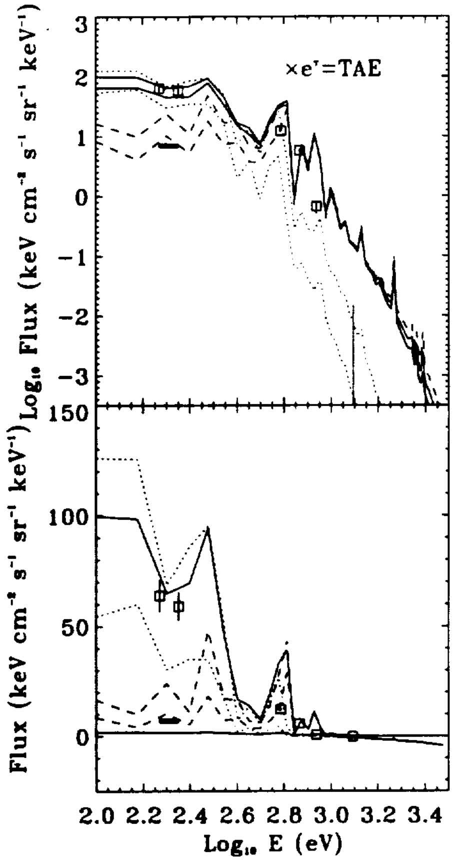

Fig. 11.4.— Graphical decomposition of the soft X-ray background. The *RASS* broad-band measurements *(boxes)* and the model spectrum at 50 eV resolution *(solid)* after the removal of the LHB contribution and after correction for Galactic absorption. *Dotted:* the contribution by the soft TAE component. *Dashed:* the contribution by the hard TAE component.A *Heavy Bar:* the maximum uniform $\frac{1}{4}$ keV flux allowed by the measurements of Snowden et al. (2000). See text for further description.

Is there some part of the band R12 emission that is constant over the sky? There have been a number of attempts to measure this value using the neutral hydrogen columns of external galaxies to shadow the extragalactic band R12 background. The value found by (Barber, Roberts, & Warwick 1996), using NGC 55 as a shadowing target, was 29.4 ± 7.2 keV cm^{-2} s^{-1} sr^{-1} keV^{-1} ($228 \pm 90 \times 10^{-6}$ counts s^{-1} arcmin^{-2}). The EPL used in the model produces 231×10^{-6} counts s^{-1} arcmin^{-2} in band R12, so there is little room for addition components.

A second measure of the background in band R12 is provided by Snowden et al. (2000). Measurements of the "distant emission" beyond many high Galactic latitude absorption features are consistent with zero. The two sigma upper limits in these directions are typically $\sim 80 \times 10^{-6}$ counts s^{-1} arcmin^{-2}. This value is shown in Figure 11.4 as a heavy bar. It is interesting that it is consistent with the band R12 emission of the hard TAE component, suggesting that the hard TAE component, more or less constant over the high latitude sky, provides the minimal band R12 emission.

The hard TAE component can only be a loose upper limit upon the diffuse extragalactic emission; from the arguments in Chapter 6, no doubt there is some contribution by the Galactic halo. The flux due to the hard TAE component is $\sim 7.4 \pm 1.0$ keV cm^{-2} s^{-1} sr^{-1} keV^{-1} in the $\frac{3}{4}$ keV band, and has a similar value in the $\frac{1}{4}$ keV band.

2.1.1. The EPL

An important point was elided above, the (Chen, Fabian, & Gendreau 1997) EPL formulation produces too much band R7 emission. The mean band R7 emission from the north Galactic polar cap ($45° < \ell < 270°, b > 85°$) after correcting the *RASS* to the (Chen, Fabian, & Gendreau 1997) point source detection limit is $40.13 \pm 0.91 \times 10^{-6}$ counts s^{-1} arcmin^{-2}. The uncertainty cited is the uncertainty in the mean due to counting statistics. However, there is also a systematic uncertainty due to the subtraction of the non-cosmic backgrounds. Since the non-cosmic backgrounds were calculated for each individual scan, the uncertainty due to the non-cosmic backgrounds appears as flux zero-point shifts between adjacent scans; a high-contrast stretch of otherwise smooth regions will reveal these features. To determine the systematic uncertainty in band R7, we measured the difference between two of the most obvious scan features; $\sim 7 \times 10^{-6}$ counts s^{-1} arcmin^{-2} peak-to-peak. The mean band R7 emission from the north Galactic polar cap is thus $40.13 \pm 3.62 \times 10^{-6}$ counts s^{-1} arcmin^{-2}. The (Chen, Fabian, & Gendreau 1997) EPL (normalization 10.5 keV cm^{-2} s^{-1} sr^{-1} keV^{-1}) produces 43.57×10^{-6} counts s^{-1} arcmin^{-2} after absorption. Therefore, the *RASS* band R7 is produced by the EPL with minor contributions by the other components ($\sim 1.5 \times 10^{-6}$ counts s^{-1} arcmin^{-2}), the normalization must be 9.5 ± 0.87 keV cm^{-2} s^{-1} sr^{-1} keV^{-1}.

2.2. Spectrum

Davé et al. (2000) plots the fraction of baryons in the WHIM as a function of the temperature. For the $z = 0$ WHIM, the distribution is peaked at $\log T \sim 6.45$, but not sharply so; the peak fraction is 0.024, and the distribution declines to 0.02 at $\log T = 6$ and 0.018 at $\log T = 7$. The fraction of emission due to each temperature, the baryon fraction weighted by the emission will be much more sharply peaked. Thus, it is of interest that the hard TAE component is characterized by a temperature of $\log T \sim 6.45$.

2.3. Angular Distribution

(Soltan & Hasinger 1994) measured the autocorrelation function in band R67 and showed that the signal is consistent with zero for $\theta > 5'$. This result is not surprising; in our formulation, only $\sim 12\%$ of the band R67 emission is *not* due to the EPL.

We have placed limits on the angular distribution of the diffuse extragalactic emission by measuring the autocorrelation function in band R45, where a larger portion of the emission may be due to the diffuse extragalactic component, and where the WHIM is thought to have its greatest emission. We show that there are indeed fluctuations on the scale $10' < \theta < 20'$ in band R45, and the signal in the ACF[2] is ~ 0.0025. This is

---

[2] As is customary the result is quoted for an im-

a direct measure; the best previous result (Chen et al. 1994) found a similar amplitude by taking the 2σ upper limit of a fit of a very noisy autocorrelation function in band R47. (By measuring in band R47, they had twice the count rate, but the half of that count rate due to band R67 had already been shown to have a vanishingly small signal for $\theta > 5'$.)

Given that Galactic absorption is small in this band, and that fluctuations in hot plasmas such as the LHB and the Galactic halo are very short lived ($\sim 10^5$ years), this signal should due to the diffuse extragalactic emission, not to one of the foregrounds. However, it is not clear how interesting this limit is; the hydrodynamical models have not yet been queried for this value.

Clearly, the hydro-cosmological simulations exist. *It is now necessary to measure the ACF of the simulations to see what order of magnitude we should expect.* The process is, in principle, straight forward. Given the density, temperature, and metallicity of every location within a model cube, one can calculate the observed field for a given instrument. This process should be done both for the PSPC and the current generation of instruments. (Given the simulations of Pierre, Bryan, & Gastaud (2000), it seems unlikely that any small collection of XMM-Newton pointings would detect a filament. What these simulations would determine is just how often one would be able to detect a filament, and what properties it should have.)

3. Improvements

3.1. Building Upon The Current Data

Can these ACFs be improved? Until high-resolution H II maps become available, it would be difficult to improve the deabsorption process. Better point source detection algorithms exist (see the discussion in Hasinger et al. 1998) than the scaled-sliding-box method that we have used on the individual pointings, though it is not clear how much better these algorithms would be in regions with large PSFs. One could design a sliding-box method to detect point sources in the mosaic, but the extent of the improvement is not clear.

One might also be able to do a better job of removing clusters of galaxies. We used the Abell catalogue because it was convenient. A number of new compilations from *ROSAT* PSPC data have been created, but are typically derived only from individual deep exposures; our individual exposures are typically not deep, merely overlapping other pointings. The signal due to clusters, however, is expected at the scale of $3'$, which is below the size of the PSF.

The ACF could be improved by modeling the contributions due to the unremoved point sources. The amplitude of the ACFs of Soltan & Hasinger (1994) were greatly reduced by modeling the point sources. Such a process is significantly more complicated for mosaics; multiple PSFs must be modelled at each point. Given that the ACF for a typical mosaic required about eight hours on the machine with which this project was started, calculating the ACF for 200 simulations per mosaic was not practicable. Newer machines have reduced the time to an hour; simulation may be practicable.

However, it should be noted that the variance is dominated by counting statistics, not the point sources. Thus, some of the large scale structure in the ACF may be removable by modeling of the point sources (which will also help remove problems due to the windowing function), the uncertainties will not be greatly reduced.

One could place tighter limits on the systematic problems by repeating this analysis in band R67 where the signal is known to be quite small.

3.2. Without Mosaics?

Mosaics have a great advantage over the *RASS* having exposures that are up to a factor of 40 greater than the *RASS* , but still covering solid angles of a few tens of square degrees. However, mosaics are not without problems; one can introduce features on the scale of individual pointings, $\sim 110'$. Since the mosaics depend upon the *RASS* for their normalization, the uncertainty at these scales is determined by the systematic problems in the *RASS* . However, these larger scales are not of much interest for the problem at hand. Nor can mosaics address the problem of

---

age that contains emission *both* from the Galactic halo/extragalactic diffuse component *and* the EPL. If the ACF is corrected to an image containing only the Galactic halo/extragalactic diffuse component, assuming that the EPL is smooth at these scales, the ACF signal would be a factor of ~ 4.7 larger.

the fluctuations at the smallest scales, $\sim 5'$ down to the resolution of the PSPC, due to large PSF at the edge of the PSPC field. Restricting ourselves to the centers of the PSPC pointings reduces the available area substantially. For these scales mosaics are not the ideal data; collections of deep pointings in low column density regions are much better. *The data collection of Soltan & Hasinger (1994), perhaps augmented by further data sets, should be reconstructed to examine the ACF in band R45.* However, without mosaicking the data, one cannot fully remove the effects of absorption.

3.3. Deconstructing the Background

Mushotzky has suggested that this dissertation has approached the problem of the WHIM in yet another, somewhat different, manner. When Chapter 6 was written, the general behavior of the spectrum of the extragalactic point sources below 0.5 keV was not known. However, the faint sources in the deep field studied by Mushotzky et al. (2000) do not, as a class, show a spectral break below 0.5 keV (as, indeed, our analysis using the known limits of the $\frac{1}{4}$ keV background showed that they could not). Chapter 6 parameterizes the flux that is not due to the extragalactic point sources and is not due to the LHB, that is, the combination of Galactic halo emission and putatative WHIM.

Of course, that parameterization is, without doubt, wrong. We know that the LHB is not in equilibrium, and it is not likely that the halo is in equilibrium either. There are a number of projects afoot to study the spectrum of the LHB and the Galactic halo with XMM-Newton using the lines of O VII and O VIII and modeling them with non-equilibrium spectra. Thus, despite the notorious non-success in modelling the high-resolution DXS spectrua of the LHB, there is some hope for progress in determining just how wrong our parameterization is.

Mushotzky has suggested that one can test the existence of a strong WHIM by comparing our model to the measure of the oxygen lines made by (as yet unpublished) rocket flights (see Deiker et al. (1997) for a description of the flights). Since equilibrium models produce stronger oxygen lines than the non-equilibrium models, scaling our models to produce the observed oxygen line strengths will produce the minimum possible broad-band flux due to the halo, and thus a measure of the maximum possible contribution due to the WHIM. The addition of the non-equilibrium results will then allow a stronger upper limit on the flux due to the WHIM.

4. Some Unfinished Business

When this dissertation was begun, one of the motivating factors was the excessive fluctuation found in the $\frac{1}{4}$ keV background by Barber, Warwick, & Snowden (1995). We suggested in the opening that these "blobs" might be the fluctuations predicted by Cen & Ostriker (1999). The ACF has clearly pointed to excess fluctuations on the scale of the Barber, Warwick, & Snowden (1995) fluctuations ($\sim 20'$), but are we still observing the same phenomena? To some extent, yes. It is difficult to compare our images directly with those of Barber, Warwick, & Snowden (1995); although the data are nearly the same, deabsorption methods have improved greatly and the point sources have been handled in a very different manner. However, comparison shows that we find generally the same pattern of positive and negative fluctuations, and the $\delta I/I$ analysis does suggest that the fluctuations have an intrinsic scale of $\sim 20'$.

Have we made any progress in determining the origin of these features? We have not identified the features with any particular phenomena, and we have not entirely eliminated as their source systematic problems with deabsorption. Given the initial results of (Reynolds 1999) (3.0×10^{19} cm^{-2} beam-to-beam variation in N_{HII}), we expect $\sim 5\%$ errors in the band R82 flux ($\sim 0.5\%$ errors in band R45). At $20'$ in band R82(R45), high-pass filtered, we find that $(\sigma_b/I)^2 \sim 1.75(1.0)$, meaning that the variation on $20'$ scales is $\sim 7\%(5\%)$. Thus, in band R82 we may still be victim to the deabsorption errors.

The standard caveat should also be given that the deabsorption model may be inherently wrong; the X-ray emission could be interleaved with the absorption. In this case the deviations from the mean $I'_O - N_H$ relation say interesting things about the degree to which the emission is interleaved, rather than *vice versa*[3].

Barber, Warwick, & Snowden (1995) suggest that the band R82 variation is due to the Galactic halo. Simple physics suggests that fluctuations do not last long in the halo (Field 1965), so if the fluctuations seen are due to the halo, the halo is a much more active place than usually imagined. Then again, the "halo" has become a very active place, with supernovae explosions and galactic chimneys, and with multiple components from 10^4 K to several times 10^6 K. Perhaps the region with all this activity should be better described as the "disk-halo" interface, while the term "halo" is left for the smoother, larger-scale-length, quasi-static, higher-temperature component. In any case, this active region, which must contain interface layers, is a more likely place to find the necessary fluctuations, but the physics is much more complicated.

5. ArrivederLa

There are still a few changes to be rung in the analysis described in this chapter. A new and more robust calculation of the stellar contribution is one of the projects being finished as this is written, the area of the sky covered by the budget calculations could be expanded, and the TAE emission could be calculated a bit more carefully. However, the bulk of the *RASS* contribution to the problem of the diffuse extragalactic emission has probably been wrung out.

Similarly, there are still a few projects to be pursued using individual PSPC pointings. Most important is determining the systematics in the band R45 ACF, both by modeling the effect of point sources interacting with the window function and by executing the same analysis in band R67. Similarly, a Soltan & Hasinger (1994) analysis in band R45, though difficult, is certainly possible, and would illuminate the smallest accessible scales.

Perhaps the most important project in the near future is querying the simulations for observable parameters. We have no clew if our ACF is a useful limit, or whether the expected value is an order of magnitude smaller than our limit. Such analysis is also important for the current generation of instruments; *Chandra* and *XMM-Newton*.

No doubt, the existance of the diffuse extragalactic emission will plague at least another generation of graduate students before it is somewhat resolved; this dissertation is but the first step.

REFERENCES

Barber, C., Warwick, R. S., & Snowden, S. L. 1995, in Röntgenstrahlung from the Universe, ed. H. Zimmermann, J. Trümper, & H. Yorke, MPE Report 263, 319

Barber, C. R., Roberts, T. P., & Warwick, R. S. 1996, MNRAS, 282, 157

Briel, U. G., & Henry, J. P. 1995, A&A, 302, L9

Cen, R., & Ostriker, J. P. 1999, ApJ, 514, 1

Chen, L.-W., Fabian, A. C., & Gendreau, K. C. 1997, MNRAS, 285, 449

Chen, L.-W., Fabian, A. C., Warwick, R. S., Branduardi-Raymont, G., & Barber, C. R. 1994, MNRAS, 266, 846

Davé, R., et al. 2000, ApJ, submitted

Deiker, S., Kelley, R. L., Lesser, A., McCammon, D., Porter, F. S., Stahle, W. T. S. C. K., & Szymkowiak, A. E. 1997, in Proceedings of the Seventh International Workshop on Low Temperature Detectors, 113

Field, G. B. 1965, ApJ, 142, 531

Hasinger, G., Burg, R., Giacconi, R., Schmidt, M., Trümper, J., & Zamorani, G. 1998, A&A, 329, 482

Kull, A., & Böhringer, H. 1999, A&A, 341, 23

Mushotzky, R. F., Cowie, L. L., Barger, A. J., & Arnaud, K. A. 2000, Nature, in press

Pierre, M., Bryan, G., & Gastaud, R. 2000, A&A, submitted

Reynolds, R. J. 1999, private communication

Scharf, C., Donahue, M., Voit, G. M., Rosati, P., & Postman, M. 2000, ApJ, 528, L73

Snowden, S. L., Freyberg, M. J., Kuntz, K. D., & Sanders, W. T. 2000, ApJS, in press

Soltan, A., & Hasinger, G. 1994, A&A, 288, 77

Warwick, R. S., & Roberts, T. P. 1998, Astronomische Nachrichten, 319, 59

Wu, K. K. S., Fabian, A. C., & Nulsen, P. E. J. 1999, MNRAS, in press

---

[3] Imagine a simple model with two sheets of absorption with optical depths τ_1 and τ_2, the closer sheet having subscript 2. If there is emission beyond both sheets, I_1, and between the sheets, I_2, but none in front of the sheets, the true observed emission will be

$$I_1 e^{-\tau_1} e^{-\tau_2} + I_2 e^{-\tau_2}$$

whereas our simple model will produce $I_1' e^{-\tau_1} e^{-\tau_2}$. Therefore, given the fits to the mean $I_O' - N_H$ relation, it must be that $I_1' \sim I_1 + I_2 e^{\tau_1}$ over a wide range of $e^{-\tau_1} e^{-\tau_2}$. So, either I_1 is small, in which case τ must also be small or I_2 is small. In neither case is reality too different than our simple model.

Appendix A: Model Temperatures

Abstract

We find that the thermal history of likely halo plasmas has little effect on the *ROSAT* broad-band ratios.

It is well known that high resolution spectra of the LHB have shown that the gas is not in equilibrium (Sanders et al. 1998; Deiker et al. 1997), but the true thermal state of the gas remains a mystery. The question has been raised whether it is valid to characterize a plasma temperature by an equilibrium temperature derived from the R2/R1 band ratio observed by the *ROSAT* PSPC

The standard response has been that equilibrium temperatures provide a universally accessible *relative* measure of the plasma temperature. The bulk of the X-ray emission from the plamsa is in lines. Even though the relative line strengths will be very different between equilibrium and non-equilibrium plasmas of the same temperature, one expects that mean energy of the lines to increase with temperature in both cases. Thus, one would expect the very broad band fluxes to behave in similar manners. However, there are some very strong lines, such as the O VII and O VIII lines, that dominate the emission. One might expect that these lines to have very different behaviors in the equilibrium and non-equilibium cases, and thus have a significant impact on the general run of R2/R1 with temperature.

To explore this problem, we obtained a set of non-equilibrium spectra from R. L. Shelton to compare with equilibrium spectra. The non-equilibrium spectra were derived from a plasma that had been shock-heated to 10^8 K and allowed to cool. The atomic models used by the non-equilibrium models are the same used by the Raymond & Smith equilibrium models. The run of R2/R1 with plasma temperature is shown in Figure A.1, where it can be seen that for $\log T > 5.5$ there are only minor differences between equilibrium and non-equilibrium models.

REFERENCES

Deiker, S., Kelley, R. L., Lesser, A., McCammon, D., Porter, F. S., Stahle, W. T. S. C. K., & Szymkowiak, A. E. 1997, in Proceedings of the Seventh International Workshop on Low Temperature Detectors, 113

Raymond, J. C., & Smith, B. W. 1977, ApJS, 35

Sanders, W. T., Edgar, R. J., Liedahl, D. A., & Morgenthaler, J. P. 1998, in The Local Bubble, ed. D. Breitschwerdt & M. Freyberg, 83

Shelton, R. L. 1999, private communication

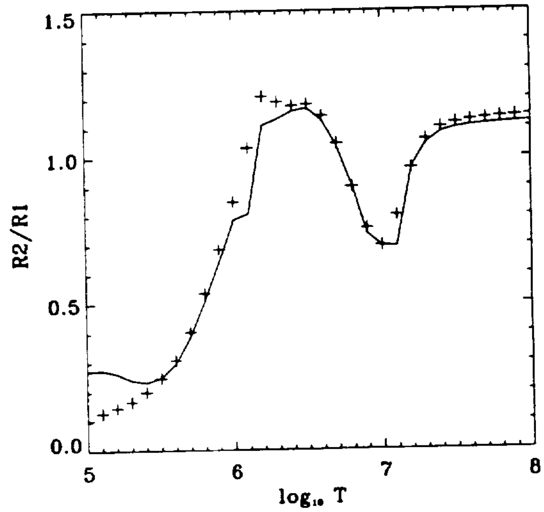

Fig. A.1.— Comparison of the R2/R1 band ratios as a function of temperature for equilibrium and non-equilibrium cooling. The solid line is for a plasma cooling from 10^8 K (Shelton 1999), the crosses are the Raymond & Smith (1977) equilibrium values.

Appendix B: Observations

This appendix presents lists of all of the pointed PSPC observations used. Each mosaic is listed in a separate table.

TABLE B.1
035+78 OBSERVATIONS

ROR	R.A.	Dec.	l	b	Exp.		Date	Target
	(J2000)				(Tot.)	(Sel.)		
701066	204.89	26.35	31.52	79.23	9040	8619	14/07/92	CHFT FIELD A/5
201037	209.04	25.92	31.83	75.48	15533	12333	19/07/92-22/07/92	ZZ BOO
700284	207.15	26.37	32.78	77.22	2025	1894	30/06/91-01/07/91	E1346+266
701064	204.40	26.63	32.79	79.70	8356	8091	12/07/92-13/07/92	CFHT FIELD A/3
701068	205.38	26.63	33.23	78.83	8669	7821	16/07/92-17/07/92	CFHT FIELD A/7
700145	207.15	26.52	33.45	77.24	18205	16702	01/07/91	1E1346+26
					1909	1544	06/01/92	1E1346+26
800105	207.23	26.59	33.80	77.18	36273	30157	04/01/92-22/01/92	ABELL 1795
800055	207.22	26.62	33.93	77.19	25803	24846	01/07/91-02/07/91	ABELL 1795
701062	204.07	27.08	35.22	80.02	9457	9073	10/07/92-14/07/92	CFHT FIELD A/1
701459	204.89	27.08	35.42	79.29	7157	6358	06/07/92-09/07/92	CFHT A/13
701063	205.71	27.08	35.63	78.57	10032	9392	15/07/92-22/07/92	CFHT FIELD A/2
701065	204.40	27.53	37.82	79.74	8971	8777	11/07/92	CFHT FIELD A/4
701069	205.37	27.53	37.87	78.88	9912	9572	13/07/92-14/07/92	CHFT FIELD A/8
701067	204.88	27.82	39.41	79.32	8209	7648	14/07/92-15/07/92	CHFT FIELD A/6
300333	205.54	28.38	42.23	78.71	13083	11904	06/06/93-22/07/93	NGC 5272
					44599	12683	02/07/94-04/07/94	NGC 5272

TABLE B.2
086+74 OBSERVATIONS

ROR	R.A. (J2000)	Dec. (J2000)	l	b	Exp. (Total)	Exp. (Sel.)	Date	Target
900626	203.65	37.91	85.56	75.91	37658	30311	19/06/93-16/07/93	DEEP SURVEY
700283	203.65	37.91	85.56	75.91	71803	71788	23/06/91-26/06/91	DEEP SURVEY
900218	203.86	38.20	85.88	75.59	6410	5173	27/12/91-02/01/92	SURVEY POSN. 1
900219	203.96	38.35	86.06	75.43	6080	4309	27/12/91-02/01/92	SURVEY POSN. 2
900220	204.07	38.50	86.21	75.26	1650	1062	26/12/91	SURVEY POSN. 3
					6026	5386	03/06/92	SURVEY POSN. 3
900221	204.17	38.64	86.36	75.10	7030	5328	27/12/91-30/12/91	SURVEY POSN. 4
900222	204.27	38.79	86.53	74.94	4792	3443	27/12/91-03/01/92	SURVEY POSN. 5
					3231	2751	02/06/92-03/06/92	SURVEY POSN. 5
900223	204.38	38.93	86.65	74.78	4745	3966	29/12/91-14/01/92	SURVEY POSN. 6
					1663	1314	02/06/92	SURVEY POSN. 6
900232	204.48	39.08	86.82	74.61	5345	4841	25/12/91-26/12/91	SURVEY POSN. 7
900233	204.58	39.23	86.99	74.45	2134	1246	30/12/91	SURVEY POSN. 8
					4075	3956	02/06/92	SURVEY POSN. 8
900234	204.69	39.37	87.10	74.29	5891	2162	15/12/91-16/12/91	SURVEY POSN. 9
900235	204.79	39.52	87.26	74.13	6202	4140	28/12/91-29/12/91	SURVEY POSN. 10
900236	204.89	39.67	87.42	73.96	6776	5512	29/12/91-16/01/92	SURVEY POSN. 11
900237	205.00	39.81	87.54	73.80	6536	5687	05/01/92-15/01/92	SURVEY POSN. 12
900226	205.10	39.96	87.69	73.64	5839	5101	07/01/92-15/01/91	SURVEY POSN 13
900227	205.20	40.10	87.82	73.49	6996	5508	30/12/91-14/01/92	SURVEY POSN 14
900228	205.31	40.25	87.95	73.32	1574	1386	06/01/92-14/01/92	SURVEY POSN. 15
					4692	3954	01/06/92-02/06/92	SURVEY POSN 15
900229	205.41	40.40	88.11	73.16	6723	4995	31/12/91-05/01/92	SURVEY POSN 16
900405	205.51	40.54	88.23	73.00	8663	7501	08/06/92	SURVEY POSN. 17
900406	205.62	40.69	88.36	72.83	7469	4713	07/07/92	SURVEY POSN 18
900407	205.72	40.83	88.48	72.68	7641	5364	03/07/92	SURVEY POSN. 19
900408	205.82	40.98	88.63	72.52	7911	6289	09/07/92	SURVEY POSN. 20
800252	203.84	41.00	92.64	73.44	15659	12297	23/06/92-29/06/92	A1763

TABLE B.3
138+52 OBSERVATIONS

ROR	R.A. (J2000)	Dec. (J2000)	*l*	*b*	Exp. (Total)	Exp. (Sel.)	Date	Target
600280	161.64	63.24	143.59	48.58	10473	7080	12/05/93-22/05/93	NGC 3359
201235	161.80	63.59	143.14	48.37	4760	3784	17/11/92-19/11/92	RX J1047.1+6335.3
701122	163.01	61.42	144.83	50.33	9349	7806	17/11/92-28/11/92	ABLS QSO J1052+612
					7804	6956	21/10/93	ABLS QSO J1052+612
					6274	4871	15/10/93-17/10/93	ABLS QSO J1052+6125
900331	164.38	62.27	143.19	50.14	9004	5569	26/05/93-27/05/93	UMA7
900330	164.39	63.40	142.03	49.29	7292	5045	23/05/93-27/05/93	UMA6
900329	164.55	64.49	140.88	48.50	10089	7604	11/05/93-24/04/93	UMA5
900328	165.66	65.62	139.28	47.91	6793	5157	10/11/92-28/11/92	UMA4
					5448	3697	05/04/93-06/04/93	UMA4
					3174	2503	11/10/93	UMA4
500157	165.72	60.89	143.86	51.60	20242	15957	18/05/93-22/05/93	G290.1-0.8
900332	167.58	64.54	139.27	49.26	6192	4465	11/04/93-14/04/93	UMA8
					9249	7493	11/10/93-13/10/93	UMA8
					3126	1986	04/05/94	UMA8
800540	168.04	63.01	140.40	50.62	5617	3864	19/10/93	A 1180
600250	169.61	58.79	143.53	54.46	4606	3740	30/11/92-04/12/92	NGC 3610
					6178	4913	10/05/93-11/05/93	NGC 3610
701412	170.58	59.08	142.54	54.52	7804	6956	21/10/93	NGC 3642
900333	170.63	64.00	138.03	50.44	5886	4171	30/11/92-01/12/92	UMA9
					3636	3077	14/10/93	UMA9
					4530	3467	04/05/94-05/05/94	UMA9
700442	172.13	58.56	141.91	55.41	1466	1018	23/04/92	NGC 3690
					3532	3442	23/04/93	NGC 3690
900148	172.96	63.84	136.76	51.10	16663	9794	29/10/91-31/10/91	UMA CLOUD 2
800260	173.34	66.41	134.67	48.90	2972	2151	29/11/92	A1302
900336	173.84	59.72	139.53	54.89	10315	7293	29/05/93-30/05/93	UMA12
900335	174.11	64.53	135.54	50.72	5823	3658	01/12/92-04/12/92	UMA11
					4397	3432	10/05/93-21/05/93	UMA11
900521	174.12	67.62	133.45	47.95	753	509	04/05/94	HS 1133+6753
					5893	4371	15/10/93-16/10/93	HS 1133+6753
900150	174.44	61.22	137.83	53.73	18289	10536	19/11/91-25/11/91	UMA CLOUD 3
900334	174.83	62.37	136.66	52.79	6000	4721	12/05/93-27/05/93	UMA10
700068	174.99	65.80	134.16	49.74	1769	1696	20/11/91-22/11/91	3C263
800402	175.71	58.13	139.43	56.75	5018	3512	30/05/93	4C58.22

TABLE B.4

161+51 OBSERVATIONS

ROR	R.A. (J2000)	Dec. (J2000)	*l*	*b*	Exp. (Total)	Exp. (Sel.)	Date	Target
900214	152.55	50.75	164.03	51.49	15664	13320	12/11/91-13/11/91	SURVEY FIELD 5
700265	152.56	51.75	162.56	51.11	3587	3191	16/04/91-09/05/91	SURVEY FIELD 4
					20122	13774	17/11/91-20/11/91	SURVEY FIELD 4
700263	152.56	52.75	161.11	50.70	13905	11132	14/04/91-10/05/91	SURVEY FIELD 3
700264	152.57	53.75	159.68	50.28	14758	13558	13/04/91-14/04/91	SURVEY FIELD 2
900213	152.57	54.75	158.29	49.83	16614	11670	10/11/91-12/11/91	SURVEY FIELD 4
900215	152.58	55.75	156.91	49.38	18824	14878	11/04/92-15/04/92	SURVEY FIELD 6
900400	154.82	52.75	160.15	51.93	2544	2065	20/11/92-21/11/92	LOCKMAN SPUR A
					13256	11760	24/04/93-03/05/93	LOCKMAN SPUR A
900401	156.81	53.49	158.15	52.62	796	727	17/11/92	LOCKMAN SPUR B
					16070	14576	25/04/93-01/05/93	LOCKMAN SPUR B
				Additional Pointings				
701401	149.41	55.38	158.60	47.93	4465	3343	08/11/93-09/11/93	0954+556
700319	150.49	55.68	157.81	48.36	18836	11024	14/11/91-15/11/91	NGC 3079
700220	153.77	49.43	165.54	52.72	5151	4688	11/05/91	GB 1011+498
600624	155.55	51.40	161.79	52.94	8427	7443	21/10/93-22/10/93	MS1019+5139
701544	157.83	50.89	161.44	54.44	10777	7628	22/10/93-23/10/93	RXJ 10313+5053
600057	158.13	54.40	156.20	52.80	3979	2109	20/04/91-21/04/91	HARO2
900149	158.78	54.24			13135	9671	01/11/91-02/11/91	UMA CLOUD 1
					4361	3978	16/04/92	UMA CLOUD 1
600156	159.69	53.50	156.61	54.06	9114	6267	17/11/91-18/11/91	NGC 3310

Table B.5
171+50 Observations

ROR	R.A. (J2000)	Dec. (J2000)	l	b	Exp. (Total)	Exp. (Sel.)	Date	Target
800102	145.73	46.99	171.63	48.28	13941	8826	17/11/91-20/11/91	A851
700167	146.25	47.50	170.77	48.52	546	213	21/04/91	HS 47.5/22 FIELD
					700	647	20/11/92	HS 47.5/22 FIELD
					1451	1317	20/10/93	HS 47.5/22 FIELD
700168	146.25	47.00	171.51	48.63	716	566	19/11/92	HS 47.5/22 FIELD
					1408	1222	25/04/93	HS 47.5/22 FIELD
700169	146.25	46.50	172.25	48.73	2394	1808	24/04/93-25/04/93	HS 47.5/22 FIELD
700451	146.25	48.00	170.04	48.41	3383	2523	10/05/92-19/05/92	HS 47.5/22 FIELD II.
700158	146.63	46.25	172.55	49.04	2505	1777	14/04/91-18/04/91	HS 47.5/22 FIELD
700171	146.63	46.75	171.80	48.94	2272	1792	14/04/91-18/04/92	HS 47.5/22 FIELD
700172	146.63	47.25	171.06	48.83	1077	776	21/04/91-23/04/91	HS 47.5/22 FIELD
700454	146.63	47.75	170.32	48.72	3183	2990	09/05/92-19/05/92	HS 47.5/22 FIELD II.
300329	146.65	44.78	174.75	49.32	5422	3739	09/11/93-10/11/93	DV UMA
700166	147.00	47.50	170.60	49.02	2157	1682	14/04/91-19/04/91	HS 47.5/22 FIELD
700170	147.00	46.50	172.09	49.24	1358	779	20/04/91	HS 47.5/22 FIELD
					1032	819	21/11/92	HS 47.5/22 FIELD
700182	147.00	47.00	171.35	49.13	2816	2358	10/05/91	HS 47.5/22 FIELD
700457	147.00	48.00	169.86	48.90	3236	3085	09/05/92-19/05/92	HS 47.5/22 FIELD II.
700157	147.38	46.25	172.38	49.54	2751	2477	15/11/91-16/11/91	HS 47.5/22 FIELD
700181	147.38	46.75	171.63	49.44	2900	2579	15/11/91-20/11/91	HS 47.5/22 FIELD
700453	147.38	47.75	170.14	49.21	4617	3238	10/05/92=19/05/92	HS 47.5/22 FIELD II.
700173	147.38	47.25	170.88	49.33	1504	1100	23/04/91	HS 47.5/22 FIELD
					575	363	11/11/92	HS 47.5/22 FIELD
700159	147.75	46.50	171.92	49.74	2604	1858	17/04/91-21/04/91	HS 47.5/22 FIELD
700165	147.75	47.50	170.42	49.51	1953	1873	15/11/91-17/11/91	HS 47.5/22 FIELD
700180	147.75	47.00	171.17	49.63	1041	613	21/04/91	HS 47.5/22 FIELD
					1354	1298	19/11/92-20/11/92	HS 47.5/22 FIELD
700456	147.75	48.00	169.67	49.39	3420	3041	10/05/92-19/05/92	HS 47.5/22 FIELD II.
700156	148.13	46.25	172.21	50.05	1757	1442	18/04/91-20/04/91	HR 47.5/22 FIELD
700174	148.13	47.25	170.70	49.82	2910	1985	10/11/91	HS 47.5/22 FIELD
700179	148.13	46.75	171.45	49.94	2063	1288	17/04/91-22/04/91	HS 47.5/22 FIELD
					2103	1973	11/11/91-12/11/91	HS 47.5/22 FIELD
700452	148.13	47.75	169.95	49.70	2911	2761	11/05/92-19/05/92	HS 47.5/22 FIELD II.
700160	148.50	46.50	171.74	50.24	2553	2422	16/11/91	HS 47.5/22 FIELD
700176	148.50	47.50	170.23	50.00	2337	1592	17/04/91	HS 47.5/22 FIELD
700178	148.50	47.00	170.98	50.13	2944	1719	15/11/91	HS 47.5/22 FIELD
700455	148.50	48.00	169.48	49.87	3487	3336	11/05/92-18/05/92	HS 47.5/22 FIELD II.
700046	148.54	49.26	167.59	49.56	3503	3029	13/04/91-14/04/91	MSS0950+49
700155	148.88	46.25	172.03	50.56	2690	1620	15/11/91	HS 47.5/22 FIELD
700175	148.88	47.25	170.51	50.31	2082	1742	10/11/91	HS 47.5/22 FIELD
700177	148.88	46.75	171.27	50.44	1890	1715	25/04/91-06/05/91	HS 47.5/22 FIELD
700450	148.88	47.75	169.75	50.19	3679	2899	12/05/92-18/05/92	HS 47.5/22 FIELD II.
700150	149.25	48.50	168.52	50.22	545	528	07/05/91	HS 47.5/22 FIELD
					1418	1243	23/04/93	HS 47.5/22 FIELD
					1922	1638	20/10/93	HS 47.5/22 FIELD
700153	149.25	48.00	169.27	50.36	2594	1900	10/11/91	HS 47.5/22 FIELD
700161	149.25	46.50	171.55	50.75	2586	1807	20/11/92-21/11/92	HS 47.5/22 FIELD
700184	149.25	47.50	170.03	50.49	3240	3063	15/11/91-21/11/91	HS 47.5/22 FIELD
700187	149.25	47.00	170.79	50.62	2524	1889	16/11/91	HS 47.5/22 FIELD
701402	149.58	47.42	170.05	50.73	3583	2830	13/11/93	0955+476
700151	149.63	48.25	168.78	50.53	1326	1204	17/11/91	HS 47.5/22 FIELD
					1298	1266	24/04/91-29/04/91	HS 47.5/22 FIELD
700154	149.63	47.75	169.54	50.67	3094	2922	07/05/91-09/05/91	HS 47.5/22 FIELD
700185	149.63	47.25	170.30	50.81	2124	1803	16/11/91	HS 47.5/22 FIELD
700188	149.63	46.75	171.06	50.94	2593	2324	11/05/91-12/05/91	HS 47.5/22 FIELD
					2885	2536	16/11/91-18/11/91	HS 47.5/22 FIELD
700149	150.00	48.50	168.29	50.70	1805	1665	16/11/91	HS 47.5/22 FIELD
700152	150.00	48.00	169.05	50.84	1576	1427	15/04/91-16/04/91	HS 47.5/22 FIELD
					569	491	23/04/91	HS 47.5/22 FIELD
700162	150.00	46.50	171.35	51.25	3042	2505	08/05/92-09/05/92	HS 47.5/22 FIELD
700183	150.00	47.50	169.81	50.98	2588	1745	15/11/91-16/11/91	HS 47.5/22 FIELD
700186	150.00	47.00	170.58	51.12	1594	1261	06/05/91	HS 47.5/22 FIELD
					716	664	21/11/92	HS 47.5/22 FIELD
700163	150.38	46.75	170.85	51.43	2145	1807	10/05/91	HS 47.5/22 FIELD
700164	150.38	47.25	170.08	51.30	890	638	17/11/91	HS 47.5/22 FIELD
					1748	1706	23/04/91	HS 47.5/22 FIELD
701546	152.05	47.09	169.80	52.43	2145	1640	24/10/93	RXJ 10081+4705

TABLE B.6
220+84 OBSERVATIONS

ROR	R.A. (J2000)	Dec. (J2000)	l	b	Exp. (Total)	Exp. (Sel.)	Date	Target
700223	185.38	28.23	201.76	83.29	15223	12087	14/06/91-15/06/91	ON 231
701056	185.34	30.18	186.34	82.73	10969	10307	18/06/92-22/06/92	2A 1218+304
701203	184.62	29.81	190.68	82.28	6608	6266	16/06/92-21/06/92	MS1215.9+3005
					2916	2572	09/12/92	MS1215.9+3005
701353	184.61	29.81	190.70	82.27	3146	2717	17/12/93-18/12/93	MKN766
700221	184.46	30.12	188.87	82.05	21999	20253	15/06/91-16/06/91	B2 1215+30
700970	184.61	30.04	189.09	82.20	19870	14489	21/12/92-23/12/93	MKN766FIELD
701413	185.03	29.28	193.78	82.77	3413	2937	16/12/93	NGC 4278
700232	181.18	27.90	205.98	79.62	27859	10580	04/06/91-05/06/91	1202+281
600444	181.66	28.17	204.35	80.03	15075	13551	24/05/93-26/05/93	NGC 4104
201170	183.00	27.50	208.24	81.23	2166	2064	16/06/92-17/06/92	CB8
201169	184.00	25.00	225.92	81.76	1814	1743	15/06/92-16/06/92	CB7
200529	184.15	26.49	215.65	82.20	3194	2020	28/12/91-31/12/91	PG 1214+268
201168	184.67	25.50	223.60	82.48	1813	1741	18/06/92	CB6
201175	184.67	23.00	240.24	81.51	4031	3112	29/06/92	CB13
201167	185.33	26.00	220.74	83.17	1678	1610	18/06/92	CB5
201176	185.50	27.00	212.38	83.45	4374	3993	19/06/92	CB14
200307	185.75	25.95	221.82	83.53	16526	11616	13/06/91-14/06/91	COM15
201166	186.00	26.50	217.24	83.85	1964	1872	20/06/92	CB4
201174	186.00	22.50	248.08	82.24	2354	2206	14/12/92-17/12/92	CB12
700308	186.10	24.61	233.92	83.42	5624	2945	19/12/91-29/05/92	MSS 1221+24
700388	186.41	24.98	231.84	83.82	8347	6453	01/06/92-05/06/92	1223+252
201165	186.67	27.00	212.85	84.49	1999	1938	21/06/92	CB3
201173	186.67	23.00	247.95	83.04	2262	2144	08/12/92-09/12/92	CB11
201164	187.33	27.50	207.34	85.07	2040	1701	20/06/92	CB2
201172	187.33	23.50	247.70	83.82	2152	1669	29/06/92	CB10
201163	188.00	28.00	200.37	85.61	1810	1740	21/06/92	CB1
201171	188.00	24.00	247.38	84.62	2200	2085	16/12/92	CB9
600162	188.48	26.27	224.31	85.99	12015	8649	15/12/91-04/01/92	NGC 4565
600415	189.09	25.99	230.74	86.44	9202	7940	30/06/92-04/07/92	NGC 4565
					10519	9496	08/12/92-15/12/92	NGC 4565
600595	188.99	27.96	198.41	86.47	17353	16100	01/07/92-02/07/92	NGC 4559
701097	189.42	26.71	219.92	86.91	5424	5085	30/06/92-01/07/92	IC 3599
701098	189.42	26.71	219.92	86.91	1772	1688	16/06/92	IC 3599
701099	189.42	26.71	219.92	86.91	1875	1807	17/06/92	IC 3599
701100	189.42	26.71	219.92	86.91	2011	1937	18/06/92	IC 3599
701528	189.42	26.71	219.92	86.91	3434	2001	17/06/92-18/06/92	IC 3599
800475	190.32	26.23	233.96	87.56	6797	4167	15/06/93-03/07/93	NGC 4615

TABLE B.7
295-89 OBSERVATIONS

ROR	R.A. (J2000)	Dec. (J2000)	l	b	Exp. (Total)	Exp. (Sel.)	Date	Target
800069	9.88	-28.81	359.66	-86.88	7465	6733	23/12/91-04/01/92	SCULPTOR C,D
800070	11.38	-29.64	329.97	-87.17	6779	6273	23/12/91-02/01/92	SCULPTOR B
700275	13.02	-29.09	298.84	-88.03	24461	16725	01/06/92-12/06/92	SGP2
700133	13.75	-28.33	269.87	-88.56	1569	1530	04/01/92	005459-281943
					19466	16675	03/06/92-15/06/92	005459-281943
900496	13.75	-28.33	269.87	-88.56	9415	8616	19/12/93	SGP3
					22693	17315	30/06/94-01/07/94	SGP3
701223	14.37	-27.64	234.16	-88.56	48943	42843	03/06/92-08/06/92	GSGP4
700081	14.49	-26.22	181.36	-88.28	3817	3664	28/12/91	0055-264
700528	14.53	-27.64	232.35	-88.43	12516	10805	08/12/92-14/12/92	SGP4
					18185	16917	04/06/92-15/06/92	SGP4
700121	15.57	-27.33	218.34	-87.58	6157	6016	05/01/92-06/01/92	Q0059-2735
					2191	1926	05/06/92-15/06/92	Q0059-2735
					6724	5412	08/12/92-09/12/92	Q0059-2735

TABLE B.8

045+00 OBSERVATIONS

ROR	R.A. (J2000)	Dec. (J2000)	*l*	*b*	Exp. (Total)	Exp. (Sel.)	Date	Target
600281	282.96	13.46	45.00	6.01	3696	2745	12/10/92-13/10/92	PLANE 45-1
600282	283.75	13.07	45.00	5.14	2421	1712	13/10/92	PLANE 45-2
					1123	789	23/03/93	PLANE 45-2
600283	284.54	12.69	45.00	4.28	2916	2609	16/10/92-17/10/92	PLANE 45-3
600284	285.32	12.30	45.00	3.43	3629	3543	28/10/92-29/10/92	PLANE 45-4
600285	286.10	11.91	45.00	2.57	4304	3760	28/10/92-29/10/92	PLANE 45-5
600286	286.88	11.52	45.01	1.71	3728	2930	18/10/92-19/10/92	PLANE 45-6
600287	287.65	11.12	45.00	0.86	4922	3594	19/10/92	PLANE 45-7
600288	288.43	10.72	45.00	-0.00	1811	1764	19/10/92	PLANE 45-8
					714	664	27/09/93	PLANE 45-8
					822	799	30/03/94	PLANE 45-8
600289	289.20	10.32	45.00	-0.86	4340	3911	19/10/92-20/10/92	PLANE 45-9
600290	289.97	9.92	45.00	-1.72	628	522	31/10/92	PLANE 45-10
					3092	1862	26/03/93-27/03/93	PLANE 45-10
600291	290.74	9.52	45.00	-2.58	2628	2497	28/10/92-03/11/92	PLANE 45-11
					1004	887	30/09/93	PLANE 45-11
600292	291.50	9.12	45.00	-3.43	926	870	28/10/92	PLANE 45-12
					2518	1683	28/03/93	PLANE 45-12
600293	292.27	8.71	45.00	-4.29	4431	3550	30/10/92-02/11/92	PLANE 45-13
600294	293.03	8.31	45.00	-5.14	3638	3083	27/10/92-28/10/92	PLANE 45-14
600295	293.79	7.90	45.00	-6.00	2580	2351	30/10/92	PLANE 45-15
					1526	1235	30/03/93	PLANE 45-15

TABLE B.9

178-22 OBSERVATIONS

ROR	R.A. (J2000)	Dec. (J2000)	Exp. (Total)	Exp. (Sel.)	Date	Target
200912	63.87	16.67	1658	1479.5	10/09/92	HYADES C
			23740	15615.6	26/02/93-03/03/93	HYADES C
200981	64.18	16.82	4495	3678.6	23/02/93-04/03/93	VLM HYADES 3
201316	64.37	20.58	4158	2356.3	14/02/93-15/02/93	LEER 1
201504	64.86	21.14	7671	7098.3	31/08/93-02/09/93	HD27295
200775	64.95	15.63	4096	3312.3	22/02/93-23/02/93	HYADES FIELD K1
200776	65.22	13.86	22995	21977.0	30/08/91-31/08/91	HYADES FIELD F1
200441	65.30	14.70	10987	6684.5	24/02/91	HYADES, POSITION 1
200442	65.30	17.53	19948	10074.5	24/02/91-27/02/91	HYADES, POSITION 2
201370	65.38	18.42	4977	3263.1	11/09/92	HYADES FIELD F4
			13662	11343.4	23/02/93-24/02/93	HYADES FIELD F4
201315	65.50	19.53	645	590.6	23/02/93	T TAU
			1545	1442.9	14/08/93-15/08/93	T TAU
700044	65.58	19.85	4704	2888.5	26/02/91-27/02/91	MSS0419+19
200020	66.21	15.10	40412	23226.9	27/02/91-01/03/91	HYADESFIELD
200777	66.40	15.94	16296	13433.3	30/08/91	Hyades field F2
201369	66.60	16.85	15551	13045.8	24/02/93-27/02/93	HYADES FIELD G1
201314	66.78	18.78	2693	2084.0	12/09/92	UX TAU
			1397	1323.3	24/02/93-26/02/93	UX TAU
200982	67.09	13.82	7727	5754.0	04/03/93-13/03/93	VLM HYADES 4
200083	67.15	16.97	2929	1226.4	25/02/91-27/02/91	VAN RHIJN 16
200576	67.15	19.18	1541	1245.6	12/03/92	EPSILON TAU
200942	67.21	13.05	7374	4868.8	09/09/92-10/09/92	79 TAU
200778	67.53	15.64	1920	1842.6	12/03/92	HYADES FIELD F3
201368	67.53	15.64	16606	11140.1	10/09/92-12/09/92	HYADES FIELD F3
200945	67.65	13.72	4101	2767.0	09/09/92	83 TAU
900353	67.85	17.96	7724	6367.3	21/02/93-24/02/93	L1551
200553	67.85	12.39	10961	9849.1	27/02/92-12/03/92	HYADES B
200911	67.85	12.39	17472	10987.0	09/09/92-11/09/92	HYADES B
			13766	9807.5	15/02/93-03/03/93	HYADES B
201313	68.07	18.03	4033	3852.6	10/09/92	V 826
200443	68.13	17.53	20074	12696.2	07/03/91-10/03/91	HYADES, POSITION 3
200444	68.13	14.70	14593	9900.1	06/03/91-07/03/91	HYADES, POSITION 4
201747	68.64	15.50	19618	18354.8	31/08/93-04/09/93	HYADES FIELD G2
200073	68.98	16.51	6833	3559.2	24/02/91	ALPHATAU

Appendix C: Reduction Scripts

Abstract

This appendix contains the description of a number of UNIX shell scripts that are useful for quasi-automating the ESAS data-reduction process. *These shell scripts should not be used until the use of the FORTRAN programs described in the previous section is well understood and a test reduction has been successfully completed.*

C.1. UNIX Scripts for Data Reduction

When reducing *ROSAT* data for diffuse background studies, it is often neccessary to execute the same program for each *ROSAT* band, typing in nearly the same long parameter lists multiple times. These scripts are intended to alleviate some of that tedium. However useful these scripts may be, they are not programmed with any semblance of elegance, and they can be difficult to read. Much of the difficulty arises from the need to feed to programs input parameters as if they were typed from the keyboard, with all the requisite carriage returns. The method for solving this problem is not elegant:

```
programname <<E
inputline1 [CR]
inputline2 [CR]
inputline3 [CR]
E
```

Here the "<<E" means to take all the text down to the matching "E" including carriage returns ("[CR]") as input. The "E" was an arbitrary choice, it could have been any character string that is unlikely to occur as a program parameter.

C.2. Prescription for Use

0.) Setup. I suggest creating a file called "reduce.log". The name is important; if it is not named properly the "cleanup" script will not work properly. The "reduce.log" file should contain the information as shown for a sample observation in Figure C.1. These lines can be copied from the "public_contents" file.

1.) The *initial* processing. The "initial" script executes every program necessary to create the observed light curve and the light curve of the scattered solar X-ray contamination.

2.) Fitting the LTE and SSX. The easiest way of fitting the LTE and SSX is to run the FORTRAN program RATE_FIT_AUTO. However, if you want to have a bit more involvement with the fitting process (which is laudable, and even recommended the first few times through) run RATE_FIT on band R4 with various orders of LTE polynomial and various orders of SSX scaling polynomial. Rather than running through all of these combinations by hand, let the computer do all the possible combinations and save plots of the results. This is the function of the "rate.fit.4" script. Once it has produced QDP format plot files of all of the possible combinations of SSX and LTE polynomial orders, I use IDL routines to review the plot files. You can then compare these results with that of RATE_FIT_AUTO.

Once you have decided which orders of polynomials to use for fitting the LTE and SSX, use the FORTRAN routine RATE_FIT to fit the other bands. Then check the output QDP plot files to check each band.

3.) The *middle* processing. The "middle" script casts the count images, the exposure images, and the scattered solar X-ray images.

4.) After-pulse fitting. As with the reductions unaided by scripts, run CAST_PART (setting afterpulse counts to zero) until it outputs the total number particle background counts; the total number of scattered solar X-ray counts can be found in the output from TILT, which was executed by the "middle" script. Then use the FORTRAN routine FIT_AP to determine the number of afterpulse counts. After fitting, I suggest saving the last several lines of output, those shown in Figure C.2, into a file named "fit_ap.log", so that it can be incorporated into the final reduction log by the "cleanup" script.

```
OBSERVATION_REQUEST_ID = "600057"
FOLLOWUP_INDEX = ""
PRINCIPAL_INVESTIGATOR = "LOOSE, DR, HANS-HERMANN"
INSTRUMENT_NAME = "PSPC B"
RIGHT_ASCENSION = " 10h 32m 31.20s"
DECLINATION = " 54d 24m 0.00s"
GALACTIC_LONGITUDE = "156d 12m 2.44s"
GALACTIC_LATITUDE = " 52d 48m 4.74s"
UT_START_TIME = "20-APR-1991 00:01:18"
UT_END_TIME = "21-APR-1991 00:26:12"
TOTAL_ACCEPTED_SECONDS = "3979"
```

Fig. C.1.— The header text to be saved in the log file.

```
6.0
22 23 6.000000 6.050000
CHISQ = 18.3, DOF = 19, REDCHISQ = 0.965
PB = 416.155 AP = 26.858
```

Fig. C.2.— Output from fit_ap to be saved in log file.

5.) The *final* processing. The "final" script casts the background images (i.e., runs CAST_PART) and calculates the count rate images.

6.) Cleanup. After finishing the reduction, there remain a large number of very small files that were used to transfer fit coefficients from one program to another, such as "rate_fit_lte.8.dat", "rate_fit_ssx_8.dat", and "T0.dat". The "cleanup" script tidies all of these data files away into the single file TRANSFER.BND, from which they can be re-extracted if neccessary. All of the ".log" files listed in Table C.2 are tidied away into the single file LOGFILE.

C.3. Scripts

The scripts and their usage are listed below in the order in which they are to be used.

C.3.1. initial

Purpose: to do all of the processing before editing the data and fitting the LTE and SSX contributions. This script executes the FORTRAN programs VALID_TIMES, RATE, and AO.

Usage: initial name gain

C.3.2. rate.fit.4

Purpose: to fit the LTE and SSX contributions to band R4. This script fits band R4 using increasing orders of polynomial to fit the LTE. It executes the fits using no SSX component (IS0 and IS1 set to zero), using only a scaling factor for the SSX component (IS0 variable, IS1 set to zero), and allowing a time variable SSX component (IS0 and IS1 both variable). Plots of the fits are placed in QDP format files named plot_4.n.0.qdp, plot_4.n.1.qdp, and plot_4.n.2.qdp for a fit to the LTE using up to nth order polynomials, and SSX fits as above. **This script is superceded by the FORTRAN routine RATE_FIT_AUTO, and is included here for pedagogical purposes only.**

Usage: rate.fit.4

C.3.3. middle

Purpose:to do all the processing after the LTE and SSX fitting, but before fitting the AP contribution. This script executes the FORTRAN programs LTE, CAST_DATA, CAST_EXP, TILT, and CAST_SSX.

Usage: middle name gain tilt

TABLE C.1

REDUCTION SHELL PARAMETERS

Name	Definition and Units
ap	the number of afterpulse counts in the exposure
gain	the gain state of the observation 1 high gain data (before 11 October 1991) 2 low gain data (after 11 October 1991) 3 high gain data, but using the R1L (R8) band
name	the root name of the data files
tilt	a flag denoting the need to run tilt 0 there were no measured solar photons (i.e. the IS0 and IS1 from RATE_FIT were both 0 for all bands) and thus tilt should not be run 1 tilt should be run

TABLE C.2

LOG FILES AND THEIR ORIGINS

Name	Source
reduce.log	created by hand
rate_fit.log	output of RATE_FIT
lte.log	output of LTE
tilt.log	output of TILT
fit_ap.log	created by hand from the output of FIT_AP
xxx_diag.out	created by CAST_DATA and augmented by CAST_PART
final_image.log	output of FINAL_IMAGE

C.3.4. final

Purpose: to execute all processing after fitting the AP contribution. This script executes the FORTRAN programs CAST_PART and FINAL_IMAGE.

Usage: final name gain ap

C.3.5. cleanup

Purpose: to consolidate into one archive file all of the transfer data files produced in the reduction process (such as ssx_x.dat, lte_x.dat). The final output file is TRANSFER.BND which, if executed as a shell script, upacks itself into all of the original files. (This is a neat trick learned from Kernighan & Pike (1984).) This script also takes all of the log files listed in Table C.2 and consolidates them into one file named LOGFILE.

Usage: cleanup

C.3.6. clearout

Purpose: to remove all files not neccessary for forming mosaics.

Usage: clearout

REFERENCES

Kernighan, B. W., & Pike, R. 1984, The UNIX Programming Environment (Prentice Hall)

Appendix D: Mosaicking

Abstract

The chapter describes the process of creating a mosaic from a number of overlapping *ROSAT* PSPC or HRI pointings. Whereas a previous chapter provided a theoretical basis for the method of mosaicking, this chapter provides a step-by-step prescription for using the FORTRAN progams developed by Kuntz and Snowden to make a mosaic. The programs described in this chapter, as well as this documentation, are avialable through the HEASARC.

D.1. Introduction

This chapter describes the FORTRAN programs in detail, as well as some UNIX scripts that make the mosaicking process less onerous.

D.2. Accessing and Compiling

D.2.1. Retrieving Files

Most of the neccessary files will have been acquired with the data reduction software (as described in Appendix B of Part I). There are a few additional data files that are needed which are to obtained through other sites.

The ROSAT *All-Sky Survey II:* The *ROSAT* All-Sky Survey II (Snowden et al, 1997) is now available. The maps can be retreived from

http://www.rosat.mpe-garching.mpg.de/survey/sxrb/12/fits.html

The ROSAT *Bright Source Catalogue:* The *ROSAT* Bright Source Catalogue can be retrieved via Internet browser from

http://www.rosat.mpe-garching.mpg.de/survey/rass-bsc/rass-bsc-1.2rxs.cat.gz

or may be obtained by anonymous ftp from ftp.rosat.mpe-garching.mpg.de, where it can be found in

archive/survey/rass-bsc/rass-bsc-1.2rxs.cat.gz.

D.2.2. Compiling

Before compiling the mosaicking software, a few directory names will need to be changed. In addition to those listed in Part I, the RASSTR variable in *get_rass_mosaic.f*, *get_rass_point.f* and *offset_dc.f* will need to be changed to point to the directory containing the *ROSAT* All-Sky Survey images. Further, in the program *get_rass_bsc.f* the CATFIL variable will need to be changed to point to the file containing the Bright Source Catalogue.

UNIX: This release of the mosaicking software includes the file *make.mosaic* which is a standard UNIX makefile. The architecture dependent FITSIO filename to be replaced is *fitsdec.for*. The EXE variable should be changed to contain the name of the directory into which you wish the executables to be placed. It will also be neccessary to edit the FFLAGS variable for your system.

VMS: The package can be compiled using the VAX script *mosaic.lnk*.

D.3. Prescription

This is a brief description of the process of making a mosaic, listing the FORTRAN routines in the Extended Source Analysis Software (Kuntz & Snowden 1998) to be used and the order in which to apply them. For detailed description of what inputs and files each FORTRAN routine requires, and suggested settings for some of the input parameters, see the program descriptions in Appendix D.5.

When forming mosaics at $\frac{1}{4}$ keV it is important to remember to reduce all of the component pointings using the same band, that is, do not attempt a mosaic where some of the pointings have band R1L and others band R1. Unless all of the component pointings were taken in the high gain mode, reduce the high gain observations with the low gain band definitions.

The mosaicking software uses the count files (PSPC: *b_n.fits*, HRI: *counts.fits*), exposure files (PSPC: *expose_n.fits*, HRI: *expose.fits*), and background files (PSPC: *back_n.fits*, HRI: *back.fits*), rather than the final products of the individual exposure reduction (PSPC: *rate_n.fits*, HRI: *rate.fits*). The object of the mosaicking software is to produce four mosaics. The first three are analogous to the count, exposure, and background images used in the individual exposure reduction. The fourth mosaic is the LTE offset mosaic. These four mosaics can then be combined analogously to the individual exposure images,

$$rate = \frac{counts - background - LTEoffset}{exposure}. \tag{D.1}$$

Assuming that the uncertainty in the model background counts is much less than $\sqrt{counts}$,

$$uncertainty = \frac{\sqrt{counts}}{exposure} \tag{D.2}$$

The mosaicking software will produce a mosaic in a zenith equal-area (ZEA) projection[1], one of the standard projections of the FITS format (Greisen & Calabretta 1993)[2]. This projection has the advantage of preserving the angular sizes of features, and thus allowing simple computation of physically meaningful quantities directly from maps. (Each pixel has the same solid angle, though not the same shape on the sky.) The projection can be in one of three coordinate frames: equatorial, ecliptic, or galactic.

Listed at the end of the description of each step, if appropriate, is the name of a useful UNIX shell script for executing that step in a quasi-automated way.

0.) Reduce the Individual Pointings. Once the individual pointings are reduced, place each in its own directory, and make sure that the count, exposure, and background files have their standard names: *b_n.fits*, *expose_n.fits*, and *back_n.fits* for the PSPC, *counts.fits*, *expose.fits*, and *back.fits* for the HRI. Figure D.1 depicts the necesary directory structure. Create a file named *dir.dat* containing the path name of all the directories, one per line. For UNIX systems, make sure that the name of each directory is terminated with a "/".

1.) Fix Broken Exposures. A "broken exposure" is a set of (sub)exposures with exactly the same pointing direction. This is often the result of an observation being scheduled over two or more half-year observing periods, but can be multiple observations proposed for the same target (e.g. SN 1987a) and processed with the same nominal pointing direction. In order to detect point sources to the faintest possible limit, the various sub-exposures should be summed, that is, the count files (*b_n.fits* or *counts.fits*), the exposure files (*expose_n.fits* or *expose.fits*), and the background files (*back_n.fits* or *back.fits*) all need to be summed over the subexposures for each band of interest. The summation can be accomplished with the program FIX_BREAK, which is described in Part I. Two exposures that are not part of a single observation should also be "fixed" so long as they have exactly the same pointing direction. The best directory structure to adopt for broken exposures is shown in Figure D.1. Remember to update the *dir.dat* file accordingly.

The resultant "summed exposure" should be used for source detection, and can be used to form the mosaic *if the mask for the summed exposure is formed from the sum of the exposure files.*

Useful UNIX shell script: add.obs.

2.) Detect Point Sources. As has been noted above, the detection of point sources in the mosaic is actually a multiple step process. The first step is to detect the point sources in each exposure. In the case of broken exposures, detect the point sources in the summed exposure, not in the subexposures. The detection of point sources is done by the FORTRAN routine DETECT by a sliding box method. At every point, the counts within 1.5 PSF radii are compared to the counts within an annulus from 1.5

---

[1] If, in a spherical coordinate system, a point has a zenith angle, azimuthal angle coordinate (θ, ϕ), then the map coordinate of the point, in the polar coordinates (radius, angle) will be (scaling factor $\sqrt{2(1-\sin\theta)}$,ϕ). See (Greisen & Calabretta 1993) for a more complete description. The advantages of this projection for studies of the diffuse background are relatively low distortion over moderate angular scales and pixels having equal solid angles.

[2] Although this software follows the standards, do not expect other software to be so careful. For example, ZEA projection images including a pole will not have the correct coordinates when displayed in SAOIMAGE.

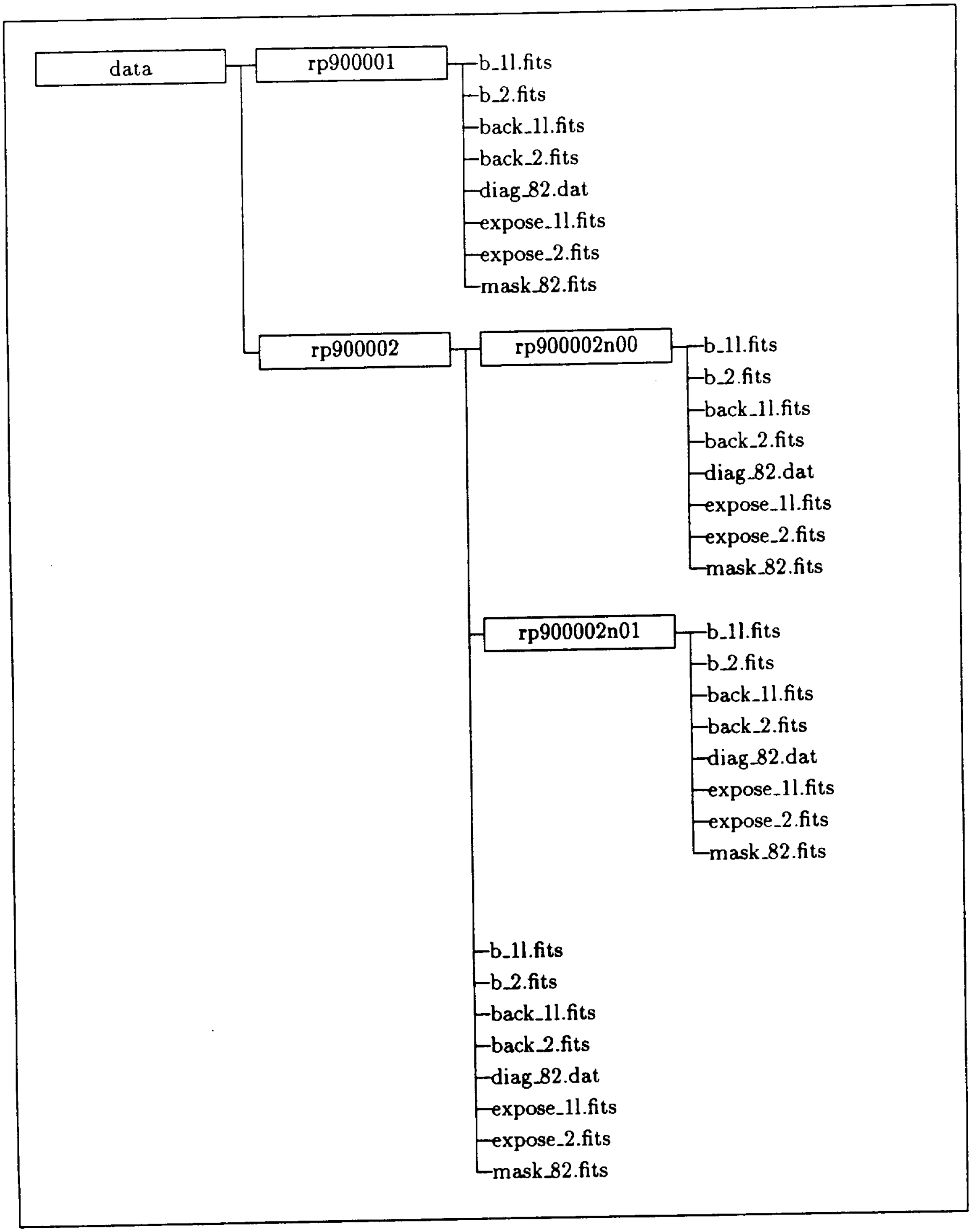

Fig. D.1.— A sample directory tree for a mosaic of the R11 and R2 bands made from two exposures. Exposure rp900002 contains two subexposures, rp900002n00 and rp900002n01. The image files in the directory rp900002 contain the sums of the images in the subdirectories, and will be used to create the mosaic.

to 2.5 PSF radii to determine the statistical significance. If the statistical significance is greater than that set by the user (typically 4σ, with no minimum number of counts needed to form a source), then a point source is "detected".

The DETECT routine automatically forms a image mask eliminating the point sources. The mask files created at this point will be called the "local" mask files as they are based on local detections using the individual images.

The suggested parameter settings are given in Table D.1. Point source detection is usually executed on wide-band images in order to have the highest count rates, and thus the lowest detection limit. The two PSPC bands usually used are R1L2 and R47.

Useful UNIX shell script: multi.detect.

3.) Determine the Point Source Detection Limits. Produce a map of the point-source detection limit over the mosaic. This task is accomplished with the FORTRAN routine PS_LIMIT. *Nota bene:* To determine the point-source limit at a given position the routine uses the mean count rate for the pointing. If there are a large number of small point sources, the mean count rate may be artificially raised, thus making the calculated point source detection limit somewhat worse than the true point source detection limit. Unless there are large bright features in the mosaic, we recommend *not* using a mask for this step.

4.) Merge the Point Source Lists. Reject false detections and low quality duplicate detections, where the quality is based upon the point source detection limit at the position of the point source. The FORTRAN routine MERGE_DETECT reads the point source detection lists for all of the exposures and rejects detections on the basis of the point source detection map produced in step 3. Accepted detections are kept in a "master list",

sources_accept_nm.fits.

Nota bene: Check the images of the "rejected" point sources for possible problems (see §2.5).

5.) Mask Out the Point Sources. Create masks for all of the exposures using the "master list" of detections, using the FORTRAN routine MASK. Specify zero as the minimum count rate (for reasons that will soon become apparent). The masks formed in this step will be called "global" mask files since they use information from the entire mosaic. If the region includes bright areas of extended emission, they should be masked out for the determination of the relative LTE offsets. The FORTRAN routine MAKEMASK allows the user to produce modified masks.

6.) Cast Images into the Mosaic Projection. Map the counts, exposures, and background counts from the projection of the individual exposures into the mosaic projection using the FORTRAN routine MERGE_RAW[3]. The units of the output images will be *counts*, *seconds*, and *counts* for the count, exposure, and model background mosaics, respectively.

If you do not want point sources to appear in your final mosaic, you should use the global mask files when you recreate the count, exposure, and background mosaic. If you are in pursuit of a pretty picture, and point sources are not important one way or the other, then it is a good idea to remove them. Due to the position dependent PSF, point sources in the regions of overlap can develop a complicated core-halo structure which, since is does not occur everywhere in the mosaic, can be distracting and/or confusing.

Useful UNIX shell script: merge.comp.

7.) Determine the LTE Offsets. Although much of this document is devoted to the measurement of the LTE offsets, the same percentage of time need not be devoted to the actual process of calculation. How the offsets are determined depends upon the *ROSAT* detector used.

PSPC (if the *RASS* is available): For programming reasons, the process of determining the offsets for the PSPC is divided into several steps.

7a.) Extract Sources from the BSC. As described above, when one compares a pointing to the *RASS*, it is essential to have removed point sources from the pointing to the same level as have been removed from the *RASS*. Create a list of the sources removed from the *RASS* by extracting those sources from the *ROSAT* Bright Source Catalogue using the FORTRAN routine GET_RASS_BSC.

---

[3] This is a change in name since the previous version due to UNIX having a *merge* command.

TABLE D.1
SUGGESTED DETECT/MASK PARAMETERS

Detector	Band	Significance (Sigma)	Count Rate (cnts/s)	Exclusion Radius (PSF Rad.)	Minimum Radius (Pixels)
PSPC	R1L2	4	0	1.5	8
PSPC	R47	4	0	1.5	1
HRI		4	0	2	3
BSC	R12		0.025	2.0	14
BSC	R47		0.04	2.0	14

7b.) Mask the BSC Sources. To form image masks removing the BSC sources, use the FORTRAN routine MASK. The routine will query for the minimum count rate for sources to be removed, these values are listed in Table 3.1 for various bands. By specifying a non-zero rate, the routine knows to put the masks in files named *bsc_mask_n.fits* rather than overwriting the standard mask files.

7c.) Calculate the Direct-Comparison (DC) LTE Offsets. For each energy band compare each pointing to the *RASS* and calculate the mean difference, as described in § 2.1. This task is accomplished by the FORTRAN routine OFFSET_DC. This routine produces the file *offset_dc_n.out*, which is used in the next step. The routine queries for a mask file, use the masks produced in the previous step. *Nota bene:* This routine produces many small FITS files in the data subdirectories (*pntd_rate_n.fits, pntd_sig_n.fits, pntd_mask_n.fits, rass_rate_n.fits,* and *rass_sig_n.fits* for each band for each pointing) which can consume vast amounts of space. They can be deleted after being used for diagnostic purposes.

7d.) Calculate the Weighted Comparison (WC) LTE Offsets. For each energy band, determine the count rates in the exposure overlap regions, and solve for the LTE offsets as described in §2.3. This is accomplished using the FORTRAN routine OFFSET. The routine will query for image masks, use the standard masks (*mask_n.fits*), not the masks using only the BSC point sources. The results will be stored in ASCII files.

Useful UNIX shell script: solve.offset.

PSPC (if the *RASS* is unavailable): The process of determining the LTE offsets for the PSPC when the *RASS* is not available is much more simple, though one should be cautious of the results (as per § 2.2 above).

7.) Calculate the Self-Consistent (SC) LTE Offsets. This task is accomplished with the FORTRAN routine OFFSET_SC. Once the the program has finished, rename the file *offset_sc_n.out* to match the output of the FORTRAN routine OFFSET, *offset_n.out*.

HRI: The process of determining the LTE offsets for the HRI is much simpler as there is no good way of direct comparison with the *RASS*, which was created with the PSPC.

7.) Calculate the Self-Consistent (SC) LTE Offsets. This task is accomplished with the FORTRAN routine OFFSET_SC. Once the the program has finished, rename the *offset_sc_n.out* file to match the output of the FORTRAN routine OFFSET, *offset_n.out*.

Useful UNIX shell script: solve.hri.off.

8.) Create Mosaic of LTE Offsets Create a mosaic image of the LTE offset counts using the FORTRAN routine MERGE_OFFSET. The units of this mosaic will be *counts*.

Useful UNIX shell script: merge.offset.

9.) Calculate Rate Calculate the final rate and significance images (units will be counts s^{-1} $arcmin^{-2}$) using the FORTRAN routine MERGE_IMAGE. As with the FINAL_IMAGE routine, images can be made from a range of energy bands as well as from a single energy band.

Useful UNIX shell script: merge.image.

D.3.1. Further Refinements

Those who would apply the mosaicking software to fields at high galactic latitude or fields with low absorbing columns will find a few more complications.

Extended Objects such as galaxy clusters may or may not have been detected by the point source detection algorithm, but in any case, will not be sufficiently masked. Many of these regions will only be recognizable in the final rate images. Therefore, one must make the mosaic *interatively*. Once the rate image has been created, determine the position of the centers of these objects and the radius of the region which they effect, both measures typically being in mosaic pixels. Convert the positions to decimal degrees in whatever coordinate system you are using, and create a detection file of the same format as that produced by DETECT or MERGE_DETECT. Then use the MASK routine to create a new set of extended source masks that include only these objects. Remember, the MASK routine expects a radius in pixels, not the mosaic pixels, but pixels of the original pointings (14.'947). The extended source masks can then be multiplied by the regular masks, using ROARITH, to get the mask to be used when calculating offsets. It may also be a good idea to use the extend source mask files to improve the *bsc_mask_nn.fits* masks. Then one must remerge the components and recalculate the offsets.

Given that you will have created a rate mosaic to detect the extended sources, one may as well improved the point source removal before remerging the components. Use BETTER_LIMIT to calculate a better value for the point source detection limit, and use its output to re-run MERGE_DETECT. (You will have to do some renaming of files so that MERGE_DETECT will be able to use the output from BETTER_LIMIT.)

D.4. A Final Word

The software described in this document was developed over several years by S. L. Snowden in support of the *ROSAT* project. Much of the mosaicking software has been modified by K. D. Kuntz in the process of his dissertation work. Although a great deal of effort has been expended to make sure that the software behaves as described, the software changed a great deal in the process of writing this document. Therefore, do not be surprised if it does not act *exactly* as advertised.

D.5. Program Descriptions

The programs in this section are used to mosaic individual observations (processed by the software in § 3) into larger area maps. They require that the names for the fits files produced by the reduction software to remain unchanged and that the files are found in separate directories. Specifically, for the PSPC, they use the *b_n.fits*, *expose_n.fits*, *back_n.fits*, and *mask_m.fits* files where n is the band number and m is a band or band range (e.g., *b_5.fits*, *expose_5.fits*, *back_5.fits*, and *mask_47.fits*). For the HRI, they use the *counts.fits*, *expose.fits*, *back.fits*, and *mask.fits* files.

The output files for the mosaic programs are in the zenith equal-area projection (ZEA). For small regions, there is little difference between the ZEA projection and the tangential projection ($\sim 1\%$ at a radius of 9°). If your favorite image display package doesn't support ZEA, the header information can be changed from ZEA to TAN.

The programs are listed in alphabetical order.

TABLE D.2
MOSAICKING PROGRAMS

Program	Description
PS_LIMIT	determines the point source detection limit over the mosaic
MERGE_DETECT	merges point source detection files for all pointings
MASK	masks out the point sources from individual exposures
MERGE_COMP	merges event, exposure, or background maps into a mosaic
OFFSET_DC	determines the mean difference between *RASS* and pointing count rates
OFFSET_SC	determines the relative offsets in the zero levels by comparing the overlap regions between pointings (Obsolete)
OFFSET	combines the output of OFFSET_DC and the method of OFFSET_SC to determine absolute LTE offsets
MERGE_OFF	uses OFFSET output to create an offset count mosaic
MERGE_IMAGE	same as FINAL_IMAGE but runs on mosaic images
ADAPT_MERGE	same as ADAPT but runs on mosaic images

TABLE D.3
FILES PRODUCED BY MOSAICKING PROGRAMS

Name	Producing Program	Can Be Deleted
Main Directory		
back_n.fits, back.fits	MERGE_COMP	
counts_n.fits, counts.fits	MERGE_COMP	
covariance_n.fits	OFFSET	√
covariance_sc_n.fits	OFFSET_SC	√
dir.dat		
expose_n.fits, expose.fits	MERGE_COMP	
mask_n.fits, mask.fits	MERGE_IMAGE	
off_n.fits	MERGE_OFFSET	
offset_dc_n.out	OFFSET_DC	√
offset_dc_n.dat	OFFSET_DC	√
offset_n.out	OFFSET	
offset_n.dat	OFFSET	√
offset_sc_n.out	OFFSET_SC	
offset_sc_n.dat	OFFSET_SC	√
psexp_nm.fits	PS_LIMIT	
psfld_nm.fits	PS_LIMIT	
pslim_nm.fits	PS_LIMIT	
psrad_nm.fits	PS_LIMIT	√
rate_n.fits	MERGE_IMAGE	
rej_xxx_acc.fits	MERGE_DETECT	√
rej_xxx_rej.fits	MERGE_DETECT	√
sig_n.fits	MERGE_IMAGE	
sources_accept_nm.dat	MERGE_DETECT	
sources_duplic_nm.dat	MERGE_DETECT	√
sources_reject_nm.dat	MERGE_DETECT	
Individual Pointing Directories		
diag_nm.dat	DETECT	
mask_nm.fits	DETECT	
pntd_mask_n.fits	OFFSET_DC	√
pntd_rate_n.fits	OFFSET_DC	√
pntd_sig_n.fits	OFFSET_DC	√
rass_rate_n.fits	OFFSET_DC	√
rass_sig_n.fits	OFFSET_DC	√

[a] A "√" indicates a file that is output for diagnostic purposes that need not be retained for continued analysis.

ADAPT_MERGE HRI, PSPC

To smooth the full 512 × 512 mosaicked images with an adaptive filtering algorithm. For each unmasked pixel, the program will include neighboring pixels within a circle of increasing radius until a selected number of counts is reached. The original pixel is then given the average surface brightness for the pixels within the circle.

Interactive Input

1) Coordinate control – *n*
   The coordinate system for the mosaic image. Enter 1 for ecliptic, 2 for equatorial, or 3 for galactic coordinates.
2) Number of counts for smoothing – *n*
   This is the number of counts that the adaptive filter will use as its smoothing kernel.
3) Fractional limit for masking – *f*
   ADAPT_MERGE will take the mask (either input file or exposure map), determine the average non-zero value of the mask, and mask out any pixels where the mask value is less than the average mask value multiplied by the fraction. Values of 0.02 for PSPC data and 0.2 for HRI data are reasonable when using exposure maps.
4) Band range – *n1, n2*
   The range of bands to be smoothed for the image. For the PSPC, e.g., enter 2 2 for the R2 band, 4 5 for the R45 ($\frac{3}{4}$ keV) band, 8 2 for the R1L2 band, or 4 7 for the R47 band covering bands R4, R5, R6, and R7. For the HRI enter 0 0.
5) Mask name – *file name*
   Enter the file name of an image to use as a mask. Enter a carriage return to use the exposure map.

File Input

1) Observation data set FITS files – none
2) Images – **PSPC:** *counts_n.fits, back_n.fits, expose_n.fits,* **HRI:** *counts.fits, back.fits, expose.fits*
   These are the count, model background count, and exposure images. The PSPC files must refer to individual bands. Therefore, MERGE, OFFSET, and MERGE_OFF must be run separately for all desired bands before ADAPT_MERGE is run.
3) ASCII files – none

ASCII File Output

None

Image Output

1) Smoothed image – PSPC: *smooth_n.fits*, HRI: *smooth.fits*
   A FITS file of the smoothed image where for the PSPC output *n* is the band or band range. The file contains the count rate in units of counts s^{-1} $arcmin^{-2}$.

Screen Output

Program diagnostic information.

To determine the point source detection limit at every point in a mosaic. For every pointing included in the mosaic, BETTER_LIMIT casts the exposure map into the mosaic coordinate system, determines the size of the PSF at each pixel, and calculates the point source detection limit at that pixel for that pointing. This is then compared to the point source detection limit at that pixel for all other pointings, and the best (i.e., lowest) limit is chosen.

This routine is better than PS_LIMIT, but requires a measurement of the true cosmic background count rate over the mosaic. Since PS_LIMIT uses the mean count rate (including point sources) it will produce point source detection limits that are somewhat higher than the actual limits, as can be seen by comparing Figure D.2 with Figure D.7. The output of MERGE_DETECT is normally very little changed by use of BETTER_LIMIT rather than PS_LIMIT.

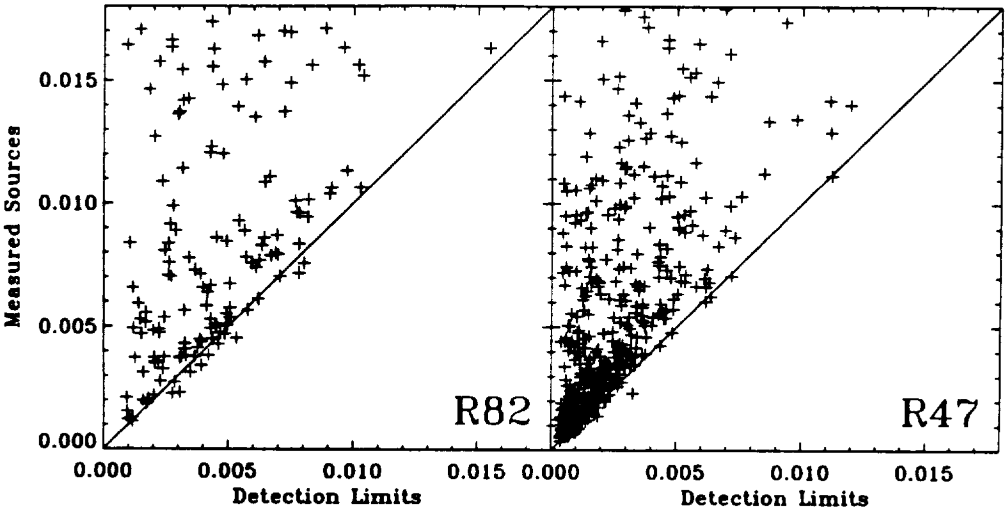

Fig. D.2.— A comparison of measured count rates and the calculated point source detection limit for BETTER_LIMIT. The few points that lie below the line (point sources that lie below the local point source detection limit) are due to the local cosmic background rate being below the mean cosmic background rate. See Figure C22 for a similar plot for PS_LIMIT.

Interactive Input

1) Coordinate control – *n*

Set the coordinate system for the mosaic image. Enter 1 for ecliptic, 2 for equatorial, or 3 for galactic coordinates. Should be identical to that used in MERGE_COMP.

2) Central coordinates – *f1, f2*

The central coordinates for the mosaic in decimal degrees in the coordinate system selected in 1). Should be identical to those used in MERGE_COMP.

3) Scale factor for mosaic – *f*

The pixel size for the mosaic in arc minutes. Should be identical to that used in MERGE_COMP.

4) Radius limit – *f*

The radius of the region in the individual pointings, in arc minutes, to be considered (applied to the sky image rather than in detector coordinates). This value should include the entire field as the extreme edge of one field may still be better than the center of another. For the PSPC a limit of 60′ will include the entire field; for the HRI *xx*′ Note that this is not the same value used for casting the mosaics.

5) Band range – *n1, n2*
   The range of bands to be combined for the final image (i.e., "2 2" will produce band R2, "4 5" will produce band R45 as a $\frac{3}{4}$ keV band, and "8 2" will produce band R1L2, "4 7" will produce band R47 combining the bands R4, R5, R6, and R7). Enter "0 0" for HRI data.

6) Cosmic background count rate – *f*
   The cosmic background rate in counts s^{-1} $arcmin^{-2}$.

7) Statistical significance and count-rate threshold – *f1, f2*
   The statistical significance can be entered either as the Poisson (i.e., $3\sigma = 0.9973002$) probability or the value in sigmas (allowed values: 1., 2., 2.5, 3., 3.5, 4., 4.5, 5., 5.5). The count-rate threshold in units of counts s^{-1} may be set to zero.

8) Mask file name for masking of the data – *filename*
   The data from each pointing will be masked using files with the input file name in the pointing directory. If no additional masking is desired, enter a carriage return.

File Input

1) Images – PSPC: *expose_n.fits* and a mask if desired from each directory listed in dir.dat, HRI: *expose.fits* and a mask if desired from each directory listed in dir.dat

2) ASCII files – *dir.dat* or *dir_add.dat*
   The file dir.dat contains a list of directory path names for the various observations to be mosaicked. This allows BETTER_LIMIT to find the observations to be mosaicked from the directory where it is being run.

ASCII File Output

None

Image File Output

1) The FITS file *pslim_n.fits*, the best point source detection limit at each pixel in the mosaic. The units are counts s^{-1}.
2) The FITS file *psfld_n.fits*, the number (line number in the dir.dat file) of the pointing containing the best point source detection limit at each pixel in the mosaic.
3) The FITS file *psexp_n.fits*, the length of the exposure corresponding to the best point source detection limit.
4) The FITS file *psrad_n.fits*, the PSF radius corresponding to the best point souce detection limit. The units are arcminutes.

Screen Output

Program diagnostic output.

To extract from the *ROSAT* Bright Source Catalogue (BSC) a list of all of the sources in a mosaic.

Interactive Input

1) Band range - *n1, n2*
   The range of bands from which the point source count rate is to be calculated
2) Coordinate control - *n*
   Set the coordinate system for the mosaic image. Enter 1 for ecliptic, 2 for equatorial, 3 for galactic coordinates.
3) Mosaic image name - *file name*
   The name of a mosaic file image (can be counts, exposure, background, etc., so long as the header has the correct information for the mosaic.)

File Input

1) Images - as selected above.

ASCII File Output

1) *bsc_extract_n.dat* - A list of point sources in nearly the same format as produced by the DETECT routine.

Image File Output

None.

Screen Output

Program diagnostic output.

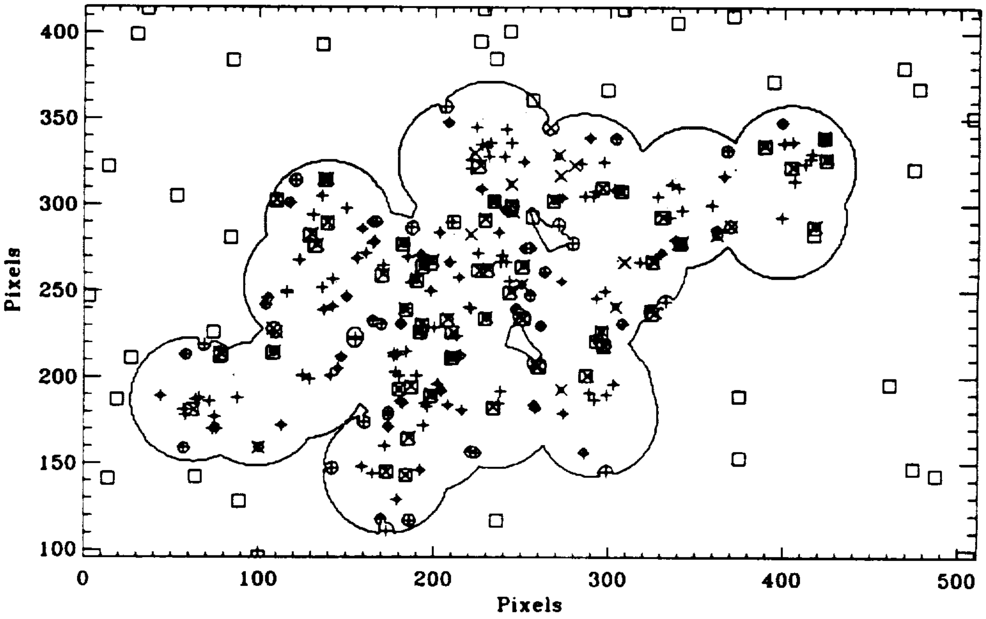

Fig. D.3.— Detected point sources in a mosaic compared to point sources in the Bright Source Catalogue. The detections were made in the R1L2 band. □: BSC detections over 0.025 counts s^{-1}, ×: detections from individual pointings over 0.025 counts s^{-1}, +: detections from individual pointings under 0.025 counts s^{-1}. Quasi-circular and irregular regions are previous removed sources.

GET_RASS_MOSAIC

To determine the offset between a mosaic and the *RASS*. This program determines which *RASS* panel has its center closest to the mosaic, and recasts the mosaic into the *RASS* coordinate system. For all pixels occupied by the mosaic, the program determines the mean and standard deviation of the count rate of the *RASS*. All *RASS* pixels exceding a user specified number of standard deviations from the mean are discarded. The offset,

$$offset = \overline{mosaic - RASS} \tag{D.3}$$

is calculated from the remaining pixels.

Interactive Input

1) Band to be compared - *n*

1a) R1L/R1 band ratio - *f*
If the band to be compared is R1L, then the R1L/R1 band ratio is needed to convert the *RASS* flux to the same band as the mosaic.

2) Sigma limit - *f*
The value in standard deviations over which pixels are discarded.

3) Coordinate control - *n*
Set the coordinate system for the mosaic image. Enter 1 for ecliptic, 2 for equatorial, 3 for galactic coordinates.

File Input

1) Images - *counts_n.fits*, *back_n.fits*, *expose_n.fits* for the moasic, *gxxxxxxrn.fits* and *gxxxxxxsn.fits* for the *RASS*.

ASCII File Output

None

Image File Output

1) *mosc_rate_n.fits*
A 512×512 FITS image in the *RASS* coordinate system containing the mosaic count rate.

2) *mosc_sig_n.fits*
A 512×512 FITS image in the *RASS* coordinate system containing the mosaic count rate uncertainty.

3) *mosc_mask_n.fits*
A 512×512 FITS image in the *RASS* coordinate system containing the mosaic mask.

Screen Output

Diagnostic output:

```
X Limits:          234          287
Y Limits:          129          161
```

The extent in *RASS* pixels of the mosaic.

```
Number of pixels in field:     1062.000
Number of pixels discarded:     2.000000
```

The number of *RASS* pixels in the mosaic, and the number of those discarded for being too far from the mean.

```
Offset :     53.01571
```

```
   +/- :     2.079403
RASS    :     189.9938
   +/- :     1.793882
Pointed:     213.7634
   +/- :    0.4400081
RASS rate has been corrected from
band R1 to band R1L using R1L/R1=   0.8227000
```

The $\overline{mosaic - RASS}$, $\overline{RASS}$, and $\overline{mosaic}$ respectively.

GET_RASS_POINT

To determine the offset between a single pointing and the *RASS*. This program determines which *RASS* panel has its center closest to the pointing, and recasts the pointing into the *RASS* coordinate system. For all pixels occupied by the pointing, the program determines the mean and standard deviation of the count rate of the *RASS*. All *RASS* pixels exceding a user specified number of standard deviations from the mean are discarded. The offset,

$$offset = \overline{pointing - RASS} \tag{D.4}$$

is calculated from the remaining pixels.

Interactive Input

1) Band to be compared - *n*

1a) R1L/R1 band ratio - *f*
If the band to be compared is R1L, then the R1L/R1 band ratio is needed to convert the *RASS* flux to the same band as the pointing.

2) Sigma limit - *f*
The value in standard deviations over which pixels are discarded.

3) Mask file name – *file name*
The data will be masked using files with the input file name in the individual directories. The mask files must be in the same directories as the data files. If no additional masking is desired, enter a carriage return.

File Input

1) Images - *b_n.fits*, *back_n.fits*, *expose_n.fits* for the moasic, *gxxxxxxrn.fits* and *gxxxxxxsn.fits* for the *RASS*.

ASCII File Output

None

Image File Output

1) *pntd_rate_n.fits*
A 41×41 FITS image in the *RASS* coordinate system containing the mosaic count rate.

2) *pntd_sig_n.fits*
A 41×41 FITS image in the *RASS* coordinate system containing the mosaic count rate uncertainty.

3) *pntd_mask_n.fits*
A 41×41 FITS image in the *RASS* coordinate system containing the mosaic mask.

4) *rass_rate_n.fits*
A 41×41 FITS image in the *RASS* coordinate system containing the mosaic mask.

5) *rass_sig_n.fits*
A 41×41 FITS image in the *RASS* coordinate system containing the mosaic mask.

It should be noted that for pointing band R1L, the *RASS* images will be band R1, will not be scaled to band R1L, and will be named rass_xxxx_1.fits.

Screen Output

Diagnostic output:

```
X Limits:          234          287
Y Limits:          129          161
```

The extent in *RASS* pixels of the mosaic.

```
Number of pixels in field:     96.00000
Number of pixels discarded:    0.0000000E+00
```

The number of *RASS* pixels in the mosaic, and the number of those discarded for being too far from the mean.

```
Offset :     21.96925
   +/- :     6.681984
RASS   :     198.4002
   +/- :     5.841153
Pointed:     172.1212
   +/- :     1.135728
RASS rate has been corrected from
band R1 to band R1L using R1L/R1=    0.8227000
```

The $\overline{mosaic - RASS}$, $\overline{RASS}$, and $\overline{mosaic}$ respectively.

MASK

To use the list of "accepted" detections to mask point sources from pointings.

Interactive Input

1) Band range – *n1, n2*
   The range of bands over which the point sources were detected.
2) Point source list file – *file name*
   The name of the file containing the point sources to be masked, usually the file *sources_accept_n.dat*.
3) Masking radius – *f*
   The radius (in PSF radii) to be removed around point sources.
4) Minimum mask size – *n*
   The minimum radius, in pixels, to be removed around point sources.
5) Minimum count rate – *f*
   The minimum count rate to be accepted as a source. This value is of particular value when creating masks from source lists extracted from the *ROSAT* Bright Source Catalogue. If the minimum count rate is not zero, the output mask will be in *bsc_mask_n.fits* rather than in *mask_n.fits*.

File Input

1) Fixed input – the *sources_accept_n.dat* file produced by MERGE_DETECT.

ASCII Output

None

Image Output

A mask files, *mask_n.fits* or, if the minimum count rate is not set to zero, *bsc_mask_n.fits*.

Screen Output

For each source masked from the pointing, a line such as

```
1   65.67660       15.05800          381        247         14
```

will appear. It contains the number of the field in which the point source had its best detection, the R.A. and dec. of the point sources, the X and Y pixel position of the source in this pointing, and the mask radius in pixels.

To merge the various component (count, background, and exposure) images from separate observations of different pointings into a large-area mosaic.

Interactive Input

1) Coordinate control – *n*
   Set the coordinate system for the mosaic image. Enter 1 for ecliptic, 2 for equatorial, or 3 for galactic coordinates.
2) Central coordinates – *f1, f2*
   The central coordinates for the mosaic in decimal degrees in the coordinate system selected in 1).
3) Scale factor for mosaic – *f*
   The pixel size for the mosaic in arc minutes.
4) Radius limit – *f*
   The radius of the region in the individual pointings, in arc minutes, to be cast into the mosaic (applied to the sky image rather than in detector coordinates). For the PSPC a limit of 53′ serves reasonably well to exclude the worst problems caused by the large point response function at large off-axis angles. For the HRI typically the entire field can be used.
5) Band to be cast – *n*
   The program will cast only one band at a time. Enter 0 for HRI data.
6) Component to be cast – *n*
   The program will cast only one component at a time. Enter 1 for counts, 2 for exposure, or 3 for background counts. For the PSPC, the program FINAL_IMAGE must be run on the individual bands to create the back_n.fits files for the background counts. All files to be cast must have the same names as they were labelled when generated, i.e., b_n.fits, expose_n.fits, and back_n.fits. Counts.fits, expose.fits, and back.fits for HRI data.
7) Mask file name – *file name*
   The data will be masked using files with the input file name in the individual directories. The mask files must be in the same directories as the data files. If no additional masking is desired, enter a carriage return.
8) Add flag – *n*
   Enter 1 to add to an existing image, 0 to cast a new image. If data are to be added to an existing image then MERGE_COMP will query for the file name. If data are to be added to an existing image the new directories must be listed in the file dir_add.dat.

File Input

1) Images – PSPC: *b_n.fits* or *back_n.fits* or *expose_n.fits* and a mask if desired from each directory listed in dir.dat. HRI: *counts.fits* or *back.fits* or *expose.fits* and a mask if desired from each directory listed in dir.dat
   The program will query for the component to be mosaicked and a mask name.
2) ASCII files – *dir.dat* or *dir_add.dat*
   The file dir.dat contains a list of directory path names for the various observations to be mosaicked. This allows MERGE_COMP to find the observations to be mosaicked from the directory where it is being run.

ASCII File Output

None

Image Output

1) Mosaicked image – PSPC: *counts_n.fits* or *expose_n.fits* or *back_n.fits*, HRI: *counts.fits* or *expose.fits* or *back.fits*

The output file depends on the chosen component. Note that for PSPC data expose_n.fits and back_n.fits have the same names as the files for the individual observations. For the HRI all files have the same names.

Screen Output

Program diagnostic information.

To merge the lists of point source detections made in the separate pointings, discarding duplicate detections.

Method

This process is accomplished in three steps. First, every point source detection is checked to see if it was made in the pointing which has the best point source detection limit at the position of the detection. If it is, the detection is "accepted" and is output to the file *sources_accept_n.dat*, if not, the detection is rejected. Second, the list of rejects is compared to the list of accepted detections. If the reject falls within the "match radius" (a user defined multiple of the PSF radius) of an accepted detection (or an accepted detection falls with that same multiple of the PSF radius of the rejected detection) the detection is considered a "duplicate" detection and is output to the file *sources_duplic_n.dat*. Third, rejected detections that do not "duplicate" accepted detections are output to the file *sources_reject_n.dat*. Figure D.4 shows the distribution of the three types of detections over a mosaic. One can see that a "match radius" of 1.5 PSF provides reasonable matches.

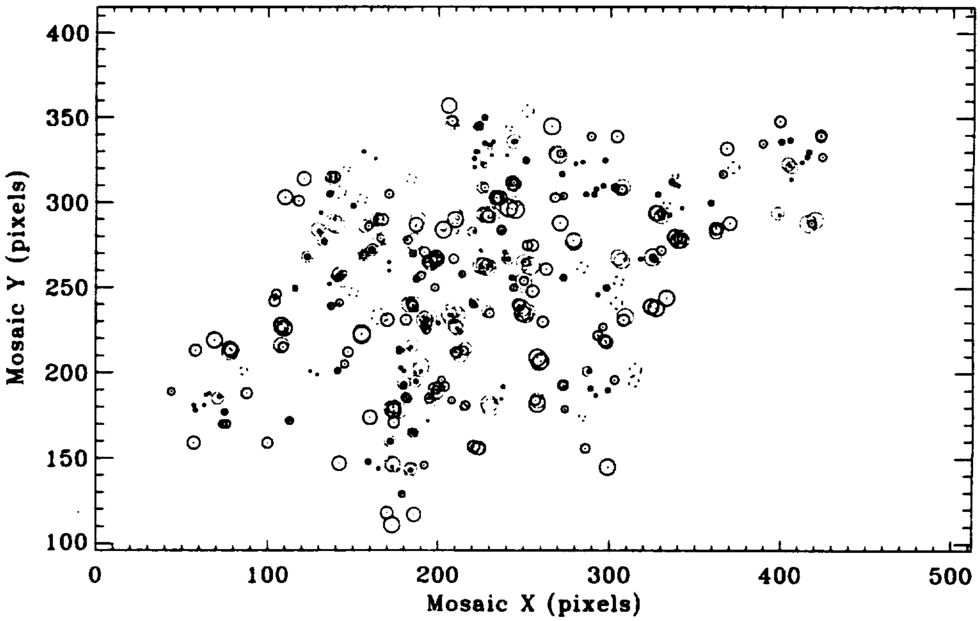

Fig. D.4.— Detected point sources in a mosaic. *Solid:* accepted detections, *Light:* duplicate detections, *Dashed:* rejected detections. In all cases, the 1.5 PSF radius is drawn. The mosaic scale is 1.'5 per pixel. Instances of two overlapping accepted detections are due to both detections being made in the same pointing.

For each rejected detection a 201 × 201 pixel region surrounding the rejected detection position is extracted and placed in the file *rej_xxx_rej.fits*, where "xxx" is the line number of the detection in the *sources_reject_n.dat* file. Similarly, a 201 × 201 pixel region surrounding the rejected detection position is extracted from the pointing with the best point source detection limit (at that position) and placed in the file *rej_xxx_acc.fits*. The user should examine the rejected detections carefully. As described in the text, some "rejected" sources may be unmasked hot-spots which should be removed before the mosaic is created. Also described in the text is a problem due to a point source falling on the boundary of two pointings. Figure D.5 shows some extracted regions, for both the rejected detections (left) and the same region in the "best detection" pointing (right), similar to Figure 3.13. Note that the top row is the reverse of the bottom row. In this case, the detection in each pointing fell in the region for which the other pointing was to be accepted. This problem does not occur often, and is easily noticed in a brief examination of the "rejected" sources.

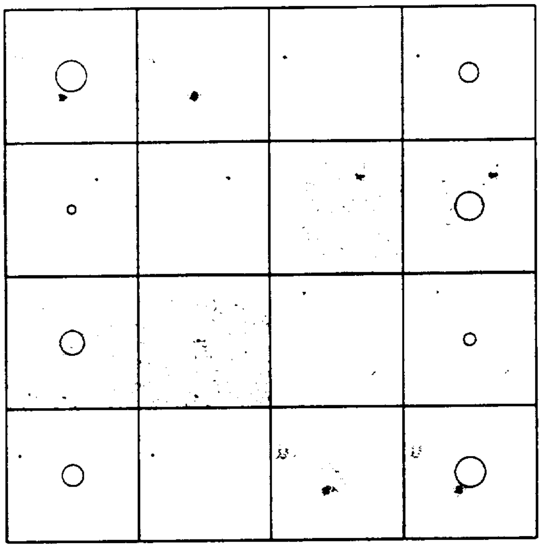

Fig. D.5.— Comparison of "rejected" sources to better exposures of the same regions. *Left two panels:* four "rejected detections". The leftmost panel is overplotted with the local PSF. *Right two panels:* the same positions (R.A., dec.) in the pointings with the best point source detection limit at those positions. The right-most panel is overplotted with the local PSF. Each panel has been scaled by the extremes within that panel. Note that the bottom row is the reverse of the top row.

Interactive Input

1) Band range – *n1, n2*
   The range of bands over which point sources were detected.
2) Coordinate control – *n*
   Set the coordinate system for the mosaic image. Enter 1 for ecliptic, 2 for equatorial, or 3 for galactic coordinates.
3) PSF scale – *f*
   The multiple of PSF radii within which two sources must reside in order to be deemed the same object.
4) Postage stamp flag – *n*
   Enter 1 if the extracted image files *rej_xxx_rej.fits* (containing the region around the rejected detection xxx extracted from the pointing in which the detect was made) raend *rej_xxx_acc.fits* (containing the region around the rejected detection xxx extracted from the region with the best detection limit) are to be formed, otherwise, 0.

File Input

1) Images – *psfld_n.fits* and *psrad_n.fits*,
   output by PS_LIMIT.

2) ASCII files – *dir.dat*
   The file dir.dat contains a list of directory path names for the various observations to be mosaicked. This allows MERGE_DETECT to find the observations to be compared from the

directory where it is being run.

3) ASCII files – *diag_n.dat*, output by DETECT in each pointing directory.

ASCII File Output

1) *sources_accept_n.dat* – a list of "accepted" detections.
2) *sources_duplic_n.dat* – a list of "duplicate" detections.
3) *sources_reject_n.dat* – a list of rejected detections that were not duplicates.

Image File Output

1) FITS files – *rej_xxx_rej.fits*, a 201 × 201 pixel image surounding the rejected detection extracted from the pointing in which the rejected detection was made. The number *xxx* is the corresponding line number in *sources_reject_n.fits*.
2) FITS files – *rej_xxx_acc.fits*, a 201 × 201 pixel image surounding the rejected detection extracted from the pointing which has the best point source detection at the position of the rejected detection. The number *xxx* is the corresponding line number in *sources_reject_n.fits*.

Screen Output

Program diagnostic information.

TABLE D.4

COLUMNS IN DETECT, MERGE_DETECT, AND GET_RASS_BSC OUTPUT

Column	DETECT	MERGE_DETECT	GET_RASS_BSC	Format
1	detection number	field number	index number	I6
2	image X (pixel)	mosaic X (pixel)	mosaic X (pixel)	I6
3	image Y (pixel)	mosaic Y (pixel)	mosaic Y (pixel)	I6
4	R.A. (decimal degrees)	R.A. (decimal degrees)	R.A. (decimal degrees)	F9.4
5	Dec. (decimal degrees)	Dec (decimal Degrees)	Dec. (decimal Degrees)	F9.4
6	Count Rate (cnts/s)	Count Rate (cnts/s)	Count Rate (cnts/s)	F12.7
7	Significance	Significance	BSC Probability/10^4	F13.8

MERGE_IMAGE HRI, PSPC

To combine the count, modeled background count, modeled offset count, exposure map, and mask (usually just the exposure map) into final surface-brightness (count rate and count-rate uncertainty) images. Nearly the same as FINAL_IMAGE but runs on mosaic images.

Interactive Input

1) Coordinate control – *n*
   Set the coordinate system for the mosaic image. Enter 1 for ecliptic, 2 for equatorial, or 3 for galactic coordinates.
2) Band range – *n1, n2*
   The range of bands to be combined for the final image (i.e., "2 2" will produce band R2, "4 5" will produce band R45 as a $\frac{3}{4}$ keV band, and "8 2" will produce band R1L2, "4 7" will produce band R47 combining the bands R4, R5, R6, and R7). Enter "0 0" for HRI data.
3) Fractional limit for masking – *f*
   ADAPT will take the mask (either input file or exposure map), determine the average non-zero value of the mask, and mask out any pixels where the mask value is less than the average mask value multiplied by the fraction. A value of 0.02 for is reasonable in most cases.
4) Mask name – *file name*
   Enter the file name of an image to use as a mask. Enter a carriage return to use the exposure map.

File Input

1) Images – PSPC: *counts_n.fits, back_n.fits, expose_n.fits, off_n.fits* and a mask if desired, HRI: *counts.fits, back.fits, expose.fits, off.fits* and a mask if desired
   The program will query for the band range to be mosaicked and a mask name.
2) ASCII files – none

ASCII File Output

None

Image Output

1) Final mosaicked images – PSPC: *rate_n.fits, sig_n.fits, mask_.fits*, HRI: *rate.fits, sig.fits, mask.fits*
   Fits files of the mosaicked count-rate, count-rate uncertainty, and an output mask. The PSPC files rate_n.fits and sig_n.fits (where n is the band number or band range) and HRI files rate.fits and sig.fits contain count rate and count-rate uncertainty (in units of counts s^{-1} $arcmin^{-2}$) for the full 512 × 512 image.

Screen Output

Program diagnostic information.

To combine the count, modeled background count, modeled offset count, exposure map, and mask (usually just the exposure map) into final surface-brightness (count rate and count-rate uncertainty) images. Nearly the same as MERGE_IMAGE, but bins by a factor of 2, 4, 8, or 16.

Interactive Input

1) Coordinate control – *n*
   Set the coordinate system for the mosaic image. Enter 1 for ecliptic, 2 for equatorial, or 3 for galactic coordinates.
2) Band range – *n1, n2*
   The range of bands to be combined for the final image (i.e., "2 2" will produce band R2, "4 5" will produce band R45 as a $\frac{3}{4}$ keV band, and "8 2" will produce band R1L2, "4 7" will produce band R47 combining the bands R4, R5, R6, and R7). Enter "0 0" for HRI data.
3) Binning parameter – *n*
   The multiple by which to bin the output image.
4) Fractional limit for masking – *f*
   ADAPT will take the mask (either input file or exposure map), determine the average non-zero value of the mask, and mask out any pixels where the mask value is less than the average mask value multiplied by the fraction. A value of 0.02 for is reasonable in most cases.
5) Mask name – *file name*
   Enter the file name of an image to use as a mask. Enter a carriage return to use the exposure map.

File Input

1) Images – PSPC: *counts_n.fits, back_n.fits, expose_n.fits, off_n.fits* and a mask if desired, HRI: *counts.fits, back.fits, expose.fits, off.fits* and a mask if desired
   The program will query for the band range to be mosaicked and a mask name.
2) ASCII files – none

ASCII File Output

None

Image Output

1) Final mosaicked images – PSPC: *bin_x_rate_n.fits, bin_x_sig_n.fits, bin_x_mask_.fits*, HRI: *bin_x_rate.fits, bin_x_sig.fits, bin_x_mask.fits*,
   FITS files of the mosaicked count-rate, count-rate uncertainty, and an output mask. The x is the binning factor. The PSPC files *bin_x_rate_n.fits* and *bin_x_sig_n.fits* (where n is the band number or band range) and HRI files *bin_x_rate.fits* and *bin_x_sig.fits* contain count rate and count-rate uncertainty (in units of counts s^{-1} arcmin^{-2}) for the full 512 × 512 image.

Screen Output

Program diagnostic information.

MERGE_OFF HRI, PSPC

Uses the output of OFFSET (offset_n.out for PSPC data for band n; offset.out for HRI data) and exposure arrays to create offset count maps for the individual observations. When cast with the count, background, and exposure maps, the offset count maps will produce a relatively uniform zero level across the field.

Interactive Input

1) Coordinate control – *n*

   Set the coordinate system for the mosaic image. Enter 1 for ecliptic, 2 for equatorial, or 3 for galactic coordinates. Should be identical to that used in MERGE.

2) Central coordinates – *f1, f2*

   The central coordinates for the mosaic in decimal degrees in the coordinate system selected in 1). Should be identical to those used in MERGE.

3) Scale factor for mosaic – *f*

   The pixel size for the mosaic in arc minutes. Should be identical to that used in MERGE.

4) Radius limit – *f*

   The radius of the region in the individual pointings, in arc minutes, to be cast into the mosaic (applied to the sky image rather than in detector coordinates). For the PSPC a limit of 53′ serves reasonably well to exclude the worst problems caused by the large point response function at large off-axis angles. For the HRI typically the entire field can be used. Should be identical to that used in MERGE.

5) Band to be cast – *n*

   The program will cast only one band at a time. Enter 0 for HRI data.

6) Mask file name – *file name*

   The data will be masked using files with the input file name in the individual directories. The mask files must be in the same directories as the data files. If no additional masking is desired, enter a carriage return.

7) Add flag – *n*

   Enter 1 to add to an existing image, 0 to cast a new image. If data are to be added to an existing image then MERGE will query for the file name. If data are to be added to an existing image the new directories must be listed in the file dir_add.dat.

File Input

1) Images – PSPC: *expose_n.fits* and a mask if desired from each directory listed in offset_n.dat, HRI: *expose.fits* and a mask if desired from each directory listed in overlap.dat

   The program will query for the mask name.

2) ASCII files – PSPC: *offset_n.dat*, HRI: *offset.dat*

   The files offset_n.dat and overlap.dat are output from OFFSET and contain a list of directory path names for the various observations to be mosaicked and offset count rates. This allows MERGE_OFF to find the observations to be mosaicked from the directory where it is being run and to scale the exposure maps for mosaicking.

ASCII File Output

None

Image Output

1) Mosaicked image – PSPC: *off_n.fits*, HRI: *off.fits*

   Mosaic of the model offset counts.

Screen Output

Program diagnostic information.

To calculate the LTE offsets for all of the pointings within a mosaic using both the self-consistent and direct-comparison equations. The relative offsets between all adjacent pointings in their regions of overlap are determined, the LTE offsets determined by OFFSET_DC are read in, and a singular-value decomposition finds the optimal solution. The relative weight of the direct-comparison offsets can be adjusted. This routine determines the absolute LTE offsets, unlike OFFSET_SC, which only determines relative offsets. See § 2.3 for a full explanation.

The use of point-source masks is highly recommended as bright sources can contribute substantially to the mean count rate in a region of overlap. Bright extended regions may also need to be masked.

Interactive Input

1) Coordinate control – *n*
   Set the coordinate system for the mosaic image. Enter 1 for ecliptic, 2 for equatorial, or 3 for galactic coordinates.

2) Central coordinates for analysis – *f1, f2*
   The central coordinates for the mosaic in decimal degrees.

3) Scale factor for mosaic – *f*
   The pixel size for the mosaic in arc minutes. This can be the same size as for the mosaic.

4) Radius limit – *f*
   The radius of the region in the individual pointings, in arc minutes, to be cast into the mosaic (applied to the sky image rather than in detector coordinates). If a point-source mask is used, generally the entire field can be used (default to 100′). If no point-source mask is used, a limit of 53′ for PSPC data will again serve reasonably well (hopefully) to exclude the worst problems caused by the large point response function at large off-axis angles. The entire field can be used for the HRI.

5) Weightings – *f*
   The relative weightings to be given to the direct comparison equations.

6) Band to be analyzed – *n*
   The program will analyze only one band at a time. Enter 0 for HRI data.

7) Mask file name – *file name*
   The data will be masked using files with the input file name in the individual directories. The mask files must be in the same directories as the data files. If no additional masking is desired, enter a carriage return.

File Input

1) Images – PSPC: *b_n.fits, back_n.fits, expose_n.fits* and a mask if desired from each directory listed in dir.dat, HRI: *counts.fits, back.fits, expose.fits* and a mask if desired from each directory listed in dir.dat
   The program will query for the band to be analyzed and a mask name.

2) ASCII files – *dir.dat* or *dir_add.dat*
   The file dir.dat contains a list of directory path names for the various observations to be mosaicked. This allows OFFSET to find the observations to be compared from the directory where it is being run.

3) ASCII file – *offset_dc.out* This file contains the output of OFFSET_DC, the difference in count rate between each pointing and the corresponding region of the *RASS*. (This program does do a consistency check between the directories listed in *dir.dat* and those listed in *offset_dc.out*.)

ASCII File Output

1) File *offset_n.dat* (*offset.dat* for HRI data) contains the record of the individual overlap region

offsets plus the final offset values.

2) File *offset_n.out* (*offset.out* for HRI data) contains the directory name of each pointing, the central coordinates of the individual observations, the LTE offset solution for each pointing, and the LTE offset uncertainties. This file is required as input to the program MERGE_OFF.

Image Output

1) FITS file *covariance_n.fits* which contains the covariance matrix for the solution.

Screen Output

Program diagnostic information.

TABLE D.5

COLUMNS IN OFFSET(_XX) OUTPUT

Column	Quantity	Units	Format
1	Directory name		a50
2	R.A.	decimal degrees	f10.2
3	dec.	decimal degrees	f10.2
4	LTE Offset	counts s^{-1} $arcmin^{-2}$	f10.2
5	LTE Offset uncertainty	counts s^{-1} $arcmin^{-2}$	f10.2

OFFSET_DC HRI, PSPC

To determine the LTE offset for all of the pointings within a mosaic by calculating the mean difference between each pointing and the same region in the *RASS*. The point source mask is used to remove the point sources from the pointed images. This removal is important; point sources can contribute significantly to the mean pointed count rate. As discussed in § 2.1, this method of measuring LTE offset can produce problems. We recommend that the LTE offsets from this routine not be used by themselves, but be combined with the self-consistent solution by using the OFFSET routine.

Interactive Input

1) Band to be compared - *n*

1a) R1L/R1 band ratio - *f*
 If the band to be compared is R1L, then the R1L/R1 band ratio is needed to convert the *RASS* flux to the same band as the mosaic.

2) Sigma limit - *f*
 The value in standard deviations over which pixels are discarded.

3) Coordinate control – *n*
 Set the coordinate system for the mosaic image. Enter 1 for ecliptic, 2 for equatorial, or 3 for galactic coordinates.

4) Central coordinates for analysis – *f1, f2*
 The central coordinates for the mosaic in decimal degrees.

5) Mask file name – *file name*
 The data will be masked using files with the input file name in the individual directories. The mask files must be in the same directories as the data files. If no additional masking is desired, enter a carriage return.

ASCII File Output

1) File *offset_dc_n.dat* (*offset_dc.dat* for HRI data) contains the record of the individual overlap region offsets plus the final offset values.

2) File *offset_dc_n.out* (*offset_dc.out* for HRI data) contains the directory name of each pointing, the central coordinates of the individual observations, the LTE offset solution for each pointing, and the LTE offset uncertainties. This file is required as input to the program MERGE_OFF.

Image File Output

1) *pntd_rate_n.fits*
 A 41×41 FITS image in the *RASS* coordinate system containing the mosaic count rate.

2) *pntd_sig_n.fits*
 A 41×41 FITS image in the *RASS* coordinate system containing the mosaic count rate uncertainty.

3) *pntd_mask_n.fits*
 A 41×41 FITS image in the *RASS* coordinate system containing the mosaic mask.

4) *rass_rate_n.fits*
 A 41×41 FITS image in the *RASS* coordinate system containing the mosaic mask.

5) *rass_sig_n.fits*
 A 41×41 FITS image in the *RASS* coordinate system containing the mosaic mask.

It should be noted that for pointing band R1L, the *RASS* images will be band R1, will not be scaled to band R1L, and will be named rass_xxxx_1.fits.

Screen Output

Program diagnostic output.

To determine the relative offsets in the zero levels of the observations to be merged. While the resulting zero level after the observations have been merged may still include an additive offset from true zero, it will be considerably more uniform across the field. OFFSET_SC determines the relative offsets between all adjacent pointings in their region of overlap, and then uses a single-value deconvolution algorithm to solve for the best-fit group of offsets. The use of point-source masks is highly recommended as bright sources can mess up the works. Bright extended regions may also need to be masked. Unless there is some good reason to use this program (such as using HRI images), the OFFSET_DC/OFFSET combination should be used instead.

Interactive Input

1) Coordinate control – *n*
   Set the coordinate system for the mosaic image. Enter 1 for ecliptic, 2 for equatorial, or 3 for galactic coordinates.
2) Central coordinates for analysis – *f1, f2*
   The central coordinates for the mosaic in decimal degrees in the equatorial coordinate system.
3) Scale factor for mosaic – *f*
   The pixel size for the mosaic in arc minutes. This can be the same size as for the mosaic.
4) Radius limit – *f*
   The radius of the region in the individual pointings, in arc minutes, to be cast into the mosaic (applied to the sky image rather than in detector coordinates). If a point-source mask is used, generally the entire field can be used (default to 100′). If no point-source mask is used, a limit of 53′ for PSPC data will again serve reasonably well (hopefully) to exclude the worst problems caused by the large point response function at large off-axis angles. The entire field can be used for the HRI.
5) Band to be analyzed – *n*
   The program will analyze only one band at a time. Enter 0 for HRI data.
6) Mask file name – *file name*
   The data will be masked using files with the input file name in the individual directories. The mask files must be in the same directories as the data files. If no additional masking is desired, enter a carriage return.

File Input

1) Images – PSPC: *b_n.fits, back_n.fits, expose_n.fits* and a mask if desired from each directory listed in dir.dat, HRI: *counts.fits, back.fits, expose.fits* and a mask if desired from each directory listed in dir.dat
   The program will query for the band to be analyzed and a mask name.
2) ASCII files – *dir.dat* or *dir_add.dat*
   The file dir.dat contains a list of directory path names for the various observations to be mosaicked. This allows OFFSET to find the observations to be compared from the directory where it is being run.

ASCII File Output

1) Overlap diagnostic data – PSPC: *offset_sc_n.dat*, HRI: *offset_sc.dat*
   Contains the record of the individual overlap region offsets plus the final offset values.
2) Overlap parameters – PSPC: *offset_sc_n.dat*, HRI: *offset_sc.dat*
   Contains in addition to the final results, the directories and central coordinates of the individual observations to be used as input to the program MERGE_OFF.

Image Output

None

Screen Output

Program diagnostic information.

To determine the point source detection limit at every point in a mosaic. For every pointing included in the mosaic, PS_LIMIT casts the exposure map into the mosaic coordinate system, determines the size of the PSF at each pixel, and calculates the point source detection limit at that pixel for that pointing. This is then compared to the point source detection limit at that pixel for all other pointings, and the best (i.e. lowest) limit is chosen.

The detection limit is calculated from the mean count rate, which includes the point sources. Thus the mean background rate will be somewhat higher than the true background rate, thus increasing the point source detection limit. For the purposes of MERGE_DETECT, this inaccuracy in the true point source detection limit is inconsequential due MERGE_DETECT looking at *relative* point source detection limits. One can imagine situations in which the inaccuracy *could* cause difficulties for MERGE_DETECT, but in practice these difficulties have not arisen.

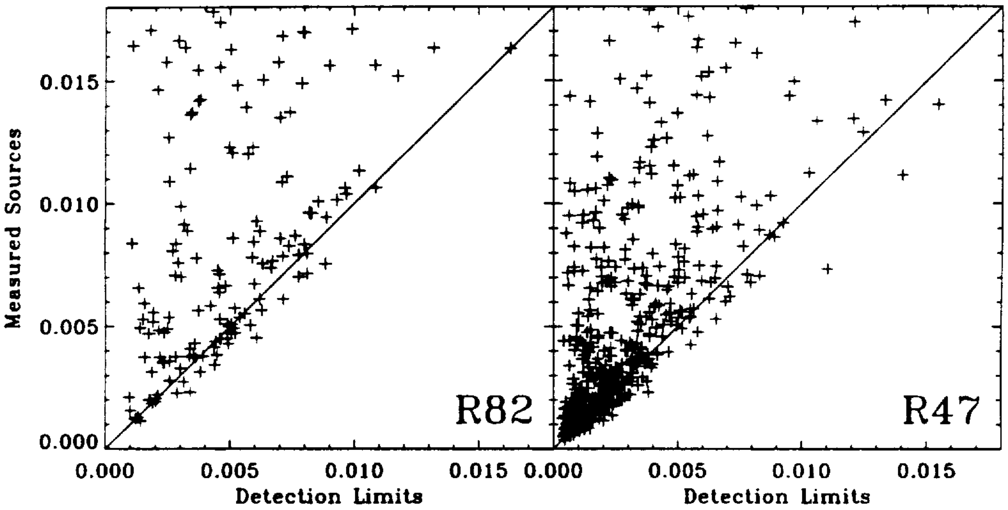

Fig. D.6.— A comparison of measured count rates and the calculated point source detection limit for PS_LIMIT. The few points that lie below the line (point sources that lie below the local point source detection limit) are due to the local cosmic background rate being below the mean cosmic background rate. See Figure C18 for a similar plot from BETTER_LIMIT.

Interactive Input

1) Coordinate control – *n*

Set the coordinate system for the mosaic image. Enter 1 for ecliptic, 2 for equatorial, or 3 for galactic coordinates. Should be identical to that used in MERGE.

2) Central coordinates – *f1, f2*

The central coordinates for the mosaic in decimal degrees in the coordinate system selected in 1). Should be identical to those used in MERGE.

3) Scale factor for mosaic – *f*

The pixel size for the mosaic in arc minutes. Should be identical to that used in MERGE.

4) Radius limit – *f*

The radius of the region in the individual pointings, in arc minutes, to be considered (applied to the sky image rather than in detector coordinates). This value should include the entire field as the extreme edge of one field may still be better than the center of another. For the

PSPC a limit of 60′ will include the entire field; for the HRI xx' Note that this is not the same value used for casting the mosaics.

5) Band range – *n1, n2*
   The range of bands to be combined for the final image (i.e., "2 2" will produce band R2, "4 5" will produce band R45 as a $\frac{3}{4}$ keV band, and "8 2" will produce band R1L2, "4 7" will produce band R47 combining the bands R4, R5, R6, and R7). Enter "0 0" for HRI data.

6) Statistical significance and count-rate threshold – *f1, f2*
   The statistical significance can be entered either as the Poisson (i.e., $3\sigma = 0.9973002$) probability or the value in sigmas (allowed values: 1., 2., 2.5, 3., 3.5, 4., 4.5, 5., 5.5). The count-rate threshold in units of counts s^{-1} may be set to zero.

8) Mask file name for masking of the data – *filename*
   The data from each pointing will be masked using files with the input file name in the pointing directory. If no additional masking is desired, enter a carriage return.

File Input

1) Images – PSPC: *expose_n.fits, counts_n.fits* and a mask if desired from each directory listed in dir.dat, HRI: *expose.fits, counts.fits* and a mask if desired from each directory listed in dir.dat

2) ASCII files – *dir.dat* or *dir_add.dat*
   The file dir.dat contains a list of directory path names for the various observations to be mosaicked. This allows PS_LIMIT to find the observations to be mosaicked from the directory where it is being run.

ASCII File Output

None

Image File Output

1) The FITS file *pslim_n.fits*, the best point source detection limit at each pixel in the mosaic. The units are counts s^{-1}.
2) The FITS file *psfld_n.fits*, the number (line number in the dir.dat file) of the pointing containing the best point source detection limit at each pixel in the mosaic.
3) The FITS file *psexp_n.fits*, the length of the exposure corresponding to the best point source detection limit.
4) The FITS file *psrad_n.fits*, the PSF radius corresponding to the best point souce detection limit. The units are arcminutes.

Screen Output

Program diagnostic output.

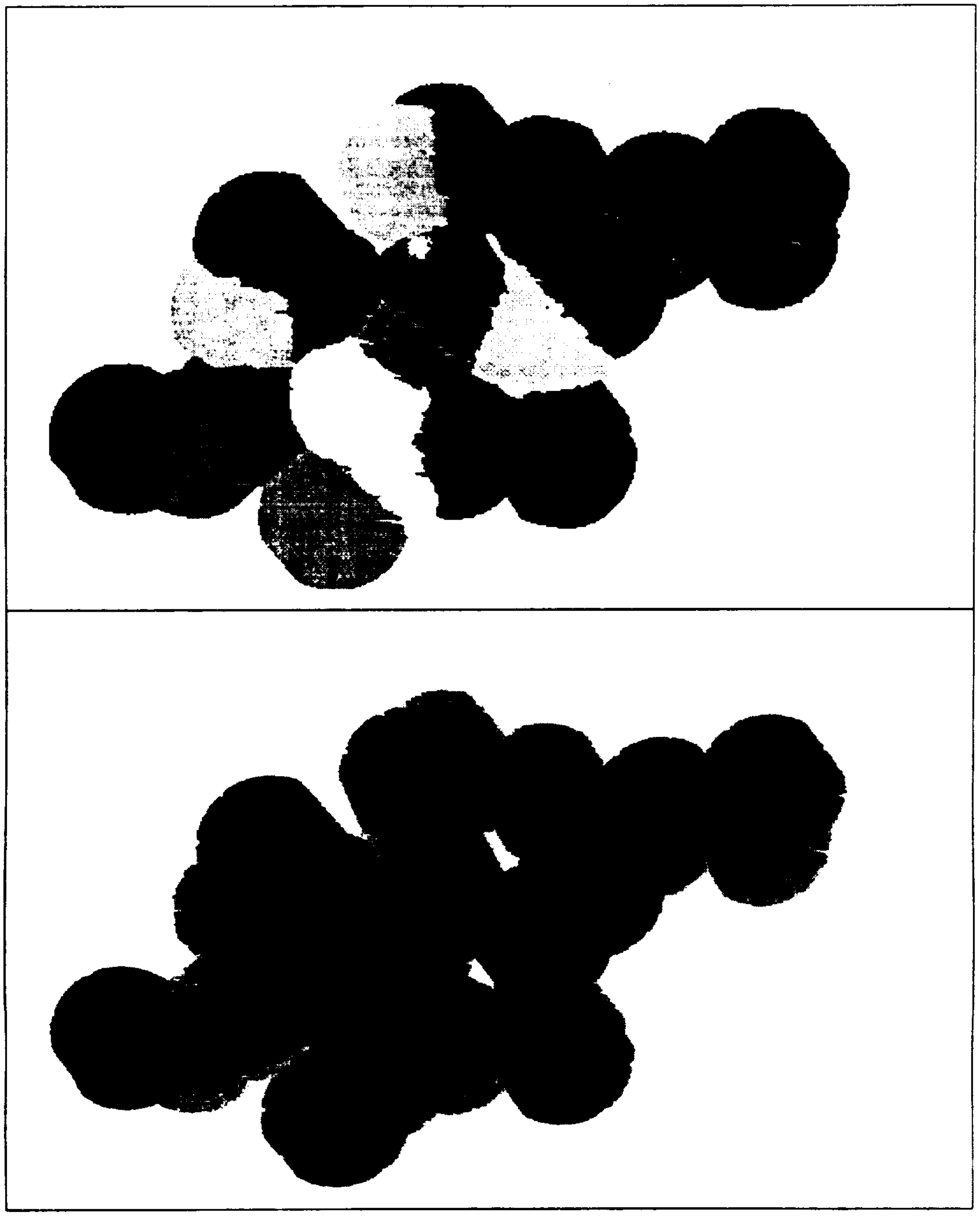

Fig. D.7.— Two of the images output by PS_LIMIT: the field number image and the point source detection limit image. *Top:* The image containing the number of the pointing with the best point source detection limit. *Bottom:* The $\log_{10}$ of the point source detection limit. The grey scale runs from -3.1 to -1.0.

ROARITH HRI, PSPC

To perform simple mathematical operations on images; adding two images together, subtracting one from another, multiplying two images, or dividing one by another.

Interactive Input
1) The name of the first input FITS file.
2) The code of the operation to perform, "+" for addition, "-" for subtraction, "*" for multiplication, and "/" for division. 3) The name of the second input FITS file.
4) The name of the output FITS file.

File Input
1) Two 512×512 FITS images.

Image Output
The output FITS image.

D.6. UNIX Scripts

When making a mosaic, one does the same thing to many different exposures (such as DETECT and MASK), or one does the same thing for each different band (such as MERGE_RAW and OFFSET). This section describes some UNIX script files that make these processes easier. In order to understand the order in which they are used, see § D.3.

Caveat: These scripts were created as they were needed. They are not models of good shell programming, nor are they anything that anyone with the slightest modicum of shell programming experience could not do, and better.

As a matter of organization, it is a good idea to put subexposures into subdirectories of the directory containing the summed exposure. A model directory tree is shown in Figure D.1

Table D.6 contains definitions of parameters required by these shell scripts. The parameters required for any script can be found by typing the name of the script without any arguments.

The scripts are listed in alphabetical order. Their method of employ should be clear from the prescription in § D.3.

add.obs

To add together two subexposures of the same field. It is assumed that the names of the subdirectories are in the file *dir.dat*. The result is put into the current directory.

Usage: add.obs

merge.comp

To create a mosaicked image of a given component (i.e., count, exposure, or background) for all bands of interest (R1L, R2, R4, R5, R6, and R7).

Usage: merge.comp coor long lati scal excl mask comp

merge.image

To create a mosaicked image of the count rate and the associated uncertainty for each band of interest (R1L, R2, R4, R5, R6, and R7), as well as the combinations R1L2, R45, R67, and R47.

Usage: merge.image coor frac

merge.off

To create a mosaicked image of the LTE offsets far all bands of interest (R1L, R2, R4, R5, R6, and R7).

Usage: merge.offset coor long lati scal excl mask

multi.detect

To execute DETECT on each individual exposure. This routine assumes that every directory named *dir.dat* contains an individual exposure. It removes any files created by DETECT in the past and runs DETECT for the R1L2 and R47 bands.

Usage: multi.detect sgma 1L2cr 47cr exrd 1L2rd 47rd 1L2cr 47cr

multi.mask

To execute MASK on each individual exposure. This routine assumes that every directory named *dir.dat* contains an individual exposure. It removes any mask files (mask_xx.fits) created by DETECT or MASK in the past and runs MASK for the R1L2 and R47 bands. Note that the name of the files containing the point source lists should include whatever part of the path is needed to point to these files from within the directory of an individual pointing.

Usage: multi.mask 1L2sf 47sf exrd 1L2rd 47rd

multi.move

To move a file of one name, "oldname", to a new name, "newname", in every directory named ?p*. This is useful to move all of the mask files produced by DETECT before creating new ones with MASK.

Usage: multi.move oldname newname

multi.remove

To remove a file named "name" from every directory named in *dir.dat*. This is useful for correcting many mistakes, but has the potential for making many more. To use wild-cards, enclose the file name in quotation marks.

Usage: multi.remove name

solve.off

To execute OFFSET and OFFSET_DC for every band of interest (R1L, R2, R4, R5, R6, R7).

Usage: solve.off long lati scal excl

TABLE D.6
MOSAICKING SHELL PARAMETERS

Name	Definition and Units
47cr	minimum valid countrate for a point source in band R47 in units of counts/second
1L2cr	minimum valid countrate for a point source in band R1L2 in units of counts/second
47rd	minimum radius around a point source to remove for band R47 in units of pixels
1L2rd	minimum radius around a point source to remove for band R1L2 in units of pixels
47sf	name of file containing the "master list" of sources detected in band R47
1L2sf	name of file containing the "master list" of sources detected in band R1L2
coor	coordinate system to use for mosaic 1 ecliptic coordinates 2 equatorial coordinates 3 galactic coordinates
comp	component to be cast into a mosaic 1 counts 2 exposure 3 background
excl	radius beyond which exposure is to be discarded
exrd	radius around point source to remove in units of PSF radii
frac	the minimum fraction of the mean exposure to be accepted as good
lati	latitude of center of mosaic
long	longitude of center of mosaic
mask	mask flag 0 if no mask is to be used 1 if mask is to be used
scal	scale of mosaic in arcmin/pixel
sgma	minimum significance for a point source detection

REFERENCES

Greisen, E. W., & Calabretta, M. 1993, Representations of celestial coordinates in fits

Kuntz, K. D., & Snowden, S. L. 1998, Cookbook for analysis procedures for *rosat* xrt observations of extended objects and the diffuse background, part ii: Mosaics, Technical report, NASA/GSFC

Appendix E: The TAE in the Southern Galactic Hemisphere

Abstract

We have made a preliminary investigation of the spectrum of the TAE in the southern Galactic hemisphere. Although the emission in the southern Galactic hemisphere has poorer statistics than the emission in the northern Galactic hemisphere, we find the component temperatures to be consistent with those of the north.

We calculated the SED of the TAE in the southern Galactic hemisphere using the method described in Chapter 6. In order to exclude contamination by Loop I, we excluded regions with $\ell < 60^\circ$ and $\ell > 270^\circ$. This is a somewhat larger region than used in the northern Galactic hemisphere, but is justified by examination of the *RASS* R45 band image. We have restricted analysis to the region $b > 45^\circ$. We also excluded regions with $N_H > 3.0 \times 10^{20}$ cm^{-2}.

Assuming the same soft TAE component temperature found for the northern Galactic hemisphere, we attempted the standard local/distant separation. For the local component we found a peak R2/R1 ratio of 1.06, a FWHM of 0.89-1.27, and corresponding model temperatures $\log T =$ 6.11 and 6.02-6.25, assuming a foreground absorbing column of $N_f = 4.0 \times 10^{18}$ cm^{-2}. The temperature of the local component is consistent with the results from the northern Galactic hemisphere, $\log T = 6.12^{+0.13}_{-0.11}$. For the local component we found a peak R2/R1 of 0.69, a FWHM of 0.41-1.22, and corresponding model temperatures $\log T =$ 5.90 and 5.72-6.25. Note that the upper bounds of neither of the distributions correspond to a Raymond & Smith model temperature.

The reason for the large difference between these results and those for the northern Galactic hemisphere is poor statistics. Figure E.1, shows a histogram of the R2/R1 band ratio for both the local and distant components. Since the number of pixels available for analysis is only ~ 0.75 that available in the north, both the local and the distant distributions are somewhat broader than those for the northern hemisphere. The flux of the distant component in the south is ~ 0.67 that of the north, but with similar uncertainties. Thus, the distribution for the distant component is much broader, and it is difficult to determine the mode of the distribution. The peak value of the R2/R1 ratio of the distant component could be placed anywhere from 0.7 to 0.9 ($5.9 < \log T < 6.03$). The distribution does suggest that the temperature in the southern Galactic hemisphere is somewhat lower than in the north. These results are consistent with those of Snowden et al. (1998), and a lower temperature for the sourthern Galactic hemisphere can be inferred from Figure 11 of Snowden et al. (2000).

REFERENCES

Snowden, S. L., Egger, R., Finkbeiner, D., Freyberg, M. J., & Plucinsky, P. P. 1998, ApJ, 493, 715

Snowden, S. L., Freyberg, M. J., Kuntz, K. D., & Sanders, W. T. 2000, ApJS, in press

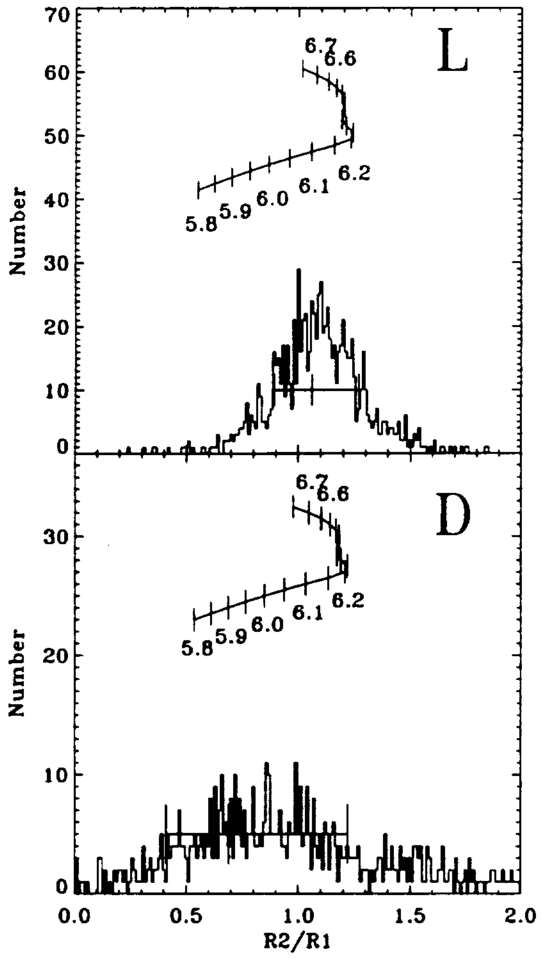

Fig. E.1.— The distribution of the R2/R1 band ratios for the local and distant components. The squiggle above the histogram shows the conversion to Raymond & Smith model temperature. For the distant component, both the R2/R1 and Raymond & Smith conversion are after deabsorption. For the local component, the histogram is of the R2/R1 derived from I'_L values; the temperature conversion assumes a 4×10^{18} cm^{-2} absorption. Note that only the lower branch of the temperature conversion is of interest as the upper branch would over-predict the R47 flux.

Appendix F: A Note on the L_X to Count Rate Conversions

Abstract

This appendix describes the method by which we calculated the relation between the intrinsic stellar X-ray luminosity and the hardness ratio.

This section describes the intrinsic X-ray luminosity, L_X, to count rate conversion used in Chapter 7 for the Schmitt (1997) and Schmitt, Fleming, & Giampapa (1995) data. Unlike other data sets where the original count rate to L_X conversion used a single factor, Schmitt (1997) and Schmitt, Fleming, & Giampapa (1995) use the function

$$(5.3HR + 8.31) \times 10^{-12} \text{ergs cm}^{-2}\text{counts}^{-1} \tag{F.1}$$

where

$$HR = \frac{R_{47} - R_{1L2}}{R_{47} + R_{1L2}}. \tag{F.2}$$

and R_{XX} is the count rate in band XX. Thus, the conversion factor depends upon the hardness ratio which, in turn, depends upon the intrinsic X-ray luminosity of the star.

Schmitt (1997) and Schmitt, Fleming, & Giampapa (1995) have shown that the hardness ratio is correlated with the X-ray luminosity L_X. These correlations are shown in F.1. The function

$$HR = a + b \log L_X \tag{F.3}$$

was fitted to the correlation for each spectral type using the procedure of Akritas & Bershady (1996), OLS(Y—X), for data with errors in both dependent and independent variables[1]. The fit values are listed in Table F.1.

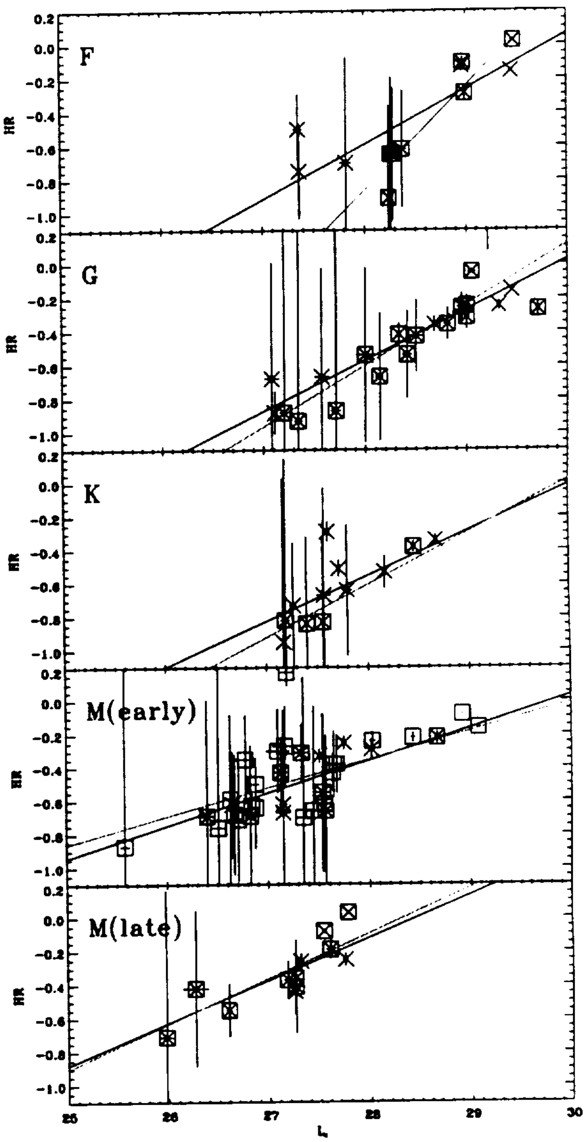

Fig. F.1.— Fit of HR *vs.* $\log L_X$ for each spectral type. *Dotted Line:* Fit excluding URBs, *Solid Line:* Fit including URBs. Data points of URBs are shown as squares.

---

[1] Only the uncertainties in $R_{47} + R_{1L2}$ are published; one can calculate the the uncertainties in L_X and HR in a straight forward way. Since

$$\log L_X = \log (5.3HR + 8.31 \cdot 10^{-12})(R_{47} + R_{1L2})(4\pi d^2) \tag{F.4}$$

where d is in centimeters, the uncertainty is

$$\sigma_{\log L_X} = \frac{\sigma_{R_{47}+R_{1L2}}}{(\ln 10)(R_{47} + R_{1L2})}. \tag{F.5}$$

I have estimated uncertainties in HR in the following manner; since R_{47} and R_{1L2} are independent measurements

$$\sigma_{R_{47}+R_{1L2}} = \sigma_{R_{47}-R_{1L2}} \tag{F.6}$$

TABLE F.1
FITS TO THE HR - L_X RELATION

Spectral	Excluding URB[a]		Including URB	
Type	a	b	a	b
F	-18.09±1.99	0.615	-9.71±1.99	0.326±0.069
G	-10.65±2.22	0.359±0.079	-8.92±1.28	0.298±0.046
K	-9.410±1.85	0.314±0.067	-8.16±1.29	0.272±0.046
M (early)	-5.10±0.62	0.169±0.022	-5.80±0.66	0.194±0.024
M (late)	-7.66±1.54	0.270±0.057	-7.22±1.49	0.253±0.055
		Unversal Slope Fits		
F	-9.54±0.99	0.317±0.031	-8.41±0.55	0.280±0.021
G	-9.45±0.99	0.317±0.031	-8.41±0.55	0.280±0.021
K	-9.48±0.96	0.317±0.031	-8.39±0.54	0.280±0.021
M (early)	-9,17±0.98	0.317±0.031	-8.15±0.54	0.280±0.021
M (late)	-8.92±0.94	0.317±0.031	-7.94±0.53	0.280±0.021

[a]Un-Resolved Binaries

From the catalogue of Schmitt (1997) and Schmitt, Fleming, & Giampapa (1995) all stars for which only upper limits existed for $R_{47} + R_{1L2}$, or for which HR was listed as -1 (due to R_{47} being only an upper limit) were discarded. Measurements for unresolved binaries (URBs) are also suspect, since the flux must be divided between the members in some more or less arbitrary fashion. Thus fits were made both including and excluding the URBs. As can be seen from Figure F.1, there is a substantial intrinsic scatter around any linear relation. Thus, given the small number of stars in any single spectral class, fits are quite uncertain (despite the small formal uncertainties), and the situation is made much worse by excluding the unresolved binaries.

The slopes from fits including the unresolved binaries have overlapping 1σ confidence intervals, leading one to suspect that 1.) the $\log L_X - HR$ relation has a single "universal" slope for all spectral classes (a suspicion first voiced by Schmitt (1997)), perhaps with an offset for each spectral class, and that 2.) the large differences in the slopes from the fits excluding the unresolved binaries is due to the large uncertainties inherent in fitting a small number of intrinsically scattered points. Acting upon these suspicions, we employed an iterative scheme for determining a single "universal" slope all spectral classes[2].

The "universal slope" fit can be seen in Figures F.3 and F.2, where the data for each spectral type has been given the appropriate offset. A "universal slope" was determined both including and excluding unresolved binaries. Although the two slopes are different, their 1σ confidence regions overlap. The offsets for individual spectral classes span an interval comparable to the uncertainties in HR. The "universal slope" fits are compared to the data from individual spec-

---

and thus

$$\sigma_{HR} = |HR|\sigma_{R_{47}+R_{1L2}}\left(\frac{1}{R_{47} - R_{1L2}} + \frac{1}{R_{47} + R_{1L2}}\right). \tag{F.7}$$

It is interesting to note that $\sigma_{L_X} \sim 0.4\sqrt{R}$ whereas $\sigma_{HR} \sim 1.4\sqrt{r}$ for very soft or very hard sources.
The published values of $\sigma_{R_{47}+R_{1L2}}$ often fall below $\sqrt{R_{47} + R_{1L2}}$, the lower limit imposed by Poisson counting statistics. In these cases I have set $\sigma_{R_{47}+R_{1L2}} = \sqrt{R_{47} + R_{1L2}}$

[2] In the first step, I calculated the means, $\bar{x}$ and $\bar{y}$ from the data for each spectral class. I then calculated the HR offset needed to place all of the centroids, the $(\bar{x}, \bar{y})_i$, for all of the spectral classes onto the fitted relation for one arbitrarily chosen class. These offsets were added to the HR, and all the data from all the spectral classes were merged and fit by a single line. In the second step, I determined the offsets needed to place the centroids on the new fit. Those offsets were added to the (original) HR, and step two was repeated until the value of the slope did not change between iterations. Only a few iterations were needed.

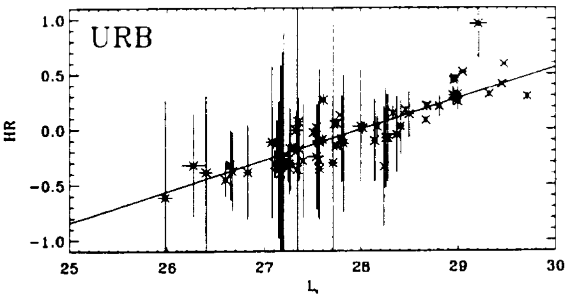

Fig. F.2.— Fit of HR *vs.* $\log L_X$ for all spectral classes together using the iterative fitting technique described in the text. Data from URBs are included.

tral classes in Figure F.4.

REFERENCES

Akritas, M. G., & Bershady, M. A. 1996, ApJ, 470, 706

Schmitt, J. H. M. M. 1997, A&A, 318, 215

Schmitt, J. H. M. M., Fleming, T. A., & Giampapa, M. S. 1995, ApJ, 450, 392

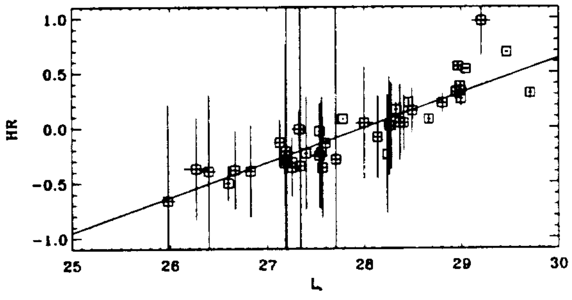

Fig. F.3.— Fit of HR *vs.* $\log L_X$ for all spectral classes together using the iterative fitting technique described in the text. Data from URBs are not included.

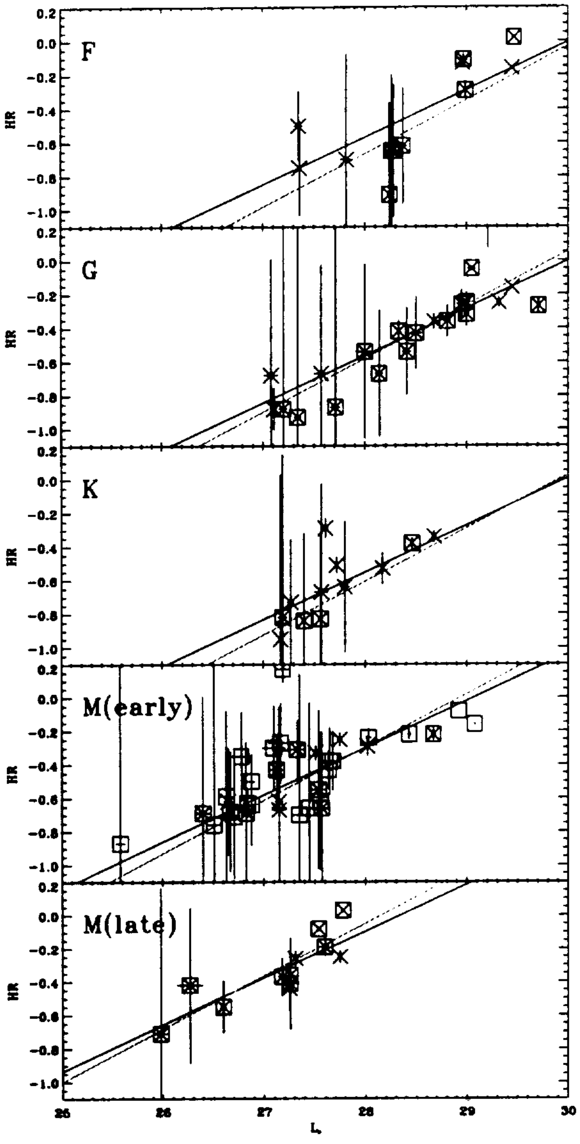

Fig. F.4.— Comparison of the "Universal Slope" fit to the data for each spectral type. *Dotted Line:* Fit excluding URBs, *Solid Line:* Fit including URBs. Data points of URBs are shown as squares.

Appendix G: The Uncertainty in $W(\theta)$

Abstract

This appendix discusses various methods for finding the uncertainty in $W(\theta)$. We present a more efficient form of the "shuffle" method, and show that in noise dominated images that it is equivalent to other methods used for determining the uncertainty in $W(\theta)$. However, we also show that in the presence of structures with amplitudes larger than the noise the shuffle method (or, indeed, any method that relies on the independence of neighboring pixels) can produce uncertainties that are a factor of a few too large at small θ and a factor of ~ 10 too small at large θ.

While writing a proposal to extend this work, we attempted to find a method that would allow us to determine the uncertainty in the ACF without reducing each pointing and calculating the ACF. Clearly, the uncertainty will be proportional to $\frac{1}{\sqrt{n}}$, where n is the number of pairs of pixels used to calculate the ACF on a given scale. The uncertainty in R can be easily estimated from the length of the exposure and the expected cosmic background rate. However, the calculation of the uncertainty in RR' involves a substantial correlation term, $\sigma^2_{RR'}$, which has a magnitude similar to σ^2_R. Thus, an *ab initio* estimation of the uncertainty in the ACF is not practicable.

There are two common methods for determining the uncertainty once the autocorrelation function has been calculated. Both of these methods are discussed by Chen et al. (1994).

The first method is to take the variance at each scale,

$$\sigma^2_{W(\theta)} = \frac{1}{\overline{R}^4}\left[\frac{\sum[(R-\overline{R})(R'-\overline{R})\sqrt{ww'}\,]^2}{\sum\sqrt{ww'}} - \left(\frac{\sum[(R-\overline{R})(R'-\overline{R})\sqrt{ww'}\,]}{\sum\sqrt{ww'}}\right)^2\right] \quad (G.1)$$

Then, by the standard propagation of uncertainties and the application of the central limit theorem, the uncertainty in the mean will be $\sigma_{W(\theta)}/\sqrt{n_\theta}$ where n_θ is the number of pairs in the sum. This method has the advantage that it is easy to calculate, but it slows the calculation of the autocorrelation, an already slow calculation[1].

The second method requires the image to be randomly "shuffled"; for all of the pixels to be reordered. The ACF is then measured upon this new image. The process is repeated many times in order to measure the variance in the distribution of $W(\theta)$ produced by all of the trial shuffles. Chen et al. (1994) found this latter method consistent with the former and preferred it because it "takes into account the correlation of the data". What is not clear is how many shuffles need to be executed to determine the variance.

We have developed a more efficient form of this latter method; a "maximal shuffle". If we consider an image to be a list of n pixels, then there are $(n-1)n/2$ possible pixel pairs. For each pixel pair, we may calculate whatever form of the ACF is desired, and then calculate the variance of that quantity, ς^2. The uncertainty of $W(\theta)$ is then given by $\varsigma/\sqrt{n_\theta}$, where n_θ is the number of pairs of pixels used to calculate $W(\theta)$. This method has the advantage over previous shuffle methods; it provides the maximum possible number of shuffles with a minimum of computing.

Consideration will show that these three methods, given the appropriate conditions, must be consistent. All three methods rely upon the central limit theorem by setting the uncertainty of the quantity RR' to be the variance of that quantity divided by the root of the number

---

[1] On a DECα with a minimal amount of memory (64M, the standard amount) an autocorrelation of a 512x512 pixel image containing a mosaic takes up to 24 hours, using a FORTRAN algorithm. The same mosaic on a PC, using IDL, takes about 2 hours.

of samples made. The three methods vary in the number of samples from which the variance of RR' is determined. The "maximal shuffle" method uses the maximum number of independent samples of RR' to determine the variance. The shuffling method takes a large number of samples in a duplicitive manner. The variance method uses a small number of samples, just the values of RR' used to calculate the ACF on a particular scale. Chen et al. (1994) suggested that if the pixels are strongly correlated, then the variance method will significantly overestimate the true variance of RR'.

Chen et al. (1994) state a preference for a shuffling method for measuring the uncertainty in $W(\theta)$ "because it takes into account the correlation of the data". They find that the shuffling method produced uncertainties consistent with those produced by the variance method, where the variance method is presumably the application of Equation G.1.

We have compared the shuffling method with the results of the variance method used in Chapter 10, which is not the same as the variance method used by Chen et al. (1994)[2]. In practice, we find that the shuffling method can produce an uncertainty that is a factor a few larger than the variance method at small θ, and that the shuffling method can produce and uncertainty that is a factor ~ 10 smaller than the variance method at large θ. (See Figure G.1.)

This difference can be understood in the following terms. In the presence of correlations, the samples are no longer independent and so the uncertainty of the mean of a subregion is not the square root of variance of all of the pixels divided by the root of the number of pixels in the subregion. If we look at the variance of II' where I and I' are separated by a distance that is much shorter than the correlation length, that variance will be much smaller than one calculated from an equivalent number of pixel pairs drawn at random from over a larger region. Thus, shuffling will overestimate the uncertainty at small θ. If we look at the variance of II' where I and I' are separated by a distance that is much on the order of than the correlation length, that variance will be much larger than one calculated from an equivalent number of pixel pairs drawn at random from over a larger region. Thus, shuffling will underestimate the uncertainty at θ comparable to the correlation length.

Therefore, for images with structure, the variance method is superior to the shuffling method.

REFERENCES

Chen, L.-W., Fabian, A. C., Warwick, R. S., Branduardi-Raymont, G., & Barber, C. R. 1994, MNRAS, 266, 846

---

[2] Since the method given by Equation G.1 is computationally intensive, it is to be avoided even in cases where the noise dominates. It is computationally little more costly to calculate $W(\theta_x, \theta_y)$ than it is to calculate $W(\theta)$. It is then trivial to compute the variance from all the W for which $\theta_x^2 + \theta_y^2 = \theta^2$.

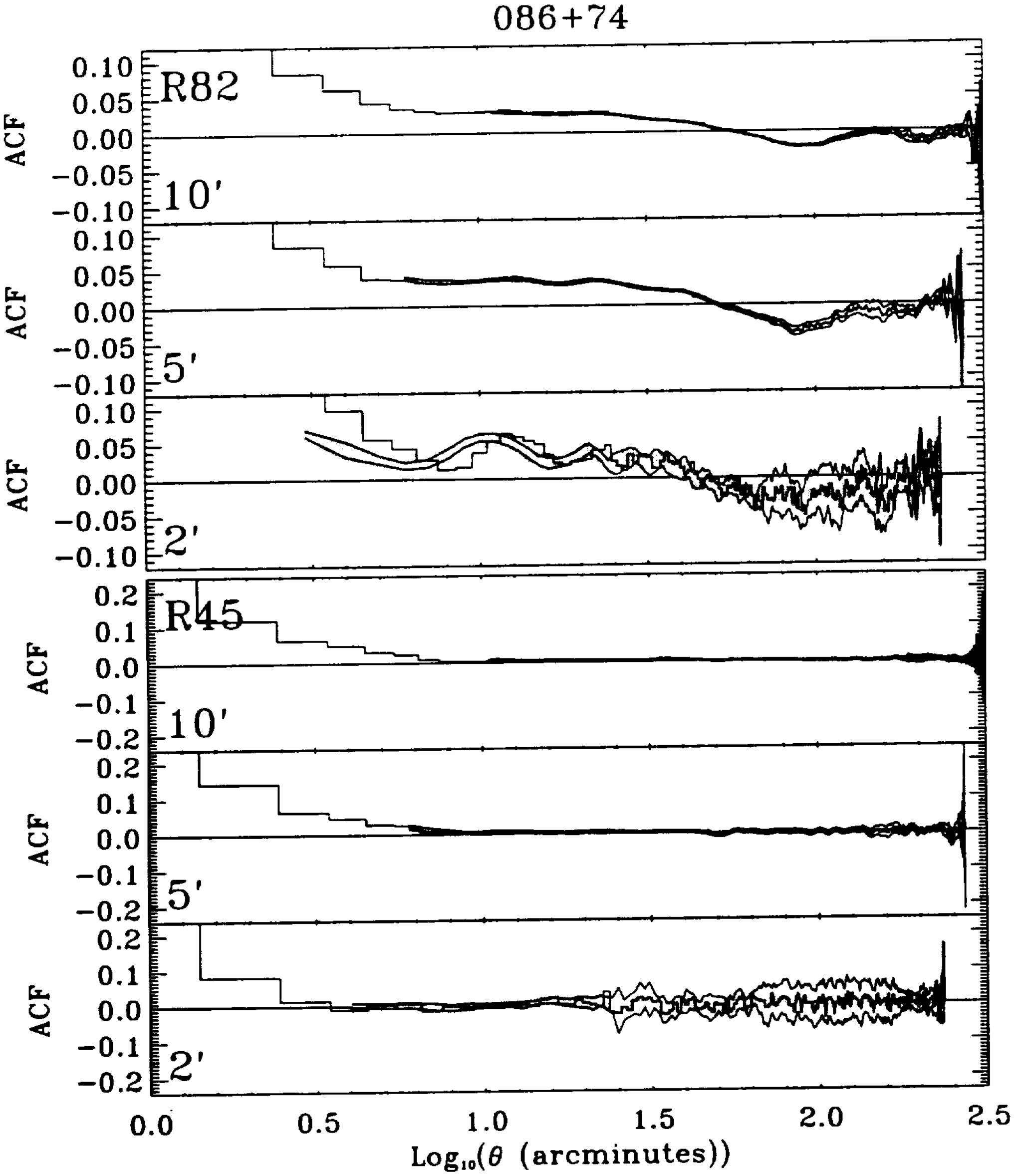

Fig. G.1.— Comparison of the uncertainty in $X(\theta)$ determined by the variance and shuffle methods. The histogram line is the ACF, the shaded region is the smoothed ACF plus-or-minus the uncertainty determined by the suffle method. The irregular solid lines are the smoothed ACF plus-or-minus the uncertainty determined by the variance method. Note that band R82 is the same as band R1L2.

Appendix H: Fluctuation Figures

Abstract

Because there are seven data sets, two bands, three exclusion radii (i.e., maximal PSF sizes), and two "modes" (raw and high-pass filtered), the number of different data sets to display is quite large. Chapter 10 extracts the most interesting data for display and discussion, but the critic justifiably wants to examine the data themselves to confirm the analysis. In order to make Chapter 10 manageable, the bulk of the data display has been exiled to this appendix. The ACFs are displayed first in four figures. They are followed by four plot of $\delta I/I$ in terms of $\sigma_b(\phi)/I$.

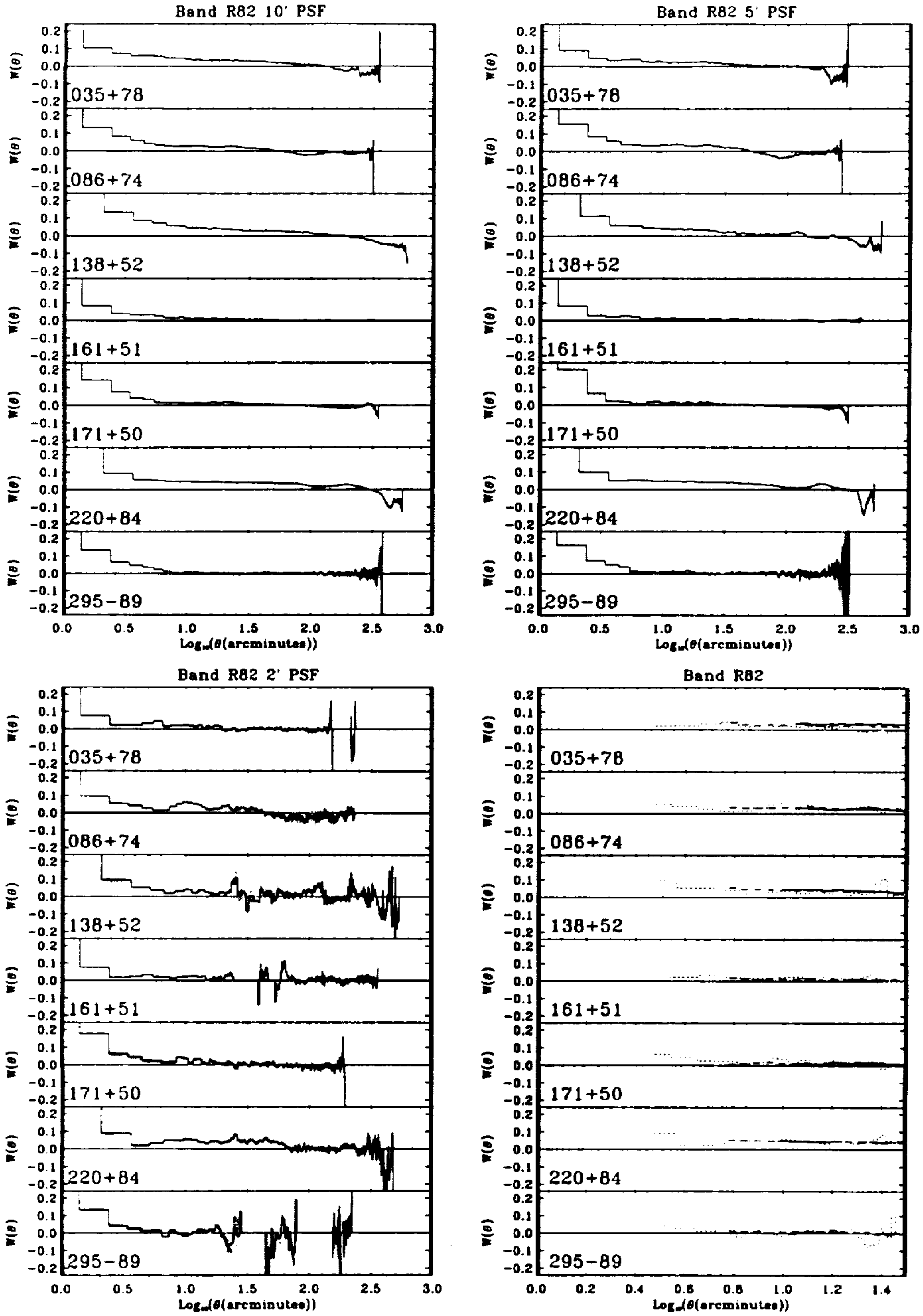

Fig. H.1.— ACFs for band R1L2(=R82). *Top Left:* for 10′ maximum PSF. *Top Right:* for 5′ maximum PSF. *Bottom Left:* for 2′ maximum PSF. Shaded regions in the first three panels show the uncertainty. *Bottom Right:* ACFs for all three PSF sizes. **Solid:** 10′, **Dashed:** 5′, and **Dotted:** 2′.

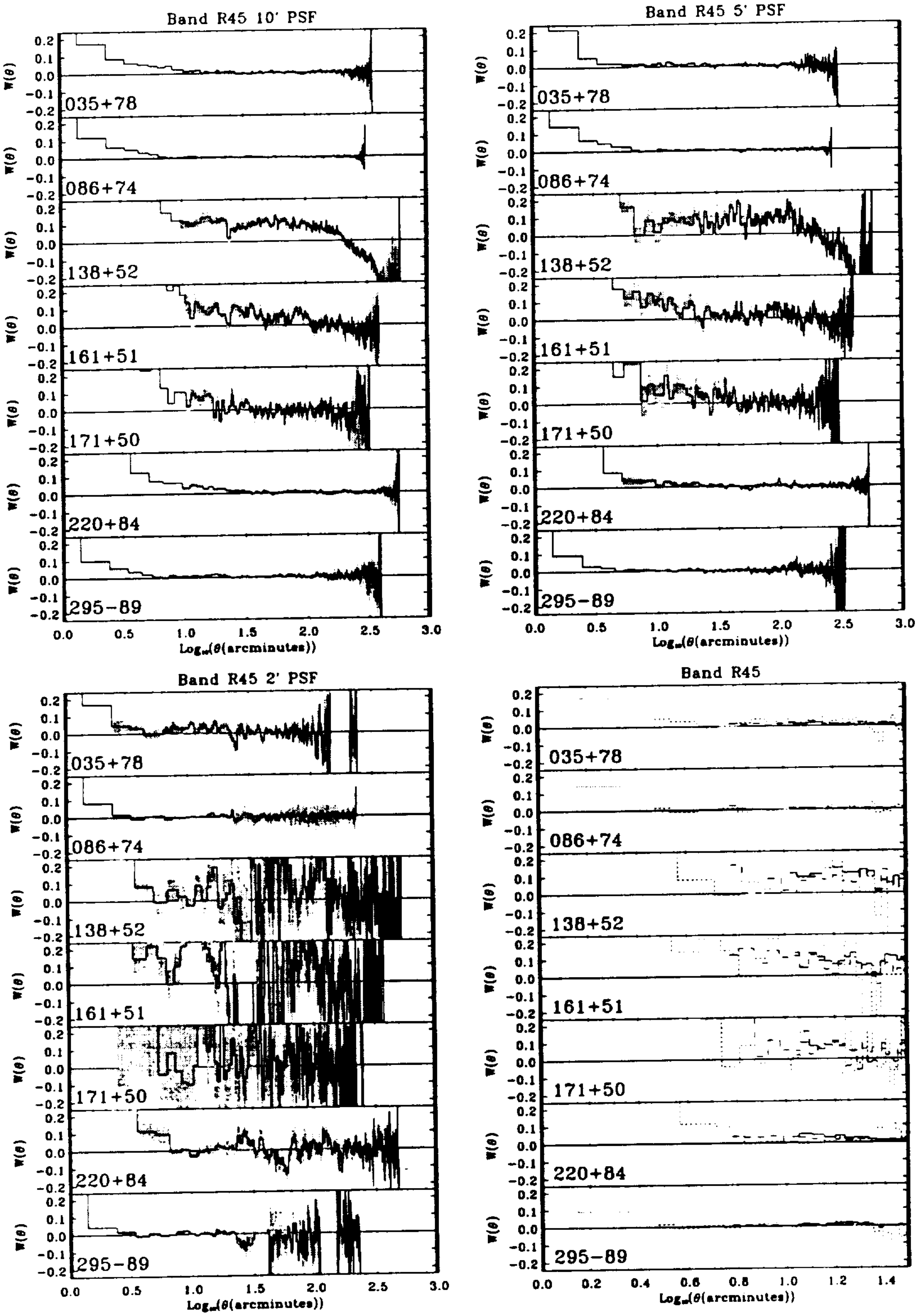

Fig. H.2.— ACFs for band R45. Legend as for previous figure.

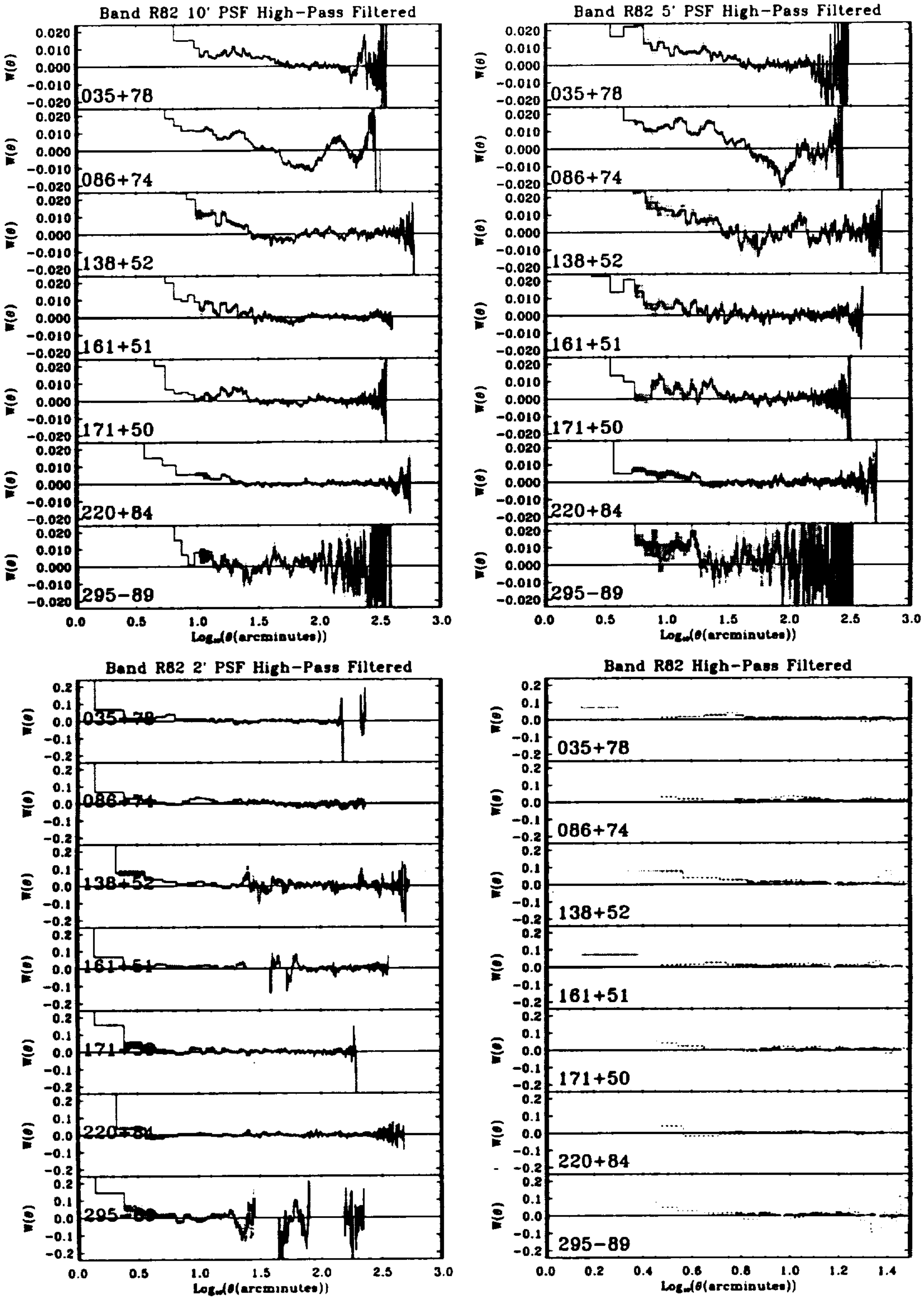
Band R82 10' PSF High-Pass Filtered

Band R82 5' PSF High-Pass Filtered

Band R82 2' PSF High-Pass Filtered

Band R82 High-Pass Filtered

Fig. H.3.— ACFs for high-pass filtered images of band R1L2(=R82). Legend as for previous figure. Note the changes of scales.

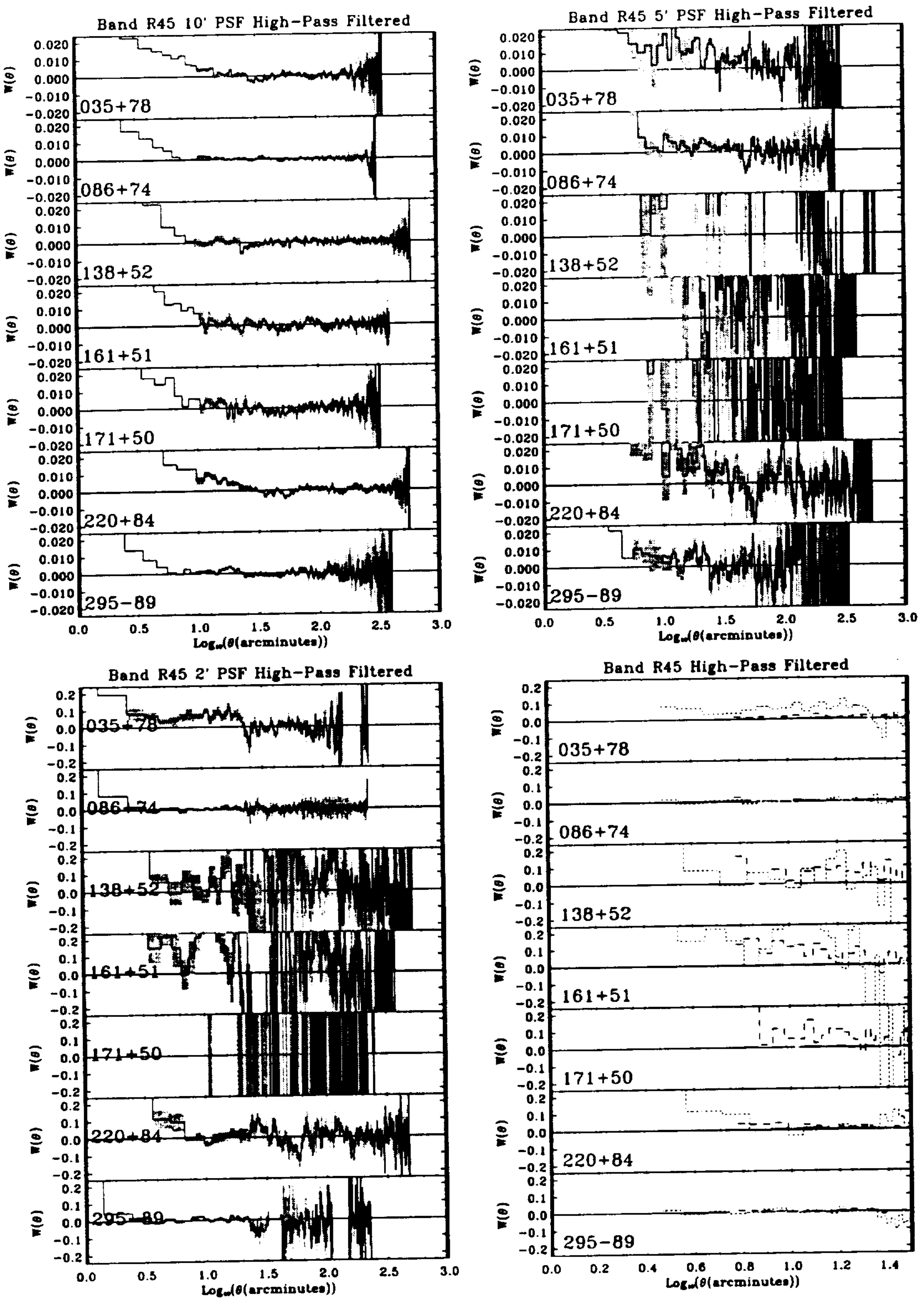

Fig. H.4.— ACFs for high-pass filtered images of band R45. Legend as for previous figure. Note the changes of scales.

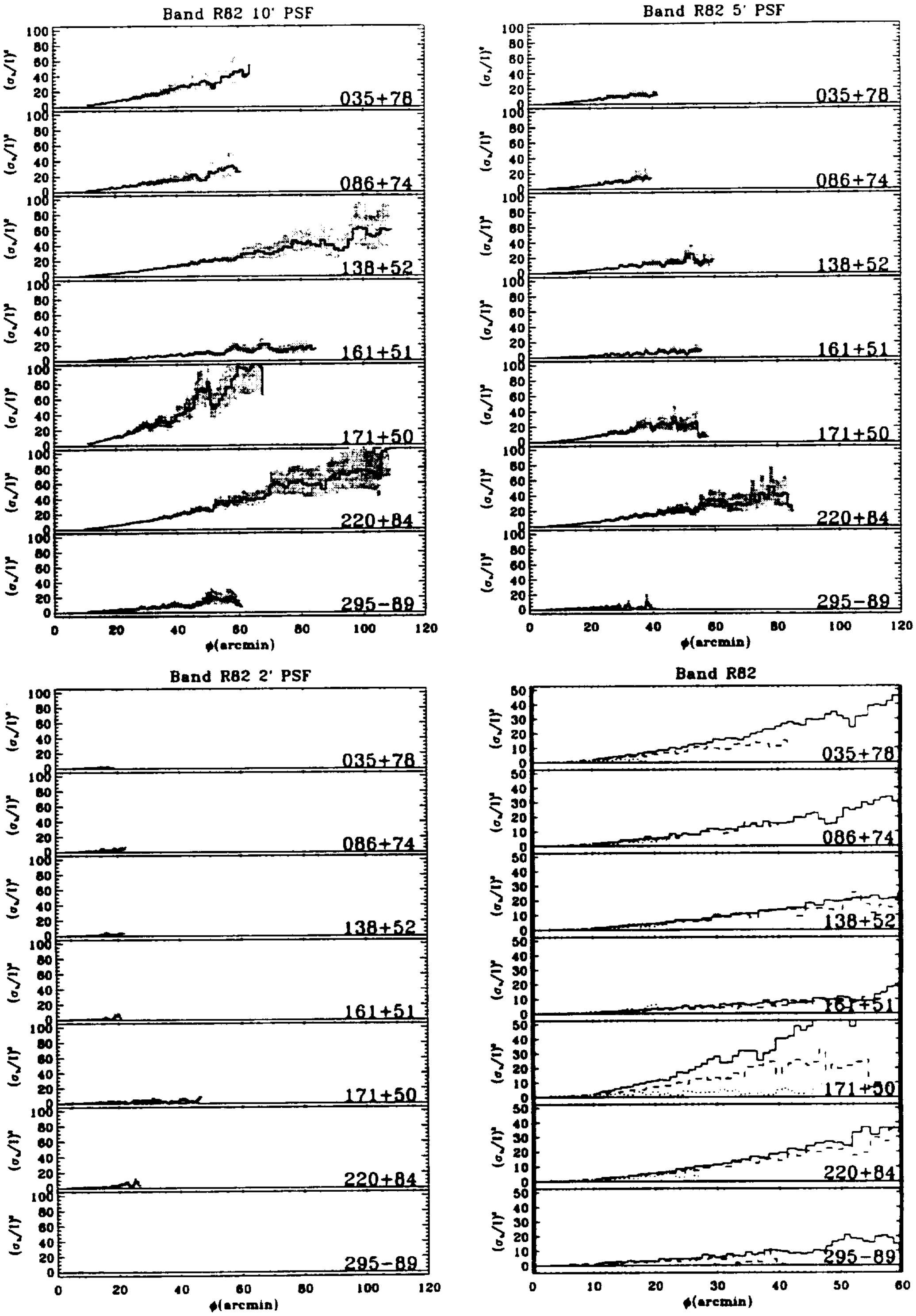

Fig. H.5.— Measures of $\sigma_b(\phi)/I$ for band R1L2(=R82). *Top Left:* for 10′ maximum PSF. *Top Right:* for 5′ maximum PSF. *Bottom Left:* for 2′ maximum PSF. Shaded regions in the first three panels show the uncertainty. *Bottom Right:* Measures of $\sigma_b(\phi)/I$ for all three PSF sizes. **Solid:** 10′, **Dashed:** 5′, and **Dotted:** 2′.

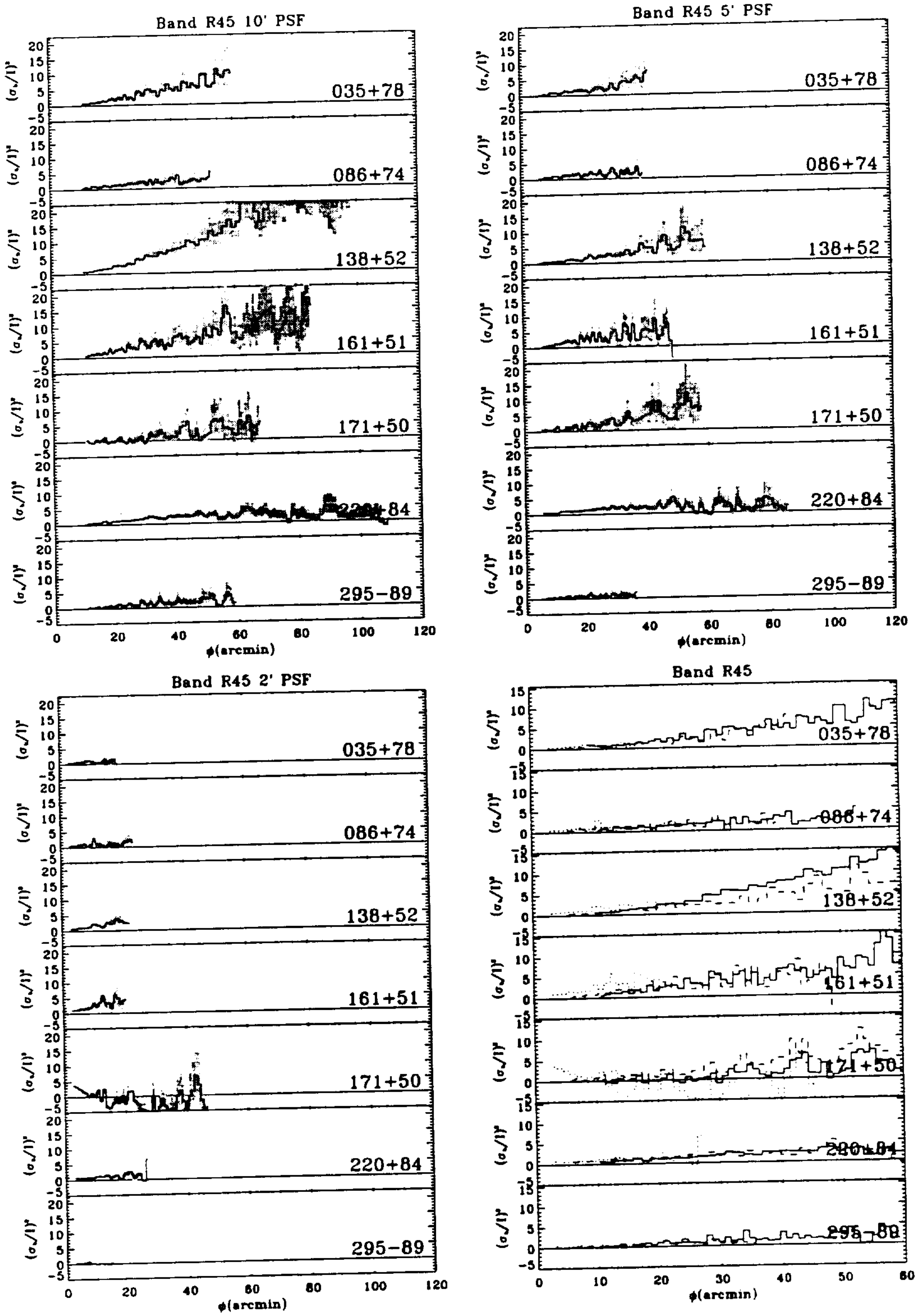

Fig. H.6.— Measures of $\sigma_b(\phi)/I$ for band R45. Legend as for the previous figure.

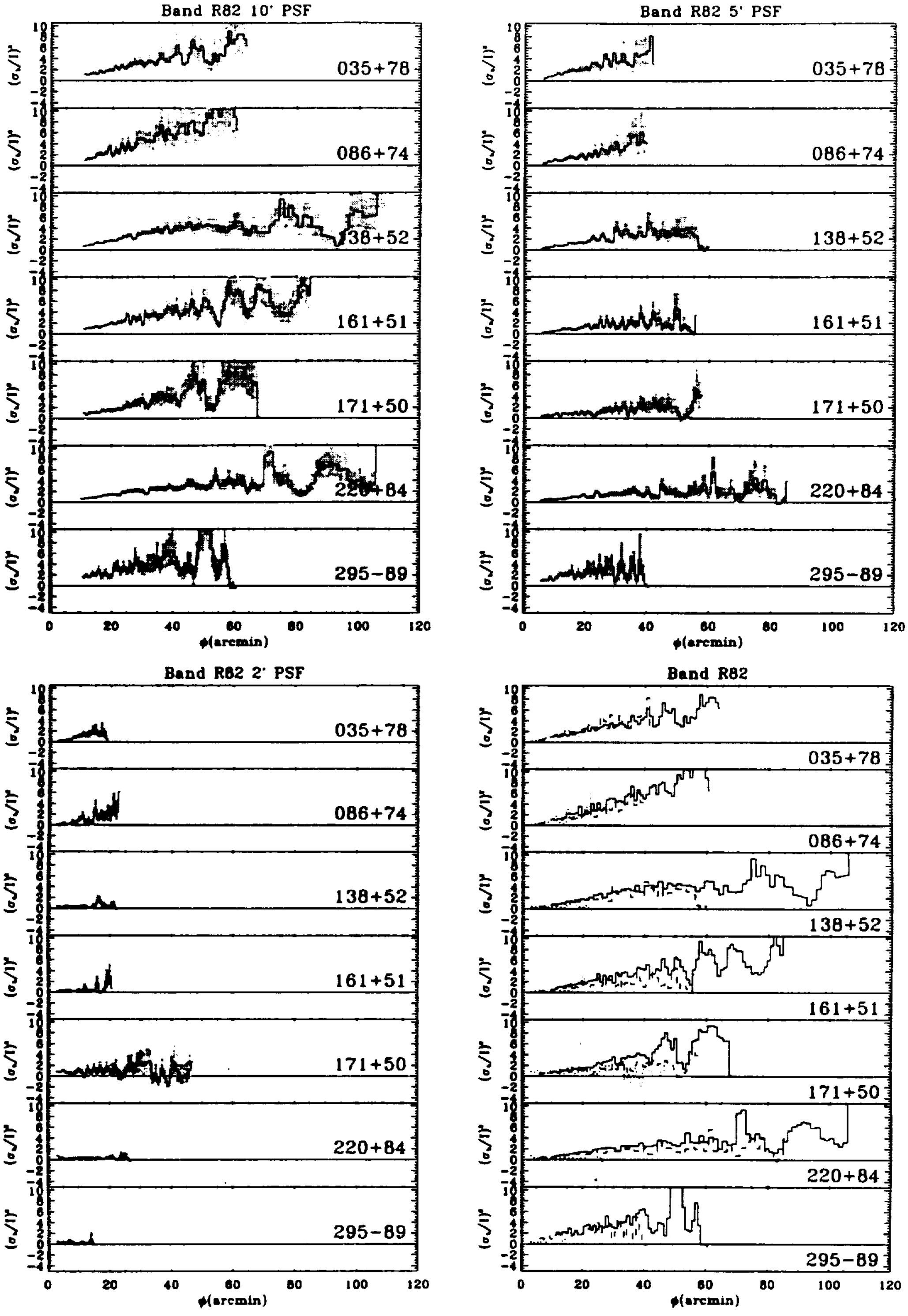

Fig. H.7.— Measures of $\sigma_b(\phi)/I$ for high-pass filtered images of band R1L2(=R82). Legend as for the previous figure.

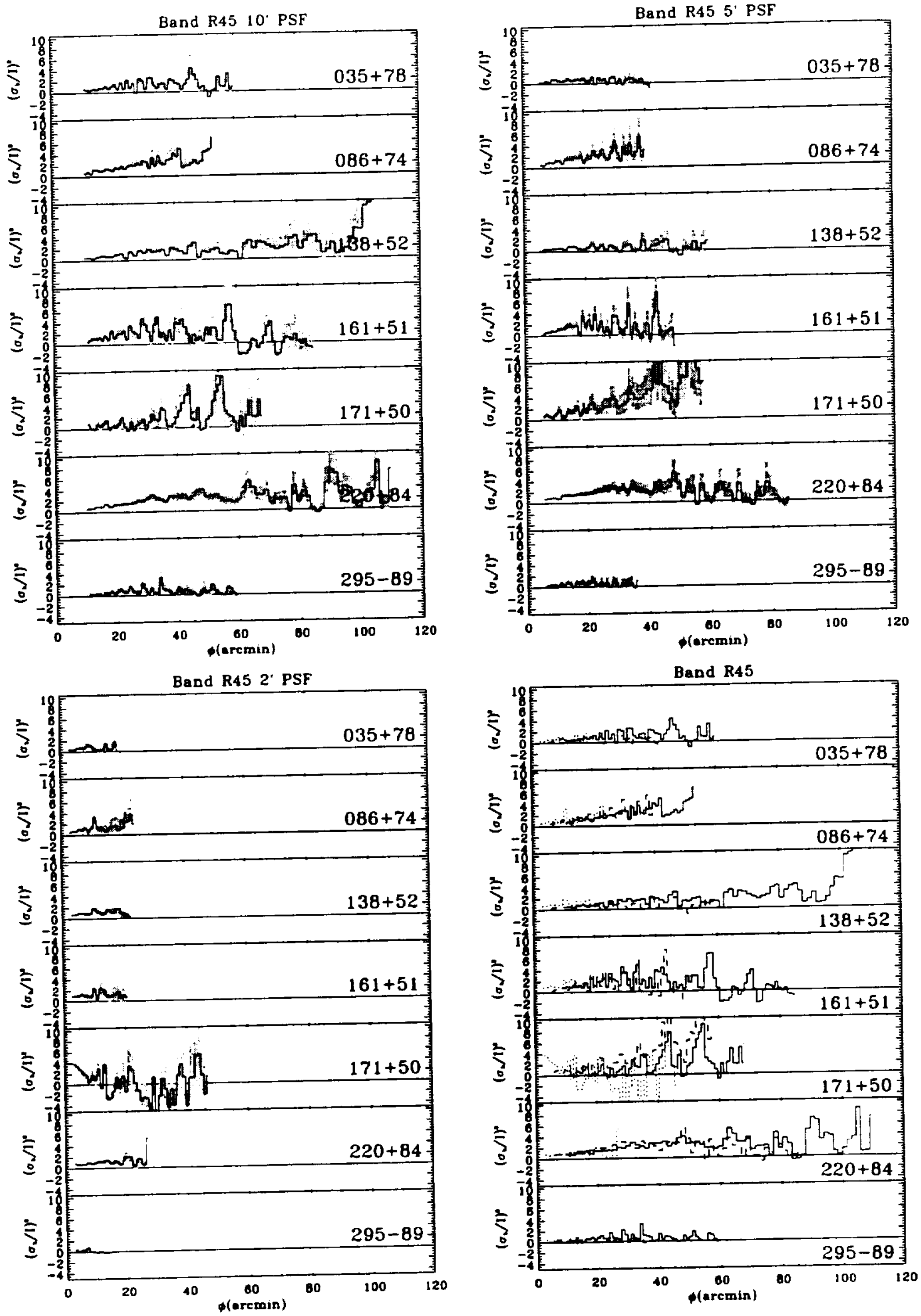

Fig. H.8.— Measures of $\sigma_b(\phi)/I$ for high-pass filtered images of band R45. Legend as for the previous figure.

Appendix I: Calculating the Suppression Factor

Abstract

This appendix provides a rough derivation of the factor by which fluctuations of scale ϕ_F are suppressed by high-pass filtering with a threshold of ϕ_S. We also show, non-rigorously, that the calculated value of the excess fluctuations at scale ϕ is the linear combination of the fluctuations at all other scales.

Assume that an image I contains only fluctuations of scale ϕ_F and amplitude $\sigma_{I,F}$ (i.e., the variance of pixels of size ϕ_F in image I). Assume also that the image is pixellated at scale ϕ_P, where $\phi_F/\phi_P \sim$ a few. At the pixels size, the variance will be

$$\sigma^2_{I,p} = \left(\frac{\phi_F}{\phi_P}\right)^2 \sigma^2_F \qquad (I.1)$$

(N.B., with respect to the text in Chapter 10 this is σ^2_B, *not* σ^2_b). The smoothed image, S, is the original image smoothed by ϕ_S, where $\phi_S/\phi_F \gtrsim$ a few. The variance of the smoothed image on the scale of ϕ_P will be

$$\sigma^2_{S,p} = \sigma^2_{I,p}\left(\frac{\phi_F}{\phi_S}\right)^2 \qquad (I.2)$$

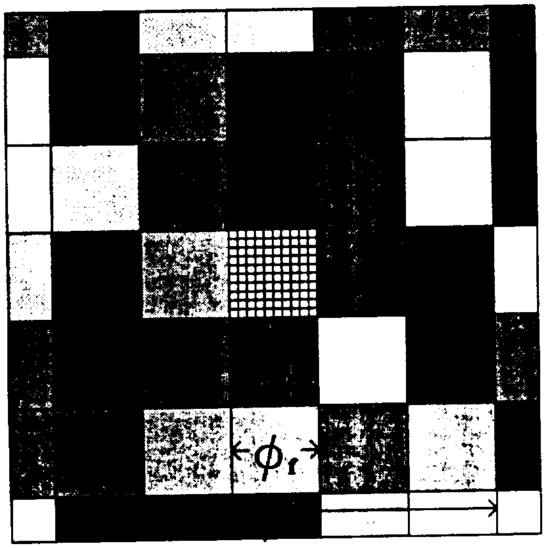

Fig. I.1.— Cartoon demonstrating values used in calculating the suppression factor. The meanings of the variables is given in the text.

The high-pass filtered image. H, is constructed by subtracting S from I, so the variance of the high-pass filtered image will be

$$\sigma^2_{H,p} = \sigma^2_{I,p} + \sigma^2_{S,p} - 2\sigma^2_{IS,p} \qquad (I.3)$$

where σ_{IS} is the correlation of the image and the smoothed image. It is shown in the footnote[1] that the correlation term is given by

$$\sigma^2_{IS,p} \sim \sigma^2_{I,p}\left(\frac{\phi_F}{\phi_S}\right)^2, \qquad (I.8)$$

thus,

$$\sigma^2_{H,p} \sim \sigma_{I,p}\left[1 - \left(\frac{\phi_F}{\phi_S}\right)^2\right] \qquad (I.9)$$

This formulation, of course, makes the assumption that there are no fluctuations at any other scale, which is clearly not the case.

Since the fluctuations at different scales are statistically independent, one can pursue a similar course assuming that there are fluctuations

---

[1] The correlation term may be calculated as follows. Assume that a pixel in the initial image is the central pixel of a smoothing region of area n pixels and has the value P. The sum of all of the other pixels in the smoothing region is Q. The mean value of a pixel is M The value of the same pixel in the low-pass filter will be $(S+Q)/n$. The correlation between the value of the pixel in the initial image, and the same pixel in the low-pass filtered image is given by

$$\sigma^2_{IS} = \frac{1}{n}\sum\left[\left(\frac{Q+P}{n} - M\right)(P-M)\right]. \qquad (I.4)$$

This expression can be expanded as

$$\frac{1}{n}\sum\left[\frac{QP}{n} + \frac{p^2}{n} - \frac{Q+P}{n}M - PM + M^2\right] \qquad (I.5)$$

and if we make the approximation that

$$\frac{Q}{n} \sim \left[\frac{(n-1)M}{n}\right] \qquad (I.6)$$

then

$$\sigma^2_{IS} \sim \frac{1}{n}\sigma^2_P. \qquad (I.7)$$

at both ϕ_F and ϕ_P. Then the variance of the original image on the scale of ϕ_P is

$$\sigma_{I,p}^2 = \sigma_P^2 + \left(\frac{\phi_F}{\phi_P}\right) \sigma_F^2 \tag{I.10}$$

The variance in the smoothed image is then

$$\sigma_{S,p}^2 = \sigma_P^2 \left(\frac{\phi_P}{\phi_S}\right)^2 + \sigma_F^2 \left(\frac{\phi_F}{\phi_P}\right)^2 \left(\frac{\phi_F}{\phi_S}\right)^2 \tag{I.11}$$

The variance in the high-pass-filtered image is then

$$\sigma_P^2 \left[1 - \left(\frac{\phi_P}{\phi_S}\right)^2\right] \sigma_F^2 \left(\frac{\phi_F}{\phi_P}\right)^2 \left[1 - \left(\frac{\phi_F}{\phi_S}\right)^2\right] \tag{I.12}$$

Thus, the variance at a given scale is the linear sum of the variances at all scales. The variance at a given scale of a high-pass-filtered image is the linear sum of the variances, each multiplied by $[1 - (\phi_F/\phi_S)^2]$ where ϕ_F is the scale of the fluctuation.

Glossary

ACF - AutoCorrelation Function, see Equation 10.7.

AGN - Active Galactic Nuclei, one of the major sources of the cosmic X-ray background. These objects are typically a nuisance for those studying the truly diffuse background.

ASCA - Advanced Satellite for Cosmology and Astrophysics (Tanaka, Inoue, & Holt 1994).

BCES - Bivariate Correlated Errors and Scatter, a linear regression model developed by Akritas & Bershady (1996) for data with errors in both variables.

CFG - Chen, Fabian, & Gendreau (1997)

CLF - The Cumulative Luminosity Function, the number of sources brighter than a given luminosity (or brightness) as a function of luminosity (or brightness).

COBE - The COsmic Background Explorer satellite (Boggess et al. 1992).

DIRBE - The Diffuse Infra-Red Background Experiment, an instrument on *COBE* (Silverberg et al. 1993).

EPL - The Extragalactic Power Law, the emission due to unresolved extragalactic sources, typically AGN and QSOs. The spectrum of the emission in the 0.5-2.0 keV energy range is well modeled as a power-law with a photon index of ~ 1.4.

HEASARC - The High Energy Astrophysics Science Archive Research Center, a service of the GSFC LHEA.

HR - Hardness Ratio, usually defined for *ROSAT* PSPC bands as $(R_{47} - R_{82})/(R_{47} + R_{82})$, but is may be defined differently by other authors.

HRI - The High Resolution Imager, the secondary instrument on *ROSAT*.

HVC - High Velocity Cloud, a cloud of neutral hydrogen with a line-of-sight velocity not produced by galactic rotation and $|v| > 100$ km s^{-1}.

IDL - Interactive Data Language, a relatively expensive high level programming language developed and marketed by Research Systems Inc. that emulates FORTRAN, but has extensive visualization support and similarly extensive function libraries.

IGM - The InterGalactic Medium.

IMF - The Initial Mass Function, the number of stars of a given mass created per unit time per unit mass.

IRAS - The Infra-Red Astronomical Satellite, which created an all-sky survey at 12 μm, 24 μm, 60 μm and 100μm.

ISM - The InterStellar Medium, all that which occupies the space between the stars.

IVC - Intermediate Velocity Cloud, a cloud of neutral hydrogen with a line-of-sight velocity not produced by galactic rotation and 40 km s^{-1} $< |v| <$ 100 km s^{-1}.

LDS - The Leiden-Dwingeloo Survey of galactic neutral hydrogen (Hartmann & Burton 1997). See Chapter 2 for a description.

LHB - The Local Hot Bubble, the irregular region of million degree gas that extends for 50 to 100 pc in every direction from the sun. The LHB is contained within but does not fill the Local Cavity. The source of the gas in the LHB is unknown but generally attributed to a sequence of supernovae, each one reheating the cavity left by the previous one (Smith 1997). The most recent observational study of the LHB is Snowden et al. (1998). (Audiences not familiar with X-ray astronomy have been known to express absolute disbelief in the existence of this phenomenon as it violates the principle that the earth is not in a preferred location. It should be noted that this principle is *cosmological*, and has no application to galactic astronomy of the ISM.)

LIC - The Local Interstellar Cloud, a tenuous asymmetric cloud of neutral hydrogen surrounding the sun and extending a few parsecs in every direction. The cloud is detected in absorption in lines of sight to nearby stars (Lallement et al. 1995) There are other similar features within the Local Cavity, see the work on the Local ISM by Lallement, Vidal-Madjar, & Ferlat (1986).

LF - The Luminosity Function, the number of objects with a given luminosity (or brightness) as a function of luminosity (or brightness).

LMB - The Lampton, Margon, and Bowyer criteria for determining a probability interval (Lampton, Margon, & Bowyer 1976).

Local Cavity - An irregular region surrounding the sun with a lower than average density of neutral gas, and having a clear boundary at which the column density increases abruptly. The Local Cavity was first discussed by Knapp (1975), was studied by Paresce (1984) and Frisch & York (1983), and most recently mapped by Sfeir et al. (1999).

Local Fluff - The Local Interstellar Cloud.

LTE - Long-Term Enhancements. A temporally variable component of the SXRB of unknown source. The time scales of variability range from hours to months. See Chapter 2.

PSDL - The Point Source Detection Limit, the flux of the faintest point source detectable.

PSF - The Point Spread Function, the function describing the fraction of flux due to a point source detected at a given radius and position angle from the expected detector location of the point source.

PSPC - The Position Sensitive Proportional Counter, the primary instrument on *ROSAT*. See Chapter 2 for a more detailed description.

RASS - The *ROSAT* All-Sky Survey. See Chapter 2.

ROSAT - The RÖntgen SATellite, a satellite sensitive to soft X-ray emission (0.1-2 keV) which produced an All-Sky Survey (the *RASS*) as well as a substantial archive of pointed observations. See Chapter 2 for a more detailed description.

R&S - Raymond and Smith model thermal spectra (Raymond & Smith 1977).

SED - The Spectral Energy Distribution

SFD - Schlegel, Finkbeiner, & Davis (1998), a set of destriped and recalibrated *IRAS* 100 μm maps.

SFR - The Stellar Formation Rate, the mass of stars (in solar masses) created per unit time.

SXRB - The Soft X-Ray Background. The exact energy range of the SXRB depends upon the author, but generally is taken to mean 0.1-2 keV.

TAE - The Trans-Absorptive Emission, the X-ray emission originating beyond the absorption of the Galactic ISM. The TAE includes emission from the Galactic halo as well as emission due to extragalactic point sources and any diffuse extragalactic emission.

URB - UnResolved Binary.

WHIM - The Warm-Hot Intergalactic Medium, intergalactic gas with temperatures from 10^5 K to 10^7 K.

XSPEC - A common program for spectral analysis in the X-ray energy band (Arnaud 1996).

REFERENCES

Akritas, M. G., & Bershady, M. A. 1996, ApJ, 470, 706
Arnaud, K. A. 1996, in Astronomical Data Analysis Software and Systems V, ed. G. Jacoby & J. Barnes, 17
Boggess, N., et al. 1992, ApJ, 397, 420
Chen, L.-W., Fabian, A. C., & Gendreau, K. C. 1997, MNRAS, 285, 449
Frisch, P. C., & York, D. E. 1983, ApJ, 271, L59
Hartmann, D., & Burton, W. B. 1997, Atlas of Galactic Neutral Hydrogen (Cambridge University)
Knapp, G. R. 1975, AJ, 80, 111
Lallement, R., Ferlet, R., Lagrange, A. M., Lemoine, M., & Vidal-Madjar, A. 1995, A&A, 304, 461
Lallement, R., Vidal-Madjar, A., & Ferlat, R. 1986, A&A, 168, 225
Lampton, M., Margon, B., & Bowyer, S. 1976, ApJ, 208, 177
Paresce, F. 1984, AJ, 89, 1022
Raymond, J. C., & Smith, B. W. 1977, ApJS, 35
Schlegel, D. J., Finkbeiner, D. P., & Davis, M. 1998, ApJ, 500, 525
Sfeir, D., Lallement, R., Crifo, F., & Welsh, B. Y. 1999, A&A, submitted
Silverberg, R. F., Hauser, M. G., Boggess, N. W., Kelsall, T. J., Moseley, S. H., & Murdock, T. L. 1993, Proc. SPIE, 2019, 180
Smith, R. K. 1997, Ph.D. thesis, University of Wisconsin
Snowden, S. L., Egger, R., Finkbeiner, D., Freyberg, M. J., & Plucinsky, P. P. 1998, ApJ, 493, 715
Tanaka, Y., Inoue, H., & Holt, S. S. 1994, PASJ, 46, L37

REFERENCES

Abell, G. O., Corwin, H. G., & Olowin, R. P. 1989, ApJS, 70, 1

Akritas, M. G., & Bershady, M. A. 1996, ApJ, 470, 706

Arabadjis, J. S., & Bregman, J. N. 1999, ApJ, 510, 806, submitted

Arendt, R. G., et al. 1998, ApJ, 508, 74

Arnaud, K. A. 1996, in Astronomical Data Analysis Software and Systems V, ed. G. Jacoby & J. Barnes, 17

Babu, G. J., & Feigelson, E. D. 1996, Astrostatistics (Chapman & Hall)

Balucinska-Church, M., & McCammon, D. 1992, ApJ, 400, 699

Barber, C., Warwick, R. S., & Snowden, S. L. 1995, in Röntgenstrahlung from the Universe, ed. H. Zimmermann, J. Trümper, & H. Yorke, MPE Report 263, 319

Barber, C. R., Roberts, T. P., & Warwick, R. S. 1996, MNRAS, 282, 157

Barber, C. R., & Warwick, R. S. 1994, MNRAS, 267, 270

Benjamin, R. A., Venn, K. A., Hiltgen, D. D., & Sneden, C. 1996, ApJ, 464, 836

Bessell, M. S., & Stringfellow, G. S. 1993, ARA&A, 31, 433

Bienaymé, O., Robin, A. C., & Crézé, M. 1987, A&A, 180, 94

Bloch, J. J., Jahoda, K., Juda, M., McCammon, D., Sanders, W. T., & Snowden, S. L. 1986, ApJ, 308, L59

Boggess, N., et al. 1992, ApJ, 397, 420

Boulanger, F., Abergel, A., Bernard, J.-P., Burton, W. B., Désert, F.-X., Hartmann, D., Lagache, G., & Puget, J.-L. 1996, A&A, 312, 256

Bower, R. G., et al. 1996, MNRAS, 281, 59

Bowyer, C. S., Field, G. B., & Mack, J. E. 1968, Nature, 217, 32

Boyle, B. J., Wilkes, B. J., & Elvis, M. 1997, MNRAS, 285, 511

Bregman, J. N., & Houk, J. C. 1997, ApJ, 485, 159

Briel, U. G., & Henry, J. P. 1995, A&A, 302, L9

Bryan, G. L., & Norman, M. L. 1998, ApJ, 495, 80

Bunner, A. N., Coleman, P. L., Kraushaar, W. L., McCammon, D., Palmieri, T. M., Shilepsky, A., & Ulmer, M. 1969, Nature, 233, 1222

Burles, S., & Tytler, D. 1998, ApJ, 499, 699

Burrows, D. N. 1989, ApJ, 340, 775

Burrows, D. N., McCammon, D., Sanders, W. T., & Kraushaar, W. L. 1984, ApJ, 287, 208

Burrows, D. N., & Mendenhall, J. A. 1991, Nature, 351, 629

Carballo, R., Warwick, R. S., Barcons, X., Gonzalez-Serrano, J. I., Barber, C. R., Martinez-Gonzalez, E., Peres-Fournon, I., & Burgos, J. 1995, MNRAS, 277, 1312

Cen, R., Kang, H., Ostriker, J. P., & Ryu, D. 1995, ApJ, 451, 436

Cen, R., & Ostriker, J. P. 1999, ApJ, 514, 1

Chen, L.-W., Fabian, A. C., & Gendreau, K. C. 1997, MNRAS, 285, 449

Chen, L.-W., Fabian, A. C., Warwick, R. S., Branduardi-Raymont, G., & Barber, C. R. 1994, MNRAS, 266, 846

Cox, D. P. 1998, in The Local Bubble, ed. D. Breitschwerdt & M. Freyberg, 121

Cox, D. P., & Reynolds, R. J. 1987, ARA&A, 25, 303

Cox, D. P., & Snowden, S. L. 1986, Advances in Space Research, 6(2), 97

Cravens, T. E. 1996, Geophysical Research Letters, 24, 105

Cui, W., Sanders, W. T., McCammon, D., Snowden, S. L., & Womble, D. S. 1996, ApJ, 468, 117

Dahlem, M., Weaver, K. A., & Heckman, T. M. 1998, ApJS, 118, 401

Danly, L., Albert, C. E., & Kuntz, K. D. 1993, ApJ, 416, L29

Davé, R., et al. 2000, ApJ, submitted

Davidsen, A., Shulman, S., Fritz, G., Meekins, J. F., Henry, R. C., & Friedman, H. 1972, ApJ, 177, 629

Deiker, S., Kelley, R. L., Lesser, A., McCammon, D., Porter, F. S., Stahle, W. T. S. C. K., & Szymkowiak, A. E. 1997, in Proceedings of the Seventh International Workshop on Low Temperature Detectors, 113

Dempsey, R. C., Linsky, J. L., Fleming, T. A., & Schmitt, J. H. M. M. 1993, ApJS, 86, 599

Domgörgen, H., & Mathis, J. S. 1994, ApJ, 428, 647

Donahue, M., Aldering, G., & Stocke, J. T. 1995, ApJ, 450, L45

Fiegelson, E. D., & Nelson, P. I. 1985, ApJ, 293, 192

Field, G. B. 1965, ApJ, 142, 531
Fixsen, D. J., Dwek, E., Mather, J. C., Bennett, C. L., & Shafer, R. A. 1998, ApJ, 508, 123
Fleming, T. A., Molendi, S., Maccacaro, T., & Wolter, A. 1995, ApJS, 99, 701
Fleming, T. A., Snowden, S. L., Pfeffermann, E., Briel, U., & Greiner, J. 1996, A&A, 316, 147
Freyberg, M. J. 1998, in The Local Bubble, ed. D. Breitschwerdt & M. Freyberg, 113
Frisch, P. C., & York, D. E. 1983, ApJ, 271, L59
Fukugita, M., Hogan, C. J., & Peebles, P. J. E. 1998, ApJ, 503, 518
Gehrels, N., & Williams, E. D. 1993, ApJ, 418, L25
Greisen, E. W., & Calabretta, M. 1993, Representations of celestial coordinates in fits
Gruber, R. 1992, in Data Analysis in Astronomy IV, ed. V. D. Gesù, 153
Guillout, P., Haywood, M., Motch, C., & Robin, A. C. 1996, A&A, 316, 89
Hartmann, D., & Burton, W. B. 1997, Atlas of Galactic Neutral Hydrogen (Cambridge University)
Hartmann, D., Kalberla, P. M. W., Burton, W. B., & Mebold, U. 1996, A&A, 119, 115
Hasinger, G., Burg, R., Giacconi, R., Hartner, G., Schmidt, M., Trümper, J., & Zamorani, G. 1993, A&A, 275, 1
Hasinger, G., Burg, R., Giacconi, R., Schmidt, M., Trümper, J., & Zamorani, G. 1998, A&A, 329, 482
Hauser, M. G., et al. 1998, ApJ, 508, 25
Haywood, M., Robin, A. C., & Crézé, M. 1997, A&A, 320, 428
Henry, T. J., & McCarthy, D. W. 1993, AJ, 106, 773
Herbstmeier, U., Heithausen, A., & Mebold, U. 1993, A&A, 272, 514
Herbstmeier, U., Mebold, U., Snowden, S. L., Hartmann, D., Burton, W. B., Moritz, P., Kalberla, P. M. W., & Egger, R. 1995, A&A, 298, 606
Hernquist, L., Katz, N., Weinberg, D. H., & Miralda-Escudé, J. 1996, ApJ, 457, L51
Hünsch, M., Schmitt, J. H. M. M., Schröder, K.-P., & Zickgraf, F.-J. 1998, A&A, 330, 225
Hünsch, M., Schmitt, J. H. M. M., Sterzik, M. F., & Voges, W. 1999, A&AS, 135, 319
Hutchinson, I. B., Warwick, R. S., & Willingale, R. 1998, in The Local Bubble, ed. D. Breitschwerdt & M. Freyberg, 283
Jakobsen, P., & Kahn, S. M. 1986, ApJ, 309, 682
Juda, M., Bloch, J. J., Edwards, B. C., McCammon, D., Sanders, W. T., Snowden, S. L., & Zhang, J. 1991, ApJ, 367, 182
Kalberla, P. M. W. 1978, Ph.D. thesis, University of Bonn
Kalberla, P. M. W., Westphalen, G., Mebold, U., Hartmann, D., & Burton, W. B. 1997, in The Local Bubble, ed. D. Breitschwerdt & M. Freyberg, 479
Kelsall, T., et al. 1998, ApJ, 508, 44
Kernighan, B. W., & Pike, R. 1984, The UNIX Programming Environment (Prentice Hall)
Kerp, J. 1994, A&A, 289, 597
Kerp, J., Burton, W. B., Egger, R., Freyberg, M. J., Hartmann, D., Kalberla, P. M. W., Mebold, U., & Pietz, J. 1999, A&A, 342, 213
Knapp, G. R. 1975, AJ, 80, 111
Krautter, J., et al. 1999, A&A, 350, 743
Kroupa, P., Tout, C. A., & Gilmore, G. 1993, MNRAS, 262, 545
Kull, A., & Böhringer, H. 1999, A&A, 341, 23
Kuntz, K. D. 2000, Ph.D. thesis, University of Maryland
Kuntz, K. D., & Danly, L. 1992, PASP, 104, 1256
Kuntz, K. D., & Danly, L. 1996, ApJ, 457, 703
Kuntz, K. D., & Snowden, S. L. 1998, Cookbook for analysis procedures for *rosat* XRT Observations of Extended Objects and the Diffuse Background, Part II: Mosaics, Technical report, NASA/GSFC
Kuntz, K. D., & Snowden, S. L. 2000, ApJ
Kuntz, K. D., Snowden, S. L., & Verter, F. 1997, ApJ, 484, 245
Kuntz, K. D., Snowden, S. L., & Warwick, R. S. 1998, in The Local Bubble, ed. D. Breitschwerdt & M. Freyberg, 329
Lallement, R., Ferlet, R., Lagrange, A. M., Lemoine, M., & Vidal-Madjar, A. 1995, A&A, 304, 461
Lallement, R., Vidal-Madjar, A., & Ferlat, R. 1986, A&A, 168, 225
Lampton, M., Margon, B., & Bowyer, S. 1976, ApJ, 208, 177
Landini, M., & Monsignori-Fossi, B. C. 1990, A&AS, 82, 229
Laor, A., Fiore, F., Elvis, M., Wilkes, B. J., & McDowell, J. C. 1997, ApJ, 477, 93
Lilienthal, D., Wennmacher, A., Herbstmeier, U., & Mebold, U. 1991, A&A, 250, 150
Lisse, C. M., et al. 1996, Science, 274, 205
Lockman, F. J. 1984, ApJ, 283, 90
Lockman, F. J., & Gehman, C. S. 1991, ApJ, 382, 182
Lockman, F. J., Jahoda, K., & McCammon, D. 1986, ApJ, 302, 432
Long, K. S., Agrawal, P. C., & Garmire, G. P. 1976, ApJ, 206, 411
Mather, J. C., et al. 1994, ApJ, 420, 439

McCammon, D., Meyer, S. S., Sanders, W. T., & Williamson, F. O. 1976, ApJ, 209, 46
McHardy, I. M., et al. 1998, MNRAS, 295, 641
McKee, C. F., & Ostricker, J. P. 1977, ApJ, 218, 148
Mewe, R., Gronenschild, E., & van den Oord, G. H. J. 1985, A&AS, 62, 197
Miyaji, T., Ishisaki, Y., Ogasaka, Y., Ueda, Y., Freyberg, M. J., Hasinger, G., & Tanaka, Y. 1998, A&A, 334, L13
Morrison, R., & McCammon, D. 1983, ApJ, 270, 119
Mortiz, P., Wennmacher, A., Herbstmeier, U., Mebold, U., Egger, R., & Snowden, S. 1998, A&A, 336, 682
Mushotzky, R. F., Cowie, L. L., Barger, A. J., & Arnaud, K. A. 2000, Nature, in press
Ostriker, J. P., & Cen, R. 1996, ApJ, 464, 27
Ottmann, R., Fleming, T. A., & Pasquini, L. 1997, A&A, 322, 785
Ottmann, R., & Schmitt, J. H. M. M. 1992, A&A, 256, 421
Paresce, F. 1984, AJ, 89, 1022
Parmar, A. N., Guainazzi, M., Oosterbroek, T., Orr, A., Favata, F., Lumb, D., & Malizia, A. 1999, A&A, submitted
Peebles, P. J. E. 1993, Principles of Physical Cosmology (Princeton University Press)
Pierre, M., Bryan, G., & Gastaud, R. 2000, A&A, submitted
Pietz, J., Kerp, J., Kalberla, P., Burton, W. B., Hartmann, D., & Mebold, U. 1998, A&A, 332, 55
Plucinsky, P. P., Snowden, S. L., Briel, U. G., Hasinger, G., & Pfeffermann, E. 1993, ApJ, 418, 519
Press, W. H., Flannery, B. P., Teukolsky, S. A., & Vetterling, W. T. 1986, Numerical Recipes (Cambridge University Press)
Prieto, M. A., Hasinger, G., & Snowden, S. L. 1996, A&A, 120, 187
Rand, R. J. 1998, Proc. Astron. Soc. Aust., 15, 106
Rand, R. J., Kulkarni, S. R., & Hester, J. J. 1992, ApJ, 396, 97
Rand, R. J., & Stone, J. M. 1996, AJ, 111, 190
Randich, S., & Schmitt, J. H. M. M. 1995, A&A, 298, 115
Randich, S., Schmitt, J. H. M. M., & Prosser, C. 1996, A&A, 313, 815
Raymond, J. C. 1992, ApJ, 384, 502
Raymond, J. C., & Smith, B. W. 1977, ApJS, 35
Reach, W. T., Koo, B.-C., & Heiles, C. 1994, ApJ, 429, 672
Reach, W. T., Wall, W. F., & Odegard, N. 1998, ApJ, 507, 507
Read, A. M., Ponman, T. J., & Strickland, D. K. 1997, MNRAS, 286, 626,668
Reynolds, R. J. 1985, ApJ, 333, 341
Reynolds, R. J. 1991, in The Interstellar Disk-Halo Connection in Galaxies, ed. H. Bloemen, 67
Reynolds, R. J. 1999, private communication
Reynolds, R. J., Tufte, S. L., Haffner, L. M., Jaenig, K., & Percival, J. W. 1998, Proc. Astron. Soc. Aust., 15, 14
Reynolds, R. J., Tufte, S. L., Kung, D. T., McCullough, P. R., & Heiles, C. 1995, ApJ, 448, 715
Sanders, W. T., Burrows, D. N., McCammon, D., & Kraushaar, W. L. 1983, in Supernova Remnants and their X-ray Emission, ed. J. Danziger & P. Gorenstien, 361
Sanders, W. T., Edgar, R. J., Liedahl, D. A., & Morgenthaler, J. P. 1998, in The Local Bubble, ed. D. Breitschwerdt & M. Freyberg, 83
Sanders, W. T., Kraushaar, W. L., Nousek, J. A., & Fried, P. M. 1977, ApJ, 217, L87
Savage, B. D., Bohlin, R. C., Drake, J. F., & Budich, W. 1977, ApJ, 216, 291
Scalo, J. M. 1986, Fundamentals of Cosmic Physics, 11, 1
Scharf, C., Donahue, M., Voit, G. M., Rosati, P., & Postman, M. 2000, ApJ, 528, L73
Schlegel, D. J., Finkbeiner, D. P., & Davis, M. 1998, ApJ, 500, 525
Schmidt, M., et al. 1998, A&A, 329, 495
Schmitt, J. H. M. M. 1985, ApJ, 293, 178
Schmitt, J. H. M. M. 1997, A&A, 318, 215
Schmitt, J. H. M. M., Fleming, T. A., & Giampapa, M. S. 1995, ApJ, 450, 392
Schmitt, J. H. M. M., Snowden, S. L., Aschenbach, B., Hasinger, G., Pfeffermann, E., Predehl, P., & Trümper, J. 1991, Nature, 349, 583
Schmutzler, T., & Tscharnuter, W. M. 1993, A&A, 273, 318
Schröder, K.-P., Hünsch, M., & Schmitt, J. H. M. M. 1998, A&A, 335, 591
Sfeir, D., Lallement, R., Crifo, F., & Welsh, B. Y. 1999, A&A, submitted
Shelton, R. L. 1998, ApJ, 504, 785
Shelton, R. L. 1999a, ApJ, 521, 217
Shelton, R. L. 1999b, private communication
Sidher, S. D., Summer, T. J., Quenby, J. J., & Gambhir, M. 1996, A&A, 305, 308
Silverberg, R. F., Hauser, M. G., Boggess, N. W., Kelsall, T. J., Moseley, S. H., & Murdock, T. L. 1993, Proc. SPIE, 2019, 180
Smith, R. K. 1997, Ph.D. thesis, University of Wisconsin

Snowden, S. L. 1998, ApJS, 117, 223
Snowden, S. L., Cox, D. P., McCammon, D., & Sanders, W. T. 1990, ApJ, 354, 211
Snowden, S. L., Egger, R., Finkbeiner, D., Freyberg, M. J., & Plucinsky, P. P. 1998, ApJ, 493, 715
Snowden, S. L., et al. 1997, ApJ, 485, 125
Snowden, S. L., & Freyberg, M. J. 1993, ApJ, 404, 403
Snowden, S. L., Freyberg, M. J., Kuntz, K. D., & Sanders, W. T. 2000, ApJS, in press
Snowden, S. L., et al. 1995, ApJ, 454, 643
Snowden, S. L., Hasinger, G., Jahoda, K., Lockman, F. J., McCammon, D., & Sanders, W. T. 1994a, ApJ, 430, 601
Snowden, S. L., & Kuntz, K. D. 1998, Cookbook for analysis procdures for *rosat* XRT Observations of Extended Objects and the Diffuse Background, Part I: Individual Observations, Technical report, NASA/GSFC
Snowden, S. L., McCammon, D., Burrows, D. N., & Mendenhall, J. A. 1994b, ApJ, 424, 714
Snowden, S. L., McCammon, D., & Verter, F. 1993, ApJ, 409, L21
Snowden, S. L., Mebold, U., Hirth, W., Herbstmeier, U., & Schmitt, J. H. M. M. 1991, Science, 252, 1529
Snowden, S. L., & Pietsch, W. 1995, ApJ, 452, 627
Snowden, S. L., Plucinsky, P. P., Briel, U., Hasinger, G., & Pfeffermann, E. 1992, ApJ, 393, 819
Snowden, S. L., Schmitt, J. H. M. M., & Edwards, B. C. 1990, ApJ, 364, 118
Snowden, S. L., Turner, T. J., & Freyberg, M. J. 1999, A&A
Sodroski, T. J., Odegard, N., Arendt, R. G., Dwek, E., Weiland, J. L., Hauser, M. G., & Kelsall, T. 1997, ApJ, 480, 173
Soltan, A., & Hasinger, G. 1994, A&A, 288, 77
Soltan, A. M., Hasinger, G., Egger, R., Snowden, S., & Trümper, J. 1996, A&A, 305, 17
Spitzer, L. 1956, ApJ, 124, 20
Stark, A. A., Gammie, C. F., Wilson, R. W., Bally, J., Linke, R. A., Heiles, C., & Hurwitz, M. 1992, ApJS, 79, 77
Stauffer, J. R., Caillault, J.-P., Gagné, M., Prosser, C. F., & Hartman, L. W. 1994, ApJS, 91, 625
Stern, R. A., Schmitt, J. H. M. M., & Kahabka, P. T. 1995, ApJ, 448, 683
Strang, G. 1976, Linear Algebra and its Applications (Academic Press)
Tanaka, Y., Inoue, H., & Holt, S. S. 1994, PASJ, 46, L37
Vallerga, J., & Slavin, J. 1998, in The Local Bubble, ed. D. Breitschwerdt & M. Freyberg, 79
Vikhlinin, A., & Forman, W. 1995, ApJ, 455, L109
Voges, W., et al. 1992, in Proceedings of Satellite Symposium 3, Space Science with Particular Emphasis on High-Energy Astrophysics, ed. T. D. Guyenne & J. J. Hunt, 223
Voges, W., et al. 1996, http://www.rosat.mpe-garching.mpg.de/survey/rass-bsc/
Voges, W., et al. 1999, A&A, 349, 389
Vogler, A., Pietsch, W., & Kahabka, P. 1996, A&A, 305, 74
Wakker, B. P., & Boulanger, F. 1986, A&A, 170, 84
Wang, Q. D. 1997, in The Local Bubble, ed. D. Breitschwerdt & M. Freyberg, 503
Wang, Q. D., Walterbos, R. A. M., Steakley, M. F., Norman, C. A., & Braun, R. 1995, ApJ, 439, 176
Warwick, R., Hutchinson, I., Willingale, R., Kuntz, K., & Snowden, S. 1997, in The Local Bubble, ed. D. Breitschwerdt & M. Freyberg, 321
Warwick, R. S., & Roberts, T. P. 1998, Astronomische Nachrichten, 319, 59
Weliachew, L., Sancisi, R., & Guélin, M. 1978, A&A, 65, 37
Wu, K. K. S., Fabian, A. C., & Nulsen, P. E. J. 1999, MNRAS, in press
Yan, M., Sadeghpour, H. R., & Dalgarno, A. 1998, ApJ, 496, 1044
Zamorani, G., et al. 1999, A&A, 346, 731
Zhang, Y., Anninos, P., Norman, M. L., & Meiksin, A. 1997, ApJ, 485, 496

REPORT DOCUMENTATION PAGE

Form Approved
OMB No. 0704-0188

1. AGENCY USE ONLY *(Leave blank)*	**2. REPORT DATE** February 2001	**3. REPORT TYPE AND DATES COVERED** Technical Memorandum

4. TITLE AND SUBTITLE
Small-Scale Spatial Fluctuations in the Soft X-Ray Background

5. FUNDING NUMBERS
662

6. AUTHOR(S)
K.D. Kuntz

7. PERFORMING ORGANIZATION NAME(S) AND ADDRESS (ES)
Goddard Space Flight Center
Greenbelt, Maryland 20771

8. PEFORMING ORGANIZATION REPORT NUMBER
2001-01596-0

9. SPONSORING / MONITORING AGENCY NAME(S) AND ADDRESS (ES)
National Aeronautics and Space Administration
Washington, DC 20546-0001

10. SPONSORING / MONITORING AGENCY REPORT NUMBER
TM—2001-209981

11. SUPPLEMENTARY NOTES

12a. DISTRIBUTION / AVAILABILITY STATEMENT
Unclassified–Unlimited
Subject Category: 90
Report available from the NASA Center for AeroSpace Information,
7121 Standard Drive, Hanover, MD 21076-1320. (301) 621-0390.

12b. DISTRIBUTION CODE

13. ABSTRACT *(Maximum 200 words)*

In order to isolate the diffuse extragalactic component of the soft X-ray background, we have used a combination of *ROSAT* All-Sky Survey and *IRAS* 100 μm data to separate the soft X-ray background into five components. We find a *Local Hot Bubble* similar to that described by Snowden et al (1998). We make a first calculation of the contribution by *unresolved Galactic stars* to the diffuse background. We constrain the normalization of the *Extragalactic Power Law* (the contribution of the unresolved extragalactic point sources such as AGN, QSO's, and normal galaxies) to 9.5±0.9 keV $cm^{-2}s^{-1}$ $sr^{-1}keV^{-1}$, assuming a power-law index of 1.46. We show that the remaining emission, which is some combination of Galactic halo emission and the putative diffuse extragalactic emission, must be composed of at least two components which we have characterized by thermal spectra. *The softer component* has log $T \sim 6.08$ and a patchy distribution; thus it is most probably part of the Galactic halo. *The harder component* has log $T \sim 6.46$ and is nearly isotropic; some portion may be due to the Galactic halo and some portion may be due to the diffuse extragalactic emission. The maximum upper limit to the strength of the emission by the diffuse extragalactic component is the total of the hard component, ~ 7.4±1.0 keV cm^{-2} s^{-1} sr^{-1} keV^{-1} in the $\frac{3}{4}$ keV band. We have made the first direct measure of the fluctuations due to the diffuse extragalactic emission in the $\frac{3}{4}$ keV band. Physical arguments suggest that small angular scale (~ 10′) fluctuations in the Local Hot Bubble or the Galactic halo will have very short dissipation times (~ 10^5 years). Therefore, the fluctuation spectrum of the soft X-ray background should measure the distribution of the diffuse extragalactic emission. Using mosaics of deep, overlapping PSPC pointings, we find an autocorrelation function value of ~ 0.0025 for $10' < \theta < 20'$, and a value consistent with zero on larger scales. Measurement of the fluctuations with a $\delta I/I$ method produces consistent results.

14. SUBJECT TERMS
Soft x-ray background; ROSAT; IRAS.

15. NUMBER OF PAGES
256

16. PRICE CODE

17. SECURITY CLASSIFICATION OF REPORT Unclassified	**18. SECURITY CLASSIFICATION OF THIS PAGE** Unclassified	**19. SECURITY CLASSIFICATION OF ABSTRACT** Unclassified	**20. LIMITATION OF ABSTRACT** UL

NSN 7540-01-280-5500

Standard Form 298 (Rev. 2-89)
Prescribed by ANSI Std. Z39.18